THE UNIVERSITY *of* EDINBURGH

Indirect structural health monitoring:

estimation and variation of dynamic vehicle-bridge interaction parameters

Richard May

Doctor of Philosophy

The University of Edinburgh
2024

“When information is cheap, attention becomes expensive.”

(James Gleick [1])

Declaration

I declare that this thesis is an original report of my research, has been written by me and has not been submitted (in whole or in part) for any previous degree or professional qualification. The experimental work is almost entirely my own; the collaborative contributions have been indicated clearly and acknowledged. Due references have been provided on all supporting literature and resources. Where aspects of the presented work have been included in collaborative publications, this has been indicated in the text.

Hazel Taylor operated the full-scale test vehicle described in chapter 4. Brackets for fitting accelerometers to the unsprung mass location were fabricated and installed by Mr Stephen James Glover, Mr Andrew Brown and Mr Calum Melrose.

Python code for implementation of the matrix pencil method and visualisation of mode shapes (chapters 4 and 7) was adapted from working examples provided by Dr Zachariah Wynne.

Access to the laboratory-scale bridge and vehicle models and additional accelerometer sensors described in chapter 7 was provided by Professor Abdollah Malekjafarian and Dr Robert Corbally. Dr Corbally also provided input towards the design and specification of the experimental regime, provided the pro forma for recording traversal data and the method of identifying when the traversal began and ended from the acceleration response data, and operated the model vehicle during traversals.

Some prior literature by others was particularly informative. I have endeavoured to clearly highlight where aspects such as methods, interpretations, and assembled groups of citations have been reproduced from prior literature.

(Richard May)

Funding statement

This work was supported by the Engineering and Physical Sciences Research Council [grant number EP/R513209/1].

Contribution to project costs from the Moray Endowment Fund at The University of Edinburgh is gratefully acknowledged.

Abstract

Bridge damage detection by indirect structural health monitoring (SHM) using vehicle-mounted accelerometers relies on vehicle-bridge interaction (VBI) in which the vehicle and bridge form a coupled dynamic system. Changes in bridge frequencies have been proposed as damage indicators. Acceleration amplitudes in frequency sub-bands are correlated with bridge operational mode shapes, changes in which can be indicative of damage location. However, treating the vehicle as combined exciter and sensor carrier introduces confounding, since even the presence of non-moving vehicles changes the effective bridge modal parameters in relation to vehicle-to-bridge mass and natural frequency ratios. Additionally, when natural frequency ratios are close to unity, vehicle movement along the bridge induces non-stationarity for the combined VBI system frequencies, a phenomenon only recently identified and little studied to date. Finally, vehicle kinematics form a filter through which the bridge response is viewed. These confounding effects can reduce or prevent visibility of bridge damage by changing observed frequencies and the associated acceleration amplitudes. The confounding is additional to the challenges inherent to direct SHM: particularly environmental and operational variation (EOV) which can mask the visibility of bridge damage or lead to spurious identification of damage where none exists, and limited availability of baseline data representing the healthy bridge condition. Indirect SHM is often suggested as a way to address the economic and practical challenge of monitoring a large number of bridges simultaneously. This thesis argues that the challenges and confounders mean that it is not yet clear how and where indirect SHM can add value. For indirect SHM to reach a state of operational readiness, greater understanding of the effects of vehicle parameters and vehicle-to-bridge parameter ratios on VBI system dynamics is required.

This study first explores vehicle parameter estimation, leveraging output-only methods to fit a representative reduced-order model reflecting current vehicle condition, configuration, and sensor location. Numerical simulation is used to demonstrate the approach, comparing time- and frequency-domain methods for model fitting in response to synthesised road profiles. Bias due to road profile variation and spectral flatness is considered. Measurements of the wheel hop frequency are presented based on responses to operational driving, alongside estimates of cabin bounce frequency using traditional accelerometers and the application of a smartphone device for the same purpose. Variation in estimated

parameters is considered and compared to a second phase of fieldwork featuring a different vehicle suspension condition and configuration. Recommendations are given for future estimation campaigns including vehicle model abstractions, data processing strategies and vehicle speed and road profile roughness class consistency.

Practically, labelled data representing damaged bridge conditions are rarely available and baseline bridge modal parameters may be unknown. In response, this study explores visibility and accuracy of bridge frequencies through prominent peak identification (PPI) assuming limited knowledge of bridge properties. The effects of the (practically immeasurable) vehicle mass ratio, vehicle-to-bridge frequency ratio, vehicle speed and sensor position are explored in a parametric study using finite element simulation. VBI-induced frequency non-stationarity is noted as a confounder and is further explored in the hybrid time-frequency domain, including the first known presentation of such effects for two degree-of-freedom quarter car models. In the presence of vehicle-to-bridge frequency matching, a robust damage identification method would be of great value. The potential for one-class classification (OCC) in latent space after dimensionality reduction of hybrid time-frequency domain inputs is investigated, showing promising results and appearing to facilitate damage identification as well as differentiating between damage locations and intensities.

The study concludes with a laboratory-scale test of the proposed OCC method. Vehicle and bridge system identification by time-domain impulse response curve fitting is complemented by frequency-domain exploration of the vehicle acceleration response in a manner reflecting the earlier field-scale experiments. The potential confounding effects of tyre out-of-roundness or mass asymmetry are discussed. A novel simplified expression is proposed for recovering an estimate of the contact point (CP) response (the acceleration of the bridge deck at the temporally varying vehicle-bridge interface) and the accuracy of such estimates is discussed in relation to vehicle-to-bridge parameter ratios. It is demonstrated that this simplified expression produces comparable outcomes to the existing formulation while reducing the requirement for knowledge of vehicle parameters, while in unfavourable conditions neither approach performs adequately. Investigations of the vehicle response show that despite best efforts, bridge frequencies are not clearly and consistently visible. The initial vehicle-to-bridge acceleration amplitude ratio is found to be unsuited to bridge frequency visibility using indirect SHM, suggesting that prior positive results using this physical model may have managed to suppress vehicle-related acceleration amplitudes in a manner not achieved here. The importance of controlling such behaviour is thus highlighted and recommendations are made for future laboratory-scale experiments relating to VBI phenomena. Despite this, approximate frequency matching between the vehicle axle hop and bridge second bending modes allows one damage condition (simulated by the addition of static mass at bridge quarter-span) to be detected based on changes to VBI-induced time-frequency behaviour of the vehicle. Data derived from traversals of different bridge configurations are compared and the statistical significance of damage detection is confirmed, thus validating the proposed method.

Lay summary

Bridges are a critical part of our infrastructure; we rely on them for the movement of people and freight. The economic cost of bridge closure is significant. However, all materials and structures are subject to damage and degradation. The traditional approach to maintaining the integrity and serviceability of bridges relies on scheduled inspections to check condition and look for defects. Such inspection regimes are a well-established and integral part of bridge operation and maintenance practices. However, some question whether cost and time savings, as well as increased objectivity, could be achieved through a regime of constant data gathering from sensors in a paradigm known as structural health monitoring (SHM).

Research into SHM has been underway for several decades. Emerging from prior efforts to detect damage in rotating machinery such as turbines or gearboxes, one of the main methods for damage detection in bridge structures is based on vibration. Through inspection of the frequencies and amplitudes of vibration, anomalous behaviour is used as an indicator of damage. Presently, there are examples of sensor networks installed on a number of bridges worldwide; typically these are long-span landmark structures. The cost of installing and maintaining a sensor network is significant, but for these bridges it is deemed acceptable.

Not all bridges are landmarks. In fact, the majority of bridges worldwide are short- or medium-span structures of less obvious interest. Nevertheless, they also represent critical links in our global infrastructure networks, but installing permanent sensors on them all is generally seen as impractical. In recent years a possible alternative way forward has emerged based on the vibration of vehicles as they pass over such bridges. During a traversal the vehicle dynamic response is influenced by the motion of the bridge. This *indirect* approach to SHM assumes that vibrations inside the vehicle can be used as the source of bridge monitoring data in order to detect damage.

Direct SHM (in which sensors are fixed directly to the bridge) is subject to challenges, some of which are significant. Perhaps the most important is that changes in the conditions in which the bridge operates – known as environmental and operational variation (EOV) – can mask the visibility of damage in the sensor data, or lead to spurious indications of damage where none exists in reality. Addressing this is non-trivial and while general frameworks for doing so have emerged, their application tends to be unique for each bridge. This is because

bridges are usually bespoke structures. In such cases it is difficult to generalise regarding how damage would manifest in the monitoring data. A period of monitoring of the healthy structure is necessary to establish a baseline for normal behaviour, and it remains challenging to determine whether deviations from this baseline represent damage or changes due to EOV.

The indirect method is subject to the same issues. The use of vehicles as sensor carriers in fact introduces further challenges, relating mainly to the vehicle's own properties (which may not be known); the interaction of the vehicle with the rough surface of the road (which generates vibrations that further mask the visibility of bridge damage); and aspects of the interaction of the vehicle and bridge leading to apparent changes in the bridge properties (further confounding the visibility of damage). As the indirect approach is still relatively new, these challenges have not yet been fully explored. Instead, the most promising outcomes from field tests rely on exerting control by using specially-made vehicles; having the vehicles move slowly (or remain stationary while recording data); and in some cases combining the vehicle sensor data with responses from other sensors directly attached to the bridge. These mitigation efforts highlight that the indirect vehicle-based approach to SHM still faces significant challenges if it is to realise its potential as a low-cost, continuous monitoring method suitable for use without interruption to normal bridge operations. This thesis addresses several of these challenges, arguing that without solving these issues the indirect approach is holistically outperformed by direct monitoring. The exploration seeks to support ongoing efforts to determine how and where novel bridge monitoring techniques can add value – not just for bridge owners and operators, but for society at large.

Acknowledgements

This thesis represents a substantial period of my life. Although it was an individual pursuit, it would not exist in its current form without the generosity, patience, and skill of many other people. Too many helped for them all to be named here, but some should be given particular credit.

I am delighted to acknowledge the support of my supervisory team. Dr Hwa Kian Chai, Professor Yong Lu and Dr Thomas Reynolds provided guidance and critique, shared ideas, listened and explained throughout. It was a pleasure to work with them all. Thanks are also due to other academics. I would particularly like to thank Dr Robert Corbally and Professor Abdollah Malekjafarian at University College Dublin for their enthusiastic and generous assistance with laboratory-scale testing. Back at the University of Edinburgh, I felt supported by the whole community. Special thanks are due to Dr David García Cava for his advice and mentoring at a time when I was struggling. I acknowledge the mentoring of Dr Marcelo Dias in helping me to navigate the academic world. I am also grateful to the examining committee: Dr David García Cava and Associate Professor Maria Gabriella Mulas were generous and thorough. Their feedback was valuable and the manuscript is improved as a result.

In the course of this project it was a pleasure to share the research journey with others alongside. Thanks for the discussion, solidarity and support to Zach Wynne, Donghui Xu, Konstantin Popov, Haochen Zhang, Pritam Das, Alicja Pace, Nikolas Ringas, Stuart Logan, Joshua Collins and others too numerous to mention. Outside of research I am grateful to the community of cyclists in Edinburgh for friendship and distraction, whether riding, building or modifying bikes. Thank you in particular to Matthew Hawkins, Stuart Allan, Graeme Cottingham, Tom McCormick, Andrew Armour and all the Outliers.

Before and during this project I was grateful for the support of others who knew from their own experience what the journey might entail. I am grateful for the mentoring provided Jake Lever, Chantal Mustoe, Kieren Egan and Thomas Nickson.

My parents, Mary and Dave, raised me to be inquisitive and supported my interests in all things technical and practical. I have no doubt that my up-

bringing was formative in my development as an engineer. They continue to be a source of wisdom and support to this day. My brother and sister, Leo and Hannah, have shared their experiences – academic, professional and otherwise – and been generous with their time. It has been a privilege to pursue graduate-level study alongside them. My parents-in-law have always welcomed me to their home and encouraged me during my journey through this project. Visiting Helen and Steve in Etal has provided a much-needed change of scenery on many occasions.

Most important is to acknowledge the contribution of my wife, Hazel. Her patience, love and support cannot be captured in words. She also provided practical assistance with fieldwork, operating the test vehicle. Finally, I acknowledge the companionship of our late cat, Clement, who passed shortly before the end of the project. Having her in our family was a source of great joy and comfort.

Richard May
East Linton, October 2024

Publications

1. May, Richard. **Indirect Structural Health Monitoring of bridges using mobile sensor data**. In Proceedings of the 23rd Young Researchers Conference (pp. 37-38). The Institution of Structural Engineers, London, 2021.

   Awarded second prize for presentation at The Institution of Structural Engineers 23rd Young Researchers Conference (2021).

2. May, Richard. **Effects of Operational Traffic Variability on iSHM.** In European Workshop on Structural Health Monitoring, pp. 700-710. Cham: Springer International Publishing, 2022.

3. May, Richard, Thomas Reynolds, Hwa Kian Chai, Robert Corbally, Abdollah Malekjafarian, and Yong Lu. **Effects of Added Mass on Indirect Structural Health Monitoring of Bridges.** In International Conference on Experimental Vibration Analysis for Civil Engineering Structures, pp. 225-235. Cham: Springer Nature Switzerland, 2023.

4. May, Richard, Hwa Kian Chai, Thomas Reynolds, and Yong Lu. **Exploring the Use of Bicycles as Exciters and Sensor Carriers for Indirect Bridge Modal Parameter Estimation.** In International Conference on Experimental Vibration Analysis for Civil Engineering Structures, pp. 254-263. Cham: Springer Nature Switzerland, 2023.

   This paper was invited for publication in ***Journal of Civil Structural Health Monitoring*** *as one of the top 15 papers presented at 10th International Conference on Experimental Vibration Analysis for Civil Engineering Structures.*

5. May, Richard, Hwa Kian Chai, Thomas Reynolds, and Yong Lu. **Field investigation of bicycles for indirect Structural Health Monitoring.** Journal of Civil Structural Health Monitoring. Springer. *Manuscript in review.*

Contents

List of Figures

List of Tables

Abbreviations

Abbreviations used in this thesis are typically defined at their first point of use in the text and listed below in alphabetical order. They are subsequently redefined where deemed helpful to assist the reader.

2DoF	Two degree-of-freedom
ANN	Artificial neural network
CM	Condition monitoring
CNN	Convolutional neural network
CP	Contact point
CPR	Contact point residual
CWT	Continuous wavelet transform
DoF	Degree-of-freedom
DSF	Damage-sensitive feature
EMD	Empirical mode decomposition
EOV	Environmental and operational variation
FE	Finite element
FFT	Fast Fourier transform
FRF	Frequency response function
GMM	Gaussian mixture model
GPS	Global positioning system
IF	Instantaneous frequency
iSHM	Indirect structural health monitoring

ISO	International Organisation for Standardisation
KDE	Kernel density estimation
MAC	Modal assurance criterion
MFCC	Mel-frequency cepstral coefficient
ML	Machine learning
MNIST	Modified National Institute of Standards and Technology
MPM	Matrix pencil method
OCC	One-class classification
ODS	Operational deflected shape
OMA	Operational modal analysis
PCA	Principal component analysis
PP	Peak-picking
PPI	Prominent peak identification
PSD	Power spectral density
RD	Random decrement
RDS	Random decrement signature
RMS	Root mean squared
RO	Research objective
SDoF	Single degree-of-freedom
SHM	Structural health monitoring
SPI	Sampling point interval
SSI	Stochastic subspace identification
ST	Stockwell transform
STFT	Short-time Fourier transform
SWEV	Single-wheeled experimental vehicle
TF	Time-frequency
UMTRI	University of Michigan Transportation Research Institute
VBI	Vehicle-bridge interaction
WD	1-Wasserstein distance
WT	Wavelet transform

Nomenclature

Generally in this thesis matrices are denoted as bold upper case characters and vectors as bold lower-case characters.

D	Damage metric (Euclidean distance from healthy condition in reduced-dimension latent space)
$D(\tau)$	Random decrement signature
$D_{XX}(\tau)$	Auto random decrement signature (same sensor as data and trigger channel)
$D_{XY}(\tau)$	Cross random decrement signature (different sensors as data and trigger channels)
E	Young's modulus
EI	Bending stiffness (bridge modelled as Euler-Bernoulli beam)
F	Force
$G_{Ex}(f)$	Excitation power spectral density as a function of frequency
$G_{Re}(f)$	Vehicle response power spectral density as a function of frequency
$G_d(n)$	ISO 8608: road profile displacement power spectral density as a function of spatial frequency
$G_d(n_0)$	ISO 8608: road profile displacement power spectral density at reference frequency
I	Bridge cross-section second moment of area
$K(x;h)$	Gaussian kernel function, evaluated at location x using bandwidth h
L	Bridge span length
N_{sample}	Number of data points in sample of discrete signal
$PC_{i,d}$	Principal component i for damaged input

$PC_{i,h}$ Principal component i for healthy input

Q Half-power bandwidth method: signal power associated with peak centred on reference frequency ω_r

R^2 Coefficient of determination

R_b Frequency amplification ratio for bridge during coupled VBI (single-mode approximation from Yang et al. [9])

$S(\tau, f)$ Stockwell transform

T^2 Vehicle transmissibility FRF squared

$Tx(t_i)$ Tigger condition for random decrement signature calculation: see equation 2.20

$W_1(u, v)$ 1-Wasserstein distance between one-dimensional probability mass functions u and v

$\Delta\omega_r$ Half-power bandwidth method: frequency bandwidth (see Fig. 2.8.5)

$\mathbf{\Lambda}$ Diagonal matrix of eigenvalues of covariance matrix $\mathbf{\Sigma}$

Ω ISO 8608: spectral exponent

$\mathbf{\Sigma}$ Covariance matrix

α Quarter-car model: ratio of natural frequency of sprung to unsprung mass modes, from Jazar [6] (see Fig. 2.4.4)

β Ratio of vehicle-to-bridge non-interacting natural frequencies (single-mode approximation from Chang et al. [22])

$\boldsymbol{u}_{CP,K}$ Contact point response for axle K

$\boldsymbol{u}_{CP,res.}$ Residual contact point response between two axles

δ_t Simulation timestep

δ_f Effective frequency resolution

ϵ Quarter-car model: ratio of masses (upper to lower degree of freedom)

μ Mean

μ Vehicle-to-bridge mass ratio

$\boldsymbol{\omega}$ Vector of natural frequencies

ω Circular frequency [rad/s]

ω_b Bridge modal frequency during coupled VBI (single-mode approximation)

ω_i	Natural frequency for mode i
ω_i	Natural frequency for mode i
ω_r	Half-power bandwidth method: *reference frequency* at centre of spectral peak
ω_s	Quarter-car model: natural frequency of sprung mass mode, from Jazar [6] (see Fig. 2.4.4)
ω_u	Quarter-car model: natural frequency of unsprung mass mode, from Jazar [6] (see Fig. 2.4.4)
ω_v	Vehicle modal frequency during coupled VBI (single-mode approximation)
ω_{b0}	Bridge natural modal frequency when not interacting with vehicle (single-mode approximation)
$\omega_{d,i}$	Damped frequency for mode i
ω_d	Spectral peak frequency from response of damped system
ω_{v0}	Vehicle natural modal frequency when not interacting with bridge (single-mode approximation)
$\rho_K(y)$	Kernel density estimate at location y
σ	Standard deviation
ξ	Quarter-car model: approximation of damping ratio for sprung mass mode, from Jazar [6] (see Fig. 2.4.4)
ξ_i	Modal damping coefficient for mode i
ζ	Half-power bandwidth method: estimated modal damping ratio
ζ_i	Modal damping ratio for mode i
ζ_{bi}	Bridge modal damping ratio for mode i
b	Bridge cross-section breadth
c	Viscous damper coefficient
c_i	Viscous damping coefficient associated with degree of freedom i
c_s	Vehicle suspension viscous damping coefficient
d	Bridge cross-section depth
d_i	ISO 8608: amplitude associated with spatial frequency n_i
f_s	Sampling frequency

$f_{CoI,ST}$ Stockwell transform cone of influence (in terms of frequency)

f_{bi} Bridge natural frequency (non-interacting) for mode i

f_n Natural frequency for beam mode n [Hz]

$f_{sim.}$ Simulation frequency

f_{vi} Vehicle natural frequency (non-interacting) for mode i

g Gravitational acceleration constant

j Square root of -1

k Spring stiffness

k_i Spring stiffness associated with degree of freedom i

k_s Vehicle suspension spring stiffness

k_t Effective vehicle tyre stiffness

l_v Vehicle axle spacing

l_{el} Element length in finite element model

m Mass

m_b Bridge mass

m_i Mass at degree of freedom i

m_v Vehicle mass

m_{vi} Vehicle mass at degree of freedom i

n ISO 8608: spatial frequency

n_0 ISO 8608: reference spatial frequency

$r(x)$ ISO 8608: road profile

s_{ST} Scale of Stockwell transform

$t_{CoI,Morlet}$ Cone of influence (in terms of time) for the Morlet mother wavelet

$t_{CoI,ST}$ Stockwell transform cone of influence (in terms of time)

t_{SPI} Sampling point interval

u Effective displacement input at tyre-road contact point due to road surface profile and/or bridge deck vertical motion

v Velocity

x_c Vehicle horizontal position (distance along bridge span)

z_i Relative displacement at degree of freedom i

z_s Relative displacement at sprung mass degree of freedom relative to displacement at contact point

z_u Relative displacement at unsprung mass degree of freedom relative to displacement at contact point

$\boldsymbol{C}$ Damping matrix

$\boldsymbol{f}$ Vector of contact forces, or vehicle and bridge according to subscripts v and b respectively

$\hat{f}_b$ Estimated bridge modal frequency

$\boldsymbol{K}$ Stiffness matrix

$L(d, \rho)$ Objective function for fitting finite element model of bridge by varying modelled beam depth d and material density ρ

$\boldsymbol{M}$ Mass matrix

$\hat{\boldsymbol{Q}}$ Matrix of mass-normalised mode shape vectors

$\hat{\boldsymbol{q}}_i$ Mass-normalised mode shape vector for mode i

$\boldsymbol{q}_i$ Mode shape vector for mode i

$\ddot{u}$ Effective acceleration input at tyre-road contact point due to road surface profile and/or bridge deck vertical motion

$\ddot{u}_i$ Effective acceleration input at tyre-road contact point due to road surface profile and/or bridge deck vertical motion

$\boldsymbol{W}$ Matrix of eigenvectors of covariance matrix $\boldsymbol{\Sigma}$

$\boldsymbol{W}_L$ Subset of matrix of eigenvectors of covariance matrix $\boldsymbol{\Sigma}$

$\boldsymbol{X}$ Data matrix to be used for dimensionality reduction by principal component analysis

$\boldsymbol{y}$ Vector of displacements and rotations, for vehicle and bridge according to subscripts v and b respectively

$\ddot{y}_i$ Acceleration response at vehicle degree of freedom i

$\dot{y}_i$ Velocity response at vehicle degree of freedom i

y_i Displacement response at vehicle degree of freedom i

$\ddot{z}_i$ Relative acceleration at degree of freedom i

$\dot{z}_i$ Relative velocity at degree of freedom i

Chapter 1

Introduction

Civil structures are fundamentally required to maintain their integrity in use. To perform as required all structures require some degree of repair and maintenance, which will inevitably have an associated cost. Moreover, existing structures contain significant quantities of embodied carbon and thus there is an environmental and economic imperative to facilitating their continued effective service. Many structures exist that have exceeded, or will soon exceed their intended design life. It has been recognised that effective ways of tracking the condition and health of these structures would be valuable (Lynch [23]).

Reliance has traditionally been placed on manual inspection of civil structures (Brownjohn and Aktan [24], Malejafarian et al. [25]), supplemented by localised non-destructive evaluation or physical testing when deemed necessary. This framework is perceived as time-consuming, undertaken only in response to specific concerns, observed defects, or on a scheduled basis. The literature also reveals that some are concerned that the traditional inspection regimes are subjective (Moughty and Casas [26]), labour-intensive (Lynch [23]) and that some defects may not be identified (An et al. [27]). It has been suggested that there are so many existing bridges that manual inspection is impractical (Moughty and Casas [26]). It is perceived that if data could be gathered regarding the health of a structure – using embedded or retrospectively-installed instrumentation, or survey techniques using external sensors – and if this data could be processed in a suitable manner, the process of monitoring structural health could potentially be automated to some degree. These new methods of monitoring and appraising existing structures are anticipated to enable intelligently targeted and programmed proactive maintenance, reducing the risk of failure and extending service life (Figueiredo and Brownjohn [28]).

Structural health monitoring (SHM) is concerned with gathering data from a structure in order to detect damage. Such a monitoring system is anticipated to offer benefits in terms of safety and cost (Farrar and Worden [29]) in addition to reducing the risk of failure and extending serviceable life of structures (Figueiredo and Brownjohn [28]). Vibration-based SHM gathers data regarding bridge motion and seeks to identify changes in signal features — modal or

abstract — as indicators of bridge damage. Two paradigms exist for vibration-based SHM, distinguished by the location of the sensors. The first is *direct* monitoring, where the sensors are fixed directly to the subject bridge. It is confounded to some degree by various factors, perhaps most significant of which is environmental and operational variation: a broad class of phenomena that can mask the visibility of damage or cause false positives in damage detection (Farrar et al. [30]). Mitigation techniques include achieving adequate signal-to-noise ratios and collecting baseline data representing the normal reaction of the bridge over that period, such as its response to changes in temperature and traffic flow. Since bridges are typically bespoke (Rytter [31], Brownjohn [32]), this implies a requirement to acquire such baseline data for each bridge individually. Consequently, some feel that direct SHM will be hampered by the cost and time requirements of sensor installation and maintenance. Certainly the field implementations of SHM systems tend to be limited to long-span landmark bridge structures. A further challenge is that acquiring reliable examples (*labelled data*) representing bridge damage is difficult at field scale (Worden et al. [33], Rizzo and Enshaeian [34]). It is therefore a challenge to know how the response of a damaged bridge will manifest, in addition to whether the damage-related aspects of the data will be visible or unique.

Within the last 20 years, interest has developed in the second paradigm, *indirect* SHM, using vehicles as combined exciters and sensor carriers. Predicated on the bridge and vehicle forming a combined dynamic system during a vehicle traversal, it is anticipated that the vibration response of the passing vehicle can be used to highlight the health status of the bridge. Proponents highlight benefits including anticipation of reduced costs (Malekjafarian et al. [25]), continuous monitoring (Gkoumas et al. [35]) across transport networks (Locke et al. [36]), and the method's potential in relation to monitoring the large numbers of short- and medium-span bridges that exist worldwide and do not current have any installed monitoring equipment (Miyamoto et al. [37], Li et al. [38]). Indirect vehicle-based SHM is appealing, but in addition to the challenges facing the direct method, it introduces further barriers. Since the sensors are vehicle-mounted, the bridge response is viewed through a filter comprised of the vehicle's kinematics. Vehicle movement means that all points along a bridge span are explored, but the collected data are invariably spatially or temporally sparse (Sadeghi Eshkevari et al. [39]) since a vehicle can only be in one place at one time. Road surface profiles are also a challenge (Malekjafarian et al. [25] [40], Yang and Yang [41]), since they introduce vibrations leading to additional signal pollution. This is exacerbated by faster vehicle speed, which also reduces the data acquisition time, bringing further difficulties. The role of vehicles as combined exciters and sensor carriers means that the method of monitoring affects the subject of monitoring, leading to phenomena including apparent bridge frequency variation when non-interacting bridge and vehicle natural frequencies are proximal (Yang et al. [9], Chang et al. [22], Cantero et al. [11] [42]).

The additional challenges introduced by indirect vehicle-based bridge SHM have led to the current situation. Some researchers pursue the use of citizen or municipal vehicles in an approach known as *crowdsourcing* (Matarazzo and

Kondor et al. [43], Mei et al. [44]). This offers the potential for near-continuous data acquisition worldwide. However, in this paradigm the challenges associated with the unknown vehicle kinematics are particularly troublesome. Additionally, sensor placement is potentially uncontrolled, leading to further variation of the vehicles' effective filters. Vehicle-to-bridge natural frequency proximity is also likely in the crowdsourcing approach. The most promising outcomes from field-scale tests have been based on the use of bespoke sensor-carrying trailers whose design aims to avoid frequency matching with the bridge (Yang et al. [45]). Additionally, measures such as very slow traversal speed (or stationary sensing vehicles) and fusion of direct and indirect sensor data have often proven necessary to achieve visibility of the higher bridge modes expected to be most helpful for damage detection and localisation, and to avoid confounding due to background traffic effects. Further, many demonstrations of the indirect method appear to rely on prior knowledge of bridge properties (for example to allow disambiguation between vehicle and bridge frequencies, or to enable a band-pass filtering approach to isolate bridge-related aspects of the signal) as well as an understanding of how they vary in relation to environmental and operational changes. The approach therefore retains an implicit requirement for intermittent direct monitoring to establish and update a baseline.

Practicing engineers must find an appropriate balance between cost and time while maintaining quality. Contemporary sensor technologies promise vastly more data than was previously available; as the epigraph quote from Gleick [1] suggests, an ongoing challenge for engineers is to leverage this data — to transform it into useful information — in an efficient manner. More data does not in and of itself imply more insight. The vehicle-based indirect bridge SHM paradigm appears to offer potential benefits: continuous data gathering, at low acquisition cost for bridge owners and operators, without interruption to normal bridge usage. This thesis argues that for these benefits to be realised it is necessary to overcome significant barriers. The thesis addresses some of these barriers through a combination of numerical simulation, fieldwork and laboratory-scale testing. Specifically the thesis presents a systematic investigation of the viability of indirect bridge SHM by moving vehicle, considering the expected challenges caused by normal operational conditions. The work pursues estimation of unknown vehicle properties; visibility of bridge frequencies and sensitivity to bridge damage in relation to vehicle and bridge interaction parameters and sensor location on the vehicle; and development of a damage detection method robust to vehicle-to-bridge frequency proximity and avoiding the requirement for labelled examples representing bridge damage.

Chapter 2

Literature review and background

2.1 Structure of chapter

This literature review begins in section 2.2 by establishing the context and motivation for damage detection by casting bridges as critical infrastructure. In section 2.3 the established principles of structural health monitoring (SHM) are then introduced, with a specific focus on vibration-based damage detection. A class of significant confounders known as *environmental and operational variation* (EOV) are introduced and techniques for their mitigation are outlined. The current state of adoption of vibration-based bridge SHM damage detection is summarised along with recent research trends intended to assist in bringing the field closer to a state of operational readiness, one of which is the *vehicle-based indirect SHM* approach. The interaction between vehicle and bridge during a traversal is fundamental to this method, and modelling this interaction relies on understanding representative vehicle kinematics and dynamic characteristics. Section 2.4 summarises the ways in which abstract reduced degree-of-freedom models are used in the automotive and bridge engineering fields and how such models can be characterised and their parameters estimated. The coupled dynamic interaction between vehicle and bridge is what allows the detection of bridge properties from vehicle-mounted sensors. Section 2.5 reviews the ways in which this vehicle-bridge interaction is abstracted and modelled. Section 2.6 presents a detailed study of the efforts in recent years to develop the vehicle-based indirect method for bridge damage detection. Theoretical, numerical, laboratory-scale and field-scale studies are reviewed, including attempts to extract estimates of bridge modal properties based on modal and abstract data-driven damage sensitive signal features. Section 2.7 offers a summary and critical review of research gaps in relation to the indirect vehicle-based method, some of which are addressed in this thesis. Finally, section 2.8 summarises the established tools and techniques used within this thesis.

This thesis relates to a number of technical fields, for which the literature – when considered together – is substantial. However, to the best of the author's knowledge the summary and critique presented here is a unique assimilation of the existing literature relating to indirect bridge health monitoring using vehicle-mounted sensors, with consideration of both the wider context and specific relevant details. Throughout the review, effort has been made to highlight any cases in which material such as summaries, interpretations, or collections of associated literature have been adopted or reproduced from prior works by others.

2.2 Bridges as critical infrastructure

Bridges provide ways to traverse obstacles, allowing the movement of people and goods. There are vast numbers of bridges in service worldwide and their closure leads to significant economic impact and societal disruption (Argyroudis et al. [46]). As key components of transport networks, bridge operation must be maintained for transport networks to function in a resilient manner. For example, Brownjohn and Aktan highlight the closures of the Hammersmith Flyover and the M4 Boston Manor Viaduct, in the United Kingdom in 2011 and 2012 respectively, describing the collateral economic and social impact as "incalculable" [24]. More recently, the Queensferry Crossing bridge near Edinburgh, Scotland was closed for 41 hours in February 2020 due to ice and snow accretion on the stay cables. The total economic cost of the closure was estimated in the region of £3.67 Million per day (Smith et al. [47]). Bridges form part of the infrastructure deemed critical to the continuity of day-to-day life:

> **"Critical infrastructure includes the vast network of highways, connecting bridges and tunnels, railways, utilities and buildings necessary to maintain normalcy in daily life. Transportation, commerce, clean water and electricity all rely on these vital systems."** (United States Department of Homeland Security [48])

Bridge design can be "particularly sensitive to environmental actions" (Denton et al. [49]). As climate change progresses, weather events become more severe and more frequent (Stern et al. [50]), suggesting that bridges are susceptible to increasing risk of damage or failure as time passes. Moreover, all materials contain defects (Farrar and Worden [29]) and thus all structures, including bridges, contain defects. Many bridges have been in service for a significant period of time - for example, in the USA 42% of bridges were over 50 years old as of 2021 (American Society of Civil Engineers [51]) and 39% in Japan as of 2023 (estimated in 2019: Japan Ministry of Land, Infrastructure, Transport and Tourism [52]). Although a long duration of service does not itself directly imply that these bridges are in poor condition, material defects accrue over time and can eventually develop to cause an issue at structural system level (Farrar and Worden [29]). Additionally, for highway bridges the imposed traffic load increases over time with greater numbers of vehicles in service, for example as evidenced by increases to recommended design imposed loads in North America (O'Brien et al. [53]), and an approximate doubling of heavy freight traffic in Germany over the two decades leading up to 2016 (Novák [54]). This combination of existing critical infrastructure with some degree of existing defects, subject to increasing load and environmental actions, suggests that bridge condition generally could potentially be declining.

Historically, the dominant paradigm has been to inspect bridges to determine their condition on a scheduled basis. Inspections are traditionally visual (Brownjohn and Aktan [24], Manarin et al. [55], Malekjafarian et al. [25],

Turksezer et al. [56]), supported by targeted special investigation (such as non-destructive evaluation) in response to observed or suspected issues. Specific requirements vary according to region (Turksezer et al. [56]) and are defined by national bodies (for example *CS 450: Inspection of highway structures* in the United Kingdom [57]). It is believed that some defects may not be apparent under such inspection regimes (An et al. [27]). Since inspections are periodic, other defects may first manifest between inspections, thus existing for some time without being noticed. Additionally, visual inspections are considered to be subjective (Moughty and Casas [26]) and labour-intensive (Lynch [23]). In response, for several decades researchers have pursued the idea of SHM which is anticipated to become increasingly widely used to pursue financial and safety benefits (An et al. [27]) as part of a continuous (Brownjohn [32]) condition and performance monitoring strategy as well as assisting in validation of design predictions of bridge response to load (Rizzo and Enshaeian [58]).

2.3 Structural Health Monitoring

2.3.1 Background

SHM is a general area of academic interest, spanning multiple fields and finding relevance wherever there are structures. Although systematic attempts to gather monitoring data from structures date back to at least the 1930s (Carder [59] from Brownjohn [32]), Brownjohn notes [32] that the term SHM emerged in the literature in the late 1980s (Boller [60]). In the civil engineering field, vibration based damage detection has been a subject of research interest since the early 1980s (Farrar and Worden [29]). SHM as it is understood today emerged from Condition Monitoring (CM) which was applied to rotating machinery and was mostly non model-based (Farrar and Worden [29]). Instead, it relied on establishing baseline behaviour to which observed behaviour could be compared. This was facilitated by large numbers of nominally-identical units concurrently experiencing similar operational conditions. In contrast, civil structures are usually bespoke (Rytter [31], Brownjohn [32]) and thus establishing baseline expected behaviour in the manner of CM is not so feasible. This typically leads to the pursuit of targeted and unique approaches to the implementation of SHM for each bridge structure, since – as Rizzo and Enshaeian conclude – "it is difficult to design a uniform SHM paradigm valid for any bridge" [58].

SHM data and sensors can take many forms, including for example data from accelerometers, strain gauges, and fibre optic sensors (Sony et al. [61]). A recently-constructed example is the Queensferry Crossing bridge near Edinburgh, Scotland which is fitted with a wide range of sensors including anemometers, barometers, rainfall gauges, temperature sensors, tilt meters, accelerometers, static and dynamic strain gauges, global positioning system (GPS) receivers, corrosion sensors and dynamic weigh-in-motion sensors (Riches et al. [62]). However, vibration-based monitoring has become one of the major paradigms for direct SHM of bridge structures and is fundamental to the indirect vehicle-based SHM method discussed later in this chapter. GPS receivers can be used for vibration monitoring, but only for very flexible structures with low frequencies due to the low effective spatial resolution (Ou and Li [63]). The use of laser vibrometers is possible but expensive (Sony et al. [61]). More practical due to the relatively high resolution and lower cost is the use of accelerometers for this purpose. For the current review, mainly vibration-based monitoring will be considered, with some reference made to other sensor types in relation to changing environmental and operational conditions.

A very large amount of literature exists in relation to SHM (Farrar and Worden [29]), especially considering its applicability to multiple structures and contexts, not just to bridges and civil infrastructure. Selected relevant information will be discussed in this review in order to establish the context and challenges faced in relation to SHM for bridges.

2.3.2 Damage detection

Structural damage can be characterised as changes to the material properties, geometry, connectivity or boundary conditions of a structure sufficient to alter its performance (Farrar and Worden [29]). Farrar and Worden define SHM as "the process of implementing a damage identification strategy" [29] [64]. Rytter first proposed that damage detection could be considered as a four-stage process [31]: detection (whether damage exists); localisation (where the damage is located); assessment (the scale of the damage); and determination of consequences (what are the implications of the damage). These four stages, or closely-related interpretations, have been widely recognised since (for example Carden and Fanning [65] and Malekjafarian et al. [25]). In 2007, Worden et al. proposed what they called "fundamental axioms of structural health monitoring" [66] on the basis that SHM was by then a mature and established field. These axioms included universality of damage defects in all structural materials; the requirement to compare two states of a structure in order to detect damage; and the role of damage-sensitive features in enhancing damage sensitivity which is otherwise correlated with susceptibility to confounding by environmental and operational variation. Worden et al. noted that these axioms were proposed in order to establish common agreement upon which further research could be based [66].

The definition of structural damage noted above implies that modal parameters of the bridge will change due to the damage. Carden and Fanning report that most CM literature relates to the modal domain and suggest that this may be due to precedent, since much early work in the area was of this nature; and thanks to the ease of interpretation of modal frequencies and mode shapes [65]. Similarly for civil structures, Lynch states that the majority of damage detection is based on changes to global vibration characteristics [23]. More recently, Worden et al. state that two distinct approaches to vibration-based damage detection for bridges have emerged: model-based data-based SHM [67]. Model-based approaches are based to some degree on the physics assumed to represent the structure; in contrast, data-based approaches "make inferences about the structural state from measured and processed data from the structure without reference to any physics-based model" (Worden et al. [67]). However, the terminology could be questioned, as SHM using models necessarily also uses data, and data-based approaches could construct an abstract model using collected data. In this thesis, the two approaches are termed *model-based* and *non model-based*. For model-based SHM, once a representative model of the structure has been established, SHM data can be used to interrogate the model, with inconsistencies being potential indicators of damage. For smaller structures, traditional modal testing is a common way to establish a model. First emerging in the middle of the 20th century (Ewins [68]) it relies on imposing measured load conditions (such as impulsive, harmonic or broadband random) and recording the frequencies and associated amplitudes of response, thus establishing a frequency response function (FRF) which is an input-output relationship as a function of frequency (He and Fu [69]). By both applying loads and measuring

responses at multiple locations, a representative model of the structure can be established. However, traditional modal analysis is expensive and complicated for full-scale bridge structures due to their size and typically low frequency range (Rainieri and Fabbrocino [70]). Operational modal analysis (OMA) has emerged as an alternative approach in which operational conditions are used as the input loading, offering the additional benefit of avoiding interruptions to normal operation of the bridge (Hasani and Freddi [71]). For bridges, the load typically comes from factors such as wind or passing traffic (Rainieri and Fabbrocino [70]) and would ideally be *white noise* (broadband random with equal signal power across all frequencies). Since the white noise condition is not always achieved, OMA assumes that the identified structural system comprises the subject bridge combined with a filter which is assumed to take white noise loading as its input and pass to the structure the actual operational loading (Rainieri and Fabbrocino [70]). Since the input loading is not controlled, the estimated modal parameters are therefore subject to bias. A further drawback of OMA is that the amplitude of the imposed load is not controlled and may not be measurable, meaning that while relative response amplitudes can be compared when recorded simultaneously, mass-normalised operational mode shapes cannot be estimated, since they depend on the input excitation magnitude, although other approaches have been proposed such as normalising the mode shapes based on changes in associated modal parameters after the addition of mass to the bridge (Parloo et al. [72] [73]). Nevertheless, OMA is appealing for large structures such as bridges and has therefore increased in popularity in the civil engineering field (Rainieri and Fabbrocino [70]).

Model-based damage detection for bridges has generally been based on comparison of modal parameters. Fan and Qiao summarise four methods: natural frequency-based; mode shape-based; curvature/strain mode shape-based; and other modal parameter-based methods [74]. Moughty and Casas provide a more recent summary [26] which has informed the material presented below. They adopted similar categories for modal parameter-based damage detection, but notably added a discussion regarding modal damping-based methods. They report that the use of frequency changes as damage indicators dates back to at least the work by Cawley and Adams in the late 1970s [75]. Frequencies as damage indicators are appealing as they are relatively easy to measure (Fan and Qiao [74], Kim et al. [76]) however they do not directly indicate the location of damage: in general, relating a change in frequency to damage is an ill-conditioned problem, i.e. there is not a unique relationship between damage location and change in a single modal frequency (Casas and Aparicio [77]). Doebling et al. [78] highlight a further drawback: although frequencies change in relation to damage, typically higher levels of damage are required for the frequency changes to be used for the purpose of damage identification, particularly when the changes in the operational conditions of the bridge create a masking effect (discussed in more detail in section 2.3.3). Carden and Fanning report [65] that some researchers have pursued the use of simultaneous changes in multiple frequencies to mitigate ill-conditioning, citing for example Vestroni and Capecchi [79].

An alternative approach is to study mode shapes. The Modal assurance criterion (MAC) emerged in the early 1980s (Allemang and Brown [80] from Moughty and Casas [26]) and has proven to be a popular comparative tool for global mode shapes. However, global mode shapes associated with lower frequencies share the drawback of insensitivity to local damage (Kim et al. [76]). Moughty and Casas report [26] that the mode shape-based method was extended to include information about the location of discrepancies between the compared shapes by Kim et al. [81]. Studies of modal curvature, first proposed by Pandey et al. [82] (from Moughty and Casas [26]) have also aimed to identify both the existence and location of damage and in some cases have been reported to perform well (for example Wahab and De Roeck [83] from Moughty and Casas [26]). Exploration of methods based on modal strain energy (for example Kim et al. [76]) and modal flexibility (for example Toksoy and Aktan [84]) similarly address Rytter's [31] first and second stages of SHM (detection and localisation). While these methods are generally suited to bridge structures of any form, the use of modal damping as a damage indicator is more specific to the construction materials, aiming to exploit the sensitivity of damping to damage such as concrete reinforcement corrosion (Yamaguchi et al. [85] from Moughty and Casas [26]).

Relatively speaking, the non model-based SHM approach for bridges has emerged more recently. Figueiredo and Brownjohn report [28] that Farrar et al. used a pattern recognition framework to support bridge damage detection [86] as early as 1994, and that the rate of related publications has been growing as the 21st century progresses. Non model-based SHM typically applies a statistical approach to damage identification (Figueiredo and Brownjohn [28], Worden et al. [67]), with the basic idea that outliers represent damage (Figueiredo and Brownjohn [28]). Farrar et al. [87] established a four-stage process for non model-based SHM: operational evaluation; data acquisition and cleansing; feature selection; and statistical model development. This illustrates a fundamental difference between model-based and non model-based SHM. Both are motivated by the identification of damage and can be applied to Rytter's damage detection stages [31] or similar interpretations (for example Tibaduiza Burgos et al. [88]), but in the latter case features of recorded data do not *necessarily* have direct physical meaning. Non model-based SHM seeks to avoid subjectivity in model creation (Figueiredo and Brownjohn [28]) and counter the confounding effects of environmental and operational variation (Moughty and Casas [26]) which are discussed in more detail in section 2.3.3. It is "rooted in the machine learning field" (Figueiredo and Brownjohn [28]). A distinct advantage of the non model-based approach is that multiple types of data can be combined and patterns identified automatically (*unsupervised learning*). However, on the other hand large data volumes can make analysis computationally expensive (Tibaduiza Burgos et al. [88]), and automatically extracted relationships are mainly useful for detection and localisation of damage (Figueiredo and Brownjohn [28]). It is therefore common for *supervised* methods to be adopted for the latter stages of damage assessment and determination of consequences, in which some data from the healthy and damaged conditions are available to be used as training

examples (Figueiredo and Brownjohn [28]).

2.3.3 Environmental and Operational Variation

It has long recognised that environmental changes can prevent visibility of damage. In 1996 Farrar et al. presented a study [30] of the variation of the modal parameters conditions of the Alamosa Canyon bridge in New Mexico, United States in relation to environmental conditions and noted:

> **"A significant amount of work has been reported in technical literature regarding the use of changes in modal parameters to identify the location and extent of damage in structures. Curiously absent, and critically important to the practical implementation of this work, is an accurate characterization of the natural variability of these modal parameters caused by effects other than damage."** (Farrar et al. [30])

EOV has been identified as a confounder for damage detection for both the model-based and non model-based approaches. EOV can take multiple forms. It has been suggested that temperature variation is the "most problematic" (Moughty and Casas [26]) source of EOV. The primary concern is that changes in temperature could be mistaken for bridge damage, either by directly affecting the properties of the structural material of the bridge or by altering its boundary conditions. Other changes can cause similar confounding; for bridges one of the most significant other sources of EOV is traffic which can reduce the natural frequencies of a bridge due to the added mass effect; Sohn [89] summarises the general agreement that implications are more severe when the traffic-to-bridge mass ratio is larger (citing Kim et al. [90], De Roeck et al. [91] and Zhang et al. [92]). Bridge damping ratios have also been observed to change due to traffic (Zhang et al. [92] from Sohn [89]). The added mass effect can vary spatially and temporally, since traffic flow is recognised to be a complex phenomenon (Kerner et al. [93]). The effects of traffic may also be related to dynamic interaction between the vehicle and bridge (discussed further in section 2.5).

In general for SHM (not limited to bridge structures) García Cava et al. [94] explain that there are two main approaches to the mitigation of EOV in seeking damage sensitive features (DSF):

- Gather data on the source of EOV and explicitly model the relationship with the structure, for example by regression (Peters and De Roeck [95] and Worden et al. [96] from Sohn [89])
- Implicitly model the relationship when the source of EOV can't be directly measured (for example Sohn, Worden and Farrar [97] from Sohn [89]), or split the data into subsets within which EOV is minimal (for example Sohn and Farrar [98], and Sohn et al. [99] [100] all from Sohn [89]). Other implicit approaches are available; for example Cross et al. explore the

use of cointegration, outlier analysis and principal component analysis to identify such DSFs [101]

Much effort has been expended in recent years towards these approaches. The requirement to assimilate sufficient monitoring data to address EOV appears to be broadly recognised, however EOV mitigation is still a significant challenge: no single method appears to have been found to address all EOV in all situations, meaning that solutions are generally bespoke.

2.3.4 Current situation

In recent years, bridge SHM has continued to attract research interest. However, there is still a lack of operational demonstrations of the value of SHM (Brownjohn and Aktan [24], Figueiredo and Brownjohn [28]). As Brownjohn et al. note:

> **"The few recent public domain publications on UK bridge monitoring... originate from academic curiosity even if they have outcomes of practical benefit."** (Brownjohn et al. [102])

For damage detection using direct sensing, approaches are generally agreed, but implementations still tend to be bespoke. For EOV mitigation, general approaches are agreed but at a very abstract level, with research continuing as to how to actually implement them. Most demonstrations of SHM are focused on the earlier of Rytter's [31] SHM stages (identification and localisation), with few examples of the later stages (assessment of damage scale and determination of consequences) according to Figueiredo and Brownjohn [28]. Additionally, many examples of SHM are still based on numerical or laboratory simulation. Sensor installations have become more common on large, long-span bridges. For example, Cawley reports [103] that 31 bridges in China were instrumented in the period 2008–2018, with an average of 250 sensors each; Rizzo and Enshaeian report [58] that Xu and Xia [104] identified 63 major bridges worldwide in 2011 that were instrumented, and in the United States the same authors discuss 15 instrumented bridges in 2021 [58]. Implementations of this kind have included a wide array of sensor types (for example the Queensferry Crossing near Edinburgh, Scotland discussed by Riches et al. [62]), but SHM sensor installations appear to be generally limited to landmark structures. For example, Ye et al.'s interviews with practitioners in the United Kingdom confirmed "very few bridges have real time SHM systems in place" [105]. Most examples of bridge SHM systems apparent in the literature relate to long-span bridges, with very few examples in relation to shorter- and medium-span bridges (Li et al. [38]). Where sensor installations have been undertaken there is still debate as to the best way to record and process the data, as well as how to generally approach sensor network design and deployment (Yang et al. [106]) for each situation. Overall, the status of bridge SHM can be summarised as being popular in the research community but with little uptake from industry. Literature suggests that this discrepancy could be due to a number of actual or perceived challenges:

- The unique nature of bridge structures, leading to difficulties in establishing baseline data representing normal behaviour (Brownjohn [32]) and lack of data representing the damaged state (Worden et al. [33], Rizzo and Enshaeian [34]), as well as the perceived impossibility of transferring a monitoring system from one bridge to another (Yang et al. [107]); inadequate signal-to-noise ratios (Worden et al. [66], Moughty and Casas [26]); inadequacies in damage sensitive features, especially those based on modal parameters (Moughty and Casas [26]); or inadequacies in the all stages of the Statistical Pattern Recognition process (Figueiredo and Brownjohn [28])
- Inadequate attention to developing business cases for use of SHM (including where it can be most useful) (Figueiredo and Brownjohn [28], Cawley [103])
- Lack of demonstrations of function of existing SHM systems: they cannot (or have not yet) reliably detect(ed) damage (An et al. [27], Figueiredo and Brownjohn [28]) or had their damage detection performance validated on real structures (Cawley [103])
- Insufficient curriculum focus on structural resilience in engineering education (Brownjohn and Aktan [24], Cawley [103])
- EOV is still a major confounder: Cross et al. suggest that this is "one of the major reasons for the slow up-take of SHM outside the world of academic research" [101]
- Concerns regarding the number of sensors and volume of data required (Yang et al. [107])
- Perceptions that the number of bridges requiring monitoring makes such monitoring effectively impossible in financial, political or practical terms (for example Moughty and Casas [26], Gkoumas et al. [35], Sarwar and Cantero [108])
- Practitioners (in the United Kingdom) were found to have cost concerns relating to sensor installation and maintenance and data storage and processing; to expect difficulty in processing and storing data; and to have concerns about sensor reliability and lifespan (Ye et al. [105])

2.3.5 Recent research trends

In response to the challenges noted above, recent research has begun to explore a number of directions. Some of these trends are summarised below with references and examples from the literature:

- Innovative excitation and sensor-carrying paradigms including the indirect vehicle-based indirect method (Malekjafarian et al. [25] [40], Wang et al. [109]) which is the primary focus of this thesis. In some cases the

approach is combined with *crowdsourcing* approaches to data collection, utilising citizen's sensors such as accelerometers in smartphones Mei and Gül ([110], Matarazzo et al. [111])

- Use of new data processing and analysis methods generally i.e. machine/deep learning (Farrar and Worden [64], Ye et al. [112]. This has also seen recent application to vehicle-based monitoring (Malekjafarian et al. [113], Malekjafarian and Maloney et al. [114], Corbally and Malekjafarian [115] [116])

- Network-level approaches and generalisation, seeking to adopt population-based approaches to bridge monitoring in which a damage detection framework can be trained on data from a different bridge(s) from the subject of monitoring. Worden et al. describe the nascent research applicable to all applications of SHM [33]

Vehicle-based indirect SHM methods involve using sensors mounted on passing vehicles. Some research has explored this concept using instrumented trains (for example Hajializadeh [117]), but for highway bridges it means vehicles such as cars, trucks and buses. The vehicle-based approach is perceived as offering benefits: low-cost (Malekjafarian et al. [25]), low resource and time requirements compared to direct monitoring (Yang et al. [118], Corbally and Malekjafarian [116]); the possibility of continuous measurement, in real time (Gkoumas et al. [35]) across transport networks (Locke et al. [36]); outsourcing of the burden of sensor network installation and maintenance (Matarazzo and Kondor et al. [43]); the reduction or removal of the need for permanent sensor installations on bridges (Malekjafarian et al. [25]); and applicability to short- and medium-span bridges (Miyamoto et al. [37]). It is still a relatively new concept and significant challenges to operational deployment remain, including those inherent to SHM and additional challenges introduced by the indirect approach. These will be discussed in the following sections.

2.4 Vehicle properties

As noted in section 2.3.3 the presence of vehicles on a bridge is a source of EOV. Understanding and characterisation of EOV in this regard requires the vehicle properties to be estimated; likewise, modelling of vehicle-bridge interaction requires a vehicle model to be established. This section presents a summary of the literature regarding vehicle properties and representative vehicle models. Modelling of vehicle-bridge dynamic interaction is discussed in section 2.5.

2.4.1 Reduced degree-of-freedom models

In engineering it is common practice to adopt reduced degree-of-freedom (DoF) model abstractions when seeking to represent a limited set of parameters of a physical system. Such representative models of vehicles have become established for a variety of purposes. A very common model, described by Jazar as the "most useful model" [6] is known as the *quarter-car* as illustrated in Fig. 2.4.1. The model comprises lumped point masses representing the distribution of the vehicle's mass and that of its occupants and cargo. The masses are joined by linkages in such a manner as to represent the general kinematics of the vehicle. Vertical displacement between the masses and the road surface is passed through springs and viscous dampers representing the vehicle's suspension springs and dampers, and the effective spring stiffness and hysteretic damping of the tyres (Jazar [6]). Fig. 2.4.1 also includes an illustrative example of a transmissibility FRF which in general terms summarises the dynamic characteristics of the model as the ratio of relative displacement response (z_s or z_u) between each vehicle degree of freedom and the base displacement input u (created by the passage of the tyre across a profiled road surface) as a function of frequency, when the input and output are measured in the same units. It is also sometimes known as a *transfer function* or *gain* (Gillespie [119], from Ainalis [3]). An assumption underpinning work in this thesis (especially chapter 4) is that the two modes of a quarter-car are broadly independent; that is, the mode shape for each mode is comprised of a large amplitude at one of the DoF and a small amplitude at the other. This results from the design of typical cars intending to isolate the cabin from higher-frequency vibrations (Jazar [6]). Each of the two modes is thus associated mainly with one DoF. The first mode, known as *cabin bounce* or *body bounce* is associated with the upper DoF and the second mode, *wheel hop* or *axle hop* with the lower DoF. The common use of these terms (for example Jazar [6]) in the literature implies that this assumption is widely held.

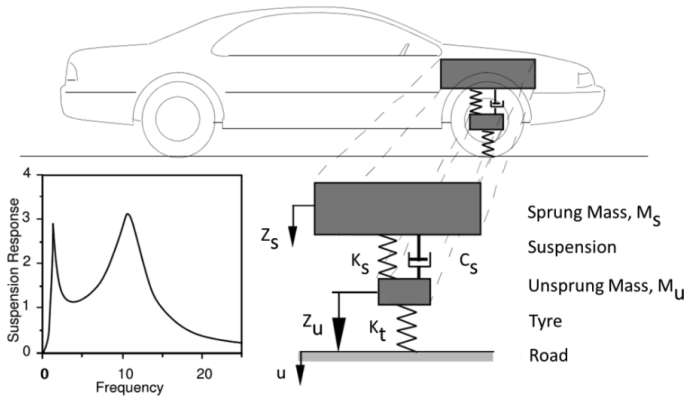

Figure 2.4.1: Illustration of a typical quarter-car model (Gillespie [2] from Ainalis [3]).

For a two-degree-of-freedom (2DoF) mass-spring-damper system as shown in Fig. 2.4.2, it is well-known (for example Villa et al. [17]) that the equation of motion in response to base acceleration input $\ddot{u}$ can be expressed in matrix form:

$$\begin{bmatrix} m_1 & 0 \\ 0 & m_2 \end{bmatrix} \begin{bmatrix} \ddot{z}_1 \\ \ddot{z}_2 \end{bmatrix} + \begin{bmatrix} c_1 + c_2 & -c_2 \\ -c_2 & c_2 \end{bmatrix} \begin{bmatrix} \dot{z}_1 \\ \dot{z}_2 \end{bmatrix} + \begin{bmatrix} k_1 + k_2 & -k_2 \\ -k_2 & k_2 \end{bmatrix} \begin{bmatrix} z_1 \\ z_2 \end{bmatrix} = \begin{bmatrix} -m_1 \\ -m_2 \end{bmatrix} \ddot{u} \tag{2.1}$$

where z_i is the relative displacement between DoF i and the displacement of the base y, with $\dot{z}_i$ and $\ddot{z}_i$ representing the relative velocity and acceleration respectively.

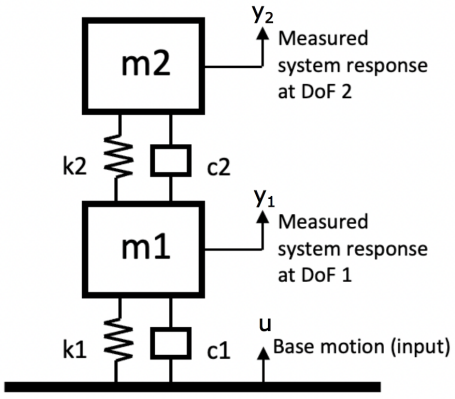

Figure 2.4.2: Idealised 2DoF model of quarter-car.

Equation (2.1) represents a system of linear differential equations of motion. In order to express the response at the DoFs as a function of the base motion input (as indicated in Fig. 2.4.2), under the well-known the classical assumption that the system response is comprised of a linear combination of *normal modes* the FRF can be expressed analytically. In order to do so, the equations of motion are decoupled.[1] Irvine [120] summarises the process. Assuming that the damping matrix is orthogonal, the damping for each mode is expressed in terms of damping ratios:

$$\boldsymbol{C} = \begin{bmatrix} 2\xi_1\omega_1 & 0 \\ 0 & 2\xi_2\omega_2 \end{bmatrix} \tag{2.2}$$

The normal mode frequencies can be determined as eigenvalues of the associated eigenproblem which is derived from the homogeneous form of equation (2.1):

$$det\{\boldsymbol{K} - \boldsymbol{\omega}^2\boldsymbol{M}\} = 0 \tag{2.3}$$

This yields a quadratic in ω^2 from which the undamped classical natural frequencies ω_i can be found. Thereafter the mode shapes $\boldsymbol{q}_i$ can be found as the eigenvector solutions satisfying equation (2.4):

$$\big[\boldsymbol{K} - \boldsymbol{\omega}^2\boldsymbol{M}\big]\boldsymbol{q}_i = 0 \tag{2.4}$$

The next required step is to normalise the eigenvectors (mode shapes) to the mass. The eigenvectors so normalised are denoted as $\hat{\boldsymbol{q}}_i$ and can be assembled as row vectors into a matrix $\hat{\boldsymbol{Q}}$ which can be used to diagonalise the mass and stiffness matrices via pre-multiplying by the transpose $\hat{\boldsymbol{Q}}^T$ and post-multiplying by $\hat{\boldsymbol{Q}}$. The full process of expressing the equation of motion in modal coordinates (thus completing the decoupling) is omitted since it is reproduced in dynamics textbooks as well as the specific source upon which this explanation is based [120]. The relevant outcome is that the acceleration response at each DoF i can be expressed as a function of frequency $\ddot{\boldsymbol{z}}_i(\omega)$, relative to the frequency of harmonic base acceleration input $\ddot{\boldsymbol{u}}(\omega)$ and in terms of the modal frequencies ω_i, mass-normalised mode shapes $\hat{\boldsymbol{q}}_i$ and damping ratios $2\xi_i\omega_i$:

$$\frac{\ddot{\boldsymbol{z}}_1(\omega)}{\ddot{\boldsymbol{u}}(\omega)} = \left\{1 + \frac{\omega^2\hat{q}_{11}[\hat{q}_{11}m_1 + \hat{q}_{21}m_2]}{\omega_1^2 - \omega^2 + j2\xi_1\omega_1\omega} + \frac{\omega^2\hat{q}_{12}[\hat{q}_{12}m_1 + \hat{q}_{22}m_2]}{\omega_2^2 - \omega^2 + j2\xi_2\omega_2\omega}\right\} \tag{2.5}$$

$$\frac{\ddot{\boldsymbol{z}}_2(\omega)}{\ddot{\boldsymbol{u}}(\omega)} = \left\{1 + \frac{\omega^2\hat{q}_{21}[\hat{q}_{11}m_1 + \hat{q}_{21}m_2]}{\omega_1^2 - \omega^2 + j2\xi_1\omega_1\omega} + \frac{\omega^2\hat{q}_{22}[\hat{q}_{12}m_1 + \hat{q}_{22}m_2]}{\omega_2^2 - \omega^2 + j2\xi_2\omega_2\omega}\right\} \tag{2.6}$$

An alternative approach to constructing a theoretical FRF is possible if the physical model parameters (masses, spring stiffnesses and viscous damper

[1] In the context of vehicle-bridge interaction, the term *coupled* takes a different interpretation which is discussed in section 2.5.

coefficients) are known. This approach avoids any error that could be caused by omitting the off-diagonal terms in the damping matrix (equation (2.2)), which is particularly relevant for highly-damped systems such as vehicles. Villa et al. [17] present the absolute-valued FRFs analytically:

$$\left|\frac{\ddot{\boldsymbol{z}}_1(\omega)}{\ddot{\boldsymbol{u}}(\omega)}\right| = \frac{\sqrt{\left(k_1k_2 - (c_1c_2 + m_2k_1)\omega^2\right)^2 + \left((k_2c_1 + k_1c_2)\omega - m_2c_1\omega^3\right)^2}}{\sqrt{B^2 + C^2}} \tag{2.7}$$

$$\left|\frac{\ddot{\boldsymbol{z}}_2(\omega)}{\ddot{\boldsymbol{u}}(\omega)}\right| = \frac{\sqrt{\left(k_1k_2 - c_1c_2\omega^2\right)^2 + \left((k_2c_1 + k_1c_2)\omega\right)^2}}{\sqrt{B^2 + C^2}} \tag{2.8}$$

$$B = m_1m_2\omega^4 + \big(-m_1k_2 - c_1c_2 - m_2(k_1 + k_2)\big)\omega^2 + k_1k_2 \tag{2.9}$$

$$C = \big(-m_1c_2 - m_2(c_1 + c_2)\big)\omega^3 + (k_2c_1 + k_1c_2)\omega \tag{2.10}$$

The quarter car model parameters adopted in the literature often make the simplifying assumption that the tyre is undamped. Strictly speaking the assumption is incorrect; Pauwelussen notes [121] that a tyre has internal energy dissipation (hysteretic damping). Additionally it is observed that a rolling tyre generates heat due to this damping, that the raise in temperature increases the inflation pressure (thus increasing the effective spring stiffness for a quarter car model) and reduces the damping, and that the magnitude of these effects is dependent on speed with the tyre approaching an equilibrium after around 20 minutes of motion [121]. Nevertheless, the tyre damping is still "so small that it can be neglected" (Guiggiani et al. [122]). A quarter-car model represents the behaviour of one side of a single axle in a single vertical plane. In an alternative model form known as the *half-car* or *bicycle car* (Jazar [6]) model, front and rear axles are represented, typically with a horizontal rigid linkage and additional spring connectors in some cases. Half-car models thus do not represent vehicle roll or yaw motion, but can – in contrast to quarter-car models – capture pitch motions. A drawback of quarter car models is therefore that they inherently do not represent vehicle kinematics other than vertical motion, meaning they do not account for pitch and roll responses of a vehicle. Nevertheless, they are deemed to be relatively simple and functional (Verros et al. [123]), providing a sound basis for more detailed studies with models of greater sophistication if required. Such models typically find their application in representing the dynamic characteristics and response of vehicles to road surface inputs, for purposes of estimating or modelling a variety of phenomena. In automotive engineering, the use of reduced DoF models has been used for studies of suspension design concerning factors such as ride quality (Hrovat [124], Hegazy and Sharaf [125], Sharma and Sharma [126]) and road holding. In fact, the design of a suspension system involves seeking a balance between these goals (Türkay and Akçay [127], Sathishkumar et al. [128], Phalke and Mitra [129], Puneet et al. [130]). Another field of application for reduced DoF vehicle models is transportation

engineering, where they have been used for such tasks as the pursuit of a suspension design to limit damage to roads (Valášek and Kejval [131], Cebon [132] from Pable et al. [133]) and their transmissibility FRFs leveraged to understand the vibration transmission from road surface to delicate cargo such as electronic items (Caldicott [134], from Ainalis [3]) or soft fruits (Lewis [135]). Other fields of application of such models are in representing VBI and the related studies around using a vehicle as a sensor carrier for bridge modal parameter estimation and damage detection (for example O'Brien et al. [136], Tan et al. [137], Sadeghi Eshkevari et al. [138], Abuodeh and Redmond [139]).

Researchers in the fields of automotive engineering and transportation have adopted a variety of values for vehicle model parameters. For example, Rouillard and Lamb report [4] that various authors (Todd et al. [140], Cebon [141], De Pont [142], Heath [143] and Prem [144]) have developed "quarter-car models representing typical vehicles using realistic mass, damper and stiffness values for transport vehicles" [4]. The resulting transmissibility FRFs are reproduced in Fig. 2.4.3. Some literature also provides parameter ratios for quarter cars. For example, Sayers provides ratios which are "based on the full spectrum of vehicles available in the United States" [5]. Jazar provides "average, minimum, and maximum of practical values of the parameters" [6] for a quarter-car. Both of these are reproduced in Fig. 2.4.4.

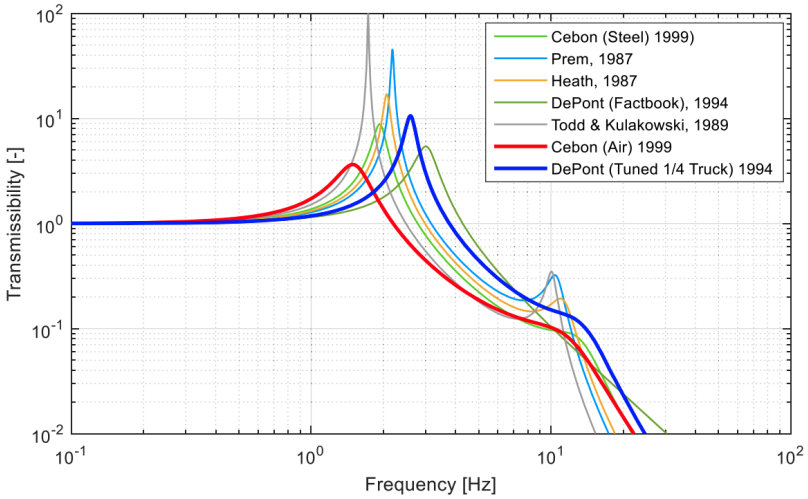

Figure 2.4.3: Various transmissibility FRFs for transport vehicles, reproduced from Rouillard and Lamb [4].

In the fields of VBI and vehicle-based indirect SHM researchers have also adopted quarter-car models. A review of the literature indicates a pervasive trend of adopting parameters from prior work in the area of vehicle dynamics and transportation engineering. For example, in a numerical study of VBI in relation to long-span bridges, Sadeghi Eshkevari et al. [138] reports having

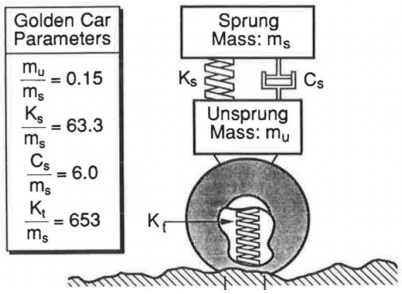

(a) Sayers' *Golden Car*

Parameter	Average	Minimum	Maximum
$\varepsilon = \frac{m_s}{m_u}$	$3-8$	2	20
$\omega_s = \sqrt{\frac{k_s}{m_s}}$	1	0.2	1
$\omega_u = \sqrt{\frac{k_u}{m_u}}$	10	2	20
$r = \frac{\omega}{\omega_s}$	$0-20$ Hz	0	200 Hz
$\alpha = \frac{\omega_s}{\omega_u}$	0.1	0.01	1
$\xi = \frac{c_s}{2m_s\omega_s}$	0.55	0	2

(b) Jazar's "practical values"

Figure 2.4.4: Parameter ratios and ranges for quarter-car models. Reproduced from Sayers [5] (left) and Jazar [6] (right).

adopted quarter-car model parameters for a commercial vehicle presented by Milliken et al. [145] and a heavy truck presented by Harris et al. [146] and Elhattab et al. [147]. Elhattab et al. [147] themselves reports having adopted their quarter-car parameters from Cebon [141]. In relation to their laboratory-scale model of VBI, Corbally and Malekjafarian [20] noted that they assumed that their model vehicle could be represented by the quarter-car parameters for an air-suspension vehicle which they adopted from Cebon [141]. In earlier work, Malekjafarian et al. [113] reported having adopted vehicle model parameters from O'Brien et al. [136] whom in turn appear to have adopted the properties from prior work based on references made to Cebon [141]. Locke et al. designed notional vehicles for their study "to represent, in a general sense, the dynamic properties of physical highway vehicles" [148] adding that these were based on Gillesipe [2]. In very recent work, O'Brien et al. [149] adopted vehicle properties from Cantero and Gonzalez [150], who adopted their parameters from Cantero [151], who based their vehicle representations on an analysis by Fu and Cebon [152] which incorporated data from studies at the University of Michigan Transportation Research Institute (UMTRI) by Fancher et al. [153] [154] and Winckler et al. [155]. In addition to the UMTRI it appears that work by Cebon (especially [141]) at the University of Cambridge as part of the Cambridge Vehicle Dynamics Consortium has been particularly influential on the basis of repeated citations regarding adopted vehicle model parameters.

2.4.2 Vehicle model parameter estimation

Estimation of vehicle model parameters can be undertaken in a variety of ways. The total vehicle mass could be measured using a weighbridge, since these are commonly available worldwide (Marshall and Murphy [156]) but this would not afford insight as to the distribution of mass between the DoFs of the representative model. Suspension springs and dampers could be laboratory tested, however this naturally requires partial disassembly of the vehicle which may be impractical. For estimation of parameters from an assembled complete vehicle,

several approaches are noted in the literature and are summarised here.

Laboratory estimation of vehicle model parameters has been undertaken in several ways. At present, the dominant methodology for establishing vehicle dynamic characteristics is laboratory testing (Ainalis et al. [157]). For example, Ainalis et al. report [157] that the Council of the European Union directive 96/53/EC [158] outlines a procedure for measurement of the sprung mass mode (frequency and damping) of heavy vehicles to establish their road-friendliness. Ainalis' PhD thesis included a detailed review of established methods of estimating vehicle dynamic characteristics both in the laboratory and in the field, including assembling relevant literature; the summary presented below is based on this [3]. Laboratory-based estimation can be characterised as (with all citations in the list as reported by Ainalis [3]):

- Output-only: in which the vehicle is perturbed (e.g. dropped, pushed and released) and the free vibration response is measured (Ainalis [3]). Examples include the transient step excitation method (Sweatman et al. [159]) which involved pulling blocks from under the wheels of a slowly moving vehicle; simultaneous dropping of the vehicle having raised all axles, proposed by Milliken et al. [160]; and Davis and Sack's suggestion [161] of driving slowly across a small diameter pipe.

- Controlled input: in which the input is provided in a measured way, for example by placing the vehicle on a servo-hydraulic shaker table (Sweatman et al. [162], Quinn and Zable [163]) and subjecting it to a series of continuous vibration periods at specific frequencies, a slow sweep through multiple frequencies, a random vibration, or vibratory impact (Caldicott [134])

The parameters estimated in a laboratory may not be sufficient to accurately represent a vehicle at a later date given anticipated operational variations (for example the condition of suspension components; replacement of components for performance reasons or due to wear; altered tyre pressure; and variation in the added mass of occupants or cargo). Additionally, there are cost and practicality constraints on laboratory testing, meaning that it is not an appealing option (Ainalis et al. [157]). Ainalis reports [3] that Cebon [141] criticised output-only techniques since they "do not attempt to determine the dynamic characteristics of a vehicle under real in-service conditions" (Ainalis [3]), and summarised the "great motivation for research into measuring and analysing the response of a vehicle during normal operation to estimate the dynamic characteristics" (Ainalis [3]). Estimation of models representing current vehicle conditions has elsewhere been recognised as valuable: Ainalis reports [3] that De Pont [164] found that whole-vehicle effects made a significant difference to suspension response and that the effects varied according to operational conditions. In response, **in-service estimation** of model parameters has been pursued. This is typically an output-only paradigm in which input excitation comes from the passage of the vehicle along a profiled road surface. Ainalis [3] outlines the principle that the vehicle's transmissibility FRF can be recovered

as the ratio of the response and input power spectra, as illustrated in Fig. 2.4.5 and equation (2.11) in which $G_{Re}(f)$ is the vehicle response power spectral density, $T^2(f)$ the vehicle transmissibility FRF squared, and $G_{Ex}(f)$ the excitation power spectral density, all as functions of frequency:

$$G_{Re}(f) = T^2(f)G_{Ex}(f) \tag{2.11}$$

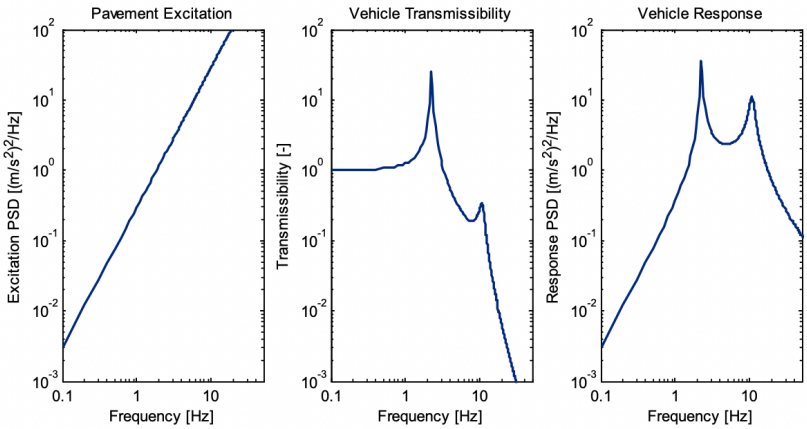

Figure 2.4.5: Illustration of the relationship between excitation and response power spectra via the transmissibility FRF. Reproduced from Ainalis [3].

Estimation of vehicle suspension characteristics during normal service offers the potential advantages of low cost and the ability to repeat measurements during the vehicle's operational life without needing to temporarily remove it from service. The input-output relationship based on the vehicle's transmissibility FRF (equation (2.11)) assumes that the vehicle's dynamic properties are linear. Under this assumption, Ainalis reports [3] that several researchers (for example Houbolt et al. [165], Gillespie [119], Sayers [166]) explored the relationship shown in this equation. Dodds and Robson noted that the outcome would be an "average linearised" spectrum on the basis that vehicle components are generally in fact not linear [167] (from Ainalis [3]). The effect of vehicle speed was investigated by Quinn and Zable [163] (from Ainalis [3]) who noted slight change in the response spectrum from testing at 40, 50 and 60 mph. Ainalis reports [3] that Quinn and Zable [163] noted that a longer duration of driving increases the statistical reliability of estimates. However, Ainalis commented that in-service testing could be challenging in this regard as "the flow of traffic may prevent the test vehicle from travelling at a constant speed" [3].

The road profile itself has also been studied alongside the effects of vehicle speed. In the field of vehicle dynamics it is common to describe road profiles based on statistical characteristics, with a power spectral density representation of pavement profile being described as useful (Andren [168]) or "indispensable" (Kropáč and Múčka [169]). The international organisation for standardisation

(ISO) code 8608 [7] describes a range of road roughness classes as spectra with the same shape (Fig. 2.4.6). Múčka [170] reports that these classes are widely adopted in automotive engineering. Selected specific examples in which the ISO 8608 classes are used to represent road surface profiles in studies relating to vehicle-based bridge damage detection include Chang et al. [171], Malekjafarian et al. [113], Corbally and Malekjafarian [115], Sarwar and Cantero [108], and Li et al. [172].

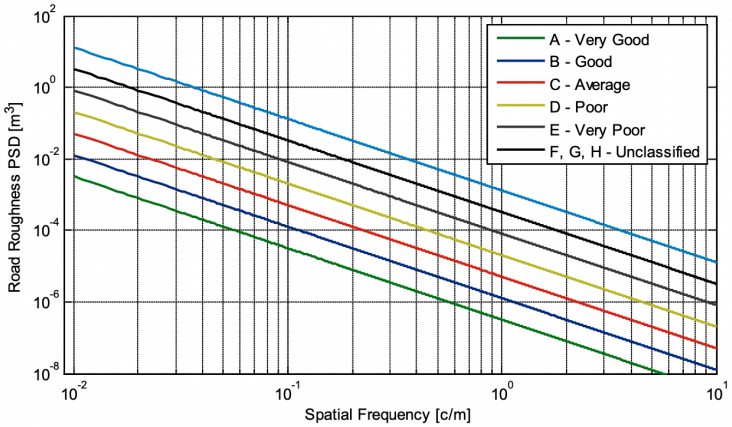

Figure 2.4.6: Spectra for ISO 8608 [7] road roughness classes. Reproduced from Ainalis [3].

Marcondes [173] (from Ainalis [3]) measured road surfaces with a profilometer and initially compared estimated vehicle transmissibilities from data gathered at 45, 52 and 60 mph. Then, using the estimated transmissibility from 52 mph driving to predict response spectra at 55 and 60 mph, they noted variation between predicted and gathered response data including frequency shifting, which was most evident at low frequencies. Gonzalez at al. [174] (from Ainalis [3]) attempted to classify road surface profiles in accordance with ISO 8608 [7] and found that vehicle speed had an influence on the estimated excitation power spectrum. Later, Rouillard and Sek [175] (from Ainalis [3]) assumed that the road profile excitation power spectrum would approach the ISO 8608 [7] spectral shape as the driving distance for data gathering increased. They proposed to use two traversals of the same road, at two different constant speeds, to establish the spectral exponent (and thus an estimate of the road roughness class according to the ISO standard). Ainalis explored this concept in their recent PhD thesis [3], comparing Rouillard and Sek's proposal [175] with the use of the Random Decrement technique which was described by Bendat and Piersol [176] as a way of approximating the free-vibration response of a dynamic system subject to broadband random excitation. Ainalis' experiments used a purpose-built trailer (Fig. 2.4.7) which they called the *Single Wheel Experimental Vehicle* (SWEV) [3]. FRF estimates derived from traversals of real roads were compared to those

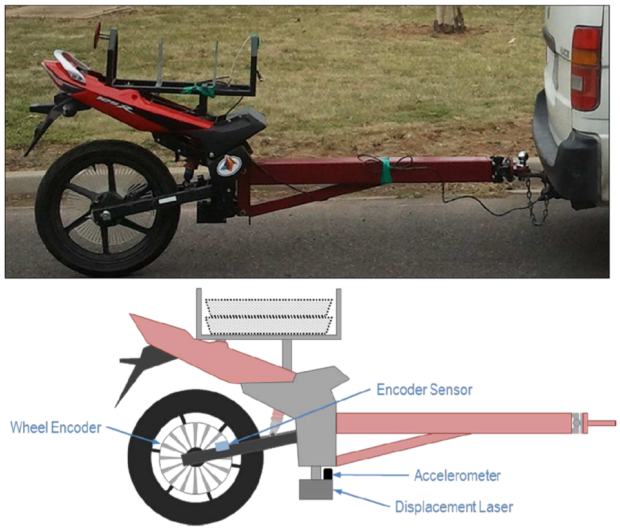

Figure 2.4.7: The Single-Wheeled Experimental Vehicle (SWEV) used for field tests. Reproduced from Ainalis [8].

based on laboratory experiments: ramp, push-release and pull-release free vibration tests, and forced random vibration tests in which hydraulic actuators were used as the source of input excitation at the wheel-road interface (for example, see the results reproduced in Fig. 2.4.8). Vehicle dynamic properties (frequency and damping ratio) for the SWEV were estimated from the FRF or free vibration response.

Ainalis' thesis [3] in addition to contemporary and subsequent related publications (Ainalis et al. [177] [8] [157] [178] and [179] [180] [181] (from Ainalis [3]) represent the most recent substantial efforts to establish reduced degree-of-freedom representative vehicle models from in-service acceleration responses that could be found in the literature. The main findings of the work by Ainalis [3] were:

- Initial on-road experiments could not be successfully verified since they relied on the assumption that the traversed road profile could be represented by the ISO 8608 spectral model, but the actual traversed road profile was not measured. Comparison to road profiles provided by another instrumented vehicle yielded inconsistent results.

- Subsequent experiments in which the test vehicle was outfitted to act as an inertial profilometer to record the traversed profile found that subsequent runs on the same road did not appear to traverse equivalent roughness spectra. This variation suggested that the assumption that the traversed road profile could be expressed by an equivalent roughness constant and spectral exponent (Rouillard and Sek [175] from Ainalis [3]) was not sound.

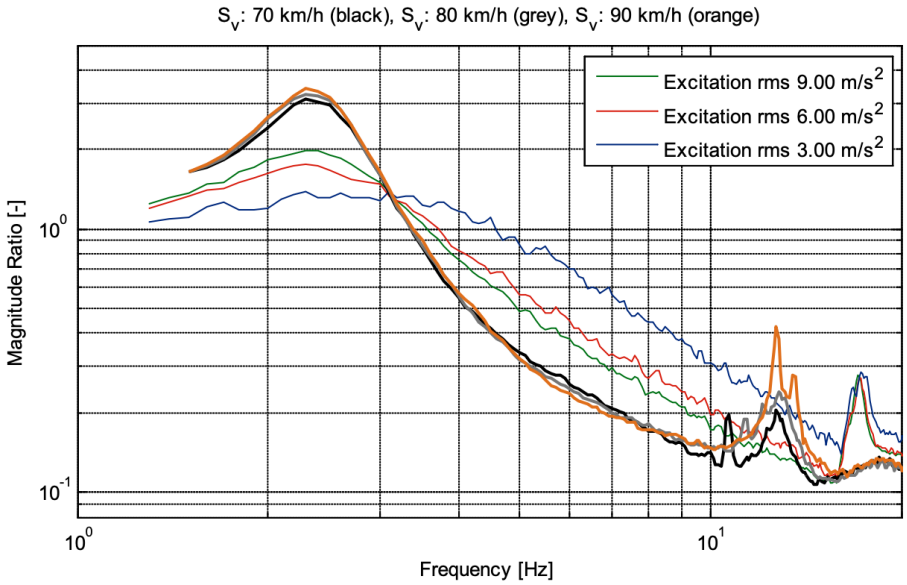

Figure 2.4.8: Example comparison of FRF estimates from field measurements (thick lines) and controlled laboratory measurement (thin lines). Reproduced from Ainalis [3].

It appeared to be impractical to repeat precisely the traversed wheel path in practice. For illustration, see Fig. 2.4.9.

- When comparing on-road and laboratory-derived estimates of FRF, the sprung mass frequency could be consistently identified but estimates of the associated damping varied significantly. The random decrement-derived estimates were believed to be biased by non-white excitation from the road profiles. It was speculated that deriving the FRF from the random decrement of velocity (rather than acceleration) might offer better performance since the velocity excitation spectrum was expected to be less subject to low-frequency bias (i.e. be more spectrally flat) than acceleration.

- Strong recommendations were made to estimate vehicle dynamic characteristics using in-service responses, rather than laboratory-based methods. The effect of vehicle speed was highlighted as requiring further investigation. The equivalent representative vehicle model used was a single degree-of-freedom sprung and damped mass, therefore it was recommended that future investigations explored more sophisticated vehicle models, particularly to estimate the unsprung mass modal parameters (i.e. to estimate parameters for a two degree-of-freedom quarter-car model).

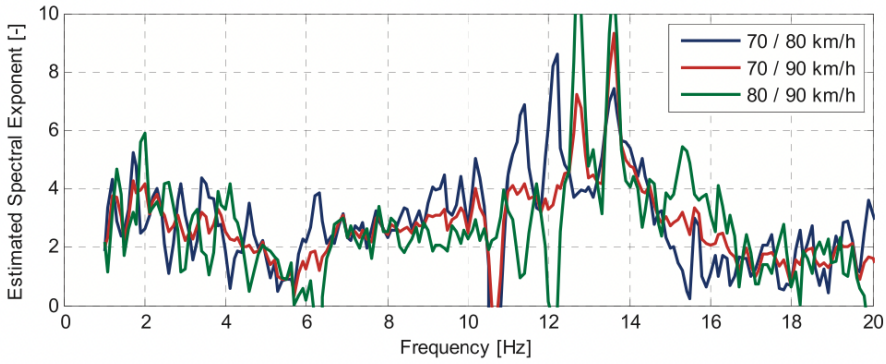

Figure 2.4.9: Example of varying spectral exponent estimates. Reproduced from Ainalis et al. [8].

2.4.3 Vehicle properties in studies of VBI and vehicle-based bridge damage detection

In relation to VBI and vehicle-based bridge damage detection, the literature suggests a common tendency for authors to adopt vehicle model parameters from prior transportation and automotive literature for numerical investigations and simulation, as noted in section 2.4.2. For laboratory-scale physical modelling of VBI, it is feasible to attempt to identify the dynamic properties of a test vehicle using tradition modal analysis techniques. More challenging, however, is identifying vehicle dynamic properties at full scale. In some cases, where field testing was performed, authors have attempted to characterise their test vehicles. For example, in their experimental verification of the extraction of bridge frequencies from a passing vehicle, Lin and Yang [182] used a single-axle trailer as the sensor carrier. They applied a load to the trailer and measured its free vibration response after the load was removed to estimate its sprung mass mode frequency and damping ratio. Miyamoto and Yabe [183] [184] used a bus as their test vehicle. They adopt a half-car numerical model and the total vehicle weight is reported, as are two frequencies for body bounce and wheel hop. The frequencies are said to be "predetermined" (Miyamoto and Yabe [183]) but it is not clear how they – or the vehicle's mass – were found. Siringoringo and Fujino [185] used a light commercial vehicle (Toyota Land Cruiser) and installed an accelerometer in the centre of the cabin equally spaced between the front and rear axles and left and right wheels. With the engine running and the driver present, but the vehicle stationary, they excited the test vehicle by having two people simultaneously jump off the vehicle from a central point. From the resulting free vibration they identified one frequency and an associated damping ratio based on the logarithmic decrement of the response. They noted that the high damping meant that the free vibration response duration was very short. Chang et al. [22] identified a single body bounce frequency of their test vehicle

by letting it drop from a brick and having installed their sensing instrumentation directly above the rear axle. Elhattab et al. [186] conducted field testing in which a truck was instrumented with a single accelerometer at its centre of gravity. They report that the truck's dynamics were conducted based on stationary acceleration with the engine running. Yang et al. [187] report results from field tests with a single-axle trailer as the sensor carrier. They note that it was intended to "mimic the single-DoF system adopted in previous theoretical investigations" [187], for example Yang et al. [118]. They note that three accelerometers were used, on the "left, center and right sides of the axle of the test vehicle" [187] but they do not appear to discuss how the trailer's dynamic characteristics were validated, other than a note in a subsequent paper that the damping coefficient was determined from a "free vibration test" (Yang et al. [188]). Aloisio and Alaggio [189] report observations from field testing using a vehicle instrumented with accelerometers. The vehicle's total mass, first frequency and associated damping ratio are reported, but they do not appear to clarify how these were estimated. Shirzad-Ghaleroudkhani and Gül [190] used a smartphone with a built-in accelerometer as the sensing apparatus in a Honda Civic car to represent the concept of a *crowdsourcing* approach to vehicle-based bridge SHM. Rather than directly identify the vehicle's dynamic characteristics, they pursued an inverse filtering approach in which off-bridge vibration response spectra were used to differentiate between vehicle- and bridge-derived frequencies recorded during traversals. They identified a "significant" dependence of vehicle response on vehicle speed and concluded that this observation "substantiates the fact that creating a speed-dependent database of the off-bridge signals is crucial in the successful performance of the inverse filtering for frequency identification of bridges" [190]. They also investigated the effect of surface roughness and sought to match on- and off-bridge acceleration records according to similar mean square acceleration amplitudes, assuming that these represented vehicle interactions with similar surface roughness conditions. Di Matteo et al. [191] report the outcomes of a field test in which a smartphone was used as the sensor. The vehicle's response spectrum was estimated using the acceleration record from 130 seconds of driving at a constant speed of 15 km/h on a "flat straight road" [191] in Palermo, Italy. After applying a frequency band-pass filter (0.5–30 Hz) they used Welch's method to estimate the power spectral density function and identified five vehicle frequencies using manual peak-picking. In another study, apparently using a different vehicle and a different test location (Dubai, United Arab Emirates), some of the same authors (Fiandaca et al. [192]) used a single accelerometer in the front right side of the vehicle cabin to record vibrations from driving on a "flat, straight road" [192] for 130 seconds. In this latter case they report a variable speed between 5 and 30 km/h. After applying a frequency band-pass filter (0.5–30 Hz) they used Welch's method to estimate the power spectral density function, from which two vehicle frequencies were identified by manual peak-picking. Locke et al. [36] identified the frequencies of their test vehicle by conducting multiple runs on the same stretch of highway at 20, 30, 40 and 50 mph with an accelerometer on the sprung mass and then unsprung mass (but not both simultaneously). Comparison be-

tween the frequencies (selected by peak-picking) for different speeds was used to validate their assumption that several observed frequencies could plausibly be caused by wheel defects (for example, out-of-balance defects) on the basis of how the observed frequencies scaled with vehicle speed. Remaining frequencies were deemed to relate to vehicle kinematics such as "pitching, rolling, etc." [36] but further characterisation of the vehicle model was deemed to be out-of-scope. Sing and Sadhu [193] conducted tests using a small car. They first identified two engine frequencies with the vehicle stationary and the engine idling; then a single suspension frequency "by performing several trial runs over a bump" [193]. The vehicle speed during this characterisation campaign is not mentioned but is assumed to be significantly lower than the 60 km/h at which the vehicle traversed the subject bridge in the later phases of their fieldwork.

An alternative in-service parameter estimation paradigm relies on image analysis. Feng and Feng [194] summarise research using computer vision techniques applied to bridge SHM tasks including estimation of vehicle properties. They report the work of Gandhi et al. [195] who leveraged computer vision applied to video of real traffic to track vehicles and group them into type classes such as car, truck or bus. Tan et al. [196] combined video with laser sensors and accelerometers to assist with moving force identification to support bridge stiffness estimation. They noted the potential for future integration of vehicle type classification from videos to be added into an SHM system for recording traffic imposed loads on bridges. Catbas et al. [197] similarly integrated object tracking of vehicles with traditional sensor data to estimate bridge influence lines from passing traffic. More recent work has further developed the concept: Ojio et al. [198] and He et al. [199] both investigated contactless bridge weigh-in-motion systems using machine vision and incorporated field testing on real bridges. The works discussed thus far generally focus on computer vision for object tracking, synthesised with other sensor data or inputs in various ways. An alternative approach is to study the vehicle's tyres via computer vision. Feng et al. [200] and Feng and Leung [201] proposed combining machine vision to identify vehicle tyre properties from their sidewall text and estimates of the tyre deflection, with tyre pressure values from on-vehicle sensors. This combination of data allowed them to estimate vehicle axle weights and the proof-of-concept study was tested on a small number of stationary and moving vehicles. The method is extended to estimate bridge influence lines for passing vehicles by Martini et al. [202].

2.5 Vehicle-Bridge Interaction

2.5.1 Overview

The dynamic interaction of a vehicle and bridge is known as vehicle-bridge interaction (VBI). In summary, VBI represents two dynamic systems (vehicle and bridge) interacting via a contact force between wheels and bridge deck or rail. The coupling of vehicle and bridge responses can be demonstrated in closed form for simple cases, but requires to be solved numerically and often via finite element (FE) approximations for any other than arbitrarily basic systems. The complexities contributing to the difficulties in obtaining a closed-form analytical solution vary depending on how the bridge and vehicle are represented but can include bridge and vehicle viscous damping; vehicle models with multiple DoFs; multiple vehicles; bridge deck or rail surface irregularities; and permission of short-term separation of contact between vehicle and bridge.

González [203] summarises the general matrix-form equations of motion of the bridge (equation 2.12) and vehicle (equation 2.13):

$$\boldsymbol{M}_b\ddot{\boldsymbol{y}}_b + \boldsymbol{C}_b\dot{\boldsymbol{y}}_b + \boldsymbol{K}_b\boldsymbol{y}_b = \boldsymbol{f}_b \tag{2.12}$$

$$\boldsymbol{M}_v\ddot{\boldsymbol{y}}_v + \boldsymbol{C}_v\dot{\boldsymbol{y}}_v + \boldsymbol{K}_v\boldsymbol{y}_v = \boldsymbol{f}_v \tag{2.13}$$

In these expressions, $\boldsymbol{M}$, $\boldsymbol{C}$ and $\boldsymbol{K}$ are matrices containing the distribution of mass, damping and stiffness terms for the bridge (subscript b) and vehicle (subscript v). The $\boldsymbol{y}$ terms are vectors of bridge and vehicle displacements and rotations respectively identified by the same subscripts, with the single and double dot notation representing the first and second derivatives of these vectors with respect to time. In this thesis (and much of the prior literature) it is assumed that the vehicle moves along the beam at a constant velocity with no friction. This means that the vehicle's response to VBI can be considered only in terms of vertical coordinates and a vertical interaction force with the bridge, while the bridge response is represented by vertical and in-plane rotational coordinates and the vertical interaction force. The two equations are coupled by an equilibrium condition between the forces at the location of the vehicle as it traverses the bridge deck ($\boldsymbol{f}_b = \boldsymbol{f}_v$). In almost all cases the contact force equilibrium is represented as enforcement of continuous contact between vehicle and bridge (González [203]).[2] Because the vehicle moves along the bridge span, equations 2.12 and 2.13 vary with time, since the location of the contact point changes. This has led to a variety of approaches featuring simplifying assumptions in pursuit of analytical solutions to the coupled equations, and the adoption of numerical approximation techniques. The following sections offer an overview.

[2] It should be noted that in the context of VBI, *coupling* usually refers to mechanical systems which have shared Lagrangian coordinates at the contact point(s).

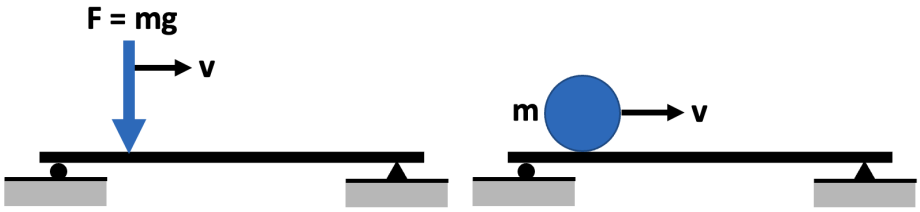

Figure 2.5.1: VBI model abstractions: moving force (left) and moving mass (right) models.

2.5.2 Vehicle-bridge interaction model abstractions

González reports that the traversal of a beam by a moving force was studied by Willis [204] and Stokes [205] in the late 1840s, and that these investigations were motivated by the mid 19$^{\text{th}}$ century Chester railway bridge collapse in the United Kingdom. In these first works, according to González [203] inertial effects of moving mass were neglected, with such effects being added in studies during the first half of the 20$^{\text{th}}$ century (Jeffcot [206], Inglis [207], and Timoshenko and Young [208]). In the mid-1960s Biggs [209] presented second order coupled differential equations linking the midspan response of a simply-supported beam oscillating in its primary mode to the response of a moving sprung mass. Both beam and sprung mass were undamped. Earlier in the same work, Biggs [209] presented the solution of a beam traversed by a moving load and a moving unsprung mass, relating to a now well-known hierarchy of model complexity:

- **Moving force model:** a force F, representing the action of gravity g on the vehicle's total mass, moves along the bridge at velocity v (Fig. 2.5.1). The inertial forces related to the movement of the vehicle's mass are not modelled. The vehicle's suspension is not modelled. This method is suitable for representing the majority of effects of the moving vehicle on the beam, for situations where the vehicle's mass is very small compared to that of the beam (González [203]). It is not suitable for modelling the vehicle's response. This model has been applied for situations in which considering only the moving forces imposed by vehicles is adequate, such as studies of resonance effects induced in bridges by automated truck platooning (for example Ling et al. [210]).

- **Moving mass model:** a mass m, representing the total vehicle mass, moves along the bridge at velocity v (Fig. 2.5.1). This approach is able to account for the inertial effects related to the movement of the vehicle mass and thus is suited to modelling interactions where the vehicle mass is non-negligible compared to that of the bridge, however the vehicle suspension is not modelled and effects due to road surface profile are not captured (González [203]). An example of the use of this approach is Mao and Lu [211] who studied resonance effects on train bridges due to the movement of successive masses representing carriages.

- **Moving sprung mass model:** a mass m on a spring k (perhaps with a viscous dashpot damper c) moves along the beam at velocity v. This method accounts for the aggregate properties of the vehicle suspension system as well as inertial effects, and can be extended to include more sophisticated representations of vehicle kinematics (i.e. vehicle models with additional degrees of freedom) as required. This is the approach which has generally been used for modelling VBI for studies of vehicle-based indirect bridge SHM. The original proposal for extracting bridge frequencies from the vehicle response modelled the vehicle as a single degree-of-freedom (SDoF) sprung mass (Yang et al. [118]). Subsequent works have generally either adopted the same approach (for example Yang and Chang [212], Yang et al. [213], Malekjafarian and O'Brien [214], Oshima et al. [215], Di Matteo et al. [191]); modelled the vehicle as a two-DoF quarter car (for example McGetrick et al. [216], O'Brien and Keenahan [217], Elhattab et al. [147], Wang et al. [218], Tan et al. [137], Sadeghi Eshkevari et al. [138], Kildashti et al. [219], Corbally and Malekjafarian [220] [20], Lan et al. [221]); extended the model to a half-car to allow representation of two axles (for example Li et al. [222], Feng and Feng [223], Li et al. [172], Liu et al. [224]); or considered a more sophisticated representation such as a full-car model (for example Li et al. [38] or a three-axle vehicle towing a two-axle trailer O'Brien and Keenahan [217]). Illustrative SDoF and 2DoF quarter-car models are shown in Fig. 2.5.2; in the latter illustration, tyre damping is omitted in accordance with the normal practice outlined in section 2.4.

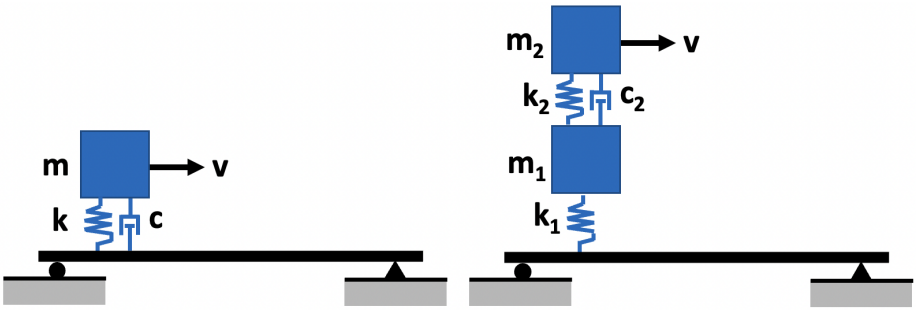

Figure 2.5.2: VBI model abstractions (damped sprung mass): single DoF (left) and two DoF (right) quarter-car models.

2.5.3 Modelling vehicle-bridge interaction

It should be noted that all of the above paradigms typically require constant contact between the vehicle and the bridge, and none inherently account for the effects of the vehicle interacting with the surface of the roadway which is, in reality, not perfectly smooth. For all but arbitrarily simple representations,

the inadmissibility of an analytical solution (González [203]) and the computational cost associated with numerical approximation mean that it is difficult to explore the effects of parameter variation on VBI when understanding the bridge dynamics via the vehicle response, for the purpose of indirect SHM, is the ultimate goal. Modelling more sophisticated vehicle bridge interaction can include multiple degree-of-freedom vehicles, considering multiple bridge modes, the effects of bridge surface profile roughness, permitting temporary separation of contact between vehicle and bridge, and modelling damage to the beam. A review of literature reveals several techniques that have been applied to the VBI problem. Aside from considerations of computational efficiency, the applicability and utility of the various methods depends upon the outcomes that are sought – for example, whether only the bridge response is desired, or if an accurate estimation of the vehicle(s) response(s) is also necessary – as well as the operational conditions to be represented. For example, Zou et al. [225] compared moving force, moving mass and moving sprung-damped-mass models and found that as the vehicle speed increased, so did the discrepancy in bridge predicted bridge response between the three abstractions. These approaches are discussed below with reference to selected relevant examples.

2.5.4 Analytical solutions

Yang and Chang [21] undertook a parametric study of the response of an SDoF vehicle to the oscillation of a simply-supported beam bridge. The bridge was assumed to be set in motion prior to the arrival of the vehicle. The effect of bridge velocity at the vehicle location was disregarded when considering the vehicle's (velocity-dependent, viscous) damping. The study thus was able to generate a closed-form expression for the response of the vehicle model to traversals of a bridge, but the system under consideration was effectively decoupled by the assumption that the vehicle would not contribute in a meaningful manner to the bridge response due to the bridge's initial state of movement and the short duration of the vehicle traverse.

Yang et al. [9] studied the variation of instantaneous frequency for a single vehicle crossing a simply-supported beam bridge. They modelled the vehicle as a single lumped mass on a spring. Only the first bridge mode was considered. Vehicle and bridge damping were neglected. Their formulation admitted an analytical solution to the coupled second-order differential equations and their study concluded that the bridge first modal frequency varied in the short term when the vehicle mass was non-trivial compared to the bridge mass, or when the resonance condition was approached.

As part of their work, Sadeghi Eshkevari et al. [138] presented a closed-form expression for a stationary vehicle at the centre of a simply-supported beam bridge. The vehicle model consisted of sprung and unsprung lumped masses, but no damping was considered. The bridge was also undamped and its mass was lumped at midspan. The authors decoupled the resulting equations of motion by solving the corresponding eigenvalue problem.

2.5.5 Uncoupled methods

When only the bridge response is sought, a simplified approach that considers the bridge and vehicle(s) to be uncoupled can suffice. In the *moving load* model, vehicles are modelled simply as point loads traversing the bridge. This approach, however, does not include the inertial effects of vehicle masses on the bridge. To address this, the *moving mass* model, in which vehicles are modelled as point masses traversing the bridge, can be utilised (Zou et al. [225]). However, even this simple model abstraction results in temporal variation in the bridge mass matrix; this frustrates the search for an analytical solution in closed form and when such a system is to be solved numerically the mass matrix must be updated at each timestep. For simply-supported bridges, Stoura and Dimitrakopoulos [226] report that the Eurocode recommends a decoupled approach in which the vehicles are treated as moving loads. An allowance for additional damping caused by VBI is given to be proportional to the bridge's length, along with an amplification factor to the bridge vibration to account for surface irregularities. They also noted that later studies by others (Doménech et al. [227] and Arvidsson et al. [228] from Stoura and Dimitrakopoulos [226]) found the Eurocode's *additional damping method* to be inaccurate in estimating the effective increase in bridge damping for some cases; improved methods of estimation were found by taking into account the bridge frequencies (Arvidsson et al. [228] from Stoura and Dimitrakopoulos [226]) and the dynamic properties of the vehicles (Yau et al. [229] from Stoura and Dimitrakopoulos [226]).

Sadeghi Eshkevari et al. [138] also investigated uncoupled simulation of VBI, noting that when the span of the bridge increases, and thus its flexibility also increases, the coupling between individual vehicles and the bridge response decreases. They developed a simple expression for coupled VBI in which the undamped vehicle is stationary at the centre of an undamped bridge with concentrated mass. Their eigenvalue solution to this coupled problem was compared to an alternative formulation in which the interaction was physically uncoupled: the bridge solution was calculated first, and the resulting vehicle response calculated subsequently, thus ensuring that the vehicle did not act as a force exciter to the bridge. Their work compared the outcomes of these two simulation approaches when a broadband random (so-called *white noise*) load was applied to the bridge. A variety of bridge span lengths were investigated. Proposing that the load from traffic on a bridge can also be considered as broadband random excitation, the authors used their decoupled model to estimate the response of a single vehicle traversing a bridge in the presence of loading to the bridge from many other vehicles.

Where both bridge and vehicle responses are sought, a number of authors have pursued uncoupled approaches where, generally, "equations of motion of bridge and vehicle are solved separately and equilibrium between both subsystems and geometric compatibility conditions are found through an iterative process" (González [203]). Relatively recent examples cited in the summary by González [203] include Green and Cebon [230], Zhu and Law [231], and Cantero et al. [232]. Feriani et al. [233] [234] also subsequently developed an uncoupled

approach which involved transfer of information (including road profile effects) between commercial FE software modelling the bridge and their own code modelling the vehicle. In more recent years computing power has been sufficient to entice researchers to pursue coupled simulations, examples of which are included below.

2.5.6 Numerical solutions

As increases in computing power began to allow numerical simulation of VBI in the mid-to-late 20th Century (González [203]), researchers initially sought simplified representations of the interaction in order to limit computational complexity. Condensation methods involve modelling the VBI "on an element level rather than on a global level" (González [203]). Garg and Dukkipati [235] (from Yang and Yau [236]) used the static condensation method to neglect the inertial terms in the vehicle equation of motion and condense the remaining vehicle DoFs to those of the bridge. Yang and Lin [237] (from Yang and Yau [236]) demonstrated the dynamic condensation method by comparison to solutions to a variety of moving load and moving mass problems as previously published by others. They developed a representation of a lumped mass vehicle model including suspension viscous damping and made it equivalent to a moving mass and moving load problem by alteration of parameters as required. However, Yang and Yau [236] report that these approaches did not adequately represent the vehicle response; to address this they considered a simply-supported beam bridge, traversed by a single DoF vehicle sprung mass model. Only the first bridge mode was considered. Contact separation between vehicle and bridge was not allowed. No damping was modelled for the vehicle or the bridge. Their approach was to discretise the vehicle equations of motion and then use the dynamic condensation method to express the vehicle equations in terms of the bridge equations for the element of the bridge in contact with the vehicle. The method allowed more efficient treatment of VBI problems when seeking a numerical approximation to the solution. The condensation method was further explored by Yang and Wu [238] who report the use of discretised vehicle equations of motion with the finite difference method. They explain that they related the contact forces between vehicle and bridge to the bridge displacement at the contact point. Disallowing contact separation between vehicle and bridge meant that they could calculate the vehicle and bridge responses without iteration. Their method was extended to include the effects of changes in contact forces parallel to the bridge deck, such as those caused by vehicle braking and acceleration.

It is also possible to model the interaction between vehicle(s) and bridge directly, and this approach has become dominant in recent years. Two variations to this approach are evident from the literature. The first entails updating the system matrices at each timestep and iteratively seeking a solution to contact force compatibility in a suitable numerical computing environment. This can require information to be passed between multiple software environments at each timestep. One example is the numerical study presented as part of the paper by Li et al. [239] where the coupled VBI equations were discretized and iteratively

solved using the *Newmark-beta* method. In recent years, this approach has been implemented by researchers utilising the *MATLAB* by MathWorks [240] environment and language (for example Lan [241]). Other algorithms to solve the iterative contact problem at each timestep are available; for example Prendergast et al. [242], Malekjafarian et al. [113] and Corbally and Malekjafarian [19] modelled VBI in MATLAB and made use of the Wilson-theta method to iteratively reach a solution. A variation to this approach involves co-simulation, in which the vehicle and bridge are modelled in separate environments and information regarding their interaction is passed back and forth. For example, Borjigin et al. modelled the bridge in *ABAQUS* by Dassault Systèmes Simulia [243] and the vehicle in MATLAB, making use of the Newmark-beta method for direct time integration [244]. However, the process of passing information between these software environments has been recognised as inefficient (Li and Feng [245]). The second approach is to model the whole VBI system in a Finite Element software environment and seek solutions by leveraging the built-in solver(s). The latter approach, using the software ABAQUS, is summarised by Lu et al. [246]. They report that train-bridge interaction was modelled using ABAQUS by Saleeb and Kumar [247] and Shih [248]. Gonzalez mentions methods based on the use of Lagrange multipliers and that an "advantage of this approach is the ease to accommodate it to a standard FE package" [203]; Lu et al. [246] report that Saleeb and Kumar [247] and Shih [248] made use of a built-in Lagrangian multiplier method to model contact interactions. This software environment offers advantages including automatic generation of system matrices, visual representations of system behaviour, and the ability to easily include in the analysis an allowance of contact separation between vehicle and bridge. The latter consideration is commonly neglected, but can affect the results of simulations (Cheng et al. [249]) and would otherwise require additional effort to implement a specific interaction model (for example Zhu et al. [250]). Lu et al. summarised the main advantages of modelling VBI directly in a single FE simulation environment as removing the need for "time-consuming coding and text-based inputting work" (Lu et al. [246]). An example of this being implemented is provided by Kildashti et al. [219] who modelled a three-dimensional cable-stay bridge structure using ABAQUS and explored its interaction with a quarter-car model. Their FE model was validated using data from field testing on the real bridge, which is located in New South Wales, Australia. Lu et al.'s publication [246] also demonstrated benchmarking against an SDoF VBI system originally presented by Yang and Yau [236]; modelling of a moving mass across a cracked simply-supported beam; and modelling of a multiple degree-of-freedom train model on a bridge including earthquake excitation and allowance for contact separation. Enthusiasm for the use of this specific software environment for modelling VBI is growing in recent years as evidenced by the literature. For example, very recently Abuodeh and Redmond [139] outline the development of a two-dimensional ABAQUS model for VBI and demonstrate benchmarking including a comparison to the results published by Yang et al. [118]. In the few literature examples of modelling coupled VBI within ABAQUS, the treatment of contact between the vehicle and bridge appears to depend on the dimension-

ality of the model. For example, Lu et al. [246] modelled the vehicle wheels as disks. Consequently they adopted a surface-to-surface contact formulation between wheel and bridge, using the penalty method which features virtual springs between the two contacting surfaces to reduce overclosure. On the other hand, Abuodeh and Redmond [139] and Kildashti et al. [219] represented the vehicle wheels as single points; they both consequently used the node-to-surface contact formulation provided by ABAQUS with a *hard* pressure-overclosure relationship, in which penetration of the node into the surface is minimised.

2.5.7 Road surface profile

In general, the numerical approach offers the advantage of allowing the road surface profile to be included in the simulation of VBI. Road profile-related effects have been identified as one of the major barriers to indirect vehicle-based bridge SHM (Malekjafarian et al. [25]). According to Abuodeh et al. [251] many researchers generate an equivalent road profile based on the ISO 8608 [7] road roughness class spectra. Examples of this include McGetrick et al. [252], Kortis et al. [253], Corbally and Malekjafarian [220], Feng et al. [254] and Aloisio et al. [255]). This profile is then used to generate additional displacement and velocity at the vehicle-bridge contact point which is included in the iterative procedure at each timestep. Zhang et al. proposed an approach for use within FE software [256] in which equivalent forces are applied. The approach has the advantage of not requiring the use of "very small elements in the FE modelling, as is the case with conventional approaches for simulating the irregularity in the profile of road surface roughness" [256] and was recently adopted by Demirlioglu et al. [257]. Abuodeh and Redmond also adopted the equivalent force approach to representing road surface roughness, finding it to be "accurate and simple" [139]. It has been noted that the vehicle's tyre radius and tyre deflection create a smoothing effect to the road roughness. To address this, some researchers opted to apply a moving average filter to the generated profile accordingly (González [203]). Such an approach was presented by Chang et al. who proposed modelling the vehicle wheel as a rigid disk, thereby addressing the spurious high frequency bridge and vehicle acceleration responses and under-emphasis of vehicle frequency in the vehicle acceleration response that are associated with modelling single-point contact [171].

2.6 Vehicle-based indirect Structural Health Monitoring

Since the idea was first suggested in 2004 by Yang et al. [118] the large number of publications illustrates the enthusiasm for the vehicle-based indirect SHM method. In addition to papers addressing specific issues, several broad-scope reviews have been published. The first comprehensive review was provided in 2015 by Malekjafarian et al. [25]. As the field developed rapidly, a further summary paper followed in 2018 from Yang and Yang [41]. Malekjafarian et al. [40] report that a subsequent review was provided in 2020 by Yang et al. [258]. Shokravi et al. [259] summarised the wider field of vehicle-assisted techniques relating to bridge SHM, including a short discussion specifically addressing bridge damage detection from sensors carried on passing vehicles. Updated reviews were provided in 2022 by Wang et al. [109] and Malekjafarian et al. [40]. Consideration of all of these papers together suggests that the majority of studies relevant to this thesis are covered by the two papers by Malekjafarian et al. [25] [40] with some interim developments summarised by Yang and Yang [41]. The summary presented here is based initially on the papers cited in these reviews, including in some cases the order in which they were cited when it relates directly to an obvious theme and/or is in chronological order, in addition to specific relevant examples from the other summaries noted above, and additional publications that have been identified during the review of the available literature. A summary of the development, achievements and challenges in the field of vehicle-based indirect bridge SHM is presented, with **focus on vehicle vibration-based monitoring for bridge damage detection**. Some additional attention is given to modal parameter estimation methods, since – as was the case for conventional direct SHM – this formed the basis of initial damage detection efforts. The review of bridge frequency extraction necessarily also discusses attempts to filter the acceleration response data. Following this, developments in non-modal damage sensitive features and machine learning techniques for pattern recognition and classification are reviewed, followed by an exploration of the emerging interest in crowdsourcing of sensor installation and data collection. The review concludes with a summary of the main confounders and challenges identified in the literature. It should be noted that the volume of literature in this field is large. The summary presented in this section does not intend to mention every paper, rather to establish the key trends and capabilities, show the general research avenues that have been pursued, highlight the current state-of-the-art and summarise the remaining challenges and possible next steps. Given the clear precedent from direct SHM (section 2.3) for changes in modal parameters to be adopted as damage indicators, the discussion below combines literature focused solely on estimating modal parameters with that explicitly pursuing damage detection.

2.6.1 Estimating bridge frequencies

As has been the case for direct SHM of bridges (see section 2.3), the exploration of bridge modal parameters as damage-sensitive features has been an important theme for the vehicle-based indirect approach. Although vehicle-bridge dynamic interaction had been studied for some time beforehand, as summarised in section 2.5, the idea of **extracting bridge frequencies from the vibration response of a passing vehicle** was first proposed in 2004 by Yang et al. [118]. The analytical study was predicated on the coupled interaction of the vehicle (modelled as a SDoF quarter-car) and the bridge (modelled as a simply-supported beam with only the fundamental mode contributing). They showed that the bridge frequency was present in the vehicle response spectrum, with an amplitude increasing as the vehicle traversal speed increased, and subject to an apparent shift, proportional to the ratio of the vehicle speed and the bridge span, of $\pm\pi v/L$ Hz. Yang and Lin [260] compared the closed-form analytical solution to a finite element numerical simulation and found good agreement, noting additionally that the visibility of the bridge frequency from the vehicle response spectrum was aided by omission of vehicle damping and the assumption of a perfectly smooth roadway surface. Lin and Yang [182] undertook a field test in which an accelerometer was mounted on a single-axle trailer towed by a moderate-sized vehicle, traversing a multi-span beam-type bridge in Taiwan. Considering a single one of the six 30 m spans, they explored the effect of vehicle speed and concurrent traffic (a heavy truck in convoy with the tractor-trailer sensing vehicle arrangement). Considering signal-to-noise ratio in terms of frequency spectrum peak height, they observed that the additional traffic load increased visibility of the bridge frequency, whilst the peak prominence was reduced at higher vehicle speeds due to the road surface roughness.

A number of other studies explored the factors contributing to **visibility of the bridge frequency peak in the vehicle response**. As noted above, Lin and Yang [182] found that higher speed reduced visibility due to the increasing effect of road surface roughness; this was a notable finding since it contrasted with Yang et al.'s prior suggestion [118] that higher speeds might increase visibility. Yang et al. [118] had also suggested that frequency matching between vehicle and bridge could increase visibility via resonance; future publications agreed (for example González et al. [261]). Although lower vehicle speeds reduced the unhelpful effects of road surface roughness, several authors noted that this also led to reduced bridge vibration, while faster vehicle speeds also increased bridge vibration amplitudes but also reduced vehicle-bridge interaction time with a corresponding reduction in frequency resolution. Malekjafarian et al. [25] report that in laboratory-scale experiments Kim et al. [262] and Toshinami et al. [263]) sought a balance between these competing demands, with Siringoringo and Fujino [185] employing a combination of simulations and field tests to the same end. The effect of damping has been studied, with McGetrick et al. [216] (from Malekjafarian et al. [25]) finding that increasing bridge damping reduced the magnitude of both the bridge frequency and the vehicle's own frequency in the vehicle response spectrum. González et al. agreed [261]. Vehicle mass

was found to be a factor, with Oshima et al. [264] (from Malekjafarian et al. [25]) agreeing with Lin and Yang's finding [182] that concurrent traversal by a heavy vehicle in convoy with the sensing vehicle was beneficial. The potential for bridge excitation prior to traversal by the sensing vehicle formed part of the parametric study presented by Yang [21] who concluded that the ratio of vehicle to bridge acceleration amplitude at the beginning of the traversal needed to be low to increase the likelihood of bridge frequency visibility from the vehicle response spectrum. Other than this parametric study and the preceding work by the same authors [118], further studies tended to use numerical methods to simulate VBI, since analytic extension of the bridge and vehicle models is precluded without additional assumptions (for example Shi and Uddin [265] who added damping to the analytical formulation, relying on the vehicle acceleration being less than the gravitational constant to enable decoupling of the equations of motion). The requirement to adopt numerical simulation to incorporate more sophisticated model abstractions and interaction effects is illustrated by citations provided by Malekjafarian et al. [40]: Yang's semi-analytical approach to the study of a three-DoF vehicle model [266], Yang and Wu's numerical simulation of the three-DoF vehicle interacting with a non-uniform beam [267], and studies relating incorporating vehicle pitching (Yang and Chen [268] and Yang and Sun [269]). Another option to improve the visibility of the bridge frequencies involves cross spectral analysis or coherence; Malekjafarian et al. [40] report that Lu et al. [270] and Lan et al. [271] both pursue this type of approach, noting that in the former case it is necessary to know the vehicle's frequencies beforehand.

Filtering and signal processing approaches have been pursued in support of increased bridge frequency visibility in the vehicle acceleration response spectrum. Oshima et al. [272] (from Malekjafarian et al. [25]) used Independent Component Analysis for their numerical study, but found it performed better for identifying road profile than it did for bridge response. Yang and Chang [212] employed empirical mode decomposition (EMD) to enhance the visibility of bridge frequencies from mode orders higher than the fundamental. They were able to detect the first and second frequencies of a bridge using this method applied to data from a field test. Yang and Lee's 2018 study [273] (from Yang and Yang [41]) numerically investigated the effect of vehicle damping and found that it improved visibility of the first bridge frequency using the EMD method in the presence of road roughness. Zhu and Malekjafarian [274] extended the method to an ensemble EMD approach, finding improved outcomes for slow vehicle speeds in their numerical study compared to the non-ensemble method, but noting that the outcomes were affected by user choices in how to apply the ensemble method. Yang et al. [275] used filtering techniques (frequency band-pass, singular spectrum analysis, and combinations thereof) in support of removing the vehicle's own frequencies from the vehicle response spectrum, to avoid confusion with bridge frequency peaks. According to Yang and Yang [41] the same group also explored stochastic subspace identification (Yang and Chen [276]) and wavelength effects (Yau et al. [277]) for the same overall aim. However, in 2017 when Hester and Gonzalez attempted to detect localised stiffness

loss from an axle acceleration record using the Continuous Wavelet Transform, they found the approach was confounded by road surface roughness effects, concluding that "there are a number of substantial challenges to be overcome before drive-by can be reliably implemented in the field" [278]. Malekjafarian and O'Brien [214] used frequency domain decomposition; Li et al. [279] (from Malekjafarian et al. [25]) adopted the Generalized Pattern Search Algorithm; and Tan et al. [280] employed the wavelet transform to assist with frequency identification from short-duration traversals, combined with the subtraction of responses from two axles to combat the effects of road roughness. Kim et al. [281] used changes in the frequency spectrum for damage identification and surface profile identification, using subtraction of spectra from two axle responses from a laboratory-scale experiment. Later, Tan and Uddin [282] (from Malekjafarian et al. [40]) used the Hilbert transform to address the short-duration problem and found that it outperformed the traditional fast Fourier transform (FFT).

Several researchers have attempted to recover an estimate of the **bridge vibration at the contact point** (CP) between vehicle and bridge, assuming that this will avoid the vehicle's frequencies obscuring bridge frequencies in the spectrum. Malekjafarian et al. [40] provide a summary of developments in this regard and insights, some of which are reproduced below. Yang et al. [283] proposed the idea, and Zhang et al. [284] noted that the CP response was nevertheless sensitive to road profile roughness. This appeared to inspire further developments; Yang et al. [285] added filtering by way of using Variational Mode Decomposition and a frequency band-pass filter, while Hashlamon et al. [286] applied the CP response method to a stationary vehicle in their numerical study. Nayek and Narasimhan [287] (from Malekjafarian et al. [40]) adopted a Gaussian process latent force model while Corbally and Malekjafarian [220] used assumed vehicle properties to recover an estimate of the CP response from multiple sensors on the vehicle. The residual response from two following axles, which was previously proposed (Kong et al. [288]) to mitigate road profile roughness was also employed for the CP response by Zhan et al. [289] (from Malekjafarian et al. [40]) who identified the first three bridge frequencies and mode shapes, in addition to damage locations (assisted by the use of the wavelet transform). One of the most successful demonstrations of bridge frequency extraction using the CP response was provided by Yang et al. [187] who used their custom-built single-axle trailer in stationary and moving states, recovering up to five bridge frequencies with the vehicle stationary and two when it was in motion along the span. They found that "perfect alignment" [187] was required between tractor and trailer to avoid yaw motion which apparently interfered with performance (it is assumed that the yawing frequency obscured some bridge frequencies in the response spectrum, but this does not appear to be clarified). Malekjafarian et al. [40] also summarise how Yang et al. [290] used the CP response combined with extreme-point symmetric mode decomposition to extract bridge frequencies, and Yang et al. [291] numerically demonstrated a method using two custom-built trailers designed with matching frequencies and damping ratios but different masses to mitigate the effects of road roughness

when the responses are combined.

During a traversal, the **vehicle and bridge can be considered as a time-varying combined dynamic system**. This means that the bridge frequencies differ to some degree from their original values when a vehicle is present. Yang et al. [9] presented a theoretical approach to predict frequency variation due to VBI, highlighting that this variation should be accounted for in studies of bridge damage detection (particularly for heavier vehicles and when vehicle and bridge frequencies were matched). Chang and Kim [22] agreed, presenting an analytical method which they investigated in field tests for a stationary vehicle. Cantero et al.'s field tests [11] and laboratory experiment [42] further demonstrated the phenomenon, with the authors concluding that "the responses are not only non-stationary, but also non-linear" [42] noting that such responses should be analysed in the hybrid time-frequency domain and calling for further studies to extend understanding and characterisation of frequency variation due to VBI. Further discussion is included in section 2.6.6.

2.6.2 Estimating bridge mode shapes

In the direct monitoring paradigm, bridge mode shape estimation has been pursued on the basis that it would support localisation of damage (Pandey [82] from Malekjafarian et al. [40], Roy and Ray-Chaudhuri [292]), thus fulfilling the second of Rytter's established SHM stages [31]. However, it has been recognised that the mode shapes estimated using output-only OMA methods will not be mass-normalised since the input excitation is not measured (Khatibi et al. [293] from Corbally and Malekjafarian [19]).

Zhang et al. [294] proposed a method of using changes in mode shape squares, extracted from the response of a passing vehicle to detect and localise damage. They employed a vehicle which imposed a harmonic load as it traversed the bridge in numerical models and laboratory-scale experiments. Following this, Zhang et al. [295] (from Malekjafarian et al. [25]) explored the use of operational deflected shape (ODS) curvature for damage detection and localisation, assuming that "the intact structure is smooth and homogenous". They found that the approach was sensitive to vehicle speed since it was linked to interaction time and thus to frequency resolution. ODSs are not mode shapes, but are similar. Corbally and Malekjafarian [19] also explored the ratio of ODS from each of two axles. Their approach was based on this ratio being "theoretically proven to be independent of the excitation level of the vehicle" [19]. Their publication included a laboratory-scale validation, in which damage was simulated by clamping additional masses onto the model bridge deck.

Yang et al. [296] proposed that bridge mode shapes could be estimated from the vibration response of a passing vehicle (without containing a harmonic exciter) as amplitude envelopes of the response at a frequency range associated with the bridge mode. Similar approaches using the Hilbert transform were reported by Malekjafarian et al. [40] to have been demonstrated by Tan et al. [137] and [297].

Oshima et al. [215] studied global detection of damage by comparing mode

shapes, using changes in the MAC as a damage metric; however they found the approach was not robust against noise.

Malekjafarian et al. [298] (from Malekjafarian et al. [40]) report a numerical investigation where bridge first and second mode shapes were estimated from the residual acceleration response of two following axles, considering the effects of road surface roughness and concurrent traffic.

In 2015, Malekjafarian et al. felt that damage detection methods based on mode shapes estimated from vehicle vibration response data needed to be "improved considerably" [25]. Since then, a number of theoretical and practical studies have attempted to address this gap. The same year, O'Brien and Malekjafarian [299] produced a numerical study in which subtracted axle responses were used to estimate the first two bridge mode shapes, subject to vehicle speed being below 4 m/s. Subtracted responses proved to be a popular approach to road profile mitigation. Kong et al. [288] presented a numerical study in which bridge mode shapes were estimated from the residual response of two trailers towed by the same vehicle. They found that the estimates improved when they also modelled concurrent background traffic. O'Brien and Malekjafarian [300] also adopted the following axle subtraction approach and demonstrated damage detection and (with partial success) localisation using mode shape squares for vehicle speeds up to 8 m/s in a numerical study. The data were collected from a laser sensor mounted on the vehicle. Malekjafarian and O'Brien's 2017 study [301] also adopted a method based on the Hilbert Huang transform for mode shape estimation, again using the subtracted response from two axles. It should be noted that Yang et al.'s proposed use of two custom-built trailers [291] appears – at least in their numerical proof-of-concept study – to mitigate road roughness to assist with estimation of mode shapes. The use of specially-made trailers is an area of interest for the group; later Yang et al. [45] use a single custom-built trailer in a field test to extract four mode shapes which compare favourably with references based on direct monitoring; however, this required the trailer to be parked stationary on the bridge.

As for frequency estimation, the CP response has been utilised for mode shape estimation. Malekjafarian et al. [40] report that Zhan and Au [302] proposed to combine the signals collected from two passes of a vehicle with non-identical mass between the passes; they found this mitigated the effects of road roughness and allowed estimation of mode shapes and localisation of damage, and that Yang et al. [303] recently pursued a similar approach with a single two-axle vehicle. Zhan et al.'s publication [289] (from Malekjafarian et al. [40]) included outputs from a laboratory-scale model; using the same treatment of the CP response they managed to extract estimates of three bridge frequencies and associated mode shapes, in addition to damage locations. Li et al. [304] also utilise the CP response for mode shape estimation; a unique aspect of their laboratory-verified approach is the use of a dual Kalman filter to estimate the two vehicle forces, from which the two CP responses are derived using vehicle parameters, the difference between which is then used for the same road profile mitigation reasons as seen in previous works.

Established direct sensing methods require many sensors in order to estimate

mode shapes [305]. In contrast, one important aspect of the drive-by vehicle approach is that the vehicle covers the whole length of a bridge span. This means that vibration responses relate only to the location of the vehicle at a specific time. Sadeghi Eshkevari et al. [39] treated such responses as a sparse representation of an array of virtual sensor locations. Adopting matrix completion methods to impute missing values, they showed that the result could be seen as the product of a "spatial matrix and a temporal matrix from which modal properties can be extracted" [39]. They were able to estimate frequencies, damping ratios and high-resolution mode shapes from a numerical study. Mei et al. [306] also adopt a matrix completion approach to mode shape estimation, based on non-parametric soft imputing for missing values.

2.6.3 Estimating bridge damping

Structural damping change has been identified as potentially indicative of the presence of bridge damage (for example Modena et al. [307], Curadelli et al. [308]), although it is difficult to quantify, "even using direct instrumentation" (Malekjafarian et al. [40]). Nevertheless, some numerical simulations suggested **damping change as a damage indicator** could be suited to the vehicle-based indirect approach (McGetrick et al. [216], Keenahan et al. [309]); laboratory validation followed, with the first investigations focused on detection of directional change. McGetrick et al. [310] and Kim et al. [311] (both from Malekjafarian et al. [25]) used repeated bridge crossings at three vehicle speeds in a laboratory-scale experiment and found that they could detect changes in bridge damping in the vehicle frequency response spectrum. González et al. [261] found that increases in bridge damping led to decreased magnitudes in the vehicle response frequency spectrum, but added that visibility of this effect was hampered by increased road surface roughness. Keenahan et al.'s study [309] found that quarter-car models were less sensitive to changes in bridge damping in the presence of increased road roughness, but that half-car models could be used to mitigate this to some extent by studying a residual response comprised of subtracting time-shifted front and rear axle responses.

Later studies attempted to identify the bridge damping ratio. González et al. [312] undertook a numerical study in which a two-axle vehicle was modelled; their approach comprised identifying which bridge damping ratio minimised the difference in estimated road profile between the two axle responses. Keenahan et al. [313] (from Malekjafarian et al. [25] adopted the approach of subtraction of response from two following axles; their numerical study found it was feasible to detect damping changes from the residual vehicle acceleration response, but that successful outcomes were dependent on the axle properties being similar. Sadeghi Eshkevari et al.'s matrix completion method [39], discussed above for mode shape estimation based on a sparse representation of bridge response also inherently estimates bridge damping as well as modal frequencies. Yang et al. [314] propose a combination of variational mode decomposition, random decrement technique and Hilbert transform to estimate bridge frequencies and associated damping ratios. In a subsequent publication [45] they demonstrate the

application of this technique to field-gathered data from a purpose-built sensor-carrying trailer. Notably, they avoid confusion of bridge and vehicle frequencies in the response spectrum by designing the vehicle so that its frequencies are higher than 20 Hz, and avoid the influence of road surface roughness by gathering data when the vehicle is parked stationary on the bridge. Bridge- and vehicle-mounted sensors show good agreement in estimating modal frequencies, mode shapes and damping ratios for two flexural and two torsional modes. The purpose-built trailer can be considered as a development of earlier work by Yang et al. [315] in which they tested a hand-drawn trailer cart as a sensor carrier, exploring construction issues including tyres in relation to the cart's own modal parameters.

2.6.4 Non-modal damage-sensitive features and Machine Learning

Several studies have suggested specific non-modal damage sensitive features, often in conjunction with a specific signal processing approach. With selected illustrative examples reproduced in the list below from those reported in the reviews by Malekjafarian et al. [25] [40], and Yang and Yang [41], these have included:

- Several studies have involved bespoke sensing vehicles fitted with velocity-measuring laser sensors also known as traffic speed deflectometers (for example Keenahan and O'Brien [316], O'Brien and Keenahan [317], Malekjafarian et al. [318])
- Some non-modal damage-sensitive signal features have been produced using signal processing techniques such as EMD or similar (for example O'Brien et al. [136], Kildashti et al. [219])
- Some studies pursued damage identification via force, flexural rigidity or strain estimation (for example Yin and Tang [319], Li and Au [320], O'Brien et al. [321], Martinez et al. [322], Hasegawa et al. [323], Hasegawa and Yano et al. [324])
- Some studies pursued other avenues, such as using vibration frequency spectra (Cerda et al. [325]), transmissibility estimates (Kong et al. [326]) or instantaneous amplitude squared (Zhang et al. [284]) as damage-sensitive features
- Several studies pursued estimation of road profiles and sought correlation of estimates with damage (Elhattab et al. [147], Yang et al. [327], Keenahan et al. [328], O'Brien et al. [329])
- One of the more popular non-modal damage-sensitive features appeared to be those based on wavelets, which are a type of time-frequency signal representation and "a means of amplifying particular features, such as discontinuities in a signal and do not need long time series for good results"

(Malekjafarian et al. [25]) but are subject to edge effects at the beginning and end of the bridge traversal [25]. Examples include Bu et al. [330], Kim and Kawatani [331], McGetrick [332], Nguyen and Tran [333], Khorram et al. [334] McGetrick and Kim [335], [336], Hester and Gonzalez [278] and Liu et al. [337]

The general trend within recent years, however, has been towards Machine Learning (ML) approaches when considering non-modal damage identification. This is assumed to be motivated by the potential for machine learning to assist with automatic identification of features while also offering the possibility of normalising environmental and operational variation given sufficient suitable data (Malekjafarian et al. [40]). Malekjafarian et al. report that the application of ML to vehicle-based indirect bridge SHM is "relatively unexplored" [40], but nevertheless examples are found in the literature. According to Malekjafarian et al. [40] one of the earliest examples of a machine learning-based approach to the use of vibration response data from vehicle-mounted sensors was Cerda et al. [338] who used labelled frequency features to train a support vector machine classifier. The experiment was extended by Lederman et al. [339] (from Malekjafarian et al. [40]); using the same model, they selected features using Principal Component Analysis and used regression to explore the relationship between these and damage. Chen et al. [340] also adopted a classification-based approach, related to wavelets and aiming to extract "hidden features in localized time-frequency regions". These early applications summarise some key paradigms in supervised machine learning. Where labelled data are available, classification methods can for example be trained to determine whether new data is likely to relate to a healthy or damaged bridge. Regression can be used to understand the relationship between data or extracted features, which may be particularly useful when environmental condition data is available alongside bridge responses.

Another approach that has proved popular is the artificial neural network (ANN), which can be adapted to learn how to map various types of input data to outputs such as distinct classes or continuous variables. Consisting of input and output layers either side of some number of interconnected hidden layers, in the *supervised learning* paradigm ANNs are automatically trained to minimise an objective function describing the mapping of a set of input data to labelled output targets. Examples of the use of ANNs for vehicle-based indirect bridge SHM include Malekjafarian et al. [113] [114] who train the ANN to predict vehicle response based on traversals of a healthy bridge, and use the difference between prediction and observation when traversing a damaged bridge as a damage indication metric. The work was extended by Corbally and Malekjafarian to include mitigation of the effects of temperature, vehicle speed and road roughness, alongside the use of the CP response [115]; comparison of damage represented by changing bridge support conditions and midspan cracking [341]; and detection of simultaneous midspan cracking and support condition change [342].

A limitation of ANNs is that they take their input data in a vector form.

This is addressed by the convolutional neural network (CNN) architecture which takes higher-dimensional inputs and uses a number of layer operations to reduce the dimensionality so that input-output patterns can be learned as for the ANN paradigm. Examples of the use of CNNs include Locke et al. [148] and Sarwar and Cantero [343] who used CNNs in combination with Autoencoders, in which the input data is compressed to a reduced-dimension *latent space*, from which the encoding can be reversed as a decoder to produce an estimate of the original input. Liu et al. [344] [345] and Li et al. [346] provide further examples of the use of autoencoders. Hajializadeh [347] [348] [117] also employed the CNN architecture for indirect bridge SHM, although in relation to instrumented trains rather than road vehicles.

Research into the application of ML to indirect vehicle-based SHM continues and some very recent examples illustrate current trends and avenues of exploration. Sarwar and Cantero [108] pursued a hybrid approach, combining vehicle response data with direct monitoring data in a probabilistic deep neural network. They found that this enabled "a more reliable damage assessment" but that "random traffic on the bridge adversely affects the ability of the proposed method to detect and localise the damage, when only vehicle sensors are used" [108] highlighting the ongoing challenges faced in relation to EOV. The bespoke nature of bridges also remains a challenge, with some researchers (for example Liu et al. [349]) beginning to explore aspects relating to *transfer learning* in which ML methods trained on data from one bridge can be used for damage detection on another.

2.6.5 Smart devices and crowdsourcing

Other than ML, the major trend to emerge very recently is an interest in crowdsourcing for vehicle response data acquisition. It is broadly agreed that, while there are examples of in-field validation of specific proposed methods, there are very few field tests of indirect vehicle-based SHM in operation (Malekjafarian et al. [25] [40], Shokravi et al. [259]). Crowdsourcing may yet become an exception to this generalisation; having only recently emerged as an area of interest, some of the studies discussed below feature field tests (perhaps most notably Matarazzo and Kondor et al. [43] due to the scale of their study). The concept of crowdsourcing (a "collaborative problem-solving process" according to Ozer et al. [350]) is that the provision and maintenance of the sensor network is outsourced to citizens (where the sensors are built-in to their vehicle or smart devices such as mobile phones), or to companies (such as transport providers, where the sensors might be carried on or built-in to buses, for example).

The first example of the crowdsourcing approach applied to bridge monitoring using vehicles appears to be Miyamoto and Yabe [183] [184] (both from Malekjafarian et al. [25]) who compared the characteristic deflection (based on acceleration responses) in a field experiment, comparing a sensor on the rear axle of a public bus to a sensor on the bridge at midspan. The outcomes from the vehicle-mounted sensor compared favourably with those from direct on-bridge measurement, on the basis of using the same bus for each traversal. The follow-

ing work by the same authors [351] (from Malekjafarian et al. [25]) considered the effects of EOV. Lan et al. [352] similarly report field experiments based on the use of a city bus. They suggest an approach leveraging coherence of frequencies from multiple traversals to estimate bridge frequencies. The approach acknowledges and even "encourages the introduction of variability in drive-by measurements" [352]. Very recently, O'Brien et al. [149] presented a concept for which they explicitly claimed that prior knowledge of bridge and individual properties was not required. This is particularly notable since most other studies appear to implicitly require prior knowledge of bridge properties to allow disambiguation between bridge-, vehicle- and road surface-related aspects of the data. Assuming knowledge only of mean vehicle properties (for example, from a fleet of vehicles under the control of a common operating authority) they pursued visibility of bridge bearing damage through differences in apparent road profile under each wheel, leading to a "special case of the moving reference influence function (MRIF)" [149] (which they note was introduced in previous work by O'Brien et al. [353]), changes in which are adopted as indicators of damage. O'Brien is reported as saying that fleet-based monitoring has "great potential" but that full-scale field tests are required (Gkoumas et al. [354]).

The use of smartphones is growing worldwide, "arguably becoming the ubiquitous appendage to humanity" (Miller et al. [355]), or is at least "ubiquitous in urban environments around the world" (Kong et al. [356]). Smartphones contain accelerometers and in recent years, community engagement has been encouraged to utilise these as low-cost distributed crowdsourcing networks for applications including monitoring seismic activity (Reilly et al. [357], Kong et al. [356]) and finding potholes in city streets (Mednis et al. [358]). Even more recently, attention has turned to the potential for a distributed sensing network for vehicle-based indirect bridge SHM. In 2018, Matarazzo et al. [359] reported being able to identify the first three bridge frequencies in field data gathered from a smartphone accelerometer. In their study, smartphones were placed on the vehicle dashboard. They combined data (power spectral densities estimated using Welch's method [360]) from forty-two traversals between two vehicles, each containing two smartphones, at slow speeds in commuting traffic. Their study investigated the proposed concept that "bridge resonant frequencies will have a persistent presence in the vehicle trips, despite data heterogeneity" [359], and was thought to benefit from having been conducted in suitable conditions; they did not explicitly account for effects of vehicle suspension characteristics, vehicle speed, concurrent traffic or road surface profile.

The nature of crowdsourcing means that it is suited to ensembles of vehicles, even if they do not come from a single unified fleet. In 2020 Sadeghi Eshkevari et al. [361] compared two methods for deconvolving vehicle and bridge-related signals in the frequency domain: first using an estimation of the vehicle's transmissibility FRF; the second being ensemble EMD, which is an already-established method by Huang et al. [362] (from Sadeghi Eshkevari et al. [361]). Following this, they remove road profile effects using a blind source separation method (previously explored by some of the same authors: Sadeghi Eshkevari and Pakzad [363] from Sadeghi Eshkevari et al. [361]) and

estimate bridge modal properties using an expectation maximisation approach which they note was proposed by Matarazzo and Pakzad [364]. In this numerical study they were able to identify the first four bridge modes (frequencies, mode shapes and damping rations) from the vehicle responses, with generally good accuracy, although in some situations the FRF-based approach seemed to yield greater accuracy. They note that their vehicle FRF is based on assumed vehicle properties and that it would be better to use true values if these were available.

Road profile effects have been identified as a confounder to vehicle-based indirect SHM as previously discussed. Sadeghi Eshkevari and Pakzad [363] reported an initial numerical study into using a blind source separation technique to distinguish between road profile- and bridge-related frequencies from a vehicle-mounted accelerometer response. Sadeghi Eshkevari et al. [138] also explored VBI modelling techniques, arguing that as bridge span increased so (typically) would flexibility and the number of concurrent vehicles on the bridge, leading to a reduction in direct coupling between the response of the bridge and that of any one vehicle. Comparing simulation techniques in their numerical study, they proposed that background traffic could be modelled as a spatially and temporally random *white noise* load, suggesting that this might prove helpful for simulation of crowdsensing-based approaches. In a related study, the author (May [365]) explored the concept that the relationship between bridge span and response coupling between bridge and individual vehicle dynamic response might indicate the existence of an optimum condition for indirect vehicle-based bridge SHM. The numerical study simulated multiple concurrent vehicle traversals, comparing damage detection from vehicle- and bridge-mounted sensors. Vehicle distributions were modelled spatially using a discrete Poisson process, with vehicle dynamic properties selected at random from assumed underlying population distributions. Different traffic densities and speeds were considered, and neural networks were trained to predict the bridge health status as a binary classification. As an exploratory study, it aimed to question whether some traffic states might be more or less amenable to vehicle-based indirect bridge SHM.

Field tests have also reported positive outcomes for crowdsourcing approaches using mobile phones. In 2022 Matarazzo and Kondor et al. [43] reported identification of bridge frequencies from the Golden Gate Bridge in California, United States and from a short-span highway bridge in Ciampino, Italy. They combined acceleration responses from smartphones on the dashboards of traversing cars, in a data processing pipeline that comprised calculating the synchrosqueezed wavelet transform for each traversal record, then estimating an empirical probability distribution across a histogram of the ensemble of wavelet ridges using kernel density estimation (KDE). They noted that accuracy could be improved by consideration of aspects such as "smartphone mount, vehicle model, roadway type, etc., and vehicle dynamical properties" [43]. A variety of vehicle speeds were included and traffic conditions were recorded, but only using a subjective scale. The data from controlled experiments were combined with uncontrolled data from taxi trips in the case of the Golden Gate Bridge. Nevertheless, they

found that as the number of traversals in the data set increased, the error in estimated bridge frequencies decreased.

Mei et al. [366] undertook numerical simulations and laboratory-scale experiments, proposing a novel damage-sensitive signal feature: Mel-frequency cepstral coefficients (MFCC), derived in part from the field of audio processing. They found these features to be sensitive to damage, but also to changes in vehicle dynamic properties and speed. To address this, they considered data from multiple vehicles and transformed the MFCCs using principal component analysis (PCA); damage detection in this ensemble case was based on changes in the distribution of these transformed features. The Euclidean distance (between the means of features relating to data from baseline and damaged states) was used as an indicator of damage severity. Contemporary publications by Mei and Gül [110] [367] appear to relate to the same experimental setup and general methodology. In subsequent work, Mei et al. [44] proposed that combined responses from multiple vehicles could be used to create baseline and testing data sets, with changes in the distribution of transformed signal features used as an indicator of damage. They felt that ensemble data from multiple different vehicles and operational conditions could mitigate EOV effects relating to vehicle types and configurations, and demonstrated the approach using a laboratory-scale experiment in which their vehicle model's mass, suspension spring stiffness and traversal speed were varied. Other work from the same research group includes Shirzad-Ghaleroudkhani et al. [368] who presented outcomes of a laboratory-scale VBI model in which the bridge support conditions, vehicle suspension stiffness and traversal speed were varied. A smartphone was mounted on the model vehicle and Welch's method [360] was used to estimate frequency spectra. Changes in the bridge frequency were detectable, however they noted that the combined properties of the vehicle and bridge during their interaction affected how much the extracted bridge frequencies were shifted and that this phenomenon was not yet fully characterised. Shirzad-Ghaleroudkhani and Gül [190] also presented a field test on two bridges in Edmonton, Canada. Their methodology was also in part based on audio processing; it employed an inverse filtering technique to remove non-transient frequencies on the assumption that the vehicle's own frequencies and those related to the road profile would be relatively persistent during a vehicle journey, while the bridge frequencies would be transient parts of the signal, relating only to the on-bridge portion of each trip. Only the first bridge mode was extracted, but the frequency and mode shape were retrieved. The use of smartphones as sensors in this study, and the field test in operational traffic, mean that it is directly applicable to the crowdsourcing paradigm. Another study by Singh and Sadhu [193] used a wavelet-derived transform to yield a high-resolution time-frequency representation of the vehicle-mounted accelerometers, and was field tested on a real bridge in London, Ontario, Canada. Three bridge frequencies were extracted. Although the experiment used traditional wired sensors and a laptop computer within the car, they speculated that it could be extended in the future to use smartphones as sensors.

Some additional novel approaches have also been suggested in recent litera-

ture. For example, Gkoumas et al. [35] anticipate that connected autonomous vehicles will play a role in the vehicle-based indirect bridge SHM landscape of the future. Other researchers suggest that human-powered vehicles could also be utilised for bridge parameter estimation and damage detection. Quqa et al. [369] present a study in which smartphones attached to bicycles were used to estimate the first modal frequency and absolute mode shape of a footbridge in Bologna, Italy. Their method required prior knowledge of the bridge frequency in order to apply a band-pass filter to the vertical acceleration responses gathered from the smartphone accelerometer. They also applied an extended Kalman filter to fuse GPS data with other (non-vertical) acceleration data from the smartphone, aiming to determine the bicycle's movement along or across the bridge deck and thus associate estimated modal parameters with the specific path taken by the bicycle in each traversal. Shortly afterward, work by the author (May et al. [370]) explored the potential for the use of bicycles as combined exciters and sensor carriers for bridge modal parameter estimation. The field-tested approach sought to compare the visibility of bridge frequencies in the bicycle-mounted accelerometer response spectrum in freewheeling and pedalling modes of operation. Concurrent sensing on the bicycle and bridge deck were used to disambiguate between bridge and vehicle frequencies. Other small-scale vehicles have also been investigated. For example, Li et al. [371] presented a numerical study of bridge frequency extraction from an accelerometer mounted on an electric scooter. The CP response was adopted, meaning that future field validations would rely on accurate knowledge of a representative vehicle dynamic model.

2.6.6 Frequency variation due to VBI

It has been recognised that bridge and vehicle modal parameters vary during VBI and some researchers have investigated the phenomenon. Cantieni's 1992 study [372] sought to simplify the vehicle-bridge system to a two degree-of-freedom representation and reported that the presence of the vehicle caused changes to the bridge frequency of up to 0.7 Hz when the vehicle was modelled as a sprung mass. Studying the same system with the vehicle represented as a lumped unsprung mass, they reported frequency changes of 0.06 Hz; in other words, both the mass and the suspension spring of the studied vehicle affected the combined vehicle-bridge system frequencies, with the consideration of the spring increasing the observed frequency change by an order of magnitude. Kim et al. [373] used field testing to compare the observed dynamic responses of a short-, medium- and long-span bridge, subject to traversal by light and heavy vehicles. This approach allowed them to vary the vehicle-to-bridge mass ratio by changing both vehicle type and bridge length. They found that the vehicle-to-bridge mass ratio was a determining factor; when this was close to zero (they reported 0.38%) the bridge response did not change significantly, but with a mass ratio of 3.8% caused a reduction in bridge frequency of 5.4%. Vehicle speed was generally constant, with "almost all" [373] of the vehicles traversing the bridge at the same speed. Cantero et al. [42] report that Kwon et al. [374]

employed a numerical modelling approach and found that the bridge damping changed during the passage of a vehicle.

Yang et al. describe their 2013 study [9] in which variation in frequency during the vehicle traversal was investigated. They developed a theoretical framework for a single-mode beam bridge interacting with an SDoF vehicle model. Assuming no damping for the vehicle or the bridge, the interacting system was described analytically. They expressed the coupled vehicle and bridge system frequencies ω as functions of vehicle position on the bridge span (x_c/L) and vehicle and bridge non-interacting frequencies ω_{v0} and ω_{b0} respectively according to equation (2.14):

$$\begin{aligned}\omega^2 =& \frac{\omega_{v0}^2}{2} + \frac{\omega_{b0}^2}{2} + \frac{m_v\omega_{v0}^2}{m_b}\sin^2\left(\frac{\pi x_c}{L}\right) \\ &\pm \sqrt{\left(\frac{\omega_{v0}^2}{2} + \frac{\omega_{b0}^2}{2} + \frac{m_v\omega_{v0}^2}{m_b}\sin^2\left(\frac{\pi x_c}{L}\right)\right)^2 - \omega_{v0}^2\omega_{b0}^2}\end{aligned} \tag{2.14}$$

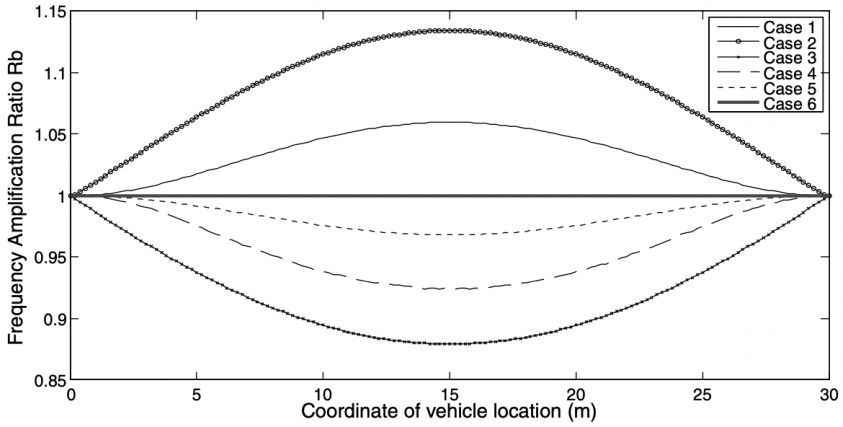

Figure 2.6.1: Analytically-predicted variation in bridge first mode frequency as a function of vehicle position, reproduced from Yang et al. [9].

Adopting their definition of the frequency amplification ratio for the bridge as $R_b \equiv \omega_b/\omega_{b0}$, Fig. 2.6.1 shows the key outcomes of the study as summarised by Yang et al. [9] for 6 hypothetical cases. They noted an increase in the apparent bridge mode 1 frequency ω_b when the bridge uncoupled frequency ω_{b0} is greater than that of the vehicle ω_{v0} (cases 1 and 2). Conversely, when the bridge uncoupled frequency is lower than that of the vehicle, the apparent bridge frequency decreases (cases 3 and 4). For a very stiff vehicle suspension (case 5, implying $\omega_{v0} >> \omega_{b0}$) they noted a decrease in apparent bridge frequency, and when the vehicle's inertia was not modelled (case 6) they noted a reversal

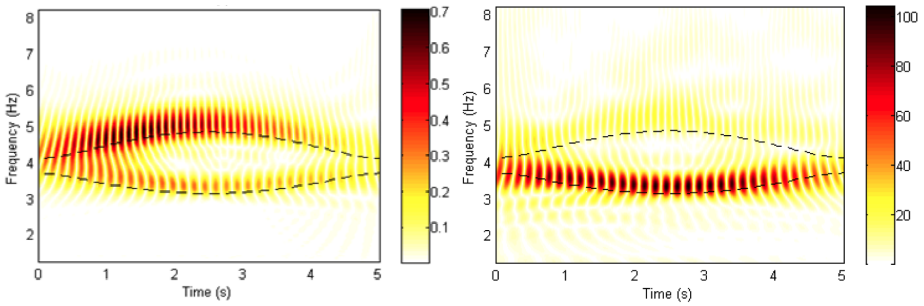

Figure 2.6.2: Frequency evolution: SDoF vehicle traversing a smooth (left) and ISO 8608 class A (right) beam. Reproduced from Cantero et al. [10]

of the trend from cases 1–4 (i.e. an apparent bridge frequency decrease when $\omega_{v0} < \omega_{b0}$ and an increase when $\omega_{v0} > \omega_{b0}$). From this investigation it can be concluded that the vehicle's mass and the vehicle-to-bridge frequency ratio both affect the bridge frequency observed during traversal. However, the study only considered a single mode bridge and vehicle model.

Also in 2013, Cantero and O'Brien [10] used numerical simulation to study the variation of frequency during VBI for a simply-supported beam bridge traversed by an SDoF vehicle. They pursued a hybrid time-frequency domain visualisation of the acceleration response of both bridge and vehicle by means of a continuous wavelet transform (CWT). They found that the frequency variation was visible when adopting a *modified Littlewood-Paley* basis wavelet, and that the trends were generally in accordance with the analytical results reported by Yang et al. [9]. They also investigated the effect of a simulated non-smooth bridge deck surface, adopting an ISO 8608 class A profile. Fig. 2.6.2 illustrates the comparison of frequency variation visible from the CWT approach in smooth and profiled surface simulations, with the expected variation based on the eigenvalue analysis indicated by a dashed line. It is noteworthy that in both cases the CWT is based on the acceleration signal from the vehicle; in other words, the vehicle-based notional acceleration sensor is able to capture both of the system frequencies, and the visibility appears to be slightly improved by the presence of a non-smooth surface. Their study investigated only one vehicle traversal speed (5 m/s) and only one mode of vibration each for the vehicle and bridge, although they stated that frequency shifts could also occur for higher modes of the bridge and for proximity of bridge frequencies to other vehicle frequencies.

Chang et al. [22] report the outcomes of a laboratory-scale and field test of a stationary vehicle parked on a bridge and present an analytical formula describing the variation of bridge frequency induced by the presence of the stationary vehicle. Reproduced here as equation (2.15) it treats the vehicle and bridge each as an SDoF system and expresses the combined system frequencies ω_i in terms of the vehicle-to-bridge frequency ratio β and mass ratio μ. The

frequency shifts due to the presence of the parked vehicle observed in both experiments were within 3% of those predicted by the formula. Inspection of the plotted results suggests that frequency shifts predicted and observed were approximately proportional to μ for $\mu > 0.05$, and with respect to β were largest when $\beta \to 1$.

$$\omega^2 = \omega_{b0}^2 \frac{1}{2}\left[1 + \beta^2 + \mu\beta^2 \pm \sqrt{(1 + \beta^2 + \mu\beta^2)^2 - 4\beta^2}\right] \tag{2.15}$$

In 2014, Westgate et al. [375] reported a study relating to the traversal of an exceptional load across a suspension bridge (the Tamar Suspension Bridge). The vehicle-to-bridge mass ratio was in excess of 8%. Responses captured by accelerometers on the bridge deck were corrupted, but they were able to study the change in deck frequency using an FE model. These changes were found to be "substantial" [375] with changes in the range of +4.8% to −7.2% for the first 6 modes of the bridge, depending on the position of the added mass with the varying direction of change being attributed to interplay between changes to the bridge's effective mass and changes to cable tension induced by the added mass. The largest changes were associated with the added mass being located at the anti-node (maximum displacement) location for each mode shape.

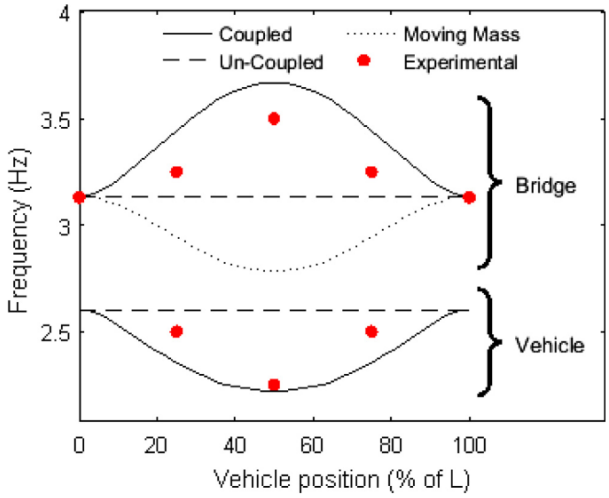

Figure 2.6.3: Experimental and numerical frequency variation for an SDoF vehicle interacting with a bridge. Reproduced from Cantero et al. [11].

Cantero et al.'s 2017 study [11] investigated the effect of vehicle traversal on bridge mode shape based on field testing and a numerical model. They noted that changes to coupled system dynamic properties during vehicle-bridge interaction were generally acknowledged but little studied. In their investigation, one speed of vehicle traversal (3.63 m/s) was considered. Considering only the first mode of vibration of the bridge and of the vehicle, they found that the bridge

mode shape was skewed according to the position of the vehicle. Additionally, the bridge first mode frequency decreased due to the presence of an added mass, but increased due to the presence of an added sprung mass as illustrated in Fig. 2.6.3.

More recently, Cantero et al.'s experimental study [42] aimed to empirically demonstrate that the change of frequency during VBI depends on the suspension properties of the vehicle (in addition to the added mass of the vehicle). Utilising a laboratory-scale model of a two-axle vehicle traversing a beam bridge and an associated FE model, they demonstrated that the change in the bridge's first modal frequency depended on both the vehicle-to-bridge mass ratio and frequency ratio. As in their prior work [11] they represented the evolution of frequency through a CWT and found that the Modified Littlewood-Paley basis wavelet (as introduced by Basu and Gupta [376]) was effective for this purpose compared to several tested alternatives.

2.6.7 Confounders and challenges

In 2015, Malekjafarian et al. [25] suggested that the main challenges were the road roughness profile; limited interaction time; and environmental effects. In 2022, an updated review paper from the same research group [40] confirmed that effects of the road roughness profile were still challenging despite progress that had been made towards their mitigation. They confirmed that environmental variation was still a challenge, but anticipated that crowdsourcing and machine learning approaches would assist in this regard. They suggested that long-term field testing of indirect vehicle-based SHM should be undertaken on bridges that were also instrumented with sensors for traditional direct SHM, in order to demonstrate the efficacy of vehicle-based indirect methods to improve uptake for bridge owners and operators. Finally, they suggested that alternatives to vibration-based monitoring should be developed for vehicle-based SHM, such as static response techniques or integrating data from cameras on vehicles, to suit different bridge types alongside the anticipated increase in autonomous and instrumented vehicles.

In 2018 Yang and Yang [41] agreed that road surface roughness was a confounder, noting that the point contact assumption in modelling led to spurious high-frequency content in the vehicle response. In general, they noted approaches presented in the literature to mitigate the effects of road surface roughness included empirical mode decomposition; data fusion from the responses of two vehicles; filtering; vehicle damping; and concurrent background traffic to increase the amplitude of bridge motion relative to the effect of the road surface on the vehicle. They highlighted that studies to date had generally been based on a SDoF quarter-car model, noting that the vehicle's kinematics, suspension and other properties contributed to the signal (bridge vibration) as received by the sensor in the vehicle. To that end, they recommended consideration of the "path of transmission" [41] which can be understood as a noting that the vehicle's kinematics form a filter through which the bridge response is viewed. They concluded by highlighting challenges in accurate laboratory-

scale modelling of VBI and lack of field testing, in both cases due to difficulties in finding or creating vehicles with characteristics accurately matching those modelled numerically in prior work.

> **"There is a long way to go before reaching a desired level of accuracy, and robustness for vehicle-assisted bridge SHM."**
> (Shokravi et al. [259])

Shokravi et al.'s 2020 summary [259] noted high cost and susceptibility to errors for some vehicle-based methods, but in this regard they referred mainly to camera-based methods. Regarding vibration-based vehicle methods, they summarised that successes were "mainly limited to bridge frequency identification under controlled conditions", adding that there was a lack of both field tests and "comprehensive experimental verification" [259]. They agreed that road profile, vehicle speed (i.e. limited interaction time) and environmental factors were the main challenges, adding that VBI modelling did not sufficiently account for vehicle dynamics and the interaction of vehicle and bridge. The quote reproduced above suggests that they were sceptical of the maturity of the field at the time of writing.

Wang et al.'s 2022 summary [109] confirmed their agreement that surface profile roughness and vehicle speed are serious confounders to the indirect vehicle-based approach; and that there was a lack of field testing. They advocated for increasing sophistication of vehicle models (i.e. beyond the SDoF quarter-car); consideration of a wider variety of bridge structure types (i.e. other than beam or girder bridges); and for further research and testing validation for the use of smartphones and similar devices as data gathering nodes in the crowdsourcing paradigm.

Malekjafarian et al.'s 2022 review [40] echoes their comments from 2015 regarding the challenges of limited interaction time, road surface roughness profile and environmental variation, noting that demonstrations of extracting bridge frequencies, mode shapes and modal damping ratios "are often in ideal conditions" [40]. They highlight the need for sufficient amplitude of bridge motion to overcome signal-to-noise limitations, suggesting that for shorter and stiffer bridges this requires higher vehicle mass, for example heavy goods vehicles or buses. They also note that signal pollution from vehicle engine vibrations has not been studied in detail. They suggest that the main barriers to be overcome to achieve success for vehicle-based bridge SHM are environmental and operational variation; damage quantification; and field testing (or more accurate and representative laboratory-scale validation).

In addition to the aspects mentioned in review papers and noted above, some other challenges and sources of confounding are evident from the literature review. Locke et al. [377] note that the vehicle-based method of estimating bridge modal properties could be seen as an application of OMA, but note that few studies have actually applied existing OMA methods in this domain. They discuss the underlying assumptions of OMA and highlight that these assumptions are violated by the presence of the vehicle and background operational

traffic. This challenge is further reinforced by Sarwar and Cantero's observation [108] that the presence of random traffic on the bridge in their numerical study reduced the effectiveness of their damage detection efforts when using only vehicle-borne sensors. Unknown vehicle properties are a challenge that has been addressed in a number of ways. Many researchers adopt assumed vehicle properties from literature, but the data are generally 25 years old or more (for example Elhattab et al. [147], Locke et al. [148], Corbally and Malekjafarian [20]). Attempts to characterise vehicle dynamics during field testing is generally limited to simple free-vibration methods with minimal sensors (for example Siringoringo and Fujino [185], Sing and Sadhu [193]) or peak picking from the response spectrum based on driving for a short time (for example Fiandaca et al. [192], Locke et al. [36]). However, the literature dedicated to vehicle parameter estimation highlights that in-service methods are in need of development, and are subject to bias due to factors such as road surface profile variations and vehicle speed (Ainalis [3]). Other factors such as vehicle drivetrain vibrations have been acknowledged (Di Matteo et al. [191]) but not studied in detail. Vehicle properties and in particular vehicle-to-bridge frequency ratios have been identified as inducing bridge frequency variation during VBI (Yang et al. [9], Chang et al. [22], Cantero et al. [11] [42]), but this has not been characterised in detail beyond the first bridge mode. An alternative approach is the use of bespoke sensing vehicles (for example the custom-built trailer by Yang et al. which was designed to avoid vehicle-bridge frequency proximity [45]). The best results from this apparatus were associated with it being stationary on the bridge (Yang et al. [187] [45]) which would in practice represent an interruption to normal traffic flow (i.e. a temporary lane closure). Improved reliability for the vehicle-based method has been associated with measures such as the fusion of direct and indirect SHM sensor data to overcome confounding due to traffic (Sarwar and Cantero [108]) or control of traffic conditions, for example synchronised traversal of a known heavy vehicle with the sensor-carrying vehicle (Lin and Yang [182], Oshima et al. [264] from Malekjafarian et al. [25]). These challenges, along with those highlighted by multiple review papers noted above, suggest that there are still several significant barriers to be overcome before implementation of indirect vehicle-based bridge SHM in operational conditions can become a reality.

2.7 Critical review and research gaps

2.7.1 Outstanding challenges

Modal-based damage detection for bridges has been the subject of much research. However, in general the following **challenges for direct bridge SHM** remain:

- Ill-conditioning: there is a lack of direct indication of the damage location and type from most changes in modal parameters.
- Higher frequency modes are more sensitive to damage (particularly localised damage) but their participation is less, meaning that signal-to-noise ratios are low for damage-sensitive features.
- EOV effects continue to be a major confounder. For bridges, temperature and traffic-related aspects appear to cause some of the biggest issues.
- ML approaches have shown promise for assimilating large volumes of data and assisting with damage detection based on non-modal based features. This is believed to offer potential for the mitigation of EOV; on the other hand, gathering the data to describe EOV is still challenging. Interpreting the results provides a further barrier, alongside the potential for identification of spurious relationships.
- Much of the value and success of condition monitoring for rotating machinery relied on the existence of a large library of nominally identical units in similar operational environments. This helped to mitigate the challenge of acquiring baseline data to which in-service responses could be compared. In contrast, bridges are bespoke, precluding the direct adoption of comparison to baseline data from other structures.
- Overall, there are commonly agreed methods and approaches to direct bridge SHM in a general sense, but the detailed implementation is bespoke to each individual bridge structure. It is difficult to identify an example of a field implementation of direct SHM that has clearly added value compared to traditional inspection methods. Practitioners remain dubious despite research enthusiasm.

The **indirect vehicle-based SHM paradigm adds further challenges**:

- Indirect vehicle-based SHM implies that measurement is abstracted from the subject bridge structure. The sensor-carrying vehicle acts as a filter. Without knowledge of the vehicle properties this filter is unknown.
- Crowdsourcing approaches mean that sensor quality is not easily controllable since the sensing devices are provided by citizens. Additionally, the position of the sensor on the vehicle may vary and may not be known; this also contributes to the effective filter through which the bridge response is viewed.

- The presence of vehicles on a bridge in traffic forms part of EOV; the added vehicle masses and moving forces can change the effective bridge modal properties. It has been recognised that the vehicle-based method violates the foundational assumptions of OMA.
- VBI means that the vehicle and bridge form a combined dynamic system during a traversal. It has been acknowledged that this leads to changes in effective bridge modal properties. Such changes are dependent on vehicle and bridge dynamic and mechanical properties. Beyond the first bridge modal frequency this has not been fully characterised.
- Road roughness profiles are a particular challenge for the vehicle-based method, reducing visibility of bridge-related aspects of the recorded vibrations at the vehicle-mounted sensor. Additionally, since the sensor is inside the vehicle, the road profile-related input is convolved by passage through the vehicle's (potentially unknown) dynamic system.
- Vehicle speed is also a challenge. Faster vehicle speeds increase the amplitude of bridge response, but also increase the amplitude of road profile-related effects. Slower speeds can be beneficial in terms of signal-to-noise ratios, but may not be practical in operational traffic conditions.
- Vehicle-to-bridge frequency proximity has been suggested as helpful to the vehicle-based method, by increasing the amplitude of bridge response through resonance. However, this frequency matching has also been identified as a major cause of VBI-induced bridge property variation, and with many bridges and vehicles apparently having similar frequencies it is plausible that such matching will occur. It is not clear if damage detection can be robustly performed in such situations.

Vehicle dynamic properties are an important factor. However, when crowdsourcing approaches are considered, these properties may not be known. There are therefore additional **challenges relating to vehicle property estimation**:

- Vehicle dynamic properties may vary due to changes in configuration or condition of the vehicle and its components.
- Established input-output methods of vehicle property estimation are expensive, time-consuming and require interruption of service. It is therefore impractical to use such approaches to track vehicle properties.
- In-service output-only vehicle parameter estimation has emerged as a potential way of estimating current vehicle dynamic properties, but is associated with further challenges:
  - Sensor placement within the vehicle is an important factor, affecting the apparent vehicle dynamics, but has been little-studied. This is of particular interest to crowdsourcing of indirect bridge SHM data,

since the sensor position may vary between vehicles and even between subsequent journeys for the same vehicle.

- Vehicle suspension systems are non-linear and thus estimated parameters are subject to variation related to speed and road surface profile. There is debate as to the appropriate spectral models of road surface profile-induced excitation, since tests of in-service methods have suggested a difference between the excitation spectra applied in laboratory simulations and those experienced on real roads.
- In-service methods have been generally limited to estimating the vehicle's sprung mass mode (cabin bounce), effectively treating the vehicle as a single degree-of-freedom sprung mass model. Further research is needed into in-service parameter estimation for more sophisticated vehicle models, initially including the vehicle's unsprung mass mode, and for estimation of vehicle modal damping ratios.

2.7.2 Questioning the value of novel methods

The difference in enthusiasm between engineering research and industry suggests that further progress is needed before a balance is found within which SHM can truly add value. In 2020, Tomé et al. suggested:

> **"The main goal of SHM should not be to replace the traditional inspection techniques, but to complement them with quantitative information."** (Tomé et al. [378])

How and where this can be achieved for indirect vehicle-based bridge monitoring methods remains an open question. Researchers have sought to address the outstanding challenges noted above using the following general approaches:

- Assumed vehicle properties have been adopted for numerical investigations, generally based on literature from the 1980s or 1990s.
- In some cases, researchers have attempted to characterise vehicle frequencies for use in field testing. This has generally been based on simple push-release tests or peak picking from single sensor response spectra generated from driving slowly; rarely are road surfaces and driving speeds clearly matched between vehicle characterisation and bridge traversal phases of fieldwork.
- Ensemble methods have been adopted in some instances based on multiple vehicles, but the distribution of vehicle properties in the population is not known or the assumptions are not made explicit.
- Bespoke sensing vehicles have been adopted in some situations. Development of these vehicles (typically trailers) has focused on maximising transmissibility of bridge motion to the sensor location and choosing the vehicle's properties with the intention of achieving separation between vehicle and bridge frequencies.

- Stationary or slow-moving sensing vehicles have been adopted to increase data acquisition time and mitigate the effects of road surface profile roughness. Otherwise, multi-vehicle or multi-axle subtraction approaches have shown some promise in this regard.
- Direct and indirect SHM sensor fusion has been pursued in order to improve the reliability of bridge parameter estimation and damage detection.
- In many studies, prior knowledge of bridge properties appears to be required in order to be able to distinguish bridge-, vehicle- and road surface-related aspects of the vehicle-mounted sensor response, or to enable focused band-pass filtering to isolate bridge-related signal features (for example in the estimation bridge mode shapes). Baseline bridge parameters must also be known (or baseline bridge response data must be available) to support the comparison of two system states required for damage detection as noted by Worden et al. [66].

In summary, at present it is typical for parameters such as vehicle properties and traversal speed to be controlled to avoid confounding effects. In some situations this extends to the use of stationary vehicles, or traversal speeds below those expected in typical highway operations. Best results are often associated with the use of bespoke custom-constructed sensor-carrying vehicles. However, many of the perceived benefits of the vehicle-based method are predicated on gathering data near-continuously in operational conditions, using uncontrolled vehicles. If bespoke sensing vehicles are required, the opportunity to simultaneously monitor large numbers of bridges is likely to be lost. Additionally, if slow traversal speeds (or stationary sensing vehicles) are necessary, this represents an interruption to normal operation of the bridge. The literature contains much discussion of reduced sensor cost, especially in relation to crowdsourcing methods. However, to achieve slow vehicle movement (or a stationary vehicle) it is in practical terms necessary to implement a temporary lane closure during data gathering campaigns. In this case, it is not totally clear what benefit comes from installing sensors in vehicles, when the supposedly low-cost accelerometers could be placed directly on the bridge deck in a temporary capacity. Additionally, requirements for prior knowledge of bridge properties – as well as attempts to fuse direct and indirect monitoring data – suggest that some degree of direct monitoring is likely to be required. Given these constraints on the utility of the vehicle-based method, in the author's opinion the benefits of vehicle-based indirect bridge SHM are not currently clear. In order to add value the method should be viable using uncontrolled vehicles (i.e. crowdsourcing) without interruption to normal bridge operations (i.e. at normal operational highway speeds) and ideally with minimal requirements for prior knowledge of bridge properties. If this cannot be achieved without the use of direct SHM, then the vehicle-based method appears to maintain the challenges associated with direct methods while adding additional challenges. It is not clear that reduced costs – as are claimed often in the literature – can be reasonably expected. Indeed, no clear substantiation of holistic cost reduction associated with indirect SHM

could be found. To the author's knowledge this critique has not previously appeared in the literature. It is therefore necessary to understand where, when and how the vehicle-based approach can add value for bridge engineers and operators. Otherwise, the benefits may be limited to being politically rather than technically and holistically useful.

2.7.3 Specific research gaps

The discussion above outlines the need to address the specific challenges that currently prevent the implementation of vehicle-based indirect bridge SHM in a meaningful way. In order to assist with developing the field towards the goal of effective, continuous monitoring in operational conditions, it is proposed to address the following specific research gaps in this thesis:

- In-service vehicle parameter estimation: exploring the effects of speed, road profile, sensor type and sensor placement. Estimating parameters for vehicle models with sophistication extending beyond single degree-of-freedom sprung masses, including the use of sensors on the unsprung mass (vehicle axle), estimation of modal damping ratios, and consideration of pitch and roll motions.
- Exploring the visibility and sensitivity of vehicle responses to bridge damage, including the effects of VBI parameters and sensor location, without requiring prior knowledge of bridge properties.
- Characterisation of VBI-induced bridge modal parameter variation beyond the fundamental bridge mode, since this otherwise confounds the detection of damage by shifts in modal parameters.
- Development of a damage detection method robust to the proximity of vehicle and bridge frequencies, since such proximity is likely to occur in practice when using non-bespoke sensor-carrying vehicles.
- Where possible, proposed damage detection methods should avoid the requirement for labelled example data from a damaged bridge, since this is extremely difficult to achieve in practice.

Section 3.1 in chapter 3 follows from the discussion above, diagrammatically summarising the additional challenges introduced by the use of vehicles as combined exciters and sensor carriers for indirect bridge SHM. This leads to a formal statement of the research aim and objectives.

2.8 Established tools and techniques adopted in this thesis

This section provides summaries of established methods that have been adopted for various aspects of the work presented in this thesis. The first general topic relates to **numerical modelling of vehicles and bridges**. Vehicle model abstractions used in the thesis are presented, along with the approach adopted for modelling vehicle-bridge interaction. The next topic is **data processing**. Filtering and smoothing of data is first considered, following by mitigation of the effects of road profile roughness in vehicle acceleration responses. Subsequently, estimation of free vibration response by the random decrement (RD) method is discussed. Following this, further specific methods are summarised: density estimation by the use of Gaussian mixture models (GMM) and kernel density estimation (KDE), and comparison of distributions using the Wasserstein distance metric. **Domain transforms** are also adopted in this thesis. This section summarises the use of Welch's method for transforming to the frequency domain by estimation of power spectra, including the application of Hanning windows; transforming to the hybrid time-frequency domain by the Stockwell transform (ST); and mapping data into latent space by application of principal component analysis (PCA). Finally, established methods for **modal parameter estimation** are adopted in this thesis. The primary methods used are summarised in this section: peak picking (PP) and the half-power bandwidth method as applied to frequency-domain data; and the application of the matrix pencil method (MPM) to time-domain data.

Throughout the work presented in this thesis, data processing and analysis made use of several open-source Python libraries. Two of these, *NumPy* [379] and *SciPy* [380], were particularly useful. Throughout the text, reference is made to specific parts of the SciPy library where particular tools or techniques are discussed. Many of the figures in this thesis where produced with the open-source Python library *Matplotlib* [381].

2.8.1 Numerical modelling

Section 2.4 discussed reduced degree-of-freedom (DoF) quarter car vehicle models as commonly adopted in the literature. In this thesis, vehicles are typically represented as two degree-of-freedom (2DoF) quarter-car models (chapters 4, 5, 6 and 7) since this allows acceleration responses from lower and upper DoFs (in practice the vehicle axle and cabin respectively) to be represented. In chapter 6 a single degree-of-freedom (SDoF) vehicle model is also used to explore aspects of vehicle-to-bridge natural frequency ratios, comparing simulation outcomes to results from prior literature before progressing to 2DoF models which have not previously been characterised in this regard.

Section 2.5 presented methods for modelling vehicle-bridge interaction (VBI). In this thesis, numerical modelling of coupled VBI is undertaken using ABAQUS (chapters 5 and 6). This method is adopted since it offers the advantage of visual

inspection of assembled interaction models, avoids the requirement to pass information between multiple software environments, and is amenable to automating analysis using Python scripts, while remaining computationally tractable for the scenarios explored in this thesis. In the simulations, the vehicle is represented as a SDoF or 2DoF sprung mass model; the more simple moving mass and moving force models were not adopted in the work presented here since they do not afford insight into the vehicle's dynamic response during VBI.

2.8.2 Filtering and smoothing

A variety of techniques exist for processing of data collected or generated in SHM. In some instances it is helpful to filter a signal to remove aspects which are unrelated to the phenomenon being studied, or to allow greater visibility of some aspect of the data. In this thesis, **frequency filtering** is employed to either remove signal content above a defined frequency, or to isolate aspects of the signal within a specific frequency range. These are respectively known as *lowpass* and *bandpass* filters. In this thesis, the adopted filter type was originally proposed by Butterworth [382] and aims to maximise flatness of response (i.e. minimise distortion of the signal) within the defined pass band. The bandpass implementation used in this thesis is derived from the open source Python library SciPy [383] and presented in the *SciPy Cookbook* [384].

Smoothing of noisy data (for example the FRFs estimated in chapter 4) is achieved in this thesis by used of a Savitzky–Golay (*Savgol*) filter. This type of filtering approach is widely used for noise reduction and is summarised by Schafer as "fitting a polynomial to a set of input samples and then evaluating the resulting polynomial at a single point within the approximation interval" [385]. The smoothed signal is generated by applying this approach sequentially to subsets of the original signal. Savgol filtering has proven extremely popular (Riordon et al. [386]); one advantage with specific relevance to this thesis is that the filtering process preserves phase. Where used in chapter 4, power spectra are smoothed using Savgol filters. The preservation of phase means that frequencies extracted by peak-picking after Savgol filtering are less likely to be spuriously estimated: the filtering process smooths the data so that the central frequency for each peak in the power spectra is maintained, while the potential for bias due to local peaks associated with noise in the data is reduced. Additionally, Savgol filters are considered to be "simple and easy to use", as well as effective at de-noising (Riordon et al. [386]).

2.8.3 Mitigation of road profile effects

In the context of vehicle acceleration response the excitation relating to road profile roughness can partially obscure other aspects of the acceleration signal of greater interest (typically relating to the motion of a bridge deck). As noted in section 2.6 multiple authors have explored using combinations of responses from multiple following axles to mitigate the effects of road profile. In this thesis the adopted approach (in chapter 7 where multiple axle responses are available, in

contrast to the single-axle vehicle representations modelled in earlier chapters) is in accordance with the time-shifted subtraction of acceleration responses from two following axles proposed by Kong et al. [288] and summarised by Li et al. [38]. The method is based on shifting one of the two discretely-sampled axle responses by the sampling point interval (SPI), denoted as t_{SPI} and calculated in relation to the axle spacing l_v, the vehicle velocity v and the sampling frequency f_s as noted by Li et al. [38] and included here as equation (2.16):

$$t_{SPI} = l_v / v f_s \tag{2.16}$$

The approach summarised by Li et al. [38] is to estimate the bridge response at the temporally-varying vehicle bridge contact location for each axle, known as the contact point (CP) response. Typically, inverse filters are constructed based on assumed or measured vehicle kinematics to estimate the CP response using the sensors located at other points on the vehicle. Established methods for doing so are explored in more detail in chapter 7. Li et al. [38] outline the procedure of estimating the CP response for two axles and then subtracting one from the other element-wise, having first time-shifted one of the CP responses by the calculated SPI and discarded the parts of the two CP responses that no longer overlap in the time domain. This yields the residual CP response ($\boldsymbol{u}_{CP,res.}$) is summarised for a pair of CP responses of total length T in equation 2.17 where the subscript refers to a slice of the vector, i.e. $\boldsymbol{u}_{CP,A}[1 : T - SPI]$ represents the slice of the first axle CP response $\boldsymbol{u}_{CP,A}$ from the 1^{st} element to the $(T - t_{SPI})^{th}$ element:

$$\boldsymbol{u}_{CP,res.} = \boldsymbol{u}_{CP,A}[1 : t_{SPI}] - \boldsymbol{u}_{CP,B}[t_{SPI} : T] \tag{2.17}$$

Subtraction of following axle responses is employed to mitigate the effects of road profile roughness in chapter 7 in pursuit of greater visibility of the bridge dynamic response in the vehicle-mounted accelerometer data. The approach is inherently unsuitable for data from a single axle vehicle where only one vehicle is present in the simulation or experiment, and is therefore not used in chapters 4, 5 or 6. In such situations, if mitigation of road profile effects is desired to assist with estimating vehicle modal parameters, the random decrement method (discussed below) can be used which yields an estimate of the system's free vibration impulse response. Alternatively, Welch's method of power spectral density estimation also counters road profile effects to some extent and is also disussed below. The preferred choice of method depends not only on whether multiple axle responses are available, but also on the desired domain (time or frequency) of the output.

2.8.4 Random decrement method

The random decrement (RD) method was originally proposed in the late 1960s and refined in the early 1970s, in both cases by Cole [387] [388]. The original

motivation related to improving modal estimates and damage detection from time-domain in-service recorded responses of space structures. In this thesis, random decrement signatures (RDS) are denoted as $D(\tau)$ and are assumed to approximate the free vibration response of the system, where the original data represent the system's response to broadband random excitation. This is particularly relevant when long samples of response data are available, with the input assumed to be broadband random and the modal parameters of the system being studied assumed to be broadly constant: for example, the output-only vehicle modal parameter estimation reported in chapter 4. In such situations, the RDS highlights the aspects of the data representing modal properties while reducing the random parts of the signal representing the road profile. The method is succinctly described by Rodrigues and Brincker [12]. First it is assumed that any given subsample, taken from a longer record of the time-domain displacement response of a structure to ambient excitation, is an additive combination of deterministic and random components, the former representing the structure's free response to some initial displacement and velocity conditions and the latter the structure's driven response to white noise excitation. The RDS is formed by summing all subsamples from the record whose initial conditions match some selected trigger condition (for example, having specified displacement and velocity values). Fig. 2.8.1 indicates this by an example of averaging subsamples meeting the condition of crossing a defined threshold with either positive or negative gradient.

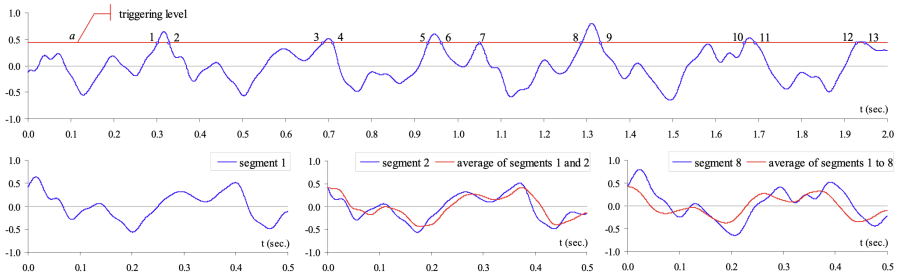

Figure 2.8.1: An example of forming the RDS, reproduced from Rodrigues and Brincker [12].

Fig. 2.8.1 shows an auto RD function, in which the triggering condition and the data to be averaged are contained within the same signal. Alternatively, one may construct a cross RD function in which the triggering condition is met in data from one sensor and the data to be averaged is from another. From Rodrigues and Brincker [12], equations 2.18 and 2.19 indicate the mathematical definition of the auto and cross RD functions respectively, for N averaged samples of response histories x or y, where the samples have length τ and are defined by the triggering condition $Tx(t_i)$:

$$D_{XX}(\tau) = \frac{1}{N}\sum_{i=1}^{N} x(t_i + \tau)|Tx(t_i) \tag{2.18}$$

$$D_{XY}(\tau) = \frac{1}{N}\sum_{i=1}^{N} y(t_i + \tau)|Tx(t_i) \tag{2.19}$$

In this thesis the auto RD function is used. Adapted from Rodrigues and Brincker [12], equation 2.20 defines the triggering condition typically used in calculating auto RD functions in this thesis: level crossing with a positive slope. Values of response history x are deemed to be equal to the trigger level b when they fall within the tolerance range $b \pm r$, noting that the first time derivative of the response history is denoted as $\dot{x}$:

$$Tx(t_i) = \{x(t_i) = b \pm r, \dot{x}(t_i) > 0\} \text{ for level } b \text{ with tolerance } r \tag{2.20}$$

The benefit of the cross-RDS is that estimates of modal parameters from multiple sensors will necessarily be in-phase, since they are constructed from samples which share a common triggering event. In this thesis, the use of the auto-RDS means that the phase relationship of modal parameter estimates from multiple sensors cannot be quantified. This is further discussed where the auto-RDS is used in chapter 4.

2.8.5 Density estimation

In this thesis, two types of density estimation are adopted. In both cases the implementation is from the open-source Python library *ScikitLearn*. The first, **kernel density estimation** (KDE) generates a non-parametric model of the distribution of a data set. It can be understood as similar to a histogram, but resulting in a smooth curve (ScikitLearn user guide [389]). From the same source, using KDE for a sample $x_1, ..., x_N$ the density estimated at some location y is given by:

$$\rho_K(y) = \sum_{i=1}^{N} K(y - x_i; h) \tag{2.21}$$

in which K is the kernel function controlled by bandwidth h. In this thesis the Gaussian kernel is adopted:

$$K(x; h) \propto \exp -(x^2/2h^2) \tag{2.22}$$

The purpose of KDE in this thesis is to allow comparison of estimated distributions based on multiple samples where each sample represents a different bridge condition. The comparisons are made in chapter 7 and use Wasserstein distance as a comparative metric, which is discussed below.

Gaussian mixture models (GMM) are also adopted in this thesis and are also a method of density estimation. GMM are used in this thesis for unsupervised clustering of modal parameter estimates in pursuit of dynamic identification of the scale model vehicle used in chapter 7. The adopted modal parameter estimation method used in that scenario generates multiple estimates, each consisting of a frequency, a damping ratio and a modal amplitude. It is necessary to infer modes of the vehicle to which clusters of estimates belong. The GMM used here was implemented through the open-source Python library Scikit-Learn [390] and uses expectation maximisation to determine a mixture of a finite number of Gaussian distributions that are deemed likely to have generated the input data.

2.8.6 Wasserstein distance

In chapter 7, data sets representing vehicle responses from different bridge states are compared. In order to explore the differences, the distribution of data in each set is estimated using KDE (discussed above). Following this, the distributions are compared using the Wasserstein distance. For the purpose of this thesis, the Wasserstein distance metric affords consistent comparison of data sets whose underlying statistics are not necessarily similar.

The 1-Wasserstein (first) distance between two one-dimensional probability mass functions u and v is:

$$W_1(u,v) = \int_{-\infty}^{+\infty} = |U - V| \tag{2.23}$$

where U and V are the cumulative distribution functions for u and v respectively (Scipy documentation [391]). Based on the field of *optimal transport*, the Wasserstein distance can be thought of as representing the amount of work required to transform one distribution into another. As a non-parametric method it has the advantage for the present application of being suited to comparisons of empirical distributions. When comparing probability density functions (which integrate to unity) the Wasserstein distance takes a value of 0 for maximal similarity and 1 for maximal dissimilarity. It has reportedly (Kolouri et al. [392]) found recent application in various fields where such a similarity measure is of value.

2.8.7 Transformation to frequency domain

The primary method employed in this thesis for estimating vehicle FRFs from in-service acceleration response is by power spectrum estimation using **Welch's method** [360]. This is a non-parametric method which comprises splitting the

time-domain acceleration signal into overlapping segments; applying a windowing function to each segment to avoid double-counting the data in the overlap regions; and averaging the modified periodogram of all the segments. A periodogram is given by the squared absolute value of discrete Fourier transform amplitudes; in Welch's method these are all scaled (*modified*) proportional to the window length and type to reduce bias. Welch's method returns a real-valued vector of signal power (in this case with units of m^2s^{-4}) or power spectral density (PSD) which comprises power normalised to frequency (in units of $m^2s^{-4}Hz^{-1}$). Power is real-valued; the method does not preserve information relating to the phase of the signal. Nevertheless, the approach is advantageous – by averaging across multiple segments, the resulting spectrum can be considered as representing the response of the system to the average spectral input received. Assuming that the system's properties do not change with time (for example as in chapters 4 and 5) Welch's method reduces the effect of random or nonstationary inputs, as may be expected from a vehicle traversing a real road surface, highlighting the system's constant modal properties.

2.8.8 Transformation to hybrid time-frequency domain

When considering dynamic systems in which the underlying modal parameters change over time, it is convenient to represent the signals in the hybrid time-frequency (TF) domain. By so doing it is possible to visualise and quantify the instantaneous frequency (IF) and how it changes as time passes. For example, in this thesis chapters 6 and 7 explore the time-varying effective modal properties of coupled vehicle-bridge systems, which vary as the vehicle traverses the bridge.

Sejdić et al. explain two general approaches to TF representation of a signal. The first involves finding a representation of the signal as some combination of "translating, modulating and scaling a basis function having a definite time and frequency localization" [13]. Examples of this approach are noted as the short time Fourier transform (STFT) and the wavelet transform (WT). The second method relies on a kernel function upon which constraints can be placed in order to construct a TF representation of the underlying function. The Stockwell transform (ST), also known as the S-transform and originally proposed by Stockwell [393] in the 1990s, is noted as being an example of this type, which in general is in accordance with ideas first outlined by Cohen [394].

Sejdić et al. discuss the utility of considering energy concentration as a way of choosing the most suitable TF representation method for a given situation [13]. Considering signals whose frequency content varies with time, greater energy concentration can be understood as a more dense representation of the true instantaneous frequency resulting from the time-domain to time-frequency domain transform. On the contrary, a lesser energy concentration is produced by a transform which shows signal power across a wider range of frequencies. Adapted from their work, Fig. 2.8.2 shows a comparison of the ST (dashed outline box) of three input signals (solid outline box). Also shown for comparison is the STFT TF representation of the same signals. The figure shows that the concentration of the STFT is the same throughout the frequency range, while

the concentration of the ST is greater (a narrower line in the plot) at lower frequencies. As summarised by Brown et al. [395], the WT and ST include a progressive frequency resolution, visible in Fig. 2.8.2; the time resolution is more fine at high frequencies and more coarse at low frequencies, while the frequency resolution is more coarse at high frequencies and more fine at low frequencies. The original ST definition as suggests that it is a "phase correction" [393] of the WT; Brown et al. explain that the WT does not provide phase information, while the ST represents phase in relation to a global reference [395].

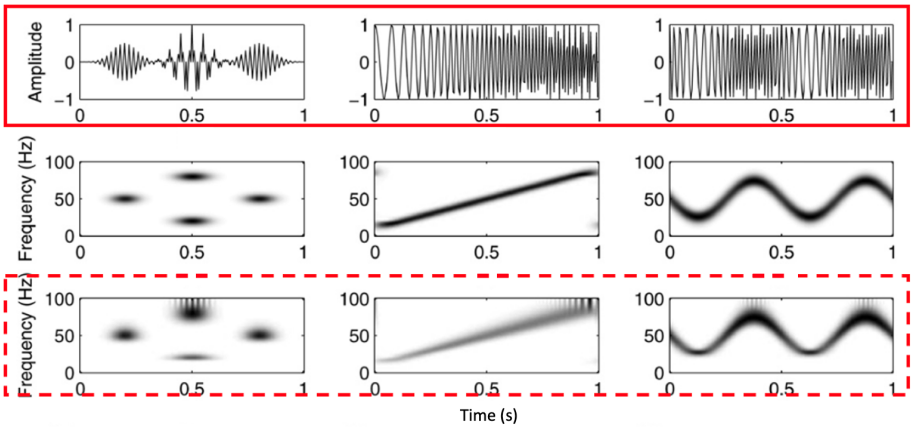

Figure 2.8.2: A comparison of the short time Fourier transform and Stockwell transform (dashed outline box) methods of representing three sample signals (solid outline box) in the hybrid time-frequency domain. Adapted from Sejdić et al. [13].

The above suggests that the ST may be well-suited to the TF representation of VBI, in which frequencies of interest tend to be low and may not be stationary. Furthermore, although not pursued in this thesis, the ST should allow phase changes to be studied if relevant. Despite these potential advantages it appears that the ST has been little used in the analysis of VBI, perhaps because it was computationally expensive until the development of the fast Stockwell transform algorithm in 2009 (Brown et al. [395]). The Stockwell transform transforming a time-domain function $h(t)$ to the time-frequency domain $S(\tau, f)$ can be given as equation 2.24 reproduced from Stockwell et al. [393]:

$$S(\tau, f) = \int_{-\infty}^{\infty} h(t) \frac{|f|}{\sqrt{2\pi}} \exp -\left(\frac{(\tau - t)^2 f^2}{2} \right) \exp(-j2\pi f t) dt \tag{2.24}$$

In this thesis, time-frequency representation of signals makes use of a Python implementation of the Stockwell transform [14]. Reproduced from the same source, Fig. 2.8.3 shows the time and time-frequency representations of a linear

chirp signal (in which the frequency changes linearly with time) using this code. The upper plot shows the signal, while the lower plot shows its Stockwell transform contours: the instantaneous frequency (which changes as time passes) is indicated by the brightest coloured contours.

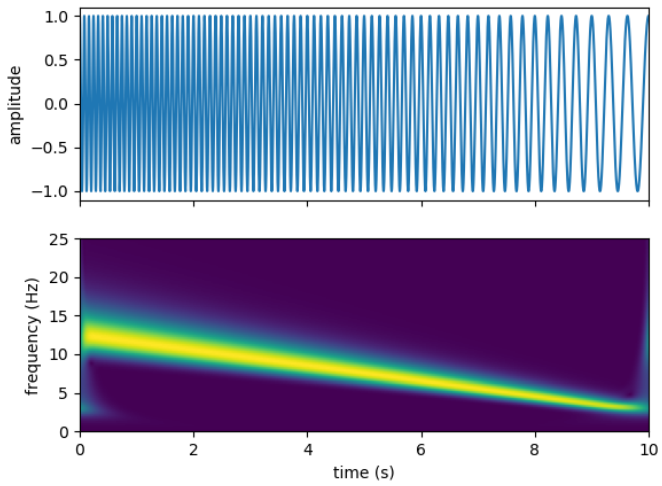

Figure 2.8.3: Above: time domain linear chirp signal. Below: time-frequency domain representation of this signal using the Stockwell transform. Reproduced from Satriano [14].

Gibson et al. assert [396] that the ST is efectively a special case of the WT with a *Morlet* mother wavelet; in this regard, the WT could have been used in this thesis. Adopting the ST for transformation to the hybrid time-frequency domain has been based primarily on ease of use of the available Python implementation, in addition to the progressive frequency resolution noted above. Phase information is not used explicitly in the parts of this thesis where the ST is leveraged (chapters 6 and 7) but is included in the discussion above as it may represent a benefit for future use of the ST in studies of indirect SHM.

2.8.9 Frequency domain modal parameter estimation

Adopted throughout this thesis, a common and well-established frequency-domain method of estimating modal frequencies is known as **peak picking** (PP), an approach in which the user visually selects a peak in the frequency-domain representation of a signal (typically having determined with their own judgement that the peak is sufficiently defined in relation to background noise). The approach is illustrated in Fig. 2.8.4. For purposes of consistency and repeatability the required height of a peak can be defined. Nevertheless, the PP approach may remain inconsistent since opinions may differ as to which fre-

quency represents the centre of a given peak. Additionally, the width of the peak is not accounted for - a wider peak could represent multiple closely-spaced modes, a mode with a non-stationary frequency, or a lack of resolution in the frequency-domain representation of the signal. Other approaches exist to address these challenges and to add further insight such as estimation of modal damping.

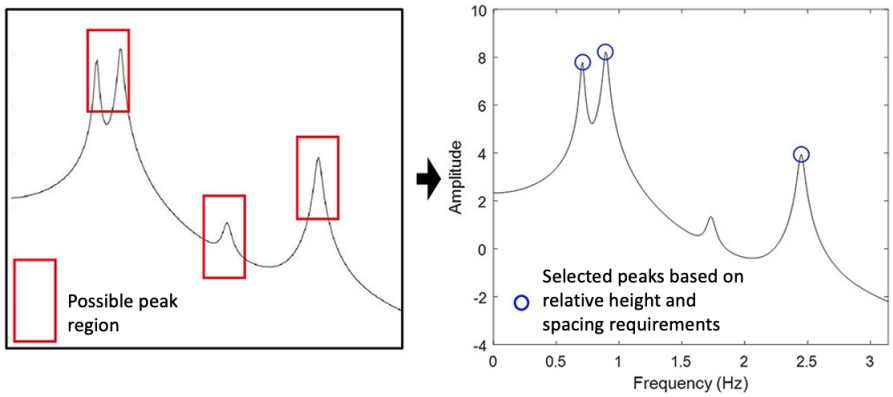

Figure 2.8.4: Illustration of peak picking method for modal parameter estimation in the frequency domain. Adapted from Kim and Sim [15]

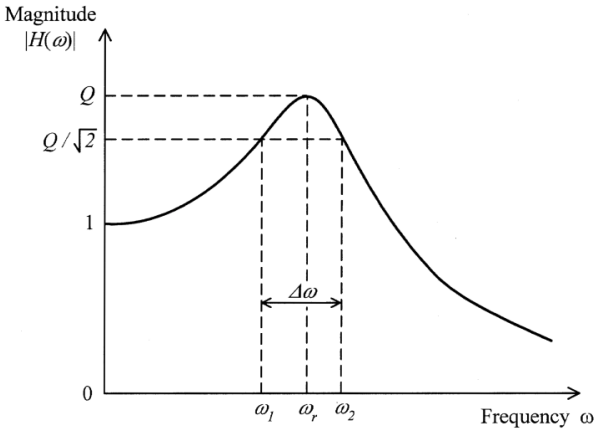

Figure 2.8.5: Half-power bandwidth method for damping estimation, reproduced from De Silva [16].

Figure 2.8.5, reproduced from [16] illustrates the **half-power bandwidth** method of damping estimationwhich is also adopted in this thesis. Having identified peak *reference frequency* ω_r and associated peak power Q (for example

by the PP method) the half-power level $Q/\sqrt{2}$ allows the associated half-power frequencies ω_1 and ω_2 to be found using the frequency difference $\Delta\omega = \omega_2 - \omega_1$. Equation 2.25 gives the estimate of modal damping ratio ζ, again reproduced from [16]. It should be noted that the half power level is found by division of the peak power by $\sqrt{2}$ since power is given in signal units squared (for the purpose of this thesis, typically acceleration squared: $m^2 s^{-4}$).

$$\zeta = \frac{\Delta\omega}{2\omega_r} \tag{2.25}$$

2.8.10 Time domain modal parameter estimation

In this thesis the matrix pencil method (MPM) is generally adopted for estimation of modal parameters from time-domain data. The MPM was outlined by Hua and Sarkar [397] (from Wynne [398]) and is a time-domain fitting technique which uses acceleration data to estimate a set of damped sinusoids which can be linearly combined to form an approximation the free vibration response signal. Each damped sinusoid must necessarily relate to a frequency, a damping ratio, a phase angle and an amplitude. The set of estimates can be understood as estimates of modal parameters for modes present in the free response of the structure at the location of the accelerometer. In all such estimation procedures, it is necessary to decide upon the number of modal estimates making up each input signal. The adopted implementation of the MPM is based on example code provided by Wynne [398] and includes their method of mode order determination. In this approach, the mode order is sequentially increased up to a pre-determined maximum order selected by the user. The approach makes use of the *coefficient of determination*, also known as the R^2 score which "represents the proportion of variance (of y) that has been explained by the independent variables in the model" [399]. The implementation used in this thesis is provided by the open-source Python library *ScikitLearn* [399] which defines the coefficient of determination as shown in equation (2.26) for predicted values $\hat{y}$ and true values y of n samples with the mean of true values denoted as $\bar{y}$:

$$R^2(y, \hat{y}) = 1 - \frac{\sum_{i=1}^{n}(y_i - \hat{y}_i)^2}{\sum_{i=1}^{n}(y_i - \bar{y})^2} \tag{2.26}$$

The R^2 score is calculated for the set of modal estimates at each model order, thus providing an estimate of the quality of fit between the original signal and the ensemble of estimated modal components. Adequate fit is deemed to have been achieved once a target R^2 score or the pre-determined maximum model order is reached. Typically-adopted R^2 targets for various applications of the MPM in this thesis are shown in Table 2.8.1. The lower R^2 score used for the laboratory-scale model vehicle impulse response (section 7.4) was adopted to allow a sufficiently large number of estimates to be retained.

Task: estimation of modal parameters for...	Typical/ illustrative R^2 target	Location in thesis
Synthetic vehicle response to ISO 8608 road profile	0.999	Section 4.2.7
Real vehicle response to real road surface profile	0.99	Section 4.5.3
Laboratory-scale model bridge (impulse response)	0.99	Section 7.3
Laboratory-scale model vehicle (impulse response)	0.9	Section 7.4

Table 2.8.1: Typical/ illustrative R^2 targets adopted for time-domain modal parameter estimation using the matrix pencil method.

2.8.11 Principal Component Analysis

Principal Component Analysis (PCA) is a broadly-used technique (Bishop [400]) with multiple applications including dimensionality reduction and feature extraction which are of relevance to this thesis. One of the broadly-used definitions of PCA is that it orthogonally projects data in such a way as to maximise the variance in the data (Hotelling [401] from Tipping and Bishop [402]).

Following the outline presented by Brownlee [403], for a n-sized set of $p \times 1$ column vectors forming a matrix $\boldsymbol{X}$ such that

$$\boldsymbol{X} = [\boldsymbol{x}_1, ..., \boldsymbol{x}_p] \tag{2.27}$$

the columns of $\boldsymbol{X}$ should be scaled to avoid bias (Groth et al. [404]). In this thesis, the data for which PCA is used (see chapters 6 and 7) represent pixel intensities and thus are already scaled in this manner. Each column should also be centered by subtracting from each element the mean of all elements in the column; incorporating this, each entry s_{ij} in the sample covariance matrix $\boldsymbol{\Sigma}_{n\times n}$ is given by (Li [405])

$$s_{ij} = \frac{1}{n-1}\sum_{i=1}^{n}(\boldsymbol{x}_i - \bar{\boldsymbol{x}}_i)(\boldsymbol{x}_j - \bar{\boldsymbol{x}}_j)^T \tag{2.28}$$

in which $\boldsymbol{x}_i$ and $\boldsymbol{x}_j$ are the i^{th} and j^{th} columns of $\boldsymbol{X}$ respectively, and the bar (for example $\bar{\boldsymbol{x}}_i$) denotes the mean. The covariance matrix $\boldsymbol{\Sigma}$ is symmetric about its leading diagonal; entries on this diagonal are variances (i.e. the covariance of a vector with itself). The eigendecomposition of $\boldsymbol{\Sigma}$ is

$$\boldsymbol{\Sigma} = \boldsymbol{W}\boldsymbol{\Lambda}\boldsymbol{W}^{-1} \tag{2.29}$$

where $\boldsymbol{W}$ is a matrix of eigenvectors, $\boldsymbol{\Lambda}$ is a diagonal matrix of eigenvalues and $\boldsymbol{W}^{-1}$ denotes the inverse of $\boldsymbol{W}$. Tipping and Bishop [402] state that the eigenvectors $\boldsymbol{W}$ are the basis upon which $\boldsymbol{X}$ can be projected to maximise variance. In order to reduce the dimensionality of $\boldsymbol{X}$ in such a projection, a truncated set of eigenvectors $\boldsymbol{W}_L$ is used, assembled in order of descending magnitude of the corresponding eigenvalues $\boldsymbol{\Lambda}$. The reduced dimension projection onto the principal axes is given by

$$\boldsymbol{T}_L = \boldsymbol{X}\boldsymbol{W}_L \tag{2.30}$$

The implementation of PCA used in this thesis is based on the open-source Python library *SciPy* [406] which adopts the approach outlined by Tipping and Bishop [402].

Chapter 3

Motivation, aim, objectives, methodology and thesis structure

3.1 Motivation

As outlined in chapter 2 there is a perceived growing need for methods of bridge monitoring which are low cost, provide reliable estimates of parameters, and can be implemented without interruption to the normal operation of the bridge. This is the general opportunity to which vehicle-based indirect structural health monitoring (iSHM) can be applied. However, further research is required before the approach can meet the required performance criteria.

Fig. 3.1.1 illustrates the general process of operational modal analysis (OMA) when applied to the estimation of bridge properties. The operational loading on the bridge is assumed to be broadband random, generated by a stochastic process. The bridge response relates to its modal properties as well as the random forcing.

Fig. 3.1.2 illustrates additional challenges when a vehicle is used as the sensor carrier. Although visibility of the bridge acceleration response is desired, it cannot be measured directly. The response is instead measured indirectly, by recording the response of the vehicle during a passage across the bridge. The vehicle's own dynamic characteristics form a filter through which the bridge acceleration at the vehicle's location is viewed. Additionally, if the vehicle is in motion (traversing the bridge), the location at which the bridge response is available is a function of time.

In the discussion within this section it has thus far been assumed that the vehicle can act as sensor carrier, but the bridge is unaffected by its presence, with the operational loading being provided by some other source (e.g. wind). Fig. 3.1.3 illustrates further challenges arising when vehicles are used as sensor

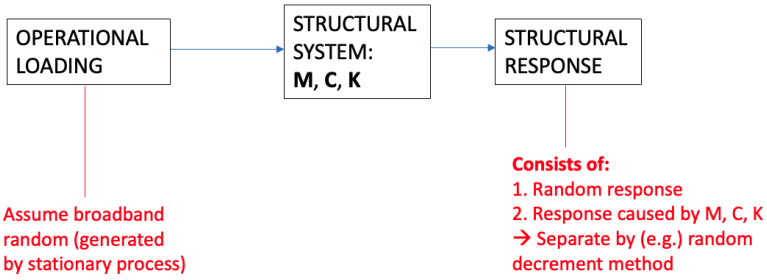

Figure 3.1.1: Outline of the OMA approach using sensors attached directly to the bridge.

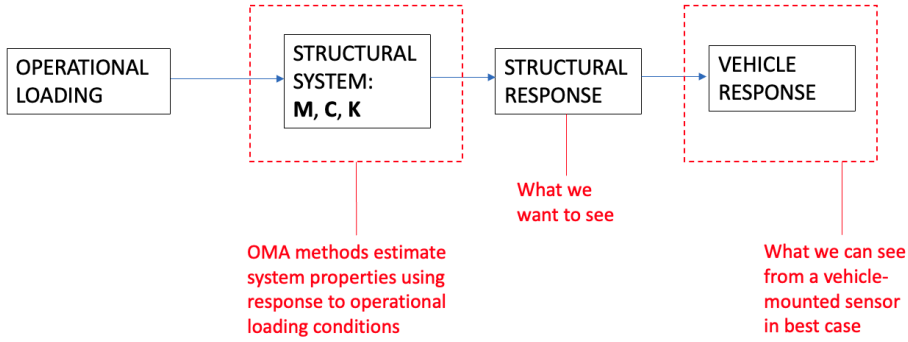

Figure 3.1.2: Additional challenges in the OMA process when a vehicle is used as a sensor carrier.

carriers and as providers of excitation to the bridge structure.

The overall goal of iSHM is to detect bridge damage from the passing vehicle acceleration response. This thesis focuses on extracting estimates of bridge modal frequencies, which can in turn be used to estimate bridge mode shapes from the vehicle-mounted sensor response. Defining bridge damage as a change in bridge modal parameters, it is clear that frequency and mode shape changes can be correlated to the existence and location of damage. However, the presence of vehicles on the bridge introduces changes to the apparent modal properties, even when the vehicles are not moving. Additionally, when the vehicle is in motion, proximity of vehicle and bridge natural frequencies leads to the combined vehicle-bridge interaction (VBI) system frequencies displaying non-stationary behaviour during the interaction. Finally, the vehicle kinematics form a filter through which the bridge response is viewed. Estimates of bridge frequencies from passing vehicle acceleration responses are therefore subject to bias relating to the VBI system parameters, including vehicle-to-bridge frequency ratio, vehicle mass ratio, vehicle speed and sensor position. Greater understanding of the visibility of bridge frequencies and their sensitivity to VBI system param-

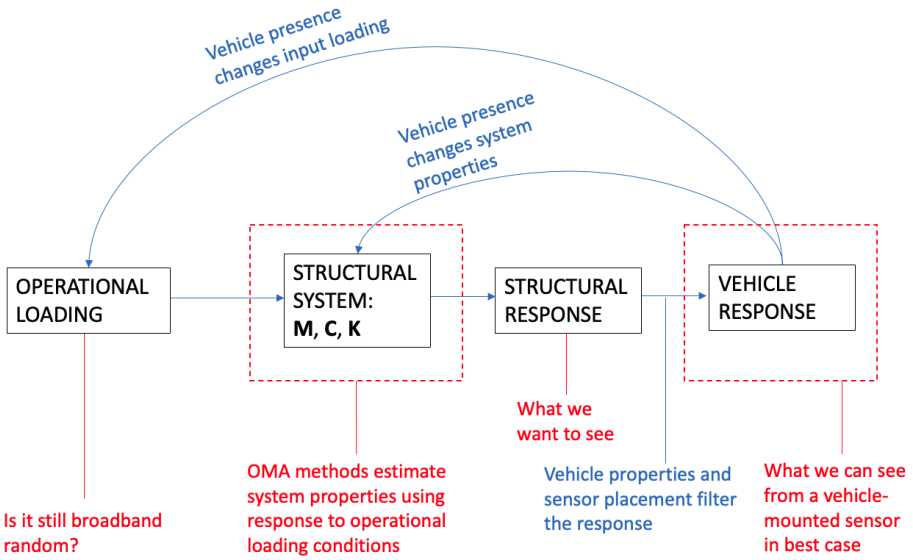

Figure 3.1.3: Further challenges in the OMA process when a vehicle is used as both exciter and sensor carrier. Key challenges to be addressed in this thesis shown in blue text.

eters is required to help iSHM move towards a state of operational readiness. The non-stationarity of coupled VBI system frequencies has only recently been acknowledged in the literature and has been little studied, but threatens to confound visibility of damage-induced frequency changes and associated time- and position-dependent sub-band acceleration amplitudes, thus affecting estimates of operational mode shapes. This phenomenon has not been fully characterised beyond consideration of the vehicle's first vertical mode of vibration.

3.2 Aim and objectives

The aim of this thesis is to systematically investigate the viability of indirect bridge damage detection based on the acceleration response of a non-bespoke traversing vehicle, given the expected operational challenges of proximal vehicle and bridge frequencies, the lack of prior knowledge of vehicle dynamic properties, and the lack of labelled data representing bridge damage.

This aim will be addressed through the following research objectives (RO):

RO.1 Estimate a representative multi-degree-of-freedom dynamic model of a vehicle, using only the vertical acceleration response of the vehicle to driving in normal operational conditions.

RO.2 Explore how variation in vehicle-to-bridge parameter ratios, vehicle model abstractions and sensor placement on the vehicle affect the visibility and sensitivity of detecting bridge frequencies from vehicle-mounted accelerometers.

RO.3 Characterise the nonstationary frequency variation for interacting vehicle-bridge systems during vehicle traversals in relation to vehicle model abstraction and vehicle-to-bridge parameter ratios.

RO.4 Establish and test a method to detect bridge damage from vehicle acceleration responses in the case of vehicle-to-bridge natural frequency matching without requiring labelled examples representing bridge damage.

3.3 Methodology

To address the stated research aim and objectives, work undertaken in this thesis comprises a combination of literature review, numerical simulation, and laboratory- and field-scale physical testing. The work is presented in the following chapters and as summarised in Table 3.3.1 [1]:

- **Chapter 2** presented a review of the known relevant existing literature.
- **Chapter 4** uses numerical simulation and field testing for estimation of vehicle properties using in-service output-only techniques.
- **Chapter 5** explores the sensitivity and visibility of bridge frequencies from vehicle-mounted sensors across a range of vehicle-bridge interaction (VBI) system parameters through a parametric study undertaken using finite element (FE) simulation of VBI.
- **Chapter 6** extends the FE study of VBI to explore the variation of VBI system frequencies during interaction and develop a method of bridge damage detection suited to cases where vehicle and bridge natural frequencies are proximal.
- **Chapter 7** uses a laboratory-scale physical model of VBI to validate the proposed damage detection method.
- **Chapter 8** concludes the thesis, summarises the fulfilment of research objectives and suggests potential avenues for further work.

Research objective	Chapter(s)
RO.1	4
RO.2	5
RO.3	6
RO.4	6,7

Table 3.3.1: Summary of chapters in which research objectives are addressed.

[1] Tables in this thesis were prepared using Tables Generator [407].

3.4 Thesis structure

This thesis can be understood as two phases of investigation. The first phase, comprising chapters 4 and 5 addresses research objectives RO.1 and RO.2. Here, the investigations primarily seek to recover estimates of vehicle and bridge dynamic properties, which are assumed to be invariant with time. The data processing and analysis methods applied therefore seek to overcome the effects of random inputs (for example the road surface profile in chapter 4). In such situations it is appropriate to employ time- or frequency-domain averaging techniques whose performance is enhanced by the relatively long samples of data available. Following this, in chapter 5 the analysis proceeds as if bridge frequencies were constant. Since this chapter is based on simulated vehicle traversals and road roughness was not modelled, frequencies can be extracted from relatively short data samples. The investigation explores the bias caused by the assumption of constant frequencies.

The second phase comprises chapters 6 and 7 and addresses research objectives RO.3 and RO.4. Here, the interaction of the traversing vehicle with the bridge leads to a combined system with dynamic properties which vary with time, according to the position of the vehicle on the bridge span. This nonstationarity was observed in chapter 5. To address it, the second phase of investigation employs data processing and analysis methods which seek to represent the variation in frequencies over time. The key challenges and constraints, main adopted methods and relative locations within the thesis are summarised in Fig. 3.4.1.

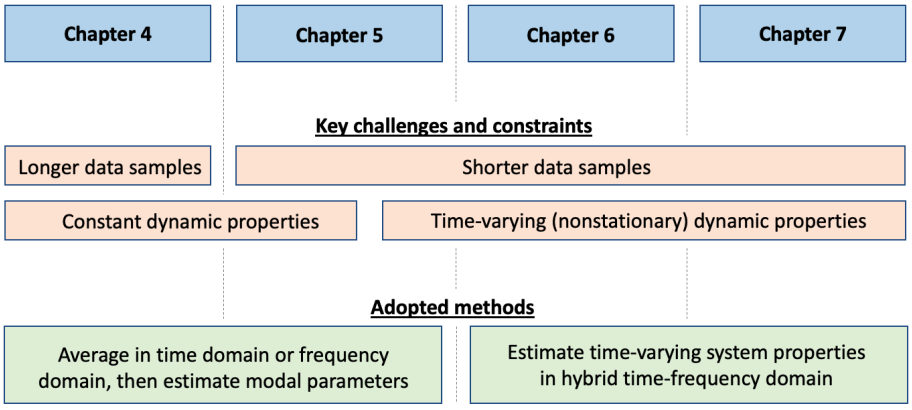

Figure 3.4.1: Structure of thesis showing key constraints and challenges for modal parameter estimation alongside main adopted methods.

Chapter 4

Vehicle parameter estimation

The fieldwork presented in this chapter was made possible by Ms. Hazel Taylor who acted as driver for the full-scale test vehicle. Thanks are also given to Mr Stephen James Glover, Mr Calum Melrose and Mr Andrew Brown who fabricated brackets to attach sensors to the vehicle.

Python code for generating modal parameter estimates using the matrix pencil method in this chapter was adapted from examples provided by Dr Zachariah Wynne [398].

4.1 Chapter outline

This chapter addresses the following research objective:

RO.1 Estimate a representative multi-degree-of-freedom dynamic model of a vehicle, using only the acceleration response of the vehicle to driving in normal operational conditions.

To address the research objective this chapter first demonstrates and validates output-only parameter estimation using numerical simulations of vehicle response. Numerical validation of the methods is necessary due to the lack of ground-truth values for full-scale vehicle parameters. Subsequently the chapter presents outcomes from applying the output-only identification methods to real vehicle responses from driving in operational conditions, including comparisons of the effects of speed, road type and vehicle configuration.

The work presented in this chapter relates to both to finite element simulations and to fieldwork tests. The source of data (synthetic or fieldwork-derived) is clarified in the section headings.

4.1.1 Method of investigation

The literature review (section 2.4) summarised the basis for a reduced degree-of-freedom model approximating the dynamic behaviour of a vehicle and explained the utility of the acceleration frequency response function (FRF) in visualising and characterising the vehicle's dynamic properties. Further discussion of experimental estimation of vehicle dynamic properties is provided in Appendix A.

- The generation of synthetic vehicle response data and the application of frequency- and time-domain methods for estimation of vehicle parameters is presented in **section 4.2**.
- Fieldwork regimes are described in **section 4.3**.
- Frequency-domain vehicle parameter estimation is undertaken in **section 4.4** using the data from the first phase of fieldwork. An alternative configuration of the field test vehicle (the second phase of fieldwork) is explored in **section 4.5** alongside adopting a low-cost smartphone device as a sensor.
- A comparison of the vehicle parameters estimated using the frequency-domain method for the two vehicle configurations is presented in **section 4.5**. Time-domain vehicle parameter estimation is employed to illustrate the potential range of variation from the second phase of fieldwork.
- **Section 4.6** comprises a discussion of the work presented in the chapter.
- **Section 4.7** presents the chapter conclusions.

4.2 Synthetic data

4.2.1 Synthesising ISO 8608 road profiles

Malekjafarian et al. [113] summarise the process of generating synthetic road profiles in accordance with ISO 8608 [7]. Their explanation is based on prior work by Yang et al. [408]. The road profile $r(x)$ is given by equation (4.1) which includes a range of spatial frequencies n_i and a random phase angle γ_i. ISO 8608 defines 8 roughness classes, A–H, each of which has an associated amplitude d_i for each spatial frequency, defined in equation (4.2). G_d is a displacement Power Spectral Density function which is defined for each spatial frequency according to equation (4.3). $G_d(n_0)$ is defined for each of the roughness classes A–H in the ISO standard. Equations (4.1), (4.2) and (4.3) are reproduced here from Malekjafarian et al. [113]:

$$r(x) = \sum_i d_i cos(n_i x_c + \gamma_i) \tag{4.1}$$

$$d_i = \sqrt{2 G_d(n_i) \Delta n} \tag{4.2}$$

$$G_d(n_i) = G_d(n_0) \left(\frac{n_i}{n_0} \right)^{-\Omega} \tag{4.3}$$

In this thesis, in accordance with the approach used by Yang et al. [408] and Malekjafarian et al. [113] the sampling interval for spatial frequency is taken as $\Delta n = 0.04$ cycles/m and the range of spatial frequencies evaluated is $i = 1$ to $i = 100$. Given this, to generate a road profile in accordance with ISO 8608 it is necessary only to select the desired roughness class and choose a value for the spectral exponent Ω (denoted as ω in ISO 8608, but shown here as Ω to avoid confusion with the use of ω for vehicle and bridge frequencies). The ISO 8608 model recommends that a value of $\Omega = 2$ is used for the spectral exponent and this is the approach used in [408] and [113]. However, Ainalis et al.'s studies of real road profiles using an inertial profilometer [157] found that estimates of spectral exponent from vehicle responses to real road conditions were not consistent: estimated values for Ω covered a range as was indicated in Fig. 2.4.9 in chapter 2, being dependent on frequency as well as varying according to the speed ratios of the vehicle runs used for estimation. Ainalis et al.'s explanation for this variation was based on non-repeatability of wheel tracks on subsequent runs. It seems reasonable to assume that even if vehicle wheel tracks were precisely repeatable, degradation of road surface over time would mean that the true spectral exponent for a given road and wheel track would not be constant. Further detailed discussion of this variation is considered to be beyond the scope of this thesis since it is not proposed to rely on classification of road surfaces encountered in fieldwork according to ISO 8608 classes, as doing so in a meaningful way would require measurement of the true profile traversed in each experimental run (as noted by Ainalis et al. [157]) and the measurement

of true road profiles in-situ was beyond the capability of the current project in practical and economic terms.

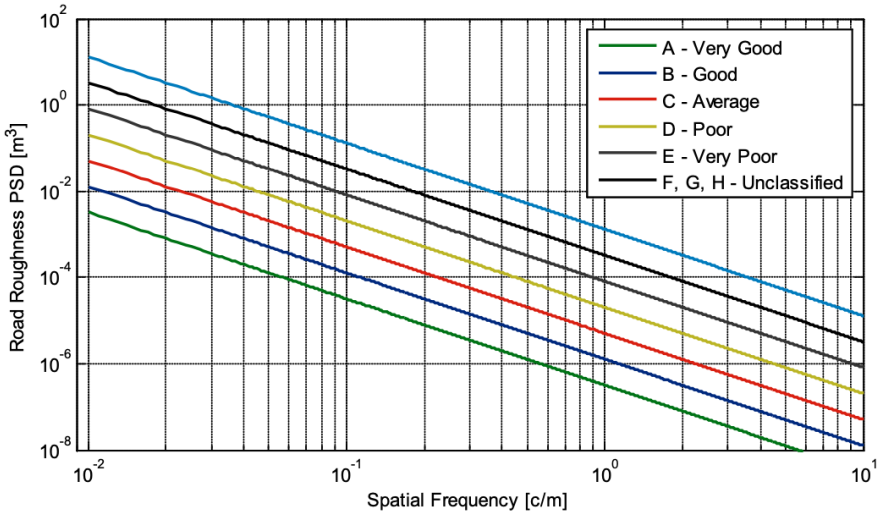

Figure 4.2.1: ISO 8608 road profile spectra. Reproduced from Ainalis [3].

Fig. 4.2.1 shows example spectra for all classes in ISO 8608. Fig. 4.2.2 shows an example profile and the corresponding spatial PSD for a simulated ISO 8608 class A road surface using the method outlined above.

4.2.2 Spectral input bias

Considering the FRF as a ratio of response to excitation spectra (equation 2.11 in chapter 2) it is intuitive that a biased spectral input will result in a biased estimate of the FRF for output-only estimation methods. Further, if it is assumed that the road surface takes the general form of an ISO 8608 profile, the acceleration input will be spectrally biased. As noted by Ainalis [3] the ISO 8608 profile is spectrally flat (unbiased) for velocity and therefore must be biased in acceleration. The bias would be more pronounced for an assumption of Gaussian white noise displacement input, since this would necessarily be spectrally flat for displacement.

To explore spectral input bias let us assume that the displacement input experienced by the vehicle at the wheel-road contact point is harmonic. Specifically, we may assume that it takes the form shown in equation (4.4); that is, the displacement as a function of time $u(t)$ is defined in relation to some circular frequency ω and is scaled by some constant A. The first derivative of this expression with respect to time gives the velocity input $\dot{u}(t)$; the second derivative gives the acceleration input $\ddot{u}(t)$ (equations (4.5) and (4.6) respectively). These expressions show that the acceleration input spectrum may be biased by the

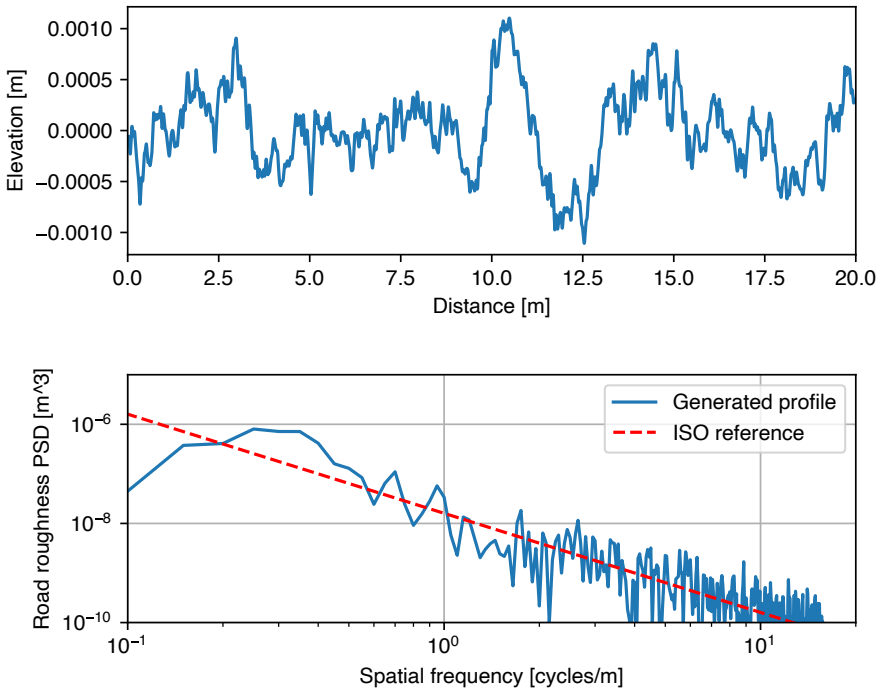

Figure 4.2.2: Example spatial PSD for simulated ISO 8608 class A road surface.

input frequency ω in the case of an ISO 8608 road profile, or by the square of input frequency in the case of a Gaussian white noise displacement input.

$$u(t) = Ae^{j\omega t} \tag{4.4}$$

$$\dot{u}(t) = j\omega Ae^{j\omega t} \tag{4.5}$$

$$\ddot{u}(t) = \omega^2 Ae^{j\omega t} \tag{4.6}$$

4.2.3 Simulated quarter-car response

To illustrate the potential effects of spectrally-biased input on estimated modal parameters, the response of a 2DoF sprung mass quarter-car model (see Fig. 2.5.2 in chapter 2) was simulated for Gaussian white noise displacement base input and ISO 8608 road profile base input. The simulated quarter car properties were selected by inspection to be reasonably representative of the full-scale test vehicle used in this chapter. It was assumed that the upper (sprung) mass of

the vehicle was 1200 kg, with two occupants (assumed combined mass 145 kg) and a half-full tank of fuel (assumed 25 kg) resulting in $m_2 = 1370$ kg for the upper DoF mass in a 2DoF quarter car model. The remaining quarter car model parameters were based on the proportions set out by Sayers [5] who presents m_1, k_1, k_2 and c_2 in terms of m_2. The resulting values were $m_1 = 205.5$ kg, $k_1 = 6.709575$ x 10^5 Nm^{-1}, $k_2 = 9.53931$ x 10^4 Nm^{-1} and $c_2 = 8.22$ x 10^3 Nsm^{-1}. For this system the expected undamped modal frequencies can be calculated as the solution to the homogeneous form of the matrix equation of motion for the system as shown in equation 2.1 (chapter 2), which for this system becomes equation (4.7). Solving for the eigenvalues w_i (here using the Python toolbox available from [409]) results in solutions indicating frequencies $f_1 = 1.24$ Hz and $f_2 = 9.73$ Hz.

$$det\left(\begin{bmatrix} k_1 + k_2 & -k_2 \\ -k_2 & k_2 \end{bmatrix} + \omega^2 \begin{bmatrix} m_1 & 0 \\ 0 & m_2 \end{bmatrix}\right) = 0 \tag{4.7}$$

The absolute value of the theoretically-expected acceleration FRF was calculated using equations 2.7 and 2.8 (chapter 2). This is compared to the power spectrum of the response at each of the two DoFs, estimated using Welch's method. In Fig. 4.2.3 the displacement power spectrum calculated from the simulated DoF displacement response is compared to the theoretically-expected acceleration FRF in the upper plot. All plotted lines are self-normalised. It is evident that the simulated response power spectra show peaks at the expected frequencies. The lower plot shows the power spectra estimated from the DoF acceleration responses. A comparison to the theoretical FRFs in the upper plot shows that the responses appear different than would be expected: the low-frequency peaks are barely distinct and a significant increase in response magnitude is apparent for DoF 2 at higher frequencies. This plot also shows the theoretically-expected FRFs for each DoF scaled by the square of the input frequency and these show good agreement with the estimated power spectra upon visual inspection. Without knowledge of the frequency bias of the input spectra, the observed outputs could be mistaken for having their lowest distinct frequencies significantly higher than those expected given knowledge of the true system parameters.

Fig. 4.2.4 illustrates a similar process for input taking the form of an ISO 8608 class A road profile. Upon visual inspection the expected acceleration FRF and estimated-from-observed-response power spectra show clear similarities once the theoretical plots are scaled according to the input frequency. Recalling that in practice acceleration will be recorded (rather than displacement or velocity) at each DoF, this exercise confirms that accounting for spectrally-biased inputs could be expected to lead to improved visibility of modal parameters.

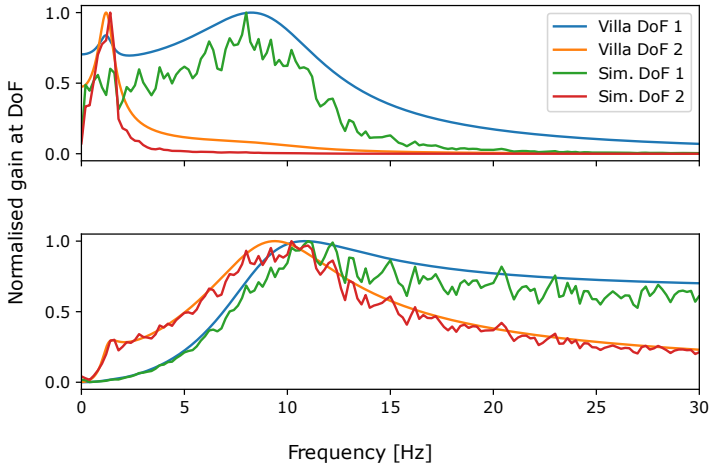

Figure 4.2.3: Displacement (upper plot) and acceleration (lower plot) vehicle FRF for base excitation input modelled as white noise (spectrally flat in displacement) compared to anticipated FRF according to Villa's method [17] (scaled by squared frequency).

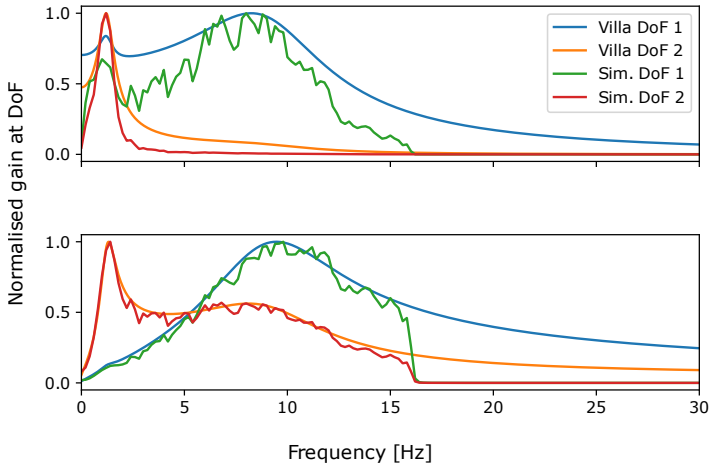

Figure 4.2.4: Velocity (upper plot) and acceleration (lower plot) vehicle FRF for base excitation input modelled as an ISO 8608 class A road (spectrally flat in velocity) compared to anticipated FRFs according to Villa's method [17] (scaled by frequency).

4.2.4 Sources of error in output-only modal parameter estimation

A key challenge inherent in the fieldwork discussed in this chapter is that the true values of the test vehicle mass, spring stiffness, damper coefficient, tyre pressure and effective tyre damping are unknown. It is assumed that potential errors in the estimated modal parameters could be caused by the following:

1. Spectral input bias.
2. Physical model not adequately represented by quarter-car approximation:
   (a) More degrees of freedom (different kinematics) in physical modal than in quarter-car model (e.g.: pitching and rolling modes are present).
   (b) Physical model is non-linear in some parameters while quarter-car model is assumed to be linear.
3. Errors inherent to estimation methods indistinguishable from other error sources due to lack of knowledge of ground-truth parameter values.

An overview of the proposed means of addressing each of these potential sources of error is given in Table 4.2.1. Item 1 in this list, spectral input bias, has been discussed above. Item 2 (a) will be discussed further in the following sections. Item 2 (b) is challenging to address and will be considered as out-of-scope for this thesis. Item 3 is the subject of the following sections, where the proposed methods of parameter estimation are demonstrated with synthetic data generated by a simulated system with known parameters.

Potential source of error in output-only vehicle modal parameter estimation	Proposed mitigation	Section reference
1 - Input bias	Assume road input takes the general form of ISO 8608 profile and scale outputs according to frequency.	4.2.2 and 4.2.3
2 (a) - Pitch and roll modes	Assume that visibility of bounce modes will persist after ensemble averaging (in time or frequency domain) while assuming pitch and roll modes are more random and thus will be de-emphasised in the ensemble average.	4.4
2 (b) - Physical model nonlinearity	Considered to be out-of-scope for the present work (i.e. assume physical model is in fact linear in all parameters whose value is sought).	–
3 - Estimation method inherent errors (lack of knowledge of ground truth values)	Demonstrate performance of estimation methods using synthetic data generated from simulated system with known parameters.	4.2.5, 4.2.6 and 4.2.7

Table 4.2.1: Summary of potential sources of error in output-only estimation of vehicle quarter-car modal parameters, and the proposed mitigation.

4.2.5 Example estimation of modal parameters

Figure 4.2.5 shows a sample of the simulated acceleration responses at each DoF of the quarter car when subject to an ISO 8608 class A road surface, alongside the power spectra estimated for each of the DoF acceleration responses using Welch's method (applied with a 5 s Hanning window with 50% overlap). The estimated power spectra are each scaled by f^{-1} and then scaled to unity at low frequency. Also shown is a smoothed estimate of each spectrum, achieved by applying a 3rd-order Savgol filter (with the smoothing length chosen as 50 for DoF 1 and 10 for DoF 2, in units of f_s^{-1}.

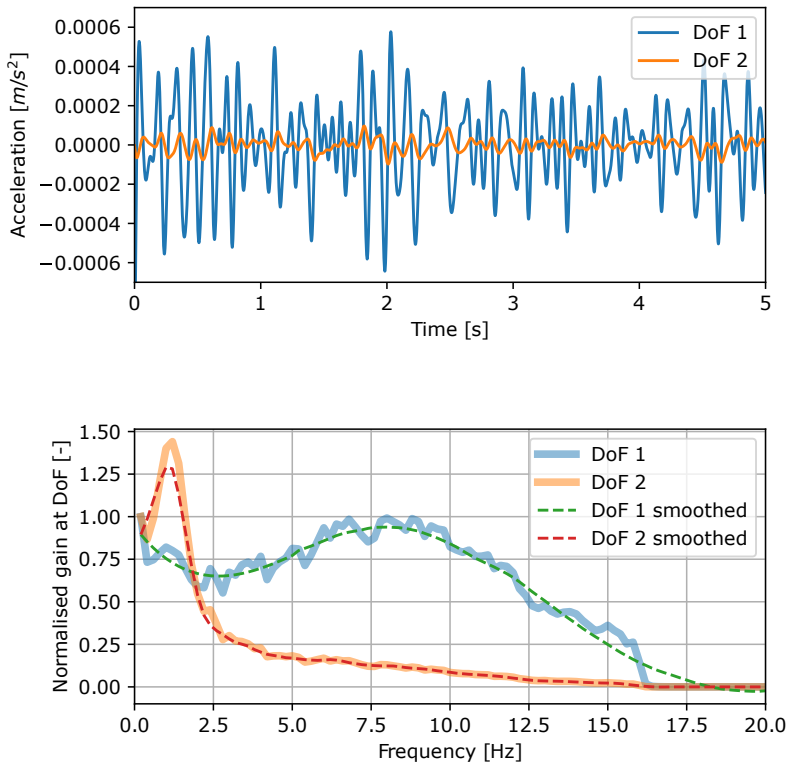

Figure 4.2.5: Example quarter car synthesised response to ISO 8608 class A road surface. Upper plot: extract from acceleration response at DoFs 1 and 2. Lower plot: estimated power spectra.

4.2.6 Frequency-domain method

Figure 4.2.6 shows a comparison of picked peak frequencies (indicated by a dot) and the bandwidth at half power associated with each peak (indicated by a horizontal line). The relative peak height is 0.5 since the signal power has been plotted as $\sqrt{S(f)}$. The estimated raw and smoothed power spectra used here are those previously calculated, using Welch's method with a 5 s Hanning window with 50% overlap. The figure compares estimation of frequency and damping from the raw and smoothed power spectrum estimates. In this example there is little change in the estimated frequency for each mode, but the figure illustrates the potential for significant bias in parameter estimation when using non-smoothed spectra. The upper plot demonstrates a reduction in half-power bandwidth due to what appears to be a spurious peak. Intuitively the estimated frequency could be subject to a similar bias. It is therefore concluded that smoothing of the estimated power spectra is beneficial here.

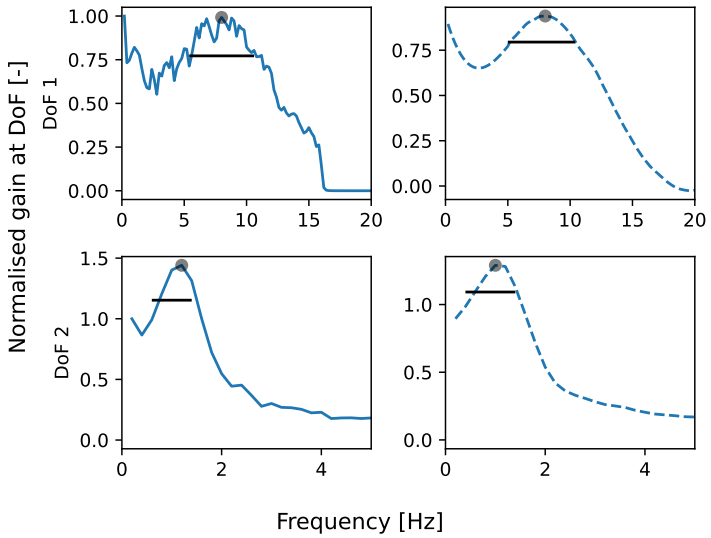

Figure 4.2.6: Example of modal frequency and damping estimation from raw (left) and smoothed (right) power spectra.

Noise inherent in power spectrum estimates has the potential for causing bias in the estimated frequencies and modal damping ratios. Smoothing the spectra before estimating modal parameters is one possible method of mitigating this bias, as demonstrated. However, it is conceivable that such smoothing could itself cause bias, as illustrated in Figs. 4.2.7 and 4.2.8 in which the smoothing length is varied and results in significant differences in bandwidth at the half-power level. Thus it is apparent that smoothing the power spectra is reliant on the user's judgement as to whether the smoothed curve is appropriately fit to the original curve. In this case, visual inspection suggests that the smoothing filter lengths indicated in Fig. 4.2.5 are reasonable.

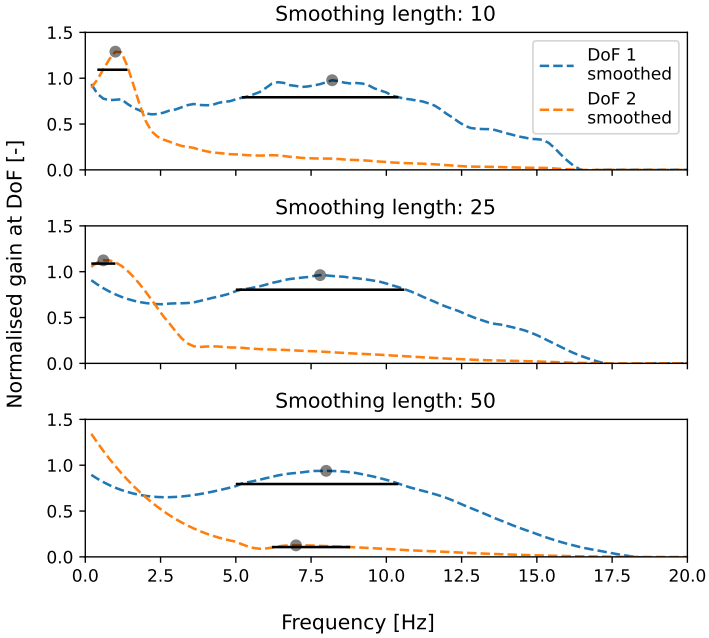

Figure 4.2.7: Illustration of bias in frequency estimates (peak-picking and half-power bandwidth methods applied to power spectrum) as a function of smoothing filter length (1 of 2).

Fig. 4.2.9 summarises the estimated modal parameters, from the raw and smoothed power spectra, recalling that the spectral peaks represent damped frequencies and thus the well-known equation (4.8) is adopted to estimate the natural frequency ω from the spectral peak damped frequency ω_d and the half-power bandwidth damping ratio ζ. Target modal frequencies are indicated. Since the vehicle could not be practically bench tested, no reference values for modal damping ratios were available, but the results are generally in accordance with expected quarter car values according to Jazar [6].

$$\omega = \frac{\omega_d}{\sqrt{1-\zeta^2}} \tag{4.8}$$

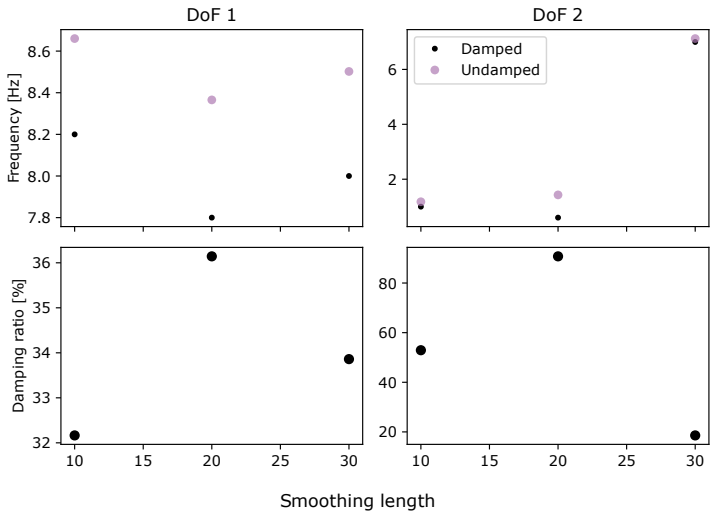

Figure 4.2.8: Illustration of bias in frequency estimates (peak-picking and half-power bandwidth methods applied to power spectrum) as a function of smoothing filter length (2 of 2).

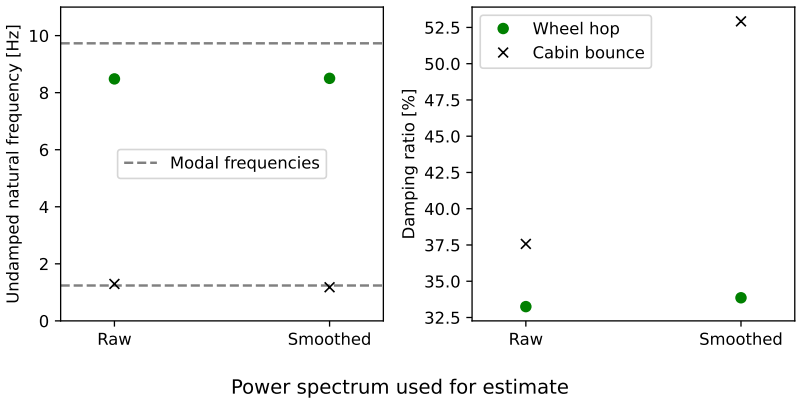

Figure 4.2.9: Summary of modal frequency and damping estimates for raw and smoothed power spectra.

4.2.7 Time domain method

Fig. 4.2.10 shows random decrement signatures (RDS) for each of the DoFs in the quarter car simulated response to the ISO 8608 class A road profile. In each case the sample length used for RDS estimation was 5 s in accordance with the recommendations given by Ainalis [3]. Also adopted from the same source was the choice of a triggering condition corresponding to zero-crossing with a positive gradient. It should be noted that the plot shows the auto-RDS i.e. the trigger and response channels are identical in each case. A trigger tolerance of $\pm 1 \times 10^{-5} m/s^2$ was adopted.

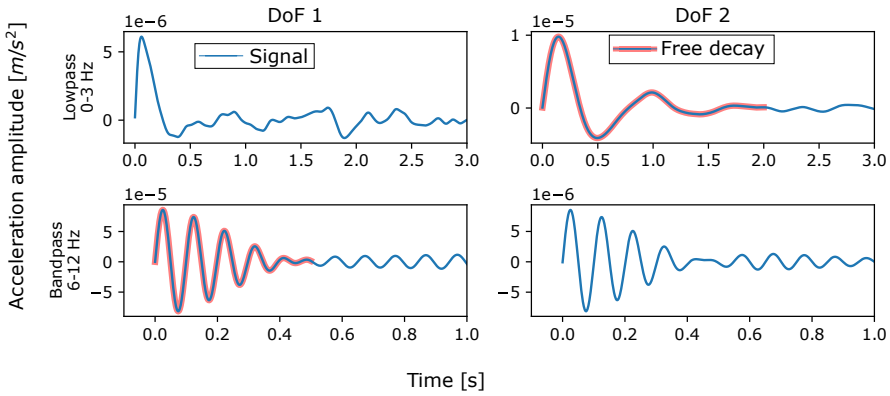

Figure 4.2.10: Random decrement estimates from frequency-filtered simulated acceleration responses.

Frequency filtering was employed to process the simulated acceleration signals prior to calculation of the RDS, again in accordance with Ainalis [3]. Lowpass filtering (below 3 Hz) and bandpass filtering (6–12 Hz) were used for the responses from DoF 2 and DoF 1 respectively. Highlighted in red in Fig. 4.2.10 is the part of the RDS deemed to represent free decay for each mode (determined by visual inspection), comprising the first 2 s for the cabin bounce at DoF 2 and the first 0.5 s for axle hope at DoF 1. This illustrates the question of optimal RDS trim length, which is revisited later in the chapter.

Fig. 4.2.11 summarises the modal parameters estimated by the matrix pencil method (MPM) applied to all four RDS estimates. In each case, the full 5 s RDS was used. Assuming that each RDS represents a single mode of response due to the frequency lowpass and bandpass filtering employed, the estimated modal parameters show good visual agreement with the expected modal frequencies. This suggests that for synthetic data the MPM can generate good parameter estimates even when visual inspection of the RDS suggests that it may not be representative of the true free response of the system (for example the upper left plot in Fig. 4.2.10) and without needing to trim the RDS. However, it is not immediately clear if this will be the case for field-gathered data.

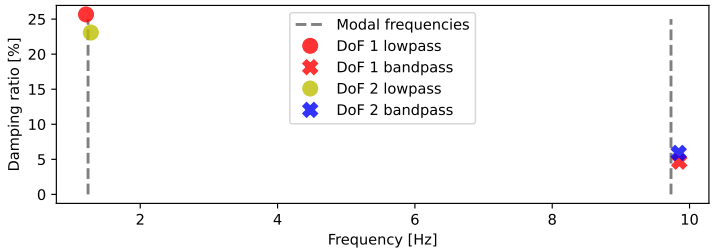

Figure 4.2.11: Matrix pencil method modal frequency and damping ratio estimates for all four RDS estimates shown in Fig. 4.2.10 compared to expected values (indicated by dashed lines).

4.2.8 Comparison of estimated parameters

Here, a comparison is made of the estimation outcomes for all three methods:

- **MPM** - Frequency filtering of signal; RDS estimation; modal parameter estimation in the time domain by Matrix pencil method.
- **PSD raw** - Power spectrum estimation by Welch method; scaling the estimated spectra; estimation of modal parameters by peak picking and half power bandwidth method.
- **PSD smoothed** - As for **PSD raw** above but including smoothing of the estimated power spectra using a Savgol filter.

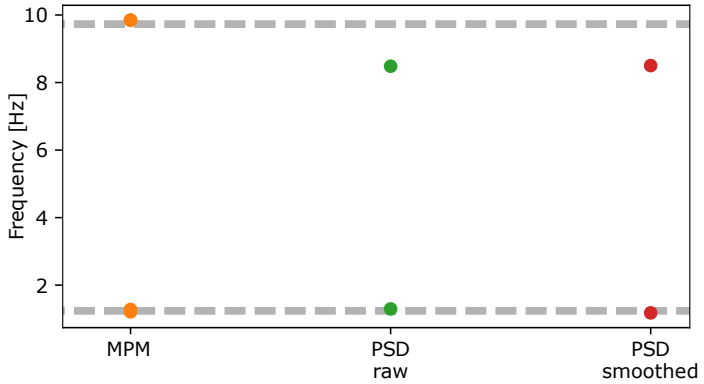

Figure 4.2.12: Estimated frequencies compared to expected values (indicated by dashed lines).

4.2.9 Estimated frequencies

Fig. 4.2.12 shows all of the predicted frequencies for the three methods compared to the ground truth modal frequencies. Fig. 4.2.13 compares the mean absolute estimation error. Regarding the first mode (cabin bounce) these plots show that the **MPM**, **PSD raw** and **PSD smoothed** methods result in estimates of the cabin bounce frequency with generally equitable accuracy, although smoothing of the power spectrum seems to slightly increase the estimation error. Regarding the second mode (wheel hop) it is apparent that only the **MPM** yields an accurate frequency estimate, with the frequency-domain methods being in error by slightly more than 1.5 Hz.

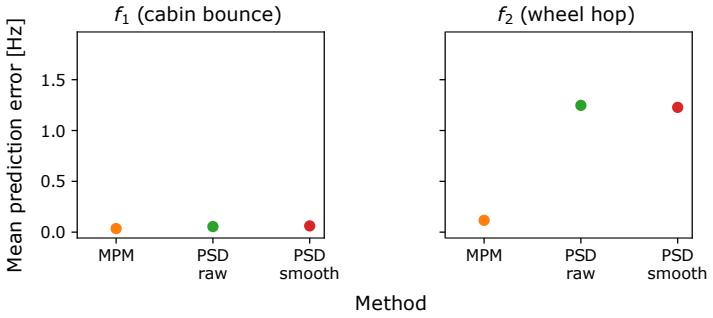

Figure 4.2.13: Comparison of frequency prediction errors.

This comparison suggests that the power spectrum-based method is adequate for estimation of the cabin bounce frequency, and that smoothing of the spectrum is not necessarily required (and may in fact induce error in the estimated frequency). The **MPM** method appears to yield accurate estimates of both the cabin bounce and wheel hop frequencies. It should be noted, however, that this method includes frequency filtering of the acceleration signals and that such filtering requires a prior estimate of the approximate frequencies of each mode. Without a reasonable prior assumption of the underlying frequencies, such estimates could be made by inspection of estimated power spectra.

4.2.10 Estimated damping ratios

Fig. 4.2.14 shows the estimated damping ratios for each of the three methods previously listed. It is difficult to directly draw conclusions from consideration of this figure, since the synthetic responses were generated based on a quarter car whose damping was directly modelled as viscous damper coefficients, rather than as modally-independent damping ratios. For this reason, Fig. 4.2.15 shows a comparison of the theoretical FRF for each DoF generated by equations 2.7 and 2.8 (directly modelling the viscous damper kinematics) with the theoretical FRF according to equations 2.5 and 2.6 (assuming modally-independent damping).

Inspection of Fig. 4.2.15 suggests the following conclusions:

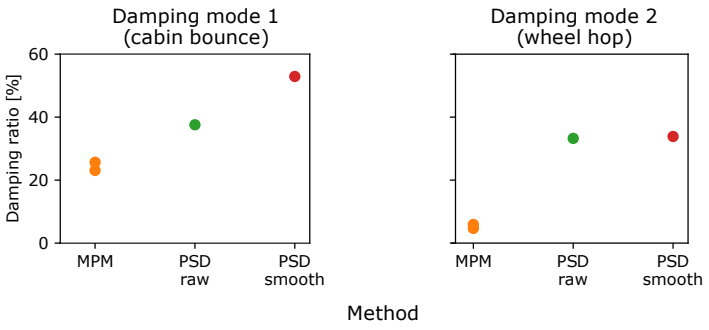

Figure 4.2.14: Comparison of damping ratio estimates.

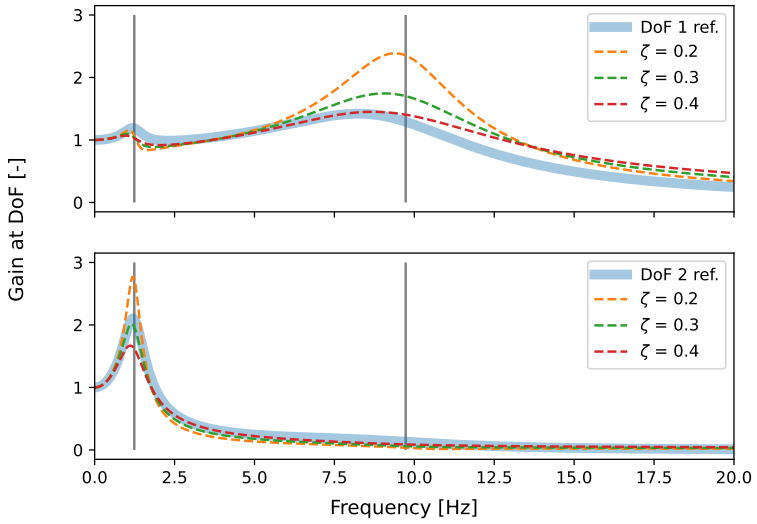

Figure 4.2.15: Theoretical FRF expressions based on varying modal damping ratios (DoF 1 upper plot, DoF 2 lower plot) compared to the reference with damper properties (Villa [17]). Expected undamped natural frequencies indicated by vertical lines.

1. Modal damping ratios in the region of $\zeta_1 = 0.4$ and $\zeta_2 = 0.3$ appear to give the best visual fit to the reference FRF curves. It is noteworthy that none of the tested parameter estimation methods achieved a good match to these damping ratios, although the power spectrum-based method yielded the best agreement, and the MPM appears to have underestimated the damping ratio for DoF 1.

2. In general terms it appears to be difficult to consistently and accurately estimate damping from in-service responses, which is a well-known challenge. Considering future application to field-gathered data, the difficulty might be further compounded by non-linear damper characteristics of dampers. Damper non-linearity can be reasonably expected, but recall that mitigation of this has been deemed to be out-of-scope for this thesis.

4.2.11 Methods for use with field-gathered data

The power spectrum and matrix pencil methods offer advantages for use with field-gathered data. It should be noted that both methods have in common a basis of averaging the signal across multiple segments, with the key difference being the domain in which this averaging is undertaken. Table 4.2.2 summarises the methods tested in this chapter thus far; notes their advantages and disadvantages based on the synthetic data fitting tests undertaken; and adds further summative commentary. Perhaps most important is that the matrix pencil method has been shown to perform well when the data are frequency filtered prior to generating the RDS. This implies approximate prior knowledge of vehicle modal frequencies. When such frequencies are unknown, the method is potentially subject to bias. Based on this and the discussion in Table 4.2.2, for modal parameter estimation from field-gathered acceleration responses in this chapter the tested methods will be used as follows:

- For comparison of estimated vehicle parameters (for both phases of fieldwork), frequency-domain estimation using the power spectrum method will be adopted.
- For evaluation of the possible range of variation of estimated parameters, time-domain estimation using RDS and MPM of frequency-filtered data will be tested, splitting the signal into segments to yield multiple estimates of modal parameters.

METHOD	ADVANTAGES	DISADVANTAGES
Power spectrum method	- Computationally light - Averages across multiple segments (counters non-stationarity of input or response) - Allows combination of multiple records into ensemble averages (counters variation related to road surface class and traversal speed) - Relatively accurate estimation of modal frequencies	- Without smoothing, sensitive to noise in data - With smoothing, sensitive to smoothing filter length - Uses only the local peak of absolute power spectrum (wider shape of curve neglected) - Phase information lost
Frequency filtering, random decrement and matrix pencil method	- Accurate estimates of modal frequencies - Maintains phase information - Averages across multiple segments (counters non-stationarity of input or response)	- Prior knowledge of approximate modal frequencies assumed - Multiple data processing stages required -Appears to underestimate modal damping ratios (particularly for wheel hop)

Table 4.2.2: Advantages, disadvantages and additional comments relating to methods of modal parameter estimation tested with synthetic data in this chapter.

4.3 Fieldwork data gathering regimes

This chapter uses data gathered in two phases of fieldwork. This section comprises a summary of the data gathering regimes and experimental procedures undertaken.

4.3.1 Fieldwork summary

The fieldwork relating to the present chapter comprised two distinct phases. The first phase discussed and analysed, here referred to as *phase 1* was undertaken on 3rd April 2023. The second phase discussed and analysed in this chapter was in fact undertaken earlier, on 5th December 2021. Since it is discussed later in the chapter and is used as an example of applying the analysis techniques under review to data gathered in an alternate vehicle configuration it is referred to here as *phase 2*.

Both phases of fieldwork comprised driving a car, instrumented with accelerometers, at nominally-constant speeds on public roads. It is assumed that by traversing the roadway the vehicle's wheels experience a time history of vertical displacement. The accelerometers were employed to record vertical acceleration during the traversals, with the ultimate aim of analysing the vehicle's acceleration response and inferring mechanical properties of reduced degree of freedom model deemed to be equivalent to the car used for testing.

4.3.2 Fieldwork test vehicle and instrumentation

The vehicle used for testing was a Honda Civic VIII FK2. This is a petrol-fuelled manual-transmission hatchback car, with this particular vehicle having been produced in 2007. The car features individually articulated front suspension, using a *MacPherson strut* system which is a popular front suspension design particularly for lower-cost and front-wheel drive cars. The rear suspension features a *torsion bar* arrangement, in which both wheels are constrained to move together in the lateral plane, but some small degree of vertical differential movement is afforded by deflection of the so-called torsion bar. The car was instrumented with Parker LORD *G-LINK-200 8G* wireless accelerometers. During phase 2, a smartphone device was also used for data gathering, leveraging its in-built accelerometer. Sensor locations, as well as the test vehicle are shown in Figs. 4.3.1 and 4.3.2 for phases 1 and 2 respectively. The figures are marked up to indicate sensor (Parker LORD G-Link-200 8G accelerometer) locations used in phase 1 (A: front cabin floor (left); B: mid-cabin floor (right); C: rear trunk floor (left); D: base of front suspension strut (left)) and phase 2 (E: Parker LORD G-Link-200 8G accelerometer on base of front suspension strut (right); F: Motorola Moto G30 smartphone on cabin centre console). In all cases, vehicle speed was maintained by the built-in cruise control system.

The test vehicle underwent alterations to its suspension system between phases 1 and 2, as noted below:

- Anti-roll bar bushes and anti-roll drop links were replaced on the front axle due to wear. This alleviated a source of play in the front suspension. The defect was present during phase 2 fieldwork. The new bushes and links were installed prior to phase 1.
- Front suspension springs were replaced between the two phases of fieldwork. The springs installed during phase 1 were more stiff, and slightly shorter than those installed during phase 2. The replacement springs were part of a sports suspension upgrade, comprising stiffer springs and a small reduction in vehicle ride height.

These changes to the test vehicle's suspension system effectively allow the application of output-only methods for vehicle parameter estimation to two different vehicle configurations. This facilitates investigation of the sensitivity and repeatability of the estimation methods, since the change in vehicle configuration is expected to lead to a change in estimated vehicle parameters.

Figure 4.3.1: Vehicle used for fieldwork, showing sensor locations in phase 1.

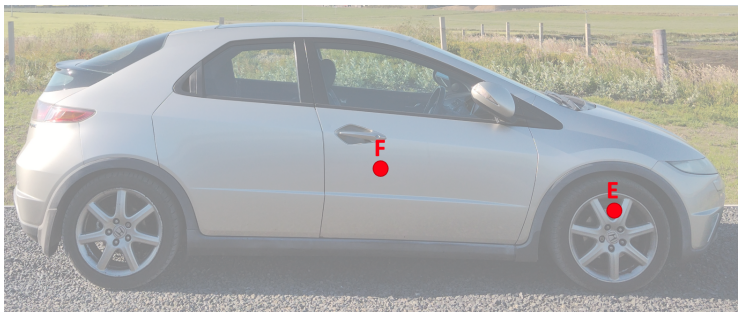

Figure 4.3.2: Vehicle used for fieldwork, showing sensor locations in phase 2.

4.3.3 Fieldwork test regimes - phase 1

Phase 1 comprised driving on two roads, at three nominally constant speeds, for two runs (out and back) each giving a total of twelve acceleration response records from the four installed accelerometers. The routes driven during fieldwork phase 1 are indicated in Fig. 4.3.3. Both roads were on the Tarbat Peninsula, between the Dornoch Firth and Moray Firth, north of Inverness on the east coast of Scotland. Data were recorded using *SensorConnect* software by Parker LORD.

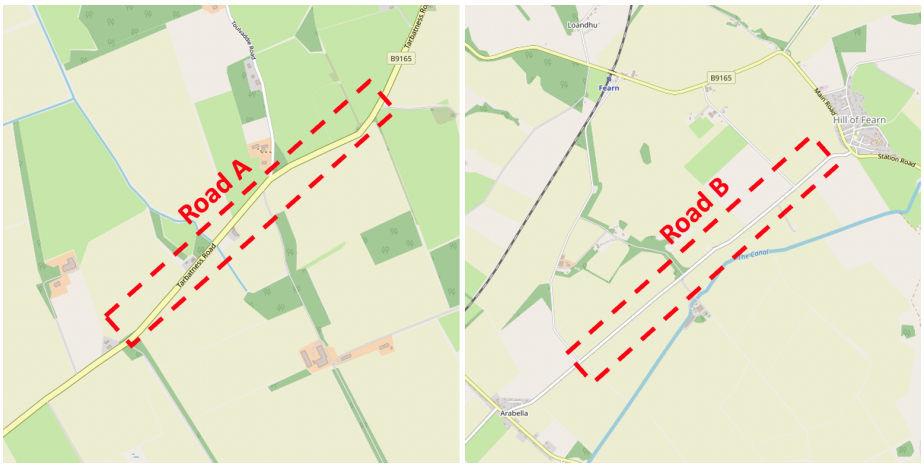

Figure 4.3.3: Road driving routes used for phase 1 of fieldwork. Orientation: north up. Map ©OpenStreetMap contributors, available under the Open Database Licence [18].

4.3.4 Fieldwork test regimes - phase 2

Phase 2 consisted of driving at one nominally constant speed on one road, for two runs (out and back) giving a total of two acceleration response records each from the one installed accelerometer and one installed smartphone device. The routes driven during fieldwork phase 2 are indicated in Fig. 4.3.4. The road was the A1 between Edinburgh and Dunbar in south-east Scotland. Smartphone data were recorded using the Android application Sensor Logger written by Kelvin Choi [410].

Tables 4.3.1, 4.3.2 and 4.3.3 summarise the test regimes and vehicle sensor instrumentation for fieldwork phases 1 and 2.

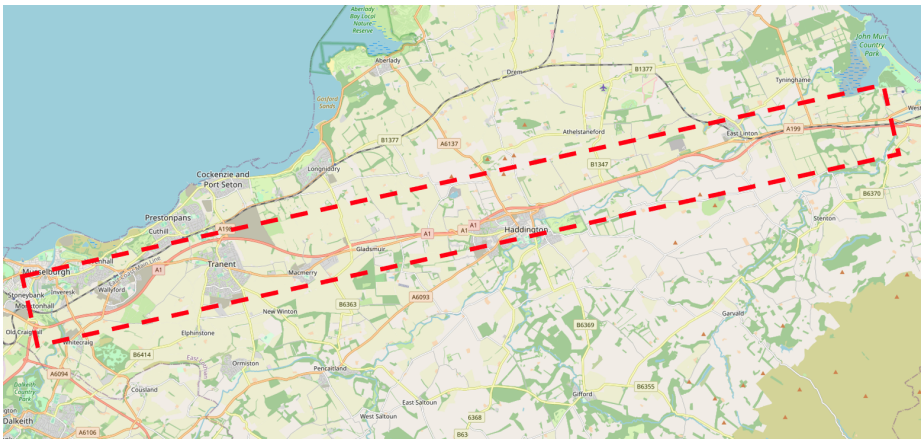

Figure 4.3.4: Route used for phase 2 of fieldwork (dashed line box denotes extent of the A1 road driven). Orientation: north up. Map ©OpenStreetMap contributors, available under the Open Database Licence [18].

	Roads	Nominal speeds	Runs each	Runs total
Phase 1	2	3 (20, 30, 40 mph)	2	12
Phase 2	1	1 (60 mph)	2	2

Table 4.3.1: Summary of test regimes for phases 1 and 2 of fieldwork.

	Accelerometers (cabin)	Accelerometers (axle)	Smartphones (cabin)	Vehicle configuration
Phase 1	3 (front left, mid right, rear left)	1 (front left)	0	*Reference configuration*
Phase 2	0	1 (front right)	1 (cabin centre)	*Alternate configuration (softer front springs; play in front anti-roll bar bushes and drop links)*

Table 4.3.2: Summary of sensor instrumentation for phases 1 and 2 of fieldwork.

	Accelerometers sampling frequency	Smartphone sampling frequency
Phase 1	512 Hz	–
Phase 2	512 Hz	500 Hz

Table 4.3.3: Summary of sensor sampling rates for phases 1 and 2 of fieldwork.

4.4 Phase 1 fieldwork data: frequency-domain parameter estimates

4.4.1 Estimates of power spectra

The process of generating averaged power spectra is illustrated by Figs. 4.4.1 and 4.4.2 for the front left cabin and axle sensors respectively, using acceleration responses from two runs on each of two roads at three different speeds. Using these two sensors implies that they can be assumed to represent the dynamic behaviour of an equivalent quarter-car model. Power spectra are first estimated by Welch's method, using a 5 s window length with 50% overlap (upper subplots). Then, they are combined to form an ensemble averages by adding spectral amplitudes element-wise and dividing the whole result by the number of estimates used in the ensemble. The middle subplots show ensembles for each vehicle speed and the lower subplots show ensembles for all speeds. These figures serve to demonstrate that the averaged power spectra for all vehicle speeds are dominated by the acceleration responses recorded at 40 mph. This is due to the amplitude of response increasing as a function of vehicle speed.

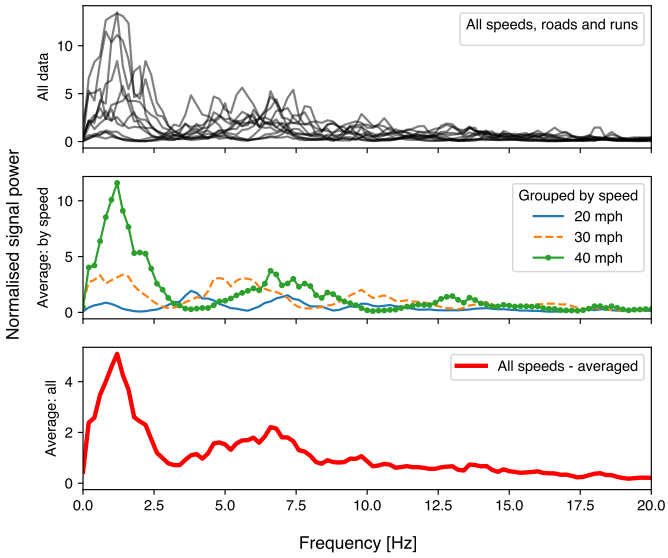

Figure 4.4.1: Illustration of the process of generating an average power spectrum (front left **cabin** sensor).

Upon inspection of Fig. 4.4.1 it is tempting to treat the two clear peaks visible in the 40 mph ensemble average spectrum as representing cabin bounce (the lower frequency) and wheel hop (the higher frequency). Indeed, this would seem to be a reasonable assumption since the previous studies of theoretical FRFs (for example as summarised in Fig. 2.4.3 from Rouillard and Lamb [4])

imply that the wheel hop frequency might be visible as a spectral peak in the spectrum generated from the sensor on the sprung mass DoF (in this case the left front cabin sensor). However, Fig. 4.4.2 shows a dominant spectral peak from the axle-mounted sensor at a different frequency, leading to the conclusion that the higher-frequency peak visible from the cabin sensor must relate to some other aspect of the vehicle's kinematics such as pitch or roll motion.

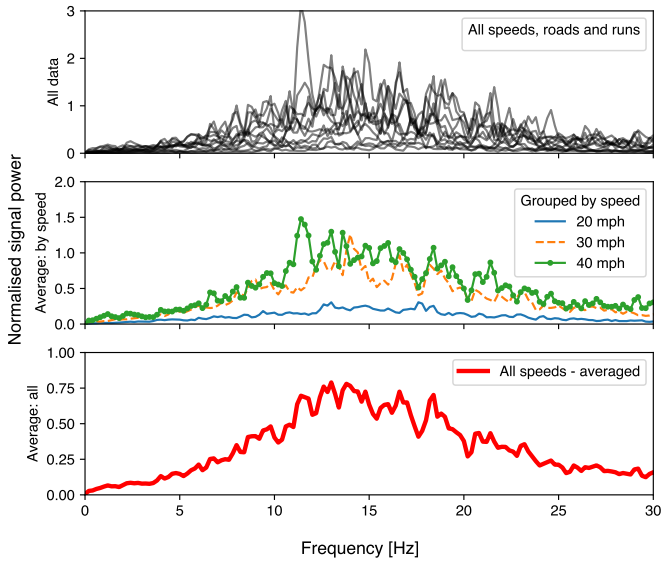

Figure 4.4.2: Illustration of the process of generating an average power spectrum (front left **axle** sensor).

The prior analysis of synthetic vehicle response suggested that the input acceleration spectra would be biased to higher energy at higher frequencies, and be spectrally flat in terms of velocity if the road surface took the general form of an ISO 8608 profile. This effect was shown to be countered by scaling the acceleration response spectra by $(1/f)$ resulting in an improved match to the expected FRFs. Fig. 4.4.3 shows the ensemble averaged power spectra for 40 mph vehicle runs, grouped by sensor location, compared with the same spectra scaled by $(1/f)$. In this case the scaling results in the loss of distinct spectral peaks and a concentration of signal power at very low frequency. This outcome suggests that the input acceleration in fieldwork phase 1 was approximately spectrally flat, and that scaling by $(1/f)$ will not improve visibility of vehicle modal parameters as was shown in the synthetic data example. This scaling was therefore not further pursued for field-gathered data in the present chapter.

In order to estimate modal parameters from power spectra using the peak-picking and half-power bandwidth methods, the shape of any particular spectrum is more important than the relative signal power magnitude compared to that seen in other spectra. Self-normalisation allows the relative shapes of

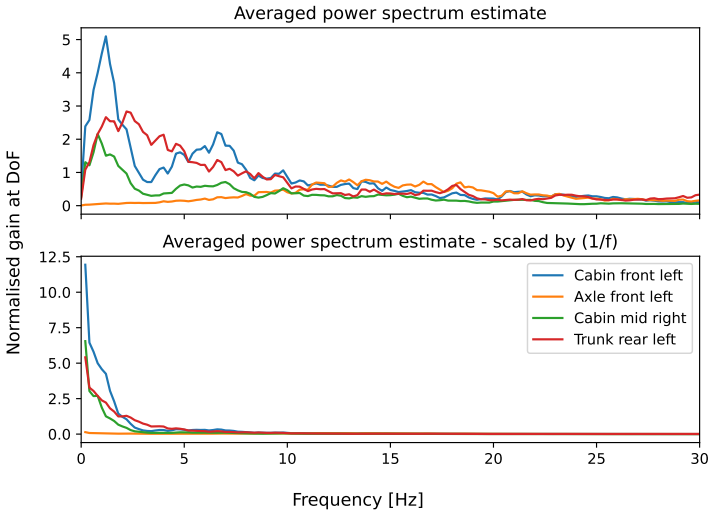

Figure 4.4.3: Upper plot: averaged power spectra grouped by sensor. Lower plot: the same spectra scaled by $(1/f)$.

spectra to be more easily visualised. Fig. 4.4.4 shows such a self-normalised comparison of the estimated power spectra grouped by speed. It is clear that, as speed increases, the shape of the power spectra from all cabin-mounted sensors seems to converge, being dominated by a spectral peak in the region of 1–2 Hz. The axle sensor spectrum maintains the same general shape at all vehicle speeds. As previously mentioned, the power spectrum does not include phase information and thus there is no way to be sure that these peaks represent in-phase motion of the vehicle. For the purpose of this thesis, it will be assumed that these spectral peaks are indeed in-phase with respect to each other. The general shape of the power spectrum estimated from the axle-mounted sensor is the same for each of the three speeds used in this phase of fieldwork, which suggests that the general nature of the road profiles traversed by the vehicle is consistent in the frequency range shown (0–30 Hz).

4.4.2 Estimates of frequency and damping

It was decided to estimate modal parameters from the spectra estimated for each sensor from an ensemble of all responses at 40 mph. This decision was based on the following:

- The estimated spectra appear (from visual inspection and comparison) to converge towards the generally-expected shapes when the vehicle speed approaches 40 mph.
- Spectra for 20 and 30 mph ensembles showed multiple peaks, which would complicate the intended process of picking a clear dominant peak and assuming its association with a mode of the vehicle's vertical response.
- The ensemble average spectra for all speeds were dominated by the response at 40 mph due to the higher amplitude of response at this speed.

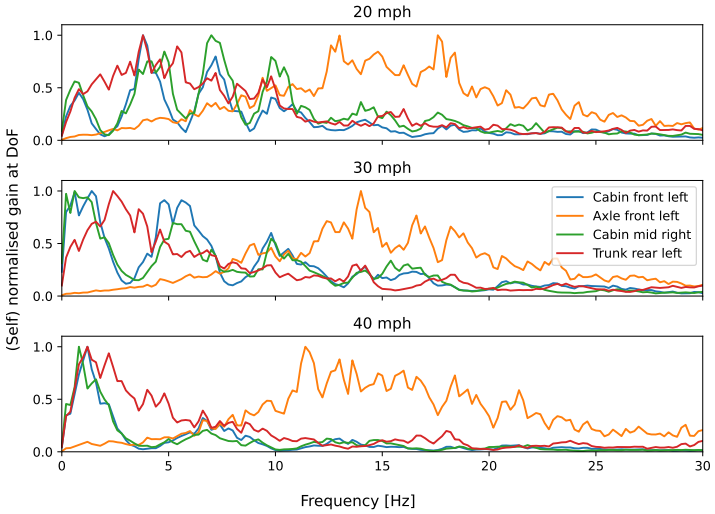

Figure 4.4.4: Ensemble averaged self-normalised power spectra (grouped by vehicle speed).

A comparison of estimates from raw and smoothed spectra was desired. The smoothed spectra are shown in Fig. 4.4.5 and are scaled to unity at low frequency with the intention of approximating FRFs in accordance with the discussion presented in the previous section.

The estimated modal parameters are shown in Fig. 4.4.6. The selection of modal parameters from the presented estimates relied on judgement and leveraged the outcomes of tests of this method of parameter estimation using synthesised vehicle responses from the prior section. In the synthetic data examples it was noted that the wheel hop frequency estimates were more reliable when using

the smoothed spectra, but when considering cabin bounce there was a risk of bias when using smoothed spectra. In this case, the undamped estimated cabin bounce frequencies from smoothed and raw spectra were approximately equal, suggesting that the selected smoothing filter length was appropriate. For consistency, it was therefore decided to use the smoothed spectra-derived estimates for both modes.

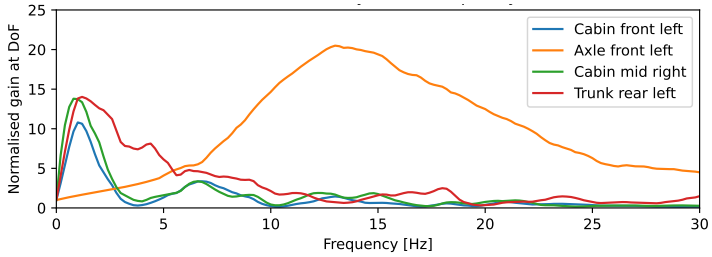

Figure 4.4.5: Ensemble averaged and smoothed power spectra, grouped by sensor location for all runs at 40 mph.

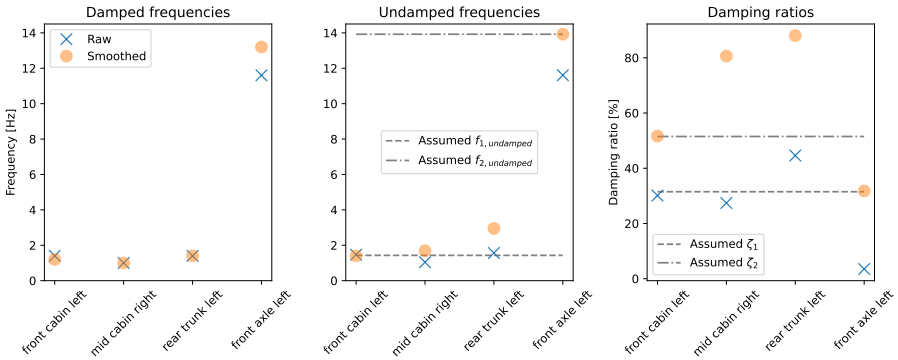

Figure 4.4.6: Summary and comparison of modal parameter estimates for all sensors generated by peak-picking and the half-power bandwidth method.

4.4.3 Effect of speed and road type

The modal parameters estimated thus far for the fieldwork data have been based on ensemble averaged power spectra using all acceleration responses from runs at 40 mph. These ensemble averages therefore include responses from both roads A and B, and runs 1 and 2 on each road respectively. Given the potential for bias due to the nature of acceleration input (being a result of the road profile) it is reasonable to investigate whether there is a discernable difference in modal parameter estimates when the ensembles are grouped by road. Further,

the ensembles considered thus far have been derived from responses gathered from runs at only one speed (40 mph). Therefore, in the present section a comparison is made of parameters estimated from ensemble averaged spectra to explore variation in estimates due to changing road and changing speed.

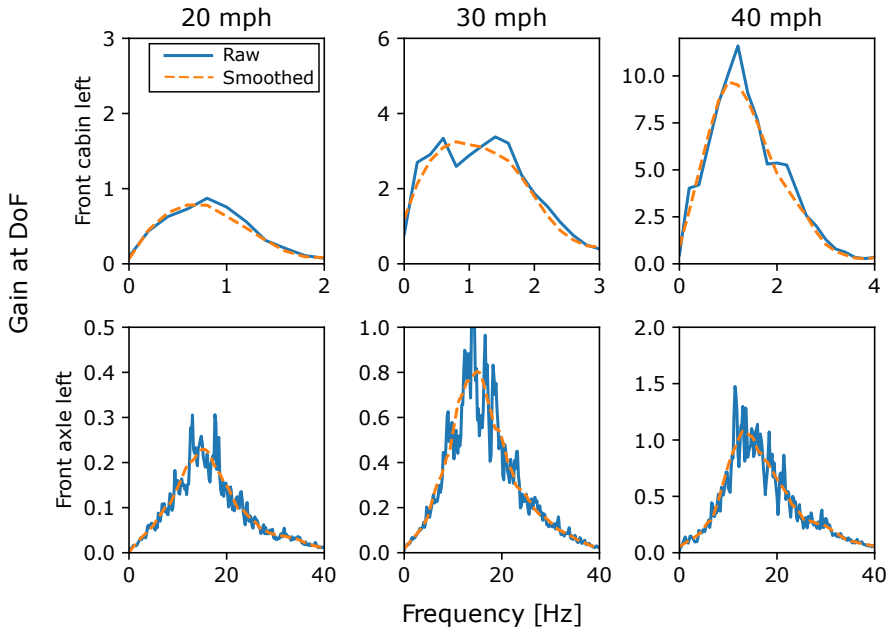

Figure 4.4.7: Illustrative example of raw and smoothed power spectra.

For the purpose of brevity, modal parameter estimates are here derived from power spectra estimated from the acceleration responses from the front left cabin and axle sensors only, thereby assuming that these two can adequately represent the vehicle as a reduced-DoF quarter car. For the purpose of illustration Fig. 4.4.7 shows ensemble averaged spectra from these sensors for both roads combined, grouped by speed. Both raw and smoothed spectra are shown; in accordance with the earlier parts of this chapter the smoothed spectra were used for estimation purposes. The spectra are shown trimmed to isolate peaks.

Fig. 4.4.8 shows the estimates of undamped frequency and damping ratio when speed is the only independent variable. Fig. 4.4.9 presents estimates of the same parameters when both speed and road are independent variables. Upon comparison of the two figures, no clear and consistent trends are immediately apparent. Instead, it appears that the damping and frequency estimates vary inconsistently, with the largest magnitude variations being for the estimates based on the axle-mounted sensor responses. This suggests that nonstationarity of the road surface profile could be the cause of the variation.

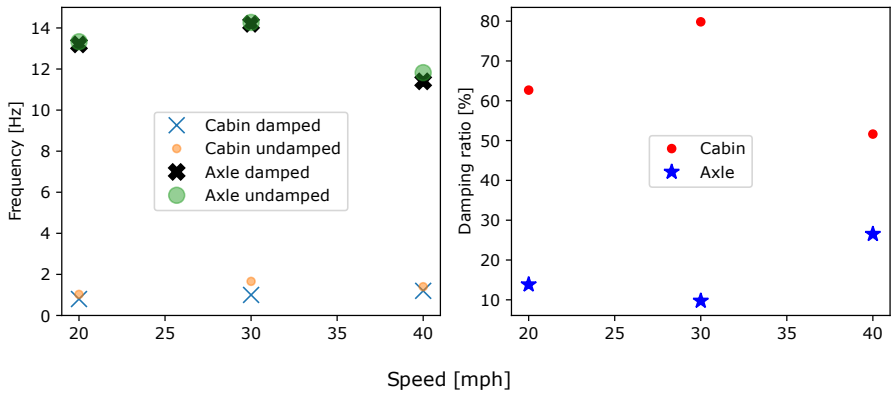

Figure 4.4.8: Estimated modal parameters with **speed** as the independent variable (ensembles for roads A and B combined).

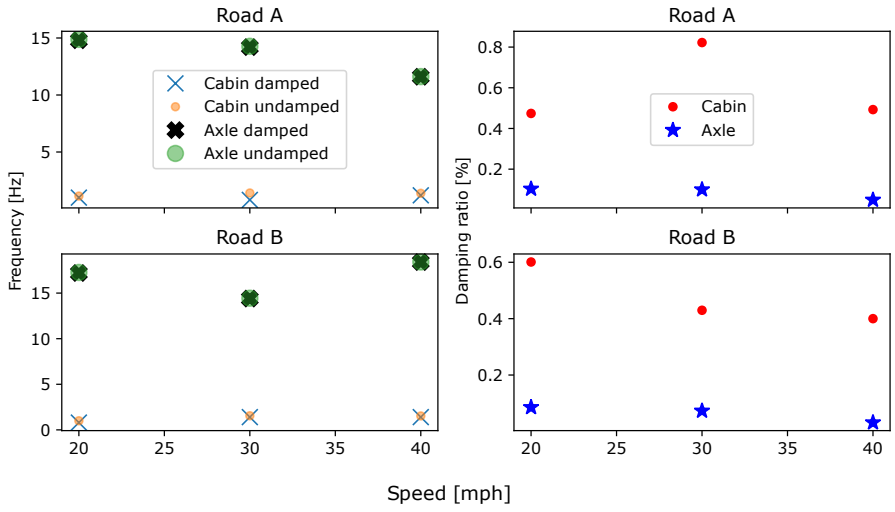

Figure 4.4.9: Estimated modal parameters with **speed and road** as independent variables.

4.4.4 Discussion

Modal parameter estimates have been presented. These parameters have been based on ensemble averaged power spectra. The factors inherent in assembling ensemble power spectra, the independent variables considered and the inferences made from the observed results are summarised in Table. 4.4.1.

Factor or variable	Comment
Ensemble power spectra grouped by speed	Average of all speeds, roads and runs approaches same general shape as average of all roads and runs at 40 mph. Second spectral peak in cabin-mounted sensor responses does not align with dominant peak in axle-mounted sensor response.
Scaling power spectra by $(1/f)$	This scaling removes visibility of clear spectral peaks. It was therefore assumed that the acceleration input was approximately spectrally flat.
Speed and road as independent variables	No clear and consistent trends observed based on visual inspection. Assume that variation occurs due to road surface nonstationarity.

Table 4.4.1: Section summary: factors and independent variables considered.

The following limitations are noted:

- **Bias** could still remain present in the estimates, inherent to the method of estimation employed.
- **Phase** information on the relative phase of signals from accelerometers is not preserved in the power spectrum. This means it is not possible with the present method to fully confirm that the dominant frequencies present in the cabin-mounted sensor responses are in-phase. A remaining challenge is therefore to disambiguate between bounce, pitch and roll modes.
- **Road surface nonstationarity** is assumed to be the cause of variation in modal parameter estimates when using data gathered from different roads or speeds, based on the relevant part of the literature review presented in section 2.4. It is therefore an outstanding challenge for future work to determine whether convergence of parameter estimates can be achieved and, if so, the measurement regime and quantity of data required to do so. The road surface profile also changes over time (due to factors such as the actions of traffic and weather exposure, as well as maintenance); this further challenges the consistency of output-only parameter estimates from different phases of fieldwork.

4.5 Fieldwork phases 1 and 2: comparison of vehicle configurations

4.5.1 Phase 2: frequency-domain parameter estimates

In this section, the acceleration responses from fieldwork phase 2 are used to generate estimates of modal parameters. Fig. 4.5.1 illustrates the power spectra estimated for the two runs comprising fieldwork phase 2. In this plot, the spectra are scaled to unity at low frequency. Based on the findings of the previous sections, the spectral acceleration input was expected to be approximately flat. The comparison of smoothed spectra presented in Fig. 4.5.2 suggests that this may not precisely be the case, as scaling by $(1/f)$ in this instance does not completely remove the distinct visibility of spectral peaks. It is concluded that the road traversed during fieldwork phase 2 was more close to the general form of an ISO 8608 profile than those for phase 1. Nevertheless, in pursuit of consistency for comparison between the two fieldwork phases the spectra used for modal parameter estimation were not scaled by $(1/f)$.

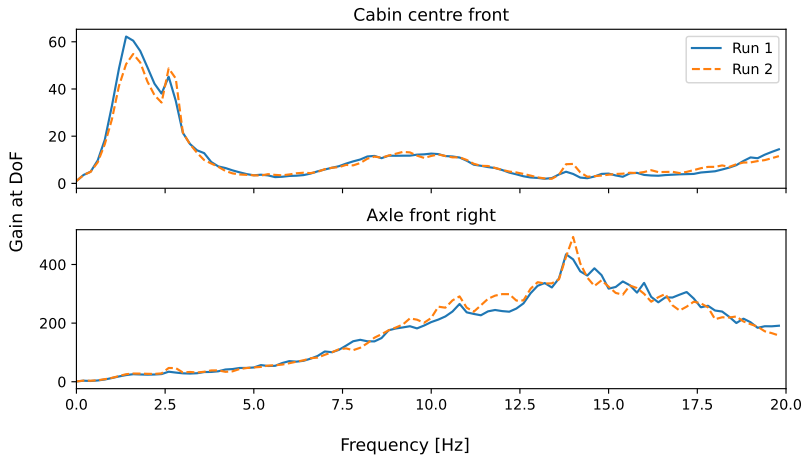

Figure 4.5.1: Power spectra for the two runs comprising fieldwork phase 2, estimated using Welch's method with a 5 s window length and 50% overlap, scaled to unity at low frequency.

4.5.2 Phases 1 and 2 - comparison of frequency domain estimates

Table 4.5.1 summarises the estimates and presents the apparent change in their values between fieldwork phases.

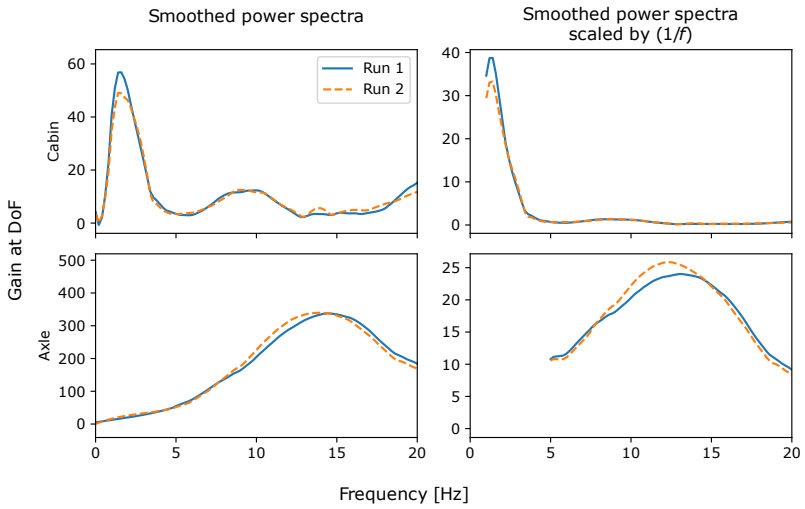

Figure 4.5.2: Comparison of smoothed power spectra for the two runs in fieldwork phase 2, with and without scaling by $(1/f)$.

Parameter	Estimate phase 1	Estimate phase 2	Change phase 1–2
Cabin bounce frequency	1.40 Hz	1.98 Hz	+ 0.58 Hz
Cabin bounce damping	51.6 %	50.5 %	- 1.1 %
Wheel hop frequency	13.9 Hz	14.9 Hz	+ 1.0 Hz
Wheel hop damping	31.8 %	25.7 %	- 6.1 %

Table 4.5.1: Summary of changes in power spectrum-based estimated modal parameters from fieldwork phase 1 to phase 2.

4.5.3 Phase 2: range of variation and RDS trim length (time-domain estimation)

The nature of the power spectrum-based estimation methods applied in this chapter means that they generate only a single frequency-damping estimate pair for every ensemble average spectrum considered. On the contrary, for the RDS and MPM approach to time domain estimation (presented in section 2.8.10 and demonstrated using synthetic data in section 4.2.7), generating multiple RDS from a signal split into segments yields multiple frequency-damping estimate pairs from which an indication of the distribution of the estimates can be inferred. The short sample lengths for fieldwork phase 1 means that such

estimation of distributions is only realistically possible for the outcome from phase 2.

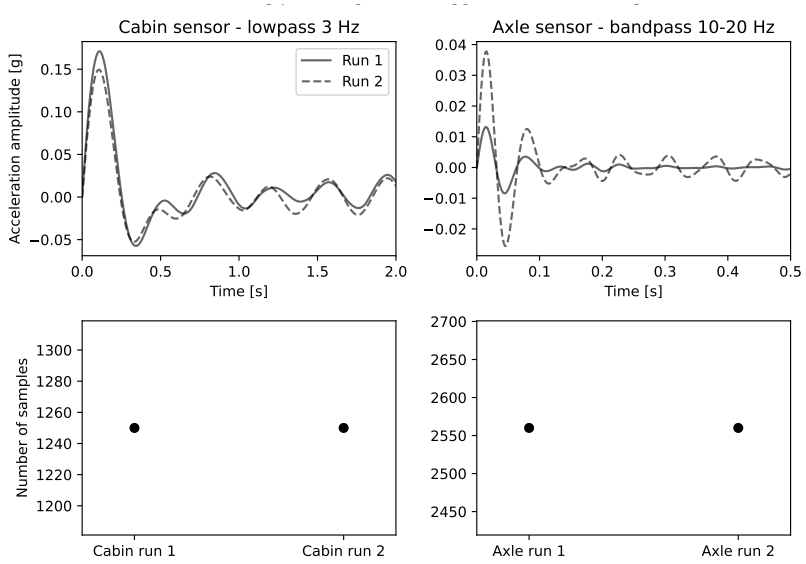

Figure 4.5.3: Comparison of RDS for runs 1 and 2. Upper: RDS estimates for cabin and axle sensors. Lower: numbers of subsamples used for estimation.

Fig. 4.5.3 shows auto-RDS for the two runs. The use of auto-RDS, rather than cross-RDS means that no inference can be made regarding the phase relationship of the modal parameter estimates for each of the DoFs. This was deemed acceptable since the purpose of the cross-RDS was in this case was only to illustrate the range of frequencies and damping ratios for each vehicle DoF during the experimental runs.

The RDS in Fig. 4.5.3 were generated using the whole of each run. The lower part of the plot shows the number of samples used in each RDS estimate; the high numbers implying that the data from each run could be split into multiple segments to generate a range of estimates for each run. Prior to pursuing this, the question of optimal RDS trim length was explored. Figs. 4.5.4 and 4.5.5 illustrate the results of a study in which the trim length was treated as the independent variable and a range of closely-spaced RDS lengths were tested. A single frequency-damping estimate pair was produced (using the matrix pencil method) for each RDS trim length. The figures indicate the trend of estimated damping and frequency with changing RDS length respectively. In each case, the estimate of damping appears to stabilise for a range of RDS lengths: around 0.9–1.7 s for the cabin bounce mode, and around 0.2–0.4 s for wheel hop. These ranges were established by visual inspection of the plots of estimated damping as a function of RDS length. A vertical line on the plots indicates the approximate centre of this range, with a horizontal line showing the damping and frequency

estimates at that RDS length (averaged between the plotted curves for runs 1 and 2).

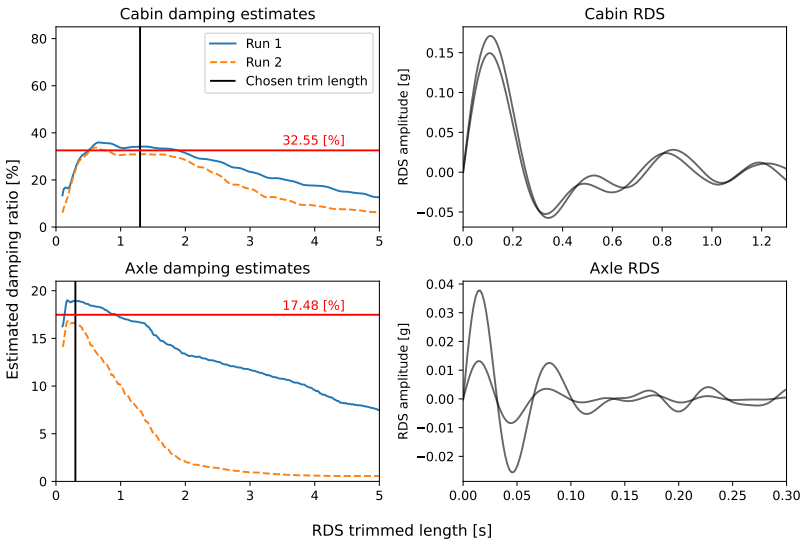

Figure 4.5.4: Estimated **damping** varying with RDS length.

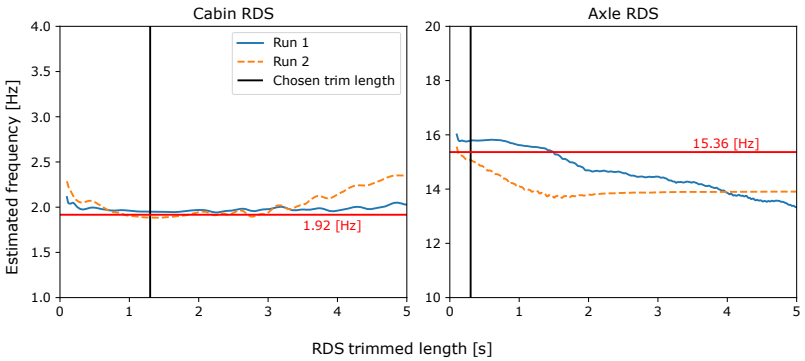

Figure 4.5.5: Estimated **frequency** varying with RDS length.

This study of RDS trim length implies that trimming to 1.3 s and 0.3 s for the cabin- and axle-mounted sensors respectively would result in a stable estimate of damping. Fig. 4.5.4 also illustrates both RDS trimmed to those lengths. With this in mind, RDS were generated from the front left axle and front left cabin sensor responses from phase 2. The acceleration response data were lowpass filtered at 3 Hz (axle sensor) or bandpass filtered at 10-20 Hz (cabin sensor), before being split into subsamples with lengths of 100 s each (non-overlapping) in order to produce multiple frequency-damping estimate pairs.

The RDS estimated from the front axle sensor were trimmed to 0.3 s and those from the cabin sensor to 1.3 s. The adopted trigger tolerance was $0.01g$ and the RDS original length was 5 s with 50% overlap.

Fig. 4.5.6 presents Gaussian probability density distributions drawn based on the mean and standard deviation of groups of frequency-damping estimate pairs produced using the matrix pencil method. The data used for these estimates are RDS trimmed to 0.3 s and 1.3 s for axle and cabin sensor acceleration responses respectively. It should be noted that the mean frequency and damping values indicated in Fig. 4.5.6 represent the mean of a group of estimates at the specified RDS length. This explains why they differ from the values indicated in Figs. 4.5.4 and 4.5.5 in which a single estimate was produced for each tested RDS length.

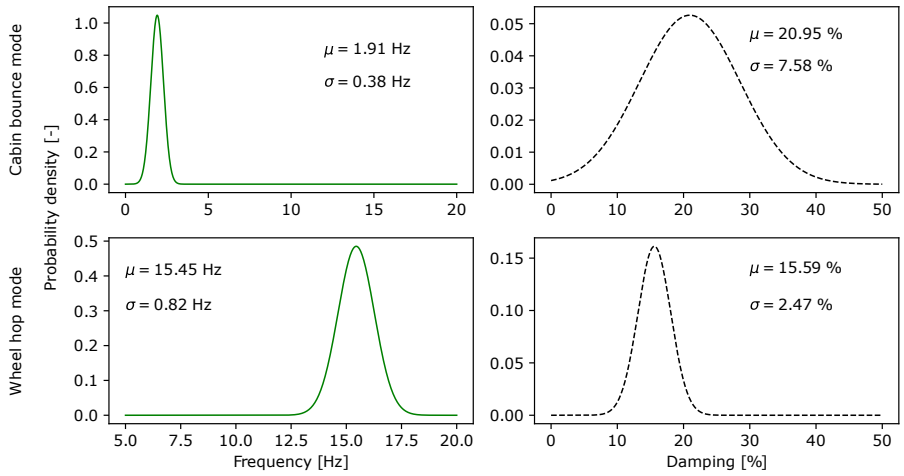

Figure 4.5.6: Gaussian distributions based on means and standard deviations of time domain frequency and damping estimates for phase 2.

	Change phase 1 to phase 2 [multiple of standard deviation of phase 2]
Cabin bounce mode frequency	1.53
Axle hop mode frequency	1.22
Cabin bounce mode damping ratio	- 0.15
Axle hop mode damping ratio	- 2.47

Table 4.5.2: Changes in estimated parameters (frequency domain method) from fieldwork phase 1 to phase 2, as multiples of standard deviation of time domain estimates (phase 2).

Considering Table 4.5.1 and Fig. 4.5.6 affords some degree of insight regarding the changes seen between phase 1 and phase 2 of the fieldwork. Table 4.5.2 presents the changes from phase 1 to phase 2 as multiples of the standard deviation of estimates from the time-domain method for phase 2. The main inferences from this are:

- The change in frequency for both modes is a similar multiple of standard deviation.
- The change in damping ratio for the cabin bounce mode is a very small fraction of the phase 2 standard deviation.
- The largest parameter change as a multiple of phase 2 standard deviation is the axle hop mode damping ratio.

Because distributions of estimates were only produced for phase 2, it is not possible to reasonably comment on whether the observed changes between the phases are significant. However, it is particularly interesting to note that the largest proportional change relates to damping of the axle hop mode. The physical changes in the vehicle between fieldwork phases related to the suspension system and could perhaps be related to play in the suspension components in this area of the vehicle. Another potential contributing factor is tyre pressure which was not measured for the fieldwork. However, the actual mechanism(s) by which these could lead to a change in effective damping ratio are not known.

4.6 Discussion

In this chapter, numerical simulation was used to model the response of a quarter-car vehicle to road surface inputs. The spectral flatness of the input profile was noted to affect the estimated vehicle FRF and scaling was employed to counter this. Subsequently, vehicle model parameters were estimated from in-service driving (fieldwork data) on a different road types at a range of speeds. The type of road and the speed of the vehicle was found to affect the estimated vehicle model parameters, suggesting that road roughness class and vehicle speed should be matched to those expected during bridge traversals when estimating vehicle models to inform vehicle-based bridge monitoring campaigns. FRF scaling did not appear to be required when processing the results from fieldwork, suggesting that real road surfaces may be approximately spectrally flat in acceleration. This is in contrast to the widely-adopted ISO 8608 road profile model which is spectrally flat in velocity. This outcome suggests the need for further consideration of the road profile input spectrum shape when using output-only methods to estimate vehicle parameters, with particular attention required when validating methods using numerical simulation and comparing the outcomes to field tests, since an assumption of spectral similarity between the modelled and actual road profiles may not be accurate and spectral bias could lead to incorrect assumptions of vehicle properties, particularly the wheel hop mode frequency. The type and position of sensors on the vehicle were not consistent between phases 1 and 2 of fieldwork in the presented study. In future studies, factors such as these should be consistent in order to increase the value of comparisons between estimates from multiple phases of fieldwork.

4.6.1 Variation of estimated quarter-car parameters

The parameters estimated using the power spectrum-based method showed some change from phase 1 to phase 2: an increase in frequency and a decrease in damping for both cabin bounce and wheel hop modes. This change of frequency is opposite to that which would be expected due to the change to softer suspension springs from phase 1 to phase 2. The expected change would be a decrease in frequency due to softer springs (for the cabin bounce mode this decrease in frequency would be approximately proportional to the square root of the change in spring stiffness). On the other hand, the largest parameter change as a proportion of the phase 2 parameter estimate standard deviation was in the damping ratio of the axle hop mode; it was speculated that this might have been related to suspension component degradation or change in tyre pressure from phase 1 to phase 2, although the actual mechanism(s) by which these could lead to a change in damping ratio are not known. The parameters for estimating the power spectra and processing the data generally were identical for the two phases with regard to this estimation method, which suggests that the changes in observed parameters between the two phases might alternatively be due to some or all of the experimental parameters which differed:

1. **Road and road surface**
   (a) Different types of road: phase 2 road surface smoother than phase 1 surface (magnitude and variation of profile).
   (b) Different lengths of road: longer samples available for phase 2 could have helped to counter nonstationarity of the surface.
2. **Vehicle speed**
   (a) Faster in phase 2 than phase 1 (nominally 60 mph and 40 mph respectively).
   (b) For a standard road profile, faster speed would result in higher magnitudes of suspension movement.
3. **Vehicle parameter nonlinearity and other variation**
   (a) True parameter values may be nonlinear in relation to rate and magnitude of suspension deflection and thus have a similar relationship to both road profile height and to vehicle speed.
   (b) Suspension damper parameters could have changed between phases 1 and 2.
   (c) Vehicle suspension kinematics include multiple degrees of freedom while model quarter-car reduces to 2 DoFs.
   (d) Effects of suspension defect present in phase 2 (anti-roll bar play) not quantified.

Considering the trends observed and the potential sources of confounding and error discussed above, a tentative conclusion is that **quarter-car model parameters measured from in-service vehicle responses may be more sensitive to road surface type and vehicle speed than to operational changes in true stiffness and damping values**. This conclusion is based on the possibility of input bias from nonstationary road surfaces, in addition to the rate-dependent nonlinearity that can be expected from real suspension damping (Calvo et al. [411]).

4.6.2 Recommendations for output-only quarter-car parameter estimation

The outcomes from this chapter suggest the following recommendations for future attempts to estimate vehicle dynamic properties using output-only methods applied to data gathered from driving on real roads:

1. **Parameter estimation to inform use of vehicle for future indirect bridge monitoring**
   (a) Estimation of vehicle properties should be based on road types with profiles nominally identical to the expected bridge deck surface.

(b) The estimated vehicle model is likely to be speed dependent. Vehicle speeds should be the same for estimation of properties of vehicle and for subsequent bridge traversals.

(c) Estimation of vehicle properties should be based on experiments undertaken with the vehicle in the same operational configuration and condition as intended for future use of the estimated parameters.

2. **Measurement of wheel hop mode parameters**

   (a) Undertake measurements using accelerometers mounted on the axles (realistically, mounting on the base of the suspension strut tower or part of the brake caliper could be potentially suitable) or as close to the wheel centre as possible, since the wheel hop mode did not appear to be visible from the sensors mounted inside the vehicle cabin or trunk.

3. **Processing of large volumes of data: measures to avoid bias**

   Although potentially applicable to similar tasks in other domains, the following measures were tested in this chapter and found to be valuable in relation to output-only estimation of vehicle properties:

   (a) Power spectra should be smoothed to avoid local peaks causing gross bias in estimated frequency and damping.

   (b) Smoothing parameters (e.g. filter length) could be chosen in an automated manner, for example by selecting the filter length as a proportion of the width of the peak to be smoothed.

   (c) The RDS should be truncated at a length chosen to allow a stable estimate of damping.

4. **Adjustment for spectral flatness of input**

   (a) Consider the potential difference in spectral shape between assumed and actual road surface profiles when comparing synthesised to real vehicle responses. Further work is suggested to determine the most suitable road profile model in this regard.

4.7 Chapter summary

- Results suggested that real road surface profiles appeared to be spectrally flat in acceleration, in contrast to widely-adopted ISO 8608 [7] profiles which are spectrally flat in velocity.
- Estimated vehicle properties varied with speed and road type, without a consistent trend. This suggested the variation could in fact relate to road surface profile. Nonlinear vehicle damping was also postulated as a potential factor. These variations appeared to obscure expected parameter changes due to vehicle condition and configuration.
- Vehicle axle hop frequency was measured from an accelerometer on the axle, but was not clearly and consistently visible from the cabin-mounted sensors.
- Cabin-mounted sensors show secondary frequency peaks which could be mistaken for the axle hop frequency without additional information to enable disambiguation.
- Variation in estimated frequency from phase 1 to phase 2 of fieldwork was in the opposite direction than expected, suggesting that this change might relate to other factors such as vehicle speed, vehicle nonlinear response, or road surface profile variation.
- The largest parameter change from phase 1 to phase 2 of fieldwork as a proportion of the standard deviation of phase 2 time-domain estimates was the axle hope mode damping ratio. It was speculated that this could have been related to suspension component degradation or tyre pressure change, but might also have related to the factors discussed above in relation to frequency changes.
- The cabin bounce frequency was visible from a low-cost smartphone device mounted in the front centre of the cabin, suggesting potential for crowdsourcing of in-service vehicle parameter estimates.

Chapter 5

Finite element simulation: visibility and sensitivity of bridge frequencies to VBI system parameters

5.1 Chapter overview

This chapter addresses the following research objective:

RO.2 Explore and how variation in vehicle-to-bridge parameter ratios, vehicle model abstractions and sensor placement on the vehicle affect the visibility and sensitivity of detecting bridge frequencies from vehicle-mounted accelerometers.

This chapter is concerned with finite element (FE) simulation of the interaction between two-degree-of-freedom quarter-car models with simply-supported beam bridges. The vehicle-bridge interaction model used in this chapter is shown in Fig. 5.1.1. In this model, the bridge is modelled as a simply-supported Euler-Bernoulli beam of uniform cross section with bending stiffness EI and length L as indicated in the figure. Other bridge properties are summarised in Tables 5.2.1 and 5.3.2. The vehicle models used in this chapter are summarised in Table 5.3.1. The vehicle traverses the bridge at constant velocity v and is represented as two masses, m_1 and m_2 representing the cabin and wheel/axle masses respectively and connected by springs.[1] The parameter k_1 represents a spring modelling the effective stiffness of the vehicle's pneumatic tyres. The work presented here aims to understand the effects of parameter variation on the

[1] In some literature these are called sprung and unsprung masses reflecting their positions above or below the suspension spring k_2.

frequency content of the acceleration response of the vehicle during a traversal of a bridge at a fixed speed.

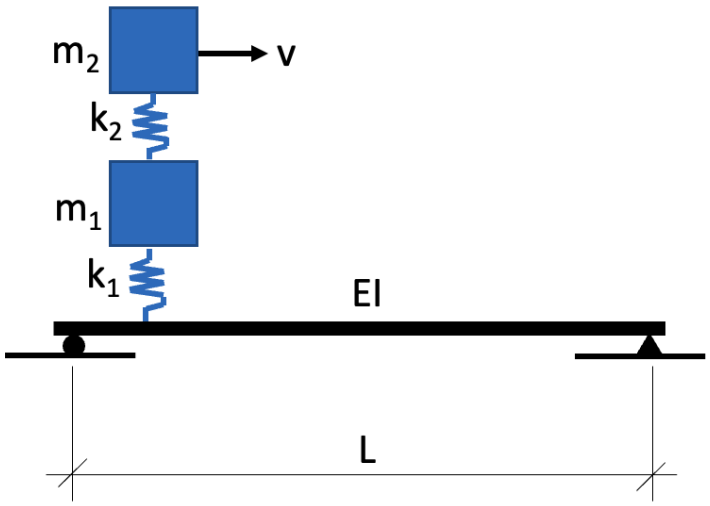

Figure 5.1.1: The two-degree-of-freedom lumped sprung mass vehicle model and simply-supported beam bridge model used in chapter 5.

In addressing research objective **RO.2**, the work presented in this chapter explores how much separation is required between vehicle and bridge frequencies to allow visibility of the bridge's fundamental frequency in the vehicle response, and the sensitivity of observed bridge frequencies to the frequency ratio. The distribution of mass between the vehicle's upper and lower degrees of freedom (DoFs) is included in the parametric investigation, to understand its effects on visibility of bridge frequencies from vehicle-mounted accelerometers, in addition to investigation of the effects of vehicle traversal speed and a comparison of the possible sensor mounting locations on the vehicle.

All of the work presented in this chapter relates to finite element simulations; the data are therefore synthetic.

5.1.1 Method of investigation

The work in this chapter will be presented in the following sections:

- **Section 5.2** describes the FE model framework used for data generation in this chapter and presents a model convergence and validation study.
- **Section 5.3** describes the range of vehicle and bridge parameters studied in this chapter.
- **Section 5.4** presents the results of an FE-based study exploring the effects of VBI system parameters on visibility and sensitivity of bridge frequency detection from vehicle mounted accelerometers.
- **Section 5.5** comprises a discussion of the work presented in the chapter.
- **Section 5.6** presents the chapter conclusions.

5.2 Finite element model validation

5.2.1 Overview of modelling and simulation regime

FE simulation for this chapter was conducted using *ABAQUS* software by Dassault Systèmes Simulia. Prior work by others (as discussed in section 2.5.6 of the literature review) has demonstrated the suitability of this software environment. Model generation and analysis was controlled by Python scripts following the method described by Overvelde [412] and extended by the author to allow iteration through a range of parameters.

Modelling was conducted in two dimensions, with vehicle and bridge motion constrained to a plane. The bridge was modelled as a simply-supported Euler-Bernoulli beam. An element length of 0.01 m was adopted based on a mesh convergence study, discussed in more detail in section 5.2.2. The modelled beam was intended to nominally represent the three-dimensional laboratory-scale bridge discussed in chapter 7 at least in terms of span length, in-plane response and the frequencies of the first two bending modes. Although modelled as a planar two-dimensional structure, ABAQUS allows the beam element properties to be defined in terms of a cross-section. Given this, and since out-of-plane effects were not intended to be studied in the present chapter, a unit breadth was adopted when defining the section properties and the density value shown in table 5.2.1 was selected in order target the first two bending mode frequencies to match those seen in the laboratory. Further discussion of the physical laboratory-scale model is included in chapter 7 including the process of estimating its modal characteristics. However it should be noted here that its first and third global mode shapes were dominated by bending; this observation supports the representation of its in-plane bending behaviour with a two-dimensional model despite the physical model having a different cross-section profile, and justifies the use of beam rather than shell elements in the FE model.

Property	Value
Span length [m]	2
Section depth [m]	0.00959
Section breadth [m]	1
Elastic modulus $[N/m^2]$	1.9×10^{11}
Second moment of area $[m^4]$	7.35×10^{-8}
Density $[kg/m^3]$	3162.92
Damping	None
Support conditions	Simply-supported
Mesh element size [m]	0.01
Timestep increment [s]	0.002

Table 5.2.1: Bridge properties used in chapter 5.

The vehicle was modelled as point masses connected by linear connector sections, which were assigned spring stiffnesses according to the vehicle parameters being investigated. The vehicle was represented as two lumped point masses (2DoF model abstraction). Normal contact between the vehicle and bridge was modelled using a surface-to-surface[2] formulation with a hard pressure-overclosure relationship, finite sliding, and adopting the default method of enforcement of contact. Contact separation was not permitted. Tangential interaction was modelled as frictionless. Modelling the vehicle-bridge interface as a contact interaction (rather than some other constraint type) allowed the representation of VBI in accordance with the assumptions outlined in the literature review for moving sprung mass models, and will allow the modelling framework to be adapted to include more sophisticated aspects of the interaction in future studies.

FE analysis was conducted in two distinct regimes:

- **Linear perturbation frequency analysis** was used to extract modal frequencies for the first two modes of the beam, without the presence of a vehicle. This is a specific analysis step within the finite element software which extracts eigenvectors (mode shapes) and eigenvalues (modal frequencies) from the model.

- **Implicit dynamic analysis**[3] was employed to simulate the vehicle moving across the bridge. The utilised output comprised vertical acceleration at each timestep for the vehicle's upper and lower DoFs; at the virtual contact point between vehicle and bridge; and at the mid-span position on the bridge.

For the implicit dynamic analysis, the simulation timestep was constant at 0.0002 s, corresponding to a *simulation frequency* of 5 kHz. For the current chapter, this simulation frequency is significantly higher than the Nyquist limit associated with the maximum frequency of 100 Hz intended to be studied. However, the adopted simulation frequency corresponds to that found to result in a stable representation of the variation of bridge frequencies with time, a phenomenon investigated in Chapter 6. Further discussion of the selection of a suitable simulation frequency in this regard is included in section 6.2.3.

[2] It is understood that surface-to-surface contact could reduce undesired overclosure, which might be beneficial if (for example) modelling the vehicle wheel as a disk. However in this case, since one of the *surfaces* was in fact a single node, the choice of surface-to-surface rather than node-to-surface contact likely had no practical implications and is mentioned only for completeness.

[3] Implicit analysis is understood to be unconditionally stable. Explicit analysis is not unconditionally stable, but would potentially be faster, as it inverts the mass matrix by discarding off-diagonal terms. In this thesis, implicit analysis was preferred since accuracy of representing the interaction of vehicle and bridge mass was sought, and the computation time for implicit analysis remained reasonable.

5.2.2 Mesh density

In order to determine the mesh density (finite element size) to be used for simulation, the eigenfrequencies were extracted for a range of different element sizes. This exercise was based on a finite element model adopting the bridge properties summarised in Table 5.2.1 which comprise a planar representation of the physical bridge model used in laboratory testing in chapter 7. Linear perturbation frequency analysis was used as noted above. Fig. 5.2.1 shows the outcomes of this study: convergence of mode 1 and 2 frequencies from the FE model (based on the *healthy* bridge properties from Table 5.2.1) with the theoretically expected values based on equation (5.1). The beam elements used to mesh the two-dimensional FE model were all of an equal length, given by the bridge span length divided by the number of elements in the model.

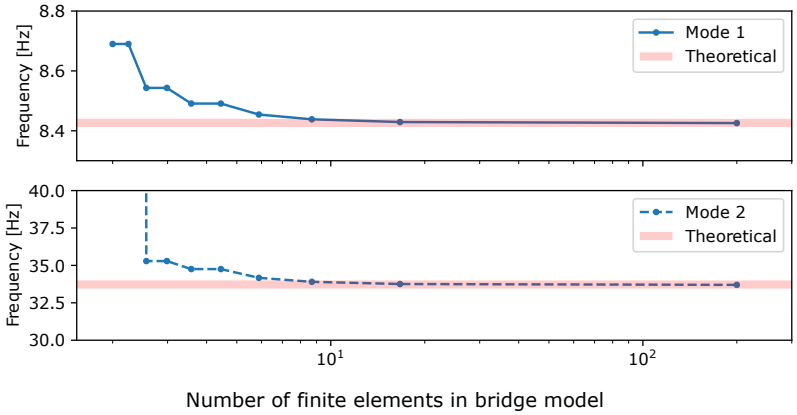

Figure 5.2.1: Mesh convergence study outcomes.

Theoretically expected modal frequencies $f_{b1} = 8.43$ Hz and $f_{b2} = 33.7$ Hz for a simply-supported beam were calculated using the well-known equation (5.1) (in which n is the mode order, with constants $K_1 = 9.87$ and $K_2 = 39.5$) and are indicated by horizontal red lines on the plots. Although representing single values, these lines are rendered as wider bars to allow the convergence to be visually apparent. Figure 5.2.1 indicated that the frequencies of the first two modes begin to converge to their theoretically expected values with around 20 or more elements used in the model ($l_{el.} >= 0.1$ m). The first two classical normal mode shapes of a simply-supported beam are well-known and thus not reproduced here. However, the first two mode shapes of the two-dimensional FE model are presented in section 7.3.3.

$$f_n = \frac{K_n}{2\pi}\sqrt{\frac{EIg}{wL^4}} \tag{5.1}$$

An element size of 0.01 m (implying 200 elements for the bridge span length of 2 m) was adopted for modelling, on the basis that this would allow accu-

rate representation of the bridge modal behaviour and by observation that the computation time was not unreasonably high at this mesh density. This mesh density was also understood to offer increased resolution regarding the effects of the position of the vehicle as its traversal of the bridge was modelled dynamically.

5.3 Range of parameters

5.3.1 Bridge and vehicle model properties

The vehicle properties adopted in this chapter are summarised in Table 5.3.1. The total vehicle mass represents the laboratory-scale test vehicle used in chapter 7. The remaining vehicle properties adopted in this chapter are intended to represent a reasonable range of upper-to-lower DoF mass ratios for quarter car models. Jazar states that the average range for this mass ratio ϵ is between 3 and 8, typically with small cars having a higher and large cars a lower mass ratio within this range (Jazar [6]). The vehicle models investigated in this chapter span this range of mass ratios with the intention of representing the expected range of parameters for real cars. The ratio of suspension spring to tyre stiffness $k_1 : k_2$ was kept constant for all modelled vehicles. A value of $k_1/k_2 = 5$ was selected for this stiffness ratio. Prior studies featured a wide range of stiffness ratios. For example, Sayers [5] adopted $k_1/k_2 = 10.32$, while Cebon [141] presents $k_1/k_2 = 1.75$. Corbally and Malekjafarian [19] assume $k_1/k_2 = 5.5$ in a study specifically using data from the same test vehicle used for the laboratory investigation presented in chapter 7. The stiffness ratio adopted in the modelling presented in this chapter was therefore deemed to be reasonable.

Table 5.3.1 also presents a range of ratios of vehicle-to-bridge non-interacting natural frequency ($f_{vi} : f_{bi}$) investigated in this chapter. the full range of vehicle parameters for this chapter are presented in Tables B.1.1 and B.1.2 which are included in Appendix B. Table 5.3.2 summarises the first three modal frequencies of the bridge model used in this chapter, including the change in frequencies induced by damage conditions A and B, with or without a point mass representing the vehicle located on the bridge.

Vehicle property	**Range of values included in study**				
Mv	3.43 kg				
$k_1 : k_2$	5.0				
Vary parameter ϵ to achieve the following vehicle mass ratios:					
$\epsilon = m_1 : m_2$	3	4.25	5.5	6.75	8
Vary spring stiffnesses to achieve the following frequency ratios:					
$f_{v1} : f_{b1}$	0.2, 0.75, 1.0, 1.25, 5.0				
$f_{v2} : f_{b2}$	0.2, 0.75, 1.0, 1.25, 5.0				
Damping	None				
For each mass ratio and frequency ratio, simulate the following traversal speeds:					
v [m/s]	0.73, 1.11, 1.52				

Table 5.3.1: Summary of vehicle properties included in the study in chapter 6.

Bridge mode	Vehicle mass position [proportion of span]	Bridge modal frequency [Hz]	Frequency change due to vehicle mass presence
1	No vehicle mass	8.4266	
	L/2[4]	7.9865	-5.22 %
	L/4	8.1963	-2.73 %
	L/6	8.3113	-1.37 %
2	No vehicle mass	33.7	
	L/2	33.7	0.00 %
	L/4	32.013	-5.01 %
	L/6	32.369	-3.95 %

Table 5.3.2: Bridge modal frequencies, with and without a point mass (not sprung) representing the total vehicle mass at midspan, quarter-span or one sixth-span.

5.3.2 Vehicle mass ratio

The quarter-car vehicle model's mode shapes are indicated in Fig. 5.3.1 for a range of values of vehicle mass ratio ϵ. The figure presents mode shapes and associated natural frequencies for a quarter-car 2DoF representation. In all presented cases, the total vehicle mass $(m_1 + m_2)$ was the same. the plotted points explore a range of ways in which the total vehicle mass is distributed between the DoFs, i.e. different values for the ratio $m_1 : m_2$. In the left-side subplots, the spring stiffness values are selected such that the vehicle's first mode frequency approximates that of the bridge ($f_{v1} \approx f_{b1}$), while for the right-side subplots $f_{v2} \approx f_{b1}$. The presentation indicates that modal participation amplitude varies as a function of upper-to-lower DoF mass ratio, which may provide an explanation for some of the observed trends in bridge frequency visibility and sensitivity discussed later in the chapter. Moreover, it shows that changing the distribution of mass between the vehicle DoFs results in a change to one of the vehicle's natural frequencies; this might reasonably be expected if the stiffness of the vehicle's springs were constant, but is notable here since the values of k_1 and k_2 were adjusted to maintain $f_v \approx f_b$. This means that, for example, if $f_{v1} \approx f_{b1}$ is maintained and the ratio $m_1 : m_2$ for the vehicle is treated as an independent variable, f_{v2} also changes and thus the ratio of vehicle-to-bridge frequencies changes for the vehicle's other mode ($f_{v2} : f_{b1}$). The mode shapes shown were generated using the *Engineering Vibration Toolbox* for Python [409].

[4] Since this position is a node (zero-displacement) point for the mode 2 shape, the result is obvious but included here for completeness.

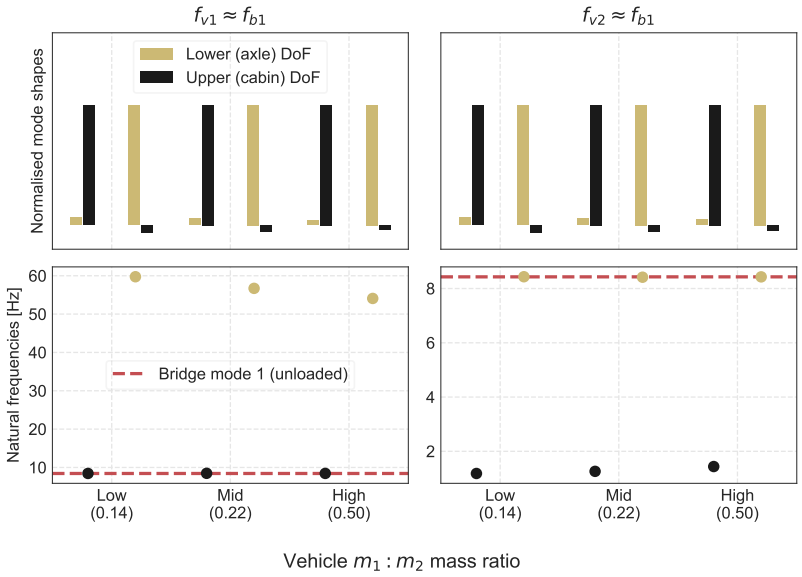

Figure 5.3.1: Mode shapes of the quarter-car vehicle model for a range of upper-to-lower DoF mass ratios.

5.3.3 Damping

Vehicle damping and bridge damping are not modelled in this chapter. Modelling undamped interaction is an approach adopted for initial studies seeking to understand aspects of the system behaviour (for example Yang et al.'s [9] frequency variation study). Based on the observations in chapter 4 it was anticipated that vehicle damping between the two DoFs (representing the viscous damper in a vehicle suspension system) would represent a significant modal damping ratio. Indeed, it is clear from the literature that vehicles are typically relatively highly damped (Jazar [6], Siringoringo and Fujino [185]). In this case, neglecting this source of damping was preferred with the intention of yielding greater visibility of the effects of vehicle mass ratio, speed, and vehicle-to-bridge frequency ratio. However, a study of the effect of vehicle damping is included in chapter 6. The contribution of tyre hysteresis to damping was assumed to be negligible in accordance with the approach generally adopted for modelling quarter-cars (Guiggiani et al. [122]). Bridge damping was assumed to be low in accordance with expectations for real bridges (for example Salcher et al.'s summary of viscous damping in rail bridges presented in relation to Eurocode specifications [413], and excepting specific scenarios such as seismic ground motion during which Feng et al. [414] report that effective modal damping ratios can be higher) and was thus also not modelled.

5.3.4 Road surface roughness

Road surface roughness is known to confound visibility of bridge frequencies by creating convolutive noise with amplitude and frequency proportional to vehicle speed, as discussed in chapter 4. Commonly in studies of VBI this is modelled as a non-smooth profile of the bridge corresponding to one of the ISO 8608 roughness classes (for example Malekjafarian et al. [113], Corbally and Malekjafarian [115], Sarwar and Cantero [108], and Li et al. [172]). However, modelling the profile directly in the FE simulation introduces additional challenges. A quarter-car traversing a non-smooth surface in an FE simulation is subject to a time history of both displacement and velocity (and thus, acceleration) due to the surface roughness. There is some debate as to the extent to which the ISO 8608 profiles can be considered to match real road surface profiles (Múčka [170]) and, as discussed in Chapter 4 the effect on the vehicle (and thus correspondingly on the bridge) would be biased by whether the resulting road profile was spectrally flat in displacement, velocity or acceleration, since all could be considered to be broadband Gaussian white noise in their respective domains. The literature review revealed that investigation has been undertaken by others into methods to reduce these confounding effects. A common and promising approach comprises subtracting time-shifted responses from following axles on the same or different vehicles (O'Brien and Malekjafarian [300], Malekjafarian et al. [298] and Zhan et al. [289] (from Malekjafarian et al. [40]), Kong et al. [288], Keenahan et al. [309], Li et al. [38]). Such an approach cannot practically be applied to a VBI model in which the vehicle is represented as a quarter car. Further challenges to the goal of modelling VBI in the presence of rough roadway surfaces relate to the effective smoothing caused by the vehicle's wheel(s), since the real contact between vehicle and bridge surface is an area rather than the single-point contact implied by the planar VBI model adopted here (Fig. 5.1.1). One promising avenue for mitigation is to represent the vehicle wheel as a disk as proposed by Chang et al. [171] however the resulting VBI simulation could still be affected by the method by which tyre deformation was modelled, and how contact overclosures were handled in the numerical simulation. An alternative approach when generating an ISO 8608 road profile would be to consider only roughness relating to spatial frequencies with corresponding wavelengths greater than the effective length of the wheel contact area. Similarly, the generative power spectrum could also be filtered to exclude wavelengths longer than the bridge span, since these would also have no effect to the resulting VBI. On the basis of the above, it was concluded that the accuracy of any representation of road surface roughness could be subject to debate, while the mitigation of its effects has already been studied in detail with promising results, but applying such methods of mitigation was arguably incompatible with the single-axle quarter car representation. Modelling of road surface roughness was therefore omitted from the FE simulations presented in this thesis.

5.4 Visibility and sensitivity of bridge frequencies from vehicle-mounted accelerometers

The study presented in this section explores the possibility that the frequency peak with the highest magnitude in the frequency spectrum derived from the vehicle acceleration response represents the fundamental frequency of the bridge. If the sensor were directly attached to the bridge, this idea would be congruent with the relative modal participation expected from the response of beam-type structures to broadband random excitation in which the response is expected to be dominated by the first mode. When considering vehicle-mounted sensors, the field of vehicle-based indirect SHM is derived from the first study by Yang et al. [118] in which the presented results show that the highest peak magnitude in the vehicle response is related to the bridge fundamental mode; their outcomes were generally in agreement between a single-mode closed-form analytical study and a finite element simulation including higher-order beam modes. A fundamentally similar approach is elsewhere referred to as prominent peak identification (PPI), for example in work by Lan et al. [352].

This approach is intended to highlight the visibility of bridge frequencies from the vehicle-mounted accelerometers. The study explores a range of vehicle speeds, sensor placement locations, vehicle mass distributions (between the quarter car's upper and lower DoFs), and vehicle-to-bridge frequency ratios. In this manner, not only can the visibility and sensitivity of bridge frequencies recorded from the vehicle-mounted sensors be explored across the parameter space. Additionally, the PPI method implicitly allows the visibility of bridge frequencies in the absence of knowledge of vehicle and VBI system properties. This is anticipated to be valuable, given the variability in estimated vehicle parameters noted in chapter 4. Further, the inclusion of a range of upper-to-lower DoF vehicle mass ratios in the investigation facilitates an understanding of the implications of this practically immeasurable parameter.

For the present study, considering the subject bridge and the vehicle model used for simulation of VBI, it is proposed to consider the frequency spectrum from 0–100 Hz. This range contains the expected first three modal frequencies of the bridge, and at least the fundamental (if not both) frequencies of the vehicle.

5.4.1 Comparative metrics

Two comparative metrics are proposed for this study. **Peak prominence** is defined as the height of the tallest peak in the acceleration power spectrum above the root mean squared (RMS) signal power level, as illustrated in Fig. 5.4.1. When considering the first (fundamental) bridge mode, the highest peak in the range 0–100 Hz is selected and prominence is compared to the RMS level in the same frequency range. For the second bridge mode, the frequency range is reduced to 25–40 Hz. **This metric thus requires no a priori knowledge of bridge or vehicle properties, other than the approximate frequency region of the bridge second mode, and highlights the visibility of bridge frequencies**. The plotted peak height above RMS signal power level is indicated by colour, according to the reference colourbar accompanying each plot. The colourbar range is identical across all plot of peak prominence, facilitating comparison.

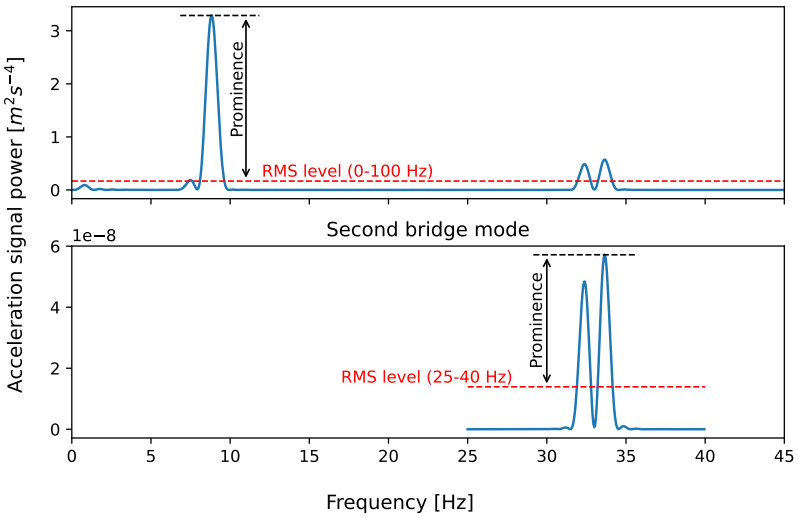

Figure 5.4.1: Illustration of peak prominence metric.

Peak drift is defined as the ratio between the tallest peak frequency and the true bridge frequency (without vehicle presence) for that mode, as illustrated in Fig. 5.4.2. A peak drift factor equal to 1.0 indicates maximal correspondence between the detected and true frequencies. The first and second bridge modes are assumed to be associated with the prominent peaks in the frequency ranges noted above. **This metric thus highlights the sensitivity of estimated bridge frequencies to the studied vehicle and VBI parameters**. Plotted frequency drift is indicated by colour, according to the reference colourbar accompanying each plot. Drift values above and below the colourbar range are indicated by a $+$ or $-$ respectively. This approach allows identification of outliers (large shifts in frequency due to VBI effects in some cases) while

maintaining visibility of relative differences of smaller values of peak drift. The colourbar range is identical across all plots of peak drift, facilitating comparison.

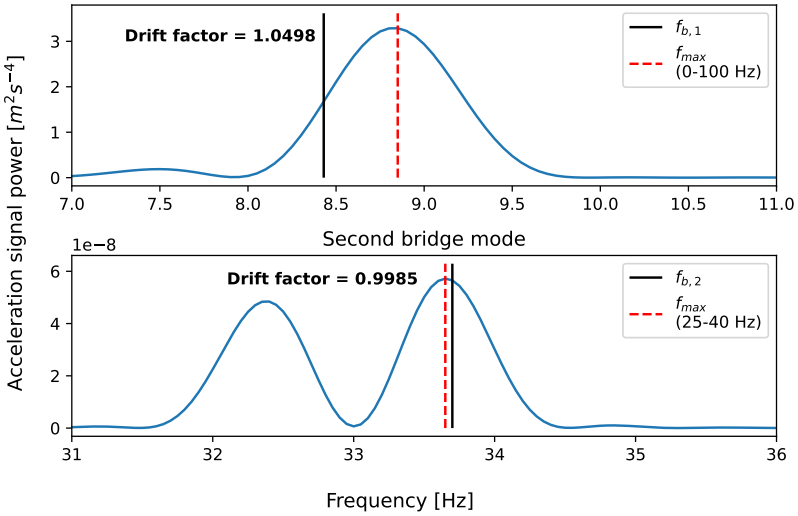

Figure 5.4.2: Illustration of peak drift metric.

The following plots (section 5.4.2) of peak prominence and peak drift graphically present the values of each of these metrics across a range of VBI system parameters. The study spans three vehicle traversal speeds (slow, medium and fast) and the metrics are presented for three sensor locations on the simulated vehicle (cabin, axle and contact point between vehicle and bridge). Within each subplot, values of the peak prominence and drift metric are presented for a range of ratios of vehicle-to-bridge frequency (f_{v1}/f_{b1} or f_{v2}/f_{b2} in the range 0.2–5.0). Each subplot also presents the metrics across a range of vehicle upper-to-lower DoF mass ratios (m_2/m_1 in the range 3–8).

5.4.2 Outcomes: vehicle properties defined relative to first bridge frequency

Fig. 5.4.3 shows the peak prominence outcomes in the range 0–100 Hz, for vehicle-to-bridge frequency ratios defined in relation to the first bridge frequency. Fig. 5.4.4 shows the associated prominent peak frequency drift outcomes. From these figures, it appears that high peak prominence is associated with the cabin sensor placement, and vehicle-bridge frequency ratios above or below unity. It is also clear that $f_{v1} = f_{b1}$ is associated with high degrees of prominent peak drift. The very highest peak prominences relate to vehicle-to-bridge frequency ratios at the upper and lower ends of the studied range.

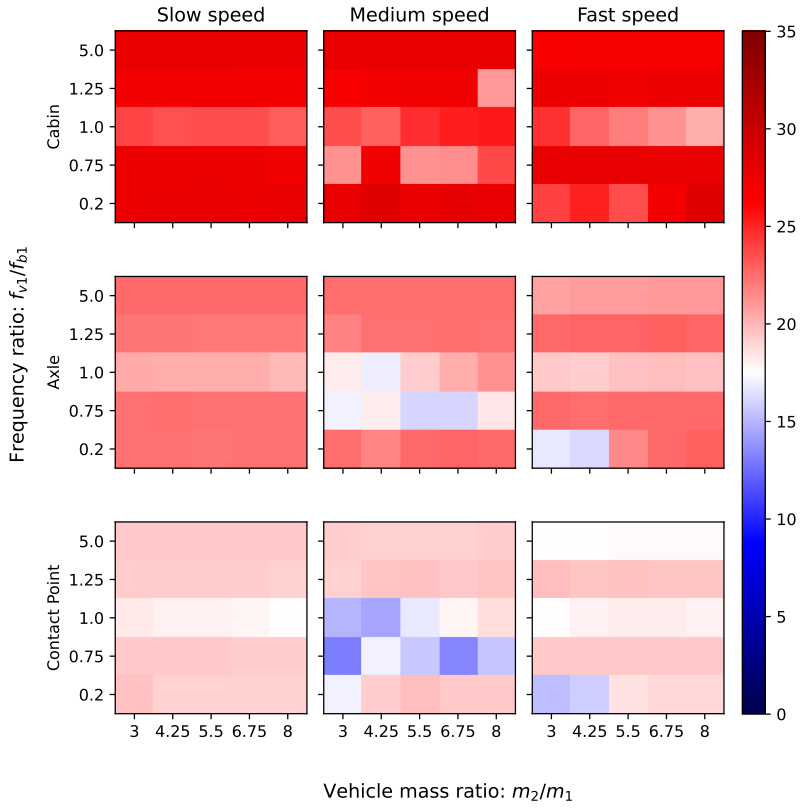

Figure 5.4.3: Peak prominence $[m^2 s^{-4}]$ above RMS level in range 0–100 Hz for vehicle properties defined in relation to f_{v1}/f_{b1}.

Frequency ratios $f_{v1}/f_{b1} = 0.2$ and $f_{v1}/f_{b1} = 0.75$ are associated with the largest under- and over-predictions of bridge frequency respectively, a trend that appears generally consistent with all vehicle mass ratios and traversal speeds. However, vehicle speed does appear to affect the results, most notably for the

medium speed which for most vehicle mass ratios is associated with a drop in prominent peak frequency (drift factor below 1.0) for $f_{v1}/f_{b1} = 1.0$ while this condition results in an increase in prominent peak frequency (drift factor above 1.0) for slow and fast speeds. Apparently the closest match between prominent peak frequency and true bridge frequency is associated with $f_{v1}/f_{b1} = 0.2$, although this trend is somewhat dependent on vehicle mass ratio, and only appears to be valid for slow and medium vehicle speeds.

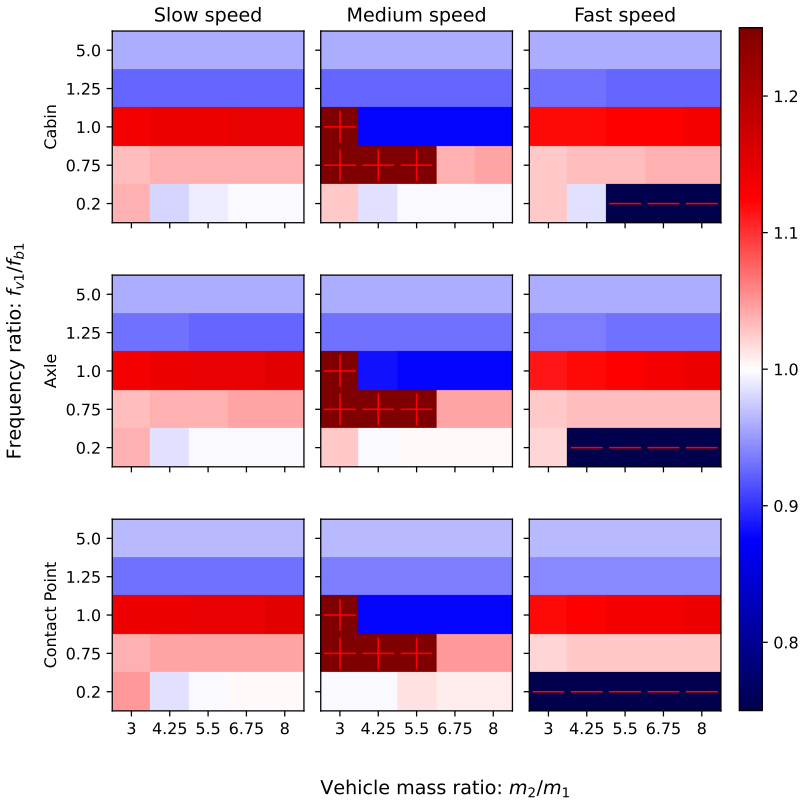

Figure 5.4.4: Prominent peak drift [Hz / Hz] in range 0–100 Hz for vehicle properties defined in relation to f_{v1}/f_{b1}.

Fig. 5.4.5 shows the peak prominence outcomes in the range 20-100 Hz, for vehicle-to-bridge frequency ratios defined in relation to the first bridge frequency. Fig. 5.4.6 shows the associated prominent peak frequency drift outcomes. These peak prominence values and frequency drifts can therefore be understood in terms of visibility and sensitivity of the second bridge frequency in the vehicle response.

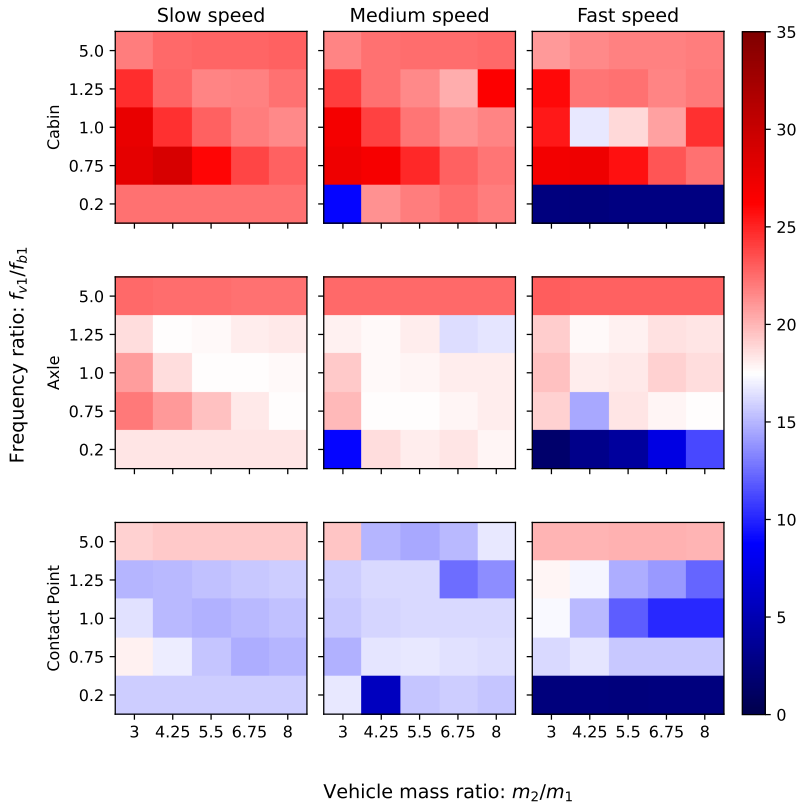

Figure 5.4.5: Peak prominence $[m^2s^{-4}]$ above RMS level in range 20–100 Hz for vehicle properties defined in relation to f_{v1}/f_{b1}.

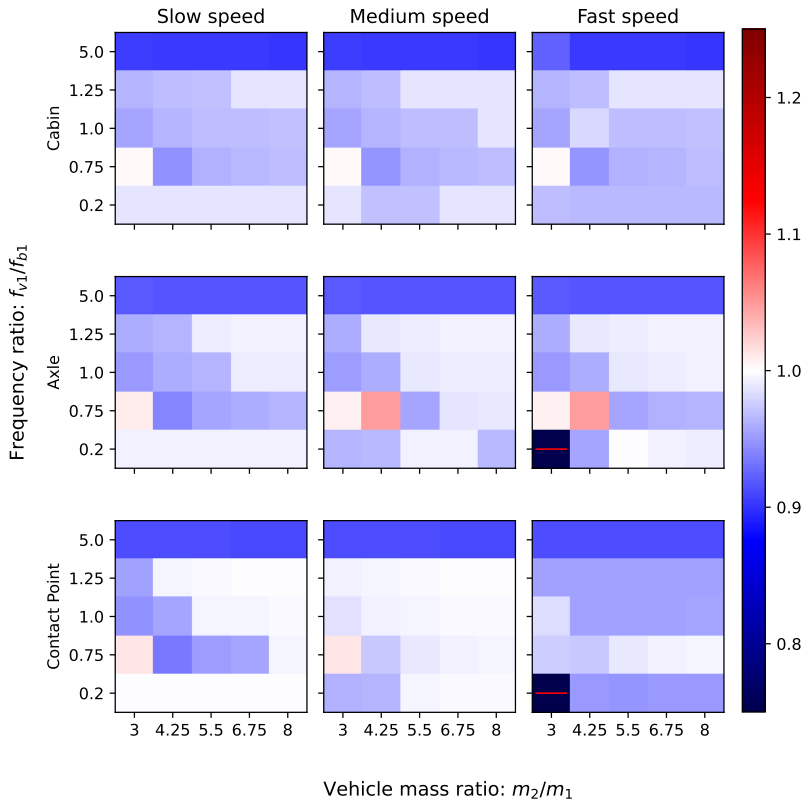

Figure 5.4.6: Prominent peak drift [Hz / Hz] in range 25–40 Hz for vehicle properties defined in relation to f_{v1}/f_{b1}.

In these plots, the higher peak prominences are generally associated with the cabin sensor location and $f_{v1}/f_{b1} = 0.75$. The lowest peak prominence values typically appear to correspond with $f_{v1}/f_{b1} = 0.2$ and the fast vehicle traversal speed. A clear trend in peak frequency drift is apparent, with slight negative drift (under-prediction of bridge frequency) associated with lower values of vehicle mass ratio, and larger negative drifts consistently associated with $f_{v1}/f_{b1} = 5.0$.

5.4.3 Outcomes: vehicle properties defined relative to second bridge frequency

Fig. 5.4.7 shows the peak prominence outcomes in the range 0-100 Hz, for vehicle-to-bridge frequency ratios defined in relation to the second bridge frequency. Fig. 5.4.8 shows the associated prominent peak frequency drift outcomes. From these figures, it appears that high peak prominence is associated with the cabin sensor placement, and all vehicle-bridge frequency ratios, with prominence slightly reduced for $f_{v2}/f_{b2} = 1.25$.

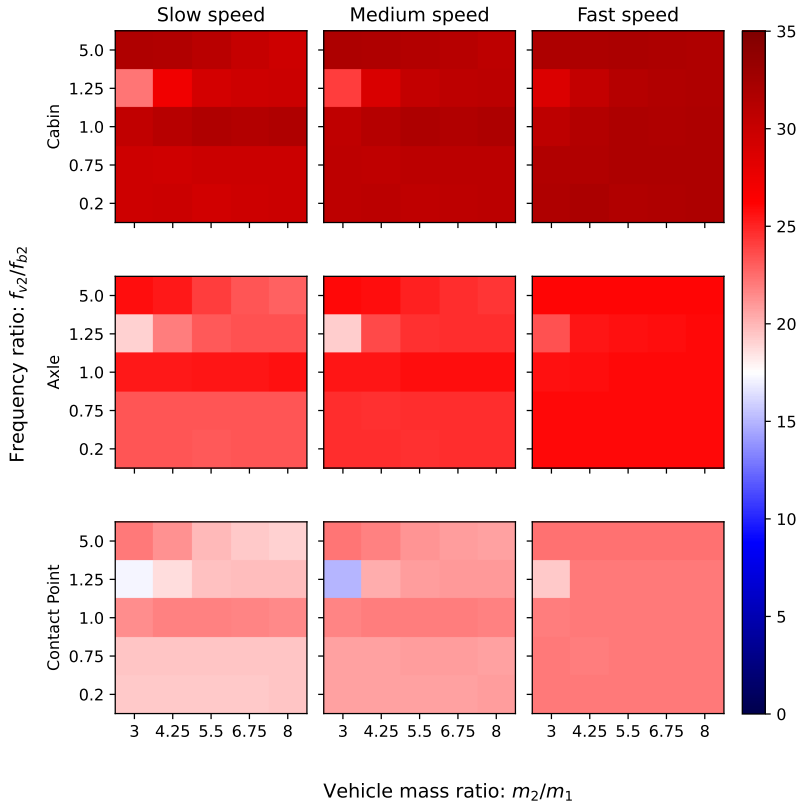

Figure 5.4.7: Peak prominence in range 0–100 Hz for vehicle properties defined in relation to f_{v2}/f_{b2}.

Generally, prominent peak frequency drift is reduced as the vehicle mass ratio increases; this can be understood as equivalent to a reduction in vehicle mass since the displacement in the vehicle's mode shape associated with f_{v2} is almost entirely at the lower DoF (see Fig. 5.3.1). Prominent peak frequency drift is also reduced as f_{v2}/f_{b2} decreases. A plausible explanation for this is that higher frequency ratios mean the vehicle's behaviour is moving closer to

the moving mass case (i.e. the vehicle acts as if it were a lumped mass without springs, leading to the well-known outcome of a reduction in the bridge natural frequency). However, when $f_{v2}/f_{b2} = 5.0$ the prominent peak frequency is reduced (drift factor less than 1.0) and this effect is consistent across all vehicle speeds, vehicle mass ratios and sensor placements. For this bridge and vehicle, some f_{v2}/f_{b2} between 1.25 and 5.0 will also represent $f_{v2} = f_{b3}$ and thus the changes in peak drift could represent VBI interaction with the vehicle's second frequency close to the bridge's third frequency.

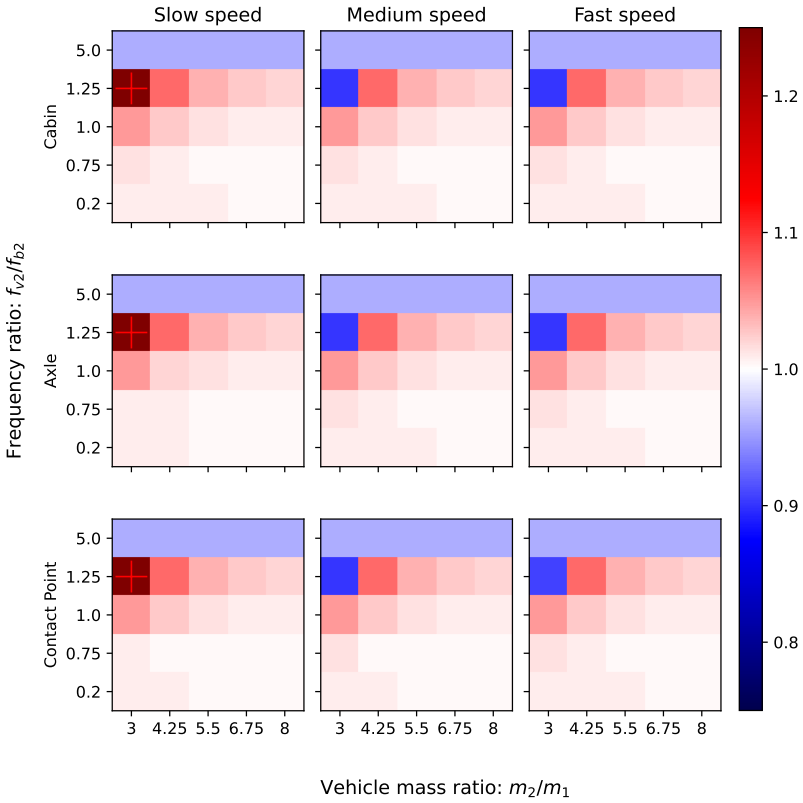

Figure 5.4.8: Prominent peak drift in range 0–100 Hz for vehicle properties defined in relation to f_{v2}/f_{b2}.

Fig. 5.4.9 shows the peak prominence outcomes in the range 20-100 Hz, for vehicle-to-bridge frequency ratios defined in relation to the first bridge frequency. Fig. 5.4.10 shows the associated prominent peak frequency drift outcomes. These peak prominence values and frequency drifts can therefore be understood in terms of visibility and sensitivity of the second bridge frequency in the vehicle response.

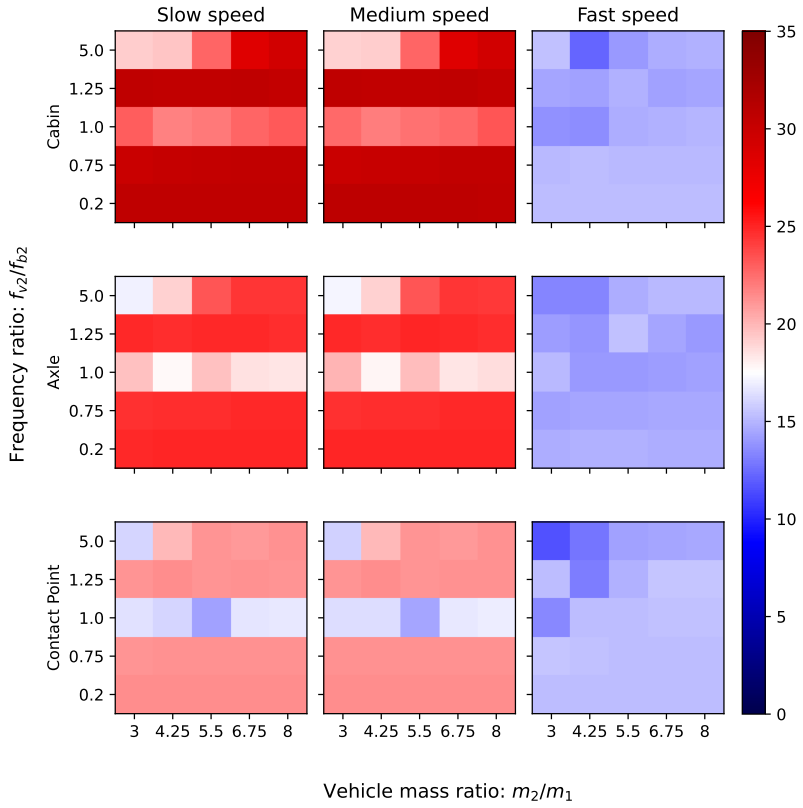

Figure 5.4.9: Peak prominence in range 20–100 Hz for vehicle properties defined in relation to f_{v2}/f_{b2}.

A clear trend is that peak prominence appears to be reduced across all vehicle-to-bridge frequency ratios and all vehicle mass ratios for the fast vehicle traversal speed. For $f_{v2}/f_{b2} < 1.0$ the fast vehicle speed is also associated with large under-prediction of bridge frequency (drift factor below 1.0). Another notable trend is that $f_{v2}/f_{b2} = 1.0$ and $f_{v2}/f_{b2} = 5.0$ appear to result in varying peak prominence and peak frequency drift as a function of vehicle mass ratio; the trend is monotonically decreasing for the contact point sensor but non-monotonic for the axle and cabin sensor placements.

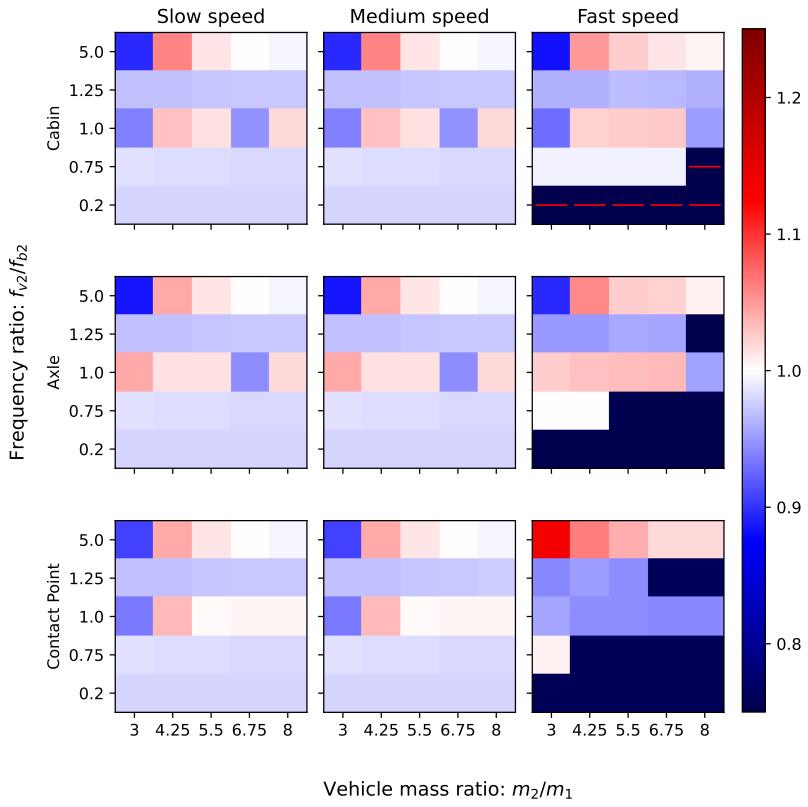

Figure 5.4.10: Prominent peak drift in range 25–40 Hz for vehicle properties defined in relation to f_{v2}/f_{b2}.

5.5 Discussion

The work presented in this chapter has used FE simulation to generate acceleration response data from a 2DoF quarter car lumped sprung mass vehicle traversing a simply-supported beam. The effects of vehicle parameters were explored, including varying the quarter car vehicle model's upper-to-lower DoF mass ratio; varying its traversal speed; and varying the stiffness of its springs such that a range of vehicle-to-bridge frequency ratios could be explored. The chapter addressed **bridge frequency visibility** for the first and second bridge modes detected directly from the vehicle response, considering the acceleration power spectrum prominent peak height above RMS signal power level; and **bridge frequency sensitivity** to explore the relative effects of vehicle and VBI system parameters by considering drift of the prominent peak frequency from the true (without vehicle presence) value.

5.5.1 Prominent peak frequencies

The prominent peak frequency study observations suggested:

- High and low vehicle-to-bridge frequency ratios lead to a situation approximating the well-known moving mass case. However, these frequency ratios in relation to one bridge mode introduce the potential for proximity with another bridge mode frequency. This may explain some of the variation in peak prominence and drift observed in the study.

- The largest peak prominence was generally associated with cabin sensor placement. However, in the case of proximity of the vehicle first mode frequency to any of the bridge frequencies, there exists a potential for misattributing the spectral peak to the bridge frequency when it is more accurately considered as representing the vehicle frequency. In such cases it would be necessary to observe the same prominent peak in the spectra relating to other sensor locations on the vehicle to confirm visibility of a bridge frequency.

- Vehicle traversal speed appears to affect frequency peak prominence and drift. A potential explanation for this relates to the observations noted in the literature review; increasing vehicle speed is understood to result in increased spectral peak height for bridge frequencies (in the absence of road roughness effects) and vehicle motion is understood to result in a frequency shift in proportion to the speed (Yang et al. [118]).

- Higher vehicle speed generally appears to lead to increased error in estimating bridge frequencies. This might be an effect of the higher vehicle speed resulting in more energy input to the bridge from the vehicle, raising the participation factor for the bridge second mode, thus reducing the mode 1 peak prominence above RMS level.

- It is understood that the presence of the total vehicle mass should affect frequency peak prominence and peak drift. However, the observations in this chapter show that the distribution of the vehicle mass between the upper and lower DoFs of a quarter car also appears to influence the resulting frequency peak prominence and peak drift. To the author's knowledge this is a novel finding that has not been previously reported. It is proposed that this may be due to the change in amplitude of response at the vehicle DoFs as a result of changing mass ratio (as shown in Fig. 5.3.1). Since measuring the mass ratio in practice is impractical unless the measurements relate to a bespoke sensor carrying vehicle whose properties are definitively known, it may be beneficial to adopt the contact point sensor location response to mitigate the effect of unknown vehicle mass ratio. The contact point response is thought to be more sensitive to bridge damage based on the available literature (Yang et al. [283], Zhang et al. [284], Yang et al. [187], Corbally and Malekjafarian [220]). **The contact point sensor response will therefore be used in the remaining parts of this thesis**. However, the formulation of the contact point estimation equation in the literature (Corbally and Malekjafarian [220]) relies on knowledge of the vehicle properties including the mass ratio. The implications of this are explored further in chapter 7.

- In practice, the vehicle spring stiffnesses would be expected to remain effectively constant (as long as a constant tyre inflation pressure was maintained). A change to the vehicle mass ratio would therefore in practice result in changes to vehicle natural frequencies. In this study, such an effect was normalised out by varying spring stiffnesses to suit mass ratios when selecting vehicle model parameters. The vehicle $k_1 : k_2$ ratio was kept constant in this study; a value in the middle of the published range was adopted as previously discussed.

- The most severe confounder to accurate estimation of bridge frequencies from the vehicle response appears to be vehicle-bridge natural frequency proximity. As noted in the literature review, this proximity is understood to induce VBI system frequency nonstationarity [42]. Time-dependent frequency variation is inherently not visible in frequency spectra. The use of hybrid time-frequency features may help to assist disambiguation in the case of vehicle-bridge frequency proximity and is pursued in chapter 6.

5.5.2 Possible effects of other VBI parameters

As discussed in sections 5.3.3 and 5.3.4, **damping** and **road surface roughness** were not modelled in this study presented in this chapter. Had they been included, it is proposed that they might have affected the observed outcomes in the following ways:

- **Vehicle damping** might have reduced the amplitude of response of some frequencies. Typically, modal damping ratios are higher for vehicles than

for bridges, expected to reach up to around $\zeta = 0.55$ for quarter-car vehicle models based on the outcomes from chapter 4 and the literature (Jazar [6]) compared to around $\zeta = 0.05$ for bridges. It is expected that inclusion of vehicle damping would reduce peak prominence for vehicle frequencies. However, in the case of proximal vehicle-to-bridge frequencies, the reduction would be expected to apply also to bridge frequency peak prominence. Exploration of the effects of vehicle damping is included in chapter 6.

- Due to the order-of-magnitude difference in damping ratios, **bridge damping** would not be expected to significantly affect the outcomes of the study.
- **Road surface roughness** is understood to represent an input to the vehicle, reducing signal-to-noise ratios. It is expected that inclusion of this effect in the study would have correspondingly reduced bridge frequency peak prominences by raising the RMS signal power level in the acceleration spectra. The RMS level would be expected to increase monotonically with vehicle traversal speed and thus the bridge frequency peak prominence would monotonically decrease with speed.
- No significant changes to **peak frequency drift** would be expected had damping and road surface roughness been included in the study. It is worth noting that damping does reduce effective frequency; a discussion of this is provided below.

As noted above, damping reduces effective frequency. However, this reduction is understood to be generally in proportion to the square root of the squared damping ratio. For example, considering an SDoF system it is well-known that the damped frequency $\omega_{d,i}$ for mode i can be expressed in terms of the natural frequency ω_i of that mode and the corresponding modal damping ratio ζ_i:

$$\omega_{d,i} = \omega_i \sqrt{1 - \zeta_i^2} \tag{5.2}$$

For a damping ratio of $\zeta = 0.55$ this results in a natural frequency reduction of approximately 16.5%. In fact, the actual reduction would be slightly different for a quarter-car model, due to the additional DoF and the non-proportional modal damping requiring the consideration of complex modes for the vehicle. However, since $k_1 >> k_2$ the SDoF model offers a coarse approximation the upper DoF's behaviour and thus yields insight to the expected magnitude of change of the vehicle's first frequency. The range of vehicle-to-bridge frequency ratios explored in this study is significantly greater than the expected frequency reduction due to vehicle damping. It is therefore concluded that effects due to changes in frequency ratios caused by vehicle damping would be less than those presented in the study of undamped vehicle bridge interaction in this chapter.

5.5.3 Implications for subsequent work in this thesis

The **virtual contact point vehicle acceleration response** is to be adopted for upcoming studies in this thesis.

The **vehicle upper-to-lower DoF mass ratio** does appear to affect the observed bridge frequency peak prominence and drift. In chapter 4 and in the discussion above it was noted that this mass ratio may change during day-to-day vehicle operation, and in practical terms cannot be measured. The vehicle mass ratio will therefore be kept constant for the study in chapter 6 to facilitate study of the effect of vehicle-to-bridge frequency ratio without confounding due to the change in modal amplitude of vehicle response induced by changing the vehicle mass ratio.

Vehicle-to-bridge frequency ratios close to unity appears to be a major confounder to accurate estimation of bridge frequencies from the vehicle response. The apparent system frequency non-stationarity discussed earlier in this thesis is believed to be the underlying cause, the time-varying aspects of effects of this nature are inherently not visible or apparent in acceleration power spectra. It is possible that adopting a hybrid time-frequency domain representation of the data will mitigate this issue by providing visibility of frequency variation. This will be explored in chapter 6.

5.6 Chapter summary

- The study adopted peak prominence and drift parameters to study the potential for accurate bridge frequency identification without prior knowledge.
- Bridge frequency peak prominence and peak drift both increased as vehicle traversal speed increased.
- Well-spaced vehicle and bridge frequencies led to outcomes approximating the moving mass case.
- The highest peak prominence was associated with the cabin sensor when the vehicle and bridge frequencies were closely-matched. However, this suggests the possibility of false positive identification of the bridge frequency.
- Vehicle-to-bridge frequency ratios close to unity induced changes in apparent bridge frequency, suggesting that VBI-induced frequency variation is a potential confounder for vehicle-based bridge modal parameter estimation and damage detection.
- Of the three vehicle sensor positions explored, the virtual contact point location appeared to be least susceptible to VBI-induced changes. However, it was noted that this sensor position cannot be literally achieved and thus relies on signal processing using known or estimated vehicle properties, meaning that in practice its utility may be compromised if the vehicle properties are not known definitively.
- Peak prominence and peak drift were affected by vehicle upper-to-lower DoF mass ratio, which is immeasurable in practice. This suggests the possibility of bias in estimates of the virtual contact point sensor response.

Chapter 6

Finite element simulation - frequency variation and damage detection

6.1 Chapter overview

This chapter addresses the following research objective:

RO.3 Characterise the nonstationary frequency variation for interacting vehicle-bridge systems during vehicle traversals in relation to vehicle model abstraction and vehicle-to-bridge parameter ratios.

This chapter is concerned with finite element (FE) simulation of the interaction between single- and two-degree-of-freedom (SDoF and 2DoF) vehicles with simply supported beam bridges. The vehicle-bridge interaction (VBI) models used in this chapter are represented in Fig. 6.1.1. These models are generally aligned with the description given in section 5.1, with the only difference being that the SDoF model combines both masses into a single m, both springs into a single k, and features a viscous dashpot damper with coefficient c. The work presented here aims to understand the effect of varying parameters on the frequencies of the combined vehicle-bridge system, including how the frequencies vary whilst the vehicle is moving along the bridge during a traversal.

Chapter 4 demonstrated that estimations of vehicle modal damping ratios can vary significantly. It is therefore difficult to reliably estimate damping properties for a representative quarter-car model. In some studies vehicle damping has been noted as a factor in the detection of bridge properties and damage from vehicle responses (for example Yang and Lin [260], Yang and Lee [273] from Yang and Yang [41]) although in general it has not received much attention; vehicles have often been modelled as undamped. If considering real vehicles and field

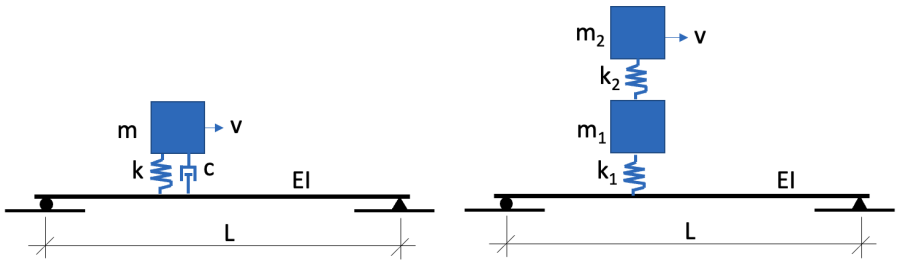

Figure 6.1.1: The single- (left) and two-degree-of-freedom (right) vehicle and simply-supported beam bridge models used in sections 6.3 and 6.4.

testing it would be necessary to choose and adopt damping ratios for vehicle models. The potential effect of errors in assumed vehicle damping ratio on the detection of bridge damage from vehicle-based sensors is a little-studied question. This chapter therefore includes an investigation of the effect of damping on instantaneous VBI system frequency for an SDoF vehicle model traversing a simply-supported beam bridge.

VBI system frequencies are understood to exhibit nonstationary behaviour during vehicle traversals when the vehicle and bridge natural frequencies are proximal (Yang et al. [9], Cantero and O'Brien [10], Cantero et al. [11] [42]). In chapter 5 this was noted as the most significant confounder to accurate estimation of bridge frequencies from vehicle-mounted accelerometer responses. It was proposed that using hybrid time-frequency representations of the vehicle response might provide mitigation. The nature of VBI system frequency nonstationarity is little-studied beyond a closed-form representation of single-mode interaction (Yang et al. [22]) and some physical testing (Cantero et al. [11], [42]). The nature of the frequency variation has not yet been explored and characterised in relation to VBI system parameters for vehicle and bridge models with more than one mode. Moreover, bridge damage detection efforts using vehicle-mounted accelerometer responses typically assume or rely on well-spaced bridge and vehicle frequencies. Since this condition may not be met in practice using uncontrolled vehicles, there would be great value in developing a bridge damage detection methodology for situations in which vehicle and bridge natural frequencies are close. In addition to exploring the nature of frequency nonstationarity for two-mode vehicle and bridge systems in VBI, this chapter proposes a bridge damage detection method and explores its efficacy across a range of VBI system parameters.

All of the work presented in this chapter relates to finite element simulations; the data are therefore synthetic.

6.1.1 Method of investigation

The work is presented in the following manner:

- **Section 6.2** describes the FE model and the simulation regimes undertaken, including the process of model development and validation. Included is the first-known application of the concept of a *cone of influence* or *radius of trust* for the Stockwell transform.
- **Section 6.3** is concerned with single degree-of-freedom vehicle models. Modal frequencies are extracted from the FE model and compared to those predicted by the existing closed-form theoretical expression. The investigation explores the change of instantaneous bridge mode 1 and 2 frequencies during vehicle traversal in relation to vehicle-to-bridge mass and frequency ratios, and vehicle damping rates.
- **Section 6.4** extends the investigation of undamped two-degree-of-freedom vehicle models from chapter 5. Simulation results are presented, showing the effects of vehicle-to-bridge frequency ratios and vehicle upper-to-lower DoF mass ratios on bridge frequencies, including the instantaneous bridge mode 1 and 2 frequencies during a vehicle traversal.
- **Section 6.5** develops an unsupervised damage detection method for situations in which the vehicle and bridge have proximal frequencies.
- **Section 6.6** comprises a discussion of the work presented in the chapter.
- **Section 6.7** presents the chapter conclusions.

6.2 Finite element model and analysis: description and validation

6.2.1 Overview of modelling and simulation regime

FE simulation for this chapter was conducted using *ABAQUS* software by Dassault Systèmes Simulia. Model generation and analysis was controlled by Python scripts.

Modelling was conducted in two dimensions, with vehicle and bridge motion constrained to a plane. The bridge was modelled as a simply-supported Euler-Bernoulli beam. An element length of 0.01 m was adopted based on a mesh convergence study, previously presented in chapter 5. The vehicle was modelled as point masses connected by linear connector sections, which were assigned spring stiffnesses and damping coefficients according to the vehicle parameters being investigated. The vehicle was either represented as one or two lumped point masses (SDoF and 2DoF model abstractions). Normal contact between the vehicle and bridge was modelled using a surface-to-surface formulation with a hard pressure-overclosure relationship and adopting the default method of enforcement of contact. Contact separation was not permitted. Tangential interaction was modelled as frictionless.

FE analysis was conducted in two distinct regimes:

- **Linear perturbation frequency analysis** was used to extract modal frequencies for the beam. The beam was analysed initially without the presence of a vehicle. Subsequently, the analysis was repeated for a range of vehicle positions along the beam. In this type of analysis, any effects relating to the movement of the vehicle are excluded. The output comprised modal frequencies (square roots of eigenvalues).

- **Implicit dynamic analysis** was employed to simulate the vehicle moving across the bridge. The output comprised vertical acceleration at all vehicle and bridge degrees of freedom at each timestep increment.

For the linear perturbation frequency analyses, results were obtained for 21 equally-spaced possible vehicle positions on the 2 m bridge span, corresponding to an inter-position spacing of 0.1 m. For the implicit dynamic analysis, the simulation timestep was constant at 0.0002 s, corresponding to a *simulation frequency* of 5 kHz. Further discussion of the selection of a suitable simulation frequency is included in section 6.2.3.

6.2.2 Mesh density

A mesh convergence study was presented in Chapter 5 and the same FE model formulation and simulation method are used in this chapter.

6.2.3 Simulation timestep

Fig. 6.2.1 shows Stockwell transforms (ST) of the bridge quarter-span acceleration response from an FE simulation of a 2DoF vehicle model traversing a beam bridge. The left plots show the ST contours in the frequency sub-band around the first bridge frequency, while the right subplots show the same for the second bridge mode. The ST contours are normalised to the maximum signal power in the frequency sub-band at each timestep, yielding a contour heatmap. The contour plots include a red line tracing the frequency with the maximum signal power (known as the *ridge*). The figure presents an exploration of varying the *simulation frequency* f_s which is the inverse of the simulation timestep length δ_t. The bridge properties match those previously presented in Table 5.2.1. Table 6.2.1 summarises the vehicle properties which were selected to yield the vehicle-to-bridge frequency ratios shown, specifically $f_{v2}/f_{b2} \approx 1$ with the intention that this would create frequency variation in the vicinity of the bridge second mode, since a suitable simulation timestep capable of capturing second mode effects can be assumed to be adequate for lower frequency phenomena also. The traversal duration was 2 s (i.e. the vehicle speed was 1 m/s). Simulation frequencies and associated simulation timesteps are summarised in Table 6.2.2.

Property	Value
m_1	0.7 kg
m_2	2.73 kg
k_1	3×10^4 N/m
k_2	38 N/m
c_1	1×10^{-10} Ns/m
c_2	1×10^{-10} Ns/m
f_{v1}	0.59 Hz
f_{v2}	32.97 Hz
$f_{v1} : f_{b1}$	0.07
$f_{v2} : f_{b1}$	3.91
$f_{v1} : f_{b2}$	0.02
$f_{v2} : f_{b2}$	0.98

Table 6.2.1: Vehicle properties and vehicle-to-bridge frequency ratios used in the convergence study in chapter 6.

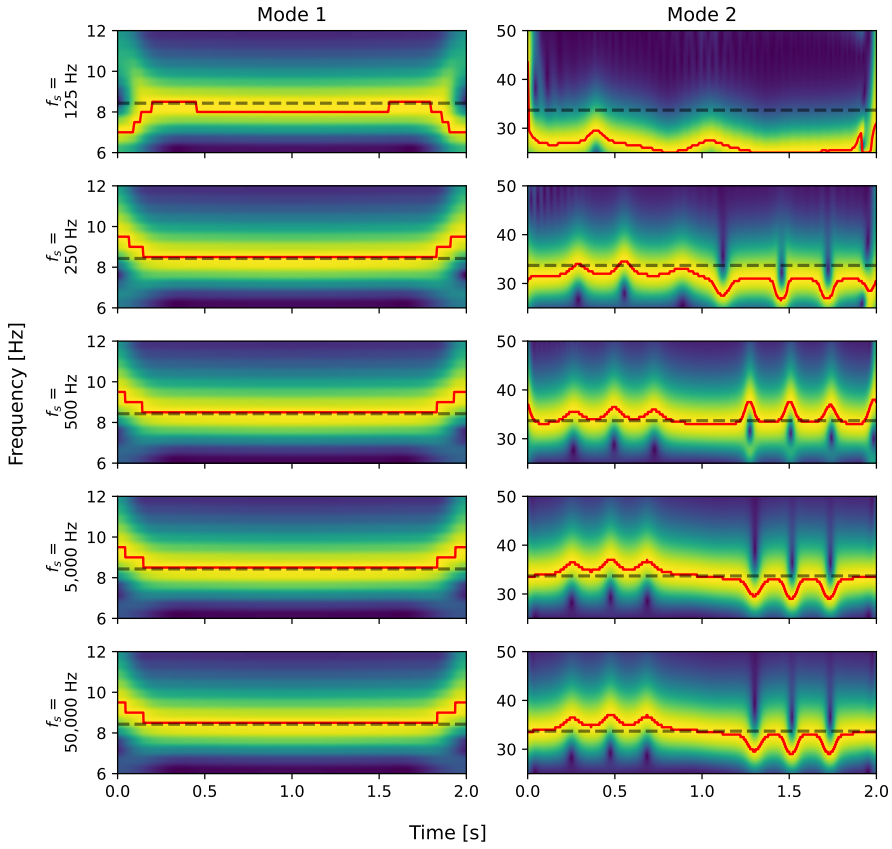

Figure 6.2.1: FE-derived instantaneous mode 1 and 2 frequencies: Stockwell transform contours featuring ridges (maximum signal power in the displayed frequency sub-bands) shown as red lines. Data from bridge quarter-span acceleration during a vehicle traversal for a range of simulation timestep lengths. Dashed grey horizontal lines represent bridge modal frequencies.

Simulation frequency $f_{sim.}$ **[Hz]**	**Simulation timestep** δt **[s]**
125	8×10^{-3}
250	4×10^{-3}
500	2×10^{-3}
5,000	2×10^{-4}
50,000	2×10^{-5}

Table 6.2.2: Simulation frequencies and associated timesteps used in the convergence study in chapter 6.

Gibson et al. state that the Stockwell transform is "a special case of the continuous wavelet transform using a Morlet-type mother wavelet, with frequency identified as inverse scale, and a minor phase and amplitude adjustment" [396]. This insight suggests the application of processing and analysis methods intended for use with Wavelet transforms (WT). Lily and Olhede [415] explain that *ridges* are curves in the wavelet transform time-scale domain which define a modulated signal whose instantaneous frequency and phase approximate those of the signal from which the transform was generated. In this thesis the instantaneous frequency is of interest. Staszewski [416] explains that picking the peak amplitude of the transform is a common method of approximating the ridge. Although it is only strictly accurate for linear ridges [416] the approach is adopted in this thesis. The red lines on the ST plots are the estimated ridges and represent the estimated time-varying frequency with maximum signal power in the bandwidth covered by the transform.

Fig. 6.2.1 presents a study of instantaneous bridge frequency variation during a vehicle traversal. Moving from the upper to lower subplots, the simulation timestep is reduced. A converged simulation is deemed to have been reached once reducing the timestep length no longer leads to a visible change in the time-frequency behaviour in the frequency sub-band in the vicinity of the first two bridge modes. Visual inspection of the figure suggests that there is little or no change in the ridge for mode 1 at simulation frequencies above 250 Hz. For mode 2, the ridge visually appears to stabilise at a simulation frequency of 5 kHz. It is interesting to note that the plotted ridge for mode 2 displays different behavioural trends at lower simulation frequencies compared to the assumed converged case, with the direction of frequency change in the second half of the vehicle traversal flipping between simulation frequencies of 250 Hz and 500 Hz, despite these both being significantly higher than the typical antialiasing Nyquist limit (twice that of the frequency of interest).

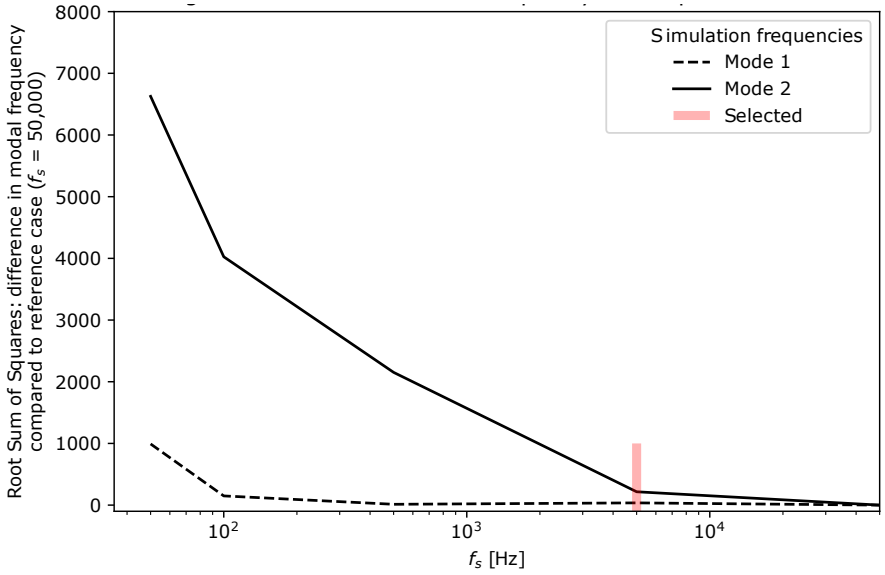

Figure 6.2.2: Square root sum of differences: instantaneous frequency during a traversal compared to the reference case.

It is assumed that the ridges for both modes at a simulation frequency of 50 kHz represent a converged simulation. Although the simulation frequency of 50 kHz is much higher than the bridge modal frequencies of interest, Fig. 6.2.2 demonstrates that this short timestep ($1/f_s = 1\times10^5$ s) appears to be necessary to capture the oscillatory behaviour of instantaneous frequency which is apparent for cases where the vehicle and bridge non-interacting natural frequencies are approximately equal (right subplots in Fig. 6.2.2. Using the converged simulation as a *reference case*), the figure presents the square root sum of squared

difference between all ridge points at each simulation frequency and the ridge points for the reference case. A vertical red line on this plot indicates the simulation frequency of 5 kHz which was adopted. The convergence trend is clear and demonstrates acceptability of the adopted simulation frequency.

6.2.4 Edge and discontinuity effects

The *radius of trust* for a Wavelet transform relates to regions at the start and end of a finite length signal. The term *cone of influence* used in some texts is also known as the *radius of trust* (Li et al. [417]). Torrence and Campo explain that, in a manner similar to the Fourier transform, the WT is subject to edge effects due to an assumption that the data are cyclic [418]. In their study they describe an example in which the signal is "padded with sufficient zeroes to bring the total length N up to the next-higher power of two, thus limiting the edge effects" [418]. When the WT is applied to finite-length samples it is conceptually helpful to imagine the signal being wrapped around such that its start and end are joined. In the case of a finite length sample where the instantaneous frequency and phase at the start and end are the same, and the signal length contains an integer number of cycles, the signal could thus be joined in this circular manner without creating a discontinuity. In reality, these conditions are not always met, leading to *edge artefacts* which can obscure the true behaviour of the signal in these regions of the resulting transform (Montenari et al. [419]).

The radius of trust is defined in relation to the *scale* of the *mother wavelet* used in the transform. In practice this allows a zone of the time-scale transform to be identified to highlight the risk of the transform in this region containing spurious and potentially misleading information. This zone is within the cone of influence, meaning that the radius of trust is the area in which the transform can be generally assumed to represent meaningful information.

To date there is no known literature discussing this concept for the Stockwell transform. To address this gap we can recall Gibson et al.'s assertion that the ST is a special case of the WT with a *Morlet* mother wavelet and scale equal to inverse frequency [396]. Torrance and Compo define the cone of influence as the "e-folding time for the autocorrelation of wavelet power at each scale" where the *e-folding time* is set such that the edge artefacts are negligible beyond the cone of influence because the power of the wavelet has decreased proportional to e^{-2} [418]. They state the e-folding time of the Morlet wavelet as $\sqrt{2}s$ [418]. Adopting this definition of the cone of influence, and recalling that the ST scale s_{ST} is given as the inverse of frequency [396]:

$$s_{ST} = 1/f \tag{6.1}$$

Torrance and Compo's cone of influence definition [418] can be expressed for a Morlet wavelet as:

$$t_{COI,Morlet} = \sqrt{2}s \tag{6.2}$$

and therefore for the ST as:

$$t_{COI,ST} = \sqrt{2}/f \tag{6.3}$$

or alternatively:

$$f_{COI,ST} = \sqrt{2}/t \tag{6.4}$$

The ST cone of influence can therefore be drawn according to equation (6.4) for values of time t advancing forward from the start of the signal sample and backward from the end, as shown in Fig. 6.2.3. In this figure the edge effect-induced deviation of estimated ridge and true signal frequency outside the radius of trust can be seen at the bottom left. Inside the radius of trust, the estimated ridge and true frequency appear to be in agreement.

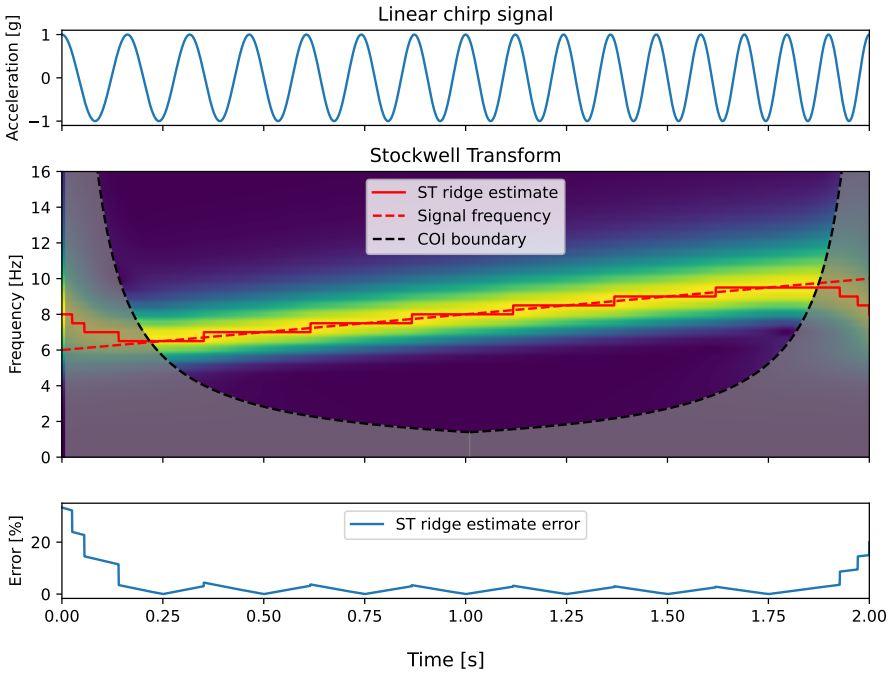

Figure 6.2.3: Ascending linear chirp signal, the corresponding Stockwell Transform, and the percentage error in the ridge estimation.

6.2.5 Time-frequency domain interpolation

Brown et al. [395] explain a compromise inherent to the Stockwell transform: it achieves more fine frequency resolution at low frequencies (at the expense of time resolution) and more fine time resolution at high frequencies (at the expense of frequency resolution). This is achieved by varying the width of the Gaussian window used in the transform as a function of frequency. In practice, this means that the frequency contours plotted around the ridge are grouped more tightly at low frequencies and spread more broadly at high frequencies. The ST's similarities to the short time Fourier transform mean that there is still a minimum discrete step in frequency δ_f to which precision the ridge can be estimated by picking the maximum power of the transform, inversely proportional to the sample length (number of points in the discrete sample) N_{sample} according to the well-known equation (6.5). For an illustration of this, refer to Fig. 6.2.4 which shows the ST and estimated ridge of a linear chirp signal. The frequency step in the estimated ridge is the same at the beginning and end of the chirp, while the width of the contours either side can be seen to increase in proportion to the chirp frequency. The constant frequency step is even more apparent in Fig. 6.2.3.

$$\delta f = \frac{1}{N_{sample}} \tag{6.5}$$

It is clear that, although more sophisticated ridge estimation techniques are available, the precision with which frequency changes can be represented by the ST depends mainly on the sample length when the nominal signal frequency is low, as it is likely to be for bridge modal frequencies. Interpolation in the frequency domain is one approach to gaining insight into the centre of a frequency peak taken from the Fourier transform of a short sample. This is equivalent to the commonly-applied method of extending the signal by padding with zeros in the time domain (Smith [420][1]). Multiple approaches are commonly applied to this time-domain padding goal. For the current purpose, options to be explored comprise padding each end of the signal with some additional information: a mirrored copy of the signal itself, a vector of zeros, or some other synthetic signal. The circular wrapping effect inherent to the transform means that the start and end effectively become adjacent parts of the signal and a discontinuity is formed. Such a discontinuity may also exist between the true sample and the synthetic padding signal after concatenation. This might be improved by applying a tapering window to the whole signal prior to padding, such that at the signal-to-padding junction the concatenated signal has zero amplitude and thus is effectively not in fact discontinuous. A visual example of these strategies is shown in Fig. 6.2.5. The upper plot shows a linear chirp signal padded with one reflected copy of itself either side. The centre upper plot shows the same signal padded with a same-length vector of zeros either side. The centre lower and lower plots show the same signal padded in the same manners respectively

[1] https://ccrma.stanford.edu/~jos/mdft/Zero_Padding_Theorem_Spectral.html

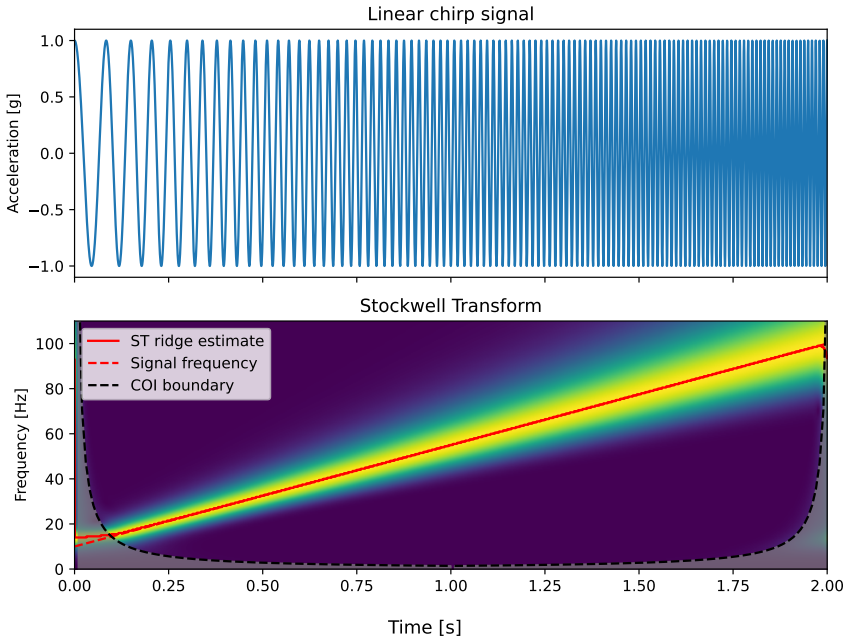

Figure 6.2.4: Ascending linear chirp signal and the corresponding Stockwell transform.

after having been subject to a Hanning window such that its amplitude reduces to zero at the start and end.

Fig. 6.2.6 plots the error in ridge estimation for these signal padding and windowing strategies for the full duration of the original signal. Fig. 6.2.7 compares the mean ridge estimation error for all points in the duration of the original signal. Padding with reflected copies of the signal results in the lowest mean error. Considering the mean error, applying the tapering window to the signal does not appear to be beneficial. Visual inspection of Fig. 6.2.6 offers clues as to where each of the approaches finds its utility.

Applying the tapering Hanning window generally appears to reduce ridge estimation error at lower frequencies, but increases it at higher frequencies. These effects appear most pronounced when the signal is padded with zeros. Without the application of the tapered window, the zero padded signal seems to result in greater error at low frequencies compared to the signal padded with reflected self-copies, with the latter approach appearing to offer generally lower errors at low and high frequencies. It should be noted that the ridge estimation errors appear to all be concentrated at the beginning and end of the signals. All signal padding and windowing methods offered similar performance away from the boundary of the edge effect cone of influence.

A comparison of Figs. 6.2.8 and 6.2.9 offers insight to the ridge estimation error performance. Padding with reflected self-copies of the signal means that

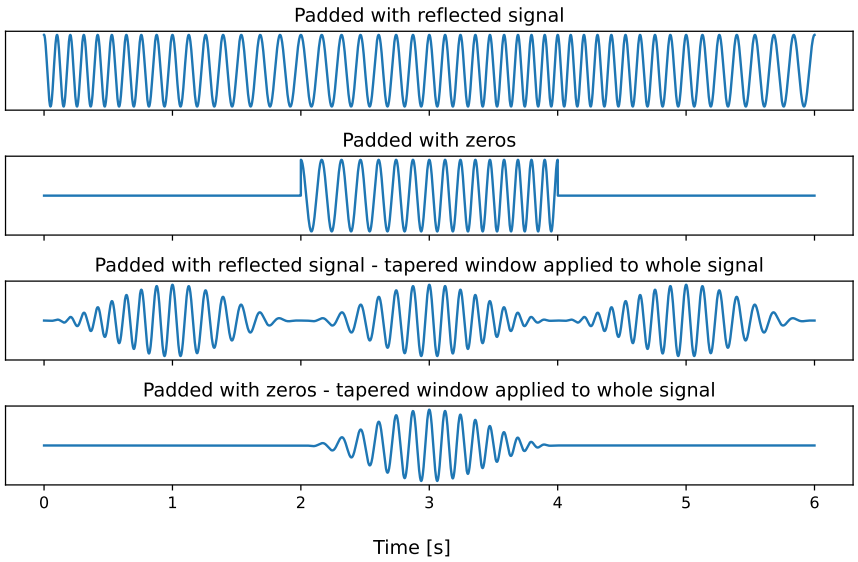

Figure 6.2.5: Illustration of typical options for padding a signal in the time domain.

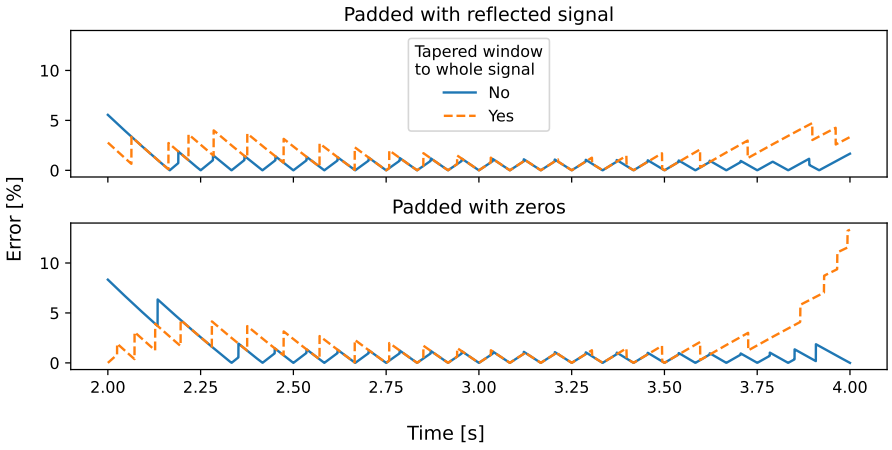

Figure 6.2.6: Comparison of percentage error (estimated ridge of Stockwell Transform compared to true instantaneous frequency) for the signals shown in Fig. 6.2.5.

the apparent frequency change immediately before and after the true signal is limited to a change in direction of gradient. In contrast, padding with zeros means that the apparent frequency rapidly drops to zero immediately before and after the true signal starts and ends. This sharp drop is a qualitatively

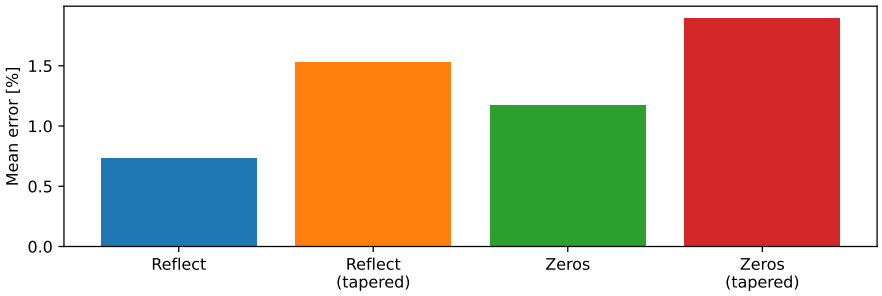

Figure 6.2.7: Mean error (estimated ridge of Stockwell transform compared to true instantaneous frequency) for the signals shown in Fig. 6.2.5.

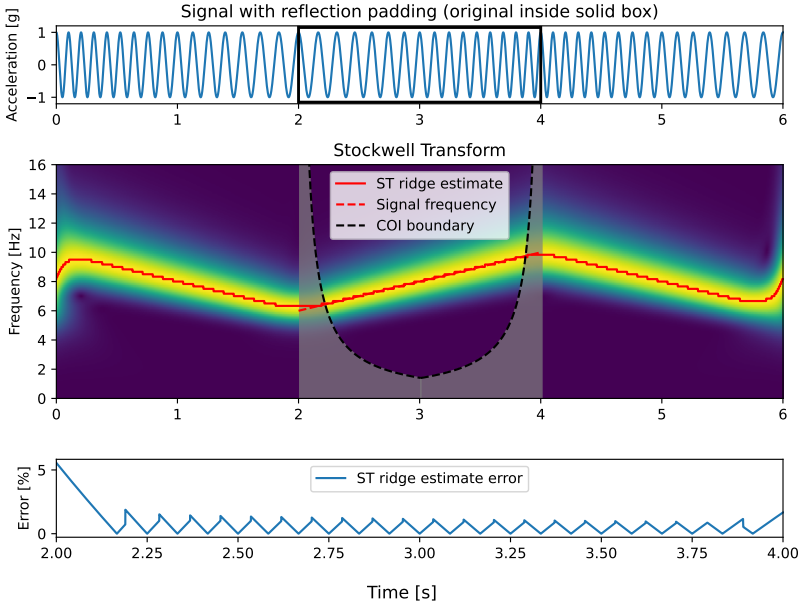

Figure 6.2.8: Ascending linear chirp signal **padded with reflected copies of the signal**, the corresponding Stockwell Transform, and the percentage error in ridge estimation.

greater discontinuity, resulting in larger ridge estimation errors within the cone of influence.

It remains to choose the length of padding to be added to the signal prior to generation of the Stockwell transform. Fig. 6.2.10 presents the outcome of a convergence study. The ascending linear chirp signal (see Fig. 6.2.3) was padded with reflected self copies repeated to cover a range of padding lengths. The mean and maximum ridge estimation error are presented for padding lengths from 0

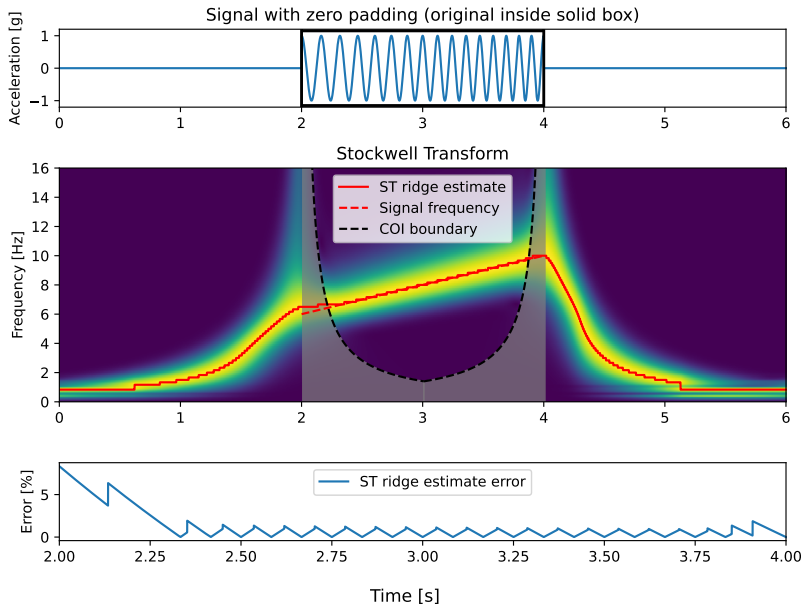

Figure 6.2.9: Ascending linear chirp signal **padded with zeros**, the corresponding Stockwell Transform, and the percentage error in ridge estimation.

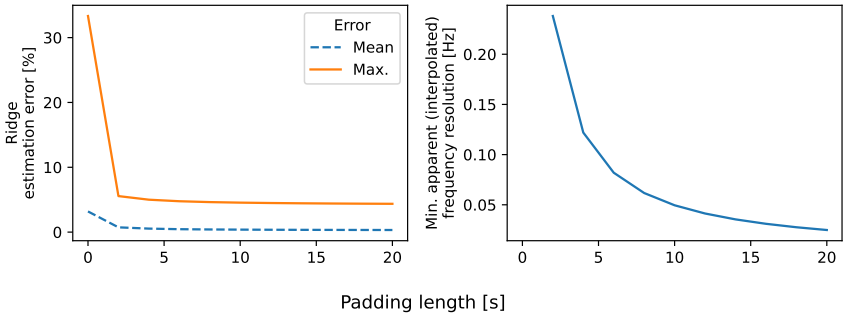

Figure 6.2.10: Padding length convergence study outcomes: ridge estimation error (left) and minimum apparent interpolated frequency resolution (right).

to 20 s, alongside the associated apparent (interpolated) frequency resolution. Increasing the padding length beyond 10 s at each end does not appear to result in a meaningful reduction in ridge estimation error for signals in this frequency range. Higher frequency signals are expected to have even lower ridge estimation error due to the tapering nature of the cone of influence boundary. The minimum apparent frequency resolution of 0.05 Hz is acceptable by inspection. The realised apparent frequency resolution will in fact be more fine due to the length of the signal itself.

6.2.6 Summary of adopted signal processing method

Based on the investigations presented in this chapter, prior to generation of the Stockwell transform it is proposed to pad the signals with reflected self-copies. Multiple copies are to be used for padding the start and end of each signal, aiming for a total padded signal length of at least 20 s or greater, yielding an expected apparent frequency resolution of $1/20 = 0.05$ Hz or higher.

6.2.7 Stockwell transform contour normalisation

It should be noted that the ST contours presented in this thesis have been normalised. The normalisation strategy adopted comprises normalisation to instantaneous maximum signal power; in other words, normalising the contours to the maximum power at each timestep within the frequency range adopted. This strategy appears to increase the visibility of VBI-induced frequency variation trends and is based on the approach used in Cantero et al's [42] study which used wavelet transforms to explore similar frequency variation based on laboratory-scale experimental measurements.

6.3 SDoF vehicle parameter variation

6.3.1 Scope of study

The results presented in this chapter relate to the SDoF vehicle model shown in Figure 6.1.1. The SDoF vehicle study in this section will be divided into the following parts:

- Comparing the linear perturbation FE-derived frequencies for the combined bridge and static SDoF vehicle system to the available closed-form expression (bridge mode 1 only). Results are shown in Figures 6.3.1 and 6.3.2, covering vehicle-to-bridge mass ratios summarised in Table 6.3.1. This serves to validate the trends of FE model predictions and to explore the nature of differences between the FE-derived and closed-form-derived results.

- Exploration of the maximum mode 1 and 2 frequency changes in the bridge as a function of the position (midspan or quarter-span); mass and frequency of a static SDoF vehicle. Results are shown in Figures 6.3.3 and C.1.1. Mass ratios explored are shown in Table 6.3.1; vehicle-to-bridge frequency ratios are shown in Table 6.3.2.

- Exploring the variation in FE-derived frequencies for the combined bridge and static SDoF vehicle system including the bridge first and second modes, and comparing the linear perturbation FE-derived outcomes (static vehicle) to the implicit dynamic (moving vehicle) FE-derived outcomes. Results are shown in Figures 6.3.4, 6.3.5 and 6.3.6. The vehicle mass used in these studies was as noted in Table 6.3.1 for the *high mass* case.

- Exploring the effect of vehicle damping ratio on instantaneous system frequencies for the SDoF vehicle traversing the bridge. Results are shown in Figures 6.3.7, C.2.1 and C.2.2. The outcomes are presented for two vehicle-to-bridge frequency ratios ($f_v \approx f_{b1}$ and $f_v \approx f_{b2}$) and vehicle damping ratios ζ from 0% (undamped) to 150% (supercritically damped). The vehicle mass used in these studies was as noted in Table 6.3.1 for the *high mass* case.

In all SDoF vehicle studies in this chapter, the modelled bridge parameters were as previously outlined in Table 5.2.1 and are reproduced here for ease of reference as Table 6.3.3. The table presents the modelled bridge span length L; cross section breadth b, depth d and second moment of area I; material density; Young's modulus E; and the natural frequencies of the first two bridge modes f_{bi}. Vehicle traversal time was 4 s (velocity 0.5 m/s) for all moving vehicle simulations. The surface of the bridge was smooth and no road roughness effects were modelled.

Identifier	**Vehicle mass** m_v **[kg]**	**Bridge mass** m_b **[kg]**	**Mass ratio** $m_v : m_b$ **[%]**
Low mass	3.43	60.66	5.65
Medium mass	6.86	60.66	11.31
High mass	10.29	60.66	16.96

Table 6.3.1: Bridge and vehicle masses and mass ratios used in the SDoF vehicle study.

Identifier	**Frequency ratio**	
	$f_v : f_{b1}$	$f_v : f_{b2}$
Very low mode 1	0.12	0.03
Low mode 1	0.73	0.18
Equal mode 1	1.00	0.25
High mode 1	1.27	0.32
Low mode 2	2.91	0.73
Equal mode 2	4.01	1.00
High mode 2	5.09	1.27

Table 6.3.2: SDoF vehicle-to-bridge frequency ratios used in the study.

L $[m]$	**b**$[m]$	**d**$[m]$	**Density** $[kg/m^3]$	**E** $[GPa]$	**I**$[m^4]$	**Damping**	$f_{b1}[Hz]$	$f_{b2}[Hz]$
2	1	0.00959	3162.92	190	7.35×10^{-8}	0	8.43	33.7

Table 6.3.3: Bridge model parameters used in SDoF vehicle study.

6.3.2 Static vehicle: eigenfrequency variation

Yang et al. [9] present a theoretical closed-form expression for the natural frequencies of a beam bridge with a static SDoF lumped sprung mass vehicle model. The expression is based on the bridge mode 1 frequency and the SDoF vehicle frequency only; these are found as the square roots ω_1 and ω_2 of the solution pair ${\omega_1}^2$ and ${\omega_2}^2$. The expression is presented in section 2.6 as equation (2.14).

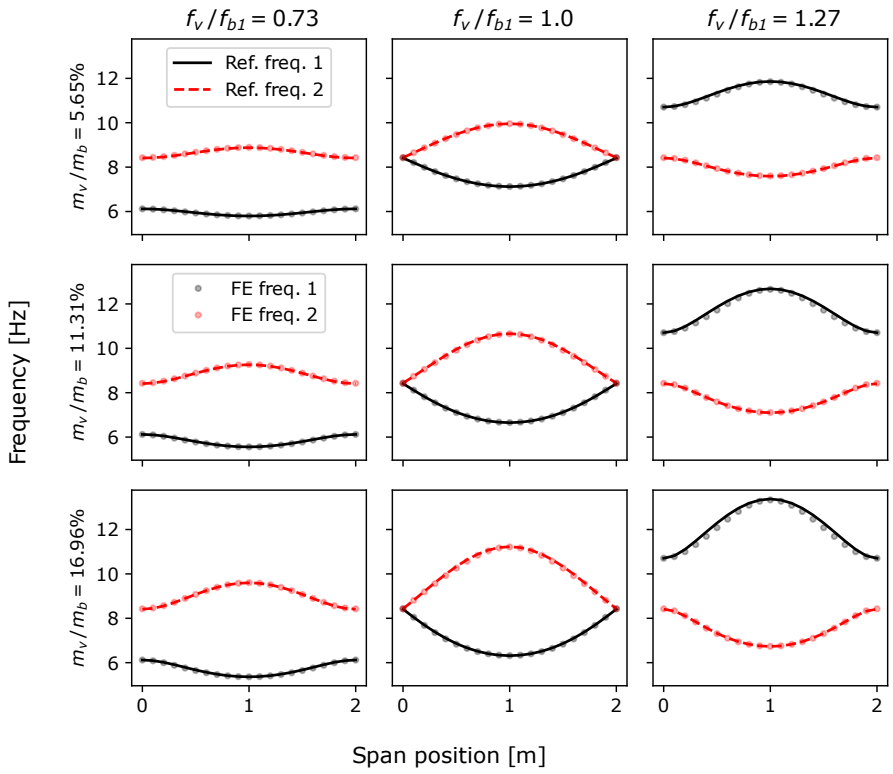

Figure 6.3.1: Mode 1 frequency variation (combined SDoF vehicle-bridge system): closed-form analytical results compared to FE-derived results.

Fig. 6.3.1 plots the frequency variation for mass ratios $m_v : m_b = 5.65\%$, 11.31% and 16.96% and frequency ratios $f_v : f_{b1} = 0.73$, 1.0 and 1.27, where f_{b1} refers to the bridge first mode. A comparison is presented between the closed-form analytical expression from Yang et al. [9] and the results derived from FE simulation. As noted in [9] the combined system has two natural frequencies for any vehicle position. Yang et al. describe one of these frequencies as associated primarily with the bridge first mode and the other with the vehicle. In Fig. 6.3.1 *frequency 1* is nominally associated with the vehicle and *frequency 2* with the bridge, although they can be thought of as natural frequencies of the combined

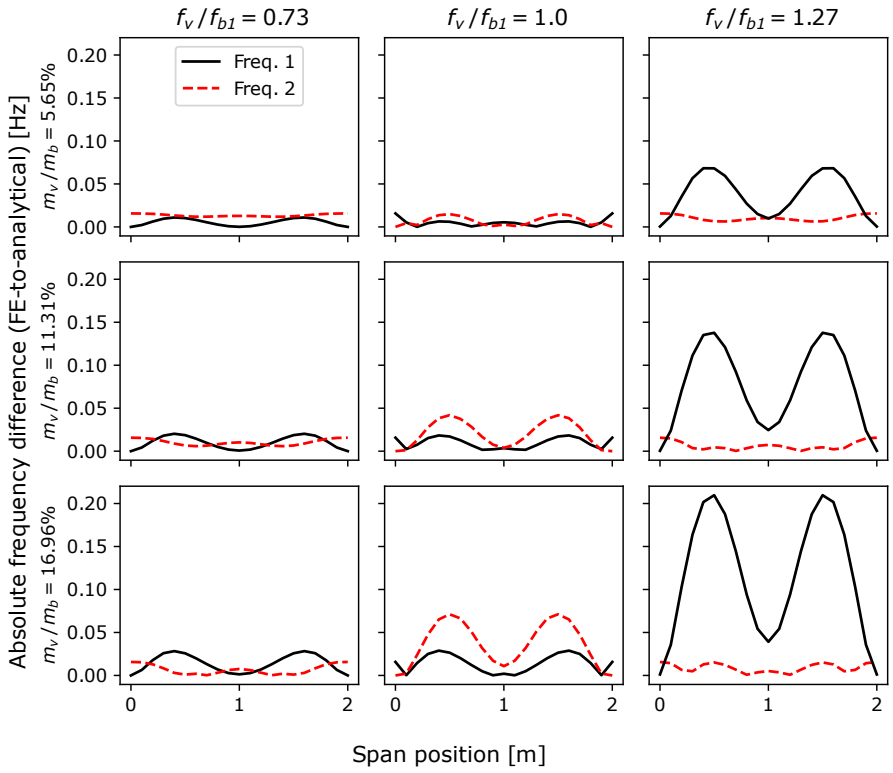

Figure 6.3.2: Mode 1 frequency variation (combined SDoF vehicle-bridge system): absolute difference between closed-form analytical and FE-derived results.

vehicle-bridge system formed during VBI corresponding to the position of the vehicle on the bridge span. It would be expected to see both of these frequencies present in the frequency spectrum of the vehicle vertical acceleration during a traversal, with the bridge frequency subject to a shift of $\pm\pi v/L$ (Yang et al. [118]).

In general, the results presented in Fig. 6.3.1 serve to validate that the trends and magnitudes of frequency variation generated by the FE model are aligned with those predicted by the analytical expression. Also, as noted in [9] when $f_v : f_{b1} < 1$ the bridge frequency appears to rise due to the presence of the vehicle, and to fall when $f_v : f_{b1} > 1$. On the other hand, small differences are visible between the plotted FE and analytical results - these are more easily visible for higher mass and frequency ratios. Fig. 6.3.2 presents the results of an investigation into these differences. Visual inspection of the plots suggests:

- For lower mass and frequency ratios, the differences between the FE- and analytically-derived frequencies are of the order of 0.05 Hz or less. In absolute terms, this is a small difference. Additionally, it should be noted

that the interpolated frequency resolution adopted for studies of variation in instantaneous frequency (section 6.4.3) and damage detection (section 6.5) is also around 0.05 Hz based on the signal padding length adopted (section 6.2.6). This implies that for these mass and frequency ratios the difference in predicted mode 1 frequency change between the analytical and FE approaches can be disregarded. Since the frequency differences are less than the effective frequency resolution of the signal processing method, they might be artefacts and in any case are small as noted above.

- For mass and frequency ratios leading to frequency differences greater than 0.05 Hz, the spatial distribution of the differences appears to follow the absolute value of the expected mode 2 shape. In other words, the difference in mode 1 frequency between the FE and analytical predictions is greatest when the vehicle is close to the anti-nodes of the expected bridge mode 2 shape.

- For $f_v/f_{b1} < 1$, the vehicle-associated mode 1 frequency varies in proportion to the vehicle's proximity to the mode 2 anti-nodes, although the magnitude of the frequency variation is low. For $f_v/f_{b1} = 1$, this type of variation is seen in both the bridge- and vehicle-associated frequencies and the magnitude of variation is still relatively low. When $f_v/f_{b1} > 1$, the same pattern of variation appears to only apply to the vehicle-associated frequency, but the magnitude of variation is much greater.

Generally, the FE and analytical predictions of frequency variation as a function of mass ratio, frequency ratio and static vehicle position are in close agreement. However, as the vehicle frequency becomes closer to the bridge mode 2 frequency, the difference in predicted frequency becomes greater. This effect is also proportional to the vehicle's proximity to the anti-nodes of the expected mode 2 shape, and the vehicle-to-bridge mass ratio. The greatest magnitude of frequency variation is seen in the vehicle-associated frequency. Since the analytical expression neglects the contributions of bridge modes 2 and above, it seems reasonable to conclude that the FE simulation results can be treated as being more representative of the variation in bridge- and vehicle-associated frequencies that would be expected in physical laboratory experiments and field tests - certainly for frequency changes greater than 0.05 Hz.

In order to characterise the maximum expected change in bridge frequency as a function of vehicle properties and position, FE-derived results for a stationary SDoF sprung mass vehicle are presented in Fig. 6.3.3. As the change in frequency caused by the presence of the vehicle appears to be partially dependent on the position of the vehicle relative to the second mode shape antinodes, the effect on bridge mode 1 and 2 frequencies of placing the vehicle at quarter-span and midspan is presented. Fig. 6.3.3 shows the maximum absolute frequency change, normalised to the *unloaded* (i.e. without the presence of a vehicle) bridge first frequency. Fig. C.1.1 included in Appendix C shows the same results normalised to the unloaded bridge second frequency. In these plots, the

three frequencies identified in subplot headings refer to the first three frequencies of the combined vehicle-bridge dynamic system. For clarity a distinction is made between the bridge frequencies with and without the presence of a vehicle (f_b and $f_{b,i}$).

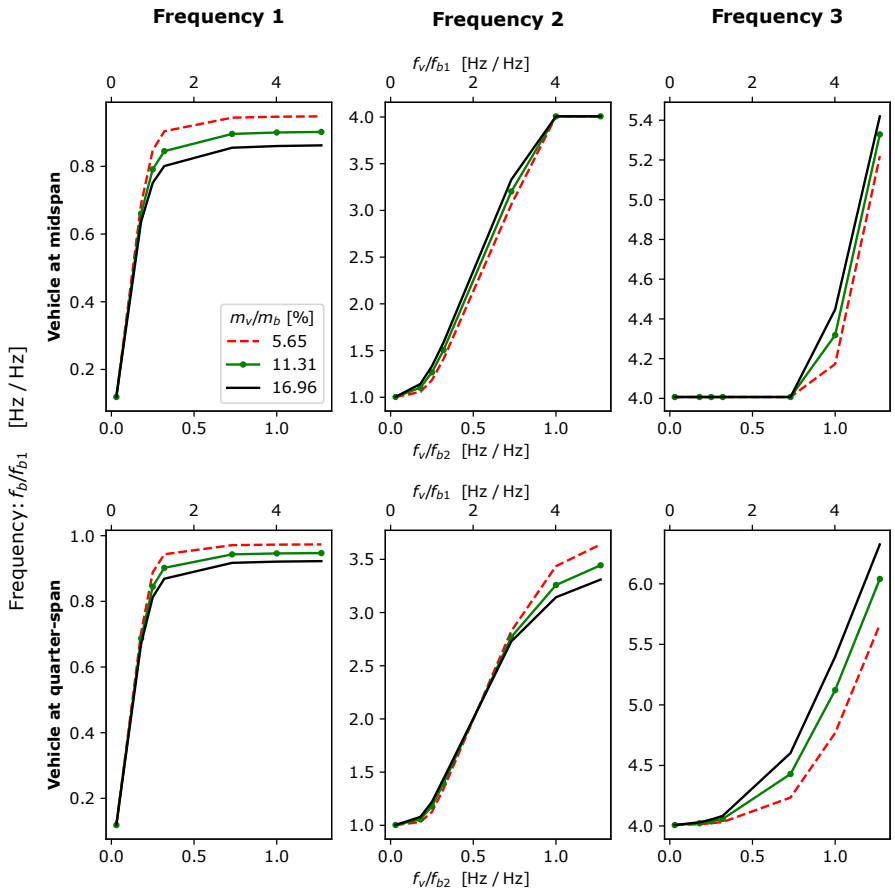

Figure 6.3.3: Change of first three VBI system frequencies due to an SDoF vehicle at quarter-span or midspan, for three vehicle-to-bridge mass ratios, in relation to the ratio of vehicle frequency to nominal (unloaded) bridge **first** mode frequency.

6.3.3 Moving vehicle: time-frequency behaviour

Figure 6.3.4 compares the ST ridges estimated from the virtual contact point and bridge quarter span location acceleration response to the expected frequencies based on linear perturbation FE analysis for vehicle frequencies proximal to

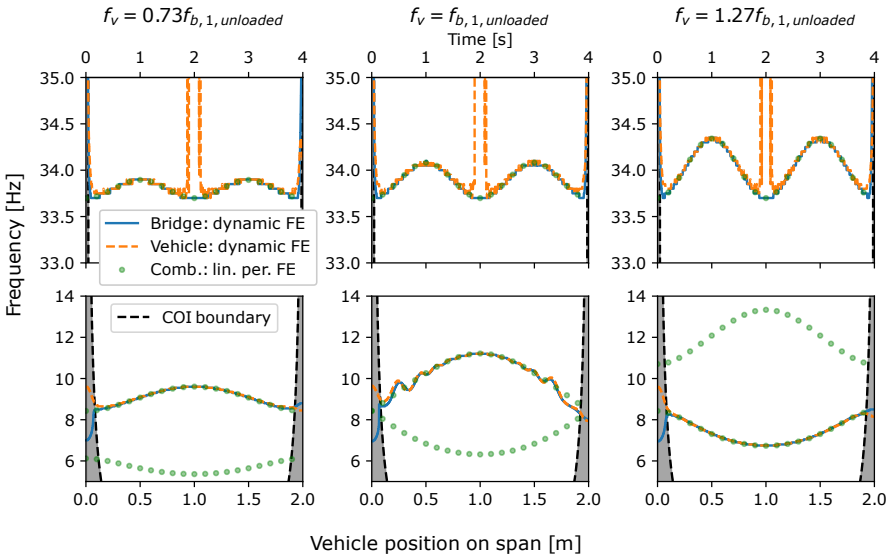

Figure 6.3.4: Time-frequency behaviour: undamped SDoF vehicle model traversing healthy bridge, for three vehicle-to-bridge frequency ratios (vehicle frequency proximal to **bridge mode 1** frequency).

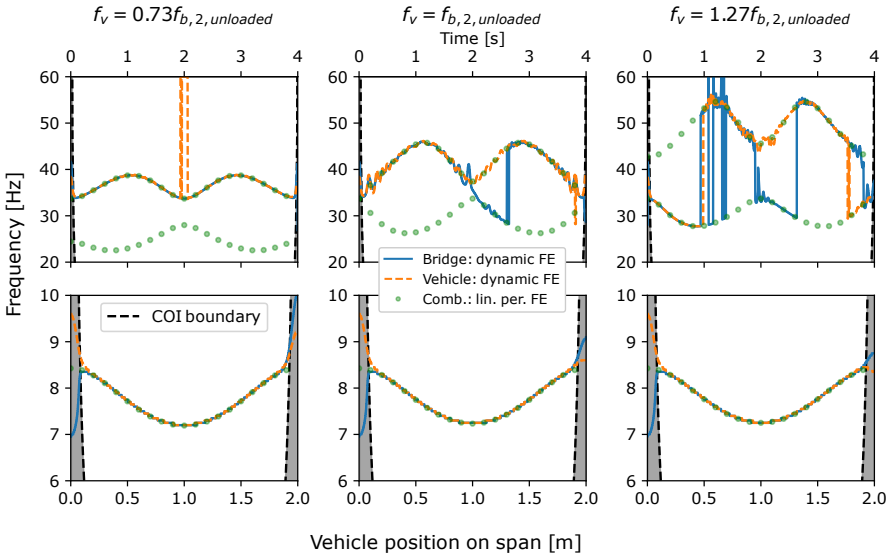

Figure 6.3.5: Time-frequency behaviour: undamped SDoF vehicle model traversing healthy bridge, for three vehicle-to-bridge frequency ratios (vehicle frequency proximal to **bridge mode 2** frequency).

the bridge **mode 1** frequency. The comparison relates to an undamped SDoF vehicle model traversing the healthy bridge, with three vehicle-to-bridge frequency ratios compared. The grey shaded zone indicates the zone of influence of edge effects for the ST. The lower and upper subplots focus on frequency ranges in the vicinity of the expected bridge first and second modes respectively. When the vehicle frequency is equal to the bridge mode 1 frequencies (lower central subplot in Fig. 6.3.4) the outcome of the dynamic FE simulation shows oscillations in instantaneous frequency at the start and end of the traversal. These oscillations occur outside the expected zone of influence of ST edge effects (the grey shaded area on the plots) and thus cannot be immediately dismissed as artefacts. The other notable feature in Fig. 6.3.4 is the divergence of the ST ridge for the virtual contact point location: a sudden rise in apparent frequency occurs when the vehicle is very close to the bridge midspan (upper central subplot). This is likely to be an artefact, since the bridge midspan location would be expected to be a node (zero displacement) point for the bridge second mode shape; in other words, the signal power associated with the bridge second frequency would be approximately zero when the vehicle passes over this part of the bridge. Other than the two matters mentioned, the ST ridge frequency variation appears to be a close match to that predicted by the linear perturbation FE analysis.

Figure 6.3.5 presents a similar comparison of the ST ridges and expected frequencies based on linear perturbation FE analysis for vehicle frequencies proximal to the bridge **mode 2** frequency. When the vehicle frequency is equal to the bridge mode 2 frequency (upper central subplot in Fig. 6.3.5) the outcome of the dynamic FE simulation shows oscillations in instantaneous frequency at the start and end of the traversal, in a similar manner to that observed in Fig. 6.3.4. Otherwise, the main differences between the ST ridge frequency and that predicted by linear perturbation FE frequency analysis appear to relate to the manner in which ST ridges were estimated. Since the ridges are extracted from transforms normalised to instantaneous maximum signal power, this results in the ridge appearing to instantaneously jump from one frequency to another at a single timestep. Effectively, this means the maximum acceleration amplitude is at some points associated with one frequency, and at other times associated with another. In contrast, the linear perturbation FE-derived results show smoother variation in frequencies with time, since they are not derived based on a maximum signal power ridge. This does not necessarily represent a difference in predictions between the two methods; rather, it can be considered as an artefact inherent to the ridge estimation method. In order to address this, in section 6.4 two ridges are extracted from the ST contours, to illustrate the divergence and convergence of VBI system frequencies during the vehicle traversal.

Figure 6.3.6 compares the ST ridges from the vehicle DoF and virtual contact point acceleration responses, for the cases in which $f_v = f_{b1}$ and $f_v = f_{b2}$. This indicates that the oscillations discussed above are likely to represent the vehicle and bridge motion being out of phase. The largest phase difference in this plot seems to be associated with a change in which frequency has the highest instantaneous signal power, resulting in the ST ridge appearing to jump from

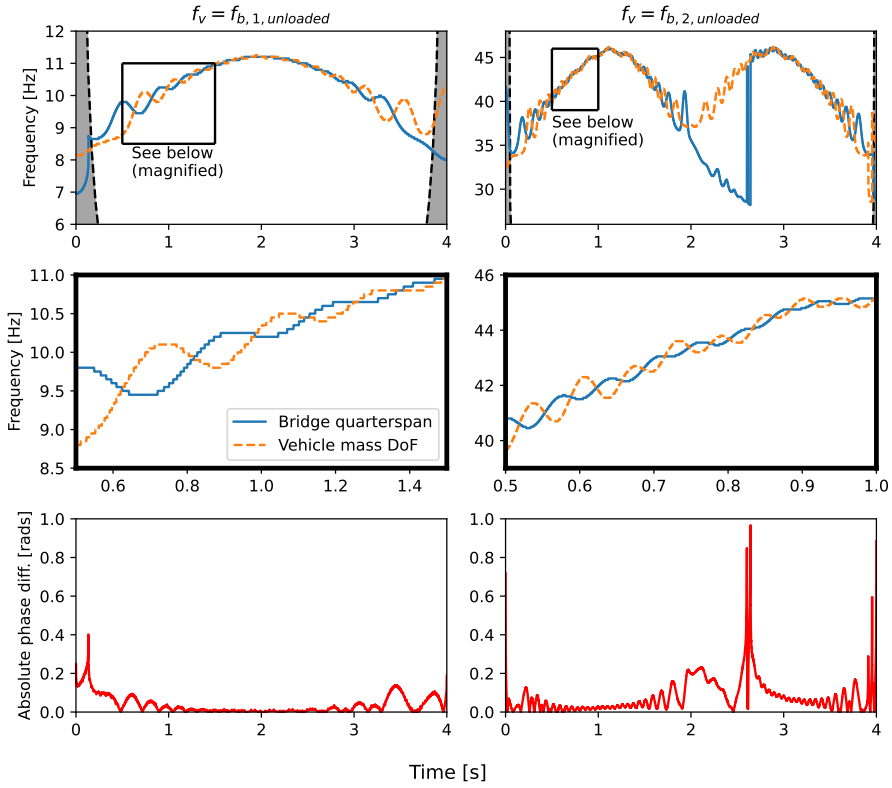

Figure 6.3.6: Comparison of instantaneous frequency (ST ridges) from the vehicle DoF and the contact point response, illustrating their phase difference.

one path to another in a discontinuous manner. As noted above, in section 6.4 the method of ridge estimation is addressed to mitigate this artefact. Here, it is sufficient to note that this behaviour appears to be a spurious artefact, in contrast to the smoother oscillatory phenomenon, although both are associated with phase difference between the vehicle DoF and the contact point response.

6.3.4 Moving vehicle: effect of vehicle damping on instantaneous frequency

Damping does not affect the vehicle's classical normal mode frequencies. However, both vehicle traversal speed and vehicle damping can change the relative phase between vehicle and bridge motion. In this study the traversal speed will be fixed while a range of vehicle damping ratios are explored. Fig. 6.3.7 shows the effect of varying the damping ratio of the SDoF vehicle model. Estimated ST ridges are compared to linear perturbation FE-derived eigenfrequencies, for vehicle damping ratios ζ of 0% (undamped), 10% and 50%.

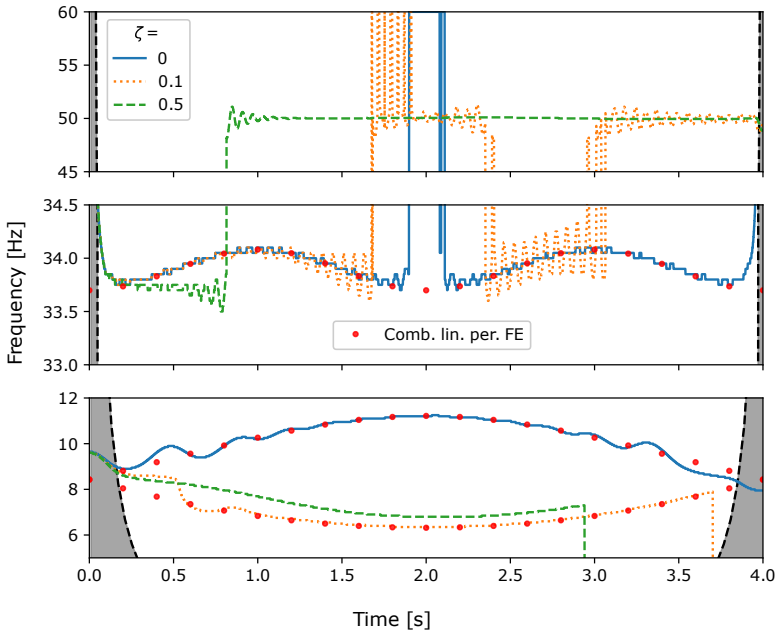

(a) $f_v \approx f_{b1}$

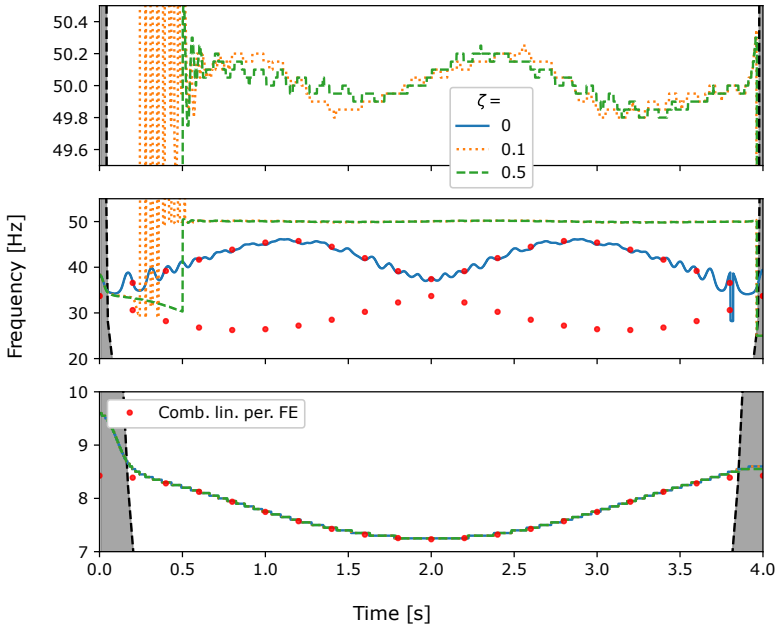

(b) $f_v \approx f_{b2}$

Figure 6.3.7: Effect of damping on SDoF vehicle, when $f_v \approx f_{b1}$ (upper subplots) and $f_v \approx f_{b2}$ (lower subplots). Dynamic and linear perturbation FE-derived results compared.

The grey zone in Fig. 6.3.7 is outside the ST radius of trust, indicating that transform edge effects may cause spurious results in this region. Recalling the earlier discussion in section 6.3.3 this figure demonstrates that adding even 10% damping – a relatively small amount, considering the expected values for real vehicles and adopted models discussed in the literature review (section 2.4) and the outcomes from field testing of a real vehicle in chapter 4 – changes which of the instantaneous VBI system frequencies has the highest instantaneous signal power. The upper and lower subplots demonstrate that this effect is apparent for the bridge first or second mode, depending on which bridge mode frequency is proximal to the vehicle frequency. Adding more damping (50%) appears to cause a more pronounced divergence in the instantaneous frequency. When $f_v \approx f_{b1}$ (upper subplot) this divergence is visible for the instantaneous frequencies in the region of both bridge modes; when $f_v \approx f_{b2}$ (lower subplot) the divergence is apparent only in the region of the bridge second mode frequency; the bridge first frequency appears to approximately follow the familiar trend associated with the well-known moving mass condition.

The divergent behaviour seen here is assumed to be a transform artefact, caused by vehicle damping reducing the acceleration amplitude associated with the frequency ranges in which the diversion occurs. Figures C.2.1 and C.2.2, included in Appendix C illustrate the effect of other damping ratios, from 0% to 150%. This serves to further suggest that the divergent behaviour is an artefact related to suppression of signal power in frequency sub-bands, since the onset of divergent behaviour appears to be proportional to the damping ratio. It is assumed that this phenomenon is not unique to the ST, but that it is more specifically induced by the method of ridge estimation. As previously noted, an alternative method of extracting multiple ridges is presented in section 6.4 and provides further insight into the nature of VBI-induced frequency variation, albeit for undamped 2DoF vehicle models.

For the current study, it can be concluded that the presence of vehicle damping alters the frequency associated with maximum instantaneous signal power. This has potential implications for vehicle-based damage detection; for example the implication of adding 10% damping is that the first bridge frequency appears to drop during the traversal when observed from the contact point response, compared to an apparent frequency rise for the undamped case. However, this could be mitigated by extracting multiple ridges from the transform to estimate the time-varying behaviour of both frequencies in each sub-band. Without knowledge of non-interacting vehicle and bridge natural frequencies and damping ratios, disambiguation of frequency change due to VBI and frequency change due to bridge damage is difficult. Chapter 4 concluded that accurately estimating the vehicle damping ratio is challenging. However, if these parameters are known, it may be possible to use the observed change in instantaneous frequency as a damage indicator, even though it appears to obscure direct visibility of the bridge frequency. This is explored in section 6.5.

6.4 Two DoF vehicle parameter variation

6.4.1 Scope of study

This section presents a study of the effects of vehicle-to-bridge parameter ratios on combined vehicle-bridge system frequencies during VBI. The study is concerned with 2DoF vehicle models and covers the range of vehicle parameters shown in Table 6.4.1. The bridge parameters considered are as summarised in Table 6.3.3.

FE simulation was used to generate combined vehicle-bridge system frequencies, first using eigenfrequencies extracted from a linear perturbation frequency analysis (see Fig. 6.4.1) and then an implicit dynamic analysis (see Fig. 6.4.2).

Vehicle ID	**A**	**B**	**C**	**D**
Vehicle parameters				
m_v [kg]	3.43			
m_2/m_1	5.5			
m_1 [kg]	0.528			
m_2 [kg]	2.902			
k_1/k_2	5			
k_1 [N/m]	49000	790000	1225	19500
k_2 [N/m]	9800	158000	245	3900
Vehicle frequencies				
f_{v1} [Hz]	8.42	33.81	1.33	5.31
f_{v2} [Hz]	53.26	213.87	8.42	33.6
Vehicle-to-bridge frequency ratios				
f_{v1}/f_{b1}	1.0	4.01	0.16	0.63
f_{v2}/f_{b1}	6.32	25.37	1.0	3.99
f_{v1}/f_{b2}	0.25	1.0	0.04	0.16
f_{v2}/f_{b2}	1.58	6.35	0.25	1.0

Table 6.4.1: Vehicle parameters used in the study of 2DoF vehicle-bridge interaction in section 6.4. Proximal vehicle-bridge frequency ratios are highlighted.

6.4.2 Static vehicle: eigenfrequency variation

As discussed in section 6.3.2, a closed-form analytical expression is available for the combined system natural frequencies of an SDoF lumped vehicle at any position on a simply-supported beam bridge, considering only the bridge's fundamental mode. The combined system frequencies can be found as solutions to the quadratic (equation 2.14) derived from the associated eigenproblem (equation 2.3). This is convenient first since it permits exploration of the effect of the vehicle-to-bridge frequency ratio, and second since the vehicle-to-bridge mass ratio appears only once in equation 2.14, meaning that its effect can also be easily explored. Considering a 2DoF vehicle interacting with a single-mode simply supported bridge suggests that the combined system frequencies derived from equation 2.3 would be found through the roots of a cubic equation, with higher degree-of-freedom vehicle models and/or multi-mode bridge behaviour leading to correspondingly higher-order equations. However, seeking a closed-form solution in such cases is not straightforward:

- For vehicle-bridge systems with more than four frequencies, the VBI system frequencies would found from the roots of a 4th-order polynomial generated by solving $det(\boldsymbol{M} - \boldsymbol{\omega}^2\boldsymbol{K}) = 0$. The order of the associated polynomial corresponds to the sum of the number of vehicle and bridge modes modelled. The Abel-Ruffini Theorem states that a general closed form solution (i.e. an equivalent to the well-known quadratic formula) for polynomials of order 4 or more does not exist (Ramond [421]).
- The quadratic form of equation 2.14 relied in part on grouping equation terms together to express ratios of vehicle-to-bridge natural frequencies, meaning that the vehicle-to-bridge mass ratio appeared only once. Considering the vehicle, this relied on expressing the single vehicle natural frequency as $\omega = \sqrt{(k/m)}$. On the contrary, a 2DoF vehicle has two natural frequencies of its own, which themselves are found through solving a quadratic; this implies that it will be difficult or impossible to isolate the vehicle-to-bridge mass ratio in the resulting cubic or higher-order equation, making the process of studying the effect of the mass ratio more cumbersome.

Given the above considerations, a practical approach is to use numerical methods to approximate the solutions to higher-order polynomials. In the case of VBI system frequencies, it is convenient to use the methods built in to FE software and this is the approach adopted for the current section of this thesis. Figure 6.4.1 shows the linear perturbation FE-derived frequencies for two vehicle-to-bridge mass ratios and four vehicle-to-bridge frequency ratios, plotted as a function of the position of the vehicle on the bridge span. The upper subplot shows the results with a common axis scale, highlighting the relative magnitude of frequency variation. From this it is clear that the largest changes in frequency are associated with natural frequency matching between vehicle and bridge.

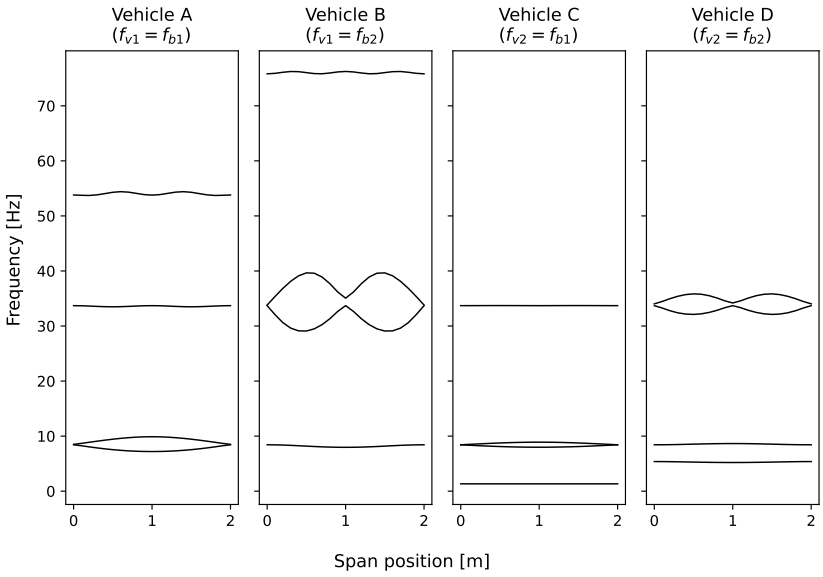

(a) Common axis scale to illustrate relative behaviour.

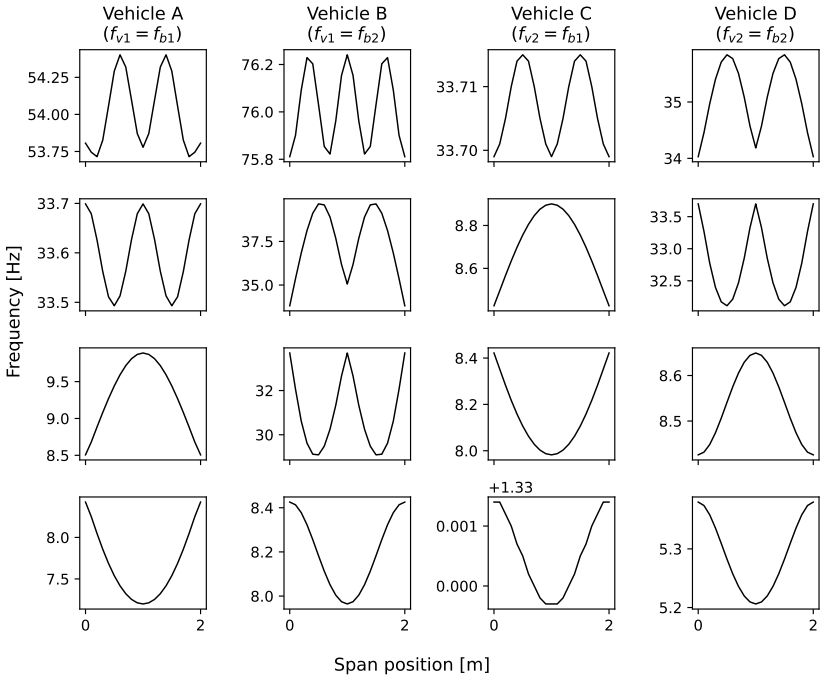

(b) Axis scales selected to illustrate patterns of frequency variation.

Figure 6.4.1: Linear perturbation FE-derived variation in frequency for static 2DoF vehicle on bridge, for two mass ratios and four frequency ratios.

The lower subplot in Fig. 6.4.1 features axis scales adjusted to illustrate that the general pattern of frequency variation is similar for all vehicle models in a given frequency sub-band.

Further inspection of these figures yields the following insights:

- When $f_{v1} = f_{b1}$ or $f_{v1} = f_{b2}$ the combined system frequencies appear to behave in a similar manner to the SDoF vehicle case, with respect to the bridge mode 1 and 2 frequencies respectively.
- When $f_{v2} = f_{b1}$ or $f_{v2} = f_{b2}$ the combined system frequencies appear to behave in a similar manner to the SDoF vehicle case, just as was noted for $f_{v1} = f_{b1}$ or $f_{v1} = f_{b2}$ but with a lower magnitude of maximum frequency shift when the vehicle is at midspan.

To understand the above observations we can recall the vehicle mode shapes presented in Fig. 5.3.1, which implied that the majority of excitation amplitude associated with the vehicle's first mode frequency occurred at the upper mass DoF, and at the lower mass DoF for the vehicle's second mode frequency. Since the upper mass is larger than the lower mass for realistic vehicle quarter-car models (Jazar, [6]), the greater frequency shift associated with $f_{v1} = f_{b1}$ or $f_{v1} = f_{b2}$ compared to $f_{v2} = f_{b2}$ or $f_{v1} = f_{b2}$ is expected to be due to the relative magnitudes of vehicle-to-bridge mass ratios $m_{v2} : m_b$ and $m_{v1} : m_b$. In other words, it appears that the magnitude of frequency shift during VBI corresponds to the vehicle-to-bridge mass ratio associated with the vehicle DoF at which the majority of excitation amplitude occurs in that frequency range.

It can also be observed that in the case of $f_{v1} = f_{b2}$ (vehicle B), it appears that the vehicle's second frequency may be close to the bridge's third frequency. This assumption is based on the variation in mode 3 frequency (around 76 Hz) which appears to be generally in proportion to the expected absolute shape of the bridge's third mode shape. Only the first four combined system frequencies are plotted in these figures and therefore it is not completely apparent whether the vehicle's effect on the bridge's third mode is related to frequency proximity (i.e. if $f_{v2} \approx f_{b3}$) or if this is solely an added mass effect, since the bridge's third mode would be the combined system's fifth mode.

6.4.3 Moving vehicle: time-frequency behaviour

The previous section reviewed the expected variation in combined vehicle-bridge system frequencies induced by VBI through estimating natural frequencies as a function of vehicle position on the bridge for a static sprung mass vehicle model. This section explores the observed instantaneous frequencies of the combined vehicle-bridge system for a moving vehicle crossing the bridge span. Fig. 6.4.2 presents the ST contours and estimated ridges in the proximity of the bridge's nominal first and second mode frequencies (lower and upper subplots respectively). Results are presented for vehicle configurations A, B, C and D presented in Table 6.4.1. In this section, two ridges are extracted from each ST, representing the highest (*ridge 1*) and second-highest (*ridge 2*) instantaneous signal power in the respective frequency sub-bands. Identifying two ridges in this manner is intended to illustrate the behaviour of two VBI system frequencies as demonstrated in section 6.3.2 and the prior work by others discussed in the literature review (section 2.6.6).

The time-frequency behaviour observed in Fig. 6.4.2 for the 2DoF vehicles A, B, C and D from dynamic FE simulations appears to be different from that seen for the same vehicles for linear perturbation FE simulations. Some of the transform ridges (lines tracing the frequency with highest signal power) appear to oscillate. Additionally, coordinated with the oscillations are loops: splitting-and-rejoining behaviour, where ridge 1 and ridge 2 part ways and then rejoin.

In some cases, the oscillations and loops are suspected to be artefacts of the transform. This includes all such behaviour in the region of the bridge second mode frequency (upper group of subplots) when the vehicle is halfway across the bridge span. Since this location is an node (zero-displacement point) for the expected bridge second mode shape, the representation of the second mode frequency here is not considered to be reliable (for example in the region of the bridge second mode frequency, for vehicles A and C in the upper group of subplots). Additionally, for all the subplots, oscillations and loops in the grey shaded zone are likely to be transform artefacts relating to the start and end of the signal, as discussed in section 6.2.4. The loops seen for transform ridges in the region of the bridge first mode frequency, for vehicles B, C and D (lower group of subplots) do not appear to show any discernible pattern and therefore are also assumed to be artefacts.

The remaining cases include:

- Vehicles B and D in the region of the bridge second mode frequency (upper group of subplots) display oscillation and loop phenomena. The rate of oscillation is faster for vehicle B than for vehicle D.
- Vehicle A in the region of the bridge first mode frequency (lower group of subplots) also displays the oscillation and loop phenomena. The rate of oscillation is slower than that seen for vehicles B and D discussed above.

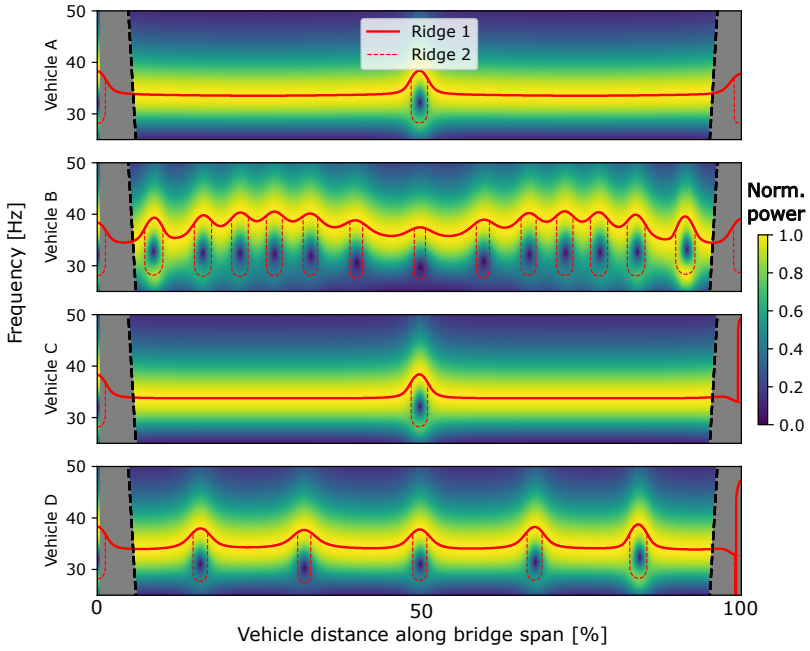

(a) ST frequency sub-band in the region of bridge second mode frequency.

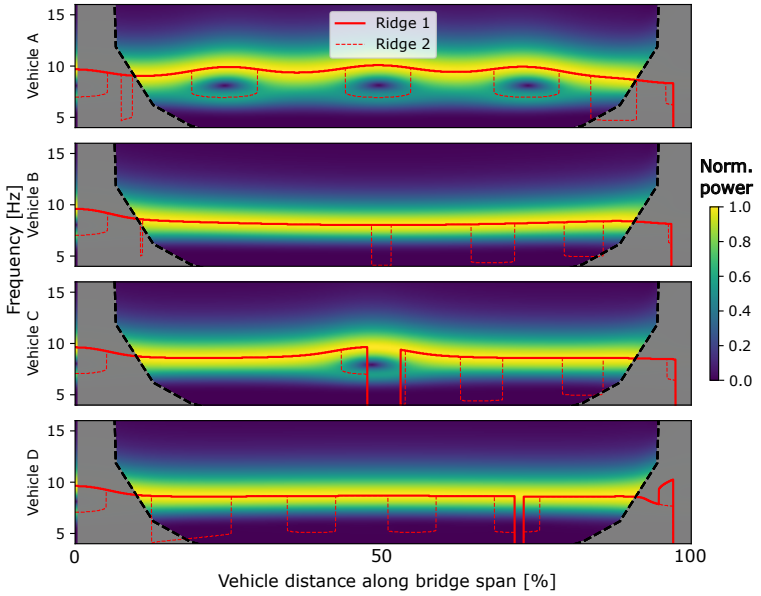

(b) ST frequency sub-band in the region of bridge first mode frequency.

Figure 6.4.2: Normalised power of contact point acceleration response Stockwell transform contours with two estimated ridges, comparing four vehicle configurations.

The oscillations visible in Fig. 6.4.2 do not appear to occur in line with any of the vehicle or bridge non-interacting frequencies. It is therefore assumed that they represent an aspect of VBI. To the author's knowledge, this behaviour has not previously been observed or characterised. The behaviour has the potential to mask the visibility of bridge damage from vehicle-mounted sensor acceleration data. All of these cases in which the behaviour is observed represent one of the vehicle frequencies being proximal to one of the bridge frequencies. Based on the investigation in section 6.3.3 it is assumed that the oscillatory and looping phenomena seen here also relate to phase difference between vehicle DoF(s) and the bridge response at the contact point. However, further investigation would be required to confirm the exact nature of this behaviour. If the observed phenomena are indeed linked to phase lag between vehicle and bridge, they might also be affected by:

- Vehicle traversal speed: this would change the phase difference between vehicle and bridge, considering the vehicle's motion across the bridge span in relation to the mode shape and time period associated with each of the bridge's modes.
- Prior excitation for the vehicle and bridge: this would change the instantaneous phase and thus the phase difference at the start of the traversal.
- Bridge or vehicle damping.

6.5 Damage detection

Section 6.4.3 demonstrated that ST contours show potential for illustrating the nonstationary nature of VBI according to the vehicle properties in situations where vehicle and bridge natural frequencies are proximal. In such situations, the nonstationarity has been noted to occlude visibility of bridge natural frequencies. The work presented in this section demonstrates the application of a conventional methodology for unsupervised damage detection in such situations.

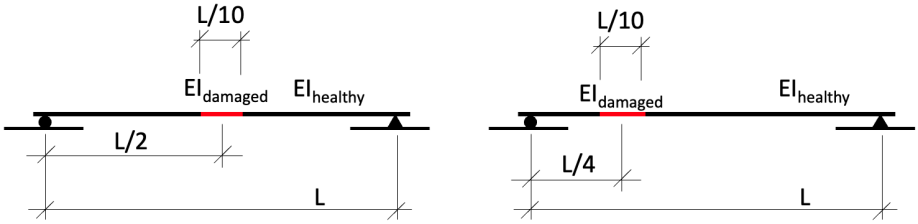

Figure 6.5.1: Illustration of midspan (left) and quarter-span (right) bridge damage modelled as local reductions in bending stiffness.

6.5.1 Modelling damage

Fig. 6.5.1 indicates the two damage locations to be considered in this work. Damage is modelled as a local reduction (10, 20, 30, 40 or 50%) in bending stiffness EI at either midspan or quarter-span, applied to a local area (10% of the span length). Modelling bridge damage in this manner is generally aligned with the approach described by Sinha et al. [422] which is adopted in the literature by others (for example O'Brien et al. [136], Malekjafarian et al. [113], Corbally and Malekjafarian [115]). Sinha et al.'s approach suggests a gradual linear stiffness change at the transition between healthy and damaged parts of the bridge, while in the work presented here the transition is modelled as a step function. The work presented in this thesis is intended to demonstrate the principles of a proposed damage detection method, rather than accurately represent a specific damage condition. The step function transition was therefore deemed acceptable for the present purpose. The damage severity levels and the associated reduction in the bridge's first two bending mode frequencies are summarised in Table 6.5.1.

Damage level (local stiffness reduction)	**10 %**	**20 %**	**30 %**	**40 %**	**50 %**
Midspan damage					
Δf_{b1}	-1.02 %	-2.20 %	-3.67 %	-5.52 %	-7.95 %
Δf_{b2}	-0.03 %	-0.06 %	-0.10 %	-0.16 %	-0.24 %
Quarter-span damage					
Δf_{b1}	-0.56 %	-1.19 %	-2.00 %	-3.04 %	-4.46 %
Δf_{b2}	-1.00 %	-2.19 %	-3.62 %	-5.38 %	-7.59 %

Table 6.5.1: Reduction in bridge mode 1 and 2 frequencies due to damage, according to location and severity.

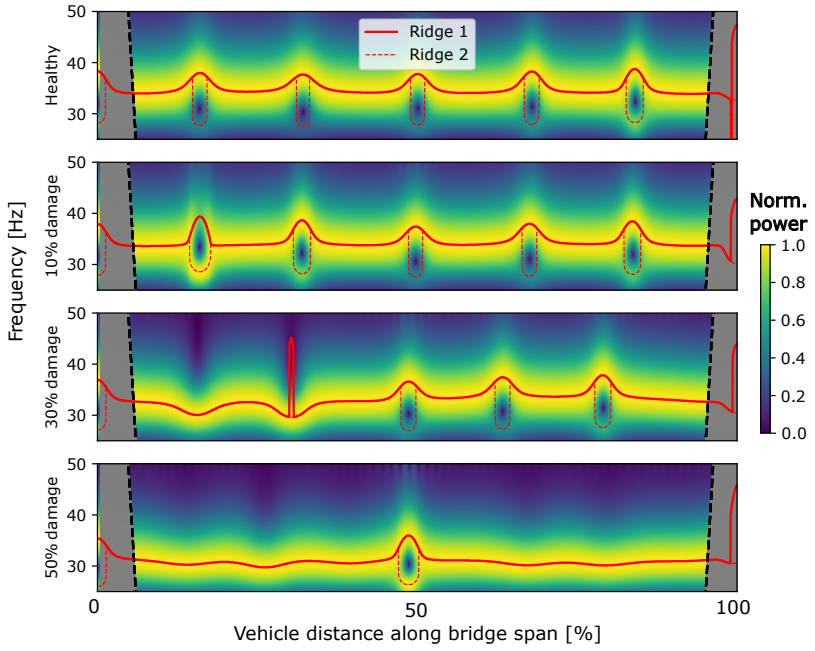

Figure 6.5.2: Vehicle D: illustration of effect of bridge damage at quarter-span.

6.5.2 Classification by latent space clustering

Chapter 4 showed that output-only estimation of vehicle properties to fit to a quarter-car model is subject to bias, but suggested methods for mitigation. In this chapter it is assumed that the vehicle properties are known. Fig. 6.5.2 illustrates ST contours for vehicle D and visual inspection confirms that they change with the increasing damage severity (illustrated for damage at quarter-span). It is proposed that changes in such ST contours could be used as a proxy indicator of bridge damage. Moreover, the change in ST contours can be expected to vary according to the location of the damage, since a local reduction in stiffness will result in different degrees of frequency change to different bridge modes according to where the reduction is applied. Using ST contours as input features is therefore expected to show some utility towards confirming the existence and the location of damage.

The proposed damage detection method can be summarised as:

1. Generate time-frequency contour images representing vehicle traversals of known healthy bridge from contact point acceleration responses, using Stockwell transform (ST)
2. Project ST contours into reduced-dimension latent space using principal component analysis (PCA)
3. Draw class boundary around cluster of projected data representing healthy bridge traversals in latent space
4. Repeat steps 1 and 2 for contact point acceleration responses from additional traversals across healthy or damaged bridge
5. For each additional traversal, calculate damage metric based on Euclidean distance in latent space from the healthy condition class boundary

The assumed clustering of data from traversals of healthy and damaged bridge conditions is shown indicatively for four notional cases A, B, C and D in Fig. 6.5.3. The following sections discuss the main challenges addressed by this damage detection framework, justify the use of PCA for projection into latent space, define the damage metric, and demonstrate the method using synthetic vehicle-bridge interaction acceleration response data generated by dynamic finite element (FE) simulation. It should be noted that drawing a decision boundary around projected data representing the healthy bridge condition is intended to allow for the effects of environmental and operational variation and random noise in the data. These aspects were not represented in the dynamic FE simulation. In the demonstration presented in this chapter, a single example of the healthy bridge condition is therefore used and so the decision boundary mentioned above (step 3) is not required, whereas it would be a necessary part of the process when applied to data from real VBI at laboratory- or field-scale.

It is generally agreed that labelled data representing the damaged bridge condition is a major challenge in SHM (Worden et al. [33], Rizzo and Enshaeian

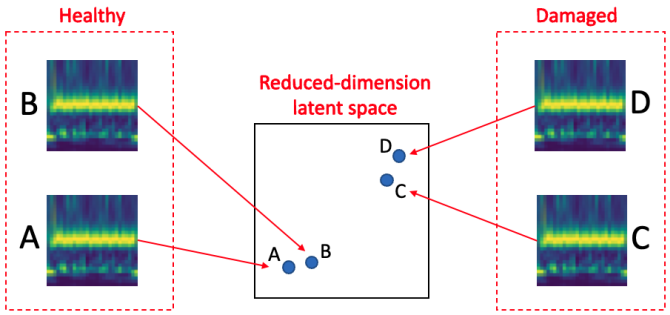

Figure 6.5.3: Indicative illustration of clustering for damage classification.

[34], Malekjafarian et al. [40], Figueiredo and Brownjohn [28]) which precludes the use of supervised classification systems in which the differences between healthy and damaged conditions can be defined or learned. An alternative paradigm would be one class classification (OCC) in which labelled examples are available for only one class (for example, data representing the healthy bridge condition). One approach for this type of classification task is to seek a projection of the input features into a reduced-dimension latent space in which the healthy examples cluster together. In OCC problems this would manifest as a *hypersphere* defining the zone into which the examples from the training class fall. Points outside the boundary would be deemed to be outliers, with an optimal boundary maximising the number of data points from each class falling to their respectively correct sides of the boundary (Khan and Madden [423]). In this manner the decision boundary could be constructed without examples representing the damaged bridge class. For a large dataset representing data from physical experiments or field tests, there could be value in using a machine learning method to perform the projection into latent space. Autoencoders are one example of a potentially suitable machine learning (ML) framework; they take an input feature and learn to reconstruct it via a series of compression (encoder) and decompression (decoder) steps. The process of learning is driven by minimisation of a loss function, for example reconstruction loss in which the input feature and reconstructed output are compared. Autoencoders are well-established and relatively recently they have been leveraged as part of strategies for image-related OCC (for example Gutoski et al. [424], Mujeeb et al. [425]). They belong to a more broad ML class known as *generative models* since the latent space (a reduced dimension space between the encoder and decoder) can be used to generate new examples similar to the input features. In principle, different regions of the latent space would relate to different aspects of the input features. Similar input features would cluster in the latent space allowing the construction of a separating hypersphere (around healthy data points, for example). A number of approaches existing to learn such separation boundaries for OCC problems, one example being support vector machines (SVM) with Khan and Madden [423] reporting examples of SVMs for this purpose by Tax

and Duin [426] [427] and Scholkopf et al. [428].

The key challenges to be addressed in the proposed damage detection method are therefore:

- VBI frequency nonstationarity due to proximal vehicle and bridge natural frequencies
- Lack of labelled data examples representing damaged bridge conditions

In the cases studied in chapter 6 of this thesis, the data are from an FE simulation and thus do not feature environmental variation or noise. There is therefore little apparent benefit in attempting to learn the latent space projection directly from the data using an autoencoder. Instead, it is proposed to adopt principal component analysis (PCA) which was introduced in section 2.8.11. This is a method which projects an input into a new coordinate system such that the variance between the coordinate directions is maximised (Shlens [429]). The literature reveals several examples of the use of PCA to generate damage-sensitive features for bridge SHM (such as Cross et al. [101], Lederman et al. [339] from Malekjafarian et al. [40], and Mei et al. [366]) and it has also already been used for image clustering tasks (for example Peng et al. [430]). Moreover, it has been argued that variational autoencoders (VAE), which differ from autoencoders in that they fit the data to a Gaussian distribution in the latent space, effectively learn PCA projection from data (Rolinek et al. [431]). In this thesis, PCA will be used to generate latent space projections. It is assumed that if the approach shows promise, it could be tested on a larger dataset using a VAE or similar method to learn a projection that effectively separates the healthy and damaged data.

6.5.3 Classification with labelled data from multiple classes

The damage classification methods in this chapter is presented in two parts. First, the separability of healthy and damaged samples will be demonstrated by learning the latent space projection using all the samples simultaneously. Following this, it will be demonstrated that projections can be determined on a sample-by-sample basis, allowing the potential for a decision boundary to be defined when only samples representing the healthy bridge condition are available.

Fig. 6.5.4 shows the principle by which samples from multiple classes could be combined. In the illustration, cases $\boldsymbol{A}$ and $\boldsymbol{B}$ represent the healthy bridge condition, while $\boldsymbol{C}$ and $\boldsymbol{D}$ represent a damaged case. The samples are single-colour images and thus can be considered as arrays of pixel intensities. Each array can be unwrapped to form a vector and these vectors can be combined into a single larger array $\boldsymbol{X}$. In this combined array the columns represent samples while the rows represent features (pixel intensity values from the original images).

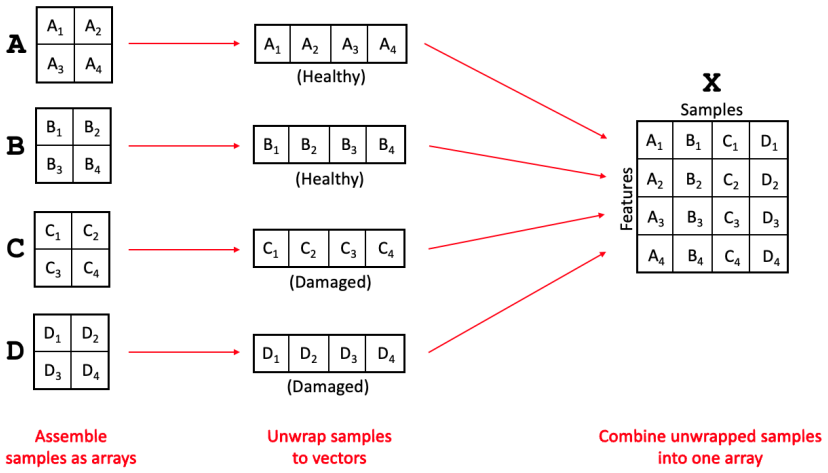

Figure 6.5.4: Illustration of multi-class PCA (part 1 of 2): combining samples into one array.

In accordance with the description of PCA in chapter 2, Fig. 6.5.5 illustrates the process of decomposing the covariance matrix of $\boldsymbol{X}$, denoted as $\boldsymbol{\Sigma}$ (equation 2.8.11). Matrix $\boldsymbol{W}$ contains eigenvectors which project the original data $\boldsymbol{X}$ into a new space which maximises the variance between samples (columns of $\boldsymbol{X}$). If $\boldsymbol{W}$ is ordered according to descending magnitude of the associated eigenvalues ($diag(\boldsymbol{\Lambda})$) and the first L rows of $\boldsymbol{W}$ retained, the projection of $\boldsymbol{X}$ by $\boldsymbol{W}_L$ is thus a reduction to dimension L for the samples. Assuming that the two classes cluster when projected into this reduced dimension subspace (which is implied by the maximisation of variance under the projection), a decision boundary can

be drawn to separate the two classes as illustrated in Fig. 6.5.5. As outlined in section 2.8.11 it should be noted that the input data are represent normalised pixel intensities, meaning that the principal components have no units.

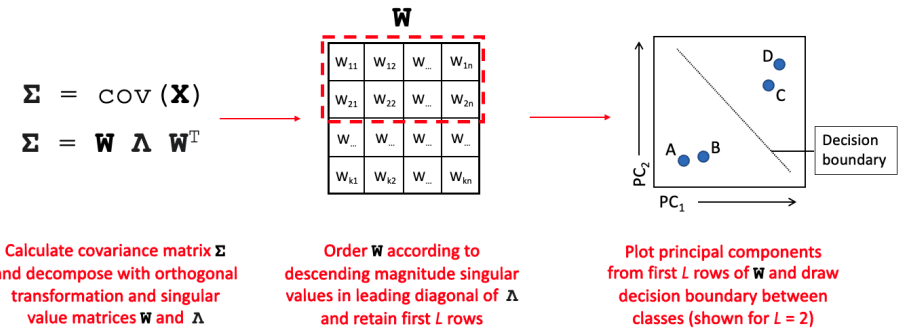

Figure 6.5.5: Illustration of multi-class PCA (part 2 of 2): decomposing the covariance matrix, selecting a reduced dimension and plotting the principal components.

6.5.4 One-class classification method

The approach adopted in this thesis is to assume that the ST contours from traversal of a damaged bridge will differ from those representing traversal of the bridge in a healthy condition. The intention is to construct a data processing pipeline in which a classifier could be trained to identify data from traversals of healthy bridges by their similarity, and classify traversals of damaged bridges as outliers based on their difference from the healthy examples. This is an established approach to one-class classification, in which the principle of *outlier detection* or *novelty detection* is leveraged, with Pimintel et al. summarising that it is "typically used when the quantity of available "abnormal" data is insufficient to construct explicit models for non-normal classes" [432]. Perera et al. state that OCC approaches "are extensively used in abnormal image detection" [433].

The process of generating latent space projections using the input images one-at-a-time relies upon the assumption that the images can be classified according to the change in frequency content over time. With each sample (image) as a matrix, the principal components which decompose the covariance matrix maximise variance between columns of the input image; since each column represents a single timestep the maximised variance represents maximised difference in the evolution of frequency content during the vehicle traversal. This is illustrated in Fig. 6.5.6. Two example input images, $\boldsymbol{A}$ and $\boldsymbol{B}$ are considered; both represent the healthy bridge condition. Assuming that the projections cluster in the reduced-dimensional latent space a decision boundary enclosing the healthy condition in this space can be drawn. When additional input images

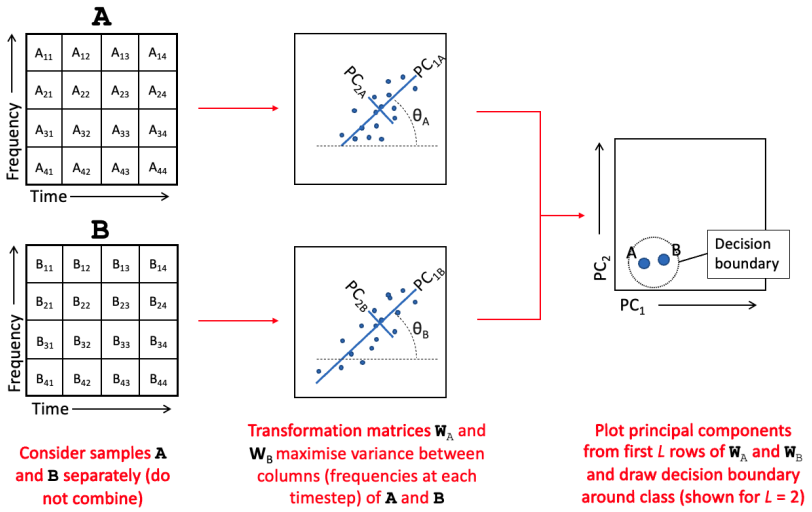

Figure 6.5.6: Illustration of single-class PCA (part 1 of 2): considering healthy samples separately, plotting their respective principal components and drawing a decision boundary.

are available, they can be similarly plotted in latent space based on the decomposition of their respective covariance matrices. As illustrated in Fig. 6.5.7 this allows damage to be detected by virtue of the projected points falling outside the decision boundary.

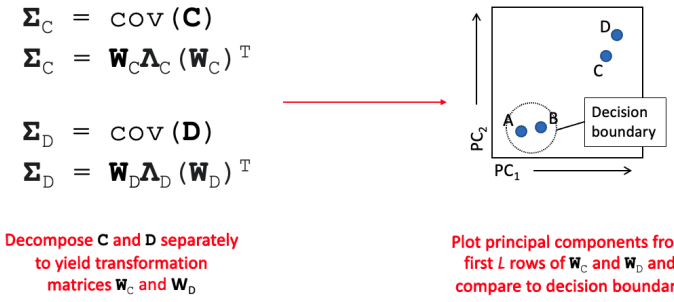

Figure 6.5.7: Illustration of single-class PCA (part 2 of 2): considering additional (damaged) samples separately, plotting their respective principal components and comparing them to the decision boundary.

6.5.5 PCA projections (multi-class)

Since labelled examples representing the damaged and healthy bridge conditions are available from the simulated vehicle traversals, projection into latent space was first pursued using the multi-class procedure outlined in section 6.5.3. Fig. 6.5.8 shows the projected first two components, comparing three ST image bandwidths as inputs. The ST contours were normalised to instantaneous maximum signal power at each timestep. It should be noted that such normalisation increases visibility of the frequencies with highest signal power across the signal length, and is separate from the necessary normalisation of input data (pixel intensities) before applying PCA as outlined in section 2.8.11. This means that principal components presented in this thesis have no units, irrespective of whether the ST contours are denoted as *normalised* or not.

In all cases the data cluster in latent space primarily according to the vehicle type. However, the plots imply that some separation between healthy and damaged classes would be visible when considering each cluster individually.

Fig. 6.5.9 presents a closer view of the clusters on a vehicle-by-vehicle basis. The axis values are omitted since the plots seek only to show the relative value of the principal components. Since the PCs have no units, this is a reasonable approach and is achieved by unifying the aspect ratio and scale for all of the subplots. Separation in latent space between the healthy and damaged data is apparent for all bandwidths of ST contour image input and for all vehicle types.

The data presented in Figs. 6.5.8 and 6.5.9 showed only the first two principal components. To justify this approach, Fig. 6.5.10 shows a *scree plot*, in which the relative magitudes of eigenvalues from the leading diagonal of eigenvalue matrix $\mathbf{\Lambda}$ (from the decomposition of the covariance matrix) are compared. This common method suggests that once the scree plot has flattened (the *elbow*) subsequent components are deemed to not add much information (Cattell [434], from Woods and Edwards [435]). The elbow visible in this plot indicates that the first two principal components capture the majority of the variation in the dataset. Additionally, projection into a two-dimensional space means that clusters are visually intuitive.

The outcomes presented in this section demonstrate that the proposed PCA projection leads to clusters in latent space which mainly relate to the vehicle type (recalling that vehicles A, B, C and D in this study are defined by the ratio of their modal frequencies to those of the bridge). Within each of the distinct clusters, separation is apparent between data points representing healthy and damaged bridge conditions, confirming the suitability of the proposed method of projection for damage detection.

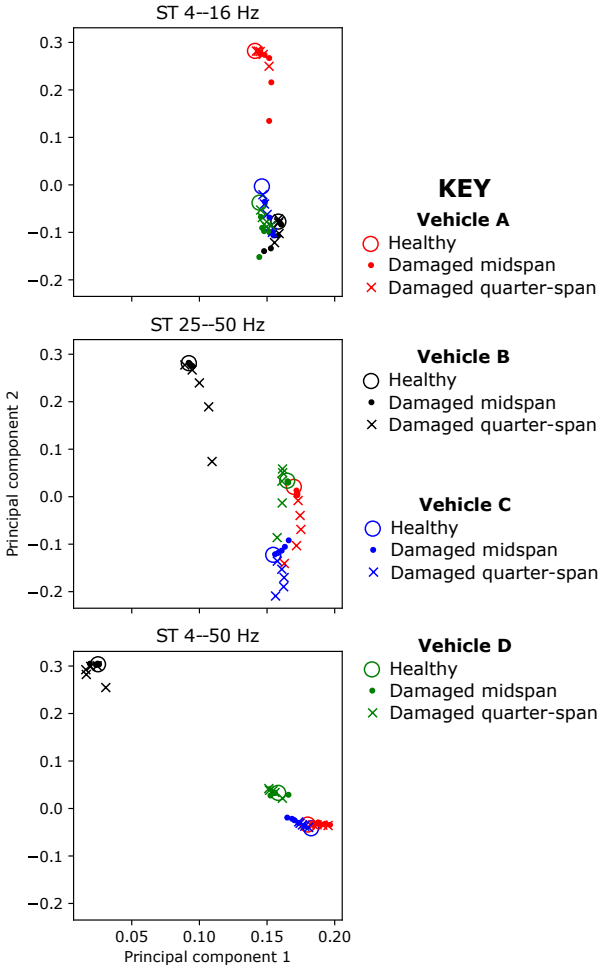

Figure 6.5.8: Multi-class PCA projections for three types of input sample image: presentation 1 of 2.

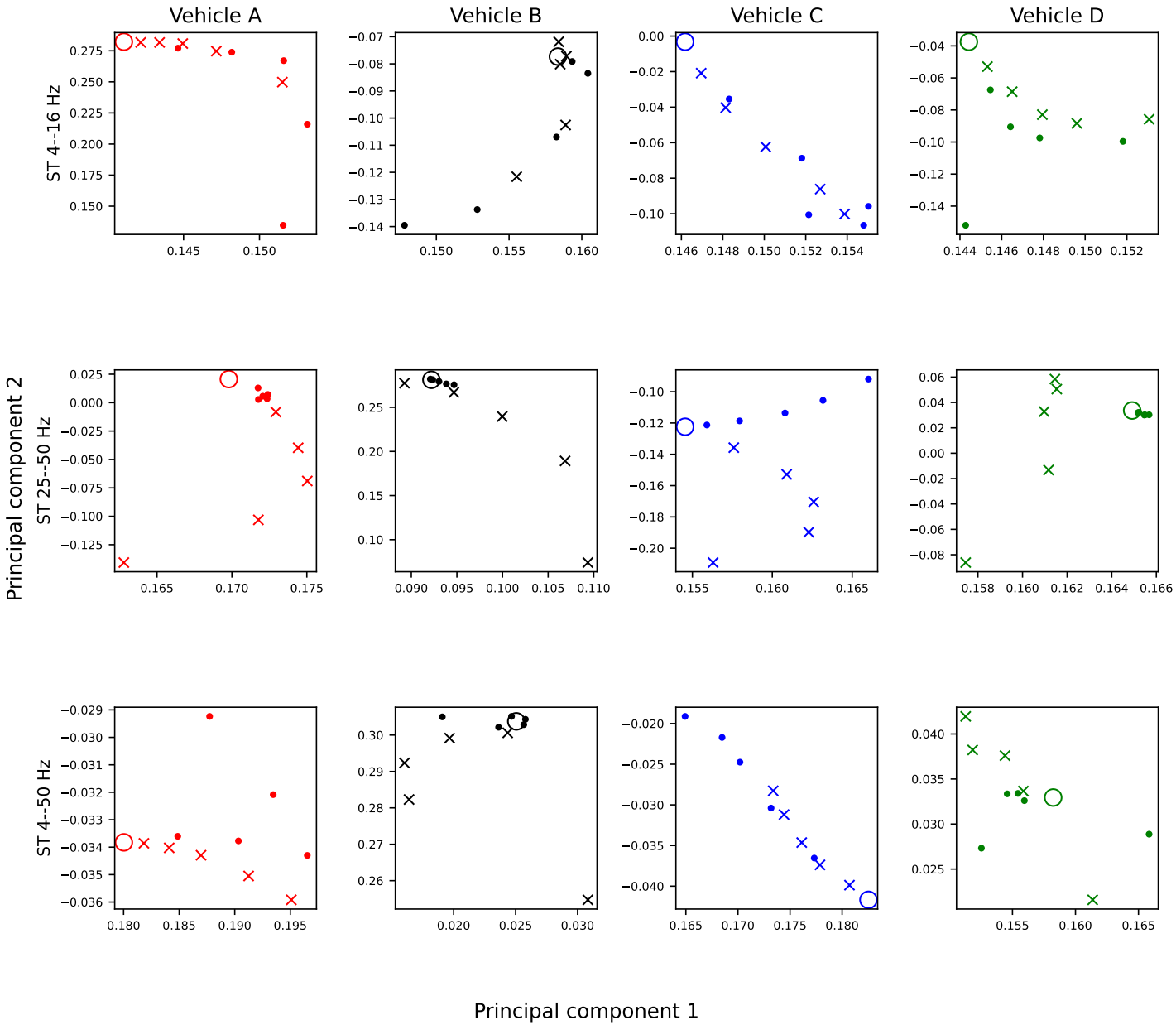

Figure 6.5.9: Multi-class PCA projections for three types of input sample image: presentation 2 of 2.

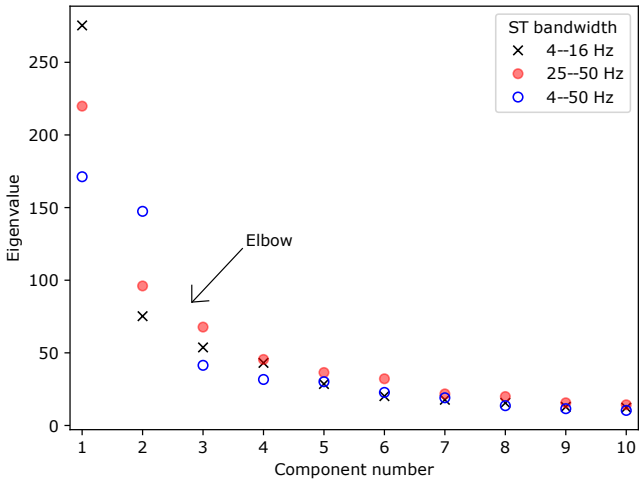

Figure 6.5.10: Multi-class PCA projection: scree plot.

6.5.6 PCA projections (single-class)

The previous section demonstrated that projection of PCs based on decomposition of the covariance matrix resulted in clustering according to vehicle properties, with apparent separation of healthy and damaged data within each cluster. These PCs represented decomposition of a covariance matrix $\boldsymbol{\Sigma}$ of a data matrix $\boldsymbol{X}$ in which all input data samples (healthy and damaged bridge conditions, and all four vehicle types) were combined. However, as previously discussed in practical situations for real bridges the labelled data representing damaged bridge conditions may not be available. It would be beneficial in such situations to pursue one-class classification in which the decision boundary (separating damaged and healthy data) is defined based only on inputs representing the healthy condition.

The current section explores the viability of an OCC approach following the outline presented in section 6.5.4. Figures 6.5.11 and 6.5.12 present the contact point acceleration responses for vehicles A, B, C and D projected into a latent space comprised of the first two principal components. The figures compare healthy and damaged conditions, with varying damage severity, across a range of Stockwell transform input features:

- Band limited to the vicinity of the first bridge mode (4–16 Hz), normalised to instantaneous maximum signal power (Fig. 6.5.11).
- Band limited to the vicinity of the second bridge mode (25–50 Hz), normalised to instantaneous maximum signal power (Fig. 6.5.11).
- Band limited to a range including the first and second bridge modes (4–50 Hz), normalised to instantaneous maximum signal power (Fig. 6.5.12).
- Band limited to a range including the first and second bridge modes (4–50 Hz), not normalised (Fig. 6.5.12).

The common axis scales used in these figures highlight that the biggest difference in the latent space projections is caused by the vehicle configuration. This is expected, given that prior exploration of VBI frequency nonstationarity showed that the ST contours varied substantially according to vehicle configuration. However, in some of the subplots it is clear that damage location and severity result in obvious differences in projection when compared to the healthy condition. Whether the largest difference is associated with the first or second PC does not appear to be consistent. Generally the plots show the same trend as was apparent for the projections based on multi-class covariance matrix decomposition presented in section 6.5.5, confirming that the proposed OCC approach is suitable for distinguishing between healthy and damaged data.

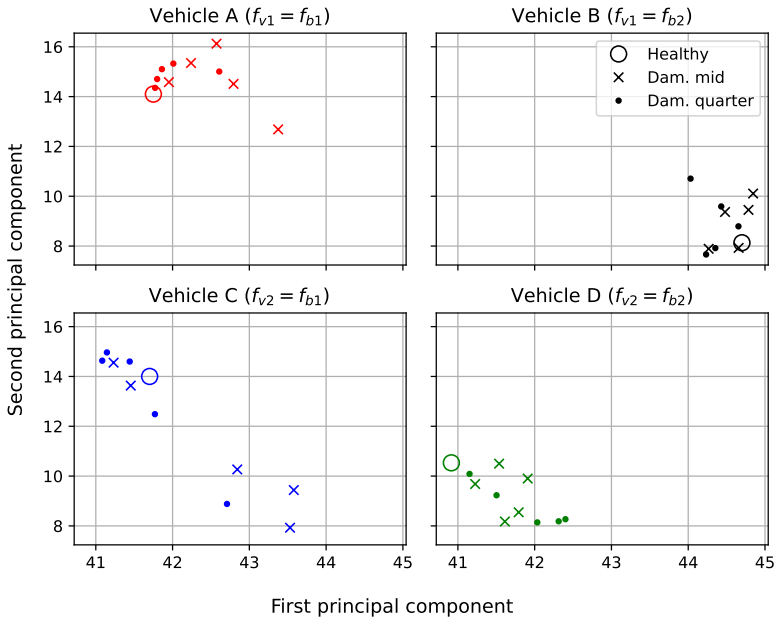

(a) Stockwell Transform 4-16 Hz

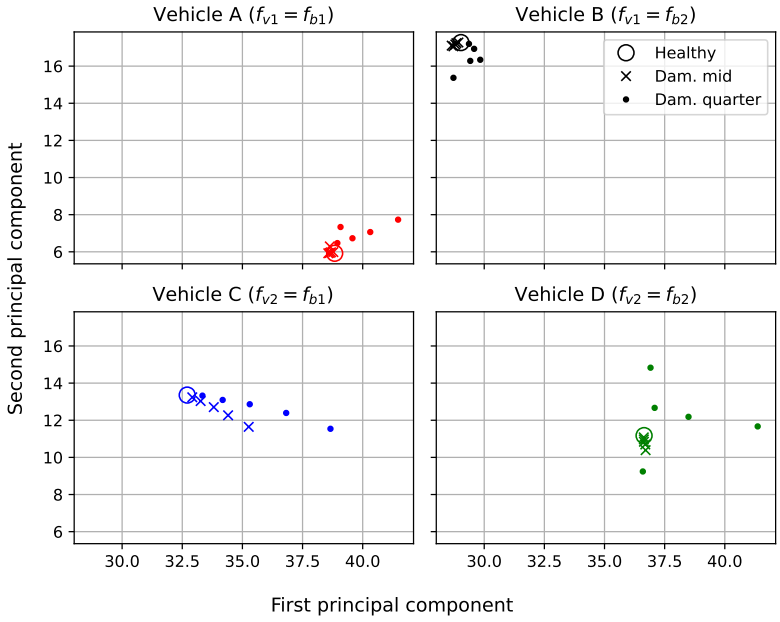

(b) Stockwell Transform 25-50 Hz

Figure 6.5.11: First and second principal components of narrowband normalised ST contours of contact point acceleration responses.

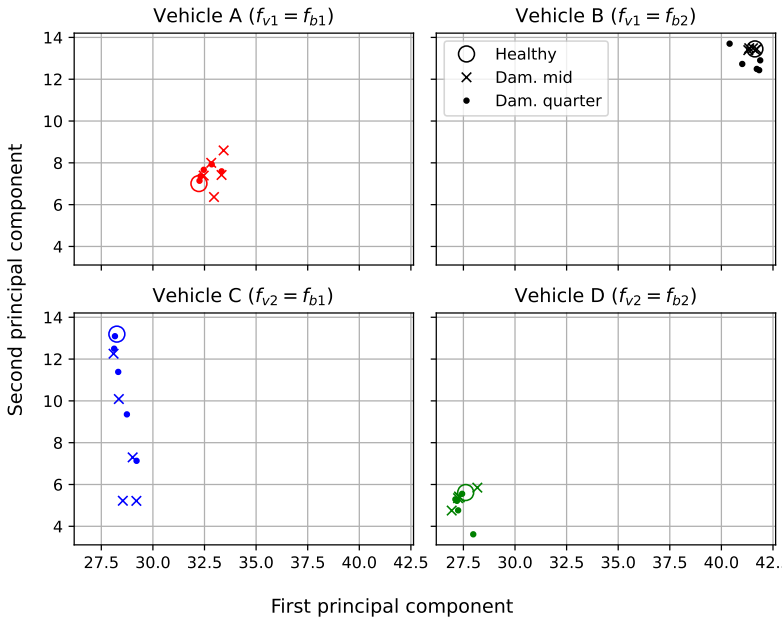

(a) Stockwell Transform 4-50 Hz, normalised

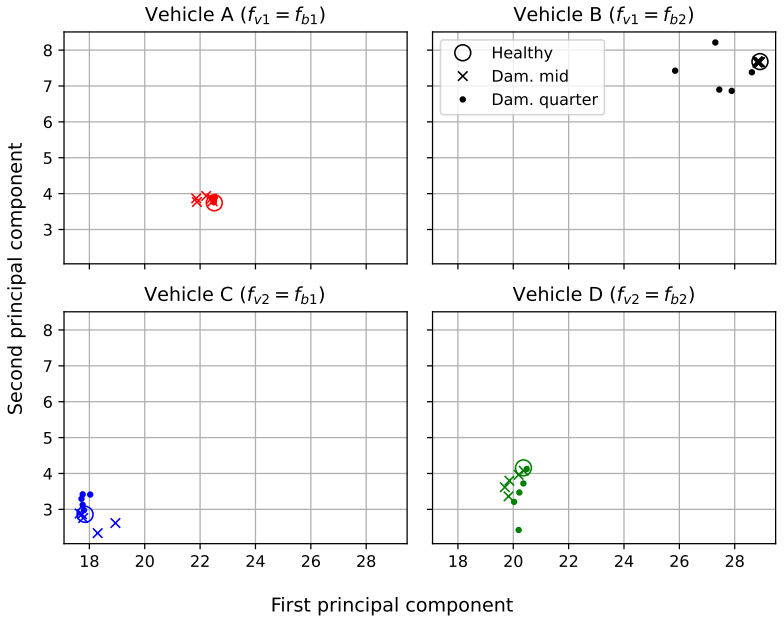

(b) Stockwell Transform 4-50 Hz, not normalised

Figure 6.5.12: First and second principal components of wideband ST contours of contact point acceleration responses (normalised compared to non-normalised).

6.5.7 Damage metric

A damage metric D is proposed as shown in equation (6.6) and illustrated in Fig. 6.5.13 as Euclidean distance in latent space from the healthy condition:

$$D = \sqrt{\left(PC_{1,h} - PC_{1,d}\right)^2 + \left(PC_{2,h} - PC_{2,d}\right)^2} \tag{6.6}$$

where PC_1 and PC_2 are the first and second principal components, and subscripts h or d refer to healthy and damaged conditions respectively. The damage index therefore represents separation from the healthy condition in latent space and it is assumed that a higher damage severity results in a greater damage index value, thus offering insight beyond binary classification. The method outlined in section 6.5.4 stated that a decision boundary would be drawn around examples of healthy data in latent space. In the current case, since the data are synthetic, only one healthy example is available for each vehicle type. This single example is assumed to represent the centre of the healthy condition cluster in latent space. If multiple healthy examples were available and a decision boundary was drawn around them, equation 6.5.7 would be defined as the distance from the class boundary.

In section 6.5.5 the input samples (ST contour images) were normalised to instantaneous maximum signal power. In the current section results are presented with and without such normalisation in order to explore its effect on separability of healthy and damaged data in latent space.

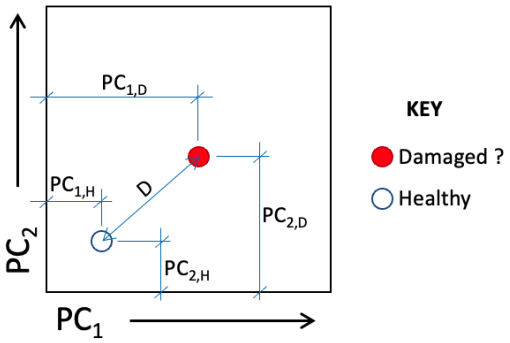

Figure 6.5.13: Illustration of Euclidean distance damage metric in latent space.

Figures 6.5.14 and 6.5.15 present the Euclidean distance damage index in the projected latent space for the PCA projections. The following trends can be observed:

- The damage index generally increases with damage severity, but this is not fully consistent for all vehicle configurations and data processing strategies.
- Normalisation of the ST appears to increase the absolute value of the damage indices.
- The best outcomes are associated with the normalised ST (either narrowband or wideband) for vehicle configuration C. In these cases, the damage index shows a mostly monotonically-increasing relationship with damage severity. Additionally, the damage index for midspan and quarter-span is consistently different here for most damage severity levels, suggesting the potential for both damage identification and damage localisation. The very best outcomes are associated with the narrowband (25–50 Hz) ST contours.

The good outcomes associated with vehicle C can be potentially understood in relation to the vehicle-to-bridge frequency ratio. For this vehicle $f_{v2} = f_{b1}$. The vehicle mode shapes previously presented in Fig. 5.3.1 confirmed that the majority of modal participation for the vehicle's second mode is at the axle DoF. Bridge damage at midspan and quarter-span both lead to a reduction in the bridge first mode frequency (Table 6.5.1) and thus a change to the vehicle-to-bridge frequency ratio is expected due to damage, leading to corresponding changes in the ST contours from the contact point acceleration response.

This damage detection test outcome based on synthetic VBI data suggests that for some damage types and severity levels, and some vehicle configurations, it may be possible to detect damage when the non-interacting vehicle and bridge natural frequencies are proximal. In chapter 7 a laboratory-scale physical VBI model is used to test this method with real data. Since the method would be confounded by inaccurate estimation of vehicle properties, vehicle system identification forms a significant part of the presented work.

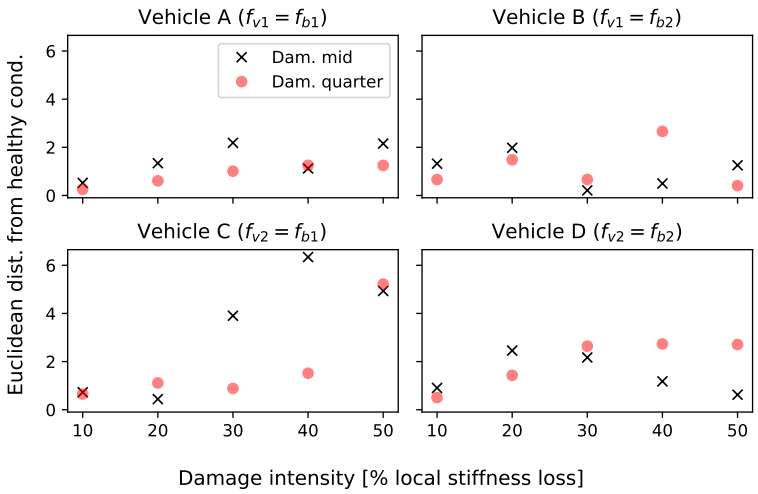

(a) Stockwell Transform 4–16 Hz

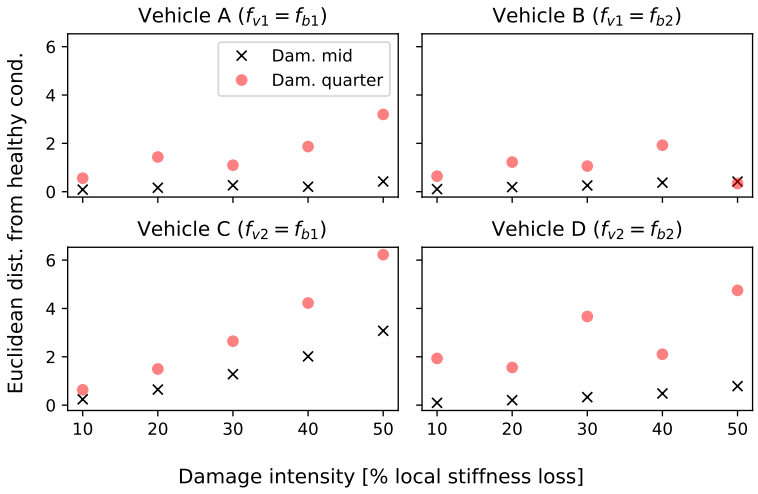

(b) Stockwell Transform 25–50 Hz

Figure 6.5.14: Damage detection by Euclidean distance from healthy condition in principal component space, comparing vehicle models A–D. Normalised narrowband ST.

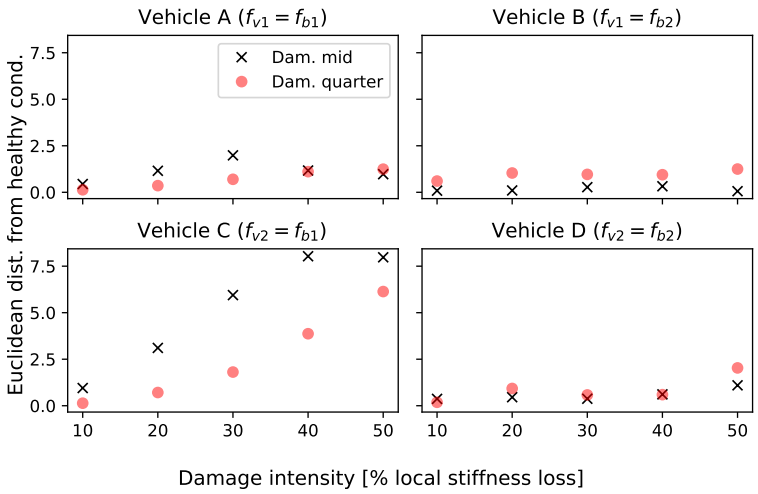

(a) Stockwell Transform 4–50 Hz, normalised

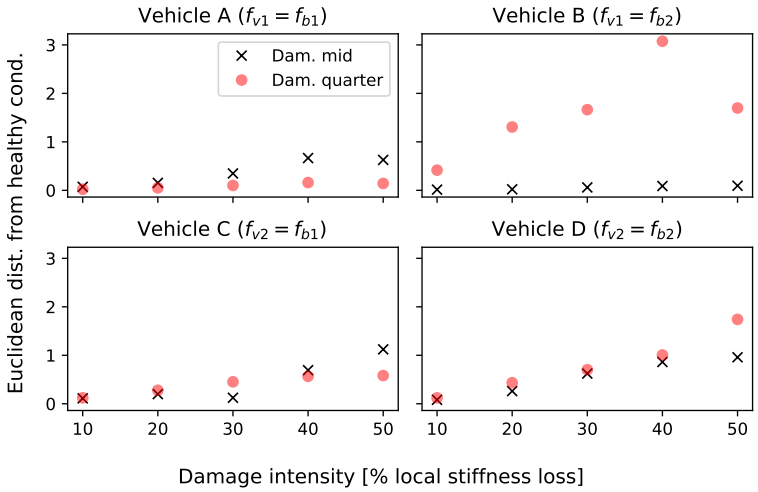

(b) Stockwell Transform 4–50 Hz, not normalised

Figure 6.5.15: Damage detection by Euclidean distance from healthy condition in principal component space, comparing vehicle models A–D. Wideband ST, showing effect of normalisation.

6.6 Discussion

6.6.1 Finite element simulation and Stockwell transform

This chapter presented FE simulation results exploring the effects of vehicle parameter variation on combined vehicle-bridge system frequencies during traversals. The performance of the FE model was validated in relation to its ability to consistently represent frequency variation for VBI. The ST was proposed as a suitable method for visualising these effects, and the first-known application of the *radius of trust* or *cone of influence* was proposed. Although widely used with the continuous wavelet transform, it is not known to have been used with the ST until now. This allowed greater disambiguation between genuine and spurious signal features by highlighting the region in which the ST contours were subject to distortion due to edge effects.

6.6.2 Single degree-of-freedom vehicle models

SDoF vehicle models were considered. Results from linear perturbation FE simulation were benchmarked against the available closed-form expression for frequency variation as a function of vehicle position for a SDoF vehicle and a single-mode simply-supported beam bridge. Good agreement was observed. The small differences between the closed-form and FE results were observed to match the absolute value of the expected bridge mode 2 shape, with the error magnitude increasing as the vehicle frequency rose towards the second bridge frequency, and as the vehicle mass increased. This highlights the potential for VBI effects relating to higher modes of the vehicle and bridge to be missed if these modes are not included in simulations. The effects not represented by the single-mode approximations in the literature may be particularly important when multiple vehicle frequencies and bridge frequencies are proximal, or when bridge frequencies are closely-spaced.

Frequency shifts for the combined SDoF vehicle-bridge system were presented with the vehicle stationary at midspan and quarter-span, normalised to the vehicle-to-bridge frequency ratios. This presentation method allows the expected maximum frequency shift to be retrieved for other vehicle and bridge parameter combinations, as long as the nominal (non-interacting) vehicle and bridge frequencies and vehicle-to-bridge mass ratio can be determined in advance.

Vehicle traversals were simulated using dynamic FE simulation and an oscillatory behaviour of instantaneous VBI system frequencies was noted. This behaviour, which has not been previously reported, was observed to be correlated with moderate phase difference between the acceleration response at the vehicle DoF and the time-varying contact point on the bridge. Existing closed-form solutions and linear perturbation FE-derived results from this chapter suggested that the combined vehicle bridge system would have two frequencies, diverging from each other to a maximum separation at the anti-node for the bridge mode. It was assumed that the virtual contact point frequency would

follow only one of these paths, based on literature identifying one frequency with the vehicle and the other with the bridge (Yang et al. [9]). After reviewing the instantaneous maximum power-normalised Stockwell Transform ridges, it was noted that larger phase angle lags (around 0.9–1.0 rad) were observed to correlate with the peak signal power jumping from one of these paths to the other. The change from one path to the other is believed to represent a change in which of the two frequencies has the higher signal power (greater participation) at that moment, and as noted this appears to correlate with phase lag. Phase differences may be expected to occur due to changes in vehicle speed, vehicle damping, prior vehicle or bridge excitation, or possibly other phenomena. This suggests that using instantaneously-normalised time-frequency representations for damage detection may prove troublesome in practice. On the other hand, the instantaneous normalisation procedure was noted to greatly increase the visibility of the frequency variation phenomenon.

The effects of SDoF vehicle damping on VBI system frequencies were explored. Relatively small amounts of vehicle damping – compared to those reported in the literature (section 2.4) and observed during field testing (chapter 4) – were observed to have large effects on the observed contact point frequency evolution with time, highlighting the importance of accurate estimation of vehicle damping ratios (a task shown to be subject to variation in chapter 4), especially considering the difference in apparent vehicle modal parameters depending on vehicle speed and road condition. Part of the observed damping-induced change was thought to be related to the manner in which a single ridge was extracted from the ST contours; the addition of damping was found to change which of the VBI system frequencies had the highest instantaneous signal power. This has implications for accurate estimation of bridge frequencies and robust visibility of bridge damage-induced effects from vehicle-mounted accelerometers if the vehicle damping ratio(s) are not known. For higher damping ratios, the resulting apparent divergence of frequency was thought to represent a suppression of response amplitude at the contact point.

6.6.3 Two degree-of-freedom vehicle models

Two-degree-of-freedom vehicle models were explored. Four vehicle configurations were tested, featuring frequency proximity between each of the vehicle's two modes and the first two bridge modes in turn. Linear perturbation FE analysis was used to highlight the expected frequency variation as a function of vehicle position on the beam. The trends of the results were found to be generally similar to the single-mode vehicle and bridge case previously reported, albeit with variation observed for more frequencies due to the higher number of vehicle and bridge modes represented. Dynamic FE simulation was used to explore frequency variation for the moving vehicle situation, considering the same range of vehicle configurations. Two ridges were extracted from the ST contours with the intention of providing greater visibility of VBI-induced frequency variation. The oscillatory phenomenon was observed for VBI system frequencies. Some degree of oscillation was noted when either of the vehicle's natural frequencies

was matched to either of the bridge's first two natural frequencies. A list of aspects of VBI that were not modelled here, but could potentially contribute to this phenomenon in practice was presented.

6.6.4 Bridge damage detection

Bridge damage detection was demonstrated using an established framework for situations in which vehicle and bridge natural frequencies are proximal. The method leveraged ST contours as input features and sought to separate healthy and damaged cases by projecting into a reduced dimension latent space comprised of the first two principal components of the features. Vehicle properties were found to have the largest effect on the distribution of data in latent space, but for some vehicle configurations a promising monotonic relationship was observed between bridge damage intensity and the proposed damage metric. In situations where the vehicle properties can be determined accurately (for example using the output-only approaches explored in chapter 4) the method may have merit, addressing the difficulties in damage visibility caused by VBI-induced frequency variation. It was speculated that this method could be applied to large datasets using deep machine learning methods, leveraging the data to learn projection methods to enhance separation of classes in latent space and thus increasing visibility of bridge damage.

6.6.5 Implications for subsequent work in this thesis

The damage detection method demonstrated in the latter part of this chapter has shown promising results for situations in which the bridge and vehicle frequencies are proximal (a situation which may unavoidably occur in practice if using citizen's or municipal vehicles rather than purpose-built sensor carriers). By leveraging the time-frequency representation of the contact point acceleration response as an input feature and assuming that the vehicle properties can be determined in advance, the potential for bridge damage detection is highlighted in a situation generally considered in prior literature to render damage detection difficult or intractable. However, it should be noted that the modelled damage locations were chosen in the simulations to maximise the effects on the bridge mode 1 or mode 2 frequencies. The work to be presented in chapter 7 will include a laboratory-scale test of this classification method.

The proposed damage detection method requires accurate estimation of vehicle properties as discussed. However, it should be noted that these vehicle properties are intended in part to allow the vehicle-to-bridge frequency ratios to be determined. As discussed in chapter 2 achieving accurate and robust bridge damage detection from vehicle-mounted sensors in operational conditions is a goal of iSHM. Considering the damage detection method proposed here, the presence of other vehicle traffic on the bridge would be a confounder. As noted in section 2.7 in chapter 2 the presence of other vehicles on the bridge during a monitoring campaign could change the effective bridge modal mass and thus the vehicle-to-bridge frequency ratios for the sensor-carrying vehicle. Restricting

background traffic would be contrary to the overall goals of iSHM. Additionally, the input from other vehicles has been noted as beneficial in addressing other signal-to-noise concerns for vehicle-based damage detection in some situations (Lin and Yang [182], Oshima et al. [264] (from Malekjafarian et al. [25]), Kong et al. [288]). Quantification of the effects of background traffic on iSHM is therefore of interest and benefit. An exploratory study conducted by the author compares the efficacy of vehicle- and bridge- mounted sensors for damage detection in the presence of multiple traversing vehicles (May, [365]). The study included vehicle properties, type classes and spacing intended to replicate real traffic.

6.7 Chapter summary

- Considering a SDoF vehicle, FE simulations (representing multiple bridge modes) of bridge frequency shift caused by a stationary vehicle showed good general agreement with single-mode analytical predictions from the literature (Fig. 6.3.1). However, the difference between the two methods' predictions increased as the vehicle frequency rose towards the bridge second mode frequency; additionally this effect manifested in accordance with the expected bridge second mode shape (absolute) as the stationary vehicle position was varied along the bridge (Fig. 6.3.2). This suggests the possibility for errors if the single-mode analytical solutions are relied upon in some situations.

- Outcomes of multi- (bridge) mode FE simulation of a stationary SDoF vehicle at midspan and quarter-span were presented (Figs. 6.3.3 and C.1.1), with vehicle and bridge relative properties normalised allowing the expected maximum bridge frequency shift to be determined in advance for future VBI exploration.

- The Stockwell transform was tested for hybrid time-frequency domain representation of vehicle response to VBI. The expected frequency variation was apparent in the normalised ST contours. Signal padding was successfully adopted to reduce edge artefacts and provide interpolation.

- Dynamic FE simulation was used to explore the effect of adding damping to a SDoF vehicle model traversing a bridge. The prior findings suggested that two frequencies would be visible. It was observed that addition of a small amount of damping (in the region of 10%, which is less than expected for real vehicles) changed which of these frequencies had the highest instantaneous signal power and thus dominated the ST contour plots. This was a potential downside of the adopted strategy of normalisation relative to instantaneous maximum signal power at each timestep).

- A previously-unreported oscillatory phenomenon was observed in the frequency response. It appeared to related to phase lag between the vehicle DoF and bridge virtual contact point responses, but could also represent a signal or transform artefact.

- A stationary 2DoF vehicle was modelled and the expected frequency shifts as a function of vehicle position on the bridge were presented for four possible resonance cases between two vehicle modes and two bridge modes.

- A damage detection method was demonstrated for situations where vehicle and bridge frequencies are proximal and labelled data representing the bridge damaged condition is unavailable. The method comprised projecting the time-frequency response into a reduced-dimension latent space (comprised of the first two principal components) and pursuing a clustering approach to one-class classification. The approach showed

promising results based on simulated VBI, suggesting the potential for monotonically-increasing latent space separation as a function of bridge damage (local stiffness loss) severity.

Chapter 7

Laboratory-scale testing

The physical testing presented in this chapter was made possible by the kind assistance of Dr. Robert Corbally and Prof. Abdollah Malekjafarian. Prof. Malekjafarian facilitated access to the laboratory at University College Dublin to allow the testing to be performed, including making equipment available. Dr. Corbally assisted with the physical testing including arranging equipment, operating the scale model vehicle, providing pro forma spreadsheets for recording results and sharing general advice on best practice in executing and recording data using this experimental setup.

Python code for generating modal parameter estimates using the matrix pencil method and inferring the associated mode shapes was adapted from examples provided by Dr. Zachariah Wynne [398].

Some aspects of the work presented in this chapter have been published as part of the proceedings of the 10$^{\text{th}}$ International Conference on Experimental Vibration Analysis for Civil Engineering Structures (May et al. [436]).

7.1 Chapter overview

This work presented in this chapter addresses one Research Outcome:

RO.8 Establish the parameters of vehicle and bridge for a laboratory-scale model of VBI. Inspect the vehicle-mounted dynamic sensor responses and test the developed method of damage detection.

The work presented in this chapter relates to laboratory-scale testing, apart from specific instances (where synthetic data is presented, reference is made in the text to finite element modelling).

7.1.1 Method of investigation

The work in this chapter is presented in the following manner:

- **Section 7.2** describes the physical apparatus and investigation schedule.

- **Section 7.3** presents the method and outcomes of a process of bridge system identification, in which the response to impulse loads was used for output-only modal parameter fitting.
- **Section 7.4** presents the vehicle system identification process and results (output-only responses to driving and to impulse loading).
- **Section 7.5** explores the established method of estimating the contact point response and proposes a novel formulation suitable for use in situations where some of the vehicle properties are not known.
- **Section 7.6** uses the estimated contact point response to explore the visibility of bridge and vehicle frequencies during traversals. The residual response (from front and rear axles) is also presented.
- **Section 7.7** demonstrates application of the damage detection method introduced in chapter 6 to the laboratory testing data and explores the statistical significance of the visibility of damage using two methods: the Wasserstein distance between sample distributions, and confidence intervals of the differences between bootstrapped sample mean distributions.
- **Section 7.8** presents the vehicle-to-bridge acceleration amplitude ratios and critically explores the likelihood of detection of bridge frequencies from the vehicle-mounted accelerometer responses.
- **Section 7.9** comprises a discussion of the work presented in the chapter.
- **Section 7.10** presents the chapter conclusions and contributions.

(a) Model bridge, with deck plate (b) Model bridge, without deck plate

Figure 7.1.1: Overview of the scale model bridge at University College Dublin. Reproduced from Corbally and Malekjafarian [19].

7.2 Description of testing regime

The physical testing described in this chapter was undertaken at the Structural Dynamics & Assessment Laboratory [437], in the Centre for Critical Infrastructure within the School of Civil Engineering, University College Dublin.

The physical bridge model comprises a steel plate, stiffened with steel angles bolted to the underside, spanning between supports comprising steel shafts turning on bearings. The bridge is positioned such that a scale model radio-controlled vehicle can be driven across the bridge. An overview of the bridge model is presented in Figure 7.1.1, illustrating the general construction details with and without the deck plate installed. Construction details are presented in Figure 7.2.1. Figure 7.2.2 shows the model vehicle, with accelerometers installed. Also visible in this figure are additional masses clamped to the bridge deck, and accelerometers installed to the underside of the deck. This bridge and vehicle model have been the subject of previous publications, for example Corbally and Malekjafarian [20] in which further details of the bridge and vehicle are available.

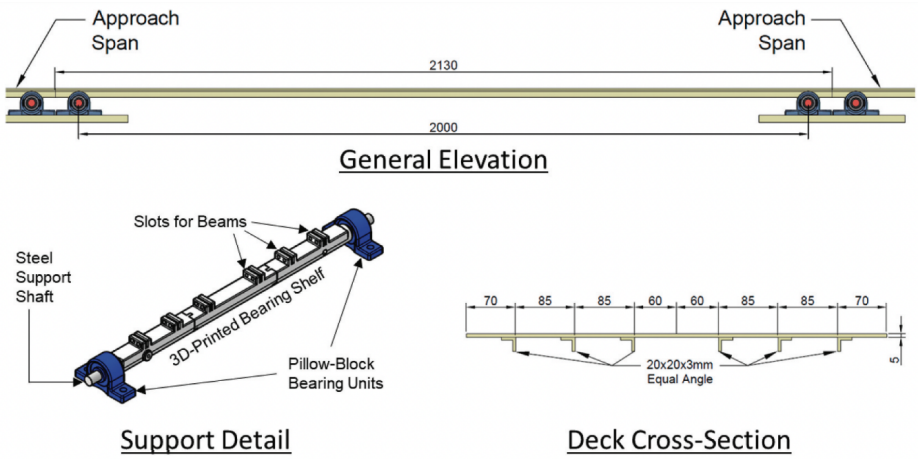

Figure 7.2.1: Details of the scale bridge model (dimensions in mm) at the SDA Laboratory, University College Dublin. Reproduced from Corbally and Malekjafarian [20].

The model vehicle used in this experiment was an *Axial SCX 10 iii* model by Axial Adventure. Other than having the outer plastic shell removed, and brackets added to facilitate mounting of accelerometers, it was unmodified from its commercially-available condition. The vehicle can be driven at three speeds. Vehicle mass including installed accelerometers was measured as 3.43 kg.

The sensors used were G-Link 200 8G wireless triaxial accelerometers produced by LORD Microstrain. Data were logged on a laptop computer running Sensor Connect[438] software. The adopted sampling frequency was 256 Hz. The layout of the accelerometers on the bridge is shown in Figure 7.2.3.

Figure 7.2.2: Vehicle used for laboratory testing at University College Dublin, showing accelerometers mounted to the vehicle and underside of bridge deck and added masses clamped to the bridge deck.

The physical testing undertaken consisted of the following regimes:

- Hammer tap impulse loading of bridge to facilitate bridge system identification, and subsequent fitting of a finite element model: see section 7.3.
- Driving vehicle on laboratory floor and using hammer tap impulse loading to facilitate vehicle system identification, and subsequent fitting of a reduced-degree-of-freedom model: see section 7.4.
- Vehicle traversals across bridge: see sections 7.5, 7.6 and 7.8.
- Damage detection: see section 7.7.

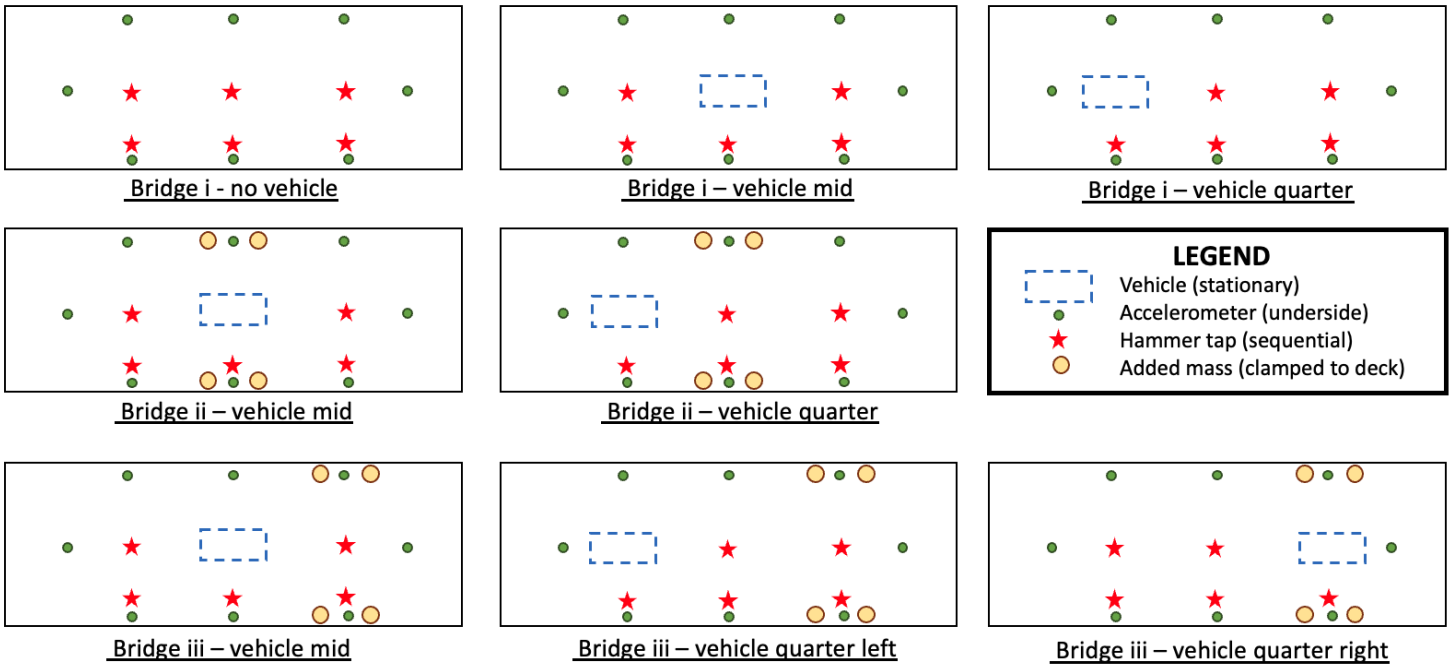

Figure 7.2.3: Bridge configurations used in bridge and vehicle-bridge system identification exercise, showing added mass locations, accelerometer locations and hammer tap locations.

7.3 Bridge system identification

This section presents outcomes from a system identification process which aimed to estimate modal parameters for the laboratory bridge model. Following this is a presentation of the process and outcomes of fitting three- and two-dimensional finite element (FE) models to the estimated parameters.

7.3.1 Estimating parameters of physical model

The bridge system identification procedure comprised instrumenting the bridge deck underside with an array of wireless accelerometers and tapping with a hammer at various locations. This is a well-known method in classical modal analysis colloquially known as the *roving hammer technique*. The exercise sought to collect records of free vibration response to impulse loading in a variety of configurations: with and without a vehicle present, and with a vehicle and added masses present. Since the data represent free vibration response, the application of the random decrement technique (as used in chapter 4) is not required here. A common trigger channel was used to select the free vibration responses from accelerometer data which were simultaneously recorded in response to the hammer taps. Some further discussion of this method of modal parameter estimation is included in Appendix A. The bridge configurations, vehicle locations, added mass locations, accelerometer locations and locations of sequential hammer taps used in the bridge system identification exercise are shown in Fig. 7.2.3. The number of hammer taps for each case are summarised in Table 7.3.1.

Ensembles of free vibration response for each of the configurations described in Table 7.3.1 were used to generate estimates of modal parameters using the matrix pencil method (MPM). The MPM is discussed in more detail in section 2.8.10, including the method of assessing goodness-of-fit based on the R^2 score, adopted from Wynne [398]. In this section, for the purpose of bridge parameter estimation a maximum model order of 20 and an R^2 target of 0.99 were adopted and only the ensemble of parameters representing the maximum R^2 was retained for each input.

Figure 7.3.1 and Table 7.3.2 summarise frequency and damping estimates for the first four modes of the laboratory bridge. The ensembles of MPM-derived estimated modal parameters were processed in the following manner:

- For each input signal, retain only the ensemble of parameters representing R^2 scores equal to or exceeding 0.99.
- Discard all estimates with damping greater than 10%, assuming such estimates are spurious, by inspection (note: in Fig. 7.3.1 the plotted means are for all estimates with damping $\leq$ 10%, but the plot scale is selected to highlight the differences between means).
- Discard estimates whose phase angle is outside the range $\pm\pi$ rad (assuming such estimates are spurious).

Bridge config. name	Vehicle location	Added mass location	Added mass magnitude	Hammer taps per location	Total hammer taps
Bridge i	-	-	-	3	18
	Midspan				15
	Quarter span (left)				15
Bridge ii	Midspan	Midspan	4 kg (4 x 1)	3	15
	Quarter span (left)				15
Bridge iii	Midspan	Quarter span (right)	4 kg (4 x 1)	3	15
	Quarter span (left)				15
	Quarter span (right)				15

Table 7.3.1: Summary of bridge configurations and hammer taps for bridge system identification exercise.

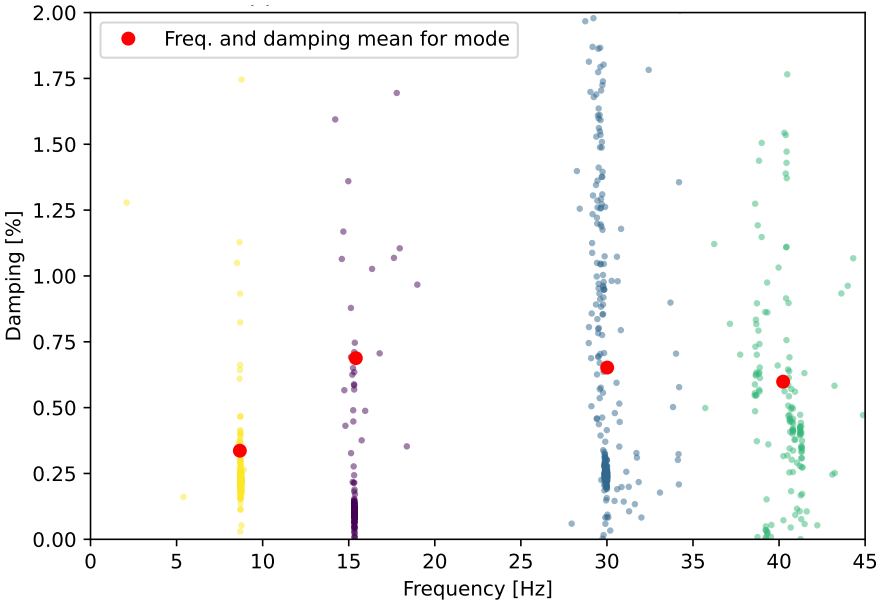

Figure 7.3.1: Gaussian Mixture Model applied to yield automated clustering of Matrix Pencil Method modal frequency and damping estimates. Plotted means relate to bridge configuration i (no vehicle, no added mass) for damping $\leq 10\%$.

Bridge modal frequency f_b [Hz]	**Bridge modal damping ratio ζ [%]**
8.67	0.34
15.41	0.69
30.01	0.65
40.24	0.60

Table 7.3.2: Mean bridge modal parameters from clusters shown in Fig. 7.3.1.

- For the purpose of comparison across the range expected to contain the first four bridge modes, consider only estimates whose frequency is less than 45 Hz.

- Generate clusters of estimates by applying a Gaussian mixture model (GMM) assuming four components (i.e. four modes in the range 0-45 Hz, by inspection), using a tied covariance matrix.

- The GMM cluster means provide an estimate of the frequency and damping for each mode, while the GMM cluster standard deviations provide an indication of certainty.

Figure 7.3.2 illustrates the estimated mode shapes for each of the clusters for bridge configuration i (see Figure 7.2.3). The mode shapes were generated by interpolation between modal amplitudes generated by the MPM analysis with GMM clustering for each sensor, using estimates for which the estimated frequency $\hat{f}_b$ met the criterion outlined in equation (7.1) where μ and σ are the mean and standard deviation of frequency for each of the GMM clusters.

$$\mu - 1.5\sigma \leq \hat{f}_b \leq \mu + 1.5\sigma \tag{7.1}$$

Visual inspection of the mode shapes plotted in Figure 7.3.2 confirms that the bending and torsion modes appear in the same order as those found in prior experiments using the same bridge by Corbally and Malekjafarian [20]. The process outlined above was repeated for all the bridge configurations shown in Figure 7.2.3. Compared to bridge configuration i (no vehicle, no added mass) the relative changes in mean and standard deviation of frequency and damping for each of the GMM cluster-derived modes are shown in Figs. 7.3.3 and 7.3.4. Tables D.1.1 and D.1.2 present the parameters estimated for each of the bridge configurations and are located in Appendix D for reference.

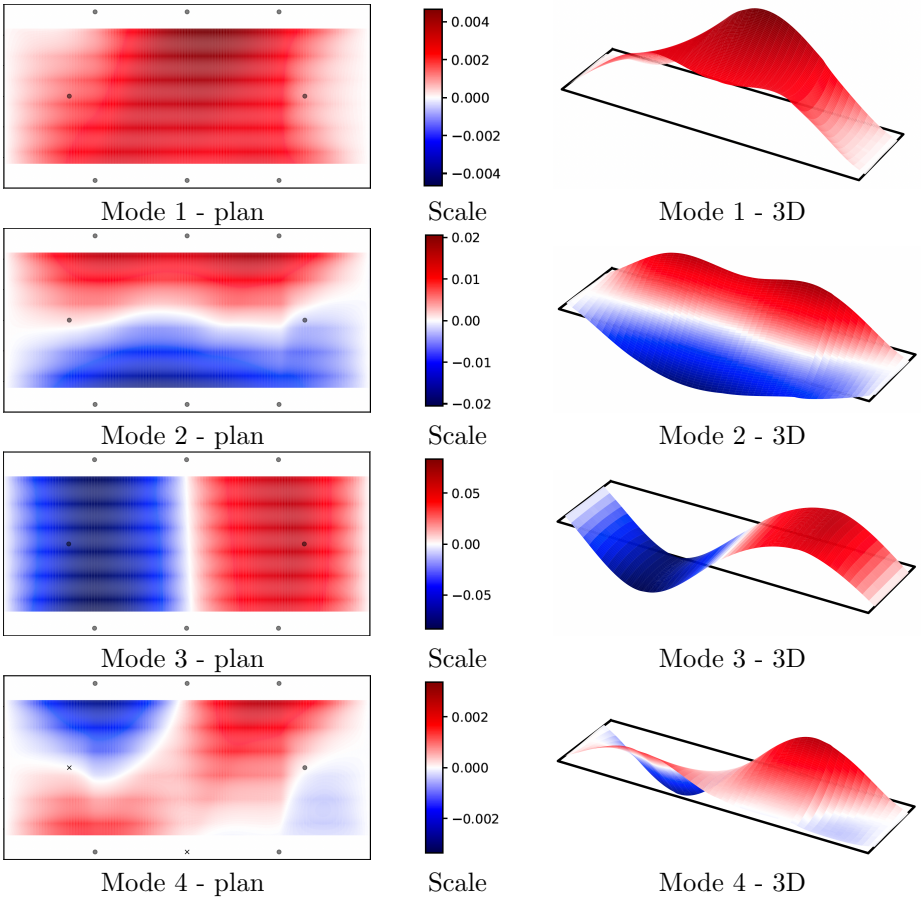

Figure 7.3.2: Estimated mode shapes for bridge configuration i (no vehicle, no added mass).

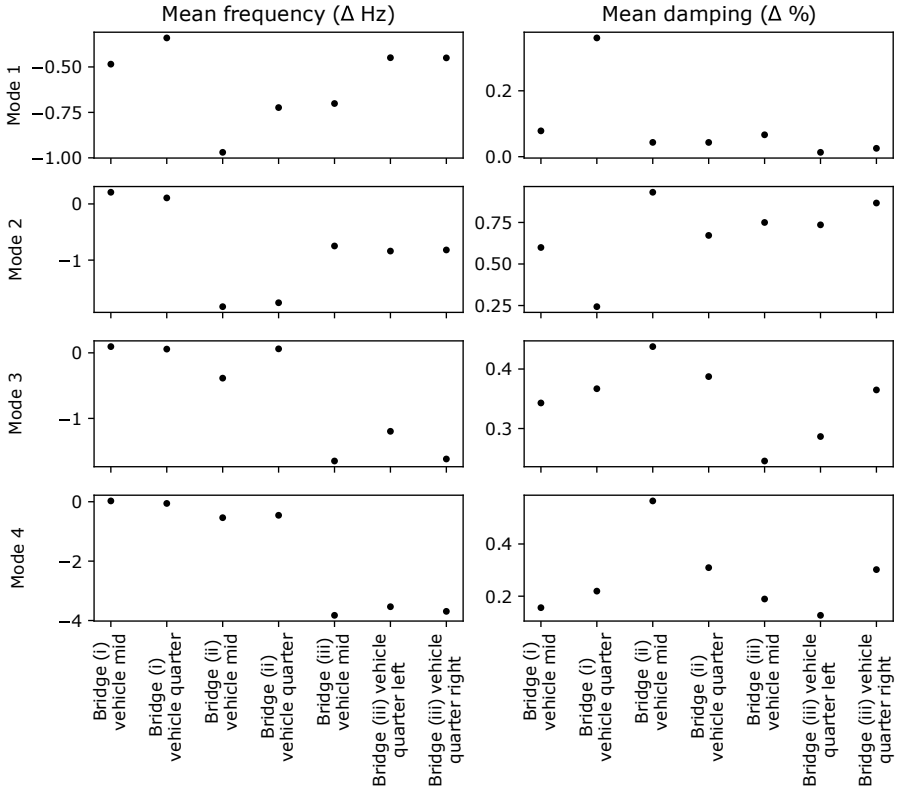

Figure 7.3.3: Relative change (compared to bridge configuration i) in **mean** estimated modal parameters for physical model bridge based on hammer tap impulse response.

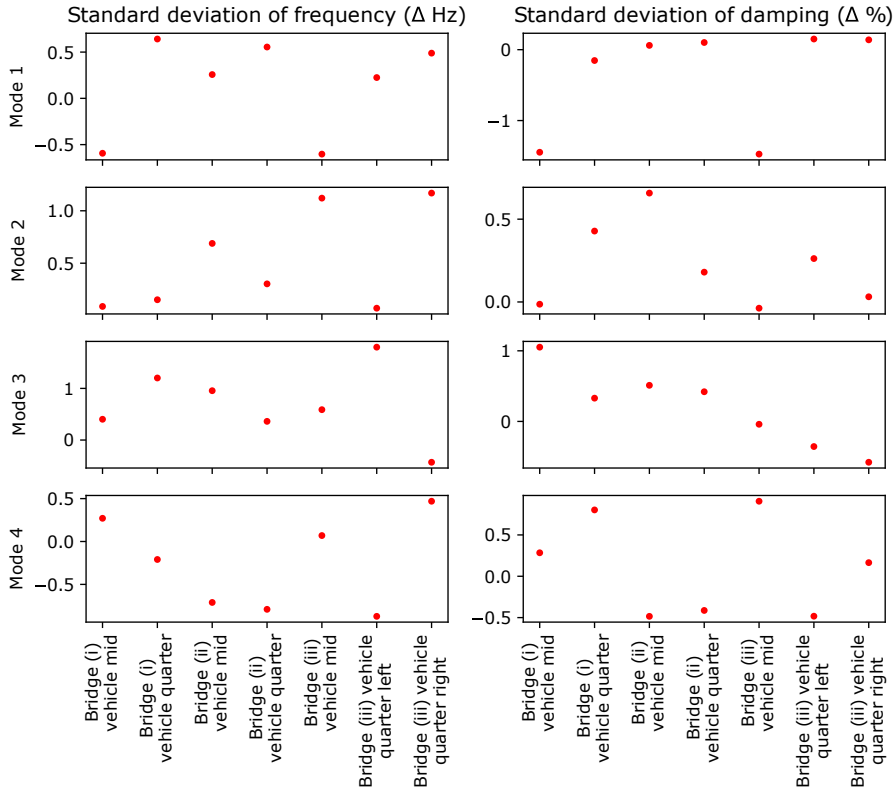

Figure 7.3.4: Relative change (compared to bridge configuration i) in **standard deviation** of estimated modal parameters for physical model bridge based on hammer tap impulse response.

7.3.2 Summary of finite element models

Three distinct FE models are discussed in this chapter: a model presented in prior literature, and 3- and 2-dimensional models developed by the author. A comparison of the modal frequencies of these three FE models and those of the laboratory-scale physical model is presented in Table 7.3.3. The FE models are outlined below.

The **FE model from prior literature** was presented by Corbally and Malekjafarian [20]. The properties of this FE model are understood to have represented the laboratory-scale physical model. The same physical model was used for the experimental work presented in the current chapter of this thesis.

A **3-dimensional FE model** developed by the author was used solely to validate output-only mode shapes and associated modal frequencies from physical testing of the laboratory-scale bridge model. The 3-dimensional FE model geometry and material properties are summarised in Table 7.3.4 and are intended to represent the physical model directly. A cross-section of the 3-dimensional FE model is shown in Fig. 7.3.5 and compared to the physical laboratory-scale model cross-section reproduced from Corbally and Malekjafarian [20].

A **2-dimensional FE model** was also developed by the author. It was first presented in chapter 5 and subsequently used in chapter 6. This FE model uses beam elements with effective properties based on a notional rectangular cross-section to represent in-plane dynamics. The material density, cross-section dimensions and elastic modulus adopted in this model were summarised in Table 5.2.1 in chapter 5. As presented in Table 7.3.5 and Fig. 7.3.6 this model has span length, mass per unit length, modal frequencies and associated mode shapes which are either an exact or a close match to both the physical model and the 3-dimensional FE model. The properties of the model were selected in order to achieve such a match. The model therefore facilitates simulation of the in-plane aspects of vehicle-bridge interaction, since the listed matching parameters wholly suffice to represent the relevant bridge dynamics. Section 7.3.3 includes a demonstration that the cross-section dimensions and material density used in the 2-dimensional FE model result in modal frequencies and mass per unit length suitable for the stated purpose.

7.3.3 Finite element model fitting

Figure 7.3.6 shows the mode shapes and associated modal frequencies for the 3- and 2-dimensional FE models developed to represent the laboratory bridge model. The three-dimensional model was used to validate the similarity of mode shapes and associated frequencies (by comparison between Figures 7.3.2 and 7.3.6 in addition to similar findings presented by Corbally and Malekjafarian [20]). This model was developed by directly representing the dimensions of the physical model as an extrusion of the cross-section presented in Figure 7.2.1. An elastic material model for steel was adopted, assuming a Young's modulus of 205 GPa and a density of 7850 kg/m^3. Supports were modelled as pinned connections. Modes 1 and 2 for the 2-dimensional model relate to modes 1 and

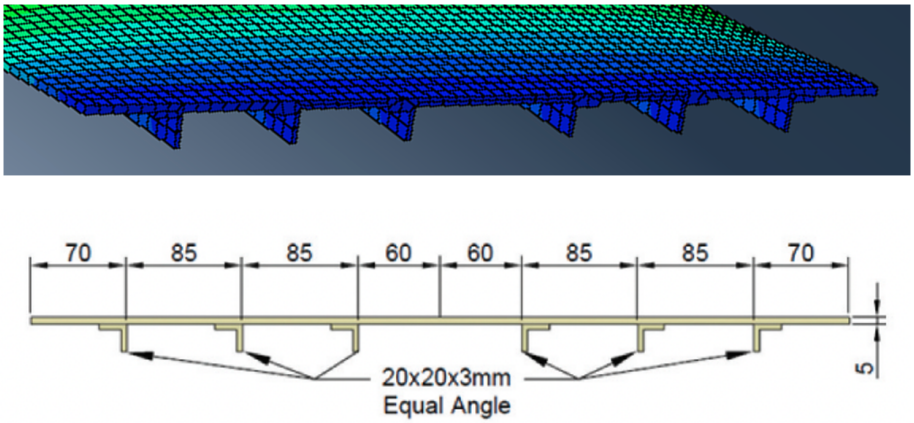

Figure 7.3.5: Cross-section of the 3-dimensional FE model developed in this thesis (above), compared to the physical model cross-section presented by Corbally and Malekjafarian [20] (below).

3 in the 3-dimensional model, since for both models these represent the first two global bending modes.

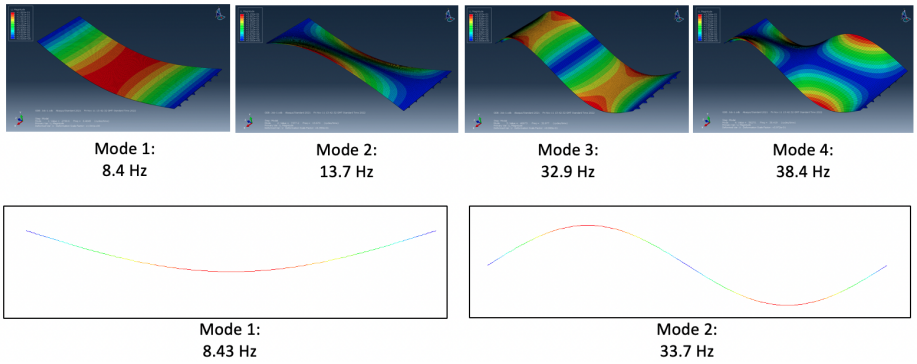

Figure 7.3.6: FE-derived bridge mode shapes and frequencies for 3- and 2-dimensional models.

The two-dimensional FE bridge model is the same as previously used in chapters 5 and 6, excepting the damage which was modelled in those chapters but was not present in the physical laboratory model.

Having confirmed that the three-dimensional FE model adequately represented the frequencies and mode shapes of the physical model, the next task was to validate the two-dimensional model. It was intended that this model would represent the first and second bending modes of the bridge (modes 1 and 3 of the 3-dimensional FE model and the physical laboratory model); since the model vehicle travelled along the bridge centreline during traversals, no signifi-

cant participation from the torsional modes (2 and 4 in the 3-dimensional FE) of the physical bridge is expected and thus a two-dimensional model will be adequate to represent vehicle-bridge interaction. Adopting a reduced-order model in this manner is aligned with the modelling principles adopted in chapters 5 and 6 as well as general practice reflected in the literature (sections 2.4 and 2.5 in chapter 2).

For the two-dimensional FE model to be representative of the physical bridge it is necessary first to confirm matching frequencies. The frequencies of a simply-supported beam are related to its span, cross-section, material elastic modulus and density. Simply-supported beam frequencies can be calculated with the previously presented and well-known equation (5.1). The span of the physical model bridge was measured in the laboratory and its total mass is assumed based on the density of steel and the cross-sectional and span length dimensions. For the FE representation in two dimensions a rectangular beam section was modelled; assuming unit cross-section breadth, a range of values for material density and beam depth were explored. Considering the first two bending mode frequencies from the three-dimensional FE model as targets, a loss function (also known as an *objective function*) was constructed (equation (7.2)). Figure 7.3.7 presents the outcomes of a process of exploring beam depth d and density ρ (where the resulting modal frequency and mass are denoted as $\hat{f_{bi}}$ and $\hat{m_b}$ respectively, with the target modal frequency and mass denoted as f_{bi} and m_b) and plotting the contours of this loss function. Considering each mode in turn, it is apparent that the two-dimensional FE model used in chapters 5 and 6 is a very close approximation of the minimum value of the loss function, representing a good match to the target frequencies and mass. Although the modal estimates presented in Figure 7.3.1 included damping, the damping ratios were very low. The undamped FE model presented in chapters 5 and 6 was therefore deemed to be representative.

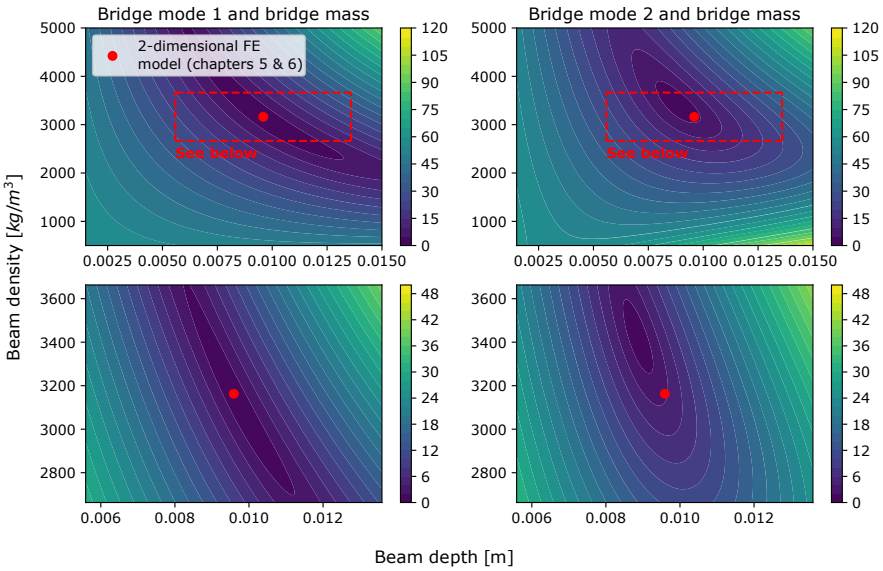

Figure 7.3.7: Minimisation of a loss function (equation (7.2)) by varying beam depth and material density, considering bridge modes 1 (left) and 2 (right). Results shown at two different scales.

As discussed in section 5.2.1 the properties of the two-dimensional bridge model used in chapters 5 and 6 (and adopted in the present chapter) were selected based on target values for the first two bending mode frequencies and the total mass representing the physical laboratory-scale model bridge. The planar FE model properties were generated using a notional cross-section; for ease of calculation this was defined as having a unit width and the cross-section depth and density were chosen to facilitate matching the first two global bending frequencies of the physical model, which were also validated using a three-dimensional FE model. For this reason, the density and depth in the FE model do not match those of the physical model, but this is of no consequence for the presented work since the relevant bridge behaviour for modelling VBI in this chapter is wholly captured by vehicle and bridge frequencies and mass ratios. Similarly the adopted elastic modulus for the steel material in the FE model has no particular significance other than to enable the approximate frequency matching between the FE and physical models.

$$L(d, \rho) = \sqrt{(\hat{f_{bi}} - f_{bi})^2 + (\hat{m_b} - m_b)^2} \tag{7.2}$$

Table 7.3.3 summarises the bridge modal frequencies estimated from the bridge system identification exercise and compares outcomes from physical testing and finite element analysis, including results previously presented by Corbally and Malekjafarian [20]. Table 7.3.5 summarises the properties of the two-dimensional FE bridge model to be adopted in order to simulate vehicle-bridge interaction in this chapter.

Bridge mode	**Description of mode**	**Hammer tap impulse response**		**3D finite element model**		**2D finite element model**
		This thesis	**Corbally and Malekjafarian [20]**	**This thesis**	**Corbally and Malekjafarian [20]**	**This thesis**
1	Bending	8.67 Hz	8.8 Hz	8.4 Hz	8.9 Hz	8.43 Hz
2	Torsion	15.41 Hz	15.3 Hz	13.7 Hz	15.4 Hz	-
3	Bending	30.01 Hz	29.9 Hz	32.9 Hz	33.8 Hz	33.7 Hz
4	Torsion	40.24 Hz	40.2 Hz	38.4 Hz	41.9 Hz	-

Table 7.3.3: Comparison of FE model- and hammer tap impulse response-derived bridge modal frequencies, comparing the physical testing and FE modelling undertaken in this thesis with that presented by Corbally and Malekjafarian [20].

The table confirms that the bridge modal frequencies identified from the physical bridge model during the work presented in this chapter are a close match to those identified in previous work by others (Corbally and Malekjafarian [20]). However, the modal frequencies of the FE models in the present work and prior work [20] are not as well-matched to those of the physical model, particularly in relation to the second global bending mode (mode 3 in the three-dimensional FE model). A potential explanation for this is apparent on inspection of Fig. 7.3.6: mode 3 appears to include some degree of torsional response, visible as higher localised deflection on each edge at quarter- and three-quarter-span positions. This implies that the physical model bridge may also have a mixture of bending and torsion for this mode, perhaps in a different proportion than is capture in the three-dimensional FE model, resulting in a discrepancy of frequency for this mode. This difference might be related to the connection of stiffening angles to the deck plate; the connection is bolted at discrete locations in the physical model while in the three-dimensional FE model the deck and angles are represented as a continuous unified cross-section. In the two-dimensional FE model torsion is not captured, leading to a similar discrepancy in frequency compared to the physical model.

Parameter	**Adopted value**
Span length	2 m
Support conditions	Simply-supported
Material elastic modulus	$2.05 \times 10^{11} N/m^2$
Material density	$7850 kg/m^3$
Cross-sectional geometry	To match physical model dimensions (Corbally and Malekjafarian [20]): 600 mm wide, 5 mm thick plate with 6 no. 20 x 20 x 3 mm downstand angles
Cross-sectional area	$3.666 \times 10^{-3} m^2$
Mass per unit length	28.78 kg/m
Flexural rigidity (EI)	14493.5 Nm^2

Table 7.3.4: Adopted parameters for 3-dimensional FE model representation of laboratory bridge.

Parameter	Adopted value	Parameter difference from 3-dimensional FE model (this thesis)	Modal parameter difference from physical model
Span length	2 m	No difference	-
Support conditions	Simply-supported	No difference	-
Mass per unit length	30.33 kg/m	+ 1.55 kg/m	-
Flexural rigidity (EI)	13965 Nm^2	-528.5 Nm^2	-
f_{b1}	8.43 Hz	+ 0.03 Hz	- 0.24 Hz
f_{b2}	33.7 Hz	+ 0.8 Hz	+ 3.69 Hz
ζ_{b1}	0.0 %	No difference	- 0.34 %
ζ_{b2}	0.0 %	No difference	- 0.65 %

Table 7.3.5: Fitted parameters for modelling two-dimensional representation of laboratory bridge.

7.4 Vehicle system identification

This section describes the process of estimating vehicle modal properties, employing two methods to explore the vehicle's response. The first approach involved time-domain curve fitting to free vibration impulse responses, using the MPM. The second involved driving the vehicle along the floor of the laboratory and inspecting peaks in the resulting acceleration power spectra, in the same manner as was found to be successful for the full-size vehicle field tests in chapter 4. Both approaches are classified as output-only methods.

7.4.1 Test vehicle and instrumentation

The vehicle used for laboratory testing was an *SCX 10 iii* by Axial Adventure. This is a 1/10 scale off-road vehicle with sprung and damped suspension, individually articulated at each wheel. The vehicle was fitted with four Parker LORD G-Link-200 8G wireless accelerometers: one on the front and back of the cabin each, and one on the front and rear axles respectively. The vehicle was modified from its stock format to permit the installation of accelerometers: custom 3D printed brackets were fabricated and the outer shell of the vehicle was removed. The customisation work was performed by the Structural Dynamics and Assessment Laboratory at University College Dublin [437]. The vehicle with installed accelerometers is shown in Fig. 7.2.2.

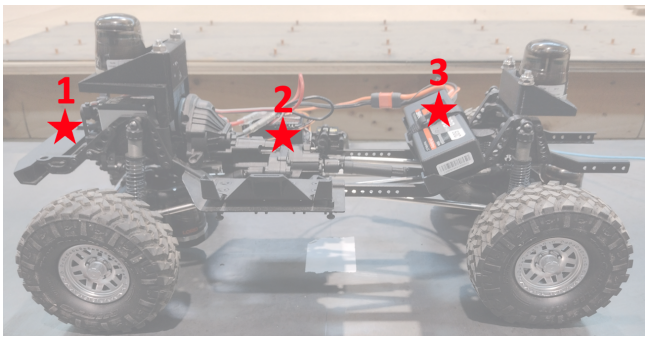

Figure 7.4.1: Vehicle used for testing at University College Dublin, with accelerometers installed, indicating hammer tap locations.

7.4.2 Test regimes

The laboratory testing comprised two distinct regimes. First, the vehicle was placed on the solid floor of the laboratory. While stationary, the vehicle was subject to hammer taps at three locations, as shown in Fig. 7.4.1 and summarised in Table 7.4.1. Time was allowed between taps so that the vehicle's free vibration acceleration response could be recorded by the attached sensors. The hammer tap force was not recorded, but the taps were administered by the

author in a manner intended to minimise differences in tap force and contact duration between the tap locations. The 6 taps for each location comprised 3 softer and 3 harder taps.

Hammer tap location	Number of hammer taps
1 (fender - front)	6
2 (transmission tunnel - middle)	6
3 (battery - rear)	6

Table 7.4.1: Summary of hammer taps in laboratory testing of scale model vehicle.

Next, the vehicle was driven along the laboratory floor at three different nominally constant speeds. The in-service acceleration response was recorded from all four accelerometers. According to measurements by Corbally and Malekjafarian [20] the vehicle's three speed settings result in measured speeds as summarised in Table 7.4.2. The outcomes from these two test regimes are discussed in the following sections.

Speed Setting	Speed Range (ms^{-1})	Avg. Measured Speeds (ms^{-1})
Low	0–0.85	0.73
Medium	0.85–1.25	1.11
High	>1.25	1.52

Table 7.4.2: Vehicle speed settings and measured speeds, reproduced from Corbally and Malekjafarian [20].

7.4.3 Time-domain impulse response

The free vibration responses to hammer tap impulse loading were processed in the manner used for bridge modal identification earlier in this chapter: the MPM was used to generate modal parameter estimates based on fitting multiple damped sinusoids to the observed data. The modal parameter estimates associated with $R^2 \geq 0.9$ were retained and are plotted in Fig. 7.4.2, overlaid on power spectra of the free vibration response. In this figure, clusters of estimates are labelled based on visual inspection and judgement to determine which mode of vehicle response they were assumed to represent (for example: axle hop frequencies assumed to be higher than cabin bounce frequencies, and front axle hop frequency assumed to be the power spectrum peak visible from both front axle and front cabin sensors).

In order to determine a single frequency and damping estimate for each of the four expected modes (front and rear cabin bounce, and front and rear axle hop) a Gaussian Mixture Model was used. The GMM utilised was as summarised in chapter 6. The intention was to use the GMM to determine clusters

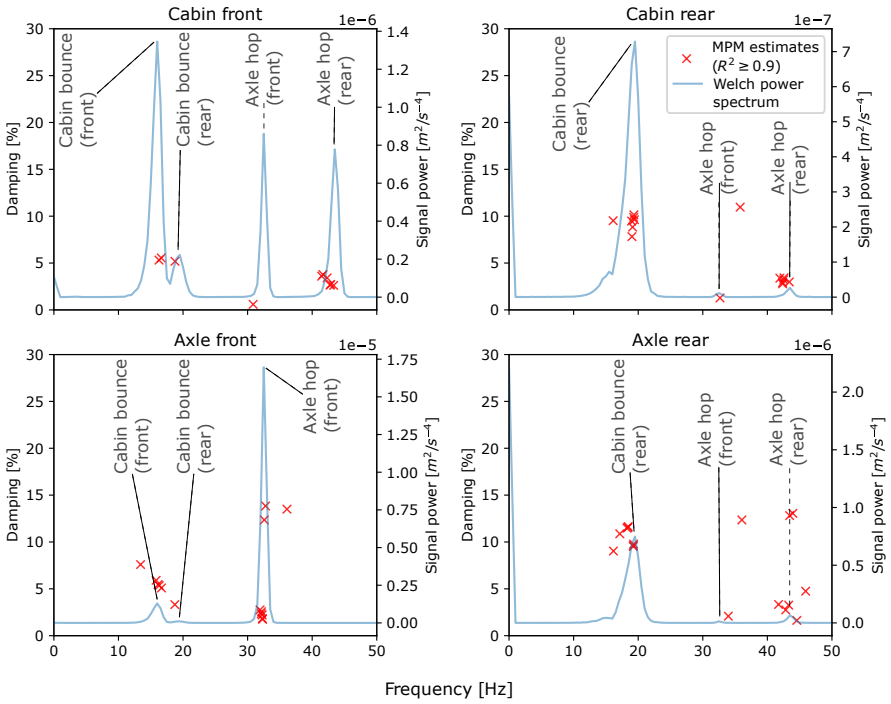

Figure 7.4.2: MPM ($R^2 \geq 0.9$) estimates of modal parameters compared to power spectra, from free vibration impulse response.

with maximum likelihood of belonging to a common mode and to then adopt the mean frequency and damping for each cluster as representative of that mode. However, GMM as applied in this thesis (using expectation maximisation) is sensitive to the initialisation parameters. As You et al. summarise, with reference to prior work by Wu [439] and Wu et al. [440] (both from You et al. [441]): Expectation maximisation is "highly sensitive to initialization and easily gets trapped in a local optimum" ([441]). This means that repeating the clustering exercise multiple times does not always result in a given data point being assigned to the same cluster. To address this, the following process (believed to be novel) was proposed and adopted:

- Repeat GMM clustering for 100 cycles, using random initialisation and an 11-component mixture (sufficient to group the MPM estimates by inspection). Record the means for each cluster on each cycle.
- Select a sub-region of the frequency-damping space deemed to include estimates for the first four vehicle modes. This region was defined by inspection, based on visual observation of cluster density; estimates outside the boundary are therefore assumed to be spurious since no clearly-defined clusters were apparent in this region.
- Repeat the GMM clustering once, using only the previously identified cluster means within the inclusion region and a four component mixture. Adopt cluster means as modal frequency and damping estimates.

The adopted process is conceptually similar to bootstrapping, an established statistical method of re-sampling to generate approximately normally-distributed sample distributions (Sainani [442]). The process is illustrated in Fig. 7.4.3. In order to generate estimated mode shapes for each cluster, the modal amplitudes for estimates within $\pm 0.75Hz$ of the cluster mean frequencies were selected (by inspection) on a per-sensor basis and the mean frequency and amplitude were calculated as indicated in Fig. 7.4.4. The resulting cluster means in frequency-amplitude space are visualised as vehicle modal displacements in Fig. 7.4.5, in which mode names provided are based on theoretical quarter-car expectations. The estimated mode shapes are a reasonable visual match for the expected cabin bounce and wheel hop displaced shapes (by inspection, and comparison to the quarter-car mode shapes from chapter 5 presented in Fig. 5.3.1). This serves to confirm that the estimated frequencies and damping ratios are suitable for use in generating a representative quarter-car model for either the front or rear axle as desired.

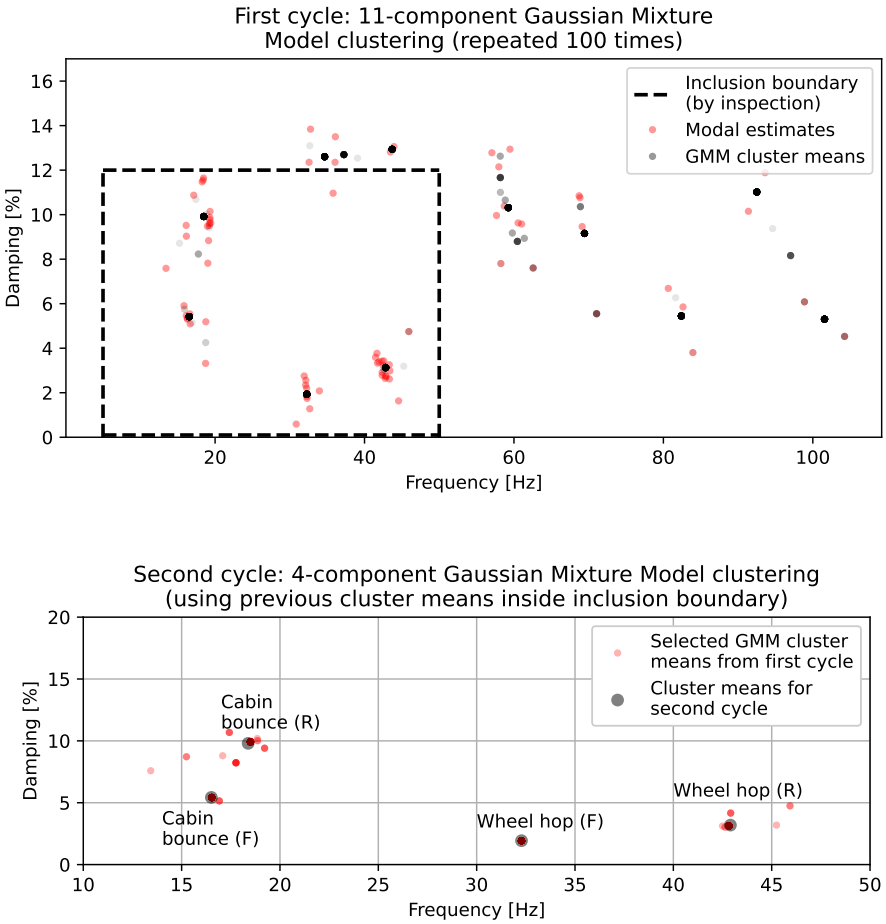

Figure 7.4.3: Illustration of multi-cycle GMM clustering for vehicle parameter estimation.

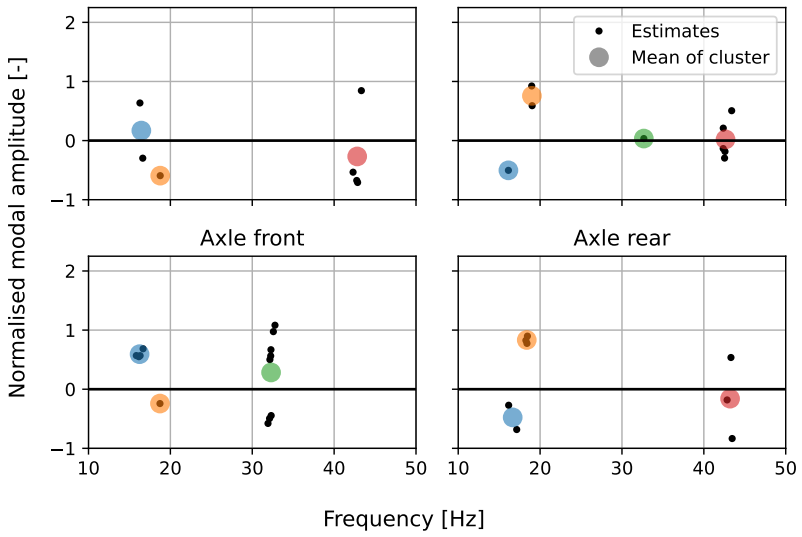

Figure 7.4.4: Estimated vehicle frequencies and associated modal amplitudes.

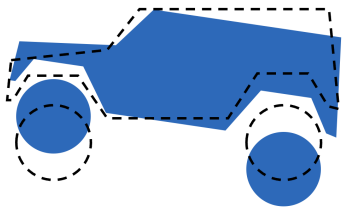

(a) Mode 1: front cabin bounce

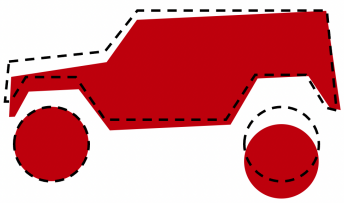

(b) Mode 2: rear cabin bounce

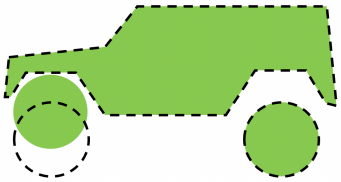

(c) Mode 3: front axle hop

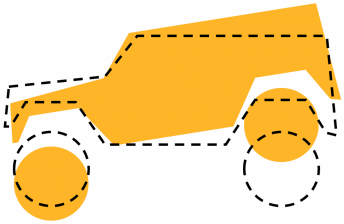

(d) Mode 4: rear axle hop

Figure 7.4.5: Visualisation of estimated vehicle mode shapes.

The adopted estimation and fitting process resulted in the modal frequencies and damping ratios summarised in Table 7.4.3. The table also includes comparison to the quarter-car model for the vehicle rear axle assumed by Corbally and Malekjafarian in their first paper on this subject [19] and adopted for subsequent work [20]: $m_1 = 0.475kg$, $k_1 = 2500Nm^{-1}$, $k_2 = 455Nm^{-1}$ and $c_2 = 20Nsm^{-1}$. No assumed value for m_2 (the cabin mass) was stated; the frequencies and damping ratios in Table 7.4.3, which were generated with the Python *Engineering vibration toolbox* functions [409] are therefore based on $m_2 = 2.755kg$ on the basis that $m_v = m_1 + m_2$, noting that values for $m_v = 3.43kg$ (vehicle mass with sensors installed) and $m_s \approx 0.2kg$ (accelerometer mass) were measured by the author as part of the work presented in this chapter (Corbally and Malekjafarian used three accelerometers while four were installed during the work reported here). Corbally and Malekjafairan's quarter-car parameters are understood to have been assumed based on notionally similar full-scale quarter-car models reported in the literature (for example Cebon [141]), to represent the plausible situation in which the true parameters of a test vehicle are not known. The frequencies and damping ratios resulting from their assumed quarter-car masses, spring stiffness and damper coefficient are noted to differ substantially from those resulting from the identification process reported in this thesis. It is concluded that the laboratory-scale model vehicle has modal parameters (in a representative 2DoF model abstraction) which differ from those typical for a full-scale vehicle. The conclusion is reinforced by the observations in chapter 4 for a full-scale vehicle, which also differ from those identified in the present chapter for the laboratory-scale vehicle. Future work should continue to seek the true parameters of test vehicles (whether reduced- or full-scale) when used to represent VBI and test damage detection methods, to reduce the potential for unexpected outcomes or misleading results when assumed vehicle parameters are used.

	This thesis		**Corbally and Malekjafarian [19] [20]**
Modal parameter	Front axle	Rear axle	Rear Axle
f_{v1}	16.5 Hz	18.4 Hz	1.91 Hz
f_{v2}	32.3 Hz	42.9 Hz	12.3 Hz
ζ_1	5.43 %	9.80 %	22.0 %
ζ_2	1.93 %	3.19 %	28.4 %

Table 7.4.3: Comparison of fitted and previously-assumed quarter-car modal parameters.

7.4.4 Outcomes: frequency domain (driving response power spectra)

Following the method set out in chapter 4, power spectra were estimated for each sensor using Welch's method based on the vehicle's response to driving on the laboratory floor at each of its three speeds. The resulting spectra are presented in Figs. 7.4.6, 7.4.7 and 7.4.8. Also indicated on these plots are bridge frequencies derived from the experimental campaign described in section 7.3 and theoretically-derived frequencies relating to the vehicle speed and wheel diameter (discussed below). Inspection of the figure reveals that the vehicle response appears to be dominated by frequencies that do not match the expected cabin bounce and wheel hop frequencies presented in section 7.4.3, nor the frequencies implicitly assumed by Corbally and Malekjafarian given their assumptions of the vehicle's properties [19]. A plausible explanation for this is the nature of the model vehicle's tyres; they were hollow rubber mouldings rather than pneumatic tyres as would be found on a full-size vehicle. Given the resulting loose fit tolerance of the tyres on the wheel rims, it is plausible that they were effectively out-of-round. Table 7.4.4 presents the harmonics that would be expected for the tyres having one high spot in the circumference (*rotation frequency*) or two high spots, making the tyre elliptical (*double rotation frequency*). Asymmetrical mass distribution on the tyre could also lead to a similar effect. These frequencies, adjusted for the vehicle speed, are plotted as red vertical solid and dashed lines respectively on Figs. 7.4.6, 7.4.7 and 7.4.8 and are based on the wheel diameter of 115 mm reported by Corbally and Malekjafarian [20].

Mean speed [m/s]	**Rotation frequency [Hz]**	**Double rotation frequency Hz]**
0.73	2.0	4.0
1.11	3.1	6.2
1.52	4.2	8.4

Table 7.4.4: Potential harmonic forcing due to suspected wheel out-of-balance, based on driving speeds and wheel diameter reported by Corbally and Malekjafarian [20].

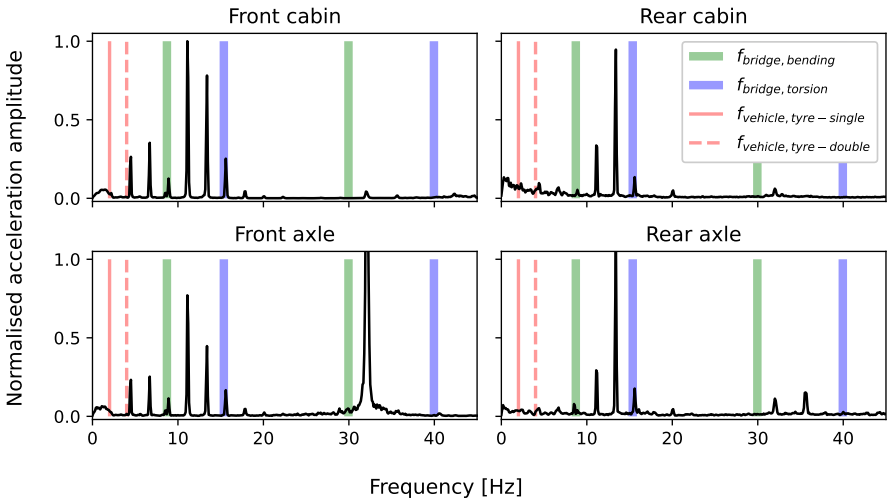

Figure 7.4.6: Welch power spectra (laboratory floor driving) - **slow speed**.

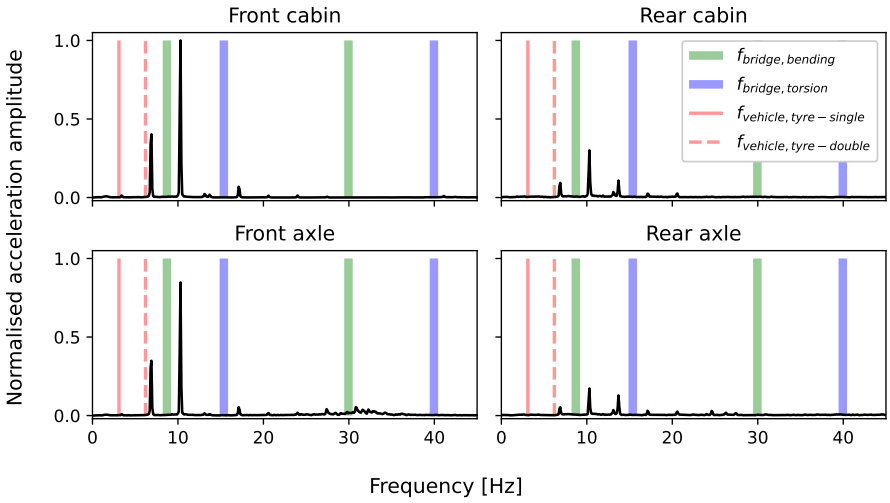

Figure 7.4.7: Welch power spectra (laboratory floor driving) - **medium speed**.

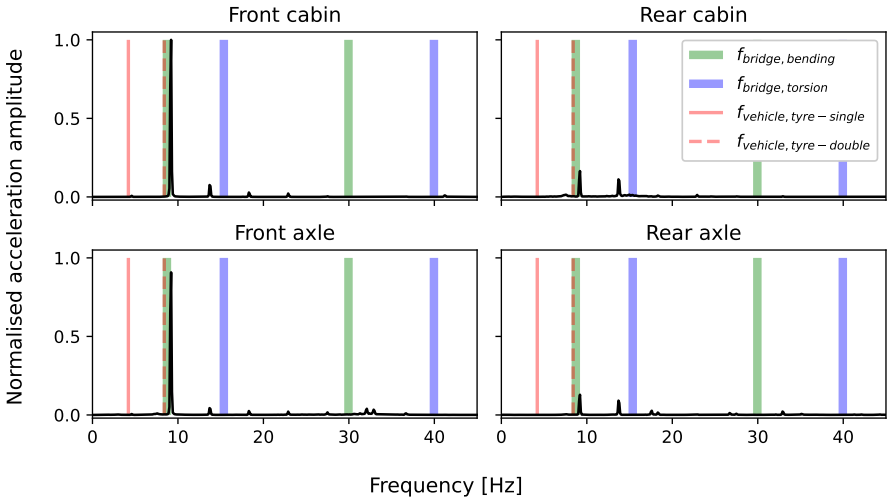

Figure 7.4.8: Welch power spectra (laboratory floor driving) - **fast speed**.

Inspection of Figs. 7.4.6, 7.4.7 and 7.4.8 reveals that a significant peak in the response spectra appears to correspond to the *double rotation frequency* for all vehicle speeds and both axles. The consistency of this observation across all speeds and axles serves to confirm that the existence of an elliptical out-of-roundness of the vehicle's tyres is a reasonable conclusion. The figure also shows the expected bridge frequencies based on the work presented in section 7.3. Notably, the wheel out-of-roundness effect appears to create a significantly prominent peak in the vehicle's front axle acceleration response at approximately the bridge fundamental frequency, even though the data relate to vehicle motion along the laboratory floor rather than traversing the bridge. This observation suggests that false positive identification of the bridge fundamental frequency is a serious risk when the vehicle traverses the bridge at the fast speed setting.

It is also notable from inspection of Figs. 7.4.6, 7.4.7 and 7.4.8 that:

- At slow speeds, a peak in the vehicle response for all sensors corresponds to one of the expected bridge torsional frequencies (from Fig. 7.3.1, Table 7.3.2 and Fig. 7.3.2). The proximity of vehicle response frequencies to the identified bridge torsion mode frequencies (indicated by blue vertical bars on Figs. 7.4.6, 7.4.7 and 7.4.8) suggests the potential for false positive identification of these bridge modes from the vehicle-mounted accelerometer responses.

- The front axle sensor (also at the slow speed setting) shows its highest magnitude response around 32 Hz, corresponding to the axle hop frequency identified in section 7.4.3.

Compared to the results reported in chapter 4, this exercise has not resulted in positive identification of vehicle modal frequencies (other than the front axle hop frequency as noted above). However, the outcomes are nevertheless valuable as they highlight the potential for the vehicle-mounted accelerometer responses to show frequencies that appear to relate to the bridge response during a traversal, but in fact could be spurious (false positives) relating in fact to the nature of the vehicle model manufacture and assembly method and tolerances. Mitigation of this (for example by installing alternative tyres with improved rotational balance) should be pursued to enhance future outcomes from this experimental apparatus.

For the purposes of this thesis, the vehicle modal parameters identified in section 7.4.3 and summarised in Table 7.4.3 (*this thesis*) will be adopted as representative of the axle hop and cabin bounce modes.

7.5 Contact point response

7.5.1 Exploring the established CP expression

Several researchers have attempted to recover estimates of the acceleration input to the vehicle, comprised of a combination of bridge deck motion and road roughness effects. Commonly known as the contact point (CP) response, this was defined for an undamped SDoF vehicle model by Yang et al. [187] as shown in equation (7.3):

$$\ddot{u} = \ddot{y}_1 + \frac{m_1}{k_1}\frac{d^2\ddot{y}_1}{dt^2} \tag{7.3}$$

in which the contact point acceleration response $\ddot{u}$ is expressed in terms of the acceleration recorded at the vehicle DoF ($\ddot{y}_1$), the mass at the vehicle DoF (m_1) and the vehicle spring stiffness (k_1). Corbally and Malekjafarian [220] extended the CP equation to accommodate a 2DoF quarter car model as shown in equation (7.4):

$$\ddot{u} = \frac{m_1}{k_1}\frac{d^2\ddot{y}_1}{dt^2} + \frac{c}{k_1}\left(\frac{d\ddot{y}_1}{dt} - \frac{d\ddot{y}_2}{dt}\right) + \frac{k_2}{k_1}\left(\ddot{y}_1 - \ddot{y}_2\right) + \ddot{y}_1 \tag{7.4}$$

In these equations, m_1 is the lower mass in a 2DoF quarter car model; k_1 and k_2 represent the lower and upper spring stiffness; and c the coefficient of a viscous damper connecting the two masses. $\ddot{y}_1$ and $\ddot{y}_2$ represent the acceleration response at the lower and upper masses respectively. The acceleration response at the virtual contact point is represented by $\ddot{u}$. The SDoF and 2DoF vehicle models are shown in Fig. 7.5.1.

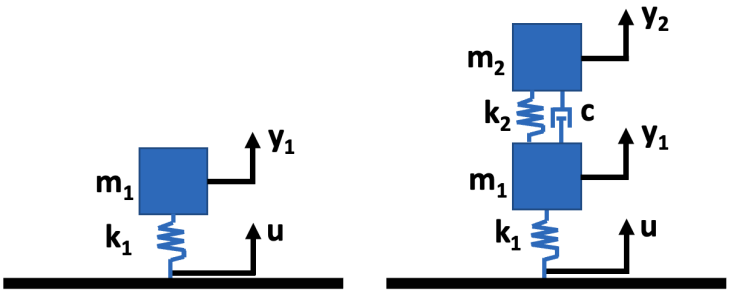

Figure 7.5.1: Vehicle models: SDoF (left) and 2DoF (right) corresponding to equations 7.3 and 7.4 respectively.

Corbally and Malekjafarian found their CP response expression to be relatively insensitive to errors in vehicle parameter estimation, which they deemed to be due to the CP response being comprised of the bridge response and road roughness effects. They stated that the bridge response was governed by the vehicle upper DoF mass m_2 and that the resilience of equation (7.4) to vehicle

parameter estimation error was because m_2 was not part of the CP equation. This interpretation is understandable, since equation (7.4) is derived from the equations of motion for a 2DoF mass-spring system subject to harmonic base excitation. However, some comments can be made regarding this formulation of the CP response equation:

- The equations of motion for a 2DoF system subject to harmonic base excitation do not include the effects of road surface profile, while in reality it does influence the vehicle response. This is acknowledged by Corbally and Malekjafarian; their numerical investigation study [220] considers modelling the vehicle wheel as a rigid disk in accordance with the procedure outlined by Chang et al. [171] and acknowledges that the bridge motion aspects of the CP response can be overwhelmed by road profile effects at higher vehicle speeds.

- The 2DoF quarter car equations of motion are in fact two coupled equations. In the CP response reproduced in equation (7.4) only one of these equations is used; the other is discarded. The unused equation of motion is shown in here as equation (7.5) in which m_2 represents the upper mass in the 2DoF quarter-car model, and y_1 and y_2 represent the displacement response at the lower and upper masses respectively, with a single superscript dot ($\dot{y}_1$ and $\dot{y}_2$) indicating the velocity. Equation (7.5) can be twice differentiated with respect to time (as for the derivation of the CP response [220]), yielding equation (7.6). Since it should evaluate to zero, they offer the potential to act as a measure of the accuracy of vehicle parameter estimation when considering vehicle responses gathered without the presence of significant road roughness (e.g. at low vehicle speeds and on smooth road surfaces).

- The purpose of the CP response equation is to suppress the effects of frequencies related to the vehicle kinematics, to afford more clear visibility of the bridge frequencies. However, the vehicle frequencies themselves relate directly to the vehicle's true properties (mass, stiffness and damping). Considering the CP response equation as an inverse filter designed to remove vehicle frequencies, it is counterintuitive that it could be resilient to errors in estimation of vehicle properties.

$$m_2\ddot{y}_2 + c\Big(\dot{y}_2 - \dot{y}_1\Big) + k_2\Big(y_2 - y_1\Big) = 0 \tag{7.5}$$

$$m_2\frac{d^2\ddot{y}_2}{dt^2} + c\Big(\frac{d\ddot{y}_2}{dt} - \frac{d\ddot{y}_1}{dt}\Big) + k_2\Big(\ddot{y}_2 - \ddot{y}_1\Big) = 0 \tag{7.6}$$

In order to investigate the queries posed above, equation (7.4) is considered as being comprised of four parts, each representing a constant (vehicle parameter ratio) multiplied by a time derivative of acceleration at vehicle DoF(s). When seeking to estimate the CP response, if accurate estimates were not available or

achievable it would be necessary to assume vehicle parameters. To reflect what is assumed to be common practice, two nominal vehicle models are assumed here for testing purposes, summarised in Table 7.5.1.

Parameter	Vehicle i	Vehicle ii
k_1	20,000 N/m	180,000 N/m
k_2	5,000 N/m	40,000 N/m
m_1	0.528 kg	
m_2	2.902 kg	
c_1	1x10^{-10} Ns/m	
c_2	117.7 Ns/m	336.9 Ns/m
ζ_1	35.6 %	37.5 %
ζ_2	58.2 %	55.7 %
f_{v1}/f_{b1}	0.76	2.16
f_{v1}/f_{b2}	3.81	11.33
f_{v2}/f_{b1}	0.19	0.54
f_{v2}/f_{b2}	0.95	2.83

Table 7.5.1: Representative vehicle models based on assuming parameters according to common methods from the literature. Proximal vehicle-to-bridge frequency ratios are highlighted.

For both vehicles, the total mass is matched to the measured experimental vehicle (section 7.4.1). The upper-to-lower DoF mass ratio, ϵ is selected from the middle of the range of normal quarter cars reported by Jazar [6]. Their spring stiffnesses are selected respectively to achieve approximate frequency matching between the axle hop frequency and the bridge second bending mode frequency (*vehicle i*) and separation between both vehicle frequencies and the first two bridge bending frequencies (*vehicle ii*). Damper coefficients are adopted assuming a damping ratio of 55%, using Jazar's equation [6], reproduced here as equation (7.7):

$$\zeta_2 = \frac{c}{2m_2\omega_2} \tag{7.7}$$

which is an approximation considered to be a common way of determining damping ratios for representative vehicle models. The target damping ratio is assumed to apply to the vehicle cabin bounce mode. Tyre damping is assumed to be negligible.

Based on the outcomes reported from the studies in chapters 5 and 6 (*vehicle i*) would be expected to induce VBI system non-stationarity and oscillations of instantaneous frequency at the contact point during traversals, while the outcomes from *vehicle ii* would be expected to approximate the moving mass condition. Moreover, *vehicle i* could be considered representative of the laboratory test vehicle, since the system identification outcomes presented in section 7.4.3 suggested a similar vehicle-bridge frequency match for the front axle quarter-car model.

Table 7.5.2 summarises the four summed parts (here called A, B, C and D) of the established contact point response (equation (7.4)) and the magnitudes of the associated vehicle parameter ratios for *vehicle i* and *vehicle ii*. By way of illustration, Figure 7.5.2 plots the magnitudes of these four parts of the CP response equation and shows the magnitude of each part multiplied by the root-mean-square value of the corresponding acceleration time derivative, taken from a sample simulated traversal from chapter 6.

Equation part	**Coefficient (parameter ratio)**	**Vehicle i**	**Vehicle ii**
A	m_1/k_1	2.64×10^{-5}	2.93×10^{-6}
B	c/k_1	5×10^{-15}	5.56×10^{-16}
C	k_2/k_1	0.25	0.22
D	k_1/k_1	1.0	1.0

Table 7.5.2: Parameter ratios for contact point response equation, for two vehicle models introduced in chapter 6.

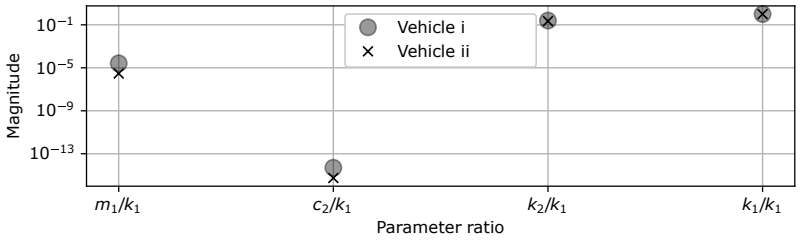

(a) Equation coefficients (parameter ratios).

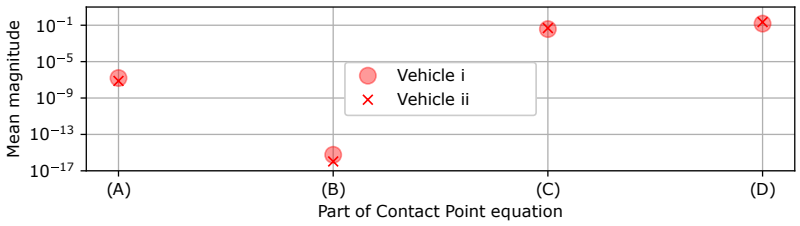

(b) Equation components.

Figure 7.5.2: Comparison of magnitudes of four additive components of established contact point response expression for vehicles i and ii.

7.5.2 Alternative simplified CP expression

It is clear that the established CP response expression (equation (7.4)) is almost entirely comprised of parts C and D, i.e. $(k_2/k_1) \times (\ddot{y}_1 - \ddot{y}_2)$ and $\ddot{y}_1$. Of this, $\ddot{y}_1$ makes up around 80% of the CP response. Parts A and B of the expression were found to be smaller than part D, by a significant factor (between 5 and 16 orders of magnitude). These trends were consistent for both vehicle models i and ii. Given these observations, a new simplified contact point expression is proposed, shown here as equation (7.8):

$$\ddot{u} = \frac{k_2}{k_1}\left(\ddot{y}_1 - \ddot{y}_2\right) + \ddot{y}_1 \tag{7.8}$$

which is comprised of only parts C and D of the established expression. This new expression has the clear benefit of only relying on knowledge of vehicle parameters k_2 and k_1, i.e. the suspension spring stiffness and effective tyre stiffness. It is plausible to assume that the suspension spring stiffness might be available by appeal to the vehicle manufacturer, and the effective tyre stiffness could be estimated using established methods as a function of manufacturer-supplied tyre properties and inflation pressure (which can be measured directly). Some researchers have proposed estimation of tyre contact forces using computer vision to recover the tyre properties from the specification cast into the tyre sidewall, and an estimate of inflation pressure based on sidewall deformation combined with on-vehicle tyre pressure measurements (Feng et al. [200], Feng and Leung [201], Martini et al. [202]), which suggests opportunities for estimation of CP response using the proposed new formulation even in situations where the manufacturer's information is not directly available.

It should also be noted that, in situations where the effective tyre stiffness is significantly larger than the suspension spring stiffness (i.e. $k_1 >> k_2$) the proposed new CP response expression further simplifies, shown here as equation (7.9):

$$\ddot{u} \approx \ddot{y}_1 \tag{7.9}$$

which offers further benefits: only one accelerometer is required (at the lower DoF) and no vehicle properties are required as long as the assumption that $k_1 >> k_2$ can be considered valid, suggesting a reduced instrumentation requirement for some vehicle classes when used for this purpose.

It should be noted that the new proposed CP response expressions (equations 7.8 and 7.9) are motivated based on consideration of only two vehicle models (*i* and *ii*). Although these vehicle models are understood to be representative of real vehicles from the literature as discussed in section 7.5.1, it is possible that other factors (such as nonstationarity of coupled VBI system frequencies during vehicle traversals) could influence the accuracy of CP response estimation. Therefore, in order to test the proposed simplified CP expressions for a range of vehicle-to-bridge frequency ratios, contact point responses from FE simulations (chapter 5) were used. From the range of vehicle parameters simulated in that chapter, those selected for use here were associated with vehicle-to-bridge

frequency ratios $f_{v1}/f_{b1} = 0.2$, $f_{v1}/f_{b1} = 5.0$, $f_{v1}/f_{b1} = 1.0$ and $f_{v2}/f_{b2} = 1.0$. The vehicle traversal speeds were *medium* and the upper-to-lower DoF vehicle mass ratio was $\epsilon = 5.5$. All of the modelled vehicles were undamped. All vehicle parameters are presented in Tables B.1.1 and B.1.2 in Appendix B.

Fig. 7.5.3 presents the outcomes of a study in which the estimated contact point responses using the established method (equation (7.4)) and the two proposed simplified methods (equations (7.8) and (7.9), recalling that the latter is simply the acceleration response from the axle-mounted accelerometer). Inspection of this figure yields the following observations:

- In all cases, the predictions from the established (equation (7.4)) and first proposed new method (equation (7.8)) are visually indistinguishable.
- In all cases, the predictions from the second proposed new method (equation (7.9), axle acceleration response) are very close to the predictions of the established or first proposed new method.
- All of the predictions are a relatively poor visual match to the true CP response, with the exception of the case when $f_{v1}/f_{b1} = 5.0$ where the predictions all show good agreement with the true CP response.

It is concluded that the proposed new simplified CP response expressions both appear to perform adequately compared to the established method. In the case of the first proposed new method (equation (7.8)) the performance was identical under visual inspection for all tested vehicle model configurations. This approach shows promise where the vehicle suspension spring and tyre stiffness are known or can be accurately estimated. The second simplified new method (equation (7.9)) shows promise to closely approximate the CP response when compared to the established method and would be preferable when $k_1 >> k_2$ can be considered a valid assumption, as the required sensor instrumentation quantity on the vehicle is reduced by 50%.

Overall, the investigation showed that estimation of contact point response using any of the tested methods only appears to be feasible for situations where the vehicle first mode frequency is significantly higher than the bridge first mode frequency. CP response estimation appears to be infeasible using acceleration responses from vehicle-mounted sensors in situations where bridge and vehicle modal frequencies are matched, or where the vehicles first mode frequency is much lower than that of the bridge. In these situations, estimation of the CP response may not improve visibility of bridge frequencies from vehicle-mounted sensors.

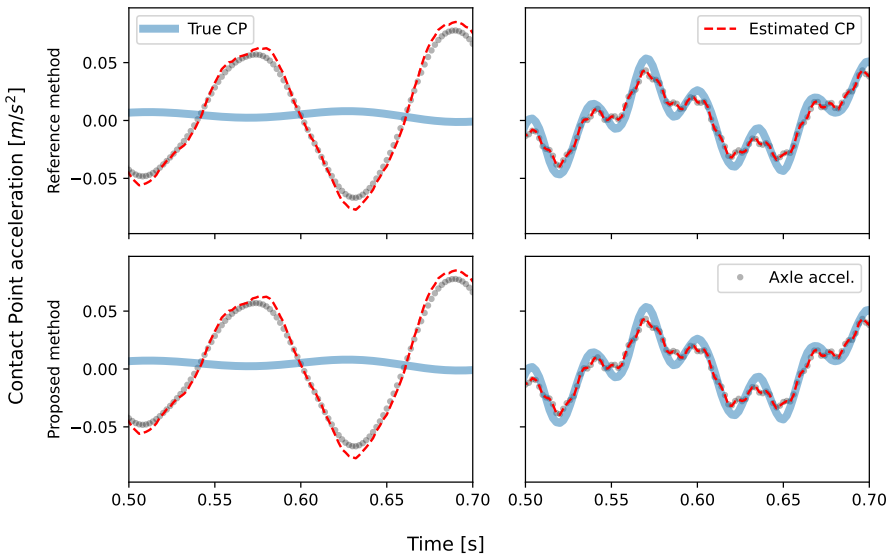

(a) $f_{v1}/f_{b1} = 0.2$ (left) and $f_{v1}/f_{b1} = 5.0$ (right)

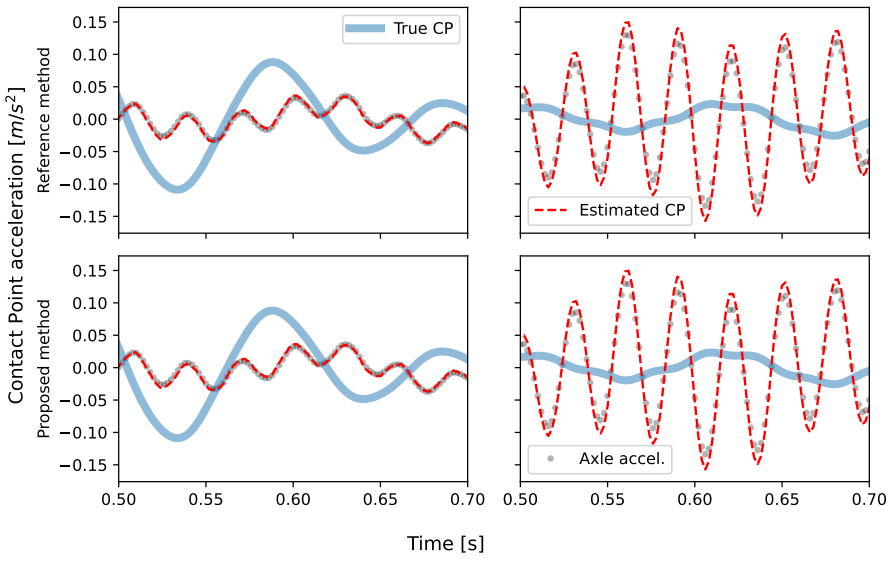

(b) $f_{v1} = f_{b1}$ (left) and $f_{v2} = f_{b2}$ (right)

Figure 7.5.3: Established and two proposed new methods for estimating CP response, compared to true CP response from FE simulations (chapter 5).

7.6 Frequencies present during traversal

This section presents analysis of the moving vehicle tests conducted using the laboratory-scale VBI model, as described at the beginning of the current chapter (sections 7.1 and 7.2). Table 7.6.1 summarises the vehicle traversals recorded during the physical testing for bridge added mass configurations *i*, *ii* and *iii* (Fig. 7.2.3). The vehicle trajectory during traversals was approximately along the centre line of the bridge, as indicated in Fig. 7.6.1. The vehicle was placed onto the pre-span roadway (as indicated in the figure) and the traversal began from that point. Following a traversal, the vehicle's orientation was reversed; subsequent traversals were therefore in opposite directions. A pause was included between subsequent traversals with the intention of allowing bridge and vehicle vibrations to dissipate.

Vehicle speed	**Bridge config.**	**No. of traversals**
Low	*Bridge i*	20
	Bridge ii	20
	Bridge iii	20
Medium	*Bridge i*	20
	Bridge ii	20
	Bridge iii	20
High	*Bridge i*	20
	Bridge ii	20
	Bridge iii	20

Table 7.6.1: Moving vehicle traversals across bridge - summary of bridge configurations and total number of traversals for each vehicle speed.

The period of the acceleration response data corresponding to the vehicle traversing the bridge span was identified by detecting local extrema in the acceleration time history, corresponding to the passage of the vehicle across the joints at each end of the bridge, in the manner outlined by Corbally and Malekjafarian [20]. This is illustrated in Fig. 7.6.2 which presents an example traversal. The portion of the acceleration signals representing the vehicle's traversal across the bridge is identified from the two prominent peaks in the vehicle front cabin sensor data.

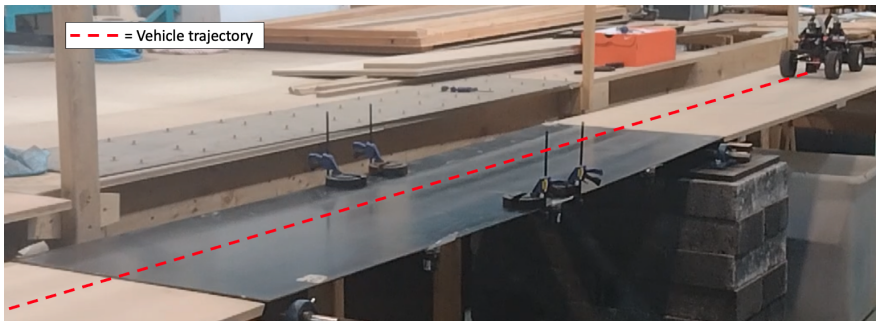

Figure 7.6.1: The approximate trajectory of the vehicle along the bridge.

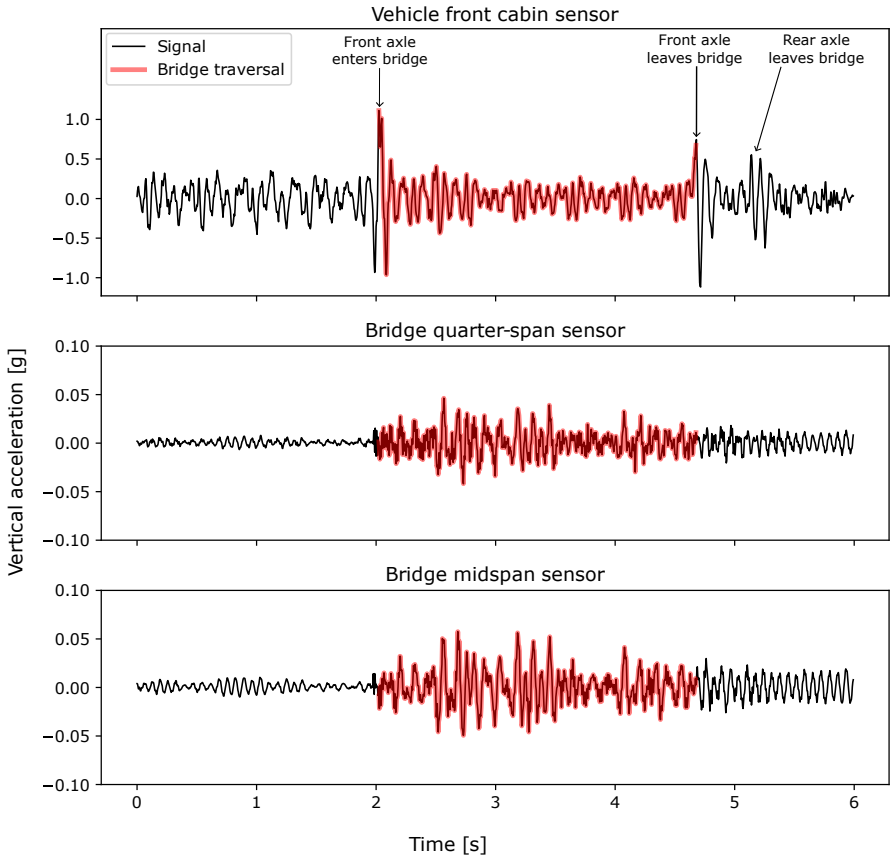

Figure 7.6.2: Acceleration data from example traversal, illustrating method of identifying vehicle-on-bridge sub-sample.

7.6.1 Contact point response

The contact point acceleration response was calculated for the vehicle traversals summarised in Table 7.6.1 using the acceleration response data from the test vehicle's front axle and front cabin sensors. A comparison was made between the proposed simplified CP response formulation (equation (7.8) and the established CP response (equation (7.4). The assumed vehicle properties used for CP response estimation are denoted as **present** for those from the vehicle system identification process presented in this thesis, and **C&M** for those based on Corbally and Malekjafarian's assumed vehicle properties ([19] [20] and as summarised in Table 7.4.3).

The ensemble power spectra (using Welch's method) for each of these CP response estimates were plotted for comparison. Figs. 7.6.3, 7.6.4 and 7.6.5 presents the comparison in the region of the expected bridge first bending frequency. These three figures relate to slow, medium and fast vehicle traversal speeds respectively. Three bridge configurations are included: *bridge i* (no added mass), *ii* (4 kg added at midspan) and *iii* (4kg added at quarter-span), all as indicated in Fig. 7.2.3. The figures also indicate the expected bridge frequencies: without a vehicle (denoted as *None*), and with a stationary vehicle at midspan (denoted *L/2*) or quarter-span (*L/4* or *3L/4*). Fig. 7.6.6 presents the outcomes for the slow vehicle traversal speed, in the vicinity of the expected vehicle front axle hop frequency. Similar plots for all vehicle speeds are presented in section D.2 in Appendix D, covering the expected frequency range for the first four bridge modes based on the identification process reported in section 7.3. All figures show power spectra which have been normalised to the square root sum-of-squares[1].

[1] Also known as l^2 or sometimes *Euclidean* normalisation.

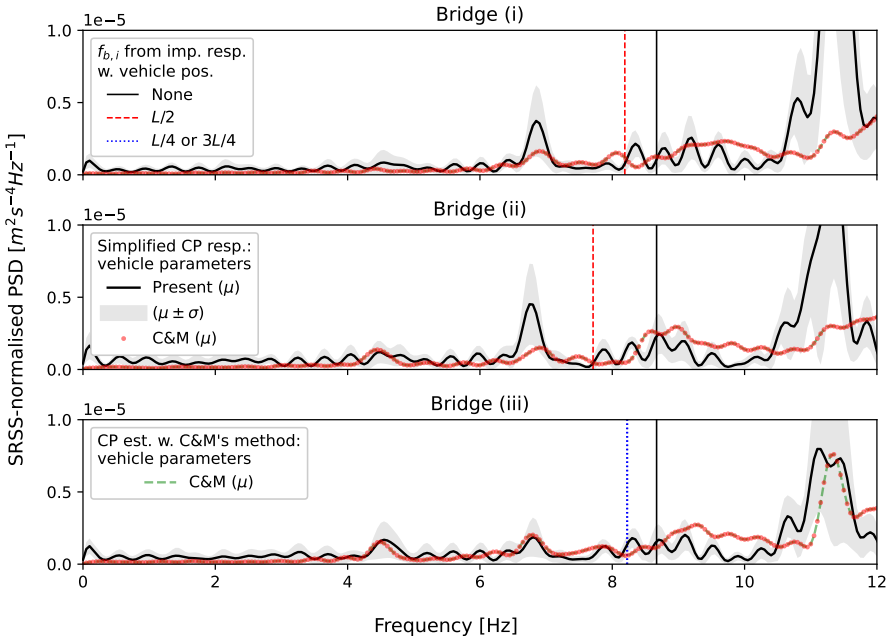

Figure 7.6.3: Power spectral density of contact point responses compared (**slow vehicle speed**).

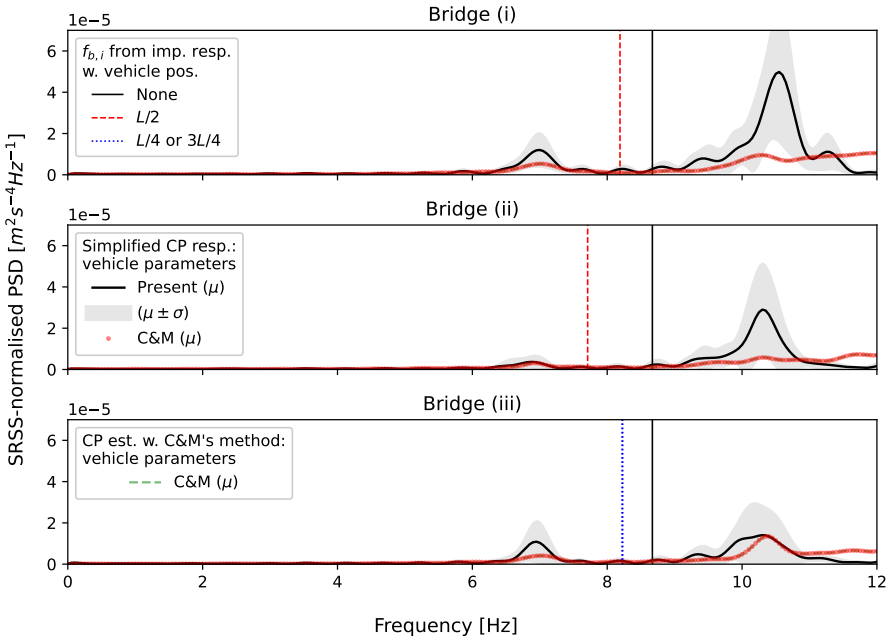

Figure 7.6.4: Power spectral density of contact point responses compared (**medium vehicle speed**).

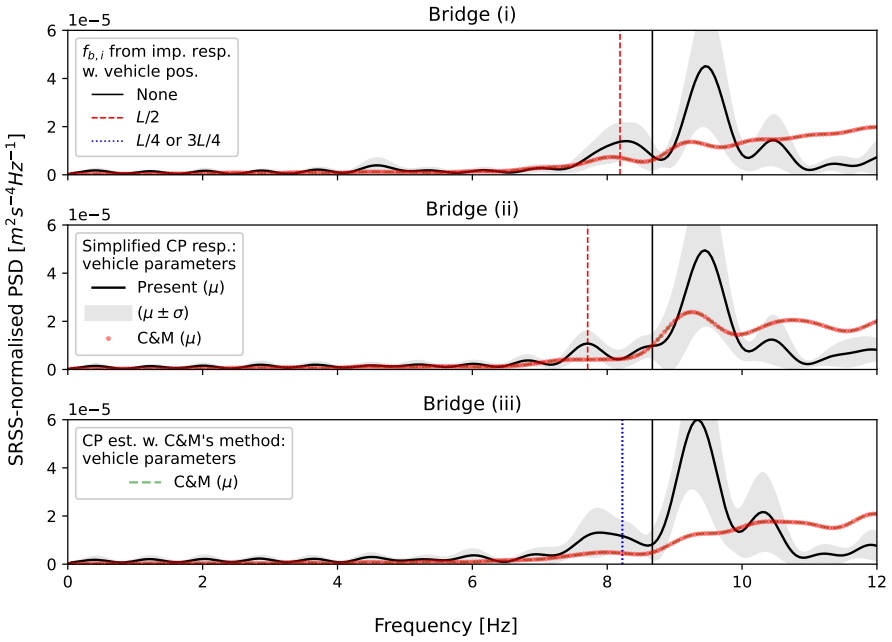

Figure 7.6.5: Power spectral density of contact point responses compared (**fast vehicle speed**).

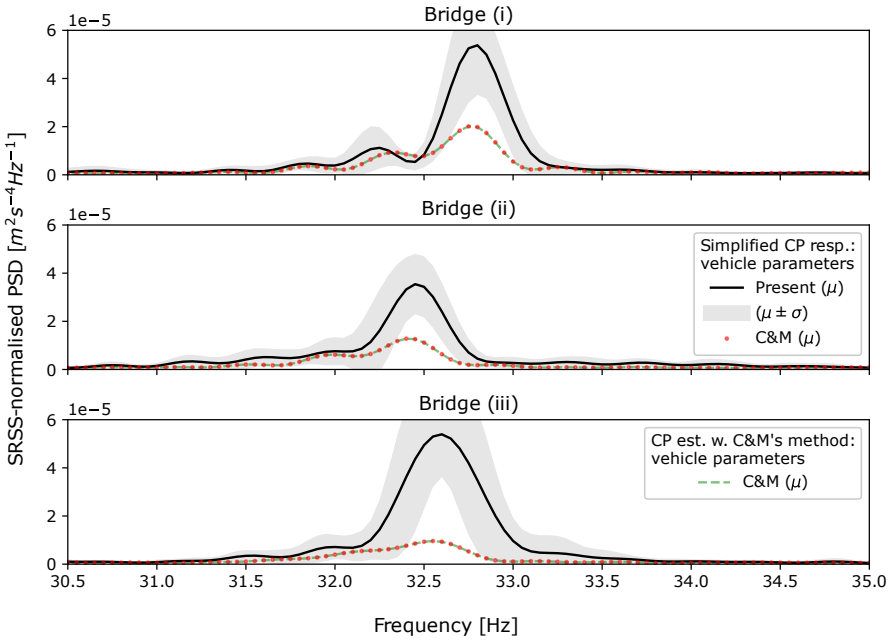

Figure 7.6.6: Power spectral density of contact point responses compared (**slow vehicle speed, frequency range around vehicle front axle hop mode**).

Comparison of the ensemble power spectra of estimated contact point response yields the following insights:

- **Visibility of bridge frequencies**
  - There is no clear and consistent visibility of the bridge first frequency, in contrast with observations by Corbally and Malekjafarian [20] who were able to see a distinct peak in the frequency domain for the bridge first frequency (slightly above 8 Hz), with particular prominence at the low vehicle speed, having similarly considered an ensemble of multiple traversals. This suggests that the lack of bridge first frequency visibility may be related to experimental conditions and procedure.
  - No clear and distinct frequency peaks are visible relating to the bridge's second bending frequency, or either of the two frequencies associated with torsional response below 50 Hz.
- **Method of contact point estimation**
  - The outcome of the proposed contact point response expression (equation (7.8) is visually indistinguishable from the established method (equation (7.4)). This serves to further confirm that the proposed new method is suitable.
- **Assumed vehicle parameters**
  - The assumed vehicle properties do appear to affect the frequency-domain outcomes, in terms of peak location and prominence.
- **Visible differences**
  - The frequencies (peak location and prominence) in the estimated CP response do appear to be affected by the bridge configuration (*i*, *ii* or *iii*), suggesting that VBI-induced frequency changes may be visible in the vehicle-related aspects of the CP response.

The above commentary suggests that the collected data do not permit visibility of the bridge frequencies, and that this is likely to relate to the experimental conditions and method rather than the data processing strategy. In other words, the frequency domain contact point response appears to be dominated by vehicle-related information. However, changes in vehicle-related frequency domain outcomes are observed to be correlated with changes in bridge configuration. Additionally the identified vehicle axle hop frequency is close to the identified bridge second bending mode frequency. This suggests that, despite lack of direct visibility of bridge frequencies, it may nevertheless be possible to detect bridge condition based on the change in vehicle response due to VBI. The method presented in chapter 6 was effective at detecting damage (modelled as local stiffness reduction) for situations with proximal vehicle and bridge frequencies. The laboratory data presented in the current chapter represent damage as a local addition of mass. Section 7.7 presents a test of the performance of the proposed damage detection method using this data.

7.6.2 Contact point residual

Prior to attempting damage detection based on vehicle response, the contact point residual was calculated in order to further confirm that direct visibility of bridge frequencies was not feasible. The outcomes are illustrated in Fig. 7.6.7 which presents the estimated CP residual (CPR) for the slow vehicle traversal speed. The contact point residual is intended to reduce the effects of convolutive noise caused by the road surface profile, thus increasing the signal-to-noise ratio (considering the signal to be comprised of bridge-related frequencies). It is based on subtracting time-shifted acceleration responses from two following axles and the method adopted here was outlined in section 2.8.3). The presented results further confirm that direct recovery of the bridge frequencies does not appear to be feasible since the CP residual is also dominated by vehicle-related frequencies. No clear and distinct peaks are apparent at the expected bridge frequencies. Similar outcomes were noted for the medium and fast vehicle traversal speeds, and figures substantiating this are included in section D.3 in Appendix D.

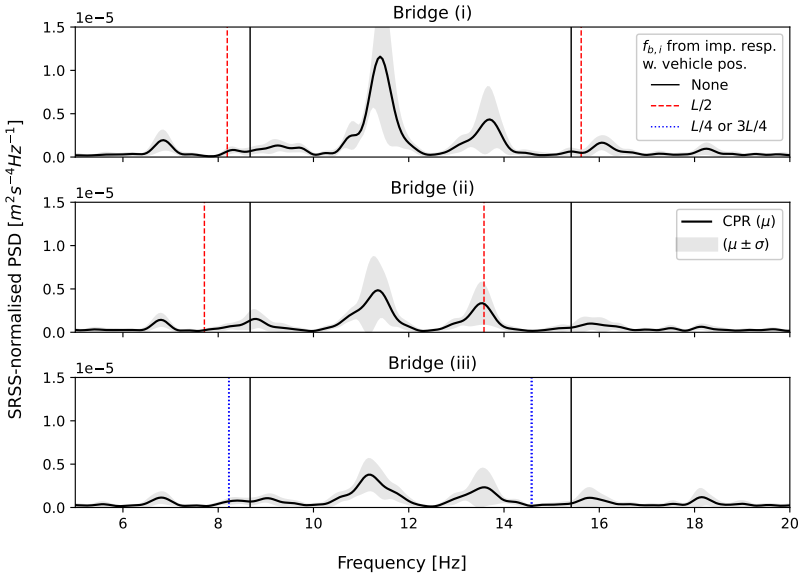

(a) Lower frequency range

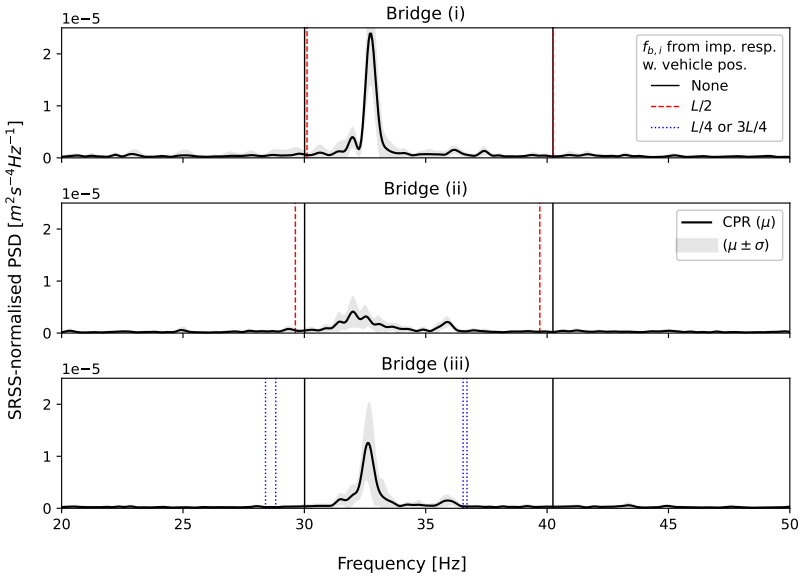

(b) Higher frequency range

Figure 7.6.7: Power spectral density of contact point response **residuals** compared - **slow vehicle speed**; frequency range as indicated.

7.7 Damage detection: one-class classification

The ensemble averaged contact point responses presented in section 7.5 appeared to be dominated by vehicle-related frequencies, with no clear and consistent indication that bridge frequencies could be directly recovered. However, vehicle-related aspects of the CP response appeared to change depending on the bridge configuration. This observation suggests that the damage detection method demonstrated in chapter 6 might be suitable for use with this dataset. Specifically, the damage detection method to be used in the current chapter is the single-class method outlined in section 6.5.4 and demonstrated using synthetic vehicle response data in section 6.5.6.

7.7.1 Time-frequency contact point response

When using images as input features in machine learning it is common to reduce the dimensions of the features where possible, in support of computation efficiency. If down-sampled input feature resolutions are sufficient for the task at hand, they are preferable. For this reason, the predictive utility of two input image resolutions will be compared here. Fig. 7.7.1 illustrates this for a single traversal. The higher resolution (200 x 200 pixels) matches that used in chapter 6; the lower resolution (28 x 28) was selected to match the resolution of the images in the Modified National Institute of Standards and Technology (MNIST) dataset [443], a widely-used example for benchmarking the performance of generative and discriminative models that use images as input features. Axis labels and units are omitted from Fig. 7.7.1; since the figure shows images, axis labels would add little insight beyond the difference in image resolution which is apparent by inspection.

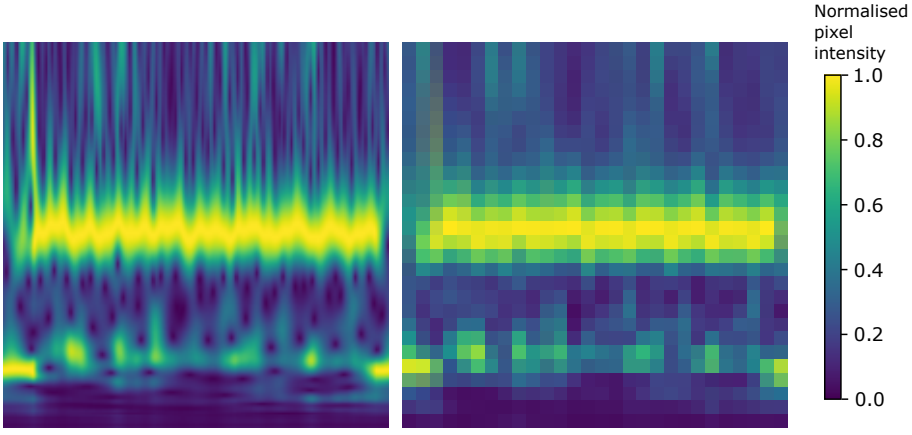

(a) Higher res.: 200x200 pixels (b) Lower res.: 28x28 pixels (c) Scale

Figure 7.7.1: Example ST contours of CP responses from a single traversal, illustrating the two image resolutions compared.

In addition to input feature resolution (pixels) a comparison is made between the frequency range represented in the Stockwell transform contours. The results presented in chapter 6 compared ST frequency bandwidths containing the expected first bridge frequency or second bridge frequency (*narrowband*) to those containing both (*midband* or *wideband*). The results were found to be more favourable considering the narrowband ST contours approximately centred on the bridge second mode, or containing both first and second modes. Given the apparent dependence on bandwidth, a similar comparison is presented here for the data derived from laboratory-scale testing. The narrowband resolution tested is focused on the expected bridge second bending mode frequency based on the previous promising outcomes for this in chapter 6. The difference between the FE and laboratory bridge second mode frequency explains the difference in bandwidth (25-50 Hz 1compared to 20-45 Hz) in order that the expected bridge frequency was close to the band centre. Table 7.7.1 summarises the ST bandwidths considered in each chapter.

Stockwell transform bandwidth	**Chapter 7 (finite element)**	**Chapter 8 (laboratory)**
Narrow (first bending mode)	4-16 Hz	-
Narrow (second bending mode)	25-50 Hz	20-45 Hz
Mid (first and second modes)	4-50 Hz	4-45 Hz
Wide (first and second modes)	-	0-65 Hz

Table 7.7.1: ST bandwidths compared in the damage detection exercises using finite element- and laboratory-derived data.

7.7.2 Principal component latent space projections

Figure 7.7.2 presents first and second principal components projected for the ensemble of traversals summarised in Table 7.6.1. The figure compares slow, medium and fast vehicle speeds and two ST image resolutions, for the *narrow* bandwidth ST contours.

Similar projections for the other two ST contour bandwidths are presented in section D.4 of Appendix D. Visually, the projected data do appear to cluster in relation to the bridge configuration (most clearly in Fig. 7.7.2 for the slow vehicle speed). However, the clusters are generally overlapping. If the clusters did not overlap it would imply that damaged and healthy data are trivially separable for each bridge configuration. Overlapping clusters do not necessarily imply that the data are not separable; on the contrary it may be possible to distinguish between healthy and damaged bridge conditions using this method but further justification is required and is explored in the following sections.

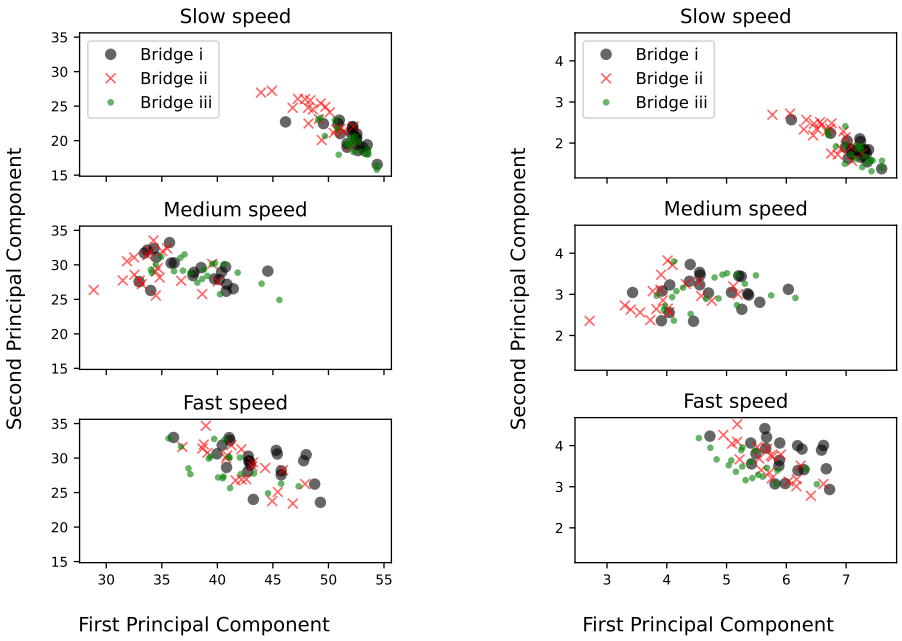

(a) Higher resolution

(b) Lower resolution

Figure 7.7.2: First and second Principal Components projected based on the ***narrow*** **(20-45 Hz)** bandwidth ST contours. Three vehicle speeds and two ST image resolutions compared for three bridge configurations.

7.7.3 Damage detection process overview

The adopted damage detection method was demonstrated in principle in chapter 6 by presenting the trend of increasing separation in latent space as a result of increasing damage intensity. It was proposed that a decision boundary could be drawn around the projected points representing the healthy bridge condition, with points outside the boundary assumed to represent bridge damage and the damage severity indicated by the Euclidean distance from the decision boundary. However, the class overlap apparent from inspection of the latent space projections (for example Fig. 7.7.2) suggests that the decision boundary would be difficult to determine without significant risk of mis-classification (damaged data points erroneously identified as healthy or vice-versa). Nevertheless, class overlap does not necessarily imply that the classes cannot be distinguished. In this chapter it is therefore proposed to explore the potential for separability of data relating to traversals of healthy and damaged bridge conditions using two methods. The first compares distributions of projected data points to determine the relative likelihood that they represent samples from differing populations (i.e. different bridge conditions). The second method directly considers whether the differences between means of each sample are statistically significant. The data processing and damage detection pipeline adopted in this chapter is presented in Fig. 7.7.3. The two methods are discussed in more detail in the following sections.

It should be noted that the damage severity index explained in chapter 6 was based on separation in two-dimensional latent space. However, visual inspection of the projected clustered data in the current chapter (for example Fig. 7.7.2) suggests that most of the difference between damaged and healthy conditions is captured by the first principal component. For this reason, in the current chapter each principal component will be considered separately during the process outlined in Fig. 7.7.3, meaning that separation of healthy and damaged data will be considered in one dimension, but for both the first and second principal components. It is anticipated that this approach will allow the data to be separated, while maintaining interpretability of the methods used.

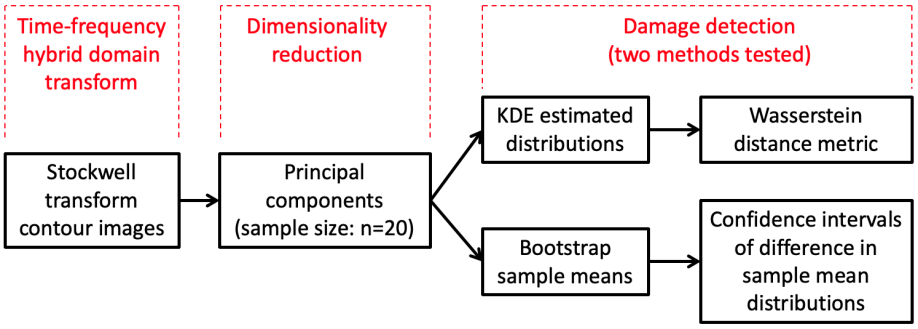

Figure 7.7.3: Overview of data processing and damage detection pipelines adopted in this chapter.

Given the observations noted above, the primary challenges to be addressed in the damage detection process in this chapter are:

- Healthy and damaged distributions overlapping in latent space projections (risk of mis-classification of damaged data if using the decision boundary approach)
- Most variation in latent space associated with first principal component (meaning that Euclidean distance damage metric is not necessary, since single-dimension distance would be sufficient)

It is therefore proposed to directly compare the distributions for each principal component in latent space. However, it is also visually apparent that the projected data do not appear to be normally-distributed (see section 7.7.4). This precludes the use of any statistical methods for comparison of small-sized samples which assume normally-distributed data. Collectively these challenges motivate an alternative approach to damage detection compared to that outlined in chapter 6. The damage detection methodology explored in the current chapter (shown graphically in Fig. 7.7.3) can therefore be summarised as:

1. Generate time-frequency contour images representing vehicle traversals of known healthy and damaged bridge conditions from contact point acceleration responses, using Stockwell transform (ST)
2. Project ST contours into reduced-dimension latent space using principal component analysis (PCA)
3. Compare distribution of data representing healthy and damaged conditions in latent space, for each of the first two principal components in turn. Two methods to be tested for comparison of the distributions, given their apparent non-Gaussian nature:
   (a) Estimate underlying distributions for each principal component using kernel density estimation (KDE). Compare healthy and damaged conditions using Wasserstein distance metric (a non-parametric measure of difference in distributions). This method is suitable for use with non-Gaussian distributions
   (b) Use bootstrapping to generate approximately Gaussian distributions of sample means. Use confidence interval approach to determine if these distributions show a statistically significant difference between data from healthy and damaged bridge conditions

7.7.4 Estimated sample distributions

Distributions of each of the projected principal components were produced using kernel density estimation. Figures 7.7.4 and D.5.1 indicate the first PC distributions, with similar plots for the lower resolution ST contours and the second PC distributions included in section D.5 in Appendix D.

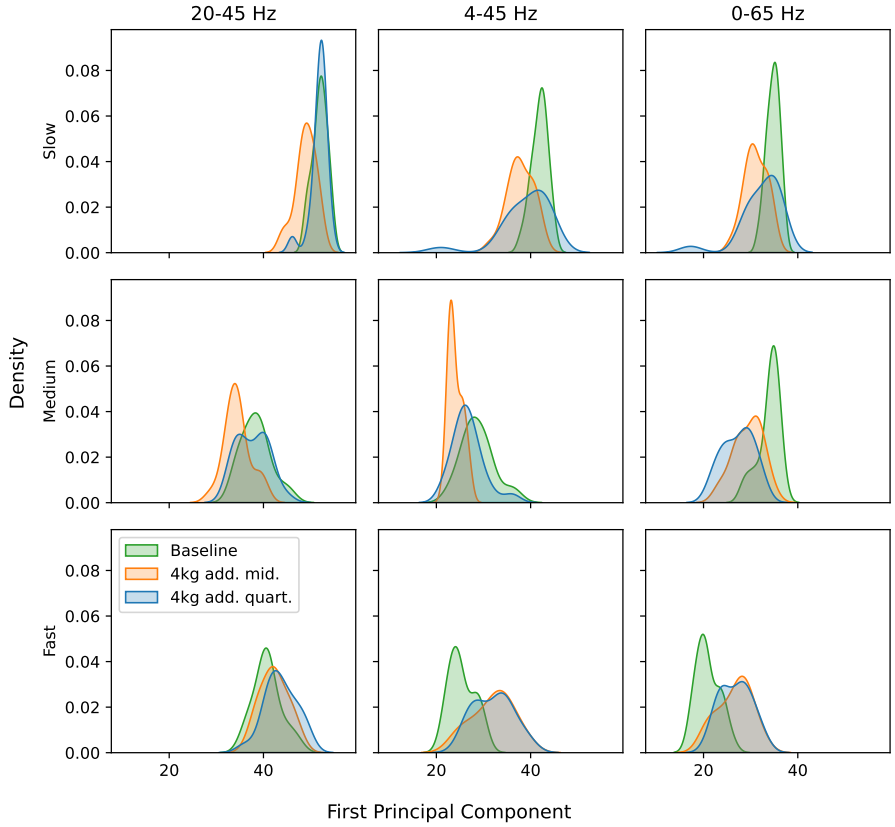

Figure 7.7.4: Estimated distributions (KDE) of first principal component from higher-resolution ST images.

Visual comparison of the estimated distributions suggests the following:

- The distributions do not all appear Gaussian, with some appearing to have multiple peaks.
- There appears to be some difference between the baseline healthy case (*bridge i*) and the damaged cases (*ii* and *iii*).

Similar observations can be made regarding the estimated distributions included in section D.5 of Appendix D.

7.7.5 Wasserstein distance metric

Figure 7.7.5 presents a comparison of the 1-Wasserstein distance (WD) metric, comparing the two damaged bridge configurations *ii* (dam. mid.) and *iii* (dam. quart.) to the baseline *i* (healthy). In order to illustrate the trend, a comparison of *i* to itself is also plotted, resulting in a WD of zero as expected. The comparisons are in each case between the KDE-derived empirical distributions (as shown in Figure 7.7.4 and the figures in section D.5 of Appendix D).

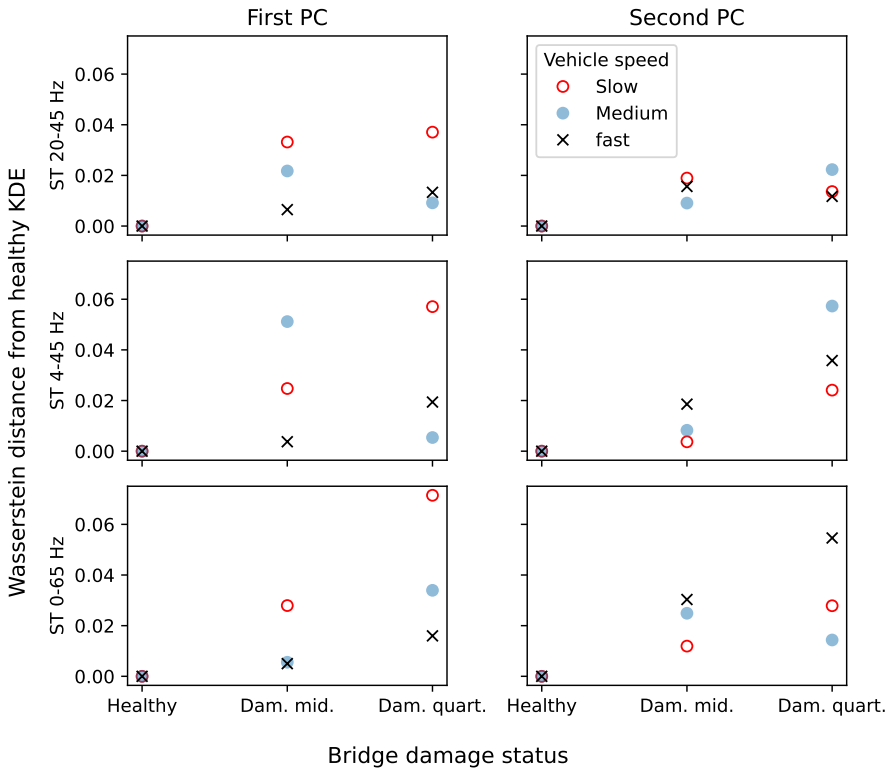

Figure 7.7.5: 1-Wasserstein Distance metric comparison for higher-resolution ST contour images.

Similar comparisons for the lower-resolution ST contour images are shown in Fig. D.6.1 in section D.6 of Appendix D. A comparison of the trends of WD suggests:

- For slow and fast vehicle speeds, quarter-span damage (bridge configuration *iii* results in a larger WD than midspan damage (bridge configuration *ii*), with the exception of the *narrow* bandwidth ST contours for the second PC.

- Generally, the first PC results in larger WD than the second PC for both damage locations.
- Figure D.6.1 shows that the relative trends (between PCs, bandwidths and speeds) for lower-resolution ST images match those for higher-resolution, but that the reduction in image resolution results in an increased absolute WD, suggesting counter-intuitively that reducing the image resolution can amplify the absolute outcomes without apparently affecting the relative trends.

7.7.6 Difference in sample means distributions

This section presents a statistical test of similarity of the projected principal components. The estimated sample distributions of PCs (for example Fig. 7.7.4) are not obviously Gaussian, with some appearing to feature multiple peaks and/or skew. Additionally, the sample size is relatively small ($n = 20$) meaning by convention that the central limit theorem should not be assumed to apply, i.e. the sample means cannot be assumed to be representative of population means. To counter this and permit comparison of a representative mean value for each sample, the samples are bootstrapped. Bootstrapping is a common strategy in statistics to address non-normal data, and consists of "empirically constructing the sampling distribution of estimates" (Pek et al. [444]) by repeatedly re-sampling (with replacement) from each original sample and calculating the mean of each re-sampled group (Sainani [442]). This results in a collection of estimates of the mean which do tend to follow a normal distribution, if the number of re-samples is sufficiently large for the central limit theorem to apply. The resulting statistic after bootstrapping retains the native units, in comparison to other strategies to address non-normal data such as transforming the sample by taking the log (Sainani [442]). Here, the implementation of bootstrapping used was from the open-source Python library *SciPy* [445]. The default number of re-samples (9,999) was adopted, along with the default confidence interval on the bootstrap distribution of 0.95.

The distributions of bootstrapped sample means will be compared. To do so in a statistically valid manner, a null and alternative hypothesis are stated to allow comparison of two samples, known to come from traversals of a healthy and damaged bridge respectively:

- **H0:** The samples appear to be from the same (healthy) population since their distributions of bootstrapped sample means do not appear to differ.
- **H1:** There is a statistically significant ($p < 0.05$, two-tailed) difference between the two distributions of bootstrapped sample means, implying that one is from a traversal of a healthy bridge and the other a damaged bridge.

As stated, the conventional significance level of 95% is adopted. The confidence interval is assumed to be two-tailed, implying that while a significant

difference is sought, no assumption is made regarding whether the healthy or damage bridge will result in a larger or smaller mean value after projection into the latent space.

In order to facilitate a comparison between data from healthy and damaged bridge traversals, distributions of the difference of bootstrapped means were constructed. To illustrate, if comparing two distributions of bootstrapped means A and B, the distribution of differences would have mean $\mu_D = \mu_A - \mu_B$ and standard deviation $\sigma_D = \sqrt{\sigma_A^2 + \sigma_B^2}$. If a 95% two-tailed confidence interval on the distribution of differences crosses zero then the distributions A and B are not considered significantly different and the null hypothesis is accepted. If the 95% confidence interval does not cross zero then the null hypothesis is rejected and the alternative hypothesis accepted, implying that a statistically significant difference is detected between A and B at the stated significance level. This approach is in accordance with normal practice for comparison of distributions. Figure 7.7.6 illustrates these distributions of differences for input features from *wideband* (0-65 Hz) ST contour images, with damage at bridge midspan and quarter-span (*bridge ii* and *iii*) compared to the healthy baseline (*bridge i*) for slow, medium and fast vehicle traversal speeds and the first two PCs. The subscript i refers to the healthy bridge configuration (e.g. $\mu - \mu_i$ refers to the distribution of differences in sample mean compared to bridge configuration i). This figure relates to higher-resolution ST contour images as inputs. Section D.7 in Appendix D includes similar plots for the lower-resolution ST contour images, and the outcomes for both image resolutions for *midband* and *narrowband* ST bandwidths.

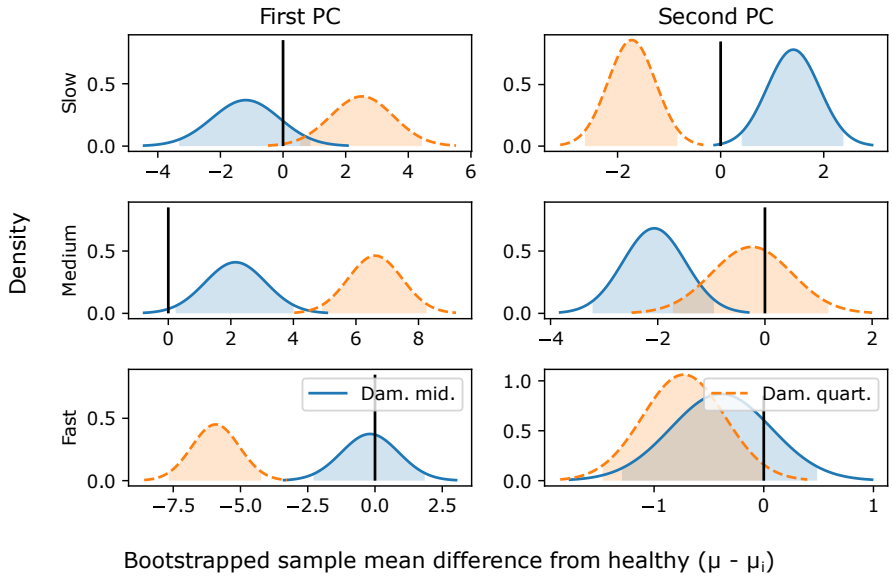

Figure 7.7.6: Gaussian probability density functions for differences in bootstrapped sample means (ST 0-65 Hz, higher resolution). 95% confidence intervals (two-tailed) shaded. Original data are first (left) and second (right) principal components.

Grouping the comparisons by damage location and PC, Table D.7.1 in Appendix D presents whether the null hypothesis was accepted or rejected. Considering all of the ST contour bandwidths for each damage location and PC, Table 7.7.2 summarises the proportion of times that the null hypothesis was rejected implying that the difference in distributions was statistically significant ($p < 0.05$, two-tailed); i.e. successful detection of damage. This demonstrates that midspan damage was detected in less than 50% of cases for both PCs, while damage at quarter-span was consistently detected in more than 50% of cases using the first PC. The best damage detection rate related to the higher-resolution ST contour images, resulting in successful detection in 77.8% of cases.

Accept alternative hypothesis (data is from traversal of damaged bridge)

LOWER RESOLUTION ST				HIGHER RESOLUTION ST			
First PC		Second PC		First PC		Second PC	
Dam. mid.	Dam. quart.	Dam. mid.	Dam. quart.	Dam. mid.	Dam. quart.	Dam. mid.	Dam. quart.
33.3%	66.7%	33.3%	44.4%	44.4%	77.8%	44.4%	44.4%

Table 7.7.2: Summary of midspan and quarter-span null hypothesis rejection rates, summed for all vehicle traversal speeds and ST contour bandwidths.

7.8 Acceleration amplitude ratios

The damage detection outcomes presented in section 7.7 appeared to show consistency with the demonstration of the method in chapter 6. However, bridge frequencies were not clearly and consistently visible in the acceleration power spectra (from ensembles of vehicle-mounted accelerometer response data) presented in section 7.6, an outcome which is not consistent with prior experimental outcomes using the same physical test apparatus (Corbally and Malekjafarian [20] in which the bridge first frequency was visible as a distinct prominent peak. In contrast, the spectra presented in section 7.6 were dominated by vehicle frequencies. This implies:

- Damage detection achieved here is likely to relate to the changes in vehicle response due to VBI as proposed in chapter 6, rather than direct visibility of changes in bridge frequencies.
- Excitation associated with vehicle-related frequencies may have been suppressed in prior work in a manner not achieved here.

To further confirm this, the ratio between vehicle and bridge acceleration amplitudes was explored. This ratio was found to be critical to accurate detection of bridge frequencies in a parametric study by Yang et al. [21]. Figure 7.8.1 presents their proposed relationship between the acceleration amplitude ratio at the start of the traversal, and the likelihood of detecting the bridge frequency. This outcome related to exploration of the closed-form analytical expression for VBI considering both the bridge and vehicle as SDoF systems.

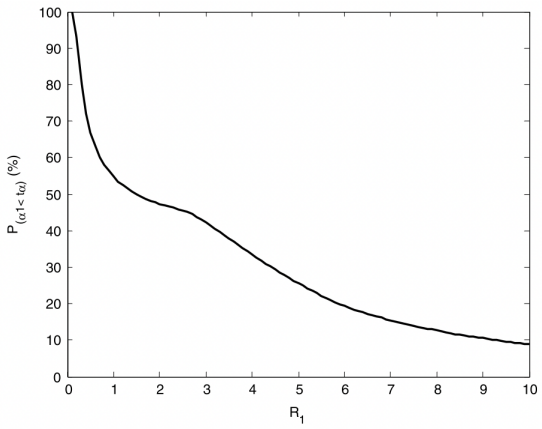

Figure 7.8.1: Probability of detecting the bridge frequency as a function of initial vehicle-to-bridge acceleration amplitude ratio for a single mode. Reproduced from Yang et al. [21].

To facilitate a comparison with the experimental outcomes from this thesis, a frequency bandpass filter was applied to the acceleration signals from the

vehicle- and bridge-mounted sensors. The filter was approximately centred on the expected bridge frequency, as summarised in Table 7.8.1. The first and second bridge bending modes are considered. The bridge sensor location was selected based on the mode under consideration (since the midspan and quarter-span locations are expected to relate to the highest modal participation for the first and second bridge bending modes respectively, based on the identified mode shapes summarised in section 7.3).

Bridge bending mode	**Frequency bandpass filter applied**	**Bridge sensor location**
First	6.4 – 10.4 Hz	Midspan
Second	28 – 32 Hz	Quarter-span

Table 7.8.1: Frequency bandpass filter limits applied in study of vehicle-to-bridge acceleration amplitude ratios.

As indicated in Fig. 7.8.1 Yang et al. [21] found the probability of detecting the bridge frequency to reduce rapidly as the vehicle-to-bridge initial acceleration amplitude ratio increased in the range 0–1. The evolution of this ratio during the traversal is shown in Fig. 7.8.2 for traversals of the healthy (configuration i) bridge with the frequency bandpass filter limits set to capture the expected first bending mode frequency. A similar plot is included here for the second bending mode frequency range (Fig. 7.8.3). The figures include horizontal lines indicating 10%, 25% and 50% probability thresholds from Fig. 7.8.1. Although the ratio defined by Yang et al. strictly relates to the initial ratio (at the start of the vehicle traversal period) it is informative to also observe the evolution of the ratio during the traversal. Comparison of these figures suggests:

- Initial vehicle-to-bridge acceleration amplitude ratios suggest a low probability of detection for the second bridge bending frequency, and an extremely low probability for the bridge fundamental frequency.
- During the traversal the ratio reduces in all cases, but the lowest values achieved (implying the highest detection of bridge frequency) consistently relate to slow and fast vehicle traversal speeds. The ratio is higher for the medium vehicle speed, with this being most apparent for the bridge fundamental frequency. This observation may explain the inconsistencies noted with detection of damage at different vehicle traversal speeds.
- The highest probability of detection achieved at the beginning of the traversal period was in the region of 25% and was associated with the bridge second bending frequency.
- The highest probability of detection achieved at any point during these traversals was in the region of 50% and was associated with the bridge first and second bending mode frequencies for at least some of the vehicle speeds and vehicle sensor positions.

- Based on visual inspection, the ratio was more variable between individual traversals when considering the bridge second bending mode frequency, but it should be noted that greater variability appears to be associated with the medium vehicle speed for both frequencies.

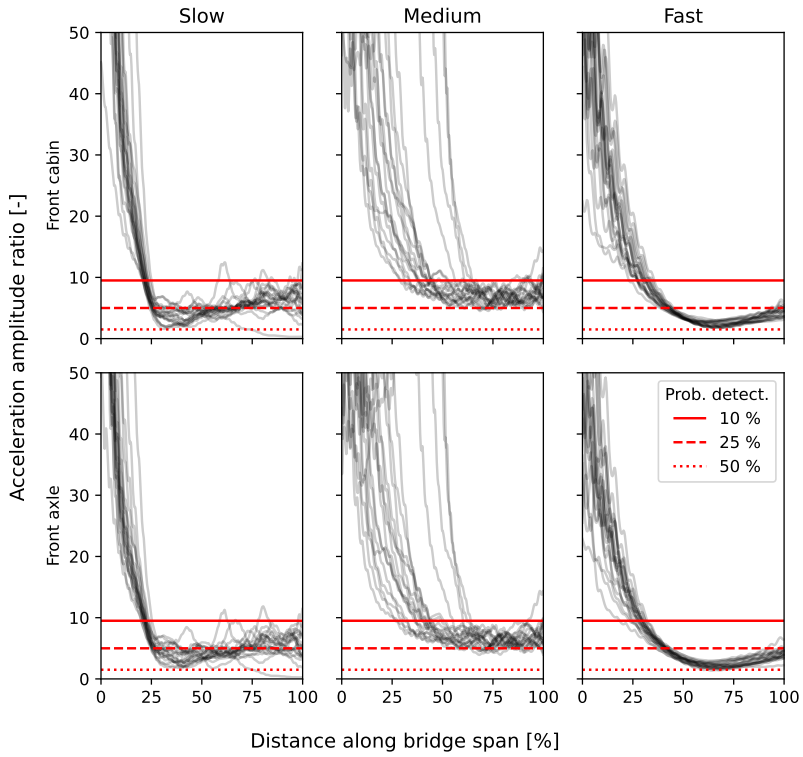

Figure 7.8.2: Acceleration amplitude ratios: vehicle (front axle and cabin sensors) compared to bridge (one **midspan** sensor) for healthy bridge (**configuration *i***) and three vehicle speeds in region of expected **first** bending mode frequency.

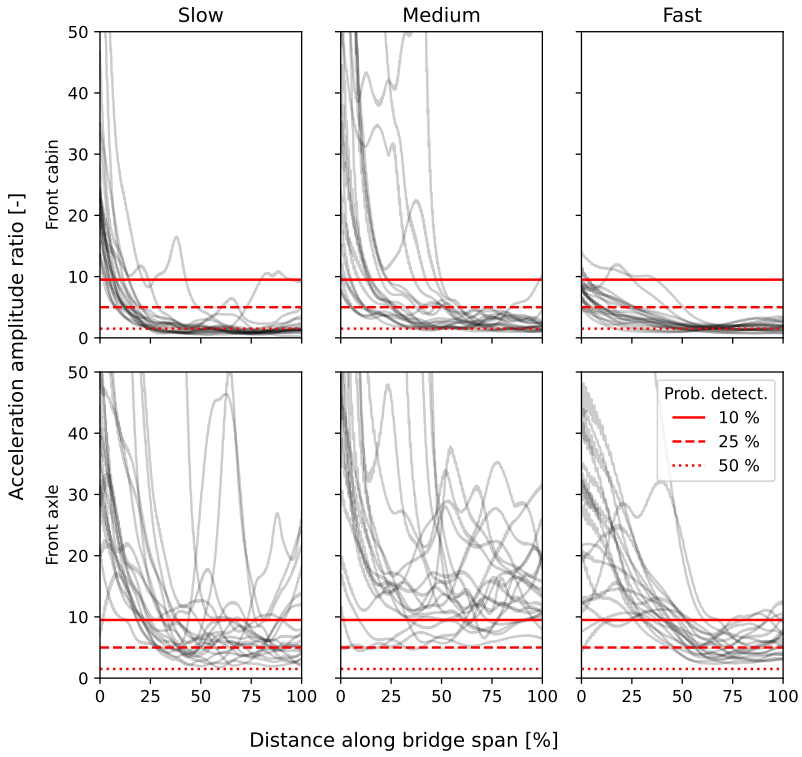

Figure 7.8.3: Acceleration amplitude ratios: vehicle (front axle and cabin sensors) compared to bridge (one **quarter-span** sensor) for healthy bridge (**configuration *i***) and three vehicle speeds in region of expected **second** bending mode frequency.

Figures D.8.1 and D.8.2 in section D.8 of Appendix D present the evolution of vehicle-to-bridge acceleration amplitude ratios for bridge configurations *ii* (considering the bridge midspan response) and *iii* (considering the bridge quarter-span response). Similar trends are apparent as observed for bridge *i*: greater variation between traversals typically associated with the medium vehicle speed, and greater probability of detection (lower ratio at the start of the traversal period) associated with the bridge second bending frequency.

7.9 Discussion

7.9.1 Bridge system identification

This chapter presented outcomes from a programme of laboratory-scale modelling of VBI. Bridge modal parameters were identified using an output-only time domain method applied to free vibration records of impulse (hammer tap) response. The outcomes were compared to prior published results for this bridge model and good agreement was noted. Parameters were also estimated for a combined vehicle-bridge system, considering a range of positions for a stationary vehicle and a range of bridge configurations with respect to added static mass. The identified bridge parameters were fitted to a two-dimensional finite element model, confirming that the bridge model adopted in finite element simulations in previous chapters 5 and 6 can be considered as representative of the physical laboratory bridge model.

7.9.2 Vehicle system identification

Vehicle modal parameters were identified using an output-only time domain method applied to free vibration records of impulse (hammer tap) response. The identified frequencies and damping ratios were fitted to two-degree-of-freedom quarter-car models representing the vehicle's front and rear axle and cabin. A comparison was made to parameters assumed for this vehicle model in previous work by others. The comparison revealed that the vehicle appears to differ significantly from those assumptions in terms of frequencies and damping ratios.

The frequency domain output-only method of vehicle parameter estimation from chapter 4 was tested on the acceleration records from driving the vehicle along the laboratory floor and the front axle hop frequency identified from impulse response parameter estimation exercise was visible. Otherwise, the results appeared to be generally dominated by frequencies relating to vehicle wheel out-of-roundess and this was noted to be apparent at all three vehicle speeds with frequency peaks appearing scaled to the wheel rotation rate. The potential for spurious (false positive) identification of the bridge fundamental frequency was noted for vehicle traversals at the fast speed, since a clear peak was visible in the power spectra at this approximate frequency even though the spectra related to vehicle motion on the laboratory floor rather than across the bridge.

7.9.3 Contact point response estimation

Outcomes from chapters 5 and 6 along with those reported in the literature had suggested that the acceleration response of a virtual sensor located at the contact point between vehicle and bridge would be more effective for damage detection compared to the physical sensors on the axle and cabin degrees-of-freedom. The established expression for contact point response estimation was interrogated. Several parts of the established expression were noted to be extremely small in comparison to the remaining components, meaning that changes in these

parts of the expression would not be expected to lead to significant impacts on the estimated contact point response. A novel simplified expression was therefore proposed with the benefit of relying only on vehicle parameters (suspension spring and effective tyre stiffness) which could be confirmed by the manufacturer or estimated. A further simplified expression was proposed for situations where the effective tyre stiffness could be confirmed as significantly greater than the suspension spring stiffness, with the distinct advantage of reducing the sensor instrumentation requirement by relying only on use of the axle-mounted sensor response. The two proposed methods were compared to the established method using results from finite element simulation of VBI and the novel methods were observed to perform well. A comparison of the effects of assumed vehicle properties was undertaken for the established and proposed methods and changes in vehicle properties were found to be significant, in contrast to prior contrary suggestions reported in the literature. Significantly, the established and proposed methods for contact point estimation were all found to perform poorly when the vehicle's frequencies were below or close to the bridge's frequencies, suggesting that well-spaced vehicle and bridge frequencies may be a necessity for accurate estimation of the contact point response. However, it should be noted that if this condition of well-spaced frequencies is achieved, the motivation for contact point response estimation is reduced since the chance of vehicle frequencies occluding bridge frequencies in the vehicle response is necessarily already reduced.

7.9.4 Visibility of bridge frequencies in vehicle response

Acceleration frequency power spectra were constructed from the contact point response estimated using the established method and the first proposed novel method. Contrary to outcomes previously published using this bridge and vehicle model, bridge frequencies were not clearly and consistently identified as dominant peaks in the frequency domain. This outcome was noted for all of the vehicle speeds and bridge configurations tested. The outcome was also observed when adopting the vehicle parameters assumed in prior published work, confirming that the spectra presented in this thesis appeared to be dominated by vehicle-related frequencies, rather than this observation being an artefact of vehicle properties or the adopted method of contact point response estimation.

Vehicle-to-bridge acceleration amplitude ratios were explored and their evolution during the vehicle traversal was plotted. Comparison was made to the probability of bridge frequency detection, presented in the literature as a function of the value of this ratio at the start of the traversal. To facilitate comparison of the experimental outcomes to this prior study, which was undertaken based on a single-mode closed-form analytical expression for VBI, frequency bandpass filters were adopted. For filters centred on the expected first and second bridge bending frequencies, the probability of detection appeared low in both cases. This observation correlated with the lack of bridge frequency visibility in the power spectra. Greater variability was noted between traversals for the medium vehicle speed compared to slow and fast.

7.9.5 Damage detection

In this study, bridge damage was represented by the addition of static mass clamped to the bridge deck. This approach has been reported in the literature as an approach to simulating damage (Cerda et al. [325]) by mimicking the frequency-reducing effects of local stiffness loss (Corbally and Malekjafarian [20]). The damage detection method demonstrated in chapter 6 was tested with the accelerations recorded from the laboratory-scale physical VBI model, using Stockwell transform contour images as inputs and projecting into a latent space comprised of the first two principal components to separate the data. A comparison was made across frequency range included in the Stockwell transform, the pixel resolution of the contour images, and the two principal components. The outcomes were first compared using the 1-Wasserstein distance metric, which derives from the concept of optimal mass transport and expresses the amount of work required to change one empirical distribution into another, thus acting as a check of similarity between data relating to different bridge configurations when considering all condition-matched traversals as a sample from a larger population. Sample distributions of principal components, generated using kernel density estimation for bridge configurations *ii* and *iii* (added mass at midspan and quarter-span respectively) were each compared to the baseline configuration *i* (no added mass). The 1-Wasserstein distance from the baseline condition was generally greater for bridge configuration *iii* (added mass at quarter-span) than for bridge *ii* although this relationship appeared to be somewhat less consistent for the medium vehicle speed, which may relate to the greater variability in vehicle-to-bridge acceleration amplitude ratios observed. In most cases the first principal component showed greater utility for separating the damaged and healthy cases. Trends were similar for both Stockwell transform contour image pixel resolutions, with the lower-resolution images appearing to magnify the absolute differences while retaining the relative trends. The wideband Stockwell transform appeared to outperform the midband and narrowband variations considering this method of damage detection and comparison, although similar trends were observed in all cases.

A comparison of sample means was then undertaken. Since the sample size of 20 was too low for the central limit theorem to apply, and the samples did not appear to be normally distributed, no direct inference could be made based on the sample means. The lack of clear normality precluded adoption of Welch's or Student's T-tests which could otherwise be used for comparisons of small samples. To counter this, bootstrapping was adopted to generate distributions of estimates of the sample means. Bridge configurations *ii* and *iii* were then compared to *i* by using the bootstrap distributions to generate distributions of difference in estimated sample mean. A conventional confidence interval of 95 % was adopted. Formal null and alternative hypotheses were stated and the acceptance and rejection rates were calculated across all Stockwell transform image contour bandwidths. A comparison was made between the rate of rejection of the null hypothesis i.e. concluding that damage could be detected due to a statistically significant difference in estimated samples means between a damaged

and healthy bridge condition ($p < 0.05$, two-tailed). The first principal component was found to result in detection of quarter-span damage in more than 50 % of cases, with the higher-resolution Stockwell transform contour images proving most effective (damage detected at the adopted significance level in 77.8 % of cases). For the second principal component (quarter-span damage) and for midspan damage (both principal components) damage was detected in less than 50 % of cases, implying an unacceptable level of type II error (false negative) since damage detection performance could have been improved in these situations by neglecting the samples and instead assuming damage was present in 50 % of cases. It is therefore concluded that quarter-span damage could be detected in a clear majority of cases using the first principal component, but midspan damage could not be reliably detected. This matches the conclusion from the finite element-based demonstration of the method presented in chapter 6 (i.e. the method is applicable to quarter-span damage, at least for the VBI system parameters and vehicle-to-bridge parameter ratios studied).

7.9.6 Laboratory-scale modelling of VBI

Based on the observed vehicle-to-bridge acceleration amplitude ratios and the lack of visibility of bridge frequencies in the estimated contact point response, it was concluded that prior results reported in the literature using this physical VBI model achieved suppression of participation of vehicle modes in a manner not achieved here. Potential causes of this are speculated:

- Sensor placement on the vehicle was approximately symmetric longitudinally and laterally during the data gathering regime. Conversely, previous results used asymmetric sensor placement, with the cabin accelerometers mounted directly to the top of the suspension struts on one side only, and the front axle sensor omitted thus creating vehicle mass biases to one side and to the back. Given the relatively high mass of the sensors compared to the vehicle itself, and the relatively soft spring rates in the vehicle suspension (based on observation of the vehicle during testing) it is deemed feasible that this asymmetric sensor placement could have induced significantly different effective vehicle modal properties compared to the experiment reported in this thesis.

- The roadway at either end of the bridge span was noted to be flexible, based on visual observation of vehicle and roadway oscillatory motion during the testing. Typically, the roadway either side of a bridge span would be more stiff vertically than the bridge deck. This aspect of the physical apparatus could conceivably have amplified motion associated with vehicle frequencies during the vehicle's drive toward the bridge, leading to the observed high vehicle-to-bridge acceleration amplitude ratios at the start of the traversals. It is suspected that the vehicle could have been oscillating vertically — due to the dynamic characteristics of the flexible pre-span roadway — before the beginning of each traversal. In practical terms, this

could have been responsible for lack of clear visibility of bridge frequencies as peaks in the vehicle acceleration response spectrum. Although this was noted visually during the experiments, the pre- and post-span roadways were not modified because the original intention was to validate prior findings (i.e. visibility of the bridge first mode frequency as a distinct peak in the vehicle CP response power spectrum). Asymmetric sensor placement on the vehicle (as previously noted) may have contributed to mitigation of the effect of the flexible roadway in prior experiments by others using this test apparatus.

To explore these ideas in the future, further testing would could be undertaken:

- Repeat traversals using symmetric sensor placement on the vehicle while providing additional vertical support under the roadways adjacent to each end of the bridge deck, thus reducing their deflection.
- Repeat traversals without additional vertical roadway support, using asymmetric sensor placement on the vehicle.
- Repeat traversals with vehicle starting position immediately prior to roadway-bridge interface.

Additional recommendations can be made regarding laboratory-scale modelling of VBI based on the observations from this chapter:

- **Observation:** Quarter-car frequencies and damping ratios fitted to the model vehicle differed considerably from those expected for full-size vehicles (based on field testing and literature).
  - **Recommendation:** Identify model vehicle parameters through a programme of physical testing to avoid issues that would be unforeseen if assuming vehicle properties (e.g. vehicle-bridge proximal frequencies or unusual upper-to-lower DoF vehicle mass distribution).
- **Observation:** Model vehicle tyres appeared to generate speed-correlated harmonics, assumed to be due to out-of-roundness of tyres. More specifically, the out-of-roundness might have been due to fit tolerance of the tyres on the rim, given that they were not pneumatic and thus the tyre-rim interface did not benefit from the effects of inflation pressure.
  - **Recommendation:** Adopt alternative tyre/wheel system (e.g. pneumatic or foam tyres and matched wheel rims.

7.10 Chapter summary

- Frequencies and mode shapes for the laboratory bridge model, identified through an output-only impulse response paradigm, showed good agreement with previously-published data for the same model. Identified modal damping ratios, which have not previously been published for this bridge, were also presented. The identified bridge parameters included combinations of static vehicle and added static mass in multiple positions.

- The output-only impulse response method was also applied to the vehicle model. The identified frequencies and damping ratios were substantially different from those assumed in prior publications by others who used the same model in their experiments.

- The frequency response of the vehicle driving on the laboratory floor was explored (in the same manner adopted for the fieldwork reported in chapter 4). A substantial component of the vehicle response was noted to be correlated with speed; it was demonstrated that this could plausibly relate to tyre out-of-roundness or mass asymmetry effects.

- An ensemble of vehicle responses to bridge traversals was used to test the damage detection method demonstrated in chapter 6. The Stockwell transform was used to generate an image for each vehicle traversal showing the time-frequency behaviour of the contact point response. Principal component analysis was employed to reduce the dimensionality of these images and project each one into a two-dimensional latent space. The distribution of the first two principal components for each bridge condition was approximated using kernel density estimation. Bootstrapping was employed to approximate distributions of the difference of sample means between the healthy and damaged conditions. Formal hypothesis testing was employed to evaluate the concept that a statistically significant different between bootstrapped healthy and damaged distributions represented successful detection of damage. The outcomes were promising, with up to 77.8 % success in identifying damage at the bridge quarter-span location.

- The ensemble power spectra from the vehicle responses were inspected and the bridge first frequency could not be clearly identified in the response. This is in contrast to previously-published observations by others using the same experimental apparatus. To explore this, the vehicle-to-bridge acceleration amplitudes were presented; they suggested that identification of bridge frequencies directly from the vehicle response was very unlikely. Based on this, two further insights were offered:

  - Since the vehicle response spectra were dominated by vehicle-related frequencies, with no clear visibility of bridge frequencies, it was speculated that vehicle excitation might have been somehow suppressed in prior studies in a manner not achieved here.

– The detection of damage at bridge quarter-span was assumed to be due to VBI-induced changes relating to the proximal vehicle and bridge frequencies, rather than due to direct visibility of changing bridge modal parameters. This suggests that — subject to accurate knowledge of vehicle properties — the confounding caused by VBI-induced frequency nonstationarity could be re-imagined as a beneficial phenomenon.

Chapter 8

Conclusions

The aim of this thesis was to **systematically investigate the viability of indirect bridge damage detection based on the acceleration response of a non-bespoke traversing vehicle, given the expected operational challenges of proximal vehicle and bridge frequencies, the lack of prior knowledge of vehicle dynamic properties, and the lack of labelled data representing bridge damage.**

This chapter reviews the fulfilment of the research objectives, reflects on the outcomes of the thesis and the current state of indirect structural health monitoring, summarises the contributions and limitations of the thesis, and makes suggestions for future work.

8.1 Fulfilment of research objectives

The work presented in thesis sought to address four research objectives, outlined in section 3.2 of chapter 3. The objectives were based on identified research gaps summarised in the critical review presented in section 2.7 following the review of literature in chapter 2.

Research objective 1 (RO.1) was to **estimate a representative multi-degree-of-freedom dynamic model of a vehicle, using only the vertical acceleration response of the vehicle to driving in normal operational conditions**. RO.1 was addressed in chapter 4. The work in this chapter included simulation of a reduced degree-of-freedom vehicle model and demonstration of output-only vehicle model parameter estimation using synthesised vehicle responses to road surface excitation. This was pursued due to the practical difficulties of establishing ground truth vehicle properties. As was noted in the literature review (chapter 2, section 2.4) the prohibitive time and cost aspects of established laboratory methods for vehicle parameter estimation are also a large part of the motivation to develop robust in-service output-only vehicle parameter estimation methods. The simulation approach pursued led to the conclusion that vehicle parameter estimates could be affected by spectral

bias in the road surface profile. A method of adjustment was demonstrated to mitigate this bias when the road profiles followed the spectral model outlined in ISO 8608 [7] and widely adopted in the literature. Methods of estimation of vehicle parameters were identified as giving consistent outcomes and were adopted for the remainder of chapter 4. Through multiple phases of fieldwork a comparison was made of the effect of road type, vehicle speed, and sensor position. A favourable comparison was also made between the use of purpose-built commercial-grade accelerometers and the acceleration sensor built in to a smartphone device.

Visibility was sought of effects related to a change in the vehicle's suspension configuration between two phases of fieldwork. The change in frequencies was opposite to that expected, suggesting that it might have been overwhelmed by variation in the road profile (or other factors) between the locations of the two experimental phases. The largest change as a proportion of the standard deviation of time-domain phase 2 estimates was in the axle hop mode damping ratio; it was speculated that this could relate to suspension component degradation or changes in tyre pressure although the mechanism(s) of such effects are not known. Alternatively the change could be related to other factors such as road profile variation or vehicle suspension nonlinear response. In contrast to the widely-adopted ISO 8608 profiles which are approximately spectrally flat in velocity, the outcomes from field tests suggested that at least some real roads are spectrally flat in acceleration and thus do not appear to be subject to the expected spectral input bias. The chapter concluded with a presentation of the range of variation seen in the estimated vehicle parameters.

Research objective 2 (RO.2) was to **explore and how variation in vehicle-to-bridge parameter ratios, vehicle model abstractions and sensor placement on the vehicle affect the visibility and sensitivity of detecting bridge frequencies from vehicle-mounted accelerometers**. RO.2 was addressed in chapter 5. Vehicle-bridge interaction was simulated for a two degree-of-freedom undamped quarter-car model traversing a beam bridge. Assuming no prior knowledge of vehicle or bridge frequencies, the frequency domain metrics of prominent peak identification and peak drift were proposed and adopted under the assumption that the largest signal power in the vehicle-mounted sensor response would be associated with the bridge first mode frequency. This study afforded a comparison of sensor position, vehicle speed, vehicle-to-bridge frequency ratio, and the vehicle's upper-to-lower degree-of-freedom mass ratio which was previously unexplored in the known literature. Generally the highest response signal power was associated with the cabin sensor location and proximal vehicle and bridge frequencies, however the potential for false positive identification of the bridge frequency was highlighted since (in the presence of real-world road profile roughness) this would also be the expected to be the prominent peak frequency for off-bridge vehicle responses.

Increased vehicle speed was associated with increased spectral peak height in accordance with prior outcomes reported in the literature. However, peak drift also increased with vehicle speed. It was observed that well-spaced vehicle-to-bridge frequency ratios led to outcomes approximating the well-known moving

mass model abstraction, while proximal frequencies between vehicle and bridge appeared to be the most significant confounder for unique and accurate identification of bridge frequency from the vehicle response. Overall, the virtual contact point sensor location appeared to be least susceptible to bias in this regard; it was therefore adopted for the subsequent investigations in the thesis. However, it should be noted that this virtual sensor location is not practical in reality. As highlighted in the literature review it has received praise from other researchers but estimation of the virtual sensor response relies on knowledge of the vehicle's properties and may therefore be subject to other biases in addition to the effects of the upper-to-lower degree-of-freedom vehicle mass ratio which was explored in chapter 5 but is suspected to be immeasurable in practice. Further exploration of the contact point response was presented in chapter 7 and is discussed below.

Research objective 3 (RO.3) was to **characterise the nonstationary frequency variation for interacting vehicle-bridge systems during vehicle traversals in relation to vehicle model abstraction and vehicle-to-bridge parameter ratios**. RO.3 was addressed in chapter 6. Frequency variation during VBI for systems with proximal vehicle and bridge frequencies was identified in chapter 5 as a potential counfounder for bridge damage detection. The literature review in chapter 2 revealed that this phenomenon had not been fully explored beyond single-mode representations of the bridge and vehicle. In order to fulfill the research objective, single- and two-degree-of-freedom quarter-car vehicle models were explored. Finite element simulation was used to extract eigenfrequencies, allowing a favourable comparison of the single degree-of-freedom vehicle outcomes to published results from the literature. However, these outcomes also highlighted the effects of the higher-order vehicle and bridge modes, justifying the exploration of more sophisticated models included in this chapter. For an SDoF vehicle, expected variations for the first three combined vehicle-bridge interaction system frequencies were presented as a function of vehicle position (midspan or quarter-span) and the ratio of nominal (non-interacting) vehicle frequency to the bridge first and second bending mode frequencies. This presentation style allows the extent of vehicle-bridge interaction-induced frequency shift to be predicted from the plots to inform future studies. For a 2DoF vehicle, the expected pattern of frequency variation for the combined vehicle-bridge system was presented for a range of vehicle positions on the bridge, considering four potential vehicle-to-bridge proximal frequency combinations.

Dynamic finite element simulation outcomes were explored using the Stockwell transform which is a time-frequency signal representation method related to the wavelet transform. The Stockwell transform contours were normalised to the instantaneous maximum signal power, which increased visibility of the frequency nonstationarity phenomenon in-line with observations from prior studies using the wavelet transform. An observed drawback of this approach is that visibility of the frequency with the second-highest signal power can be suppressed. An observed phenomenon was apparent splitting into two parts of the ST ridges; based on the observations this was attributed to phase lag between the vehi-

cle DoF and bridge contact point responses. At smaller magnitudes of phase lag the ridge appeared to oscillate. In both cases this behaviour was expected to confound damage detection (and damage localisation using mode shapes). Although the oscillation and ridge splitting phenomena were understood to be correlated with phase lag, the behaviour was not fully characterised and might also represent some kind of signal or transform artefact. Further research is required in this regard.

The effect of single degree-of-freedom vehicle model damping was explored. Prior literature, reinforced by the study of eigenfrequency variation, suggested that the frequency variation would be apparent as a pair of frequencies nominally representing the vehicle and bridge modes but in reality being a mode-splitting phenomenon for the combined vehicle-bridge system. Lower amounts of vehicle damping (below that expected for real vehicles) changed which of the frequency pair had the highest signal power and thus greater visibility in the normalised Stockwell transform contours. At damping ratios closer to those expected in reality (based on the literature review in chapter 2 and the observations from field testing in chapter 4) the ridges diverged significantly, suggesting that vehicle damping may be detrimental to the use of time-frequency transforms for this purpose. Further research is required to better understand and complete the characterisation of this phenomenon.

Overall, the eigenfrequency-based outcomes offered characterisation of the expected overall magnitudes of frequency shift during VBI for the range of vehicle-to-bridge parameter ratios investigated. However, the dynamic simulation outcomes suggest that the actual time-frequency behaviour in these situations may be more complicated during a traversal.

Research objective 4 (RO.4) was to **establish and test a method to detect bridge damage from vehicle acceleration responses in the case of vehicle-to-bridge natural frequency matching without requiring labelled examples representing bridge damage**. RO.4 was addressed in chapters 6 and 7. In chapter 6 changes in vehicle-bridge interaction-induced frequency variation were proposed as indicators of the presence of damage, which was modelled as localised stiffness reduction of the bridge deck at midspan or quarter-span. The use of machine learning methods such as autoencoders was discussed as a potential avenue for the challenging problem of one class classification with large data sets, a framework in which outlier or anomaly detection is leveraged to overcome the lack of labelled data representing bridge damage. In practice the unavailability of labelled data is a significant challenge. For the small synthetic data set used for this study, clustering of damaged and healthy responses was explored in a reduced-dimension latent space, comprised of the first and second principal components of the Stockwell transform contour images. This approach was justified by the use of principal component analysis for image classification techniques and unsupervised feature extraction in prior bridge structural health monitoring research, alongside recent observations in the literature regarding the similarity of principal component analysis and autoencoder outcomes for situations such as this. A promising trend was observed suggesting that latent space separation might monotonically increase

with damage severity. This trend was most apparent for cases where the bridge and vehicle frequencies were proximal.

Chapter 7 entailed laboratory-scale validation of the proposed damage detection method. The bridge and vehicle physical models were first characterised using operational modal analysis methods. Bridge frequencies and mode shapes showed good agreement with prior results by others, and modal damping ratios were presented for the first time for this bridge. However, the exercise highlighted that the vehicle's front axle hop modal frequency was close to the bridge's second bending mode frequency, contrasting to prior studies by others using the same physical apparatus in which wide separation of bridge and vehicle frequencies was implied based on assumed vehicle properties. Also noted was a dominant frequency in the vehicle response to driving not on the bridge, which was directly correlated with speed. It was theoretically shown that this could plausibly relate to tyre out-of-roundness or mass asymmetry. The detailed study of vehicle and bridge properties presented here, including characterisation of the combined vehicle and bridge system (with the vehicle stationary on the bridge span) will inform future investigations using this apparatus.

Close matching of estimated modal bridge properties and the finite element simulated bridge in previous chapters (5 and 6) confirmed that the damage detection method from chapter 6 could be tested using outcomes from the laboratory experiments. Vehicle responses from ensembles of traversals were used to create Stockwell transform contour images. Bridge damage was simulated by the addition of static mass to the deck. Damaged and healthy cases projected into latent space formed overlapping clusters with non-Gaussian shapes. However, comparison of the distributions using the 1-Wasserstein distance metric suggested that the cases might be separable. Sample means were bootstrapped and a distribution of sample mean differences between damaged and healthy cases was constructed. Formal hypotheses were stated. The outcomes suggested that the damage detection method was successful (rejection of null hypothesis, $p < 0.05$) in up to 77.8% of cases using the first principal component for damage modelled at the bridge quarter-span position.

In contrast to previous studies published by others using this physical model, the bridge first frequency was not clearly detectable from the vehicle acceleration response spectrum. Filtering techniques were applied, subtracting the front and rear vehicle responses to mitigate the effect of surface profile roughness in accordance with recommendations from the literature, but this did not solve the issue; the vehicle response spectra were dominated by vehicle-related frequencies (albeit subject to variation induced by vehicle-bridge interaction). Further study confirmed that the initial vehicle-to-bridge acceleration amplitude ratios (for band-limited vehicle responses and specific bridge sensor locations relating to the first and second bridge modes) were very high, implying low to negligible probability of detecting bridge frequencies directly from the vehicle response according to the literature. This outcome suggested that control of vehicle vibration response might have been present in prior studies in a manner not achieved here, perhaps relating to flexibility of the pre- and post-bridge roadway and/or the vehicle sensor mounting positions. This, along with the potential tyre irreg-

ularities, informed recommendations for future experimental campaigns using this apparatus. Since the bridge frequencies were not directly visible in the vehicle response, but the proposed damage detection method showed promising outcomes, it was concluded that the confounding caused by VBI-induced frequency nonstationarity may have potential for being re-imagined as a beneficial phenomenon for damage detection subject to accurate knowledge of vehicle and bridge modal frequencies.

8.2 Conclusions, contributions, and limitations

As time passes, damage accumulates in the built environment. Engineers have a responsibility to use reasonable skill and care towards the goal of maintaining the integrity of structures. However, cost and time are significant constraints; all built assets are subject to degradation and bridges — which are critical infrastructure — are no exception. Structural health monitoring has emerged as a potential way to decrease costs, increase objectivity and ultimately improve the process of bridge inspection and maintenance. Although it has been a focus of research for some decades, the bespoke nature of bridges means that it is still something of a novelty; installed sensor networks on long-span landmark bridge structures are becoming more common, but debate remains as to how best to use the collected data. Significant challenges, including the masking or spurious identification of damage due to environmental and operational variation, are active areas of research. Collecting baseline data representing the healthy bridge condition is necessary but difficult in practice. The same is true for data representing the manifestation of damage.

Installed sensor networks are less common for short- and medium span bridges, yet they are also critical infrastructure. The quantity of such bridges worldwide is thought by some to be a barrier to direct monitoring on a continuous basis. Indirect structural health monitoring by moving vehicle has recently emerged as a potential solution to this economic and practical challenge. It is still a nascent field.

The main contributions of this thesis are:

- The thesis has critically reviewed the emergence of indirect structural health monitoring, identifying that it maintains the challenges associated with its direct monitoring counterpart while introducing additional confounding. The additional challenges for indirect structural health monitoring, associated with using the vehicle as a combined exciter and sensor carrier, have been highlighted and placed in context.

- The key outstanding challenges for indirect structural health monitoring using frequency changes as damage indicators have been explored and addressed in a systematic and holistic manner. This has included unknown vehicle properties, the potential for matching of vehicle and bridge natural frequencies, and the resulting nonstationarity of combined vehicle-bridge system frequencies.

- Damage detection has been demonstrated and validated, using an established framework, for situations in which vehicle and bridge frequencies are matched. Using changes in vehicle-bridge interaction-induced frequency variation as indicators of damage, the approach reframes a significant challenge in iSHM as a benefit. Additionally the adopted method did not necessarily require direct visibility of bridge dynamics from the vehicle response or the availability of labelled data representing bridge damage.

The main contributions of this thesis represent positive developments for the field. Nevertheless there are also limitations. Most importantly, there are some challenges for indirect structural health monitoring that are not addressed in the thesis. Some of these, such as the interrelated effects of vehicle speed and road surface profile, were deliberately omitted as they have been extensively investigated in prior literature. However, these factors are important when considering indirect monitoring in operational traffic conditions and may in fact represent some of the most significant barriers due to the resulting decreases in signal-to-noise ratio and sample length. Other notable limitations to the presented work include:

- The results of output-only vehicle parameter estimation in chapter 4 would have been rendered more credible by comparison to ground truth reference values for the vehicle from physical laboratory testing. The comparison of estimates between phases 1 and 2 of the fieldwork appeared informative but the two phases used different sensor types and placements on the vehicle, meaning that firm conclusions were limited. Other factors such as tyre pressure were not controlled between the two phases of fieldwork. Additionally, future work should explore modal parameter estimation methods using the response of multiple sensors simultaneously, allowing the vehicle's mode shapes to be confirmed.

- The presented study of visibility and sensitivity (chapter 5), the characterisation of frequency variation in vehicle-bridge interaction systems (chapter 6) and the proposed damage detection method (chapters 6 and 7) can only be considered valid for the range of vehicle and bridge parameters and parameter ratios studied. Although efforts were made to explore realistic values for the parameters, other vehicle or bridge types might require additional validation. A particular limitation relates to the representation of bridge damage. Only two damage locations were explored. Damage was modelled as a local reduction in stiffness. Although this approach is aligned to that seen in prior literature, in reality bridge damage can manifest in a variety of ways and in many possible locations.

- The quarter-car vehicle model used in this thesis captures some of the important and arguably dominant aspects of real vehicle dynamic behaviour. Nevertheless, more sophisticated vehicle models (for example including pitch and roll motion) would allow greater insight regarding the potential applicability of the proposed damage detection method. Additionally, contact between the vehicle and bridge was modelled as a single-point interface. This is unrealistic, but was acceptable in this thesis since the road profile roughness was not modelled in the finite element studies of vehicle-bridge interaction. In reality, the nature of the tyre-road interface could influence the visibility of bridge frequencies in the vehicle-mounted sensor response.

- The bridge model used in the finite element studies captured only two-dimensional in-plane bending modes. Real bridges display lateral and torsional modes, whose frequencies may be closely-spaced. These additional modes could affect the performance of the proposed damage detection method.

- Actions on bridges include wind loads and background traffic. These were not included in the presented studies, but may affect the bridge motion and thus the nature of the vehicle-bridge interaction, especially if they manifest as actions with frequency bias or as non-stationary inputs. Equally, varying environmental conditions (such as temperature) were discussed as important influences to bridge behaviour but were not modelled. Arguably these factors were less relevant for the laboratory scale bridge, but are important when considering the applicability of the research outcomes to full-scale field testing.

- The exploration of frequency variation for vehicle-bridge interaction systems in chapter 6 found that vehicle damping influenced the apparent time-frequency behaviour in the contact point response. The influence was noted but not fully characterised. Additionally, oscillatory and ridge splitting-and-rejoining phenomena were noted in the Stockwell transform ridges in this chapter. A plausible explanation was given, based on limited finite element simulations. However, the behaviour was not completely characterised. An alternative explanation is that the phenomena were — to some degree — transform artefacts, or some other spurious signal feature. These possibilities could not be completely dismissed based on the scope and extent of investigations in the thesis and further work was suggested to explore the phenomena.

- The Stockwell transform contours used for damage detection in this thesis contained known transform artefacts. Additionally, the some aspects of the time-frequency behaviour displayed by the contours were not fully characterised as discussed above. The inclusion of artefacts in these data could cause bias in damage detection outcomes, or false positive/ false negative identification of damage. Further exploration of the sensitivity of the damage detection methodology to the transform artefacts could be undertaken in the future, and methods to mitigate the effects of artefacts could be explored if deemed necessary to improve damage sensitivity and repeatability.

- The thesis highlighted that undertaking baseline condition monitoring of bridges using direct sensing methods represents a significant time and cost burden, and may not always be practically achievable. However, the proposed damage detection method was predicated on approximate matching of natural frequencies between the vehicle and bridge. Although significant effort was expended towards vehicle parameter estimation (chapter 4), it is possible that in practice the bridge frequencies would not be

known. Additionally, the sensitivity of the proposed method to accidentally *mis*matched frequencies was not fully explored.

- The presented investigations focused on bridge and vehicle frequencies. It was argued that bridge mode shapes might offer improvements regarding the localisation of damage, but that they were derived from amplitude envelopes applied to frequency-filtered vehicle responses and thus would be subject to bias due to frequency variation during vehicle-bridge interaction. The extent and nature of this bias was not explored.

- The focus on frequency estimation arguably excluded other approaches which could improve the detection and localisation of damage. In addition to mode shapes as discussed above, the presented studies did not explore methods using responses from multiple vehicles; fusion of direct and indirect monitoring data; and other signal features (modal or abstract) which could be sensitive to damage.

Despite the advances made in this thesis and complementary research by others, there are still many challenges associated with structural health monitoring. The thesis identified that the most promising outcomes for indirect structural health monitoring have required the use of bespoke sensor-carrying vehicles and necessitated interruption to normal operation of the bridge to allow slow or stationary instrumented vehicles to scan the structure. The thesis has argued that for the indirect method to outperform direct monitoring, continuous data gathering in operational conditions is required and that the use of uncontrolled vehicles is necessary. The research presented here has addressed the key challenges associated with such an approach. However, the field is still developing and much work still remains to be done, including field-scale validation. There is still a long way to go until the indirect method reaches a state of operational readiness. Nevertheless, it remains an appealing prospect due to the practical and economic aspects of installing and maintaining direct sensor networks on all bridges worldwide. However, it could be argued that the nature of the challenges mean that indirect structural health monitoring will be most valuable not as a broadly-applied universal and continuous method, but rather in specific and considered situations, combined with other tools and techniques of engineering appraisal. Identifying such situations and combinations is one of the next major frontiers for the field.

8.3 Future work recommendations

In the critical review (section 2.7) it was argued that the engineering community should find ways to make the vehicle based method work at operational speeds, in uncontrolled vehicle types and with potentially uncontrolled sensor types and locations. Otherwise, the best outcomes reported in the literature (bespoke sensing vehicles at slow speeds, or stationary in closed traffic lanes) might be exceeded in utility by placing sensors directly on the bridge in a temporary manner. The work presented in this thesis has sought to address some of the key issues whose resolution is required to enable vehicle-based indirect bridge SHM to reach a state of operational utility. Some useful and positive outcomes have been presented. Nevertheless, the scope of challenges is broad, meaning that there are opportunities for future work. Additionally, reflection on the outcomes presented in the thesis alongside the critical review (section 2.7) suggests some particular considerations for the direction of future research. These are outlined below.

8.3.1 Vehicle property estimation

There is a perceived need to estimate vehicle properties using output-only in-service methods, as outlined in section 2.4. This is anticipated to become more pressing as vehicles change in the near future. Many representative vehicle model parameters commonly adopted in the literature date from several decades ago. At present there is an increasing trend for electrification of vehicles. Electric cars are reported to be heavier than equivalent internal combustion-powered models (Timmers and Achten [446]). The mass of batteries (and their placement) required in such vehicles may change the effective dynamic properties. Additionally, interest continues in driver assistance and autonomous control technologies (Gkoumas et al. [35]). It is feasible that built-in sensors on vehicles of this type may provide data of use to bridge monitoring efforts. On the other hand, if citizen's sensors (such as smartphones) are to be used then their position in the vehicle may vary and thus the effective vehicle model (representing the path of vibration transmission from road surface to sensor) could be different for every journey. In this case, the need for characterisation of vehicle dynamics considering the sensor location is even greater. The outcomes presented in this thesis, considered alongside the existing literature, suggest that estimation accuracy is a concern. Variability in road surface profiles is believed to be a major factor contributing to the variability of estimated properties. Methods involving multiple passes, multiple vehicles and multiple sensors per vehicle may be useful here. Reaching convergence of estimated parameters for a single road type would be useful if feasible to achieve. Investigation is warranted into the test regime, data volume and type, and data processing methods required to do so. There is also a need to consider the effects of variability in estimated vehicle models on damage detection and localisation. A sensitivity study (with comparison to damage types, extents, and locations) is warranted.

8.3.2 Traffic effects

There is also a requirement for greater understanding of traffic effects as source of EOV. The literature review highlighted some recent research (section 2.4) in which machine vision was used as part of vehicle type classification and axle weight estimation procedures. Traffic is understood to be a complex phenomenon and has been the subject of academic research for some decades (Kerner [447]). Some recent work on indirect SHM suggested an inverse relationship between traffic volume and vehicle-bridge coupling ([138]). Recalling the challenges associated with using a single vehicle as combined exciter and sensor carrier, alongside the research outcomes suggesting the potential benefits and drawbacks of concurrent traffic raises the question: could there be an optimum traffic situation in which the vehicle-based indirect method is of most use? A paper by the author (May [365]) presented an initial exploration of this question. The study should be extended to consider more traffic flow situations. Measurements of real traffic on bridges would be informative. The efficient and intuitive techniques now available for modelling VBI (section 2.5) could be combined with traffic flow modelling techniques to assist with identification of suitable conditions in a parametric manner. Such a coupled approach has been the subject of recent work; for example He et al. [448] pursued an empirical approach to eliminating the effects induced by traffic mass, but this was limited to the first bridge model. Scope for future work includes higher order bridge modes; a wider variety of bridge types and traffic conditions; integration of real traffic data; and the implications for vehicle-mounted sensors for indirect bridge SHM.

8.3.3 VBI-induced frequency variation

The thesis presented a study of nonstationarity of bridge frequencies as a function of vehicle and VBI system parameters (chapter 6). This was highlighted as a confounder to identification of bridge frequencies and visibility of damage-induced frequency changes. The literature review highlighted that bridge mode shapes are used for damage localisation, but that estimation of bridge mode shapes from the vehicle response relies on an amplitude envelope of a frequency band-limited signal (section 2.6.2). VBI induced frequency variation was therefore postulated as a potential confounder to mode shape-based damage localisation. The extent of this confounding should be studied. Estimation of vehicle properties could potentially be combined with characterisation of frequency variation to offset the effects. Research is required into the methods and practice of doing so. Potential limitations of the existing single-mode expressions describing bridge frequency variation were identified, on the basis that they do not consider effects related to other bridge modes. These effects may be particularly relevant for situations in which multiple vehicle and bridge frequencies are simultaneously proximal, or where a single vehicle frequency is proximal to multiple closely-spaced bridge frequencies. These potential situations could also be explored in future work.

8.3.4 Damage detection

In this thesis a method of damage detection was proposed for situations in which vehicle and bridge frequencies are proximal, and in which labelled data representing the damaged bridge response are not available. The literature review (chapter 2) established that the frequency matching challenge is somewhat inevitable for crowdsourcing approaches using non-bespoke sensor carrying vehicles. The difficulty in establishing baseline and labelled data is an ongoing challenge for bridge SHM. The proposed method, explored using numerically-simulated data (chapter 6) and tested on laboratory-scale physical model outcomes (chapter 7) appeared to show promise. However, the approach could be confounded by errors in vehicle property estimation which at present are to be expected (chapter 4), and outcomes have only been explored in relation to specific localised damage types. Further research is recommended to explore the sensitivity and robustness of this type of damage detection method, especially considering full-scale vehicle-bridge interaction, different vehicle types, varied damage scenarios, and the presence of other sources of EOV such as temperature variation or background traffic.

8.3.5 Transport futures

The climate crisis demands that the future of transport will be different from today. Bridge SHM has a multi-decade history, and some challenges have persisted for much of that time. It is therefore sensible to consider whether or not today's VBI and indirect SHM challenges will still apply in the future. For example, autonomous vehicle control has been the subject of research interest, but a survey of industry professions found their most significant safety concerns were around risks associated with "incorrect understanding of the surrounding objects such as humans, animals, and static and dynamic objects" (Rezaei and Caulfield [449]). These issues may be particularly critical in urban areas where vehicles must share space with more vulnerable parties such as cyclists and pedestrians. On the other hand, motorways are already restricted to access by certain subsets of vehicles. In the author's opinion it seems likely that road haulage of freight will persist for some years, if not indefinitely. Some researchers highlight the potential aerodynamic efficiency benefits of autonomous control of fleets of heavy vehicles in convoys and have begun to explore the possible impacts on bridges (for example Ling et al. [210]). If this multi-vehicle autonomous control paradigm becomes a reality, in the author's opinion it will be limited to use on motorways or other restricted-access roads. It could be seen as a help or hindrance to bridge SHM efforts. At times it may result in faster and/or more closely-spaced heavy traffic. On the other hand, autonomous control of multiple vehicles suggests the availability of data describing the traffic flow which has been found to be a factor in bridge SHM. The effective frequencies introduced by trains of moving loads could potentially be leveraged to enhance response of particular bridge modes, thus yielding a direct point of comparison to previous bridge states, perhaps with greater visibility of damage-

sensitive modes in the response. Traffic in urban areas may also change. In the author's opinion, combinations of human-powered and electrically-assisted light vehicles are the future of local urban transportation (combined with rail and bus systems). These lighter vehicles might have potential for use in the indirect bridge SHM paradigm. Some recent work by the author (May et al. [370]) has begun to explore this possibility. The effective vehicle dynamics may change due to human-vehicle interaction, presenting significant challenges and highlighting the need for further research in this area.

Bibliography

[1] James Gleick. *The information: A history, a theory, a flood*. Vintage, 2011.

[2] Thomas D Gillespie. Everything you always wanted to know about the IRI, but were afraid to ask. *The University of Michigan Transportation Research Institute. Nebraska*, 1992.

[3] Daniel Ainalis. *Estimating the dynamic characteristics of road vehicles using vibration response data*. PhD thesis, Victoria University, 2014.

[4] V Rouillard and MJ Lamb. Road vehicle shock detection algorithm using the hilbert envelope. *Computer Methods in Applied Mechanics and Engineering*, 419:116637, 2024.

[5] Michael W Sayers. Two quarter-car models for defining road roughness: Iri and hri. *Transportation Research Record*, (1215), 1989.

[6] Reza N Jazar. *Vehicle dynamics*, volume 1. Springer, 2008.

[7] Technical Committee ISO/TC, Mechanical Vibration, Shock. Subcommittee SC2 Measurement, Evaluation of Mechanical Vibration, and Shock as Applied to Machines. *Mechanical Vibration–Road Surface Profiles–Reporting of Measured Data*, volume 8608. International Organization for Standardization, 1995.

[8] Daniel Ainalis, Vincent Rouillard, and Michael Sek. On-the-road measurements to establish the dynamic characteristics of transport vehicles. *Packaging Technology and Science*, 28(8):657–671, 2015.

[9] YB Yang, MC Cheng, and KC Chang. Frequency variation in vehicle–bridge interaction systems. *International Journal of Structural Stability and Dynamics*, 13(02):1350019, 2013.

[10] Daniel Cantero and Eugene J OBrien. The non-stationarity of apparent bridge natural frequencies during vehicle crossing events. *FME transactions*, 41(4):279–284, 2013.

[11] Daniel Cantero, David Hester, and James Brownjohn. Evolution of bridge frequencies and modes of vibration during truck passage. *Engineering Structures*, 152:452–464, 2017.

[12] Jorge Rodrigues and Rune Brincker. Application of the random decrement technique in operational modal analysis. In *Proceedings of the 1st International Operational Modal Analysis Conference, April 26-27, 2005, Copenhagen, Denmark*, pages 191–200. Aalborg Universitet, 2005.

[13] Ervin Sejdić, Igor Djurović, and Jin Jiang. Time–frequency feature representation using energy concentration: An overview of recent advances. *Digital signal processing*, 19(1):153–183, 2009.

[14] Claudio Satriano. Stockwell - Python package for time-frequency analysis through Stockwell transform. https://github.com/claudiodsf/stockwell. Accessed: 2023-05-08.

[15] Hyunjun Kim and Sung-Han Sim. Automated peak picking using region-based convolutional neural network for operational modal analysis. *Structural Control and Health Monitoring*, 26(11):e2436, 2019.

[16] Clarence W De Silva. *Vibration: fundamentals and practice*. CRC press, 2006.

[17] Marco Villa, Hilaryl Au, Amir Damansouz, and Min Kee Goh. Derivation of transfer function of a two-degree-of-freedom damped system with base excitation. 2022.

[18] OpenStreetMap contributors. Available under the open database license. http://openstreetmap.org/copyright. Accessed: 2024-02-22.

[19] Robert Corbally and Abdollah Malekjafarian. Bridge damage detection using operating deflection shape ratios obtained from a passing vehicle. *Journal of Sound and Vibration*, 537:117225, 2022.

[20] Robert Corbally and Abdollah Malekjafarian. Detecting changes in the structural behaviour of a laboratory bridge model using the contact-point response of a passing vehicle. *Journal of Structural Integrity and Maintenance*, pages 1–13, 2023.

[21] YB Yang and KC Chang. Extracting the bridge frequencies indirectly from a passing vehicle: Parametric study. *Engineering Structures*, 31(10):2448–2459, 2009.

[22] KC Chang, CW Kim, Sudanna Borjigin, et al. Variability in bridge frequency induced by a parked vehicle. In *Proceedings of the 4th KKCNN Symposium on Civil Engineering*, pages 75–79, 2014.

[23] Jerome Peter Lynch. An overview of wireless structural health monitoring for civil structures. *Philosophical Transactions of the Royal Society A: Mathematical, Physical and Engineering Sciences*, 365(1851):345–372, 2007.

[24] James Brownjohn and Emin Aktan. Improving resilience of infrastructure: The case of bridges. In *Structures Congress 2013: Bridging Your Passion with Your Profession*, pages 1812–1821, 2013.

[25] Abdollah Malekjafarian, Patrick J McGetrick, and Eugene J OBrien. A review of indirect bridge monitoring using passing vehicles. *Shock and vibration*, 2015, 2015.

[26] John J Moughty and Joan R Casas. A state of the art review of modal-based damage detection in bridges: Development, challenges, and solutions. *Applied Sciences*, 7(5):510, 2017.

[27] Yonghui An, Eleni Chatzi, Sung-Han Sim, Simon Laflamme, Bartlomiej Blachowski, and Jinping Ou. Recent progress and future trends on damage identification methods for bridge structures. *Structural Control and Health Monitoring*, 26(10):e2416, 2019.

[28] Eloi Figueiredo and James Brownjohn. Three decades of statistical pattern recognition paradigm for shm of bridges. *Structural Health Monitoring*, 21(6):3018–3054, 2022.

[29] Charles R Farrar and Keith Worden. An introduction to structural health monitoring. *Philosophical Transactions of the Royal Society A: Mathematical, Physical and Engineering Sciences*, 365(1851):303–315, 2007.

[30] Charles R Farrar, Scott W Doebling, Phillip J Cornwell, and Erik G Straser. Variability of modal parameters measured on the alamosa canyon bridge. Technical report, Los Alamos National Lab.(LANL), Los Alamos, NM (United States), 1996.

[31] Anders Rytter. Vibrational based inspection of civil engineering structures. 1993.

[32] James MW Brownjohn. Structural health monitoring of civil infrastructure. *Philosophical Transactions of the Royal Society A: Mathematical, Physical and Engineering Sciences*, 365(1851):589–622, 2007.

[33] Keith Worden, Lawrence A Bull, Paul Gardner, Julian Gosliga, Timothy J Rogers, Elizabeth J Cross, Evangelos Papatheou, Weijiang Lin, and Nikolaos Dervilis. A brief introduction to recent developments in population-based structural health monitoring. *Frontiers in Built Environment*, 6:146, 2020.

[34] Piervincenzo Rizzo and Alireza Enshaeian. Challenges in bridge health monitoring: A review. *Sensors*, 21(13):4336, 2021.

[35] Konstantinos Gkoumas, Kyriaki Gkoktsi, Flavio Bono, Maria Cristina Galassi, and Daniel Tirelli. The way forward for indirect structural health monitoring (ishm) using connected and automated vehicles in europe. *Infrastructures*, 6(3):43, 2021.

[36] William Locke, Laura Redmond, and Matthias Schmid. Experimental evaluation of drive-by health monitoring on a short-span bridge using OMA techniques. In *Dynamics of Civil Structures, Volume 2: Proceedings of the 39th IMAC, A Conference and Exposition on Structural Dynamics 2021*, pages 109–127. Springer, 2022.

[37] Ayaho Miyamoto, Risto Kiviluoma, and Akito Yabe. Frontier of continuous structural health monitoring system for short & medium span bridges and condition assessment. *Frontiers of Structural and Civil Engineering*, 13:569–604, 2019.

[38] Zhenkun Li, Weiwei Lin, Youqi Zhang, et al. Bridge frequency scanning using the contact-point response of an instrumented 3d vehicle: Theory and numerical simulation. *Structural Control and Health Monitoring*, 2023, 2023.

[39] Soheil Sadeghi Eshkevari, Shamim N Pakzad, Martin Takáč, and Thomas J Matarazzo. Modal identification of bridges using mobile sensors with sparse vibration data. *Journal of Engineering Mechanics*, 146(4):04020011, 2020.

[40] Abdollah Malekjafarian, Robert Corbally, and Wenjie Gong. A review of mobile sensing of bridges using moving vehicles: Progress to date, challenges and future trends. In *Structures*, volume 44, pages 1466–1489. Elsevier, 2022.

[41] YB Yang and Judy P Yang. State-of-the-art review on modal identification and damage detection of bridges by moving test vehicles. *International Journal of Structural Stability and Dynamics*, 18(02):1850025, 2018.

[42] Daniel Cantero, Patrick McGetrick, Chul-Woo Kim, and Eugene OBrien. Experimental monitoring of bridge frequency evolution during the passage of vehicles with different suspension properties. *Engineering Structures*, 187:209–219, 2019.

[43] Thomas J Matarazzo, Dániel Kondor, Sebastiano Milardo, Soheil S Eshkevari, Paolo Santi, Shamim N Pakzad, Markus J Buehler, and Carlo Ratti. Crowdsourcing bridge dynamic monitoring with smartphone vehicle trips. *Communications engineering*, 1(1):29, 2022.

[44] Qipei Mei, Mustafa Gül, and Nima Shirzad-Ghaleroudkhani. Towards smart cities: crowdsensing-based monitoring of transportation infrastructure using in-traffic vehicles. *Journal of Civil Structural Health Monitoring*, 10(4):653–665, 2020.

[45] YB Yang, Z Li, ZL Wang, K Shi, H Xu, FQ Qiu, and JF Zhu. A novel frequency-free movable test vehicle for retrieving modal parameters of bridges: Theory and experiment. *Mechanical Systems and Signal Processing*, 170:108854, 2022.

[46] S Argyroudis, L Hofer, MA Zanini, and SA Mitoulis. Resilience of critical infrastructure for multiple hazards: Case study on a highway bridge. *ICONHIC Proceedings*, 2019.

[47] Alec W Smith, Sotirios A Argyroudis, Mike G Winter, and Stergios A Mitoulis. Economic impact of bridge functionality loss from a resilience perspective: Queensferry crossing, uk. In *Proceedings of the Institution of Civil Engineers-Bridge Engineering*, volume 174, pages 254–264. Thomas Telford Ltd, 2021.

[48] US Department of Homeland Security: Critical infrastructure. https://www.dhs.gov/science-and-technology/critical-infrastructure. Accessed: 2024-01-18.

[49] Steve Denton, Georgios Tsionis, and Bora Acun. The evolution of eurocodes for bridge design. *European Commision, Joint Research Centre, Institute for the Protection and Security of the Citizen. Luxembourg*, 2012.

[50] Paul C Stern, Kristie L Ebi, Robin Leichenko, Richard Stuart Olson, John D Steinbruner, and Robert Lempert. Managing risk with climate vulnerability science. *Nature Climate Change*, 3(7):607–609, 2013.

[51] American Society of Civil Engineers: 2021 report card for America's infrastructure. https://infrastructurereportcard.org/cat-item/bridges-infrastructure/. Accessed: 2024-01-18.

[52] Ministry of Land, Infrastructure, Transport and Tourism: White paper on land, infrastructure, transport and tourism in Japan, 2019. https://www.mlit.go.jp/common/001325161.pdf. Accessed: 2024-01-18.

[53] Eugene OBrien, Andrzej Nowak, and Colin Caprani. *Bridge traffic loading: From research to practice*. CRC Press, 2021.

[54] Balthasar Novák. German guidelines for the re-assessment of existing highway bridges. In *Maintenance, Monitoring, Safety, Risk and Resilience of Bridges and Bridge Networks*, pages 295–295. CRC Press, 2016.

[55] Silvia Manarin, Mariano Angelo Zanini, Flora Faleschini, and Carlo Pellegrino. A critical analysis based on the comparison between traditional and advanced approaches to the visual inspection of bridges and viaducts. In *International Conference on Experimental Vibration Analysis for Civil Engineering Structures*, pages 750–759. Springer, 2023.

[56] Zehra Irem Turksezer, Chiara Iacovino, Pier Francesco Giordano, and Maria Pina Limongelli. Development and implementation of indicators to assess bridge inspection practices. *Journal of Construction Engineering and Management*, 147(12):04021165, 2021.

[57] Highways England. Cs 450 inspection of highway structures, version 0.10 (2021). *The National Archives: London, UK*, 2021.

[58] Piervincenzo Rizzo and Alireza Enshaeian. Bridge health monitoring in the united states: A review. *Structural Monitoring and Maintenance*, 8(1):1, 2021.

[59] Dean S Carder. Observed vibrations of bridges. *Bulletin of the Seismological Society of America*, 27(4):267–303, 1937.

[60] Christian Boller. Encyclopedia of structural health monitoring. *(No Title)*, 2009.

[61] Sandeep Sony, Shea Laventure, and Ayan Sadhu. A literature review of next-generation smart sensing technology in structural health monitoring. *Structural Control and Health Monitoring*, 26(3):e2321, 2019.

[62] Oliver Riches, Chris Hill, and Paul Baralos. Queensferry crossing, uk: Durability, maintenance, inspection and monitoring. In *Proceedings of the Institution of Civil Engineers-Bridge Engineering*, volume 172, pages 175–188. Thomas Telford Ltd, 2019.

[63] Jinping Ou and Hui Li. Structural health monitoring in mainland china: review and future trends. *Structural health monitoring*, 9(3):219–231, 2010.

[64] Charles R Farrar and Keith Worden. *Structural health monitoring: a machine learning perspective*. John Wiley & Sons, 2012.

[65] E Peter Carden and Paul Fanning. Vibration based condition monitoring: a review. *Structural health monitoring*, 3(4):355–377, 2004.

[66] Keith Worden, Charles R Farrar, Graeme Manson, and Gyuhae Park. The fundamental axioms of structural health monitoring. *Proceedings of the Royal Society A: Mathematical, Physical and Engineering Sciences*, 463(2082):1639–1664, 2007.

[67] Keith Worden, Elizabeth J Cross, Nikolaos Dervilis, Evangelos Papatheou, and Ifigeneia Antoniadou. Structural health monitoring: from structures to systems-of-systems. *IFAC-papersonline*, 48(21):1–17, 2015.

[68] David J Ewins. *Modal testing: theory, practice and application*. John Wiley & Sons, 2009.

[69] Zhi-Fang Fu and Jimin He. *Modal analysis*. Elsevier, 2001.

[70] Carlo Rainieri and Giovanni Fabbrocino. Operational modal analysis of civil engineering structures. *Springer, New York*, 142:143, 2014.

[71] Hamed Hasani and Francesco Freddi. Operational modal analysis on bridges: A comprehensive review. *Infrastructures*, 8(12):172, 2023.

[72] Eli Parloo, Peter Verboven, Patrick Guillaume, and Marc Van Overmeire. Sensitivity-based operational mode shape normalisation. *Mechanical systems and signal processing*, 16(5):757–767, 2002.

[73] Eli Parloo, Bart Cauberghe, Francesco Benedettini, Rocco Alaggio, and Patrick Guillaume. Sensitivity-based operational mode shape normalisation: Application to a bridge. *Mechanical Systems and Signal Processing*, 19(1):43–55, 2005.

[74] Wei Fan and Pizhong Qiao. Vibration-based damage identification methods: a review and comparative study. *Structural health monitoring*, 10(1):83–111, 2011.

[75] Peter Cawley and Robert Darius Adams. The location of defects in structures from measurements of natural frequencies. *The Journal of Strain Analysis for Engineering Design*, 14(2):49–57, 1979.

[76] Jeong-Tae Kim, Yeon-Sun Ryu, Hyun-Man Cho, and Norris Stubbs. Damage identification in beam-type structures: frequency-based method vs mode-shape-based method. *Engineering structures*, 25(1):57–67, 2003.

[77] Juan R Casas and Angel C Aparicio. Structural damage identification from dynamic-test data. *Journal of Structural Engineering*, 120(8):2437–2450, 1994.

[78] Scott W Doebling, Charles R Farrar, Michael B Prime, and Daniel W Shevitz. Damage identification and health monitoring of structural and mechanical systems from changes in their vibration characteristics: a literature review. 1996.

[79] Fabrizio Vestroni and Danilo Capecchi. Damage evaluation in cracked vibrating beams using experimental frequencies and finite element models. *Journal of Vibration and Control*, 2(1):69–86, 1996.

[80] Randall J Allemang. A correlation coefficient for modal vector analysis. In *Proc. of the 1st IMAC*, pages 110–116, 1982.

[81] J-H Kim, H-S Jeon, and C-W Lee. Applications of the modal assurance criteria for detecting and locating structural faults. In *Proceedings of the international modal analysis conference*, pages 536–536. SEM Society for Experimental Mechanics Inc, 1992.

[82] AK Pandey, M Biswas, and MM Samman. Damage detection from changes in curvature mode shapes. *Journal of sound and vibration*, 145(2):321–332, 1991.

[83] MM Abdel Wahab and Guido De Roeck. Damage detection in bridges using modal curvatures: application to a real damage scenario. *Journal of Sound and vibration*, 226(2):217–235, 1999.

[84] T Toksoy and AE Aktan. Bridge-condition assessment by modal flexibility. *Experimental Mechanics*, 34:271–278, 1994.

[85] Hiroki Yamaguchi, Yasunao Matsumoto, Kousuke Kawarai, Abeykoon Jalath Dammika, Saeed Shahzad, and Ryuichi Takanami. Damage detection based on modal damping change in bridges. 2012.

[86] Charles R Farrar, WE Baker, TM Bell, KM Cone, TW Darling, TA Duffey, A Eklund, and A Migliori. Dynamic characterization and damage detection in the i-40 bridge over the rio grande. Technical report, Los Alamos National Lab., NM (United States), 1994.

[87] Charles R Farrar, Scott W Doebling, and David A Nix. Vibration–based structural damage identification. *Philosophical Transactions of the Royal Society of London. Series A: Mathematical, Physical and Engineering Sciences*, 359(1778):131–149, 2001.

[88] Diego A Tibaduiza Burgos, Ricardo C Gomez Vargas, Cesar Pedraza, David Agis, and Francesc Pozo. Damage identification in structural health monitoring: A brief review from its implementation to the use of data-driven applications. *Sensors*, 20(3):733, 2020.

[89] Hoon Sohn. Effects of environmental and operational variability on structural health monitoring. *Philosophical Transactions of the Royal Society A: Mathematical, Physical and Engineering Sciences*, 365(1851):539–560, 2007.

[90] CY Kim, NS Kim, JG Yoon, and DS Jung. Effect of vehicle mass on the measured dynamic characteristics of bridges from traffic-induced vibration test. In *Proceedings-SPIE the International Society for Optical Engineering*, volume 2, pages 1106–1111. Citeseer, 2001.

[91] Guido De Roeck, Johan Maeck, et al. Traffic-induced shifts in modal properties of bridges. In *IMAC 20, the International Modal Analysis Conference*, volume 4753, pages 630–636. Society of Photo-optical Instrumentation Engineers, 2002.

[92] QW Zhang, LC Fan, and WC Yuan. Traffic-induced variability in dynamic properties of cable-stayed bridge. *Earthquake engineering & structural dynamics*, 31(11):2015–2021, 2002.

[93] Boris S Kerner, Sergey L Klenov, and Dietrich E Wolf. Cellular automata approach to three-phase traffic theory. *Journal of Physics A: Mathematical and General*, 35(47):9971, 2002.

[94] David García Cava, Luis David Avendaño-Valencia, Artur Movsessian, Callum Roberts, and Dmitri Tcherniak. On explicit and implicit procedures to mitigate environmental and operational variabilities in data-driven structural health monitoring. *Structural Health Monitoring Based on Data Science Techniques*, pages 309–330, 2022.

[95] Bart Peeters and Guido De Roeck. One-year monitoring of the z24-bridge: environmental effects versus damage events. *Earthquake engineering & structural dynamics*, 30(2):149–171, 2001.

[96] Keith Worden, Hoon Sohn, and Charles R Farrar. Novelty detection in a changing environment: regression and interpolation approaches. *Journal of sound and vibration*, 258(4):741–761, 2002.

[97] Hoon Sohn, Keith Worden, and Charles R Farrar. Statistical damage classification under changing environmental and operational conditions. *Journal of intelligent material systems and structures*, 13(9):561–574, 2002.

[98] Hoon Sohn and Charles R Farrar. Damage diagnosis using time series analysis of vibration signals. *Smart materials and structures*, 10(3):446, 2001.

[99] Hoon Sohn, Keith Worden, and Charles R Farrar. Novelty detection using auto-associative neural network. In *ASME International Mechanical Engineering Congress and Exposition*, volume 35609, pages 573–580. American Society of Mechanical Engineers, 2001.

[100] Hoon Sohn, Charles R Farrar, Norman F Hunter, and Keith Worden. Structural health monitoring using statistical pattern recognition techniques. *J. Dyn. Sys., Meas., Control*, 123(4):706–711, 2001.

[101] EJ Cross, Graham Manson, Keith Worden, and SG Pierce. Features for damage detection with insensitivity to environmental and operational variations. *Proceedings of the Royal Society A: Mathematical, Physical and Engineering Sciences*, 468(2148):4098–4122, 2012.

[102] James MW Brownjohn, Prakash Kripakaran, Bill Harvey, Rolands Kromanis, Peter Jones, and Farhad Huseynov. Structural health monitoring of short to medium span bridges in the united kingdom. *Structural Monitoring and Maintenance*, 3(3):259, 2016.

[103] Peter Cawley. Structural health monitoring: Closing the gap between research and industrial deployment. *Structural health monitoring*, 17(5):1225–1244, 2018.

[104] You Lin Xu and Yong Xia. *Structural health monitoring of long-span suspension bridges*. CRC Press, 2011.

[105] Cong Ye, Sin-Chi Kuok, Liam J Butler, and Campbell R Middleton. Implementing bridge model updating for operation and maintenance purposes: Examination based on uk practitioners' views. *Structure and Infrastructure Engineering*, 18(12):1638–1657, 2022.

[106] Yang Yang, Yao Zhang, and Xiaokun Tan. Review on vibration-based structural health monitoring techniques and technical codes. *Symmetry*, 13(11):1998, 2021.

[107] Yeong-Bin Yang, Judy P Yang, Yuntian Wu, and Bin Zhang. *Vehicle scanning method for bridges*. John Wiley & Sons, 2019.

[108] Muhammad Zohaib Sarwar and Daniel Cantero. Vehicle assisted bridge damage assessment using probabilistic deep learning. *Measurement*, 206:112216, 2023.

[109] ZL Wang, Judy P Yang, K Shi, H Xu, FQ Qiu, and YB Yang. Recent advances in researches on vehicle scanning method for bridges. *International Journal of Structural Stability and Dynamics*, 22(15):2230005, 2022.

[110] Qipei Mei and Mustafa Gül. A crowdsourcing-based methodology using smartphones for bridge health monitoring. *Structural Health Monitoring*, 18(5-6):1602–1619, 2019.

[111] Thomas J Matarazzo, Dániel Kondor, Sebastiano Milardo, Soheil S Eshkevari, Paolo Santi, Shamim N Pakzad, Markus J Buehler, and Carlo Ratti. Crowdsourcing bridge vital signs with smartphone vehicle trips. *arXiv preprint arXiv:2010.07026*, 2020.

[112] XW Ye, T Jin, and CB Yun. A review on deep learning-based structural health monitoring of civil infrastructures. *Smart Struct. Syst*, 24(5):567–585, 2019.

[113] Abdollah Malekjafarian, Fatemeh Golpayegani, Callum Moloney, and Siobhán Clarke. A machine learning approach to bridge-damage detection using responses measured on a passing vehicle. *Sensors*, 19(18):4035, 2019.

[114] Abdollah Malekjafarian, Callum Moloney, and Fatemeh Golpayegani. Drive-by bridge health monitoring using multiple passes and machine learning. In *European Workshop on Structural Health Monitoring: Special Collection of 2020 Papers-Volume 1*, pages 695–703. Springer, 2021.

[115] Robert Corbally and Abdollah Malekjafarian. A data-driven approach for drive-by damage detection in bridges considering the influence of temperature change. *Engineering Structures*, 253:113783, 2022.

[116] Robert Corbally and Abdollah Malekjafarian. A deep-learning framework for classifying the type, location, and severity of bridge damage using drive-by measurements. *Computer-Aided Civil and Infrastructure Engineering*, 2023.

[117] Donya Hajializadeh. Machine-learning-based bridge damage detection using train-borne measurements. *Proceedings of the Institution of Civil Engineers-Smart Infrastructure and Construction*, 40(XXXX):1–15, 2023.

[118] Y-B Yang, CW Lin, and JD Yau. Extracting bridge frequencies from the dynamic response of a passing vehicle. *Journal of Sound and Vibration*, 272(3-5):471–493, 2004.

[119] Thomas D Gillespie. Heavy truck ride. Technical report, SAE Technical Paper, 1985.

[120] Tom Irvine. Two-stage isolation for harmonic base excitation, revision C. 2015.

[121] Joop Pauwelussen. *Essentials of vehicle dynamics*. Butterworth-Heinemann, 2014.

[122] Massimo Guiggiani et al. The science of vehicle dynamics. *Pisa, Italy: Springer Netherlands*, 15, 2014.

[123] G Verros, S Natsiavas, and C Papadimitriou. Design optimization of quarter-car models with passive and semi-active suspensions under random road excitation. *Journal of vibration and control*, 11(5):581–606, 2005.

[124] D Hrovat. Influence of unsprung weight on vehicle ride quality. *Journal of Sound and Vibration*, 124(3):497–516, 1988.

[125] S Hegazy and AM Sharaf. Ride comfort analysis using quarter car model. In *International Conference on Aerospace Sciences and Aviation Technology*, volume 15, pages 1–11. The Military Technical College, 2013.

[126] Sunil Kumar Sharma and Rakesh Chandmal Sharma. Simulation of quarter-car model with magnetorheological dampers for ride quality improvement. *International Journal of Vehicle Structures & Systems*, 10(3):169–173, 2018.

[127] Semiha Türkay and Hüseyin Akçay. A study of random vibration characteristics of the quarter-car model. *Journal of sound and vibration*, 282(1-2):111–124, 2005.

[128] P Sathishkumar, J Jancirani, Dennie John, and S Manikandan. Mathematical modelling and simulation quarter car vehicle suspension. *International Journal of Innovative Research in Science, Engineering and Technology*, 3(1):1280–1283, 2014.

[129] Trupti P Phalke and Anirban C Mitra. Analysis of ride comfort and road holding of quarter car model by simulink. *Materials Today: Proceedings*, 4(2):2425–2430, 2017.

[130] NP Puneet, Abhinandan Hegale, Hemantha Kumar, and KV Gangadharan. Multi objective optimization of quarter car parameters for better ride comfort and road holding. In *AIP conference proceedings*, volume 2200. AIP Publishing, 2019.

[131] Michael Valášek and Jaromír Kejval. Limited-active road-friendly truck suspension. *Vehicle System Dynamics*, 37(sup1):75–82, 2002.

[132] D Cebon. Theoretical road damage due to dynamic tyre forces of heavy vehicles part 2: simulated damage caused by a tandem-axle vehicle. *Proceedings of the Institution of Mechanical Engineers, Part C: Journal of Mechanical Engineering Science*, 202(2):109–117, 1988.

[133] MJ Pable, MM Gawture, and P Seshu. A review of 'road-friendly'suspensions. In *National Conference on Mechanisms and Machines (13th NaCoMM07)*, pages 12–13, 2007.

[134] Peter J Caldicott. Distribution testing—sine or random? *Packaging Technology and Science*, 4(5):287–291, 1991.

[135] Garren Lewis. *Isolation of Damaging Vibrations to Strawberries being Transported via a Robotic Harvest-aid*. University of California, Davis, 2016.

[136] Eugene J OBrien, Abdollah Malekjafarian, and Arturo González. Application of empirical mode decomposition to drive-by bridge damage detection. *European Journal of Mechanics-A/Solids*, 61:151–163, 2017.

[137] Chengjun Tan, Nasim Uddin, Eugene J OBrien, Patrick J McGetrick, and Chul-Woo Kim. Extraction of bridge modal parameters using passing vehicle response. *Journal of Bridge Engineering*, 24(9):04019087, 2019.

[138] Soheil Sadeghi Eshkevari, Thomas J Matarazzo, and Shamim N Pakzad. Simplified vehicle–bridge interaction for medium to long-span bridges subject to random traffic load. *Journal of Civil Structural Health Monitoring*, 10:693–707, 2020.

[139] Omar R Abuodeh and Laura Redmond. A framework for developing efficient vehicle-bridge interaction models within a commercial finite element software. In *Dynamics of Civil Structures, Volume 2: Proceedings of the 40th IMAC, A Conference and Exposition on Structural Dynamics 2022*, pages 67–73. Springer, 2022.

[140] Kevin B Todd and Bohdan T Kulakowski. Simple computer models for predicting ride quality and pavement loading for heavy trucks. *Transportation research record*, 1215:137–150, 1989.

[141] David Cebon. *Handbook of vehicle-road interaction*. 1999.

[142] John De Pont. *Road profile characterisation*. Transit New Zealand, 1994.

[143] AN Heath. Application of the isotropic road roughness assumption. *Journal of Sound and Vibration*, 115(1):131–144, 1987.

[144] H Prem. Road roughness influence on suspension performance. In *SYMPOSIUM ON HEAVY VEHICLE SUSPENSION*, 1988.

[145] William F Milliken, Douglas L Milliken, and Maurice Olley. *Chassis design: principles and analysis*, volume 400. Society of Automotive Engineers Warrendale, 2002.

[146] Niall K Harris, Eugene J OBrien, and Arturo González. Reduction of bridge dynamic amplification through adjustment of vehicle suspension damping. *Journal of Sound and Vibration*, 302(3):471–485, 2007.

[147] Ahmed Elhattab, Nasim Uddin, and Eugene OBrien. Drive-by bridge damage monitoring using bridge displacement profile difference. *Journal of Civil Structural Health Monitoring*, 6:839–850, 2016.

[148] William Locke, Justin Sybrandt, Laura Redmond, Ilya Safro, and Sez Atamturktur. Using drive-by health monitoring to detect bridge damage considering environmental and operational effects. *Journal of Sound and Vibration*, 468:115088, 2020.

[149] Eugene J OBrien, Daniel P McCrum, and Shuo Wang. Monitoring bearing damage in bridges using accelerations from a fleet of vehicles, without prior bridge or vehicle information. *Engineering Structures*, 302:117414, 2024.

[150] Daniel Cantero and Arturo González. Bridge damage detection using weigh-in-motion technology. *Journal of Bridge Engineering*, 20(5):04014078, 2015.

[151] Daniel Cantero, Arturo González, and Eugene J O'Brien. Comparison of bridge dynamic amplification due to articulated 5-axle trucks and large cranes. *Baltic Journal of Road and Bridge Engineering*, 6(1):39–47, 2011.

[152] T-T Fu and D Cebon. Analysis of a truck suspension database. *International journal of heavy vehicle systems*, 9(4):281–297, 2002.

[153] PS Fancher, RD Ervin, CC MacAdam, and CB Winkler. Measurement and representation of the mechanical properties of truck leaf springs. Technical report, SAE Technical Paper, 1980.

[154] Paul S Fancher, Robert D Ervin, Christopher B Winkler, and Thomas D Gillespie. A factbook of the mechanical properties of the components for single unit and articulated heavy trucks. Technical report, 1986.

[155] Christopher B Winkler, SM Karamihas, and SE Bogard. Roll-stability performance of heavy-vehicle suspensions. *SAE transactions*, pages 652–664, 1992.

[156] Hamish Marshall and Glen Murphy. Factors affecting the accuracy of weighbridge systems. *International Journal of Forest Engineering*, 14(1):67–79, 2003.

[157] Daniel Ainalis, Vincent Rouillard, and Michael Sek. Estimating the ride quality characteristics of vehicles with random decrement analysis of on-the-road vibration response data. *Vehicle System Dynamics*, 54(6):765–783, 2016.

[158] Council Directive. 96/53/ec laying down for certain road vehicles circulating within the community the maximum dimensions in national and international traffic and maximum weights in international traffic. *Official Journal of the European Community L*, 235:39.

[159] Peter Frank Sweatman, S McFarlane, C Ackerman, and RM George. *Ranking of the road friendliness of heavy vehicle suspensions: low frequency dynamics*. Number 13. 1994.

[160] P Milliken, J de Pont, T Mueller, and D Latto. Assessing road-friendly suspensions. *Transfund New Zealand Research Report*, (206), 2001.

[161] Lloyd Davis and R Sack. Analysis of heavy vehicle suspension dynamics using an on-board mass measurement system. In *AUSTRALASIAN TRANSPORT RESEARCH FORUM (ATRF), 27TH, 2004, ADELAIDE, SOUTH AUSTRALIA, AUSTRALIA*, volume 27, 2004.

[162] P Sweatman, S McFarlane, J Komadina, and D Cebon. *In-service Assessment of Road-friendly Suspensions: For Information*. 2000.

[163] BE Quinn and JL Zable. Evaluating highway elevation power spectra from vehicle performance. *Highway Research Record*, (121), 1966.

[164] John De Pont. Suspensions or whole vehicles? rating road–friendliness. *International Journal of Heavy Vehicle Systems*, 6(1-4):75–98, 1999.

[165] John C Houbolt, James H Walls, and Robert F Smiley. On spectral analysis of runway roughness and loads developed during taxiing. Technical report, 1955.

[166] Michael W Sayers. Dynamic terrain inputs to predict structural integrity of ground vehicles. final report. Technical report, 1988.

[167] CJ Dodds and JD Robson. Simulation of dynamic stresses in vehicles and components. *Vehicle System Dynamics*, 4(2-3):130–134, 1975.

[168] Peter Andren. Power spectral density approximations of longitudinal road profiles. *International Journal of Vehicle Design*, 40(1-3):2–14, 2006.

[169] Oldřich Kropáč and Peter Múčka. Classification scheme for random longitudinal road unevenness considering road waviness and vehicle response. *Shock and vibration*, 16(3):273–289, 2009.

[170] Peter Múčka. Simulated road profiles according to iso 8608 in vibration analysis. *Journal of Testing and Evaluation*, 46(1):405–418, 2018.

[171] KC Chang, FB Wu, and YB Yang. Disk model for wheels moving over highway bridges with rough surfaces. *Journal of Sound and Vibration*, 330(20):4930–4944, 2011.

[172] Zhenkun Li, Yifu Lan, and Weiwei Lin. Indirect damage detection for bridges using sensing and temporarily parked vehicles. *Engineering Structures*, 291:116459, 2023.

[173] Jorge Aparecido Marcondes. *Modeling vertical acceleration in truck shipments using the International Roughness Index for pavements.* Michigan State University, 1990.

[174] Arturo González, Eugene J O'brien, Y-Y Li, and K Cashell. The use of vehicle acceleration measurements to estimate road roughness. *Vehicle System Dynamics*, 46(6):483–499, 2008.

[175] Vincent Rouillard and Michael A Sek. A practical method for estimating ground vehicle frequency response function from response data. In *Proceedings of the 6th Australasian Congress on Applied Mechanics*, pages 98–108. Engineers Australia Perth, WA, 2010.

[176] Julius S Bendat and Allan G Piersol. *Random data: analysis and measurement procedures.* John Wiley & Sons, 2011.

[177] Daniel Ainalis, Vincent Rouillard, and Michael Sek. Issues with combining road elevation spectral models and vehicle vibration response to estimate vehicle dynamic characteristics. *Packaging Technology and Science*, 28(3):253–270, 2015.

[178] Daniel Ainalis, Vincent Rouillard, and Michael Sek. Practical considerations for estimating road vehicle frequency response functions from response data. *Packaging Technology and Science*, 30(4):127–144, 2017.

[179] Daniel T Ainalis, Vincent Rouillard, and Michael A Sek. Evaluation of experimental techniques for establishing vehicle suspension characteristics. In *Proceedings: the 7th Australasian Congress on Applied Mechanics (ACAM 7), 9-12 December 2012, the University of Adelaide, North Terrace Campus/National Committee on Applied Mechanics of Engineers Australia*, pages 788–799. Engineers Australia Barton ACT, 2012.

[180] Daniel T Ainalis, Vincent Rouillard, and Michael A Sek. Issues with the experimental characterisation of automotive shock absorbers for vehicle dynamic simulations. In *8th Australasian Congress on Applied Mechanics: ACAM 8: ACAM 8*, pages 323–331. Engineers Australia Barton, ACT, 2014.

[181] Daniel Ainalis, Vincent Rouillard, and Michael Sek. Estimation of road transport vehicle dynamic characteristics using random decrement analysis and on-the-road vibration data. *International Journal of Vehicle Design*, 76(1-4):140–162, 2018.

[182] CW Lin and YB Yang. Use of a passing vehicle to scan the fundamental bridge frequencies: An experimental verification. *Engineering Structures*, 27(13):1865–1878, 2005.

[183] Ayaho Miyamoto and Akito Yabe. Bridge condition assessment based on vibration responses of passenger vehicle. In *Journal of physics: conference series*, volume 305, page 012103. IOP Publishing, 2011.

[184] Ayaho Miyamoto and Akito Yabe. Development of practical health monitoring system for short-and medium-span bridges based on vibration responses of city bus. *Journal of Civil Structural Health Monitoring*, 2:47–63, 2012.

[185] Dionysius M Siringoringo and Yozo Fujino. Estimating bridge fundamental frequency from vibration response of instrumented passing vehicle: analytical and experimental study. *Advances in Structural Engineering*, 15(3):417–433, 2012.

[186] Ahmed Elhattab, Nasim Uddin, and Eugene OBrien. Drive-by bridge frequency identification under operational roadway speeds employing

frequency independent underdamped pinning stochastic resonance (fi-upsr). *Sensors*, 18(12):4207, 2018.

[187] YB Yang, Hao Xu, Bin Zhang, Feng Xiong, and ZL Wang. Measuring bridge frequencies by a test vehicle in non-moving and moving states. *Engineering Structures*, 203:109859, 2020.

[188] YB Yang, Hao Xu, ZL Wang, K Shi, and YT Wu. Refined detection technique for bridge frequencies using rocking motion of single-axle moving vehicle. *Mechanical Systems and Signal Processing*, 162:107992, 2022.

[189] Angelo Aloisio and Rocco Alaggio. Experimental estimation of the elastic modulus of concrete girders from drive-by inspections with force-balance accelerometers. *Shock and Vibration*, 2021:1–12, 2021.

[190] Nima Shirzad-Ghaleroudkhani and Mustafa Gül. An enhanced inverse filtering methodology for drive-by frequency identification of bridges using smartphones in real-life conditions. *Smart Cities*, 4(2):499–513, 2021.

[191] Alberto Di Matteo, Dario Fiandaca, and Antonina Pirrotta. Smartphone-based bridge monitoring through vehicle–bridge interaction: analysis and experimental assessment. *Journal of Civil Structural Health Monitoring*, 12(6):1329–1342, 2022.

[192] Dario Fiandaca, Alberto Di Matteo, Bernardo Patella, Nadia Moukri, Rosalinda Inguanta, Daniel Llort, Antonio Mulone, Angelo Mulone, Soughah Alsamahi, and Antonina Pirrotta. An integrated approach for structural health monitoring and damage detection of bridges: An experimental assessment. *Applied Sciences*, 12(24):13018, 2022.

[193] Premjeet Singh and Ayan Sadhu. A hybrid time-frequency method for robust drive-by modal identification of bridges. *Engineering Structures*, 266:114624, 2022.

[194] Dongming Feng and Maria Q Feng. Computer vision for shm of civil infrastructure: From dynamic response measurement to damage detection–a review. *Engineering Structures*, 156:105–117, 2018.

[195] Tarak Gandhi, Remy Chang, and Mohan Manubhai Trivedi. Video and seismic sensor-based structural health monitoring: Framework, algorithms, and implementation. *IEEE Transactions on intelligent transportation systems*, 8(2):169–180, 2007.

[196] Chin An Tan, Demeke Beyene Ashebo, Maria Q Feng, and Yoshio Fukuda. Integration of traffic information in the structural health monitoring of highway bridges. In *Sensors and Smart Structures Technologies for Civil, Mechanical, and Aerospace Systems 2007*, volume 6529, pages 471–480. SPIE, 2007.

[197] F Necati Catbas, Ricardo Zaurin, Mustafa Gul, and Hasan Burak Gokce. Sensor networks, computer imaging, and unit influence lines for structural health monitoring: Case study for bridge load rating. *Journal of Bridge Engineering*, 17(4):662–670, 2012.

[198] T Ojio, CH Carey, Eugene J OBrien, C Doherty, and Su E Taylor. Contactless bridge weigh-in-motion. *Journal of Bridge Engineering*, 21(7):04016032, 2016.

[199] Wei He, Jifan Liu, Shiqi Song, and Peng Liu. A non-contact vehicle weighing approach based on bridge weigh-in-motion framework and computer vision techniques. *Measurement*, 225:113994, 2024.

[200] Maria Q Feng, Ryan Y Leung, and Casey M Eckersley. Non-contact vehicle weigh-in-motion using computer vision. *Measurement*, 153:107415, 2020.

[201] Maria Q Feng and Ryan Y Leung. Application of computer vision for estimation of moving vehicle weight. *IEEE Sensors Journal*, 21(10):11588–11597, 2020.

[202] Alberto Martini, Eleonora M Tronci, Maria Q Feng, and Ryan Y Leung. A computer vision-based method for bridge model updating using displacement influence lines. *Engineering Structures*, 259:114129, 2022.

[203] Arturo González. Vehicle-bridge dynamic interaction using finite element modelling. In *Moratal D.(ed.). Finite Element Analysis*. InTech, 2010.

[204] Great Britain. Commissioners appointed to inquire into the application of iron to railway structures. *Report of the Commissioners Appointed to Inquire Into the Application of Iron to Railway Structures...*, volume 1. William Clowes and sons, 1849.

[205] Sir George Gabriel Stokes. *Discussion of a differential equation relating to the breaking of railway bridges*. Printed at the Pitt Press by John W. Parker, 1849.

[206] HH Jeffcott. Vi. on the vibration of beams under the action of moving loads. *The London, Edinburgh, and Dublin Philosophical Magazine and Journal of Science*, 8(48):66–97, 1929.

[207] CE Inglis. A mathematical treatise on vibrations in railway bridges, 1934.

[208] S.P. Timoshenko and D.H. Young. *Vibration Problems in Engineering*. D. Van Nostrand, New York, 1955.

[209] John M Biggs and John Biggs. *Introduction to structural dynamics*. McGraw-Hill College, 1964.

[210] Tianyang Ling, Ran Cao, Lu Deng, Wei He, Xin Wu, and Wenjie Zhong. Dynamic impact of automated truck platooning on highway bridges. *Engineering Structures*, 262:114326, 2022.

[211] Lei Mao and Yong Lu. Critical speed and resonance criteria of railway bridge response to moving trains. *Journal of Bridge Engineering*, 18(2):131–141, 2013.

[212] YB Yang and KC Chang. Extraction of bridge frequencies from the dynamic response of a passing vehicle enhanced by the emd technique. *Journal of sound and vibration*, 322(4-5):718–739, 2009.

[213] YB Yang, YC Li, and KC29575771401 Chang. Using two connected vehicles to measure the frequencies of bridges with rough surface: a theoretical study. *Acta Mechanica*, 223:1851–1861, 2012.

[214] Abdollah Malekjafarian and Eugene J O'Brien. Application of output-only modal method in monitoring of bridges using an instrumented vehicle. In *Civil Engineering Research in Ireland, Belfast, UK, 28-29 August, 2014*, 2014.

[215] Yoshinobu Oshima, Kyosuke Yamamoto, and Kunitomo Sugiura. Damage assessment of a bridge based on mode shapes estimated by responses of passing vehicles. *Smart Structures and Systems*, 13(5):731–753, 2014.

[216] Patrick J McGetrick, A Gonzalez, and Eugene J OBrien. Theoretical investigation of the use of a moving vehicle to identify bridge dynamic parameters. *Insight-Non-Destructive Testing and Condition Monitoring*, 51(8):433–438, 2009.

[217] Eugene Obrien and Jennifer Keenahan. Using instrumented quarter-cars for "drive by" bridge inspection. In *Proceedings of the 2013 International Association for Bridge and Structural Engineering Conference (IABSE 2013)*, 2013.

[218] Hao Wang, Jian-Xiao Mao, and Billie F Spencer Jr. A monitoring-based approach for evaluating dynamic responses of riding vehicle on long-span bridge under strong winds. *Engineering Structures*, 189:35–47, 2019.

[219] Kamyar Kildashti, M Makki Alamdari, CW Kim, Wei Gao, and Bijan Samali. Drive-by-bridge inspection for damage identification in a cable-stayed bridge: Numerical investigations. *Engineering structures*, 223:110891, 2020.

[220] Robert Corbally and Abdollah Malekjafarian. Examining changes in bridge frequency due to damage using the contact-point response of a passing vehicle. *Journal of Structural Integrity and Maintenance*, 6(3):148–158, 2021.

[221] Yifu Lan, Zhenkun Li, and Weiwei Lin. Physics-guided diagnosis framework for bridge health monitoring using raw vehicle accelerations. *Mechanical Systems and Signal Processing*, 206:110899, 2024.

[222] HL Li, ZR Lu, and JK Liu. Identification of distributed damage in bridges from vehicle-induced dynamic responses. *Advances in Structural Engineering*, 19(6):945–952, 2016.

[223] Dongming Feng and Maria Q Feng. Output-only damage detection using vehicle-induced displacement response and mode shape curvature index. *Structural Control and Health Monitoring*, 23(8):1088–1107, 2016.

[224] Chengyin Liu, Yipeng Zhu, and Hui Ye. Bridge frequency identification based on relative displacement of axle and contact point using tire pressure monitoring. *Mechanical Systems and Signal Processing*, 183:109613, 2023.

[225] Qiling Zou, Lu Deng, Tieding Guo, and Xinfeng Yin. Comparative study of different numerical models for vehicle–bridge interaction analysis. *International Journal of Structural Stability and Dynamics*, 16(09):1550057, 2016.

[226] Charikleia D Stoura and Elias G Dimitrakopoulos. Additional damping effect on bridges because of vehicle-bridge interaction. *Journal of Sound and Vibration*, 476:115294, 2020.

[227] A Doménech, P Museros, and MD Martínez-Rodrigo. Influence of the vehicle model on the prediction of the maximum bending response of simply-supported bridges under high-speed railway traffic. *Engineering Structures*, 72:123–139, 2014.

[228] Therese Arvidsson, Raid Karoumi, and Costin Pacoste. Statistical screening of modelling alternatives in train–bridge interaction systems. *Engineering structures*, 59:693–701, 2014.

[229] JD Yau, María D Martínez-Rodrigo, and A Doménech. An equivalent additional damping approach to assess vehicle-bridge interaction for train-induced vibration of short-span railway bridges. *Engineering Structures*, 188:469–479, 2019.

[230] MF Green and D Cebon. Dynamic interaction between heavy vehicles and highway bridges. *Computers & structures*, 62(2):253–264, 1997.

[231] XQ Zhu and SS Law. Dynamic load on continuous multi-lane bridge deck from moving vehicles. *Journal of Sound and Vibration*, 251(4):697–716, 2002.

[232] Daniel Cantero, Eugene J OBrien, Arturo González, Bernard Enright, and Cillian Rowley. Highway bridge assessment for dynamic interaction with critical vehicles. 2009.

[233] A Feriani, MARIA GABRIELLA Mulas, G Lucchini, et al. Vehicle-bridge interaction analysis: an uncoupled approach. In *Proceedings of the 2008 International Conference on Noise and Vibration Engineering-CD ROM*, pages 609–624. KATHOLIEKE UNIV LEUVEN, DEPT WERKTUIGKUNDE,, 2008.

[234] A Feriani, MARIA GABRIELLA Mulas, E Poli, et al. An uncoupled iterative approach for bridge-vehicle coupled systems. In *Proceedings of the 8th International Conference on Structural Dynamics-EURODYN 2011*, pages 1289–1296. EUROPEAN ASSOC. STRUCTURAL DYNAMICS, 2011.

[235] Dukkipati RV JGarg VK. *Dynamics of railway vehicle systems*. New York: Academic Press, 1984.

[236] Yeong-Bin Yang and Jong-Dar Yau. Vehicle-bridge interaction element for dynamic analysis. *Journal of Structural Engineering*, 123(11):1512–1518, 1997.

[237] Yeong-Bin Yang and Bing-Houng Lin. Vehicle-bridge interaction analysis by dynamic condensation method. *Journal of Structural Engineering*, 121(11):1636–1643, 1995.

[238] Yeong-Bin Yang and Yean-Seng Wu. A versatile element for analyzing vehicle–bridge interaction response. *Engineering structures*, 23(5):452–469, 2001.

[239] Jiantao Li, Xinqun Zhu, Siu-seong Law, and Bijan Samali. Time-varying characteristics of bridges under the passage of vehicles using synchroextracting transform. *Mechanical Systems and Signal Processing*, 140:106727, 2020.

[240] MathWorks MATLAB - math. graphics. programming. https://uk.mathworks.com/products/matlab.html. Accessed: 2024-01-29.

[241] Yifu Lan. Improving the drive-by bridge inspection performance by vehicle parameter optimization. In *Proceedings of the 8th Asia Pacific Workshop on Structural Health Monitoring (8AMWSHM), Cairns, Queensland, Australia*, pages 195–202, 2021.

[242] Luke J Prendergast, David Hester, Kenneth Gavin, et al. Development of a vehicle-bridge-soil dynamic interaction model for scour damage modelling. *Shock and Vibration*, 2016, 2016.

[243] Abaqus - finite element analysis for mechanical engineering and civil engineering. https://www.3ds.com/products/simulia/abaqus. Accessed: 2024-01-29.

[244] Sudanna Borjigin, Chul-Woo Kim, Kai-Chun Chang, and Kunitomo Sugiura. Nonlinear dynamic response analysis of vehicle–bridge interactive system under strong earthquakes. *Engineering Structures*, 176:500–521, 2018.

[245] Jian-An Li and Dongming Feng. A comparative study of vehicle-bridge interaction dynamics with 2d and 3d vehicle models. *Engineering Structures*, 292:116493, 2023.

[246] Xuzhao Lu, Chul-Woo Kim, and Kai-Chun Chang. Finite element analysis framework for dynamic vehicle-bridge interaction system based on abaqus. *International Journal of Structural Stability and Dynamics*, 20(03):2050034, 2020.

[247] Atef F Saleeb and Abhimanyu Kumar. Automated finite element analysis of complex dynamics of primary system traversed by oscillatory subsystem. *International Journal for Computational Methods in Engineering Science and Mechanics*, 12(4):184–202, 2011.

[248] Jou-Yi Shih. *Models for vehicle/track/ground interaction in the time domain*. PhD thesis, University of Southampton, 2017.

[249] YS Cheng, FTK Au, YK Cheung, and DY Zheng. On the separation between moving vehicles and bridge. *Journal of Sound and Vibration*, 222(5):781–801, 1999.

[250] DY Zhu, YH Zhang, and H Ouyang. A linear complementarity method for dynamic analysis of bridges under moving vehicles considering separation and surface roughness. *Computers & Structures*, 154:135–144, 2015.

[251] Omar Abuodeh, William Locke, Laura Redmond, Rakesh Vulchi Sreenivasulu, and Matthias Schmid. Examining methods for modeling road surface roughness effects in vehicle–bridge interaction models via physical testing. In *Society for Experimental Mechanics Annual Conference and Exposition*, pages 33–47. Springer, 2023.

[252] Patrick McGetrick, Chul-Woo Kim, Arturo González, et al. Dynamic axle force and road profile identification using a moving vehicle. *International Journal of Architecture, Engineering and Construction*, 2(1):1–16, 2013.

[253] Jan Kortis, Lubos Daniel, and Maros Duratny. The simulation of the influence of surface irregularities in road pavements on the response of the bridge to moving vehicle. *Procedia engineering*, 199:2991–2996, 2017.

[254] Kun Feng, Miguel Casero, and Arturo González. Characterization of the road profile and the rotational stiffness of supports in a bridge based on axle accelerations of a crossing vehicle. *Computer-Aided Civil and Infrastructure Engineering*, 2023.

[255] A Aloisio, R Alaggio, A Contento, and B Briseghella. The effect of road roughness on vehicle-bridge interaction modeling. In *Life-Cycle of Structures and Infrastructure Systems*, pages 2746–2753. CRC Press, 2023.

[256] Yao Zhang, Hai Sheng Zhao, and Seng Tjhen Lie. A simple approach for simulating the road surface roughness involved in vehicle-bridge interaction systems. *International Journal of Structural Stability and Dynamics*, 18(07):1871009, 2018.

[257] Kultigin Demirlioglu, Semih Gonen, and Emrah Erduran. Effect of road roughness on the dynamic response of vehicles in vehicle-bridge interaction modeling. In *International Conference on Experimental Vibration Analysis for Civil Engineering Structures*, pages 294–304. Springer, 2023.

[258] YB Yang, Zhi-Lu Wang, Kang Shi, Hao Xu, and YT Wu. State-of-the-art of vehicle-based methods for detecting various properties of highway bridges and railway tracks. *International Journal of Structural Stability and Dynamics*, 20(13):2041004, 2020.

[259] Hoofar Shokravi, Hooman Shokravi, Norhisham Bakhary, Mahshid Heidarrezaei, Seyed Saeid Rahimian Koloor, and Michal Petrů. Vehicle-assisted techniques for health monitoring of bridges. *Sensors*, 20(12):3460, 2020.

[260] YB Yang and CW Lin. Vehicle–bridge interaction dynamics and potential applications. *Journal of sound and vibration*, 284(1-2):205–226, 2005.

[261] Arturo González, Eugene J OBrien, and PJ McGetrick. Detection of bridge dynamic parameters using an instrumented vehicle. In *Proceedings of the Fifth World Conference on Structural Control and Monitoring*, 2010.

[262] Chul-Woo Kim, R Isemoto, T Toshinami, Mitsuo Kawatani, P McGetrick, and Eugene J O'Brien. Experimental investigation of drive-by bridge inspection. In *5th International Conference on Structural Health Monitoring of Intelligent Infrastructure (SHMII-5), Cancun, Mexico, 11-15 December, 2011*. Instituto de Ingeniería, UNAM, 2011.

[263] T Toshinami, M Kawatani, and C Kim. Feasibility investigation for identifying bridge's fundamental frequencies from vehicle vibrations. In *Proceedings of the Fifth International IABMAS Conference on Bridge Maintenance, Safety, Management and Life-Cycle Optimization*, page 108, 2010.

[264] Yoshinobu Oshima, T Yamaguchi, Y Kobayashi, and Kunitomo Sugiura. Eigenfrequency estimation for bridges using the response of a passing

vehicle with excitation system. *BRIDGE MAINTENANCE, SAFETY, MANAGEMENT, HEALTH MONITORING AND INFORMATICS*, page 591, 2008.

[265] Zhenhua Shi and Nasim Uddin. Extracting multiple bridge frequencies from test vehicle–a theoretical study. *Journal of Sound and Vibration*, 490:115735, 2021.

[266] Judy P Yang. Theoretical formulation of three-mass vehicle model for vehicle–bridge interaction. *International Journal of Structural Stability and Dynamics*, 21(07):2171004, 2021.

[267] Judy P Yang and Chun-Hsien Wu. Vehicle-bridge interaction system with non-uniform beams. *International Journal of Structural Stability and Dynamics*, 21(12):2150170, 2021.

[268] Judy P Yang and Bo-Lin Chen. Rigid-mass vehicle model for identification of bridge frequencies concerning pitching effect. *International Journal of Structural Stability and Dynamics*, 19(02):1950008, 2019.

[269] Judy P Yang and Jyu-Yi Sun. Pitching effect of a three-mass vehicle model for analyzing vehicle-bridge interaction. *Engineering Structures*, 224:111248, 2020.

[270] Xuzhao Lu, Limin Sun, Chul-Woo Kim, Kai-Chun Chang, and Zhuoran Han. Bridge frequency identification from multiple moving-vehicle dynamics using cross-spectrum method. In *Bridge Safety, Maintenance, Management, Life-Cycle, Resilience and Sustainability*, pages 1087–1094. CRC Press, 2022.

[271] Yifu Lan, Weiwei Lin, Youqi Zhang, et al. Bridge frequency identification using vibration responses from sensors on a passing vehicle. *Proceedings of the Bridge Safety, Maintenance, Management, Life-Cycle, Resilience and Sustainability*, 2022.

[272] Y Oshima, K Yamamoto, K Sugiura, and T Yamaguchi. Estimation of bridge eigenfrequencies based on vehicle responses using ica. In *Proceedings of the 10th International Conference on Structural Safety and Reliability (ICOSSAR'09)*, 2009.

[273] Judy P Yang and Wei-Chun Lee. Damping effect of a passing vehicle for indirectly measuring bridge frequencies by emd technique. *International Journal of Structural Stability and Dynamics*, 18(01):1850008, 2018.

[274] Licheng Zhu and Abdollah Malekjafarian. On the use of ensemble empirical mode decomposition for the identification of bridge frequency from the responses measured in a passing vehicle. *Infrastructures*, 4(2):32, 2019.

[275] YB Yang, KC Chang, and YC Li. Filtering techniques for extracting bridge frequencies from a test vehicle moving over the bridge. *Engineering Structures*, 48:353–362, 2013.

[276] YB Yang and Wei-Fan Chen. Extraction of bridge frequencies from a moving test vehicle by stochastic subspace identification. *Journal of Bridge Engineering*, 21(3):04015053, 2016.

[277] JD Yau, Judy P Yang, and YB Yang. Wave number-based technique for detecting slope discontinuity in simple beams using moving test vehicle. *International Journal of Structural Stability and Dynamics*, 17(06):1750060, 2017.

[278] David Hester and Arturo González. A discussion on the merits and limitations of using drive-by monitoring to detect localised damage in a bridge. *Mechanical Systems and Signal Processing*, 90:234–253, 2017.

[279] Wei-ming Li, Zhi-hui Jiang, Tai-long Wang, and Hong-ping Zhu. Optimization method based on generalized pattern search algorithm to identify bridge parameters indirectly by a passing vehicle. *Journal of Sound and Vibration*, 333(2):364–380, 2014.

[280] Chengjun Tan, Ahmed Elhattab, and Nasim Uddin. "Drive-by" bridge frequency-based monitoring utilizing wavelet transform. *Journal of Civil Structural Health Monitoring*, 7:615–625, 2017.

[281] Chul-Woo Kim, Kai-Chun Chang, Patrick John McGetrick, Shinichi Inoue, and Souichiro Hasegawa. Utilizing moving vehicles as sensors for bridge condition screening–a laboratory verification. *Sensors & Materials*, 29(2), 2017.

[282] Chengjun Tan and Nasim Uddin. Hilbert transform based approach to improve extraction of "drive-by" bridge frequency. *Smart Structures and Systems*, 25(3), 2020.

[283] YB Yang, Bin Zhang, Yao Qian, and Yuntian Wu. Contact-point response for modal identification of bridges by a moving test vehicle. *International Journal of Structural Stability and Dynamics*, 18(05):1850073, 2018.

[284] Bin Zhang, Yao Qian, Yuntian Wu, and YB Yang. An effective means for damage detection of bridges using the contact-point response of a moving test vehicle. *Journal of Sound and Vibration*, 419:158–172, 2018.

[285] YB Yang, Hao Xu, XQ Mo, ZL Wang, and YT Wu. An effective procedure for extracting the first few bridge frequencies from a test vehicle. *Acta Mechanica*, 232:1227–1251, 2021.

[286] Ibrahim Hashlamon, Ehsan Nikbakht, Ameen Topa, and Ahmed Elhattab. Numerical parametric study on the effectiveness of the contact-point response of a stationary vehicle for bridge health monitoring. *Applied Sciences*, 11(15):7028, 2021.

[287] Rajdip Nayek and Sriram Narasimhan. Extraction of contact-point response in indirect bridge health monitoring using an input estimation approach. *Journal of Civil Structural Health Monitoring*, 10(5):815–831, 2020.

[288] XUAN Kong, CS Cai, and B Kong. Numerically extracting bridge modal properties from dynamic responses of moving vehicles. *Journal of Engineering Mechanics*, 142(6):04016025, 2016.

[289] Ying Zhan, Francis TK Au, and Jing Zhang. Bridge identification and damage detection using contact point response difference of moving vehicle. *Structural Control and Health Monitoring*, 28(12):e2837, 2021.

[290] YB Yang, F Xiong, ZL Wang, and H Xu. Extraction of bridge frequencies inclusive of the higher modes by the esmd using the contact-point response. *International Journal of Structural Stability and Dynamics*, 20(04):2050045, 2020.

[291] Yang Yang, Quan Cheng, Yuanhao Zhu, Lilei Wang, and Ruoyu Jin. Feasibility study of tractor-test vehicle technique for practical structural condition assessment of beam-like bridge deck. *Remote Sensing*, 12(1):114, 2020.

[292] Koushik Roy and Samit Ray-Chaudhuri. Fundamental mode shape and its derivatives in structural damage localization. *Journal of Sound and Vibration*, 332(21):5584–5593, 2013.

[293] MM Khatibi, MR Ashory, A Malekjafarian, and Rune Brincker. Mass–stiffness change method for scaling of operational mode shapes. *Mechanical Systems and Signal Processing*, 26:34–59, 2012.

[294] Yao Zhang, Longqi Wang, and Zhihai Xiang. Damage detection by mode shape squares extracted from a passing vehicle. *Journal of Sound and Vibration*, 331(2):291–307, 2012.

[295] Yao Zhang, Seng Tjhen Lie, and Zhihai Xiang. Damage detection method based on operating deflection shape curvature extracted from dynamic response of a passing vehicle. *Mechanical Systems and Signal Processing*, 35(1-2):238–254, 2013.

[296] YB Yang, YC Li, Kai Chun Chang, et al. Constructing the mode shapes of a bridge from a passing vehicle: a theoretical study. *Smart Structures and Systems*, 13(5):797–819, 2014.

[297] Chengjun Tan, Hua Zhao, Eugene J OBrien, Nasim Uddin, Paul C Fitzgerald, Patrick J McGetrick, and Chul-Woo Kim. Extracting mode shapes from drive-by measurements to detect global and local damage in bridges. *Structure and Infrastructure Engineering*, 17(11):1582–1596, 2021.

[298] Abdollah Malekjafarian and Eugene J OBrien. Identification of bridge mode shapes using short time frequency domain decomposition of the responses measured in a passing vehicle. *Engineering Structures*, 81:386–397, 2014.

[299] Eugene J OBrien and Abdollah Malekjafarian. Identification of bridge mode shapes using a passing vehicle. In *7th International Conference on Structural Health Monitoring of Intelligent Infrastructure (SHMII)*, 2015.

[300] Eugene J OBrien and Abdollah Malekjafarian. A mode shape-based damage detection approach using laser measurement from a vehicle crossing a simply supported bridge. *Structural Control and Health Monitoring*, 23(10):1273–1286, 2016.

[301] Abdollah Malekjafarian and Eugene J OBrien. On the use of a passing vehicle for the estimation of bridge mode shapes. *Journal of Sound and Vibration*, 397:77–91, 2017.

[302] Ying Zhan and FTK Au. A double-pass method for bridge assessment considering surface roughness using normalized contact point responses. *Smart Monitoring, Assessment and Rehabilitation of Civil Structures*, 2019.

[303] YB Yang, Hao Xu, Zhi-Lu Wang, and Kang Shi. Using vehicle–bridge contact spectra and residue to scan bridge's modal properties with vehicle frequencies and road roughness eliminated. *Structural Control and Health Monitoring*, 29(8):e2968, 2022.

[304] Jiantao Li, Xinqun Zhu, and Jian Guo. Enhanced drive-by bridge modal identification via dual kalman filter and singular spectrum analysis. *Structural Control and Health Monitoring*, 29(5):e2927, 2022.

[305] Rajdip Nayek, Suparno Mukhopadhyay, and Sriram Narasimhan. Mass normalized mode shape identification of bridge structures using a single actuator-sensor pair. *Structural Control and Health Monitoring*, 25(11):e2244, 2018.

[306] Qipei Mei, Nima Shirzad-Ghaleroudkhani, Mustafa Gül, S Farid Ghahari, and Ertugrul Taciroglu. Bridge mode shape identification using moving vehicles at traffic speeds through non-parametric sparse matrix completion. *Structural Control and Health Monitoring*, 28(7):e2747, 2021.

[307] Claudio Modena, Devis Sonda, and Daniele Zonta. Damage localization in reinforced concrete structures by using damping measurements. *Key engineering materials*, 167:132–141, 1999.

[308] RO Curadelli, JD Riera, D Ambrosini, and MG Amani. Damage detection by means of structural damping identification. *Engineering Structures*, 30(12):3497–3504, 2008.

[309] Jennifer Keenahan, Patrick McGetrick, Eugene J OBrien, and Arturo Gonzalez. Using instrumented vehicles to detect damage in bridges. In *Proceedings of the 15th International Conference on Experimental Mechanics, Porto, Portugal*, pages 22–27, 2012.

[310] Patrick McGetrick, Chul-Woo Kim, and Eugene J OBrien. Experimental investigation of the detection of bridge dynamic parameters using a moving vehicle. In *Proceedings of the 23rd KKCNN Symposium on Civil Engineering*, 2010.

[311] Chul-Woo Kim, R Isemoto, P McGetrick, Mitsuo Kawatani, and Eugene J O'Brien. Drive-by bridge inspection from three different approaches. *Smart Structures and Systems*, 13(5):775–796, 2014.

[312] Arturo González, Eugene J OBrien, and PJ McGetrick. Identification of damping in a bridge using a moving instrumented vehicle. *Journal of Sound and Vibration*, 331(18):4115–4131, 2012.

[313] Jennifer Keenahan, Eugene J OBrien, Patrick J McGetrick, and Arturo Gonzalez. The use of a dynamic truck–trailer drive-by system to monitor bridge damping. *Structural Health Monitoring*, 13(2):143–157, 2014.

[314] YB Yang, K Shi, ZL Wang, H Xu, B Zhang, and YT Wu. Using a single-dof test vehicle to simultaneously retrieve the first few frequencies and damping ratios of the bridge. *International Journal of Structural Stability and Dynamics*, 21(08):2150108, 2021.

[315] Yeong-Bin Yang, Wei-Fan Chen, Hao-Wen Yu, and CS Chan. Experimental study of a hand-drawn cart for measuring the bridge frequencies. *Engineering Structures*, 57:222–231, 2013.

[316] Jennifer Keenahan and Eugene J OBrien. Allowing for a rocking datum in the analysis of drive-by bridge inspections. *Civil Engineering Research in Ireland*, pages 117–124, 2014.

[317] Eugene J OBrien and Jennifer Keenahan. Drive-by damage detection in bridges using the apparent profile. *Structural Control and Health Monitoring*, 22(5):813–825, 2015.

[318] Abdollah Malekjafarian, Daniel Martinez, and Eugene J OBrien. The feasibility of using laser doppler vibrometer measurements from a passing vehicle for bridge damage detection. *Shock and Vibration*, 2018, 2018.

[319] Shih-Hsun Yin and Chung-Yu Tang. Identifying cable tension loss and deck damage in a cable-stayed bridge using a moving vehicle. 2011.

[320] ZH Li, FTK Au, et al. Damage detection of a continuous bridge from response of a moving vehicle. *Shock and Vibration*, 2014, 2014.

[321] Eugene J OBrien, P J Mcgetrick, and Arturo González. A drive-by inspection system via vehicle moving force identification. *Smart Structures and Systems*, 13(5):821–848, 2014.

[322] Daniel Martinez, Abdollah Malekjafarian, and Eugene OBrien. Bridge flexural rigidity calculation using measured drive-by deflections. *Journal of Civil Structural Health Monitoring*, 10:833–844, 2020.

[323] S Hasegawa, CW Kim, KC Chang, and N Toshi. Bridge damage detection utilizing dynamic force obtained from moving vehicle acceleration. In *Bridge Safety, Maintenance, Management, Life-Cycle, Resilience and Sustainability*, pages 1027–1035. CRC Press, 2022.

[324] Souichirou Hasegawa, Yukihiro Yano, Chul-Woo Kim, and Kai-Chun Chang. Structural health monitoring of bridges using dynamic vehicle force. In *European Workshop on Structural Health Monitoring*, pages 668–679. Springer, 2022.

[325] Fernando Cerda, James Garrett, Jacobo Bielak, Piervincenzo Rizzo, JA Barrera, Z Zhang, Siheng Chen, Michael T McCann, and Jelena Kovacevic. Indirect structural health monitoring in bridges: scale experiments. In *Proc. Int. Conf. Bridge Maint., Safety Manag., Lago di Como*, pages 346–353, 2012.

[326] XUAN Kong, CS Cai, and B Kong. Damage detection based on transmissibility of a vehicle and bridge coupled system. *Journal of Engineering Mechanics*, 141(1):04014102, 2015.

[327] YB Yang, BQ Wang, ZL Wang, K Shi, H Xu, B Zhang, and YT Wu. Bridge surface roughness identified from the displacement influence lines of the contact points by two connected vehicles. *International Journal of Structural Stability and Dynamics*, 20(14):2043003, 2020.

[328] Jennifer Keenahan, Yifei Ren, and Eugene J OBrien. Determination of road profile using multiple passing vehicle measurements. *Structure and Infrastructure Engineering*, 16(9):1262–1275, 2020.

[329] Eugene J OBrien, Simon Wilson, Jennifer Keenahan, and Yifei Ren. A bayesian approach to the estimation of road profile and bridge damage from a fleet passing vehicle measurements. *International Journal of Structural Stability and Dynamics*, 2023.

[330] JQ Bu, SS Law, and XQ Zhu. Innovative bridge condition assessment from dynamic response of a passing vehicle. *Journal of engineering mechanics*, 132(12):1372–1379, 2006.

[331] Chul-Woo Kim and M Kawatani. Challenge for a drive-by bridge inspection. In *Proceedings of the 10th International Conference on Structural Safety and Reliability*, pages 758–765, 2009.

[332] Patrick J McGetrick. *The use of an instrumented vehicle to monitor transport infrastructure*. PhD thesis, University College Dublin, 2012.

[333] Khoa Viet Nguyen and Hai Thanh Tran. Multi-cracks detection of a beam-like structure based on the on-vehicle vibration signal and wavelet analysis. *Journal of Sound and vibration*, 329(21):4455–4465, 2010.

[334] A Khorram, F Bakhtiari-Nejad, and M Rezaeian. Comparison studies between two wavelet based crack detection methods of a beam subjected to a moving load. *International Journal of Engineering Science*, 51:204–215, 2012.

[335] Patrick J McGetrick and Chul Woo Kim. A parametric study of a drive by bridge inspection system based on the morlet wavelet. *Key Engineering Materials*, 569:262–269, 2013.

[336] Patrick McGetrick and CA Kim. A wavelet based drive-by bridge inspection system. In *Proceedings of the 7th International Conference on Bridge Maintenance Safety and Management (IABMAS'14)*, 2014.

[337] Jingxiao Liu, Bingqing Chen, Siheng Chen, Mario Bergés, Jacobo Bielak, and HaeYoung Noh. Damage-sensitive and domain-invariant feature extraction for vehicle-vibration-based bridge health monitoring. In *ICASSP 2020-2020 IEEE International Conference on Acoustics, Speech and Signal Processing (ICASSP)*, pages 3007–3011. IEEE, 2020.

[338] Fernando Cerda, Siheng Chen, Jacobo Bielak, James H Garrett, Piervincenzo Rizzo, and Jelena Kovacevic. Indirect structural health monitoring of a simplified laboratory-scale bridge model. *Smart Structures and Systems*, 13(5):849–868, 2014.

[339] George Lederman, Zihao Wang, Jacobo Bielak, H Noh, James H Garrett, Siheng Chen, Jelena Kovacevic, Fernando Cerda, and Piervincenzo Rizzo. Damage quantification and localization algorithms for indirect shm of bridges. In *Proc. Int. Conf. Bridge Maint., Safety Manag., Shanghai, China*, pages 640–647, 2014.

[340] Siheng Chen, Fernando Cerda, Piervincenzo Rizzo, Jacobo Bielak, James H Garrett, and Jelena Kovačević. Semi-supervised multiresolution classification using adaptive graph filtering with application to indirect bridge structural health monitoring. *IEEE Transactions on Signal Processing*, 62(11):2879–2893, 2014.

[341] R Corbally and A Malekjafarian. An indirect approach for long term monitoring of bridge health. In *11th International Conference on Bridge Maintenance, Safety and Management (IABMAS)*, pages 1427–1432. CRC Press, Taylor & Francis Group Barcelona, Spain, 2022.

[342] Robert Corbally and Abdollah Malekjafarian. Drive-by detection of midspan cracking and changing boundary conditions in bridges. In *Experimental Vibration Analysis for Civil Engineering Structures: Select Proceedings of the EVACES 2021*, pages 607–618. Springer, 2022.

[343] Muhammad Zohaib Sarwar and Daniel Cantero. Deep autoencoder architecture for bridge damage assessment using responses from several vehicles. *Engineering Structures*, 246:113064, 2021.

[344] Jingxiao Liu, Mario Bergés, Jacobo Bielak, James H Garrett, Jelena Kovačević, and Hae Young Noh. A damage localization and quantification algorithm for indirect structural health monitoring of bridges using multi-task learning. In *AIP Conference Proceedings*, volume 2102. AIP Publishing, 2019.

[345] Jingxiao Liu, Siheng Chen, Mario Bergés, Jacobo Bielak, James H Garrett, Jelena Kovačević, and Hae Young Noh. Diagnosis algorithms for indirect structural health monitoring of a bridge model via dimensionality reduction. *Mechanical Systems and Signal Processing*, 136:106454, 2020.

[346] Zhenkun Li, Weiwei Lin, and Youqi Zhang. Real-time drive-by bridge damage detection using deep auto-encoder. In *Structures*, volume 47, pages 1167–1181. Elsevier, 2023.

[347] Donya Hajializadeh. Deep-learning-based drive-by damage detection system for railway bridges. *Infrastructures*, 7(6):84, 2022.

[348] Donya Hajializadeh. Deep learning-based indirect bridge damage identification system. *Structural health monitoring*, 22(2):897–912, 2023.

[349] Jingxiao Liu, Mario Bergés, Jacobo Bielak, and Hae Young Noh. Knowledge transfer between bridges for drive-by monitoring using adversarial and multi-task learning. *arXiv preprint arXiv:2006.03641*, 2020.

[350] Ekin Ozer, Maria Q Feng, and Dongming Feng. Citizen sensors for shm: Towards a crowdsourcing platform. *Sensors*, 15(6):14591–14614, 2015.

[351] Ayaho Miyamoto and Akito Yabe. Development of bridge monitoring system for short-and medium-span bridges based on bus vibration.

[352] Yifu Lan, Zhenkun Li, Keijo Koski, Ludovic Fülöp, Timo Tirkkonen, and Weiwei Lin. Bridge frequency identification in city bus monitoring: A coherence-ppi algorithm. *Engineering Structures*, 296:116913, 2023.

[353] Eugene J OBrien, Daniel P McCrum, and Shuo Wang. Drive-by fleet monitoring to detect bearing damage in bridges using a moving reference influence function. *International Journal of Structural Stability and Dynamics*, page 2340003, 2023.

[354] Konstantinos Gkoumas, Maria Cristina Galassi, D Allaix, Armelle Anthoine, Sotiris Argyroudis, Gianmarco Baldini, Lorenzo Benedetti, Flavio Bono, James Brownjohn, Elsa Caetano, et al. Indirect structural health monitoring (ishm) of transport infrastructure in the digital age. Technical report, Luxembourg: Publications Office of the European Union, 2023.

[355] Daniel Miller, Laila Abed Rabho, Patrick Awondo, Maya de Vries, Marília Duque, Pauline Garvey, Laura Haapio-Kirk, Charlotte Hawkins, Alfonso Otaegui, Shireen Walton, et al. *The global smartphone: Beyond a youth technology*. UCL Press, 2021.

[356] Qingkai Kong, Richard M Allen, and Louis Schreier. Myshake: Initial observations from a global smartphone seismic network. *Geophysical Research Letters*, 43(18):9588–9594, 2016.

[357] Jack Reilly, Shideh Dashti, Mari Ervasti, Jonathan D Bray, Steven D Glaser, and Alexandre M Bayen. Mobile phones as seismologic sensors: Automating data extraction for the ishake system. *IEEE Transactions on Automation Science and Engineering*, 10(2):242–251, 2013.

[358] Artis Mednis, Girts Strazdins, Reinholds Zviedris, Georgijs Kanonirs, and Leo Selavo. Real time pothole detection using android smartphones with accelerometers. In *2011 International conference on distributed computing in sensor systems and workshops (DCOSS)*, pages 1–6. IEEE, 2011.

[359] Thomas J Matarazzo, Paolo Santi, Shamim N Pakzad, Kristopher Carter, Carlo Ratti, Babak Moaveni, Chris Osgood, and Nigel Jacob. Crowdsensing framework for monitoring bridge vibrations using moving smartphones. *Proceedings of the IEEE*, 106(4):577–593, 2018.

[360] Peter Welch. The use of fast fourier transform for the estimation of power spectra: a method based on time averaging over short, modified periodograms. *IEEE Transactions on audio and electroacoustics*, 15(2):70–73, 1967.

[361] Soheil Sadeghi Eshkevari, Thomas J Matarazzo, and Shamim N Pakzad. Bridge modal identification using acceleration measurements within moving vehicles. *Mechanical Systems and Signal Processing*, 141:106733, 2020.

[362] Norden E Huang, Zheng Shen, Steven R Long, Manli C Wu, Hsing H Shih, Quanan Zheng, Nai-Chyuan Yen, Chi Chao Tung, and Henry H

Liu. The empirical mode decomposition and the hilbert spectrum for nonlinear and non-stationary time series analysis. *Proceedings of the Royal Society of London. Series A: mathematical, physical and engineering sciences*, 454(1971):903–995, 1998.

[363] Soheil Sadeghi Eshkevari and Shamim Pakzad. Bridge structural identification using moving vehicle acceleration measurements. In *Dynamics of Civil Structures, Volume 2: Proceedings of the 36th IMAC, A Conference and Exposition on Structural Dynamics 2018*, pages 251–261. Springer, 2019.

[364] Thomas J Matarazzo and Shamim N Pakzad. Scalable structural modal identification using dynamic sensor network data with stridex. *Computer-Aided Civil and Infrastructure Engineering*, 33(1):4–20, 2018.

[365] Richard May. Effects of operational traffic variability on iSHM. In *European Workshop on Structural Health Monitoring*, pages 700–710. Springer, 2022.

[366] Qipei Mei, Mustafa Gül, and Marcus Boay. Indirect health monitoring of bridges using mel-frequency cepstral coefficients and principal component analysis. *Mechanical Systems and Signal Processing*, 119:523–546, 2019.

[367] Qipei Mei and Mustafa Gül. Monitoring populations of bridges in smart cities using smartphones. In *Structures Congress 2019*, pages 27–37. American Society of Civil Engineers Reston, VA, 2019.

[368] Nima Shirzad-Ghaleroudkhani, Qipei Mei, and Mustafa Gül. Frequency identification of bridges using smartphones on vehicles with variable features. *Journal of Bridge Engineering*, 25(7):04020041, 2020.

[369] Said Quqa, Pier Francesco Giordano, and Maria Pina Limongelli. Shared micromobility-driven modal identification of urban bridges. *Automation in Construction*, 134:104048, 2022.

[370] Richard May, Hwa Kian Chai, Thomas Reynolds, and Yong Lu. Exploring the use of bicycles as exciters and sensor carriers for indirect bridge modal parameter estimation. In *International Conference on Experimental Vibration Analysis for Civil Engineering Structures*, pages 254–263. Springer, 2023.

[371] Zhenkun Li, Yifu Lan, and Weiwei Lin. Using contact residual responses of a 3-dof scooter to identify first few frequencies of the footbridge. In *International Conference on Experimental Vibration Analysis for Civil Engineering Structures*, pages 132–143. Springer, 2023.

[372] R Cantieni. Investigation of vehicle-bridge interaction for highway bridges. In *Heavy vehicles and roads technology, safety and policy*, pages 130–137. Thomas Telford Publishing, 1992.

[373] Chul-Young Kim, Dae-Sung Jung, Nam-Sik Kim, Soon-Duck Kwon, and Maria Q Feng. Effect of vehicle weight on natural frequencies of bridges measured from traffic-induced vibration. *Earthquake Engineering and Engineering Vibration*, 2:109–115, 2003.

[374] Soon-Duck Kwon, Chul-Young Kim, and Sung-Pil Chang. Change of modal parameters of bridge due to vehicle pass. In *IMAC-23: Conference and Exposition on Structural Dynamic, Orlando*, pages 213–219, 2005.

[375] Robert Westgate, Ki-Young Koo, James Brownjohn, and David List. Suspension bridge response due to extreme vehicle loads. *Structure and Infrastructure Engineering*, 10(6):821–833, 2014.

[376] Biswajit Basu and Vinay K Gupta. Seismic response of sdof systems by wavelet modeling of nonstationary processes. *Journal of Engineering Mechanics*, 124(10):1142–1150, 1998.

[377] William Locke, Laura Redmond, and Matthias Schmid. Evaluating oma system identification techniques for drive-by health monitoring on short span bridges. *Journal of Bridge Engineering*, 27(9):04022079, 2022.

[378] Emanuel Sousa Tome, Mario Pimentel, and Joaquim Figueiras. Damage detection under environmental and operational effects using cointegration analysis–application to experimental data from a cable-stayed bridge. *Mechanical Systems and Signal Processing*, 135:106386, 2020.

[379] Charles R. Harris, K. Jarrod Millman, Stéfan J. van der Walt, Ralf Gommers, Pauli Virtanen, David Cournapeau, Eric Wieser, Julian Taylor, Sebastian Berg, Nathaniel J. Smith, Robert Kern, Matti Picus, Stephan Hoyer, Marten H. van Kerkwijk, Matthew Brett, Allan Haldane, Jaime Fernández del Río, Mark Wiebe, Pearu Peterson, Pierre Gérard-Marchant, Kevin Sheppard, Tyler Reddy, Warren Weckesser, Hameer Abbasi, Christoph Gohlke, and Travis E. Oliphant. Array programming with NumPy. *Nature*, 585(7825):357–362, September 2020.

[380] Pauli Virtanen, Ralf Gommers, Travis E. Oliphant, Matt Haberland, Tyler Reddy, David Cournapeau, Evgeni Burovski, Pearu Peterson, Warren Weckesser, Jonathan Bright, Stéfan J. van der Walt, Matthew Brett, Joshua Wilson, K. Jarrod Millman, Nikolay Mayorov, Andrew R. J. Nelson, Eric Jones, Robert Kern, Eric Larson, C J Carey, İlhan Polat, Yu Feng, Eric W. Moore, Jake VanderPlas, Denis Laxalde, Josef Perktold, Robert Cimrman, Ian Henriksen, E. A. Quintero, Charles R. Harris, Anne M. Archibald, Antônio H. Ribeiro, Fabian Pedregosa, Paul van Mulbregt, and SciPy 1.0 Contributors. SciPy 1.0: Fundamental Algorithms for Scientific Computing in Python. *Nature Methods*, 17:261–272, 2020.

[381] J. D. Hunter. Matplotlib: A 2d graphics environment. *Computing in Science & Engineering*, 9(3):90–95, 2007.

[382] Stephen Butterworth et al. On the theory of filter amplifiers. *Wireless Engineer*, 7(6):536–541, 1930.

[383] SciPy documentation. https://docs.scipy.org/doc/scipy/index.html. Accessed: 2024-06-25.

[384] SciPy Cookbook: Butterworth Bandpass. https://scipy-cookbook.readthedocs.io/items/ButterworthBandpass.html. Accessed: 2024-06-25.

[385] Ronald W Schafer. What is a savitzky-golay filter?[lecture notes]. *IEEE Signal processing magazine*, 28(4):111–117, 2011.

[386] James Riordon, Elizabeth Zubritsky, and Alan Newman. Top 10 articles., 2000.

[387] H COLE, JR. On-the-line analysis of random vibrations. In *9th structural dynamics and materials conference*, page 288, 1968.

[388] Henry A Cole Jr. On-line failure detection and damping measurement of aerospace structures by random decrement signatures. Technical report, NASA, 1973.

[389] ScikitLearn user guide: 2.8: density estimation. https://scikit-learn.org/stable/modules/density.html. Accessed: 2024-06-25.

[390] sklearn.mixture.gaussianmixture. https://scikit-learn.org/stable/modules/generated/sklearn.mixture.GaussianMixture.html. Accessed: 2023-11-01.

[391] scipy.stats.wasserstein_distance. https://docs.scipy.org/doc/scipy/reference/generated/scipy.stats.wasserstein_distance.html. Accessed: 2023-12-12.

[392] Soheil Kolouri, Yang Zou, and Gustavo K Rohde. Sliced wasserstein kernels for probability distributions. In *Proceedings of the IEEE Conference on Computer Vision and Pattern Recognition*, pages 5258–5267, 2016.

[393] Robert Glenn Stockwell, Lalu Mansinha, and RP Lowe. Localization of the complex spectrum: the s transform. *IEEE transactions on signal processing*, 44(4):998–1001, 1996.

[394] Leon Cohen. Generalized phase-space distribution functions. *Journal of Mathematical Physics*, 7(5):781–786, 1966.

[395] Robert A Brown, M Louis Lauzon, and Richard Frayne. A general description of linear time-frequency transforms and formulation of a fast, invertible transform that samples the continuous s-transform spectrum nonredundantly. *IEEE Transactions on Signal Processing*, 58(1):281–290, 2009.

[396] Peter C Gibson, Michael P Lamoureux, and Gary F Margrave. Stockwell and wavelet transforms. *Journal of Fourier analysis and applications*, 12:713–721, 2006.

[397] Yingbo Hua and Tapan K Sarkar. Matrix pencil method for estimating parameters of exponentially damped/undamped sinusoids in noise. *IEEE Transactions on Acoustics, Speech, and Signal Processing*, 38(5):814–824, 1990.

[398] Zachariah Wynne. *Closing the loop: the integration of long-term ambient vibration monitoring in structural engineering design*. PhD thesis, University of Edinburgh, 2022.

[399] sklearn.metrics.r2_score. https://scikit-learn.org/stable/modules/model_evaluation.html#r2-score. Accessed: 2024-02-22.

[400] Christopher M Bishop and Nasser M Nasrabadi. *Pattern recognition and machine learning*, volume 4. Springer, 2006.

[401] Harold Hotelling. Analysis of a complex of statistical variables into principal components. *Journal of educational psychology*, 24(6):417, 1933.

[402] Michael E Tipping and Christopher M Bishop. Mixtures of probabilistic principal component analyzers. *Neural computation*, 11(2):443–482, 1999.

[403] Jason Brownlee. How to Calculate Principal Component Analysis (PCA) from Scratch in Python. https://machinelearningmastery.com/calculate-principal-component-analysis-scratch-python/. Accessed: 2024-07-03.

[404] Detlef Groth, Stefanie Hartmann, Sebastian Klie, and Joachim Selbig. Principal components analysis. *Computational Toxicology: Volume II*, pages 527–547, 2013.

[405] Xiaodong Li. STA135 Lecture 2: Sample Mean Vector and Sample Covariance Matrix. https://www.stat.ucdavis.edu/~xdgli/Xiaodong_Li_Teaching_files/135Note2.pdf. Accessed: 2024-07-03.

[406] Scikit learn: PCA. https://scikit-learn.org/stable/modules/generated/sklearn.decomposition.PCA.html. Accessed: 2024-07-03.

[407] Latex tables generator. https://www.tablesgenerator.com/. Accessed: 2024-02-23.

[408] YB Yang, YC Li, and KC Chang. Effect of road surface roughness on the response of a moving vehicle for identification of bridge frequencies. *Interaction and multiscale mechanics*, 5(4):347–368, 2012.

[409] The Engineering Vibration Toolbox for Python. http://vibrationtoolbox.github.io/vibration_toolbox/index.html. Accessed: 2023-06-18.

[410] Kelvin, Tsz Hei Choi (ORCID: [0000-0002-5796-5263]). One-tap sensor logger in your pocket. https://www.tszheichoi.com/sensorlogger. Accessed: 2023-11-29.

[411] JA Calvo, B Lopez-Boada, JL San Román, and A Gauchia. Influence of a shock absorber model on vehicle dynamic simulation. *Proceedings of the Institution of Mechanical Engineers, Part D: Journal of Automobile Engineering*, 223(2):189–203, 2009.

[412] JTB Overvelde. Learn abaqus script in one hour. *overvelde. com [en línea].[Consulta: 09-02-2015]. Disponible en: http://www. overvelde. com/wpcontent/uploads/2011/05/LearnAbaqusScriptInOneHour. pdf*, 2010.

[413] Patrick Salcher, Helmuth Pradlwarter, and Christoph Adam. Reliability assessment of railway bridges subjected to high-speed trains considering the effects of seasonal temperature changes. *Engineering Structures*, 126:712–724, 2016.

[414] Maria Q Feng, Sung Chil Lee, et al. Determining the effective system damping of highway bridges. Technical report, California. Dept. of Transportation, 2009.

[415] Jonathan M Lilly and Sofia C Olhede. On the analytic wavelet transform. *IEEE transactions on information theory*, 56(8):4135–4156, 2010.

[416] WJ1693779 Staszewski. Identification of non-linear systems using multi-scale ridges and skeletons of the wavelet transform. *Journal of Sound and Vibration*, 214(4):639–658, 1998.

[417] Hongnan Li, Tinghua Yi, Ming Gu, and Linsheng Huo. Evaluation of earthquake-induced structural damages by wavelet transform. *Progress in Natural Science*, 19(4):461–470, 2009.

[418] Christopher Torrence and Gilbert P Compo. A practical guide to wavelet analysis. *Bulletin of the American Meteorological society*, 79(1):61–78, 1998.

[419] Lorenzo Montanari, Biswajit Basu, Andrea Spagnoli, and Brian M Broderick. A padding method to reduce edge effects for enhanced damage identification using wavelet analysis. *Mechanical Systems and Signal Processing*, 52:264–277, 2015.

[420] Julius O. Smith. *Mathematics of the Discrete Fourier Transform (DFT)*. `http:`http://ccrma.stanford.edu/ jos/mdft/`//ccrma.stanford.edu/-~jos/mdft/`, accessed 13/02/2024. online book, 2007 edition.

[421] Paul Ramond. The abel–ruffini theorem: Complex but not complicated. *The American Mathematical Monthly*, 129(3):231–245, 2022.

[422] Jyoti K Sinha, MI Friswell, and S Edwards. Simplified models for the location of cracks in beam structures using measured vibration data. *Journal of Sound and vibration*, 251(1):13–38, 2002.

[423] Shehroz S Khan and Michael G Madden. A survey of recent trends in one class classification. In *Artificial Intelligence and Cognitive Science: 20th Irish Conference, AICS 2009, Dublin, Ireland, August 19-21, 2009, Revised Selected Papers 20*, pages 188–197. Springer, 2010.

[424] Matheus Gutoski, Manassés Ribeiro, Nelson Marcelo Romero Aquino, André Eugenio Lazzaretti, and Heitor Silverio Lopes. A clustering-based deep autoencoder for one-class image classification. In *2017 IEEE Latin American conference on computational intelligence (LA-CCI)*, pages 1–6. IEEE, 2017.

[425] Abdul Mujeeb, Wenting Dai, Marius Erdt, and Alexei Sourin. One class based feature learning approach for defect detection using deep autoencoders. *Advanced engineering informatics*, 42:100933, 2019.

[426] David MJ Tax and Robert PW Duin. Data domain description using support vectors. In *ESANN*, volume 99, pages 251–256, 1999.

[427] David MJ Tax and Robert PW Duin. Support vector domain description. *Pattern recognition letters*, 20(11-13):1191–1199, 1999.

[428] Bernhard Schölkopf, Robert C Williamson, Alex Smola, John Shawe-Taylor, and John Platt. Support vector method for novelty detection. *Advances in neural information processing systems*, 12, 1999.

[429] Jonathon Shlens. A tutorial on principal component analysis. *arXiv preprint arXiv:1404.1100*, 2014.

[430] Yu Peng, Jesse S Jin, Suhuai Luo, Min Xu, and Yue Cui. Vehicle type classification using pca with self-clustering. In *2012 IEEE International Conference on Multimedia and Expo Workshops*, pages 384–389. IEEE, 2012.

[431] Michal Rolinek, Dominik Zietlow, and Georg Martius. Variational autoencoders pursue pca directions (by accident). In *Proceedings of the IEEE/CVF Conference on Computer Vision and Pattern Recognition*, pages 12406–12415, 2019.

[432] Marco AF Pimentel, David A Clifton, Lei Clifton, and Lionel Tarassenko. A review of novelty detection. *Signal processing*, 99:215–249, 2014.

[433] Pramuditha Perera, Poojan Oza, and Vishal M Patel. One-class classification: A survey. *arXiv preprint arXiv:2101.03064*, 2021.

[434] Raymond B Cattell. The scree test for the number of factors. *Multivariate behavioral research*, 1(2):245–276, 1966.

[435] Carol M Woods and Michael C Edwards. 12 factor analysis and related methods. *Handbook of statistics*, 27:367–394, 2007.

[436] Richard May, Thomas Reynolds, Hwa Kian Chai, Robert Corbally, Abdollah Malekjafarian, and Yong Lu. Effects of added mass on indirect structural health monitoring of bridges. In *International Conference on Experimental Vibration Analysis for Civil Engineering Structures*, pages 225–235. Springer, 2023.

[437] Structural Dynamics & Assessment Laboratory. https://sdal.ucd.ie/. Accessed: 2023-10-30.

[438] Sensorconnect. https://www.microstrain.com/software/sensorconnect. Accessed: 2023-10-30.

[439] CF Jeff Wu. On the convergence properties of the em algorithm. *The Annals of statistics*, pages 95–103, 1983.

[440] Chong Wu, Can Yang, Hongyu Zhao, and Ji Zhu. On the convergence of the em algorithm: From the statistical perspective. *arXiv preprint arXiv:1611.00519*, 2016.

[441] Jie You, Zhaoxuan Li, and Junli Du. A new iterative initialization of em algorithm for gaussian mixture models. *Plos one*, 18(4):e0284114, 2023.

[442] Kristin L Sainani. Dealing with non-normal data. *Pm&r*, 4(12):1001–1005, 2012.

[443] MNIST dataset. https://www.kaggle.com/datasets/hojjatk/mnist-dataset. Accessed: 2024-02-22.

[444] Jolynn Pek, Octavia Wong, and Augustine CM Wong. How to address non-normality: A taxonomy of approaches, reviewed, and illustrated. *Frontiers in psychology*, 9:2104, 2018.

[445] Scipy.stats.bootstrap. https://docs.scipy.org/doc/scipy/reference/generated/scipy.stats.bootstrap.htm. Accessed: 2023-12-12.

[446] Victor RJH Timmers and Peter AJ Achten. Non-exhaust pm emissions from electric vehicles. *Atmospheric environment*, 134:10–17, 2016.

[447] BS Kerner. *The physics of traffic*. Springer, 2004.

[448] Wen-Yu He, Lin-Qing Gu, Zhu Liang, Wei-Xin Ren, and Xu-Cong Ding. Elimination of stochastic traffic flow effects on modal identification of beam type bridge under ambient excitation. In *Structures*, volume 58, page 105623. Elsevier, 2023.

[449] Amin Rezaei and Brian Caulfield. Safety of autonomous vehicles: what are the insights from experienced industry professionals? *Transportation research part F: traffic psychology and behaviour*, 81:472–489, 2021.

Appendices

Appendix A

Output-only experimental estimation of frequency response and modal parameters

A.1 Methods for experimental estimation of frequency response function

The literature review (section 2.4) summarised methods of vehicle parameter estimation and methods to construct a theoretical frequency response function (FRF). This section provides additional discussion of methods by which an estimate of the FRF for a system can be achieved without knowledge of all of its properties, in cases where the input can be measured or can be reasonably be assumed to take the form of an impulse or an assumed spectral shape.

A.1.1 Measured input-output method

An established method of estimating the FRF of a system with unknown properties, especially at laboratory scale, is to subject it to an impulse load condition. Another approach, which offers particular utility in the full-scale laboratory testing of vehicles, involves subjecting the structure (vehicle) of interest to a continuous harmonic input at a range of frequencies. The output-to-input relationship can thus be established across the frequency band of concern. For vehicles, such testing requires access to hydraulically-actuated *shaker rigs* of the 4- or 7-post type (referring to the number of locations where concurrent input or restraint can be applied). Such rigs are expensive and rare, typically being found only in industrial settings or at highly-specialised research and testing facilities.

The ideal impulse can be described by the Dirac delta function, which in the time domain is unity-valued at a single point in time and zero-valued elsewhere. In the frequency domain the Dirac delta represents equal signal power across an infinitely wide frequency band, i.e. in the frequency domain it can be considered as equivalent to *white noise* excitation in that neither have any frequency bias. The FRF is constructed by dividing the frequency-domain response at a given degree-of-freedom (DoF) by the frequency-domain input. Given that the input took the form of an impulse, the system response can be considered as its free vibration condition. Since the input power is flat across all frequencies, the FRF represents the system's proportional acceleration response to input acceleration at any frequency.[1] It follows that peaks in the FRF represent natural frequencies of the system being studied. The FRF peaks represent damped frequencies and are related to the equivalent undamped frequencies as shown in equation A.1 which relates the observed damped frequency for mode i ($\omega_{d,i}$) to the undamped natural frequency for that mode (ω_i) in terms of the modal damping ratio (ζ_i). This is particularly relevant for vehicles since they are heavily damped; the square root serving to allow the damped and undamped frequencies to tend towards convergence with decreasing damping. In the case

[1] In this thesis, the FRF will be assumed to be the ratio of output to input acceleration in the frequency domain unless noted otherwise. In the wider literature this is typically known as the accelerance FRF. Other forms of the FRF can be constructed, for example the mobility FRF (ratio of output to input velocity) and the receptance FRF (displacement).

of vehicle suspensions, the damping may be non-trivial and thus an immediate utility of the estimated modal damping ratio is revealed, affording the improved estimation of undamped natural frequencies in cases where the observed FRF indicates that damping is high for a given mode.

$$\omega_i = \frac{\omega_{d,i}}{\sqrt{1-\zeta_i}} \tag{A.1}$$

By varying the location at which the impulse is applied to the structure it is possible to assemble a set of FRFs describing the response at the given DoF to input at any position of interest. This is colloquially known as the *roving hammer* technique. As the name implies, the impulse is delivered by a single tap from a hammer. Although the Dirac delta is the ideal impulse, practical considerations limit its use to theoretical studies or numerical simulations. The use of a hammer instrumented with a force transducer in the tip allows the same method of FRF estimation to be employed in physical testing situations, as the frequency domain output can be divided by the frequency domain input to achieve an FRF normalised to input amplitude. From this it follows that unless the system's response displays amplitude-related nonlinearity, or its stiffness, mass or damping change, the FRF can be used to predict the response at the DoF to any harmonic loading at the input location. The FRF has no units but since it is based on acceleration it is sometimes denoted as having units of g/g where $g = 9.81m/s^2$.[2]

The measured input-output method is not used in this thesis, but is explained here to provide context for the adopted methods (*assumed impulsive input* and *assumed spectral input*) discussed below.

A.1.2 Assumed impulsive input method

In physical modal testing scenarios for structures (for example the bridge and vehicle identification exercises reported in chapter 7) it may not be practical or possible to apply a known and measured input, whether impulsive or harmonic in nature. In such situations the methods applied to FRF estimation belong to the field of *operational modal analysis* (OMA). Since the magnitude of the input is not known or not measurable, the output must be arbitrarily scaled in a consistent manner to afford comparison of input-output relationships between multiple forcing locations and DoFs. In the case of FRF estimation a useful scaling method is found by recalling that at zero frequency the system's input-output behaviour under harmonic excitation should be equivalent to a static

[2] It should be noted that the input and output acceleration records in the frequency domain are typically complex-valued, comprising a magnitude of response and a phase angle of that response. Typically, such complex-valued information would be represented by a Bode plot which includes both amplitude and phase angle plotted against frequency. However, this thesis will typically consider only the absolute value of the FRF, neglecting phase information, which seems reasonable given the overall goal of estimating vehicle frequencies and damping. Additionally, outputs from the method used in chapter 4 for power spectrum estimation (Welch's method, discussed in section 2.8.7 are real-valued due to the nature of the averaging inherent to the method.

condition. This allows the FRF to be constructed by scaling to unity at zero frequency.

This approach finds particular utility in situations where the system being studied is understood to have received an impulsive excitation, but the magnitude of the impulse is not known. Alternatively, if the free vibration response of the system can be estimated by other means, this method of FRF estimation can be employed for responses to non-impulsive excitation. This scenario is discussed further in section A.1.3.

A.1.3 Assumed spectral input method

In some cases the input excitation is not practically measurable. For estimation of vehicle properties, Ainalis et al. [157] proposed the method of using the random decrement technique to estimate the free vibration response of the vehicle system at the DoF of interest.[3] The approach assumes that the acceleration input created by the vehicle traversing a road surface includes random excitation across the range of frequencies of interest, and that – in accordance with the assumptions underlying the development of the random decrement technique – the response at the DoF relates to the stochastic forcing and the modal properties of the structure. Further discussion of the random decrement method is provided in section 2.8.4.

[3] It should be noted that the work presented by Ainalis et al. [157] investigated a proprietary SDoF vehicle.

A.2 In-service estimation of vehicle modal parameters

The methods discussed in this section adopt an assumption that the two modes of a 2DoF quarter-car are broadly independent. In other words, for the first mode (known as *cabin bounce*) the upper DoF experiences vibration while the lower DoF is essentially unmoving. The situation is reversed for the second mode (*wheel hop*). This is intuitive considering one of the key purposes of vehicle suspension which is to isolate the upper DoF (the cabin) from vibrations caused by the road surface. Illustrations of quarter-car mode shapes, supporting this intuitive explanation, are included in Fig. 5.3.1. The implication of the assumption is that frequencies and damping ratios can be estimated using the acceleration response at each DoF independently, as is described below and adopted in chapter 4 through the power-spectrum method and the auto-RDS/matrix pencil method. The limitation of these approaches is that they do not facilitate estimation of mode shapes, and may misrepresent vehicle modal frequencies and damping ratios in cases where the above assumption does not apply.

A.2.1 Power spectrum-based method

The adopted procedure (and key assumptions) for vehicle parameter estimation in the frequency domain (chapters 4 and 7) based on the power spectrum is as follows:

1. Install accelerometers on the vehicle at locations equivalent to the upper and lower mass of a quarter-car, attached (for example) to the front left axle and the front left of the cabin.

2. Assume that the input from the road surface takes the general form of an ISO 8608 profile (or is spectrally flat in acceleration) when averaged across multiple speeds and sections of roadway.

3. Assume that average vehicle response will be dominated by vertical displacement; in other words, assume that cabin bounce and wheel hop modes will dominate the averaged response while pitch and roll modes will be transient and of lower magnitude, tending towards zero in the averaged response.

4. Estimate the power spectra (using Welch's method) from cabin and axle sensors for each experimental run, road, and speed. Scale the spectra by frequency^{-1} to account for the assumed input being spectrally flat in velocity rather than acceleration.

5. Combine the estimated spectra into ensemble averages to demonstrate that the response converges towards the general form of the FRF for a quarter car model with only vertical deflection permitted.

6. Use the peak picking and half-power bandwidth methods (discussed in more detail in section 2.8.9) to estimate damped natural frequency and modally independent damping ratios respectively.

7. Estimate the undamped natural frequency from the estimated damped natural frequency and damping ratio for each observed mode.

A.2.2 Random decrement and matrix pencil method

An alternative approach, not requiring estimation of the FRF is to estimate modal parameters in the time domain. In this thesis, a combination of the random decrement (RD) method (discussed in more detail in section 2.8.4) and the matrix pencil method (MPM) method (summarised in section 2.8.10) is adopted for estimation of vehicle parameters from in-service acceleration responses (chapter 4).[4] In summary, the RD method estimates free vibrations of the subject structure by means of averaging across multiple samples of the acceleration response in the time domain. The MPM fits these estimates of free vibration to modal parameters in time domain. The adopted experimental procedures and assumptions outlined in steps 1–3 (above) apply.

[4] The matrix pencil method is also used for parameter identification of the laboratory-scale bridge and vehicle models in chapter 7.

Appendix B

Supplementary material for chapter 5

B.1 Vehicle properties

m1: m2	3	3	3	3	3
Mv	3.43	3.43	3.43	3.43	3.43
m1	0.86	0.86	0.86	0.86	0.86
m2	2.57	2.57	2.57	2.57	2.57
k1	1750	24500	43500	68000	1095000
k2	350	4900	8700	13600	219000
k1 : k2	5	5	5	5	5
f_v1 / f_b1	0.20	0.75	1.00	1.25	5.00
f_v2 / f_b1	0.94	3.51	4.68	5.85	23.48
f_v1 / f_b2	0.05	0.19	0.25	0.31	1.25
f_v2 / f_b2	0.23	0.88	1.17	1.46	5.87

4.25	4.25	4.25	4.25	4.25
3.43	3.43	3.43	3.43	3.43
0.65	0.65	0.65	0.65	0.65
2.78	2.78	2.78	2.78	2.78
1950	26500	47000	74000	1175000
390	5300	9400	14800	235000
5	5	5	5	5
0.20	0.75	1.00	1.25	5.00
1.13	4.18	5.57	6.98	27.83
0.05	0.19	0.25	0.31	1.25
0.28	1.05	1.39	1.75	6.96

5.5	5.5	5.5	5.5	5.5
3.43	3.43	3.43	3.43	3.43
0.53	0.53	0.53	0.53	0.53
2.90	2.90	2.90	2.90	2.90
2000	27500	49000	76500	1230000
400	5500	9800	15300	246000
5	5	5	5	5
0.20	0.75	1.00	1.25	5.00
1.28	4.73	6.32	7.89	31.66
0.05	0.19	0.25	0.31	1.25
0.32	1.18	1.58	1.97	7.92

m1: m2	6.75	6.75	6.75	6.75	6.75
Mv	3.43	3.43	3.43	3.43	3.43
m1	0.44	0.44	0.44	0.44	0.44
m2	2.99	2.99	2.99	2.99	2.99
k1	2000	28500	50500	79000	1265000
k2	400	5700	10100	15800	253000
k1 : k2	5	5	5	5	5
f_v1 / f_b1	0.20	0.75	1.00	1.25	5.00
f_v2 / f_b1	1.39	5.26	7.00	8.76	35.04
f_v1 / f_b2	0.05	0.19	0.25	0.31	1.25
f_v2 / f_b2	0.35	1.32	1.75	2.19	8.76

8	8	8	8	8
3.43	3.43	3.43	3.43	3.43
0.38	0.38	0.38	0.38	0.38
3.05	3.05	3.05	3.05	3.05
2000	29000	52000	80000	1290000
400	5800	10400	16000	258000
5	5	5	5	5
0.20	0.75	1.00	1.25	5.00
1.50	5.72	7.65	9.49	38.12
0.05	0.19	0.25	0.31	1.25
0.38	1.43	1.91	2.37	9.53

Table B.1.1: Vehicle properties used in study of Contact Point response in chapter 7: varying **suspension** spring stiffness to achieve target vehicle-to-bridge **first** frequency ratio.

m1: m2	3	3	3	3	3
Mv	3.43	3.43	3.43	3.43	3.43
m1	0.86	0.86	0.86	0.86	0.86
m2	2.57	2.57	2.57	2.57	2.57
k1	1300	18000	32000	49500	793000
k2	260	3600	6400	9900	158600
k1 : k2	5	5	5	5	5
f_v1 / f_b1	0.17	0.64	0.86	1.06	4.26
f_v2 / f_b1	0.81	3.01	4.01	4.99	19.98
f_v1 / f_b2	0.04	0.16	0.21	0.27	1.07
f_v2 / f_b2	0.20	0.75	1.00	1.25	5.00

4.25	4.25	4.25	4.25	4.25
3.43	3.43	3.43	3.43	3.43
0.65	0.65	0.65	0.65	0.65
2.78	2.78	2.78	2.78	2.78
1000	13800	24200	38000	605000
200	2760	4840	7600	121000
5	5	5	5	5
0.15	0.54	0.72	0.90	3.59
0.81	3.02	3.99	5.00	19.97
0.04	0.14	0.18	0.22	0.90
0.20	0.75	1.00	1.25	5.00

5.5	5.5	5.5	5.5	5.5
3.43	3.43	3.43	3.43	3.43
0.53	0.53	0.53	0.53	0.53
2.90	2.90	2.90	2.90	2.90
800	11100	19500	30500	490000
160	2220	3900	6100	98000
5	5	5	5	5
0.13	0.48	0.63	0.79	3.16
0.81	3.01	3.99	4.98	19.98
0.03	0.12	0.16	0.20	0.79
0.20	0.75	1.00	1.25	5.00

m1: m2	6.75	6.75	6.75	6.75	6.75
Mv	3.43	3.43	3.43	3.43	3.43
m1	0.44	0.44	0.44	0.44	0.44
m2	2.99	2.99	2.99	2.99	2.99
k1	650	9300	16500	25800	411000
k2	130	1860	3300	5160	82200
k1 : k2	5	5	5	5	5
f_v1 / f_b1	0.11	0.43	0.57	0.71	2.85
f_v2 / f_b1	0.79	3.00	4.00	5.00	19.97
f_v1 / f_b2	0.03	0.11	0.14	0.18	0.71
f_v2 / f_b2	0.20	0.75	1.00	1.25	5.00

8	8	8	8	8
3.43	3.43	3.43	3.43	3.43
0.38	0.38	0.38	0.38	0.38
3.05	3.05	3.05	3.05	3.05
550	8000	14200	22000	355000
110	1600	2840	4400	71000
5	5	5	5	5
0.10	0.39	0.53	0.65	2.63
0.79	3.00	4.00	4.98	20.00
0.03	0.10	0.13	0.16	0.66
0.20	0.75	1.00	1.25	5.00

Table B.1.2: Vehicle properties used in study of Contact Point response in chapter 7: varying **tyre** spring stiffness to achieve target vehicle-to-bridge **second** frequency ratio.

Appendix C

Supplementary material for chapter 6

C.1 Effects of vehicle-to-bridge mass and frequency ratios

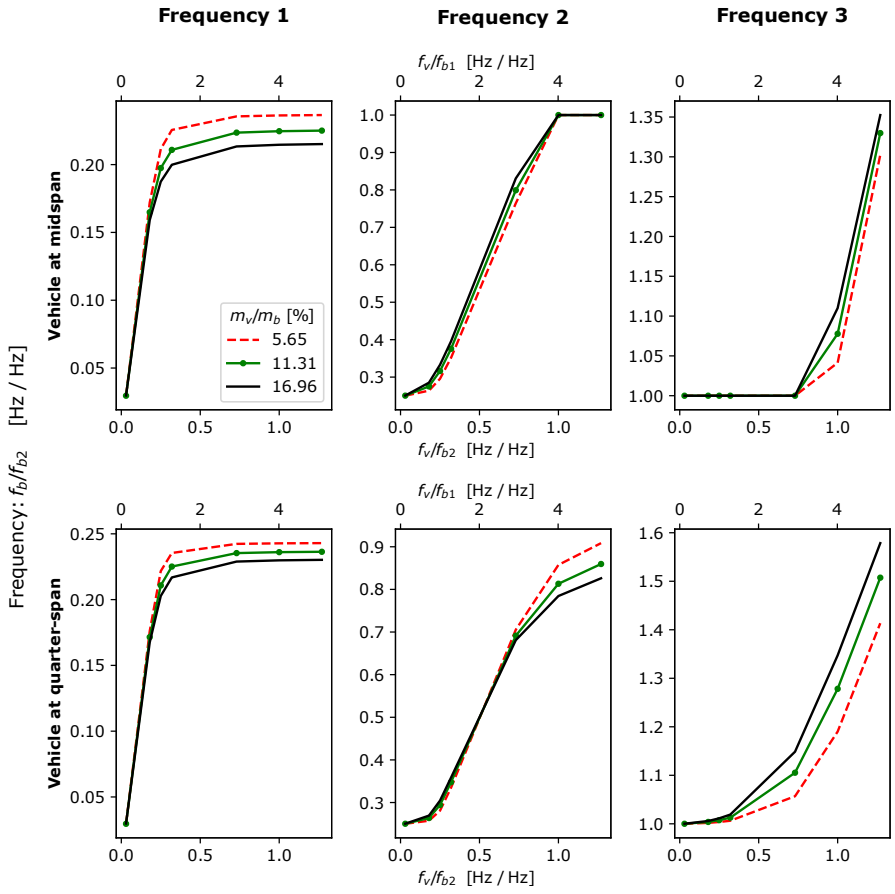

Figure C.1.1: Frequency change due to a single degree-of-freedom vehicle at quarter-span or midspan, for three vehicle-to-bridge mass ratios, in relation to the ratio of vehicle frequency to nominal (unloaded) bridge **second** mode frequency.

C.2 Effects of vehicle damping

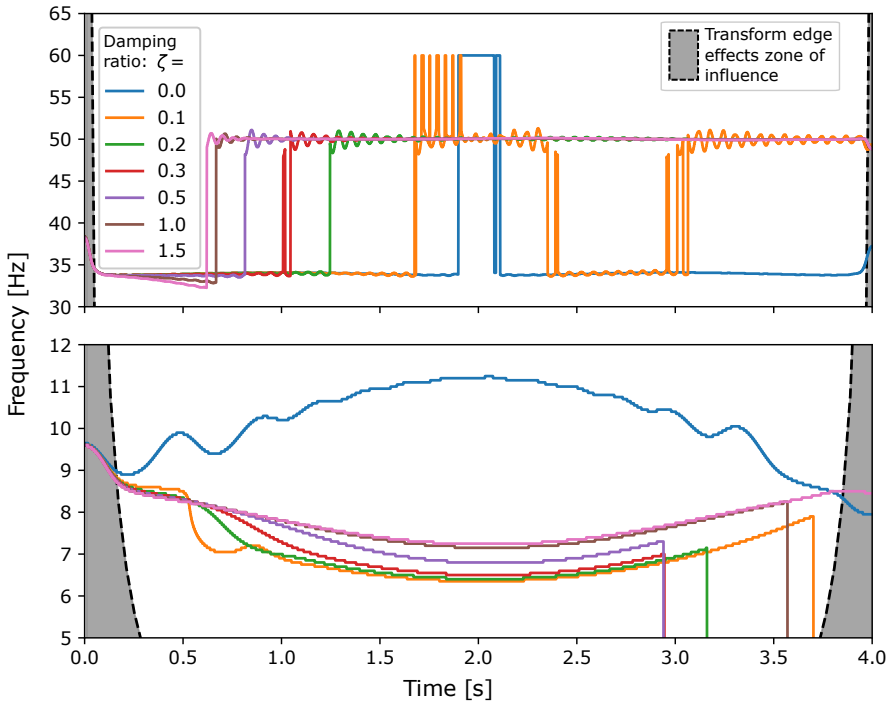

Figure C.2.1: Effect of adding damping to the single degree-of-freedom vehicle model (finite element simulation): estimated ridges of Stockwell transforms of the contact point acceleration response normalised to instantaneous maximum power. **Vehicle frequency proximal to bridge first mode frequency.**

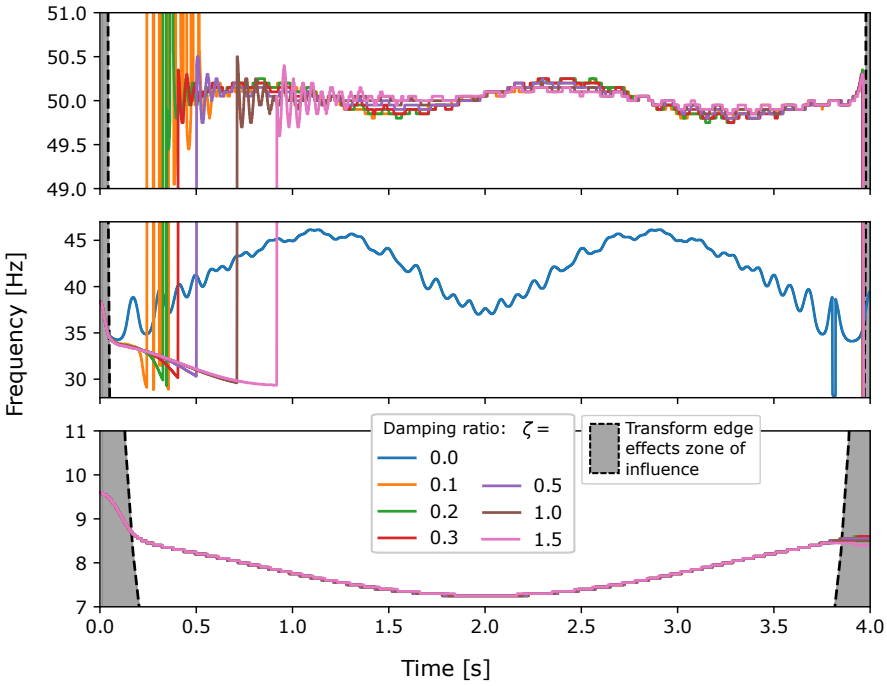

Figure C.2.2: Effect of adding damping to the single degree-of-freedom vehicle model (finite element simulation): estimated ridges of Stockwell transforms of the contact point acceleration response normalised to instantaneous maximum power. **Vehicle frequency proximal to bridge second mode frequency.**

Appendix D

Supplementary material for chapter 7

D.1 Bridge identification

Mean frequencies [Hz]

Bridge config.	(i)			(ii)		(iii)		
Vehicle loc.	-	Mid.	Quarter	Mid.	Quarter	Mid.	Quarter left	Quarter right
Added mass loc.	-			4 kg mid.		4 kg quarter right		
Mode 1	8.67	8.19	8.33	7.71	7.95	7.97	8.23	8.22
Mode 2	15.41	15.62	15.52	13.58	13.65	14.66	14.57	14.59
Mode 3	30.01	30.11	30.07	29.63	30.08	28.36	28.82	28.40
Mode 4	40.24	40.26	40.18	39.70	39.78	36.41	36.70	36.54

Standard deviation of frequency [Hz]

Bridge config.	(i)			(ii)		(iii)		
Vehicle loc.	-	Mid.	Quarter	Mid.	Quarter	Mid.	Quarter left	Quarter right
Added mass loc.	-			4 kg mid.		4 kg quarter right		
Mode 1	1.44	0.01	1.25	0.86	1.16	0.00	0.83	1.10
Mode 2	0.55	1.53	1.59	2.13	1.74	2.56	2.35	2.61
Mode 3	0.61	0.95	1.75	1.51	0.91	1.14	1.51	0.12
Mode 4	0.91	1.18	0.70	0.20	0.12	0.98	0.03	1.38

Table D.1.1: Outcomes of the bridge identification exercise: frequencies.

Mean damping [%]

Bridge config.	(i)			(ii)		(iii)		
Vehicle loc.	-	Mid.	Quarter	Mid.	Quarter	Mid.	Quarter left	Quarter right
Added mass loc.	-			4 kg mid.		4 kg quarter right		
Mode 1	0.34	0.41	0.70	0.38	0.38	0.40	0.35	0.36
Mode 2	0.69	1.29	0.93	1.62	1.36	1.44	1.42	1.55
Mode 3	0.65	1.00	1.02	1.09	1.04	0.90	0.94	1.02
Mode 4	0.60	0.75	0.82	1.16	0.91	0.79	0.73	0.90

Standard deviation of damping [%]

Bridge config.	(i)			(ii)		(iii)		
Vehicle loc.	-	Mid.	Quarter	Mid.	Quarter	Mid.	Quarter left	Quarter right
Added mass loc.	-			4 kg mid.		4 kg quarter right		
Mode 1	0.56	0.06	1.35	1.56	1.60	0.03	1.65	1.64
Mode 2	0.70	0.55	0.99	1.22	0.74	0.53	0.34	0.60
Mode 3	1.50	1.75	1.03	1.21	1.12	0.66	0.83	0.12
Mode 4	0.59	0.87	1.39	0.11	0.18	1.50	0.11	0.76

Table D.1.2: Outcomes of the bridge identification exercise: damping ratios.

D.2 Contact point response comparison

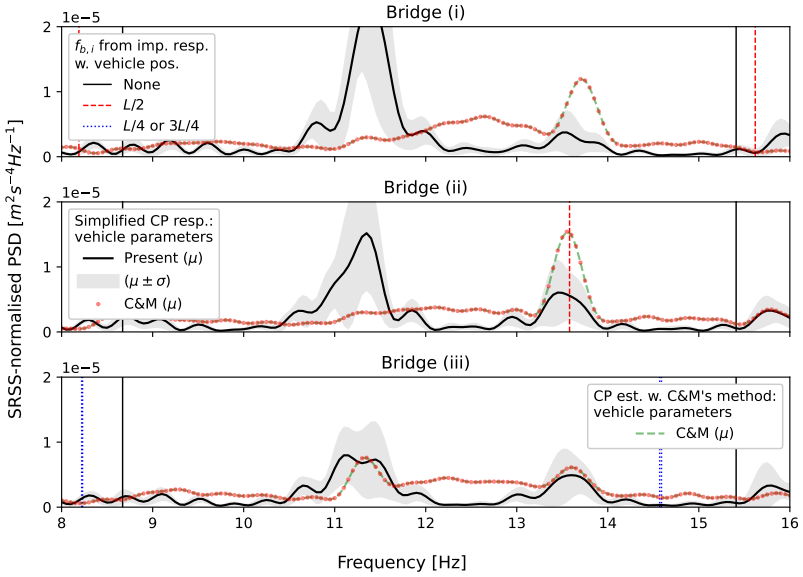

Figure D.2.1: Power spectral density of contact point responses compared (**slow vehicle speed**; frequency range as indicated).

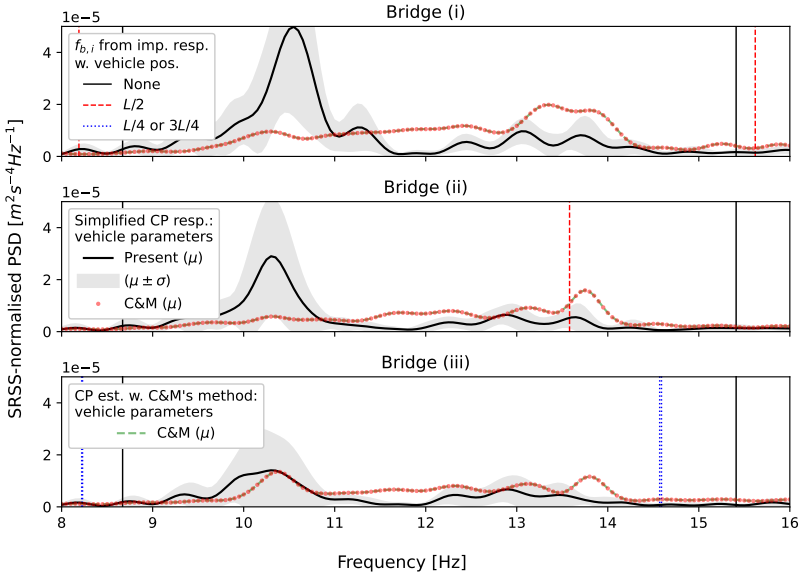

Figure D.2.2: Power spectral density of contact point responses compared (**medium vehicle speed**; frequency range as indicated).

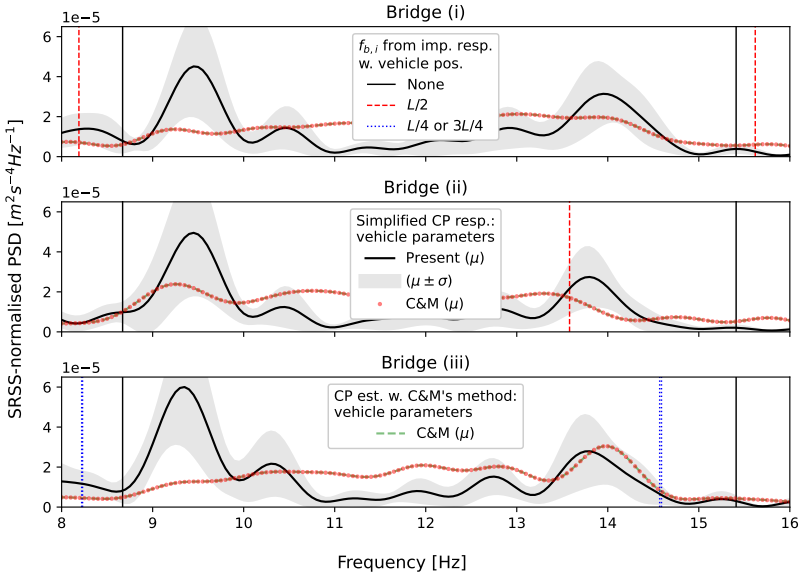

Figure D.2.3: Power spectral density of contact point responses compared (**fast vehicle speed**; frequency range as indicated).

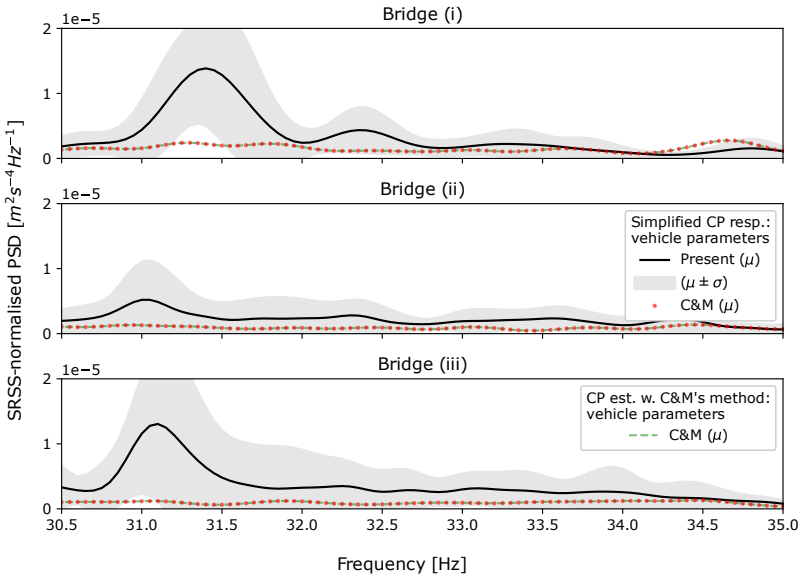

Figure D.2.4: Power spectral density of contact point responses compared (**medium vehicle speed**; frequency range as indicated).

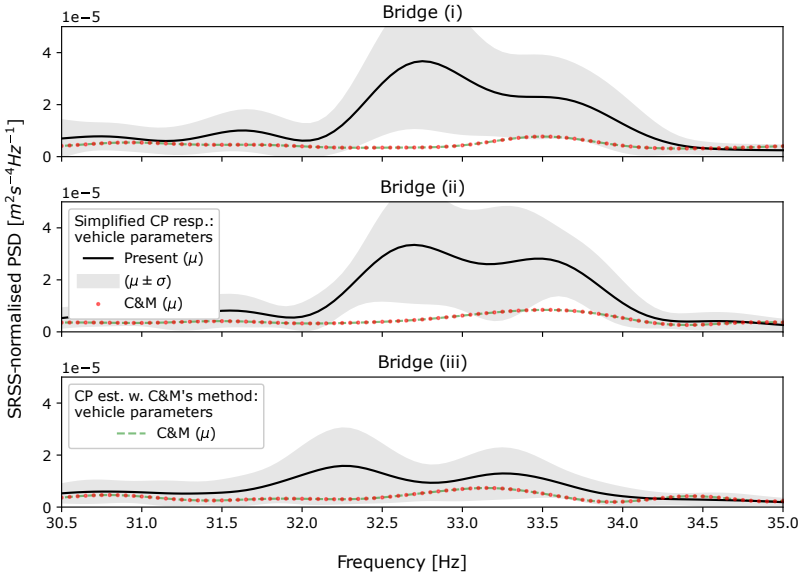

Figure D.2.5: Power Spectral Density of Contact Point responses compared (**fast vehicle speed**; frequency range as indicated).

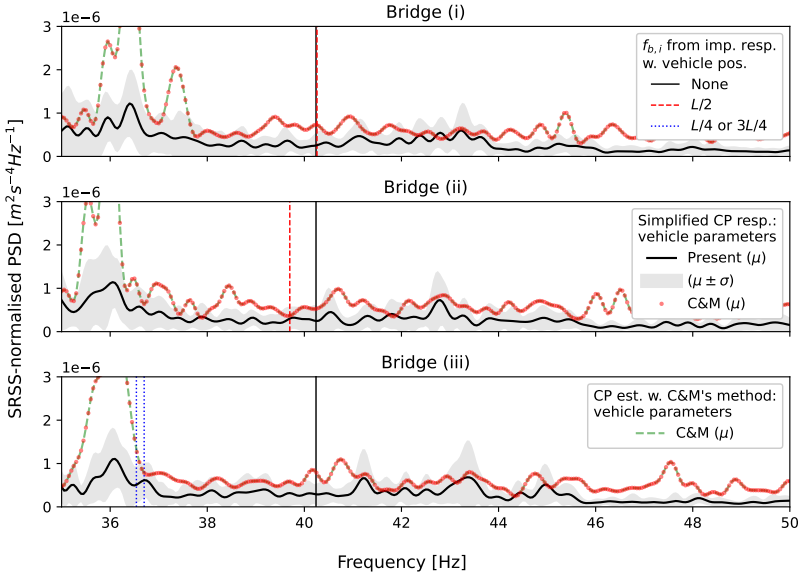

Figure D.2.6: Power spectral density of contact point responses compared (**slow vehicle speed**; frequency range as indicated).

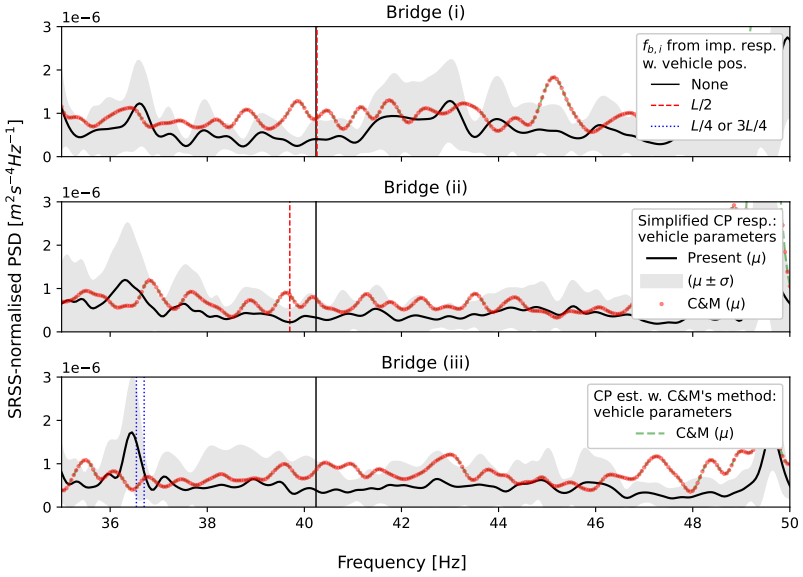

Figure D.2.7: Power spectral density of contact point responses compared (**medium vehicle speed**; frequency range as indicated).

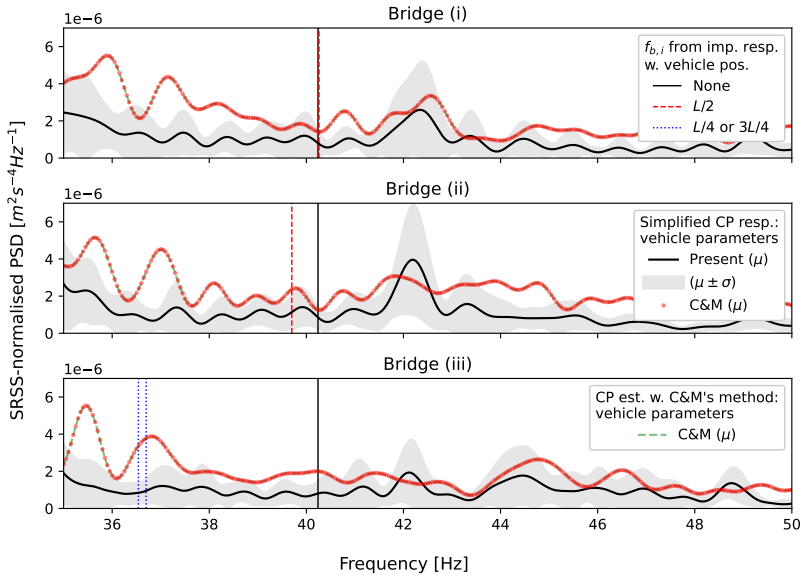

Figure D.2.8: Power spectral density of contact point responses compared (**fast vehicle speed**; frequency range as indicated).

D.3 Contact point residual comparison

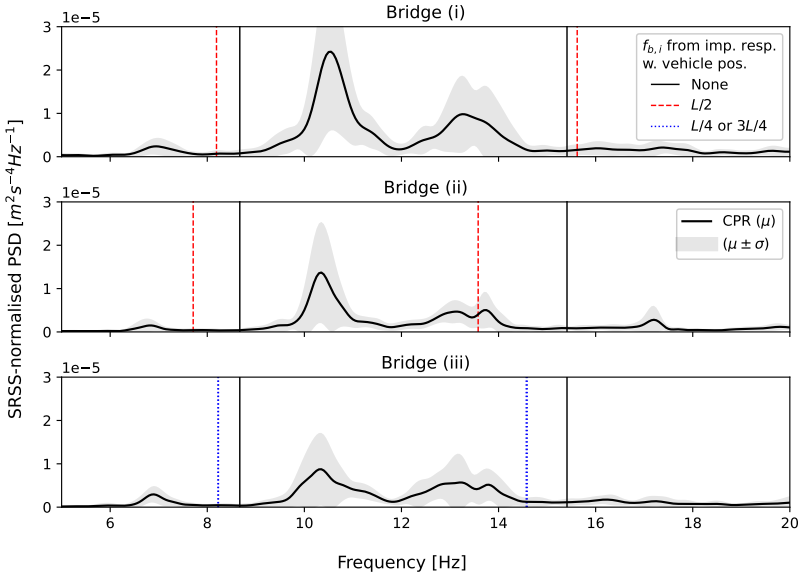

Figure D.3.1: Power spectral density of contact point response **residuals** compared - **medium vehicle speed**; lower frequency range (as indicated).

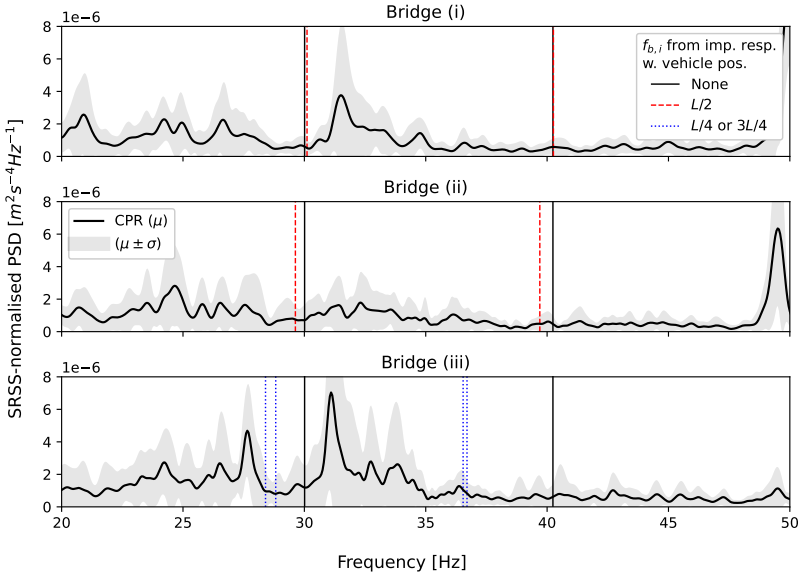

Figure D.3.2: Power spectral density of contact point response **residuals** compared - **medium vehicle speed**; higher frequency range (as indicated).

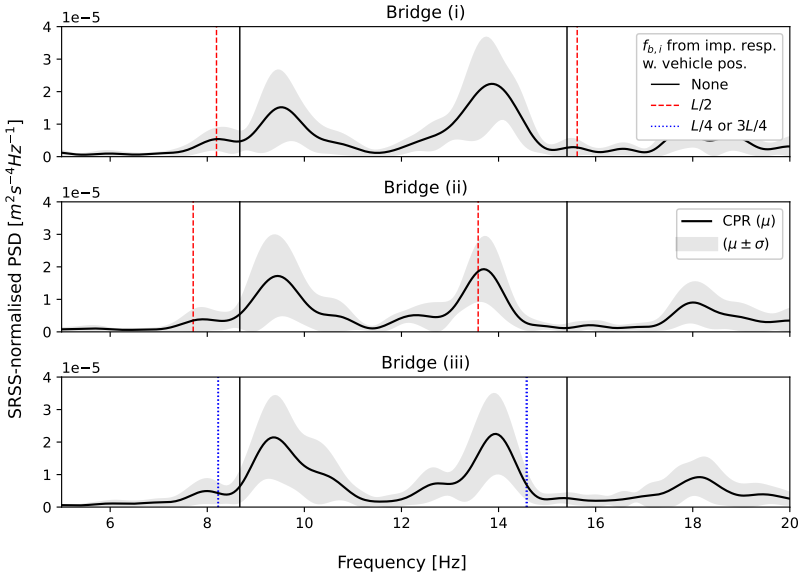

Figure D.3.3: Power spectral density of contact point response **residuals** compared - **fast vehicle speed**; lower frequency range (as indicated).

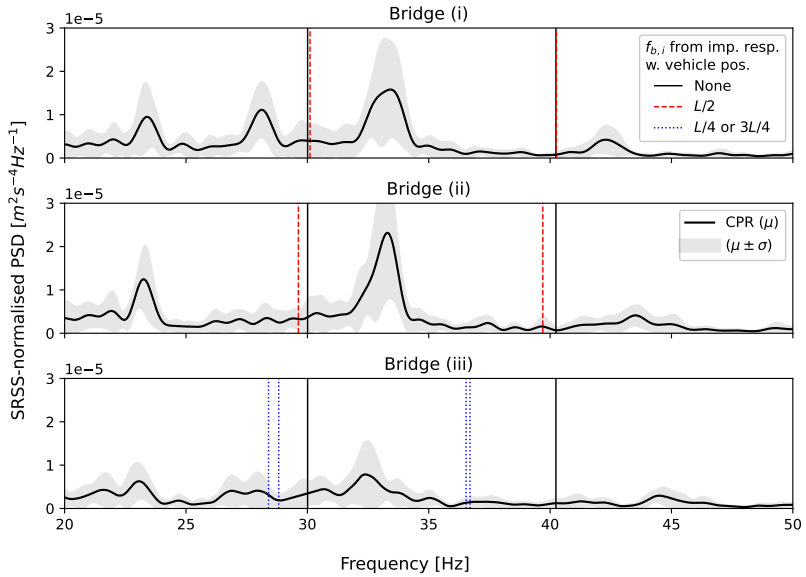

Figure D.3.4: Power spectral density of contact point response **residuals** compared - **fast vehicle speed**; higher frequency range (as indicated).

D.4 Principal Component projections

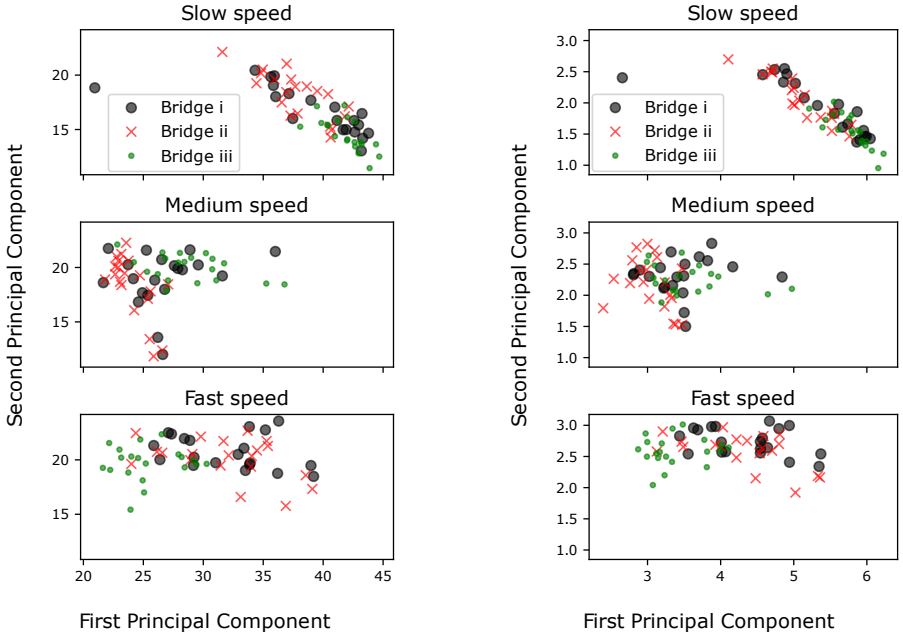

(a) Higher resolution

(b) Lower resolution

Figure D.4.1: First and second principal components projected from ***wide A* (4-45 Hz)** bandwidth Stockwell transform (ST) contour images. Three vehicle speeds and two ST image resolutions compared for three bridge configurations.

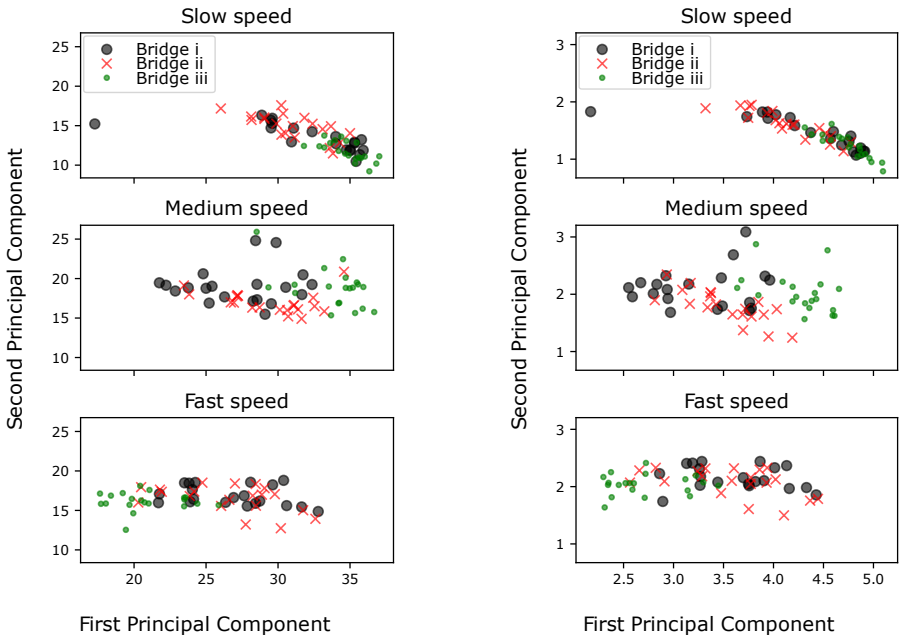

(a) From ST at higher resolution

(b) From ST at lower resolution

Figure D.4.2: First and second principal components projected from ***wide B* (0-65 Hz)** bandwidth Stockwell transform (ST) contour images. Three vehicle speeds and two ST image resolutions compared for three bridge configurations.

D.5 Estimated sample distributions

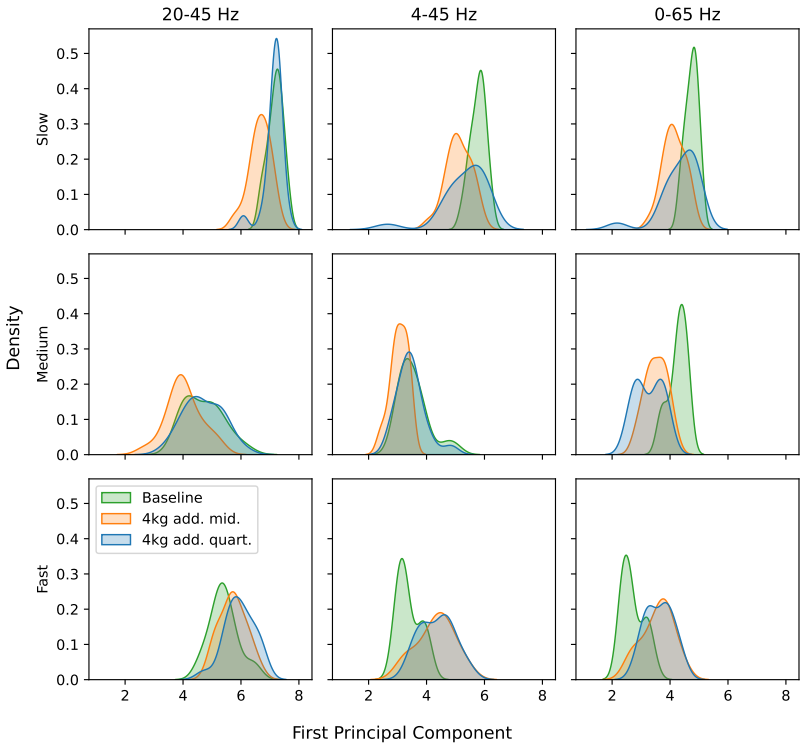

Figure D.5.1: Estimated distributions (kernel density estimation) of first principal component from lower-resolution Stockwell transforms.

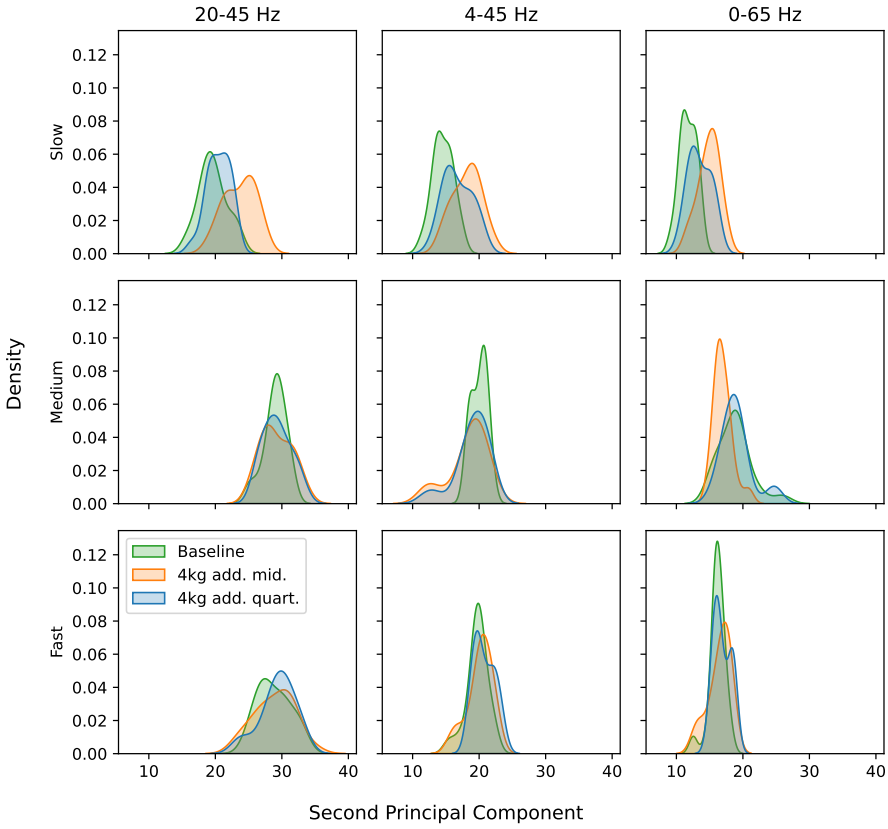

Figure D.5.2: Estimated distributions (kernel density estimation) of second principal component from higher-resolution Stockwell transforms.

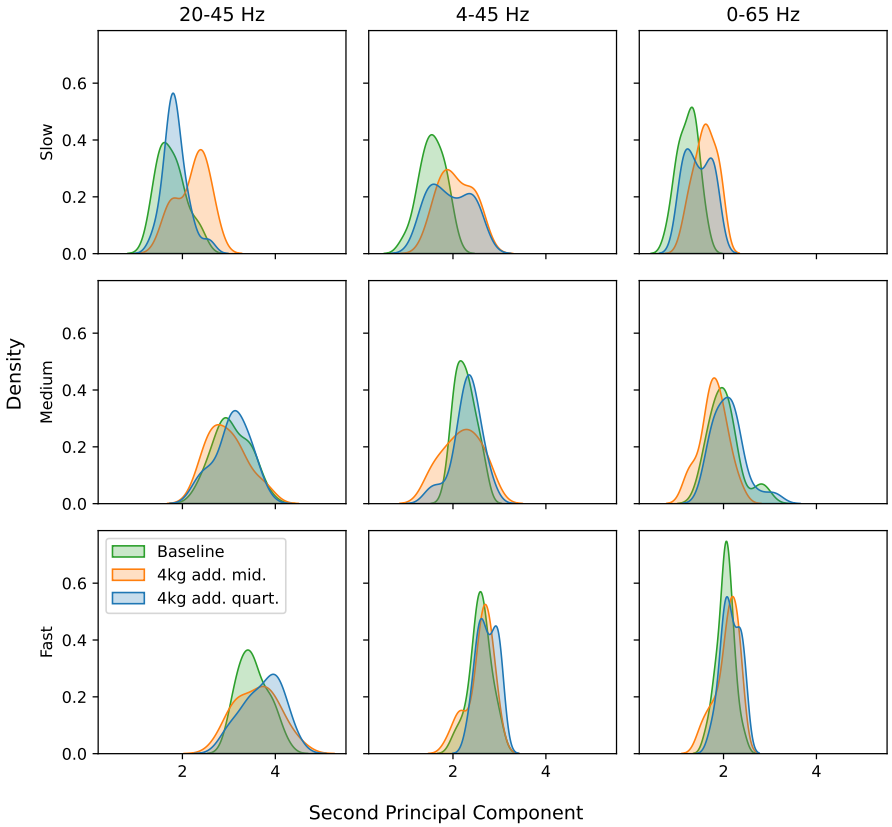

Figure D.5.3: Estimated distributions (kernel density estimation) of second principal component from lower-resolution Stockwell transforms.

D.6 Wasserstein distance metric comparisons

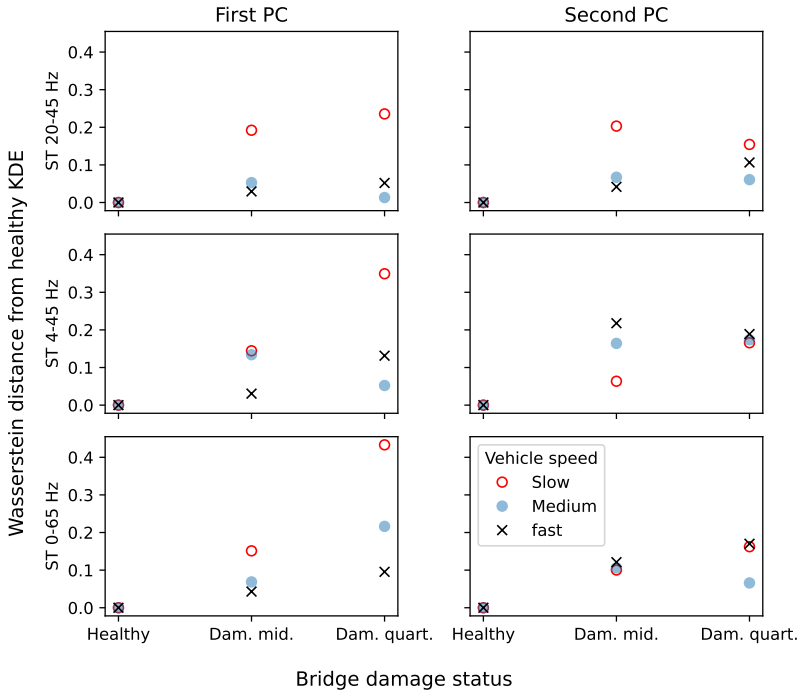

Figure D.6.1: 1-Wasserstein distance metric comparison for lower-resolution Stockwell transform contour images.

D.7 Difference in bootstrapped sample means distributions

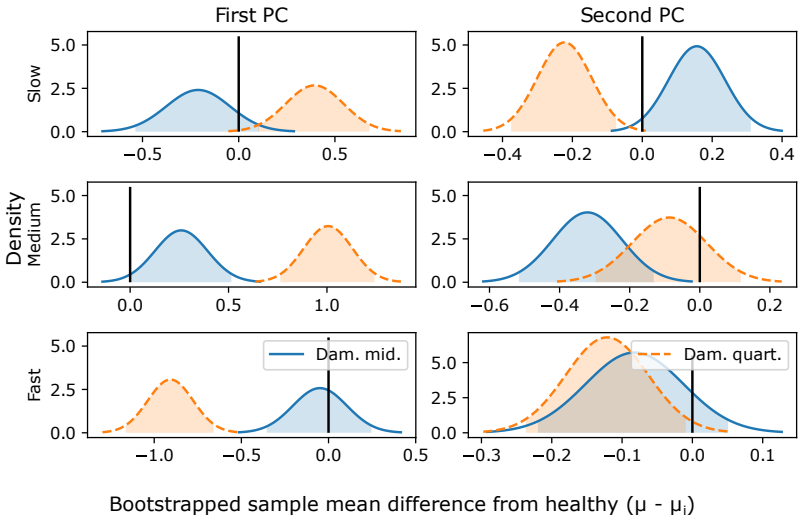

Figure D.7.1: Gaussian probability density functions for differences in bootstrapped sample means (**Stockwell transform 0-65 Hz, lower image resolution**). 95% confidence intervals (two-tailed) shaded. Original data are first (left) and second (right) principal components.

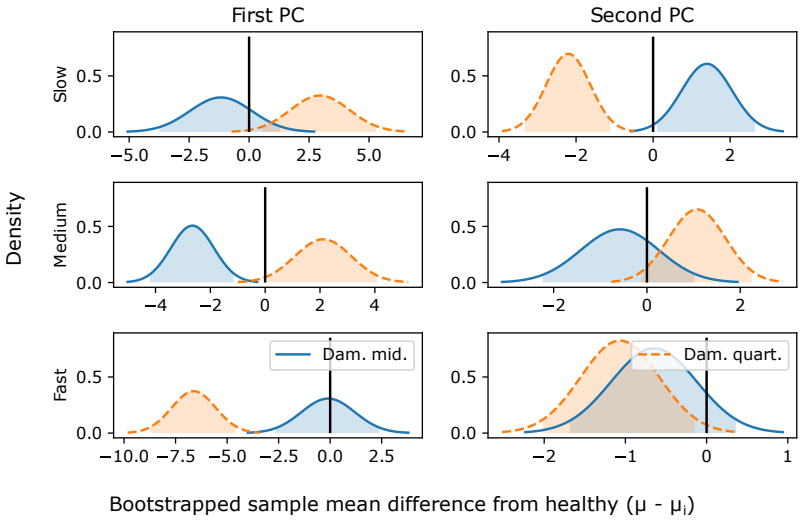

Figure D.7.2: Gaussian probability density functions for differences in bootstrapped sample means (**Stockwell transform 4-45 Hz, higher image resolution**). 95% confidence intervals (two-tailed) shaded. Original data are first (left) and second (right) principal components.

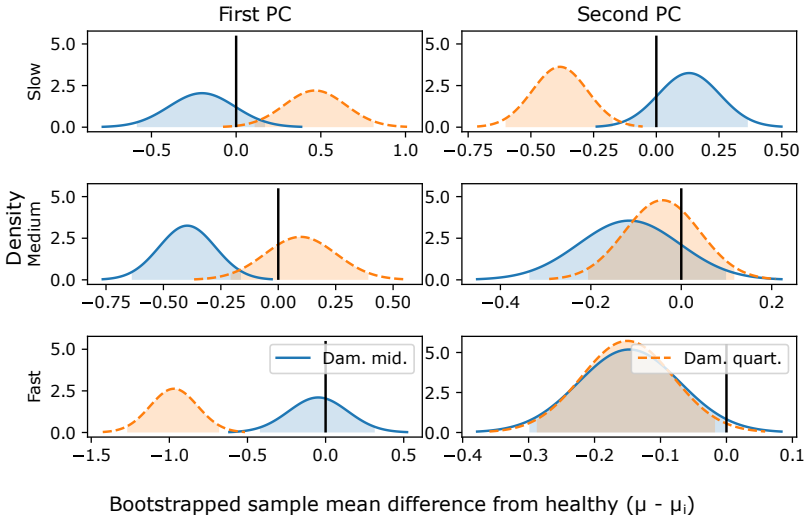

Figure D.7.3: Gaussian probability density functions for differences in bootstrapped sample means (**Stockwell transform 4-45 Hz, lower image resolution**). 95% confidence intervals (two-tailed) shaded. Original data are first (left) and second (right) principal components.

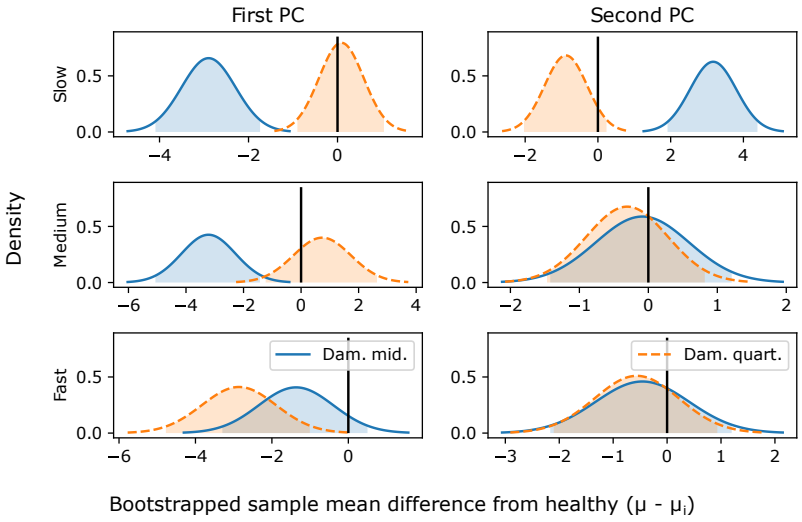

Figure D.7.4: Gaussian probability density functions for differences in bootstrapped sample means (**Stockwell transform 20-45 Hz, higher image resolution**). 95% confidence intervals (two-tailed) shaded. Original data are first (left) and second (right) principal components.

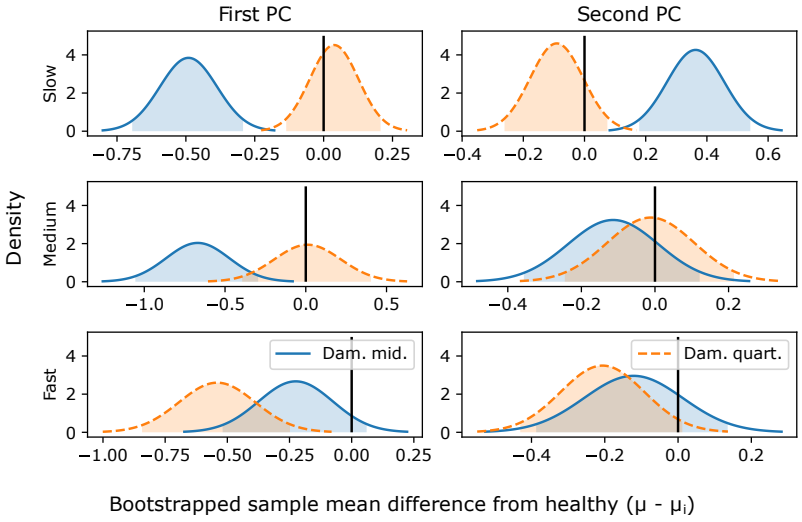

Figure D.7.5: Gaussian probability density functions for differences in bootstrapped sample means (**Stockwell transform 20-45 Hz, lower image resolution**). 95% confidence intervals (two-tailed) shaded. Original data are first (left) and second (right) principal components.

95% two-tailed Confidence Interval crosses zero, therefore accept null hypothesis (data is from traversal of healthy bridge)

ST bandwidth	Vehicle speed	LOWER RESOLUTION ST				HIGHER RESOLUTION ST			
		First PC		Second PC		First PC		Second PC	
		Dam. mid.	Dam. quart.	Dam. mid.	Dam. quart.	Dam. mid.	Dam. quart.	Dam. mid.	Dam. quart.
20-45 Hz ("narrow")	Slow	No	Yes	No	Yes	No	Yes	No	Yes
	Medium	No	Yes	Yes	Yes	No	Yes	Yes	Yes
	Fast	Yes	No	Yes	Yes	Yes	No	Yes	Yes
4-45 Hz ("mid")	Slow	Yes	No	Yes	No	Yes	No	No	No
	Medium	No	Yes	Yes	Yes	No	No	Yes	Yes
	Fast	Yes	No	No	No	Yes	No	Yes	No
0-65 Hz ("wide")	Slow	Yes	No	Yes	No	Yes	No	No	No
	Medium	Yes	No	No	Yes	No	No	No	Yes
	Fast	Yes	No	Yes	No	Yes	No	Yes	No

Accept alternative hypothesis (data is from traversal of damaged bridge)

Mean damage detection rate (all ST bandwidths and vehicle speeds)	LOWER RESOLUTION ST				HIGHER RESOLUTION ST			
	First PC		Second PC		First PC		Second PC	
	Dam. mid.	Dam. quart.	Dam. mid.	Dam. quart.	Dam. mid.	Dam. quart.	Dam. mid.	Dam. quart.
	33.3%	66.7%	33.3%	44.4%	44.4%	77.8%	44.4%	44.4%

Table D.7.1: Acceptance and rejection of null hypothesis for all Stockwell transform contour bandwidths, vehicle traversal speeds and both principal components.

D.8 Vehicle-to-bridge acceleration amplitude ratios

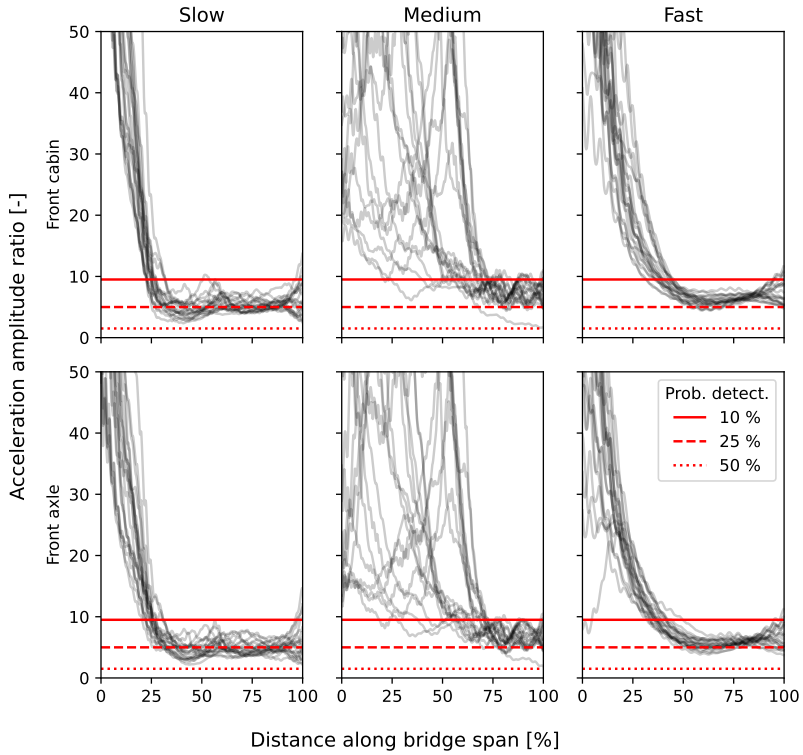

Figure D.8.1: Acceleration amplitude ratios: vehicle (front axle and cabin sensors) compared to bridge (one **midspan** sensor) for **bridge configuration *ii*** and three vehicle speeds in region of expected **first** bending mode frequency.

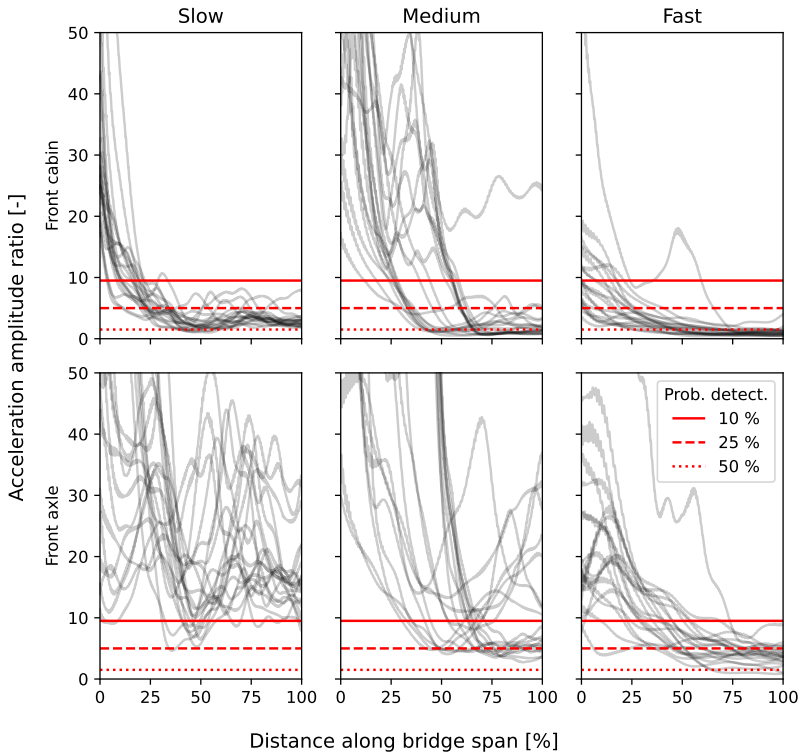

Figure D.8.2: Acceleration amplitude ratios: vehicle (front axle and cabin sensors) compared to bridge (one **quarter-span** sensor) for **bridge configuration *iii*** and three vehicle speeds in region of expected **second** bending mode frequency.